ISSN en trámite

volumen 60, número 2, abril 2024

instituto de astronomía

unam

revista mexicana de astronomía y astrofísica

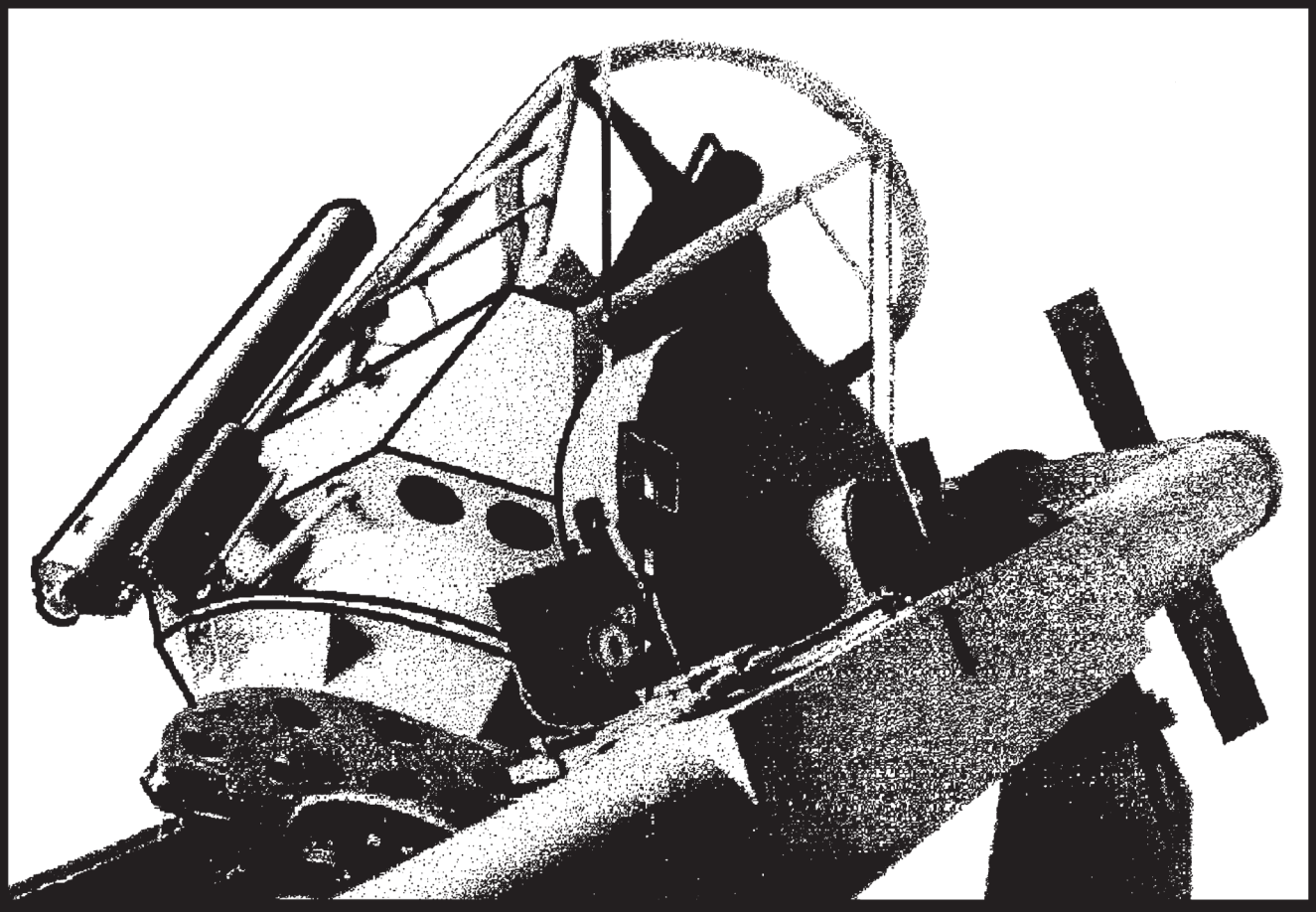

volumen 60
número 2
octubre 2024

revista mexicana de astronomía y astrofísica

Instituto de Astronomía
Universidad Nacional Autónoma de México

revista mexicana de astronomía y astrofísica

ISSN en trámite

URL de DOI: https://doi.org/10.22201/ia.01851101p.2024.60.02

rmaa@astro.unam.mx

http://www.astroscu.unam.mx/RMxAA/

La *RMxAA* aparece indexada en Current Contents, Science Citation Index, Astronomy and Astrophysics Abstracts, Physics Briefs, Publicaciones Científicas en América Latina, Astronomy and Astrophysics Monthly Index, PERIODICA, RedALyC, Latindex y SciELO.

Revista Mexicana de Astronomía y Astrofísica, volumen 60, número 2, octubre 2024, es una publicación semestral, editada y distribuida por el Instituto de Astronomía, UNAM, Circuito Exterior, Ciudad Universitaria, 04510, Alcaldía Coyoacán, Ciudad de México, Teléfono: 5556223906, Correo Electrónico: rmaa@astro.unam.mx, ISSN en trámite. Editora responsable: Christine Patricia Allen Armiño. Distribución: Bienes y Servicios del Instituto de Astronomía, UNAM. Impresa por Grupo Edición, S.A. de C.V., Xochicalco 619, Colonia Letrán Valle, 03650, Alcaldía Benito Juárez, Ciudad de México. Fecha de impresión: 27 de septiembre de 2024. Número de ejemplares impresos: 500 en papel Couché de 100 gramos los interiores y en cartulina Couché de 250 gramos los forros. Precio de la publicación: gratuito.

CONTENTS

Revista Mexicana de Astronomía y Astrofísica, **60**, 205–216 (2024)

https://doi.org/10.22201/ia.01851101p.2024.60.02.01

LIGHT AND FREQUENCY ANALYSIS OF DETACHED ECCENTRIC BINARY SYSTEM DT CAM WITH PRE-MAIN SEQUENCE COMPONENT

Tuncay Özdemir[1] and Birol Gürol[2]

Received September 3 2023; accepted February 27 2024

ABSTRACT

In this study we analyzed *TESS* data of detached eccentric binary system DT Cam and we obtained the first physical parameters of the components. We found that the out-of-eclipse variation of the system shows a small amplitude periodic feature. Most of the frequencies obtained are related with the orbital variation except one, for which the period was determined as ≈0.605 days. The masses and radii of the primary and secondary components were calculated as $M_1 = 1.793 M_\odot$, $M_2 = 1.414 M_\odot$, $R_1 = 1.355 R_\odot$, and $R_2 = 1.522 R_\odot$, respectively. Considering the physical properties of the primary component we concluded that it is a rotational variable. We found that the massive component is smaller than the low-mass component. It seems that the secondary component is a pre-main sequence star, which is important for the understanding of stellar structure and evolution.

RESUMEN

Se analizan datos de *TESS* sobre la binaria excéntrica DT Cam y se obtienen por primera vez los parámetros físicos de las componentes. Encontramos una variación periódica de pequeña amplitud fuera de eclipse. Muchas de las frecuencias obtenidas se relacionan con la variación orbital, excepto una, cuyo período se determinó como ≈0.605 días. Se calculan las masas y radios de las componentes primaria y secundaria, y se obtienen como resultados $M_1 = 1.793 M_\odot$, $M_2 = 1.414 M_\odot$, $R_1 = 1.355 R_\odot$, y $R_2 = 1.522 R_\odot$. Dadas las propiedades físicas de la primaria concluimos que es un variable rotacional. Encontramos que la componente masiva es más pequeña que la compañera de baja masa. Al parecer, la secundaria es una estrella pre-secuencia principal, lo cual es importante para entender la estructura y evolución estelares.

Key Words: binaries: eclipsing — stars: fundamental parameters — stars: individual: DT Cam — stars: rotation — techniques: photometric

1. INTRODUCTION

DT Cam (TIC 87251422, HD 33500, $\alpha_{2000} = 05^h13^m57^s.69$, $\delta_{2000} = +56^\circ\,30'\,28''.61$, $V = 8^m.13$) is classified as a spectroscopic binary in the Simbad[3] database. The spectral type and distance of the system are given as A2 (Cannon and Pickering 1993) and 184 pc (*Gaia* Collaboration 2022), respectively. The system is defined as an Algol-type eclipsing binary by Otero et al. (2005) with an orbital period of P=14.132500 days, and it is included in the GCVS catalogue[4].

In the catalogue published by McDonald et al. (2012), the system's distance (d), effective temperature ($T_{\rm eff}$), and luminosity (L) are given as $d = 255.750$ pc, $T_{\rm eff} = 7948$ K, and $L = 27.52 L_\odot$, respectively. In the Eclipsing Binary Catalogue published by Avvakumova et al. (2013) the system is classified as DM (detached main sequence system) with depth of the primary minima as $0^m.06$ which is probably mistyped. By analyzing the eclipse timing diagram of the system, Kim et al. (2018) found the orbital period and the phase of the secondary minima as $P = 7.0662668$ days and 0.578, respectively.

[1]Department of Physics, Faculty of Arts and Sciences, İnönü University, Malatya, Turkey.
[2]Department of Astronomy and Space Sciences, Ankara University Science Faculty, Tandoğan, Ankara, Turkey.
[3]https://simbad.cds.unistra.fr/simbad/.
[4]http://www.sai.msu.su/gcvs/cgi-bin/search.html.

TABLE 1

PARAMETERS OF THE LIGHT CURVE AND THE $(O-C)$ ANALYSES OF DT CAM*

Parameter	Value
i(deg)	87.69 (0.19)
T_1(K)	8800
T_2(K)	7382 (75)
L_1(%)	66.4 (0.7)
L_2(%)	33.6 (0.6)
L_3(%)	0.0
R_1/a	0.068(3)
R_2/a	0.064(2)
e	0.188(0.010)
$\omega(deg)$	49.2(1.3)
U(yr)	>100

*Obtained by Zasche et al.(2018).

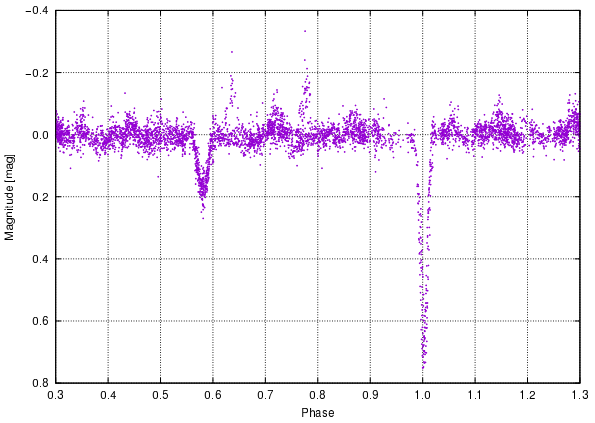

Fig. 1. Unfiltered light curve of ASCC 178636 (DT Cam) observed from MASCARA published by Burggraaff et al. (2018). The color figure can be viewed online.

Zasche et al. (2018) obtained the first light curve and $(O-C)$, and analysed the system by using unfiltered and special SuperWASP observations; their system parameters are given in Table 1.

By using Gaia DR2 data, Kervella et al. (2019) obtained the color excess, system's radial velocity, mass and radius of the primary component as $E(B-V) = 0.087$, $V_R = 33.881\,\mathrm{km/s}$, $M_1 = 2.2M_\odot$ and $R_1 = 1.862R_\odot$, respectively. Later, using Gaia EDR3 data, Kervella et al. (2022) updated some of the parameters as $V_R = 33.76\,\mathrm{km/s}$, $M_1 = 2.20M_\odot$ and $R_1 = 1.85R_\odot$. In the catalogue of EA-type eclipsing binaries observed by *TESS* and published by Shi et al. (2022) the system's orbital period was given as 14.1325 days. Based on the Multi-site All-Sky CAmeRA (MASCARA) observations (see Figure 1) published by Burggraaff et al. (2018) the depth of the primary and secondary minima were given as $0^m.75$ and $0^m.2$, respectively. In Figure 1, although scattering is observed at maximum light, there are also traces of a periodic variation which can be related to pulsation in the system.

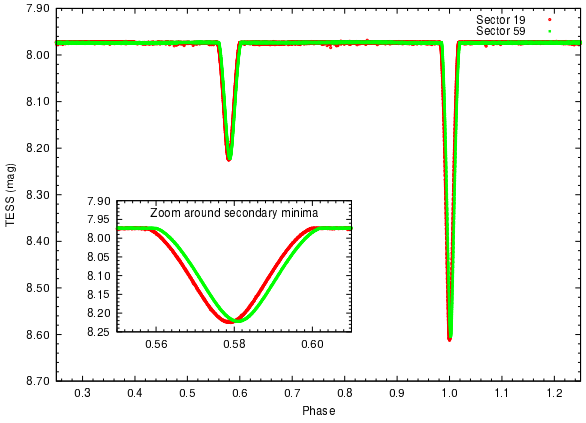

Fig. 2. The light curve of DT Cam (TIC 87251422) obtained from MAST archive for Sectors 19 (red) and 59 (green). The orbital phase is calculated by using equation (1). The color figure can be viewed online.

2. THE *TESS* DATA AND LIGHT ELEMENTS

The observations of DT Cam were made by the Transiting Exoplanet Survey Satellite (*TESS*) (Ricker et al. 2015) in Sectors 19 and 59 with each sector having ≈27.4 days of observations with nearly 2 min (SC: Short Cadence) exposure time. The *TESS* data are available in the MAST (Barbara A. Mikulski Archive for Space Telescopes[5]) archive. In this study we prefer to use the raw SAP (simple aperture photometry) data. A total of 35,860 observations of the system were obtained and the time span is nearly 1120.6 days. The light elements of the system are given in the *TESS* Eclipsing Binary Catalogue[6] published by Prša et al. (2022) as,

$$Min.I(BJD) = 2458825.166288(0.000014) + 7.0661708(0.000206) \times E\,. \quad (1)$$

In Figure 2 we plot the light curve of the system obtained in Sectors 19 and 59 by using the light elements given by Prša et al. (2022). As can be seen in the zoomed inner plot the secondary minima for both sectors do not overlap with each other which indicates that the light elements of the system need

[5] https://mast.stsci.edu/portal/Mashup/Clients/Mast/Portal.html.

[6] http://tessebs.villanova.edu/.

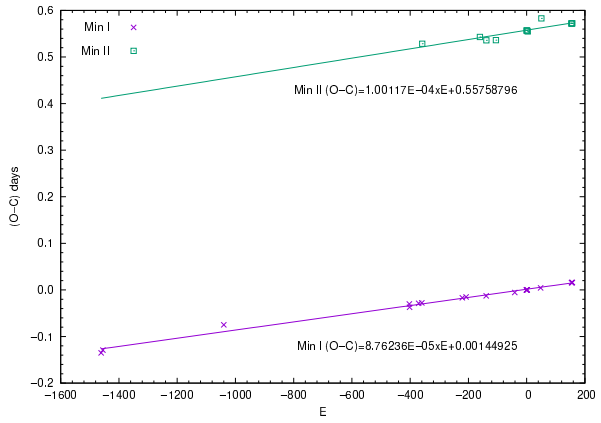

Fig. 3. $(O-C)$ variation and linear fit obtained for DT Cam by using equation (1) of Prša et al. (2022). The color figure can be viewed online.

to be refined. The same situation occurs for the primary minima too but it is not shown here. Additionally from the light curve we can say that the eclipsing system is composed of two spherical components in detached (D) configuration, and because the secondary minima occurred out of 0.5 phase (including the duration of the eclipse times which are different from each other) we can say that the eccentricity of the system must be larger than zero.

Since the light elements given with equation (1) by Prša et al. (2022) were derived using only Sector 19 data, we primarily obtained a full set of minima times from the current observations. Using the *TESS* observations, we obtained 8 primary and 7 secondary eclipse times. The eclipse times were calculated by using the Minima27[7] software published by Dr. Bob Nelson. In Table 2 we present the calculated minima times with their errors. Additionally, we include the minima times found in the literature. The minima times published in HJD were converted to BJD using the algorithm published by Eastman et al. (2010)[8].

The time span of the primary and secondary minima is about 11,433 and 3639 days, respectively. Applying a linear fit to the $(O-C)$ data (see Figure 3) we obtained new light elements as,

$$Min.I(BJD) = 2458825.167737(0.00109) + 7.06625839(0.00000202) \times E\,, \quad (2)$$

$$Min.II(BJD) = 2458822.747588(0.00214) + 7.06622709(0.00001452) \times E\,. \quad (3)$$

[7] https://www.variablestarssouth.org/resources/bob-nelsons-softwaretools/softwareby-bob-nelson.

[8] https://astroutils.astronomy.osu.edu/time/hjd2bjd.html.

The difference in orbital periods calculated for the primary and secondary minima is about 1.079 sec which is smaller than the obtained errors. Probably this difference occurred because of the different time span of the times of minima used in the fit. The ratio of the slopes obtained for the fit is ≈0.875. Because of this, the $(O-C)$ values between the primary and secondary minima is going to be larger at larger Epoch values. We think that there are not enough data or time span to draw a firm conclusion about apsidal motion as mentioned by Zasche et al. (2018). For the rest of the calculation, we used the light elements obtained for the primary minima.

3. LIGHT CURVE ANALYSIS

Because of the calculation time we obtained a total of 1000 points by averaging at 0.001 phase intervals. By using these phase intervals, we see that the depth of both minima was not changed. For the light curve analysis, we prefer to use the Wilson-Devinney code (2015 version which in 2019 added the *TESS* band to the code) which can solve light curves in magnitudes or in flux. The subscripts 1 and 2 refer to the primary (hotter) and the secondary (cooler) component, respectively.

Before light curve analysis we can find the eccentricity and argument of periastron of the orbit by using the widths of the primary (w_1) and secondary (w_2) eclipses and the phase of the secondary eclipse (φ_2).

$$e_0 \cos w_0 = \frac{\pi}{2}\left[(\varphi_2 - \varphi_1) - 0.5\right] = 0.1241\,, \quad (4)$$

$$e_0 \sin w_0 = \frac{w_2 - w_1}{w_2 + w_1} = 0.1136\,. \quad (5)$$

The required data are given as 0.039, 0.049, and 0.579, respectively by Prša et al. (2022). Using the formulae given by Kopal (1978) (equations 4 and 5) and the phase of the primary eclipse as $\varphi_1 = 0$ we obtained the eccentricity and argument of periastron as 0.1683 and 42.48 deg, respectively. These are used as input parameters in the light curve analysis of the eclipsing system.

In Table 3 we compiled effective temperatures published in different sources (except the last one which was obtained according to the $\log T_{\rm eff} - (B-V)_0$ relation given by Eker et al. 2020) but using the $(B-V) = 0.20$ color and $E(B-V) = 0.087$ reddening values given by Kervella et al. (2019). The median and average of the effective temperatures are found to be 8006 ± 329 K and 8200 ± 329 K, respectively, and we prefer to use these values for the primary component in the light curve analysis of DT Cam.

TABLE 2

THE OBTAINED ECLIPSE TIMES AND ERRORS OF DT CAM

No	Min.Type	HJD (2400000+)	BJD (2400000+)	$\pm\sigma$	References
1	I	48501.35500	48501.35568	-	Otero et al. (2005)
2	I	48543.75800	48543.75868	0.03	Kim et al. (2018)
3	I	51476.27300	51476.27373	0.02	Kim et al. (2018)
4	I	55977.46852	55977.46928	0.00011	Zasche et al. (2014)
5	I	55984.52776	55984.52852	0.00292	Zasche et al. (2018)
6	I	56203.58753	56203.58830	0.00016	Zasche et al. (2014)
7	I	56281.31626	56281.31703	0.00019	Zasche et al. (2017)
8	II	56292.47172	56292.47249	0.00058	Zasche et al. (2017)
9	I	57263.52491	57263.52570	0.0001	Juryšek et al. (2017)
10	I	57355.38700	57355.38780	0.01	Paschke (2017)
11	II	57691.58808	57691.58889	0.00066	Zasche et al. (2017)
12	I	57842.95506	57842.95588	0.00302	Zasche et al. (2018)
13	II	57847.03660	57847.03742	0.0103	Zasche et al. (2018)
14	II	58080.22056	58080.22139	0.0063	Zasche et al. (2018)
15	I	58535.44700	58535.44784	0.0020	Paschke (2019)
16	I	58832.23170	58832.23253	-	Jeong et al. (2020)
17	I	-	58818.10004	0.00001	*TESS*
18	II	-	58822.19000	0.00003	*TESS*
19	I	-	58825.16628	0.00001	*TESS*
20	II	-	58829.25608	0.00003	*TESS*
21	I	-	58832.23254	0.00001	*TESS*
22	II	-	58836.32227	0.00004	*TESS*
23	I	-	58839.29886	0.00001	*TESS*
24	I	59164.34600	59164.34683	0.005	Paschke (2021)
25	II	59182.59000	59182.59083	0.010	Paschke (2021)
26	II	-	59910.39548	0.00002	*TESS*
27	I	-	59913.37222	0.00001	*TESS*
28	II	-	59917.46170	0.00002	*TESS*
29	I	-	59920.43845	0.00001	*TESS*
30	II	-	59924.52798	0.00002	*TESS*
31	I	-	59927.50474	0.00001	*TESS*
32	II	-	59931.59433	0.00002	*TESS*
33	I	-	59934.57104	0.00001	*TESS*

TABLE 3

DT CAM $T_{\rm EFF}$ VALUES FROM LITERATURE

$T_{\rm eff}$ (K)	References
8970	Wright et al. (2003)
8589	Ammons et al. (2006)
7948	McDonald et al. (2012)
7947	Chandler et al. (2016)
7962	McDonald et al. (2017)
8006	Tonry et al. (2018)
8006	*Gaia* Collaboration (2018)
8200	Stassun et al. (2019)
7987	Bai et al. (2019)
8200	Paegert et al. (2021)
8381	Eker et al. (2020)

In the catalogue of Gaia DR3 Part 3 for non-single stars (*Gaia* Collaboration 2022) we found the system's center of mass velocity as $V_\gamma = 13.111 \pm 0.170$ km/s, the semi-amplitude of the primary and secondary component as $K_1 = 73.246 \pm 0.406$ km/s and $K_2 = 92.856 \pm 0.400$ km/s, respectively. Additionally, the system's eccentricity, $e = 0.160 \pm 0.003$, and the argument of periastron, $\omega = 39.123 \pm 1.285$ deg, were obtained, which are compatible with the calculated data by using equations (4) and (5). According to the values given in Gaia DR3 catalogue the mass ratio of the system is obtained as $q(m_2/m_1) = 0.7888$.

The Wilson & Devinney method (Wilson & Devinney 1971; Wilson 1979, 1990) was applied to solve the light curve of the DT Cam. In the light curve analysis of the DT Cam, we used Mode 2 appropriate for detached type systems. Ad-

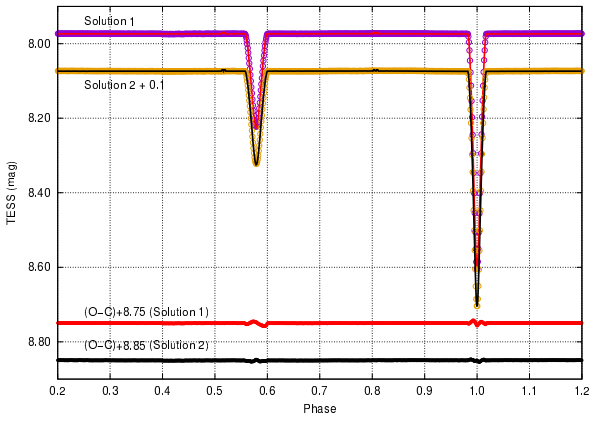

Fig. 4. The observational and theoretical light curves of DT Cam including the residuals of the fit for both solutions. The color figure can be viewed online.

ditionally, we selected the starting parameters as $T_{\rm eff,1} = 8006\,{\rm K}$ (Solution 1) and 8200 K (Solution 2), $e = 0.168$, $\omega = 42.48$ deg, $P = 7.06626244$ days. Because $T_{\rm eff,1}$ is higher than 7200 K, we used the primary's albedo and gravity darkening parameters as 1.0. Assuming the secondary temperature is lower than the primary's we selected $T_{\rm eff,2} = 6500\,{\rm K}$, and included albedo and gravity darkening parameters as 0.5 and 0.32, respectively.

By using the initial parameters (T_1, q, i, e, ω) as input values we solved the light curves until the solution converged. After a coarse solution was obtained, we let the l_3 (third-light) parameter free because of the system is located in a crowded region. The convergent solution was obtained with the adjustable parameters by iteration, until the correction of the parameters became smaller than the corresponding standard deviations. The observed and theoretical light curves, calculated with the final elements, are shown in Figure 4 including the residuals of the fit with the observations.

The parameters obtained from the light curve analysis are given in Table 4. The absolute parameters of the components obtained by the Wilson-Devinney LC code for the DT Cam system are given in Table 5. Since the LC code does not give the errors of the absolute parameters, we estimated them from the input parameters. The errors given here correspond to the propagated errors of the calculated parameters.

Using the bolometric magnitude and bolometric correction for the primary component as 2.694 ± 0.178 and 0.022, respectively, we obtained the absolute magnitude of the primary component as $M_{V,1} = 2.672 \pm 0.279$. In the ASAS-SN Catalogue of Variable Stars II database[9] the mean V magnitude of the system is given as $8^m.63$ and it is nearly 0.5 magnitudes dimmer than the given value in the Simbad database. The $(B-V)$ and $E(B-V)$ values given in the ASAS-SN Catalogue as 0.093 and 0.577, respectively, are different from the values found in the literature. By using $(B-V) = 0.2$ and $E(B-V) = 0.07$ we obtained the interstellar extinction in the V filter as $A_v = 3.1 \times E(B-V) = 0.317$. Using those values, we obtained the distance of the DT Cam as 174 ± 10 pc, which is consistent with that given in the *TESS* Input Catalogue (Stassun et al. 2019) and in Gaia DR3 catalogues as 183.927 and 183.479 pc, respectively.

4. OUT-OF-ECLIPSE LIGHT VARIATION

Due to the relatively large amplitude of the eclipse variation, we cannot visually see any light variations at the maxima of the light curve. In Figure 4, we see that the light at the maxima is fairly smooth. Since the primary component's temperature is located in the instability strip, we suspect that it could be a pulsator, similar to stars δ Scuti or γ Dor. In Figure 5 we plot the out-of-eclipse variation for Sectors 19 (upper panel) and 59 (lower panel) included the eclipse boundaries with the regions of ingress and egress to the eclipse indicated by horizontal error bars. As can be seen in Figure 5 despite scattering (gray dots) there are multi periodic variations which can be attributed to pulsation or any other type of variation, like rotation. Because of scattering, we prefer to smooth the light curves by obtaining an average of 5 successive observations (black dots in Figure 5).

The time gap between Sector 19 and 59 is approximately 1069 days. Because of this we prefer to analyze the data separately in the frequency domain. The obtained frequencies are given in Table 6, and the amplitude variation in Figure 6 includes the Fourier fit in Figure 7. The Rayleigh resolution for Sectors 19 and 59 were obtained as $0.040 d^{-1}$ and $0.038 d^{-1}$, respectively. All of the marked combinations given in Table 6 are obtained as the difference between the observed and the predicted frequencies which are smaller than or equal to the Rayleigh criterion.

The existence of periodic variations can be clearly seen by using the normal points created. We found that most of the frequencies obtained are related to the orbital period, except the frequency obtained at $1.65 d^{-1}$, which corresponds to 0.605 days. The

[9] https://asas-sn.osu.edu/variables/531066b2-10c7-52cb-8856-d6a54c9843ee.

TABLE 4

THE LIGHT CURVE SOLUTION OF DT CAM

	Solution 1		Solution 2	
Parameters	**Value**	$\pm\sigma$	**Value**	$\pm\sigma$
T_0(BJD)	2458825.16774	0.00109	-	-
P (day)	7.06625839	0.000002	-	-
a($R_\odot$)	22.859	0.024	-	-
V_γ(km/s)	13.111	0.170	-	-
K_1(km/s)	73.246	0.406	-	-
K_2(km/s)	92.856	0.400	-	-
e	0.167	0.001	0.164	0.002
ω(deg)	42.643	0.029	41.060	0.059
$q(m_2/m_1)$	0.7888	-	-	-
Phase Shift	0.0360	-	0.0360	-
i(deg)	87.675	0.006	88.194	0.010
T_1(K)	8006*	329*	8200*	329*
T_2(K)	6368	250*	6448	250*
A_1	1.000	-	1.000	-
A_2	0.500	-	0.500	-
g_1	1.000	-	1.000	-
g_2	0.320	-	0.320	-
Ω_1	17.82053	0.00665	18.10684	0.01549
Ω_2	13.15815	0.00381	13.08262	0.00824
x_1 (bolo)	0.651	-	-	-
x_2 (bolo)	0.640	-	-	-
y_1 (bolo)	0.255	-	-	-
y_2 (bolo)	0.234	-	-	-
L_1/L_{tot}(TESS)	0.60057	0.00078	0.59815	0.00148
$L_3/L_{tot}(TESS)$	0.00920	-	0.01639	-
$r1$(mean)	0.05928	0.00002	0.05827	0.00003
$r2$(mean)	0.06658	0.00002	0.06697	0.00003
σ(fit)	-	2.6245E-07	-	5.3357E-07

Assumed values are marked with asterisks.

strongest amplitude (essentially semi-amplitude) is of the order of 0.0003 mag in the *TESS* filter. The amplitude in Johnson V is not known but we can estimate it using the relation given by Paunzen et al. (2020) as $Amp(V)/Amp(TESS) = 1.44(4)$. According to this relation, the estimated amplitude in Johnson V is about 0.00086 mag and we cannot obtain such a low magnitude variation with ordinary photometric Earth bound observations. As can be seen in Figure 6, the real amplitude of the periodic variation is probably larger than that obtained by Fourier analysis.

Grigahcène et al. (2010) characterized the δ Scuti type variables as short period pulsating stars, with periods between 0.014 (f = 71.428 d^{-1}) and 0.333 (f = 3.003 d^{-1}) days and pulsation constant Q (Handler et al. 2002) lower than 0.055 days, but generally the accepted lower limit is smaller than 0.033 days (Stellingwerf 1979; Breger 1990).

The binary model yields a mean density of $\rho_1 = 0.721\rho_\odot$ and $\rho_2 = 0.401\rho_\odot$ for the primary and secondary component, respectively. The frequency for the highest amplitude variations for Sector 19 found to be $f_1 = 1.650234d^{-1}$ ($P_1 = 0.60597$ days). Using the relation given as $Q = P_{puls}\sqrt{(\rho/\rho_\odot)}$, we obtained the pulsation constant as $Q_1 = 0.514$ and $Q_2 = 0.384$ days for the primary and secondary component, respectively. As can be seen all of the pulsation constants are larger than 0.055 days. According to these results (including the period of the cyclic variation) we conclude that none of the components can be a δ Scuti pulsator.

TABLE 5

ABSOLUTE PARAMETERS OF DT CAM

	Solution 1		Solution 2	
Parameters	Primary	Secondary	Primary	Secondary
Mass ($M_\odot$)	1.793 ± 0.007	1.414 ± 0.006	1.793 ± 0.007	1.414 ± 0.006
Radius ($R_\odot$)	1.340 ± 0.002	1.538 ± 0.002	1.332 ± 0.002	1.531 ± 0.002
Luminosity* ($L_\odot$)	6.796 ± 1.117	3.432 ± 0.539	7.227 ± 1.160	3.651 ± 0.566
$\rho(\rho_\odot)$	0.721	0.401	0.759	0.394
M_{bol}	2.669 ± 0.178	3.411 ± 0.171	2.603 ± 0.174	3.344 ± 0.168
Bol.Corr.(BC)	0.022	0.062	0.003	0.068
M_v	2.647 ± 0.279	3.349 ± 0.274	2.600 ± 0.277	3.276 ± 0.273
log g (cgs)	4.428 ± 0.002	4.224 ± 0.002	4.443 ± 0.002	4.219 ± 0.002
d(pc)	174 ± 10	-	178 ± 10	-

*Calculated by using components' temperature and radius.

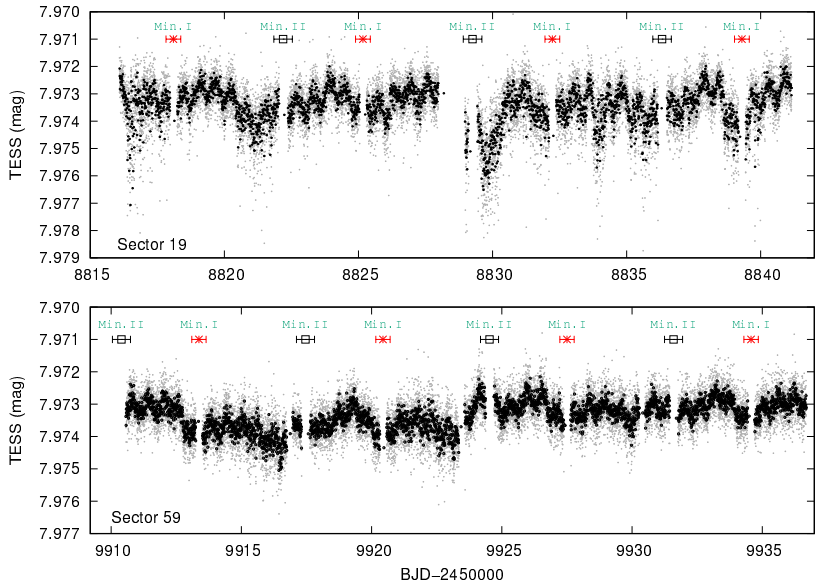

Fig. 5. Out-of-eclipse variation of DT Cam for Sectors 19 (upper panel) and 59 (lower panel). Black dots represent the average of 5 successive observations. The color figure can be viewed online.

The location of the secondary component in the HR diagram coincides with the Solar-like pulsators but the pulsation period is much larger than the 3 to 10 min ranges given by Aerts et al. (2010). Because of this we conclude that the secondary component cannot be a Solar-like pulsator.

Kaye et al. (1999) characterized the γ Doradus (GDOR) type variables as high-order, low-degree, non-radial gravity mode pulsators and showed that the period range is $0.3 \leq P(day) \leq 3 (0.33 \leq f(d^{-1}) \leq 3.33)$. Among the GDOR type pulsators there are low- and high-amplitude examples; the high-amplitude ones are explained by the superposition of several base frequencies (Paunzen et al. 2020). Most of the GDOR pulsators are in the region of A- and F-type main sequence stars within the temperature range of $6100 < T_{\rm eff} < 7500\,{\rm K}$ (Bradley et al. 2015). Additionally, Q pulsation constants for GDOR type stars are given as $Q > 0.24$ days (Grigahcène et al. 2010).

All of the parameters obtained for the secondary component; effective temperature ($T_2 = 6368\,{\rm K}$), Q pulsation constant ($Q_2 = 0.384$ days), and frequency of the periodic variation ($f = 1.65 d^{-1}$) show that the secondary component can be a GDOR type pulsator. In Figure 8 we see that the secondary component is located out of the instability strip given for GDOR type pulsators. But we also see that a small number

TABLE 6

THE OBTAINED SIGNIFICANT FREQUENCIES OF DT CAM USING OUT-OF-ECLIPSE DATA FOR SECTORS 19 AND 59

No	Frequency (d^{-1})	Amplitude *TESS* (mag)	Phase (rad)	P(days)	P_{orb}/P	n	Difference	Combination
			Sector 19					
f_1	1.650234	0.000324	0.119240	0.60597	11.661	-	-	-
f_2	0.227481	0.000198	0.613891	4.39598	1.607	-	-	-
f_3	0.431016	0.000162	0.622711	2.32010	3.046	3	-0.0065	$3f_{orb}$
f_4	0.277367	0.000325	0.363430	3.60533	1.960	2	0.0057	$2f_{orb}$
f_5	0.133695	0.000213	0.403955	7.47972	0.945	1	0.0078	f_{orb}
f_6	0.319271	0.000168	0.512517	3.13213	2.256	-	-	-
f_7	0.041904	0.000141	0.513211	23.86387	0.296	-	-	-
			Sector 59					
f_1	0.034459	0.000330	0.634004	29.02023	0.243	0.25	0.0009	$f_{orb}/4$
f_2	1.652104	0.000180	0.165151	0.60529	11.674	-	-	-
f_3	0.141664	0.000170	0.828329	7.05898	1.001	1	-0.0001	f_{orb}
f_4	0.428820	0.000206	0.133727	2.33198	3.030	3	-0.0043	$3f_{orb}$
f_5	0.070832	0.000153	0.887096	14.11795	0.501	0.5	-0.0001	$f_{orb}/2$
f_6	0.277584	0.000103	0.481096	3.60251	1.961	2	0.0055	$2f_{orb}$
f_7	0.111034	0.000097	0.965751	9.00628	0.785	-	0.0038	$f_3 - f_1$ (f_{orb}-$f_{orb}/4$)

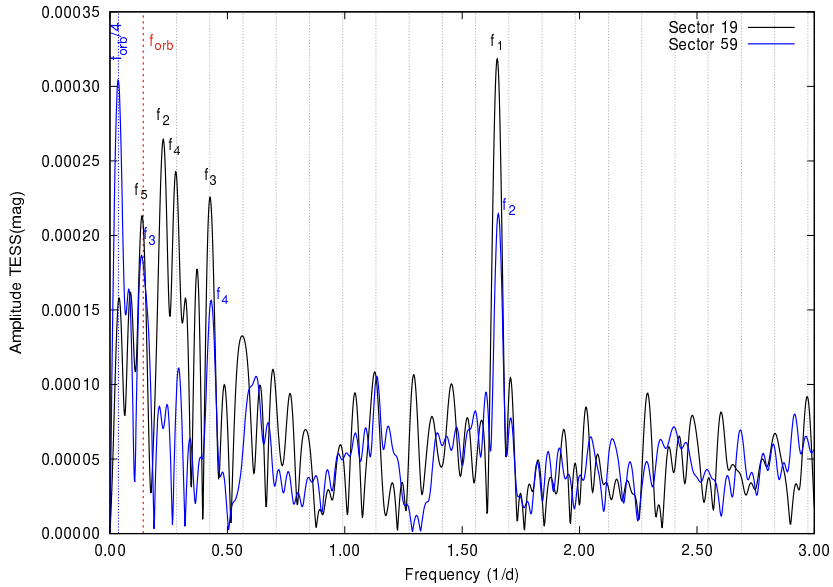

Fig. 6. The amplitude spectrum for the out-of-eclipse light variation of DT Cam for Sectors 19 (black line) and 59 (blue line). We marked the location of the orbital frequency (red vertical line) including the harmonics of orbital frequency f_{orb} with dotted vertical lines. The color figure can be viewed online.

of GDORs are located outside this instability strip too, which can be a sign of the type of the pulsator.

By using Kepler observations, Balona (2011) showed that low-frequency variations are present in most A-type stars and that the dominant period is consistent with the expected rotational periods of these stars. Using this finding Balona (2011) suggested that star spots, or other co-rotating structures, may be responsible for the low-amplitude light variations in normal A-type stars. Comparison of the two sectors with each other in Figure 6 (the amplitude of frequency at 1.65 d^{-1}) we see that the am-

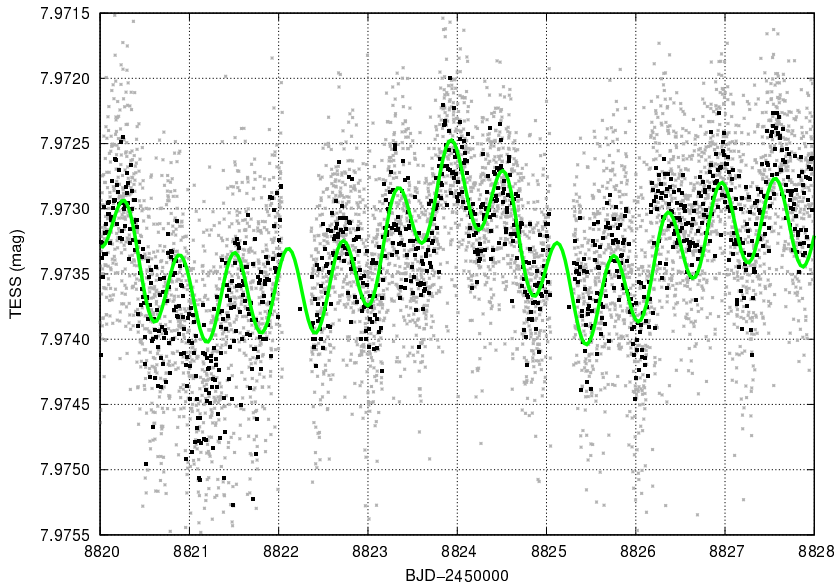

Fig. 7. Small amplitude periodic variation of DT Cam at Sector 19 (a small portion is plotted). The synthetic curve was computed using all the frequencies detected. Gray dots are for the original data, black dots represent the average of 5 successive observations, and the green line is the Fourier fit obtained by using all of the frequencies given in Table 6 for Sector 19. The color figure can be viewed online.

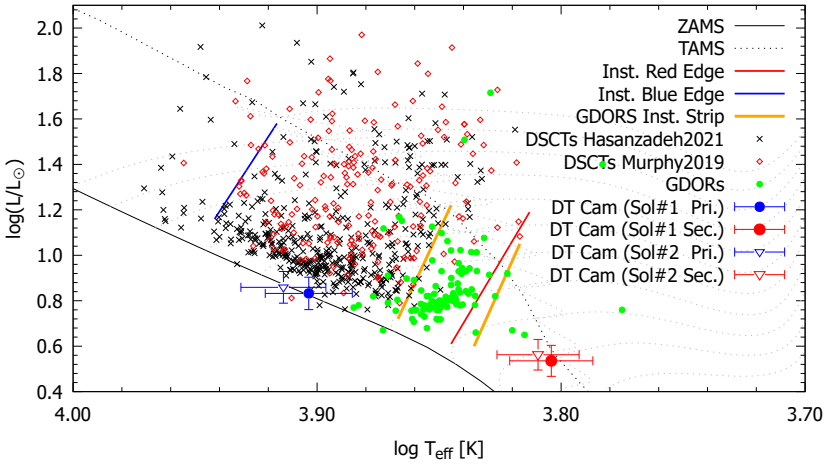

Fig. 8. Position of the primary and secondary component of DT Cam in the Hertzsprung-Russell diagram (HRD) (blue and red points, respectively). Black and gray continuous lines show the ZAMS and evolutionary tracks of stars for solar metallicity composition Z=0.008, taken from Girardi et al. (2000). Dotted red and blue lines represent the boundaries of the instability strip. Dashed orange lines indicate the theoretical cool and hot boundary of the γ Doradus instability strip (Warner et al. 2003). The other small dots represent the location of δ Scuti type stars obtained from Hasanzadeh et al. (2021) (black) and Murphy et al. (2019) (red). Green dots show confirmed γ Doradus stars compiled from Kaye et al. (1999), Henry et al. (2005), and Paunzen et al. (2020). The color figure can be viewed online.

plitude is essentially different in both sectors, which can be a sign of variable amplitude. And this can be a sign of stars pots as mentioned by Lanza et al. (2009) for cool stars. Because of this, there is a possibility of the secondary component, the cooler component, having star spots on the surface. Balona (2011) showed that there is a possibility of the A-type component also having star spots on its surface, and found that a total of 208 A-type stars which are coded as SPOT in their work show only a single peak

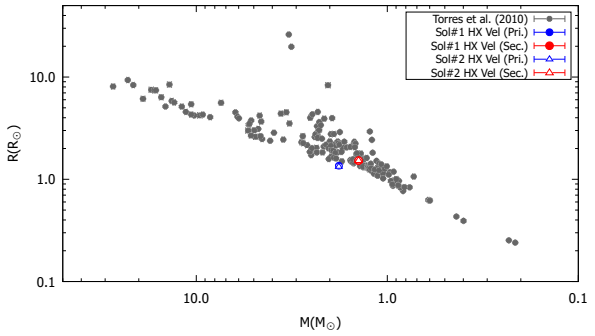

Fig. 9. Position of the primary and secondary component of DT Cam on the mass-radius diagram (blue and red points, respectively). The mass and radius values were taken from Torres et al. (2010). The color figure can be viewed online.

in the frequency domain, as we obtained for the DT Cam system

Assuming that the frequency of highest amplitude is the rotation frequency we can calculate the rotational velocity of the components separately by using the radius values given in Table 5. The rotational velocities obtained for the primary and secondary components are $v_1 = 112.57$ km/s and $v_2 = 129.20$ km/s, respectively. In the literature we found that the average rotational velocities of A0 and F5 type main-sequence stars were given as 190 and 25 km/s, respectively (McNally 1965). Using the corresponding spectral types for the components as A2+F4 we concluded that the low amplitude periodic variation with a period of 0.60597 days can be caused by the rotation of the primary component. In the literature e.g. Sikora et al. (2019) we find some examples, such as HD 13709, HD 19398, and HD 54558, for which the rotational period is smaller than that obtained for the A2-type primary component in DT Cam system.

5. RESULTS AND DISCUSSION

We derived for the first time the absolute and geometrical parameters of the Algol type eccentric eclipsing binary DT Cam by using *TESS* and Gaia observations.The results of the light-curve modelling reveal that DT Cam is a detached system with one of the components probably in the PMS phase. Using the semi-amplitudes of the radial velocity data of the system given in the catalogues, combined with our light curve solution, enabled us to find the physical and geometric parameters of the components. In this sense, we conclude that the system will provide an important contribution to the literature.

We updated the light elements of the system by using all of the times of minima obtained by the *TESS* observations and data found in the literature. The difference of the orbital period obtained for the primary and secondary minima is 1.079 seconds, and it is probably caused by the different time spans of the observations. In addition, we think that there is not enough time span for obtaining apsidal motion parameters.

In Figure 8 we plot our results with the δ Scuti type variables compiled from Uytterhoeven et al. (2011) and Murphy et al. (2019) including the γ Doradus pulsators compiled from Kaye et al. (1999), Henry et al. (2005), and Paunzen et al. (2020). The primary component is located on the Main Sequence of the instability strip. Because of the location of the components on the HRD we suspected that the primary or secondary component can be a pulsator like δ Scuti or γ Doradus, or a rotational variable. Based on the physical and frequency analysis parameters discussed in the previous section we cannot strictly figure out which of the components shows a small amplitude periodic variation. As a result, the secondary component can be a GDOR type pulsator or the A2-type component can be a rotating variable. Because most of GDOR type pulsators show multi-period variations (Zhou 2015; Paunzen et al. 2020; Takata et al. 2020; Henry et al. 2005) and since we see only one for DT Cam, we accepted that the primary component is a rotating variable.

The number of eclipsing binaries with a pre-main sequence component whose absolute parameters are determined is very small. In this sense we think that the system will make an important contribution for the understanding of stellar structure and evolution.

In Figure 9 we plot our results in the mass-radius diagram given by Torres et al. (2010). The primary component seems to have a small radius and low luminosity. Most likely, the primary component has a very fast rotating core, as in the EK Cep system investigated by Yıldız (2003).

As obtained in § 4 the out-of-eclipse variations are mostly related to the orbital frequency, except for the low amplitude periodic variation with a period of 0.60597 days. It is not possible to say whether these small-amplitude periodic variations are caused by one or both components. If the periodic variation of 0.60597 days is caused by rotation of the primary component we can say that system is not synchronized.

We thank the anonymous referee for helpful comments and suggestions that greatly improved

the quality of this paper, especially because of the warning that the secondary component may be a pre-main sequence object. This research has made use of VizieR the Simbad database, operated at CDS, Strasbourg, France, and NASA's Astrophysics Data System Abstract Service. This work has made use of data from the European Space Agency (ESA) mission Gaia (https://www.cosmos.esa.int/gaia), processed by the Gaia Data Processing and Analysis Consortium (DPAC7). Funding for the DPAC has been provided by national institutions, in particular the institutions participating in the Gaia Multilateral Agreement. The *TESS* data presented in this paper were obtained from the Mikulski Archive for Space Telescopes (MAST). Funding for the *TESS* mission is provided by the NASA Explorer Program.

REFERENCES

Aerts, C., Christensen-Dalsgaard, J., Kurtz, D. W. 2010, Asteroseismology (Springer), https://doi.org/10.1007/978-1-4020-5803-5

Ammons, S. M., Robinson, S. E., Strader J., et al. 2006, ApJ, 638, 1004, https://doi.org/10.1086/498490

Avvakumova, E. A., Malkov, O. Y., & Kniazev, A. Y. 2013, AN, 334, 860, https://doi.org/10.1002/asna.201311942

Bai, Y., Liu, J. F., Bai, Z. R., Wang, S., & Fan, D. W. 2019, AJ, 158, 93, https://doi.org/10.3847/1538-3881/ab3048

Balona, L. A. 2011, MNRAS, 415, 1691, https://doi.org/10.1111/j.1365-2966.2011.18813.x

Bradley, P. A., Guzik, J. A., Miles, L. F., et al. 2015, AJ, 149, 68, https://doi.org/10.1088/0004-6256/149/2/68

Breger, M. 1990, Delta Scuti Star, ed. M. Breger and Michael Montgomery (San Francisco, CA: ASPC)

Burggraaff, O., Talens, G. J. J., Spronck, J., et al. 2018, A&A, 617, 32, https://doi.org/10.1051/0004-6361/201833142

Cannon, A. J. & Pickering, E. C. 1993, yCat, 3135, 0

Chandler, C. O., McDonald, I., & Kane, S. R. 2016, AJ, 151, 59, https://doi.org/10.3847/0004-6256/151/3/59

Eastman, J., Siverd, R., & Gaudi, B. S. 2010, PASP, 122, 935, https://doi.org/10.1086/655938

Eker, Z., Soydugan, F., Bilir, S., et al. 2020, MNRAS, 496, 3887, https://doi.org/10.1093/mnras/staa1659

Gaia Collaboration. 2018, 2018yCat.1345, 0G, https://doi.org/10.26093/cds/vizier.1345

Gaia Collaboration. 2022, 2022yCat.1355, 0G, https://doi.org/10.26093/cds/vizier.1355

Girardi, L., Bressan, A., Bertelli, G., & Chiosi, C. 2000, A&AS, 141, 371, https://doi.org/10.1051/aas:2000126

Grigahcène, A., Antoci, V., Balona, L., et al. 2010, ApJ, 713, 192, https://doi.org/10.1088/2041-8205/713/2/L192

Handler, G. & Shobbrook, R. R. 2002, MNRAS, 333, 251, https://doi.org/10.1046/j.1365-8711.2002.05401.x

Hasanzadeh, A., Safari, H., & Ghasemi, H. 2021, MNRAS, 505, 1476, https://doi.org/10.1093/mnras/stab1411

Henry, G. W., Fekel, F. C., & Henry S. M. 2005, AJ, 129, 2815, https://doi.org/10.1086/429876

Henry, G. W., Fekel, F. C., & Williamson M. H. 2022, AJ, 163, 180, https://doi.org/10.3847/1538-3881/ac540b

Jeong, M. -J., Kim, C. -H., Song, M. -H., et al. 2020, OEJV, 205, https://doi.org/0.5817/OEJV2020-0205

Juryšek, J., Hoňková, K., Šmelcer, L., et al. 2017, EIJV, 179, 1

Kaye, A. B., Handler, G., Krisciunas, K., et al. 1999, PASP, 111, 840, https://doi.org/10.1086/316399

Kervella, P., Arenou, F., Mignard, F., & Thévenin, F. 2019, A&A, 623, 72, https://doi.org/10.1051/0004-6361/201834371

Kervella, P., Arenou, F., & Thévenin, F. 2022, A&A, 657, 7, https://doi.org/10.1051/0004-6361/202142146

Kim, C. -H., Kreiner, J. M., Zakrzewski, B., et al. 2018, ApJS, 235, 41, https://doi.org/10.3847/1538-4365/aab7ef

Kopal, Z. 1978, ASSL, 68, https://doi.org/10.1007/978-94-009-9780-6

Lanza, A. F., Pagano, I., Leto, G., et al. 2009, A&A, 493, 193, https://doi.org/10.1051/0004-6361:200810591

McDonald, I., Zijlstra, A. A., & Boyer M. L. 2012, MNRAS, 427, 343, https://doi.org/10.1111/j.1365-2966.2012.21873.x

McDonald, I., Zijlstra, A. A., & Watson, R. A. 2017, MNRAS, 471, 770, https://doi.org/10.1093/mnras/stx1433

McNally, D. 1965, The Observatory, 85, 166

Murphy, S. J., Hey, D., Van Reeth, T., & Bedding T. R. 2019, MNRAS, 485, 2380, https://doi.org/10.1093/mnras/stz590

Otero, S. A., Wils, P., & Dubovsky, P. A. 2005, IBVS, 5586, 1

Paegert, M., Stassun, K. G., Collins, K. A., et al. 2021, arXiv:2108.04778, https://doi.org/10.48550/arXiv.2108.04778

Paschke, A. 2017, OEJV, 181

_____. 2019, BAVJ, 30, 1

_____. 2021, BAVJ, 55, 1

Paunzen, E., Bernhard, K., Hümmerich, S., et al. 2020, MNRAS, 499, 3976, https://doi.org/10.1093/mnras/staa2905

Prša, A., Kochoska, A., Conroy, K. E. et al. 2022, ApJS, 258, 16, https://doi.org/10.3847/1538-4365/ac324a

Ricker, G. R., Winn, J. N., Vanderspek, R., et al. 2015, JATIS, 1. 014003, https://doi.org/10.1117/1.JATIS.1.1.014003

Shi, Xiang-dong, Sheng-bang, Qian, & Lin-Jia Li. 2022, ApJS, 259, 50, https://doi.org/10.3847/1538-4365/ac59b9

Sikora, J., David-Uraz, A., Chowdhury, S., et al. 2019, MNRAS, 487, 4695, https://doi.org/10.193/mnars/stz1581

Stassun, K. G., Oelkers, R. J., Paegert, M., et al. 2019, AJ, 158, 138, https://doi.org/10.3847/1538-3881/ab3467

Stellingwerf, R. F. 1979, ApJ, 227, 935, https://doi.org/10.1086/156802

Takata, M., Ouzzani, R.-M., Saio, H., et al. 2020, A&A, 635, 106, https://doi.org/10.1051/0004-6361/201936297

Tonry, J. L., Denneau, L., Flewelling, H., et al. 2018, ApJ, 867, 105, https://doi.org/10.3847/1538-4357/aae386

Torres, G., Andersen, J., & Giménez, A. 2010, A&ARv, 18, 67, https://doi.org/10.1007/s00159-009-0025-1

Uytterhoeven, K., Moya, A., Grigahcène, A., et al. 2011, A&A, 534, 125, https://doi.org/10.1051/0004-6361/201117368

Warner P. B., Kaye A. B., & Guzik, J. A. 2003, ApJ, 593, 1049, https://doi.org/10.1086/376727

Wilson, R. E. & Devinney, E. J. 1971, ApJ, 166, 605, https://doi.org/10.1086/150986

Wilson, R. E. 1979, ApJ, 234, 1054, https://doi.org/10.1086/157588

———. 1990, ApJ, 256, 613, https://doi.org/10.1086/168867

Wright, C. O., Egan, M. P., Kraemer, K. E., & Price, S. D. 2003, AJ, 125, 359, https://doi.org/10.1086/345511

Yıldız, M. 2003, A&A, 409, 689, https://doi.org/10.1051/0004-6361:20031118

Zasche, P., Uhlar, R., Kucakova, H., Svoboda, P., & Masek, M. 2014, IBVS, 6114, 1

Zasche, P., Uhlar, R., Svoboda, P., et al. 2017, IBVS 6204, https://doi.org/10.22444/IBVS.6204

Zasche, P., Wolf, M., Uhlar, R., et al. 2018, A&A, 619, 85, https://doi.org/10.1051/0004-6361/201832793

Zhou, A. Y. 2015, arXiv:1501.05166, https://doi.org/10.48550/arXiv.1501.05166

B. Gürol: Ankara University, Science Faculty, Dept. of Astronomy and Space Sciences, 06100 Tandoğan, Ankara, Turkey (Birol.Gurol@ankara.edu.tr).

T. Özdemir: İnonu University, Faculty of Arts and Sciences, Malatya, Turkey (tuncay@inonu.edu.tr).

Revista Mexicana de Astronomía y Astrofísica, **60**, 217–226 (2024)

https://doi.org/10.22201/ia.01851101p.2024.60.02.02

INVESTIGATING THE HYPERBOLIC AND HYBRID SCALAR FIELD COSMOLOGIES WITH VARYING COSMOLOGICAL CONSTANT IN $F(R,T)$ GRAVITY

Nasr Ahmed [1,2] and Tarek M. Kamel[2]

Received October 30 2023; accepted March 1 2024

ABSTRACT

This paper investigated two scalar field cosmological models in $f(R,T)$ gravity with cosmic transit and varying cosmological constant $\Lambda(t)$. The cosmological constant tends to have a tiny positive value at the current epoch. The scalar field pressure p_ϕ shows a sign flipping for normal scalar field. For the phantom field, the scalar potential $V(\phi)$ is negative and the energy density $\rho_\phi = E_k + V$ takes negative values when the equation of state parameter ω_ϕ is less than -1. The WEC, $\rho = \sum_i \rho_i \geq 0$ and $p_i + \rho_i \geq 0$, is not violated but with an instability for the second model at late times. For a scalar field ϕ, the condition $\rho_\phi + p_\phi = \rho_\phi(1+\omega_\phi) = 2E_k \geq 0$ allows for $\rho_\phi < 0$ if $\omega_\phi < -1$. The causality and energy conditions have been discussed for both models. The cosmology in both models was studied using a given function $a(t)$ derived from the desired cosmic behavior, which is the opposite of the traditional view.

RESUMEN

Investigamos dos modelos cosmológicos de campo escalar suponiendo gravedad $f(R,T)$, con tránsito cósmico y constante cosmológica $\Lambda(t)$ variable. La constante cosmológica tiende a un valor pequeño y positivo en el presente. La presión del campo escalar p_ϕ cambia de signo para un campo escalar normal. Para el campo fantasma, el potencial escalar $V(\phi)$ es negativo y la densidad de energía $\rho_\phi = E_k + V$ adquiere valores negativos cuando el parámetro ω_ϕ de la ecuación de estado es menor que -1. No se viola la WEC, $\rho = \sum_i \rho_i \geq 0$ y $p_i + \rho_i \geq 0$, pero se obtiene una inestabilidad en el segundo modelo, a tiempos tardíos. Para un campo escalar ϕ, la condición $\rho_\phi + p_\phi = \rho_\phi(1+\omega_\phi) = 2E_k \geq 0$ permite una $\rho_\phi < 0$ si $\omega_\phi < -1$. Se discuten las condiciones de causalidad y energía para ambos modelos. Se estudia la cosmología en ambos modelos con una función dada $a(t)$ derivada del comportamiento cósmico deseado, lo cual es contrario a la visión tradicional.

Key Words: cosmological parameters — cosmology: theory — dark energy

1. INTRODUCTION

Accelerated cosmic expansion (Percival et al. 2001; Stern et al. 2010) has become a basic motivation for a variety of modified gravitational theories (Nojiri & Odintsov 2006; Nojiri et al. 2008; Ferraro & Fiorini 2007; Bengochea & Ferraro 2009; De Felice & Tsujikawa 2010; Alves et al. 2011; Maeder 2017; Gagnon & Lesgourgues 2011; Ahmed 2009, 2010; Ahmed & Pradhan 2022; Ahmed & Kamel 2021). In order to find a satisfactory explanation, an exotic form of energy with negative pressure, called dark energy, was hypothesized. Several dynamical scalar fields models of dark energy were introduced such as Quintessence, Phantom and Tachyons (Tsujikawa 2013; Kamenshchik et al. 2001; Caldwell 2002; Chiba et al. 2000; Sen 2002; Arkani-Hamed et al. 2004; Ahmed et al. 2023). For a zero curvature FRW universe driven by a scalar field ϕ, Einstein's equations are

$$3H^2 = \frac{1}{2}\dot{\phi}^2 + V(\phi), \quad \dot{H} = -\frac{1}{2}\dot{\phi}^2, \quad \ddot{\phi} + 3H\dot{\phi} + V' = 0. \tag{1}$$

[1]Mathematics and Statistics Department, Faculty of Science, Taibah University, Saudi Arabia.
[2]Astronomy Department, National Research Institute of Astronomy and Geophysics, Helwan, Cairo, Egypt.

With units $8\pi M_{Pl}^{-2} = c = 1$. $H = \frac{\dot{a}}{a}$ is the Hubble parameter and $V(\phi)$ is the potential. The prime denotes differentiation with respect to ϕ, and the dots denote differentiation with respect to t. While this nonlinear system is insoluble in general, progress can be made through postulating a particular form of the scale factor $a(t)$ and then obtaining the form of both $\phi(t)$ and $V(\phi)$ (Barrow & Parsons 1995; Ellis & Madsen 1991). In Banerjee & Pavón (2001), it was shown that a minimally coupled scalar field in Brans-Dicke theory leads to an accelerating universe. A power function forms of the scale factor a and the scalar field ϕ were assumed as

$$a(t) = a_1 t^{\alpha}, \qquad \phi(t) = \phi_1 t^{\beta}, \tag{2}$$

with a_1, ϕ_1, α and β constants. An accelerated expansion was also achieved in a modified Brans-Dicke theory through considering the following power-law form of both a and ϕ (Bertolami & Martins 2000).

$$a(t) = a_0 \left(\frac{t}{t_0}\right)^{\alpha}, \qquad \phi(t) = \phi_0 \left(\frac{t}{t_0}\right)^{\beta}. \tag{3}$$

Cosmology in the scalar-tensor $f(R,T)$ gravity has been studied in Gonçalves et al. (2022) where three particular forms of $a(t)$ have been used.

1.1. *Negative Potentials and Energy Densities*

The case of negative potential cosmologies has become interesting after the prediction of Ads spaces in string theory and particle physics. Negative potentials also exist in ekpyrotic and cyclic cosmological models in which the universe goes from a contracting to an accelerating phase (Steinhardt & Turok 2002; Khoury et al. 2001). They are commonly predicted in particle physics, supergravity and string theory where the general vacuum of supergravity has a negative potential. It has also been suggested that negative potentials lead to an explanation of the cosmological scale in terms of a high energy scale such as the supersymmetry breaking scale or the electroweak scale (Garriga & Vilenkin 2000). A detailed discussion of scalar field cosmology with negative potentials was carried out in Felder et al. (2002). The effect of negative energy densities on classical FRW cosmology has been investigated in Nemiroff et al. (2015) where the total energy density can be expanded as

$$\rho = \sum_{n=-\infty}^{\infty} \rho_n^{+} a^{-n} + \sum_{m=-\infty}^{\infty} \rho_m^{-} a^{-m}, \tag{4}$$

where ρ_n^{+} is the familiar positive energy density and ρ_m^{-} is the negative cosmological energy density. The cosmic evolution with negative energy densities was also examined in Saharian et al. (2022) where vacuum polarization was mentioned as an example for a gravitational source with $\rho < 0$ that may have played a significant role in early cosmic expansion.

An interesting study was carried out in De La Macorra & Germán (2022) where the equation of state parameter is negative ($\omega_\phi = p_\phi/\rho_\phi < -1$) with no violation of the weak energy condition ($\rho = \sum_i \rho_i \geq 0$ & $p_i + \rho_i \geq 0$) which requires a negative potential $V(\phi) < 0$. It has been shown that $\rho_\phi = \frac{1}{2}\dot{\phi}^2 + V(\phi)$ becomes negative with $\omega_\phi < -1$, the negative ρ_ϕ leads to a small value of the cosmological constant. However, while cosmic expansion exists in such scenario, the negative potential V leads to a collapsing universe.

The classical energy conditions are "the null energy condition (NEC) $\rho + p \geq 0$; weak energy condition (WEC) $\rho \geq 0$, $\rho + p \geq 0$; strong energy condition (SEC) $\rho + 3p \geq 0$ and dominant energy condition (DEC) $\rho \geq |p|$". Since the SEC implies that gravity should always be attractive, this condition fails in the accelerating and inflation epochs (Visser 1997a,b). As was mentioned in Barceló et al. (2002), even the simplest scalar field theory we can write down violates the SEC. The NEC is the most fundamental energy condition on which the singularity theorems, and other key results, are based (Alexandre & Polonyi 2021). If the NEC is violated, all other point-wise energy conditions (ECs) are automatically violated. A very useful discussion about the validity of classical linear ECs was given in Barceló et al. (2002) where it was shown that these classical conditions cannot be valid in general situations. The scalar field potential $V(\phi)$ is restricted by the ECs where the scalar field ϕ (with $\rho_\phi = \frac{1}{2}\dot{\phi}^2 + V(\phi)$ & $p_\phi = \frac{1}{2}\dot{\phi}^2 - V(\phi)$) satisfies the NEC for any $V(\phi)$, the WEC if and only if $V(\phi) \geq -\frac{1}{2}\dot{\phi}^2$, the DEC if and only if $V(\phi) \geq 0$, the SEC if and only if $V(\phi) \leq \dot{\phi}^2$. The detailed proof of this theorem can be found in Westmoreland (2013).

1.2. $\Lambda(t)$ *Models*

A new model for the time-dependent cosmological constant $\Lambda(t)$ was proposed in Lopez & Nanopoulos (1996) using the following ansatz

$$\Lambda = \frac{\Lambda_{Pl}}{(t/t_{Pl})^2} \propto \frac{1}{t^2}, \tag{5}$$

Λ starts at the Planck time as $\Lambda_{Pl} \simeq M_{Pl}^2$ and leads to the value $\Lambda_0 \approx 10^{-120} M_{Pl}^2$ for the current epoch. The decay of $\Lambda(t)$ during inflation and as Bose condensate evaporation was studied in Dymnikova &

Khlopov (2001, 2000). Other models for $\Lambda(t)$ have been suggested in Basilakos et al. (2009; Pan (2018); Oikonomou et al. (2017); Ahmed & Alamri (2018, 2019a). The following ansatz was first introduced in Basilakos et al. (2009) where a variety of cosmologically relevant observations were used to put strict constraints on $\Lambda(t)$ models

$$\Lambda(H) = \lambda + \alpha H + 3\beta H^2, \tag{6}$$

where H is the Hubble parameter, λ, α and β are constants. It has been found in Pan (2018); Basilakos et al. (2013); Gómez-Valent & Solà (2015) that the zero value of λ does not agree with observations, while $\lambda \neq 0$ behaves like the ΛCDM model at late-time. Examples of varying Λ models in terms of the Hubble parameter H are (Pan 2018)

$$\Lambda(H) = \beta H + 3H^2 + \delta H^n, \quad n \in R - \{0, 1\}, \tag{7}$$
$$\Lambda(H, \dot{H}, \ddot{H}) = \alpha + \beta H + \delta H^2 + \mu \dot{H} + \nu \ddot{H}. \tag{8}$$

A generalized holographic dark energy model where the effective cosmological constant depends on H and its derivatives was proposed in Nojiri et al. (2021, 2020, 2022a).

1.3. $f(R,T)$ *Modified Gravity*

The action of $f(R,T)$ modified gravity is given as (Harko et al. 2011)

$$S = \int \left(\frac{f(R,T)}{16\pi G} + L_m \right) \sqrt{-g}\ d^4x, \tag{9}$$

where L_m is the matter Lagrangian density. $f(R,T)$ is an arbitrary function of the Ricci scalar R and the trace T of the energy-momentum tensor $T_{\mu\nu}$ is defined as

$$T_{\mu\nu} = g_{\mu\nu} L_m - 2\frac{\partial L_m}{\partial g^{\mu\nu}}. \tag{10}$$

Varying the action (9) gives

$$\begin{aligned} f_R(R,T) R_{\mu\nu} - \frac{1}{2} f(R,T) g_{\mu\nu} \\ + (g_{\mu\nu} \Diamond - \nabla_\mu \nabla_\nu) f_R(R,T) \\ = 8\pi T_{\mu\nu} - f_T(R,T) T_{\mu\nu} - f_T(R,T) \Theta_{\mu\nu}, \end{aligned} \tag{11}$$

where $\Diamond = \nabla^i \nabla_i$, $f_R(R,T) = \frac{\partial f(R,T)}{\partial R}$, $f_T(R,T) = \frac{\partial f(R,T)}{\partial T}$ and ∇_i denotes the covariant derivative. $\Theta_{\mu\nu}$ is given by

$$\Theta_{\mu\nu} = -2T_{\mu\nu} + g_{\mu\nu} L_m - 2g^{\alpha\beta} \frac{\partial^2 L_m}{\partial g^{\mu\nu} \partial g^{\alpha\beta}}. \tag{12}$$

The cosmological equations for $f(R,T) = R + 2h(T)$ with cosmological constant Λ considering a scalar field ϕ coupled to gravity were given in Aygün et al. (2018) as

$$\frac{2\ddot{a}}{a} + \frac{\dot{a}^2}{a^2} = 4\pi\epsilon\dot{\phi}^2 - 8\pi V(\phi) + \mu\epsilon\dot{\phi}^2 - 4\mu V(\phi) - \Lambda, \tag{13}$$
$$\frac{3\dot{a}^2}{a^2} = -4\pi\epsilon\dot{\phi}^2 - 8\pi V(\phi) - \mu\epsilon\dot{\phi}^2 - 4\mu V(\phi) - \Lambda, \tag{14}$$

where $h(T) = \mu T$ and μ is a constant; $\epsilon = \pm 1$ corresponding to normal and phantom scalar fields respectively. In the current work, two cosmological models in modified $f(R,T)$ gravity were investigated using a given scale factor $a(t)$ deduced from the desired cosmic behavior which is the opposite of the conventional viewpoint. Such ad hoc approach to the cosmic scale factor and cosmological scalar fields was widely used by many authors in various theories (Ellis & Madsen 1991; Chervon et al. 1997; Sen & Sethi 2002; Maharaj et al. 2017; Silva & Santos 2013; Ahmed & Alamri 2019b; Sazhin & Sazhina 2016; Ahmed et al. 2020; Ahmed 2020; Ahmed & Kamel 2021; Ahmed & Pradhan 2020; Nojiri et al. 2022b). We will make use of the following hyperbolic and hybrid scale factors:

$$a(t) = A \sinh^{\frac{1}{n}}(\eta t) \quad , \quad a(t) = a_1 t^{\alpha_1} e^{\beta_1 t}, \tag{15}$$

where A, η, n, $a_1 > 0$, $\alpha_1 \geq 0$ and $\beta_1 \geq 0$ are constants. The first scale factor generates a class of accelerating models for $n > 1$; the models also exhibit a phase transition from the early decelerating epoch to the present accelerating era in good agreement with recent observations. The second hybrid ansatz is a mixture of power-law and exponential-law cosmologies, and can be regarded as a generalization of each of them. The power-law cosmology can be obtained for $\beta_1 = 0$, and the exponential-law cosmology can be obtained for $\alpha_1 = 0$. New cosmologies can be explored for $\alpha_1 > 0$ and $\beta_1 > 0$. A generalized form of the hybrid scale factor has been proposed in Nojiri et al. (2022b); Odintsov et al. (2021) to unify the cosmic evolution of the universe from a non-singular bounce to the viable dark energy

$$a(t) = \left[1 + a_0 \left(\frac{t}{t_0}\right)^2\right]^{\frac{1}{3(1+\omega)}} \exp\left[\frac{1}{(\alpha-1)} \left(\frac{t_s - t}{t_0}\right)^{1-\alpha}\right], \tag{16}$$

where ω, α and t_s are various parameters. Setting $t_0 = 1$ billion years, this can be re-written as the product of two scale factors

$$a(t) = \left[1 + a_0 t^2\right]^{\frac{1}{3(1+\omega)}} \times \exp\left[\frac{1}{(\alpha-1)} (t_s - t)^{1-\alpha}\right]. \tag{17}$$

In the current work, we are going to use the ansatz (6) for the time varying cosmological constant, which leads to a very tiny positive value of Λ at the current epoch as suggested by observations (Perlmutter et al. 1999; Tonry et al. 2003).

2. MODEL 1

Starting with the hyperbolic solution in (15), which gives the desired behavior of the deceleration and jerk parameters, we obtain the Hubble, deceleration, and jerk parameters as:

$$H = \frac{\eta}{n}\coth(\eta t), \quad q = -\frac{\ddot{a}a}{\dot{a}^2} = \frac{-\cosh^2(\eta t)+n}{\cosh^2(\eta t)}, \quad j = \frac{\dddot{a}}{aH^3} = 1 + \frac{2n^2-3n}{\cosh^2(\eta t)}. \tag{18}$$

In order to solve the system of equations (13) and (14) for the scalar field and the potential, we utilize the hyperbolic scale factor in (15) along with the time-dependent anstaz for the cosmological constant (6). Then, we will have a system of two equations in two unknowns which we have solved using Maple software and have obtained

$$\phi(t) = \frac{\mp\ln(e^{\eta t}+1) \pm \ln(e^{\eta t}-1)}{\sqrt{-2\epsilon(4\pi+\mu)}} + \phi_0, \tag{19}$$

$$V(t) = -\frac{\left(\eta^2(1+3\beta)\coth^2(\eta t) + 2\eta\alpha\coth(\eta t) + 2(\eta^2+4\lambda)\right)}{16(2\pi+\mu)}, \tag{20}$$

$$V(\phi) = -\frac{\left((3\beta+1)\,\eta^2\chi^2 + 4\eta\alpha\chi + 2\eta^2(3\beta+5)\right)}{64(2\pi+\mu)} - \frac{\left(16\lambda + 4\eta\alpha\chi^{-1} + \eta^2\chi^{-2}(3\beta+1)\right)}{64(2\pi+\mu)}, \tag{21}$$

where $\chi \equiv e^{(\phi_0-\phi)\sqrt{-2\epsilon(4\pi+\mu)}}$ and we have used $t(\phi) = \frac{1}{\eta}\ln(\mp\frac{1+\chi}{\chi-1})$ to get the expression for $V(\phi)$. The expression for $\phi(t)$ shows that ϵ can be -1 provided that $(4\pi+\mu) > 0$, and it can be $+1$ provided that $(4\pi+\mu) < 0$. Plotting $t(\phi)$ leads to same graph for both signs (Sen 2002). We also obtain the same expressions for $V(\phi)$ (Ahmed et al. 2023), energy density ρ and pressure p for both ϕ solutions. Actually, Figure 1(g) shows that both solutions for ϕ, although they have a different start, unite in one solution. We can use $\phi_0 = 0$ without loss of generality. Recalling that $\rho_\phi = E_k + V$ and $p_\phi = E_k - V$ we obtain

$$p_\phi(t) = -\frac{\eta^2 e^{2\eta t}}{\epsilon(4\pi+\mu)(e^{\eta t}+1)^2(e^{\eta t}-1)^2} - V(t),$$
$$\rho_\phi(t) = -\frac{\eta^2 e^{2\eta t}}{\epsilon(4\pi+\mu)(e^{\eta t}+1)^2(e^{\eta t}-1)^2} + V(t). \tag{22}$$

The evolution of the cosmological constant in this work agrees with observations where it has a very tiny positive value at the current epoch (Figure 1c). The expressions for the parameters q, j and the cosmological constant in equation (6) are all independent of ϵ. The rest of the parameters are all plotted for $\epsilon = \pm 1$. For $\epsilon = +1$, which corresponds to a normal scalar field, the scalar field pressure p_ϕ changes sign from positive to negative. We can also see that $V(\phi)$, $V(t)$ and ρ_ϕ are all positive where both $V(t)$ and ρ_ϕ tend to ∞ as $t \to 0$. For $\epsilon = -1$, which corresponds to a phantom scalar field, the pressure $p_\phi > 0$ all the time while ρ_ϕ takes negative values when $\omega_\phi < -1$ with a negative scalar potential V. In the literature, it is known that the vacuum phantom energy has some unusual physical properties such as the increasing vacuum energy density, violation of the DEC $\rho + p < 0$ and the superluminal sound speed (González-Díaz 2004).

According to the WEC, the total energy density and pressure should follow the inequalities $\rho + p = \rho(1+\omega) \geq 0$ and $\rho \geq 0$. For a scalar field ϕ, the condition $\rho_\phi + p_\phi = \rho_\phi(1+\omega_\phi) = 2E_k \geq 0$ allows for $\rho_\phi < 0$ if $\omega_\phi < -1$ as long as the total energy density $\rho \geq 0$ with the total equation of state parameter $\omega > -1$. In general, the phantom energy does not obey the WEC where it has $\rho_{ph} > 0$ but $\rho_{ph} + p_{ph} = \rho_{ph}(1+\omega_{ph}) = 2E_k < 0$ which means that the phantom field has a negative (non-canonical) kinetic term (De La Macorra & Germán 2004). Testing the classical energy conditions (Visser 1997b) shows that both the null and the dominant are satisfied all the time. The highly restrictive SEC $\rho + 3p \geq 0$ is violated as expected where we have a source of repulsive gravity represented by the negative pressure, which can accelerate cosmic expansion. Because the strong condition implies that gravity should always be attractive, it is expected to be violated during any accelerating epoch dominated by a repulsive gravity effect such as cosmic inflation. In addition to the ECs, the sound speed causality condition $0 \leq \frac{dp}{d\rho} \leq 1$ is satisfied only for $\epsilon = +1$.

The possible values of the parameters in the figures are restricted by observations, whereas the theoretical model should predict the same behavior obtained by observations. For that reason, we have to

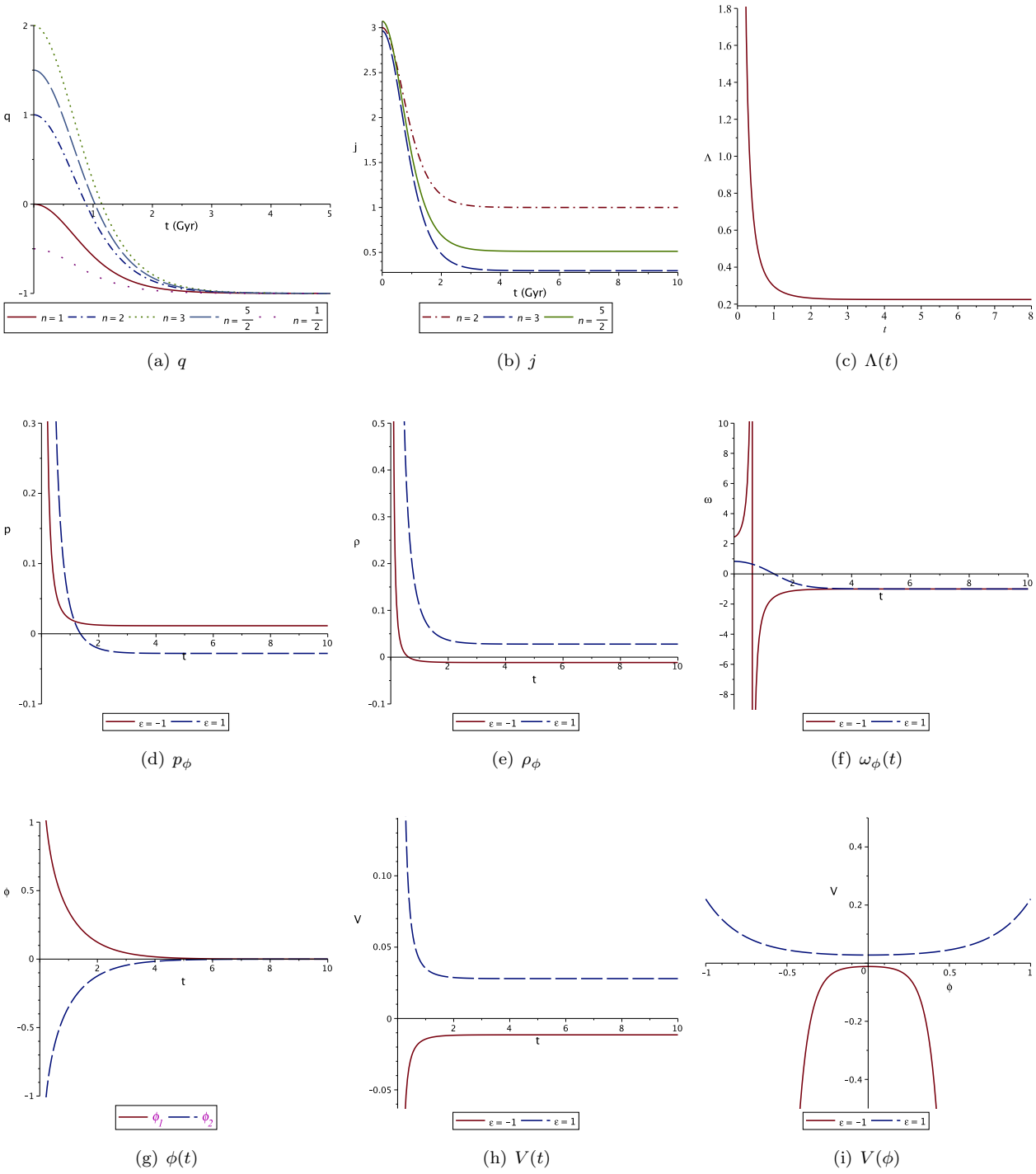

Fig. 1. The hyperbolic solution: (a) The deceleration parameter q shows a decelerating-accelerating cosmic transit. (b) The jerk parameter approaches unity at late-times where the model tends to a flat ΛCDM model. (c) The cosmological constant reaches a very tiny positive value at the current epoch. (d), (e) & (f) show p_ϕ, ρ_ϕ and ω_ϕ for $\epsilon = \pm 1$. For the phantom case, the energy density $\rho_\phi = E_k + V < 0$ when $\omega_\phi < -1$. (g) The two solutions of $\phi(t)$ obtained in Sen (2002). (h) The scalar potential evolution with time. (g) scalar potential V verses ϕ . Here $n = 2, \eta = 1, \phi_0 = 0, A = \lambda = \beta = \alpha = 0.1$, $\mu = 15$ for $\epsilon = -1$ and -15 for $\epsilon = 1$. The color figure can be viewed online.

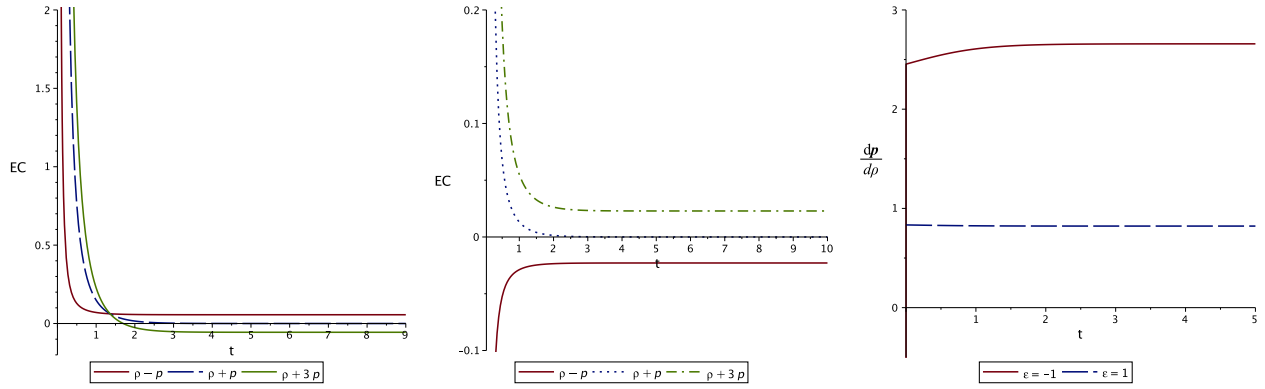

(a) $\epsilon = +1$ (b) $\epsilon = -1$ (c) dp/dt

Fig. 2. ECs and sound speed for the hyperbolic model. Superluminal sound speed for the phantom field. The color figure can be viewed online.

fine-tune the parameters' values to agree with observational results. We have taken $n = 2$ as it allows for a decelerating-accelerating cosmic transit and also allows the jerk parameter j to approach unity at late-times in agreement with the standard ΛCDM model. The constants A, η, and the integration constant ϕ_0 are arbitrary and we have chosen the values 0.1, 1 and 0 respectively without loss of generality. The value of the constant μ has been adjusted such that the quantity under the quadratic root in (19) is always positive for both normal and phantom fields. If we choose $\mu = 15$, then $(4\pi + \mu) > 0$ for the normal field where $\epsilon = +1$. For the phantom field with $\epsilon = -1$, we choose $\mu = -15$ so $(4\pi + \mu) < 0$ and then $-2\epsilon(4\pi+\mu) > 0$. As we have indicated in § 1.2, the zero value of λ does not agree with observations while $\lambda \neq 0$ behaves like the ΛCDM model at late-time. Based on this, we have chosen the non-zero value 0.1 for λ, β and α.

3. MODEL 2

Considering the second hybrid scale factor in (15), which also leads to the desired behavior of both q and j (Ahmed 2020), we get the expressions for H, q and j as:

$$H = \beta_1 + \frac{\alpha_1}{t}, q = \frac{\alpha_1}{(\beta_1 t + \alpha_1)^2} - 1,$$
$$j = \frac{{\alpha_1}^3 + (3\beta t - 3)\,{\alpha_1}^2 + \left(3\beta^2 t^2 - 3\beta t + 2\right)\alpha_1 + \beta^3 t^3}{(\beta\, t + \alpha_1)^3}. \tag{23}$$

For the scalar field and the potential, making use of (6), we get

$$\phi(t) = \pm\frac{\sqrt{-\epsilon(4\pi+\mu)\alpha_1}\ln t}{\epsilon(4\pi+\mu)} + C_1, \tag{24}$$

$$V(t) = \frac{\left(3\beta_1^2(\beta_0+1) + \alpha_0\beta_1 + \lambda_0\right)t^2}{-4(\mu+2\pi)t^2} + \frac{\left(6\alpha_1\beta_1\left(\beta_0+1\right) + \alpha_0\alpha_1\right)t}{-4(\mu+2\pi)t^2} + \frac{3\alpha_1^2\left(\beta_0+1\right) + \alpha_1}{-4(\mu+2\pi)t^2}, \tag{25}$$

$$V(\phi) = \frac{3\left(\beta_1^2+\alpha_1^2\right)(\beta_0+1) + \alpha_0\beta_1}{-4(\mu+2\pi)} + \frac{\xi^{-1}\alpha_1\left(6\beta_0\beta_1 + \alpha_0 + 6\beta_1\right) + \lambda_0 - \alpha_1}{-4(\mu+2\pi)}, \tag{26}$$

where $\xi = e^{\frac{\epsilon(|C_1-\phi)(4\mu+\pi)}{\sqrt{-\epsilon\alpha_1(4\mu+\pi)}}} = t(\phi)$. Plotting $t(\phi)$ leads to same graph for both signs. Also, both solutions for ϕ give the same expressions for ρ and p as

$$p(t) = \frac{-\alpha_1}{2\epsilon(4\pi+\mu)t^2} - V(t),\ \ \rho(t) = \frac{-\alpha_1}{2\epsilon(4\pi+\mu)t^2} + V(t). \tag{27}$$

In comparison to the first hyperbolic model, a similar behavior has been obtained for different parameters in the hybrid model. For $\epsilon = +1$, p_ϕ changes sign from positive to negative indicating a cosmic transit. $V(\phi)$, $V(t)$ and ρ_ϕ are > 0 where both $V(t)$ and $\rho_\phi \to \infty$ as $t \to 0$. For $\epsilon = -1$, p_ϕ is always positive while ρ_ϕ takes negative values when $\omega_\phi < -1$ with a negative scalar potential V. In the current work, we argue that the WEC is not violated for the two models considered with an instability at late-times for the second model, which now can be seen in Figure 4(c). The WEC, asserting that the total energy density ρ must be non-negative, is challenged by the notion that a negative term in the energy density can coexist if the overall energy density remains

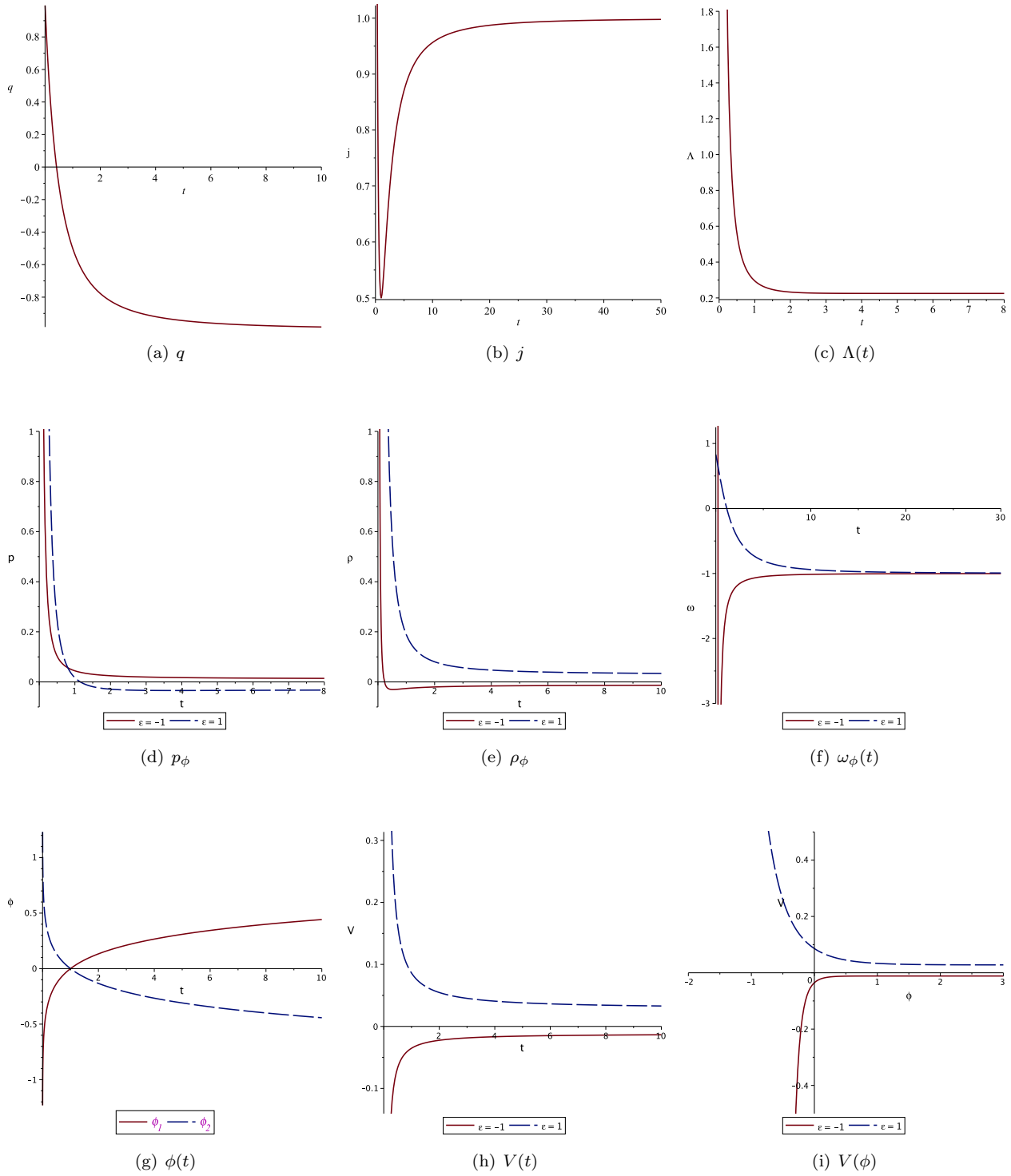

(a) q (b) j (c) $\Lambda(t)$

(d) p_ϕ (e) ρ_ϕ (f) $\omega_\phi(t)$

(g) $\phi(t)$ (h) $V(t)$ (i) $V(\phi)$

Fig. 3. The second model: (a) A decelerating-accelerating cosmic transit. (b) The jerk parameter $j = 1$ at late-times. (c) The cosmological constant reaches a very tiny positive value at the current epoch. (d), (e), & (f) show p_ϕ, ρ_ϕ and ω_ϕ for $\epsilon = \pm 1$. For the phantom case, the energy density $\rho_\phi < 0$ when $\omega_\phi < -1$. (g) The two solutions of $\phi(t)$ obtained in Sen (2002). (h) The scalar potential evolution with time. (g) Scalar potential V verses ϕ . Here $\alpha_1 = \beta_1 = 0.5$, $\eta = 1, \phi_0 = 0, A = \lambda = \beta = \alpha = 0.1$, $\mu = 15$ for $\epsilon = -1$ and -15 for $\epsilon = 1$. The color figure can be viewed online.

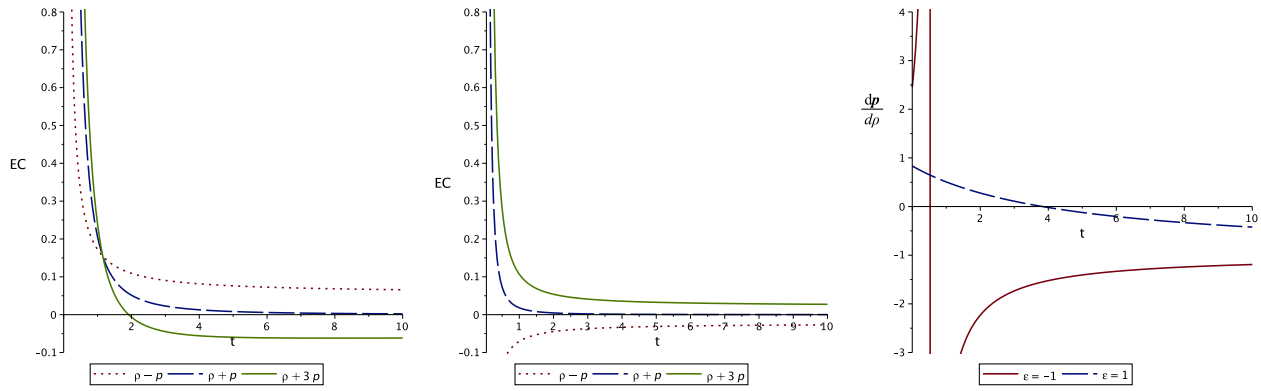

(a) $\epsilon = +1$ (b) $\epsilon = -1$ (c) dp/dt

Fig. 4. ECs and sound speed for the hybrid model. Negative sound speed for the phantom field. The color figure can be viewed online.

positive. Figure 4(c) shows that the sound speed causality condition is satisfied only within a specific time interval (for late-times) for a normal scalar field, while it is always violated for the phantom field. The phantom field, for both the hyperbolic and hybrid models, has a positive pressure $p_\phi > 0$ and a negative scalar potential $V(\phi)$. Also, its energy density $\rho_\phi = E_k + V$ takes negative values when the equation of state parameter $\omega_\phi < -1$. Figure 4(b) shows that $p_i + \rho_i \geq 0$ for both normal and phantom fields.

4. CONCLUSION

We revisited the scalar field cosmology in $f(R,T)$ gravity through two models. The main points can be summarized as follows:

- The evolution of the deceleration parameter indicates that a decelerating-accelerating cosmic transit exists in both models . The jerk parameter also tends to 1 at late-times, where the model tends to a flat ΛCDM model.
- The evolution of the varying cosmological constant in both models shows that it tends to a tiny positive value at the current epoch.
- The scalar field pressure p_ϕ in both models shows a sign flipping from positive to negative for a normal scalar field $\epsilon = +1$, but it's always positive for the phantom field $\epsilon = -1$.
- In both models, the scalar potential $V(\phi) > 0$ for $\epsilon = +1$ and < 0 for $\epsilon = -1$.
- For the normal field, $\rho_\phi > 0$ with no crossing to the phantom divide line for ω_ϕ. For the phantom field we have $\rho_\phi < 0$ when $\omega_\phi < -1$.
- Classical energy conditions have been tested for both cases. For the hyperbolic model, the sound speed causality condition $0 \leq \frac{dp}{d\rho} \leq 1$ is valid only for $\epsilon = +1$. For the hybrid model, this condition is satisfied only for a specific interval of time for the normal scalar field.

REFERENCES

Ahmed, N. 2009, Brane-worlds and low energy heterotic M-theory, PhD thesis, Newcastle University
Ahmed, N. 2010, AIPC 1316, Brane-world Gravity in Normal Coordinates, 269, https://doi.org/10.1063/1.3536438
Ahmed, N. 2020, MPLB, 35, 20500007, https://doi.org/10.1142/S0217732320500078
Ahmed, N. & Alamri, S. Z. 2018, RAA, 18, 123, https://doi.org/10.1088/1674-4527/18/10/123
_____. 2019a, IJGMM, 16, 1950159-104, https://doi.org/10.1142/S0219887819501597
_____. 2019b, Ap&SS, 364, 100, https://doi.org/10.1007/s10509-019-3590-4
Ahmed, N., Bamba, K., & Salama, F. 2020, IJGMM, 17, 1750075, https://doi.org/10.1142/S0219887820500759
Ahmed, N., Fekry, M., & Kamel, T. M. 2023, CaJph, 101, 712, https://doi.org/10.1139/cjp-2022-0338
Ahmed, N. & Kamel, T. M. 2021, IJGMM, 18, 1850070A, https://doi.org/10.1142/S0219887821500705
Ahmed, N. & Pradhan, A. 2020, NewA, 80, 101406, https://doi.org/10.1016/j.newast.2020.101406
_____. 2022, InJPh, 96, 301, https://doi.org/10.1007/s12648-020-01948-4
Alexandre, J. & Polonyi, J. 2021, PhRvD, 103, 105020, https://doi.org/10.1103/PhysRevD.103.105020

Alves, M. E. S., Miranda, O. D., & de Araujo, J. C. N. 2011, PhLB, 700, 283, https://doi.org/10.1016/j.physletb.2011.05.022
Arkani-Hamed, N., Cheng, H.-C., Luty, M. A., & Mukohyama, S. 2004, JHEP, 2004, 074, https://doi.org/10.1088/1126-6708/2004/05/074
Aygün, S., Aktaş, C., Sahoo, P. K., & Bishi, B. K. 2018, GrCo, 24, 302, https://doi.org/10.1134/S0202289318030039
Banerjee, N. & Pavón, D. 2001, CQGra, 18, 593, https://doi.org/10.1088/0264-9381/18/4/302
Barceló, C., Visser, M., & Ahluwalia, D. V. 2002, IJMPD, 11, 1553, https://doi.org/10.1142/S0218271802002888
Barrow, J. D. & Parsons, P. 1995, PhRvD, 52, 5576, https://doi.org/10.1103/PhysRevD.52.5576
Basilakos, S., Lima, J. A. S., & Solà, J. 2013, IJMPD, 22, 1342008, https://doi.org/10.1142/S021827181342008X
Basilakos, S., Plionis, M., & Solà, J. 2009, PhRvD, 8, 083511, https://doi.org/10.1103/PhysRevD.80.083511
Bengochea, G. R. & Ferraro, R. 2009, PhRvD, 79, 124019, https://doi.org/10.1103/PhysRevD.79.124019
Bertolami, O. & Martins, P. 2000, PhRvD, 61, 4007, https://doi.org/10.1103/PhysRevD.61.064007
Caldwell, R. R. 2002, PhLB, 545, 23, https://doi.org/10.1016/S0370-2693(02)02589-3
Chervon, S. V., Zhuravlev, V. M., & Shchigolev, V. K. 1997, PhLB, 398, 269, https://doi.org/10.1016/S0370-2693(97)00238-4
Chiba, T., Okabe, T., & Yamaguchi, M. 2000, PhRVD, 62, 3511, https://doi.org/10.1103/PhysRevD.62.023511
De Felice, A. & Tsujikawa, S. 2010, LRR, 13, 3, https://doi.org/10.12942/lrr-2010-3
De La Macorra, A. & Germán, G. 2004, IJMPD, 13, 1939, https://doi.org/10.1142/S0218271804006061
Demianski, M., Piedipalumbo, E., Sawant, D., & Amati, L. 2017, A&A, 598, 113, https://doi.org/10.1051/0004-6361/201628911
Dymnikova, I. & Khlopov, M. 2000, MPLA, 15, 2305, https://doi.org/10.1142/S0217732300002966
_____. 2001, EPJC, 20, 139, https://doi.org/10.1007/s100520100625
Ellis, G. F. & Madsen, M. S. 1991, CQGra, 8, 667, https://doi.org/10.1088/0264-9381/8/4/012
Felder, G., Frolov, A., Kofman, L., & Linde, A. 2002, PhRvD, 66, 3507, https://doi.org/10.1103/PhysRevD.66.023507
Ferraro, R. & Fiorini, F. 2007, PhRvD, 75, 084031, https://doi.org/10.1103/PhysRevD.75.084031
Gagnon, J.-S. & Lesgourgues, J. 2011, JCAP, 09, 026, https://doi.org/10.1088/1475-7516/2011/09/026
Garriga, J. & Vilenkin, A. 2000, PhRvD, 61, 083502, https://doi.org/10.1103/PhysRevD.61.083502
Gómez-Valent, A. & Solà, J. 2015, MNRAS, 448, 2810, https://doi.org/10.1093/mnras/stv209
Gómez-Valent, A., Solà, J., & Basilakos, S. 2015, JCAP, 2015, 004, https://doi.org/10.1088/1475-7516/2015/01/004
Gonçalves, T. B., Rosa, J. L., & Lobo, F. S. 2022, PhRvD, 105, 064019, https://doi.org/10.1103/PhysRevD.105.064019
González-Díaz, P. F. 2004, PhLB, 586, 1, https://doi.org/10.1016/j.physletb.2003.12.077
Harko, T., Lobo, F. S. N., Nojiri, S., & Odintsov, S. D. 2011, PhRvD, 84, 024020, https://doi.org/10.1103/PhysRevD.84.024020
Kamenshchik, A., Moschella, U., & Pasquier, V. 2001, PhLB, 511, 265, https://doi.org/10.106/S0370-2693(01)00571-8
Khoury, J., Ovrut, B. A., Steinhardt, P. J., & Turok, N. 2001, PhRvD, 64, 123522, https://doi.org/10.1103/PhysRevD.64.123522
Lima, J. A. S., Basilakos, S., & Solà, J. 2013, MNRAS, 431, 923, https://doi.org/10.1093/mnras/stt220
Lopez, J. L. & Nanopoulos, D. V. 1996, MPLA, 11, 1, https://doi.org/10.1142/S02117732396000023
Maeder, A. 2017, ApJ, 849, 158, https://doi.org/10.3847/1538-4357/aa92cc
Maharaj, S. D., Goswami, R., Chervon, S. V., & Nikolaev, A. V. 2017, MPLA, 32, 1750164, https://doi.org/10.1142/S0217732317501644
Nemiroff, R. J., Joshi, R., & Patla, B. R. JCAP, 06, 006, https://doi.org/10.1088/1475-7516/2015/06/006
Nojiri, S. & Odintsov, S. D. 2006, PhRvD, 74, 086009, https://doi.org/10.1103/PhysRevD.74.086009
Nojiri, S., Odintsov, S. D., Oikonomou, V. K., & Paul, T. 2020, PhRvD, 102, 023540, https://doi.org/10.1103/PhysRevD.102.023540
Nojiri, S., Odintsov, S. D., & Paul, T. 2021, Symm, 13, 928, https://doi.org/10.3390/sym13060928
_____. 2022a, PHLB, 825, 136844, https://doi.org/10.1016/j.physletb.2021.136844
_____. 2022b, AtOO, 35, 100, https://doi.org/10.1134/S1024856023010062
Nojiri, S., Odintsov, S. D., & Tretyakov, P. V. 2008, PThPS, 172, 81, https://doi.org/10.1143/PTPS.172.81
Odintsov, S. D., Paul, T., Banerjee, I., Myrzakulov, R., & SenGupta, S. 2021, PDU, 33, 100864, https://doi.org/10.1016/j.dark.2021.100864
Oikonomou, V. K., Pan, S., & Nunes, R. C. 2017, IJMPA, 32, 1750129, https://doi.org/10.1142/S0217751X17501299
Pan, S. 2018, MPLA, 33, 1850003, https://doi.org/10.1142/S0217732318500037
Percival, W. J., Baugh, C. M., Bland-Hawthorn, J., et al. 2001, MNRAS, 327, 1297, https://doi.org/10.1046/j.1365-8711.2001.04827.x
Perlmutter, S., Aldering, G., Goldhaber, G., et al. 1999, ApJ, 517, 565, https://doi.org/10.1086/307221

Saharian, A., Avagyan, R., de Mello, E. B., et al. Ap, 65, 427, https://doi.org/10.1007/s10511-022-09751-1

Sazhin, M. V. & Sazhina, O. S. 2016, ARep, 60, 425, https://doi.org/10.1134/S1063772916030136

Sen, A. 2002, JHEP, 07, 065, https://doi.org/10.1088/1126-6708/2002/07/065

Sen, A. A. & Sethi, S. 2002, PHLB, 532, 159, https://doi.org/10.1016/S0370-2693(02)01547-2

Silva, J. G. & Santos, A. F. 2013, EPJC, 73, 2500, https://doi.org/10.1140/epjc/s10052-013-2500-0

Steinhardt, P. J. & Turok, N. 2002, PhRvD, 65, 126003, https://doi.org/10.1103/PhysRevD.65.126003

Stern, D., Jimenez, R., Verde, L., Kamionkowski, M., & Stanford, S. A. 2010, JCAP, 02, 008, https://doi.org/10.1088/1475-7516/2010/02/008

Tonry, J. L., Schmidt, B. P., Barris, B., et al. 2003, ApJ, 594, 1, https://doi.org/10.1086/376865

Tsujikawa, S. 2013, CQGra, 30, 214003, https://doi.org/10.1088/0264-9381/30/21/214003

Visser, M. 1997a, Sci, 276, 88, https://doi.org/10.1126/science.276.5309.88

_____. 1997b, PhRvD, 56, 7578, https://doi.org/10.1103/PhysRevD.56.7578

Westmoreland, S. 2013, Energy Conditions and Scalar Field Cosmology, Master of Science Thesis, Kansas State University

Nasr Ahmed: Mathematics and Statistics Department, Faculty of Science, Taibah University, Saudi Arabia.
Nasr Ahmed and Tarek M. Kamel: Astronomy Department, National Research Institute of Astronomy and Geophysics, Helwan, Cairo, Egypt.

Revista Mexicana de Astronomía y Astrofísica, **60**, 227–239 (2024)

https://doi.org/10.22201/ia.01851101p.2024.60.02.03

NEW CATALOG OF DISTANCES TO PLANETARY NEBULAE BASED ON *GAIA* PARALLAXES AND STATISTICAL DISTANCES

Diego Hernández-Juárez[1], Mónica Rodríguez[2], and Miriam Peña[1]

Received December 6 2023; accepted March 6 2024

ABSTRACT

We have developed a method to determine the most reliable distances for a large group of planetary nebulae. For this purpose, we analyze the distances obtained from *Gaia* parallaxes and three determinations of statistical distances. The most reliable distance is derived for 2211 objects, and uncertainties for these distances are calculated in a homogeneous way. Using our most reliable distances, we compare the distributions of Galactic heights of hydrogen-poor and hydrogen-rich central stars of planetary nebulae. We find that [WR] central stars are closer to the Galactic plane than hydrogen-rich central stars and than other hydrogen-poor central stars. The latter have a similar distribution to hydrogen-rich central stars, which is significantly different from the one of [WR] central stars. This result disagrees with the proposed evolutionary sequence for hydrogen-poor central stars.

RESUMEN

Desarrollamos un método que determina las distancias más fiables de un grupo amplio de nebulosas planetarias a partir de las distancias obtenidas con paralajes de *Gaia* y tres determinaciones de distancias estadísticas. Calculamos las distancias más fiables para 2211 objetos y les asignamos incertidumbres. Con estas distancias, comparamos las distribuciones de alturas sobre el plano galáctico de objetos con estrellas ricas y pobres en hidrógeno. Encontramos que las nebulosas planetarias con estrellas [WR] están más cerca del plano galáctico que aquellas con estrellas ricas en hidrógeno y con otras estrellas pobres en hidrógeno. Estas últimas se distribuyen de manera similar a los objetos con estrellas ricas en hidrógeno, y de forma significativamente distinta que los objetos con estrellas [WR]. Esto está en desacuerdo con la secuencia evolutiva propuesta para estrellas centrales pobres en hidrógeno.

Key Words: parallaxes — planetary nebulae: general — stars: distances

1. INTRODUCTION

In the study of planetary nebulae (PNe) and stellar evolution, it is necessary to have accurate distances to calculate parameters such as luminosity, gaseous mass, and others. Several methods can be used to obtain distances to PNe, and they can be grouped into two classes: individual and statistical methods. Individual methods provide direct estimates of the distances to PNe. Some examples of individual distance estimate methods are trigonometric parallaxes, spectroscopic distances, expansion parallaxes, or the extinction method (see the review by Kwitter & Henry 2022, for other methods and examples). On the other hand, statistical estimates rely on the assumption that PNe have certain properties in common, or that they fulfill some empirical relation between two parameters, from one of which the distance can be derived. Some examples are the Shklovsky (1956) method, based on a constant ionized mass for all PNe, and the relation between radio continuum surface brightness and physical radius of the nebula, first explored by van de Steene & Zijlstra (1995).

Statistical estimates are usually considered less reliable than individual estimates, but this is not always true. In some cases, statistical estimates have

[1]Instituto de Astronomía, Universidad Nacional Autónoma de México, Ciudad de México, México.

[2]Instituto Nacional de Astrofísica, Óptica y Electrónica, Luis Enrique Erro 1, Tonantzintla, Puebla, México.

errors comparable to those of the individual estimates (Buckley & Schneider 1995). Besides, very different distances are sometimes obtained with different individual methods for some objects (Zhang 1993; Ali et al. 2022).

The only individual method that is model independent and that in principle can lead to small uncertainties for a large quantity of PNe heliocentric distances is the trigonometric parallax of *Gaia*. *Gaia* is a space probe launched by the European Space Agency at the end of 2013 (Hodgkin et al. 2013; Gaia Collaboration et al. 2016, 2021), and has provided trigonometric parallaxes for billions of objects (Lindegren et al. 2021). This has been a milestone in distance estimation for the astronomical community. However, not all of these distances are entirely reliable. Some parallaxes are negative or have very large errors. In those cases, Bayesian statistics must be used to infer distances from parallaxes (Bailer-Jones et al. 2021). However, the Bayesian estimates can be highly dependent on the assumed prior. Besides, even when the parallaxes are positive and have small errors, they could result from spurious solutions (Fabricius et al. 2021). In addition, it can be complicated to identify the central star of a PN in the *Gaia* database. Chornay & Walton (2021) and González-Santamaría et al. (2021) have developed methods to identify the central stars of PNe, but the methods are not perfect and there may be misidentifications.

Due to these problems, we decided to revise the distances obtained with parallaxes from the Early Data Release 3 (EDR3) of *Gaia*, in order to decide when it is necessary to use other distance estimates. The aim of this work is to determine the most reliable distance estimate for a large sample of PNe. We explore several sets of statistical distances and the distances derived from *Gaia* EDR3, compare them with each other, and create a procedure to determine the most reliable distance for each PN and its uncertainty.

This paper is organized as follows. In § 2 we comment on the catalogs of statistical distances we will be using, in § 3 we explore the *Gaia* parallaxes and their problems, and in § 4 we compare the statistical distance estimates with the distances implied by the parallaxes. In § 5 we present the procedure we follow to determine the most reliable distance estimate for each object, and in § 6 we compare our most reliable estimates with individual distance estimates available for several dozens of objects. In § 7 we use our most reliable distances to analyze the Galactic height distribution of hydrogen-poor and hydrogen-rich PNe. Finally, we present our conclusions in § 8.

2. STATISTICAL DISTANCES

We use the catalogs of statistical distances of Zhang (1995), Stanghellini & Haywood (2018) and Frew et al. (2016). We choose these catalogs because they have the largest number of objects and are based on a variety of methods to calculate the distance, although some of them use the same observational data. The methods are described below.

Zhang (1995) uses two methods to estimate the distance. These methods are based on new calibrations of previously known empirical relations between the ionized mass and the brightness temperature with the intrinsic radius of PNe. The ionized mass and the brightness temperature are obtained from the flux at 5 GHz. To calibrate both methods, Zhang (1995) uses a sample of 134 Galactic PNe with known individual distances determined by Zhang (1993). He provides the mean of the distances implied by both methods as his best estimate. His final sample contains 647 PNe.

The distances listed by Stanghellini & Haywood (2018) are based on the approach of Stanghellini et al. (2008), who re-calibrate the method of Daub (1982) using 70 Magellanic Cloud PNe. This method assumes that density-bounded PNe, which are optically thin to Lyman continuum radiation, have the same ionized mass, whereas both optically thick radiation-bounded PNe and bipolar PNe show a relation between their ionized mass and their surface brightness. Like Zhang (1995), Stanghellini et al. (2008) calculate all their parameters using the PN angular sizes and the fluxes observed at 5 GHz. The final sample of Stanghellini & Haywood (2018) contains distances for 900 PNe.

Frew et al. (2016) use an empirical relation between the Hα surface brightness and the intrinsic radius of PNe to estimate their distances. They calibrate this relation using data for 322 PNe, of which 206 are Galactic and 126 are extragalactic objects. They find that optically-thick and optically-thin PNe have somewhat different behaviors and provide three relations, one for the full sample, one for optically thick objects, and one for optically thin PNe. They obtain distances for 1133 PNe, and for 515 of them they have the information required to estimate their optical thickness so that they can assign to these objects better distance estimates based on the relations for either optically thick or optically thin nebulae.

2.1. *Final Sample of Statistical Distances*

Since Frew et al. (2016) and Zhang (1995) have more than one distance estimate for each PN, we must decide which one to use. In the case of the distances of Frew et al. (2016), we use those obtained with the formulas for optically thick and thin nebulae whenever possible (515 objects). Otherwise, we use the distance obtained with the general formula (618 objects).

We have compared the three distance estimates of Zhang (1995), the ones based on the ionized mass and the brightness temperature, and the mean of these two estimates, with the distances of Stanghellini & Haywood (2018) and Frew et al. (2016). We find that the distances based on the brightness temperature method are in much better agreement with those of the other authors. For the other two sets of distances, 20−40% of the objects have distances that disagree by more than 75% from the distances of Stanghellini & Haywood (2018) and Frew et al. (2016), whereas the brightness temperature method leads to this kind of disagreement for only 5 to 8% of the PNe. Hence, we use here only the distances of Zhang (1995) that are based on the brightness temperature method.

3. DISTANCES FROM *GAIA* PARALLAXES

In principle, the distances derived from *Gaia* parallaxes, p, will be reliable when the objects are well identified and when the parallaxes are positive, do not have a considerable error, and are corrected for systematic errors. Besides, we must consider the quality of the fit to the astrometric observations. The RUWE (Renormalised Unit Weight Error) parameter is used to measure this quality (Lindegren et al. 2018). RUWE values above 1.4 suggest that there are problems with the astrometric solutions[3], and we will not use those parallaxes here.

Identifying the central stars of PNe can be complicated, as the stars are faint, they can be hidden behind nebular material, and there might be several candidates in the central region of the nebula. Besides, some of the candidates may not be real objects; they can be *Gaia* misidentifications arising from the effects of the surrounding gas and its nebular emission. Chornay & Walton (2021) and González-Santamaría et al. (2021) have developed methods to identify the central stars of PNe in *Gaia* EDR3. Both methods follow similar procedures: they look for the objects closest to the geometric center of the PNe and refine the selection by using colors, with González-Santamaría et al. (2021) giving more importance to the latter criterion.

The catalogs by Chornay & Walton (2021) and González-Santamaría et al. (2021) contain in total 1140 objects with positive parallax and RUWE lower than 1.4, and they have in common 872 objects. From this sample in common, 25 objects have different identifications in the two catalogs, and eight of these 25 objects have estimates of statistical distances. If we use the identifications of Chornay & Walton (2021) to determine the distances implied by the parallaxes (with the procedure described below), the differences between these distances and the statistical distances have an average lower than 0.05 dex, with a maximum difference of 0.5 dex. When the same procedure is done using the identifications of González-Santamaría et al. (2021), an average difference of more than 0.3 dex is obtained, with a minimum difference of 0.1 dex and a maximum of 0.7 dex. Therefore, we decided to use the identifications by Chornay & Walton (2021) for the 872 objects in common, but we will also use the unique identifications of Chornay & Walton (2021) for 190 objects, and those of González-Santamaría et al. (2021) for 78 objects.

Once the objects are identified, the next step is to correct the parallaxes for systematic errors. We applied these *zero-point* corrections using an available Python code that requires information on the source magnitudes, colors, and celestial positions to interpolate the values of the corrections (Lindegren et al. 2021).

Some objects in the *Gaia* database have negative parallaxes or considerable errors. To be able to use the information for these objects, it is necessary to use a Bayesian approach, as Bailer-Jones et al. (2021) do. These authors calculate a distance estimate for each object with parallax in *Gaia* EDR3 using Bayesian statistics. Bailer-Jones et al. (2021) use a prior based on a Milky Way model from the mock stellar catalog of Rybizki et al. (2020), which is based on a three-dimensional model of the Galaxy. These distances should not be used indiscriminately, since for objects with large parallax errors, the distances converge to the prior (Oudmaijer et al. 2022). In this work, we will not use the results derived from negative parallaxes, and the distances based on parallaxes with large errors will be used with caution, as described below.

There are problems for the *Gaia* parallaxes that cannot be completely solved, such as the spurious parallax solutions. Fabricius et al. (2021) mention

[3] https://gea.esac.esa.int/archive/documentation/GDR2/Gaia_archive/chap_datamodel/sec_dm_main_tables/ssec_dm_ruwe.html.

that even in the region of parallaxes with errors smaller than 20%, spurious parallax solutions can exist. To arrive at this result, they look for those objects with $p/\delta p < -5$, where they are sure that *Gaia* is giving wrong results. Fabricius et al. (2021) find that at least 1.6% of the objects have spurious solutions in this region, and consider that the same percentage will be present in the region of positive parallaxes with errors lower than 20%.

In the next section, we explore further the problems that can arise from the use of *Gaia* parallaxes in order to decide in which cases we should not use these data.

4. COMPARISON OF STATISTICAL AND *GAIA* DISTANCES

We have selected a sample of 411 PNe that have positive parallaxes in *Gaia* and the three estimates of statistical distances discussed above. For these objects, we are going to compare the two distances implied by the *Gaia* parallax ($D_{\rm G}$) —the one implied by the inverse of parallax, $1/p$, and the Bayesian estimate, $D_{\rm B}$— with the statistical estimates ($D_{\rm S}$) by Frew et al. (2016), $D_{\rm FPB16}$, Stanghellini & Haywood (2018), $D_{\rm SH18}$, and Zhang (1995), $D_{\rm Z95}$. This comparison is presented in Figure 1, where we plot the ratio $D_{\rm S}/D_{\rm G}$ as a function of the relative error of the parallax, $\delta p/p$. We use stars for the distances derived from the inverse of the parallax and squares for the Bayesian distances. The statistical catalogs are identified with colors in the online version: blue for the distances of Frew et al. (2016), orange for those of Stanghellini & Haywood (2018), and brown for the distances of Zhang (1995).

We can see in Figure 1 that the three statistical distance estimates generally agree with each other. In fact, if we compare every possible pair of statistical distances (1744 pairs for 788 PNe), most of the differences (68%, the traditional 1-σ result) are smaller than ≈ 0.07 dex, and 85% of them are smaller than 0.2 dex. If we now compare the statistical values with those implied by *Gaia*, we see in Figure 1 that when the parallax errors are smaller than 15% (the vertical dotted line in Figure 1), $D_{\rm G}$ and $D_{\rm S}$ show a broad agreement for most of the objects, whereas for errors larger than 15%, the differences between $D_{\rm G}$ and $D_{\rm S}$ are increasingly larger. On the other hand, for parallax errors $\approx$15%, most of the differences (68%) between $1/p$ and $D_{\rm B}$ are smaller than 0.07 dex, and all of them are smaller than 0.2 dex, but, as Figure 1 shows, $1/p$ is an increasingly unreliable distance estimate as the parallax errors increase.

There are some objects in Figure 1 that show large differences between $D_{\rm G}$ and $D_{\rm S}$, even in the region of small parallax errors. An example is Abell 19, the object with the smallest parallax error in the figure. This is likely a misidentification of the PN central star. In fact, Chornay & Walton (2020) argue that the centrally located star is probably a nearby field star. Other objects with large differences are likely to be also misidentifications or to have spurious parallaxes.

Therefore, we will use 15% as the defining line between the regions where $1/p$ is a good estimate of distance ($\delta p/p \leq 0.15$) and where the Bayesian estimates are a better choice ($\delta p/p > 0.15$). Besides, we will only use the parallax distances when they show agreement (better than or equal to 0.07 dex, see §5) with any of the statistical distance estimates, or when they are the only available distance estimates. Our approach is described below.

5. PROCEDURE FOR DETERMINING THE MOST RELIABLE DISTANCE FOR EACH PN AND ASSIGNMENT OF UNCERTAINTIES

In order to obtain an extended catalog with as many distances as possible, we have compiled a sample of PNe that have at least one of the distance estimates considered here: the statistical distances of Frew et al. (2016), Stanghellini & Haywood (2018), and Zhang (1995), and the distances obtained from *Gaia*. In those cases where the PNe have several distance estimates and include the *Gaia* parallax, we consider that the inverse of the parallax will provide the best distance estimate when the parallax errors are small, below 15%, and when there is a good agreement between this distance and any of the statistical distance estimates. If this is not the case, we will use the median of the available values as the best distance estimate. When the parallax errors are larger than 15%, we will only use the Bayesian estimate in our calculations. The procedure and the criteria we use are defined below.

5.1. *Inverse of the Parallax*

As discussed in § 4, the distance obtained from the inverse of the parallax is very similar to the Bayesian estimate when the parallax error is small, $\delta p/p < 0.15$. We use in this case the inverse of the parallax as the *Gaia* distance estimate. However, this distance must be similar to the statistical estimates in order to avoid problems with misidentifications and spurious parallaxes. Hence, in order to assign this distance to a given object, we require it to fulfill the conditions: $\delta p/p < 0.15$ and $\log(pD_{\rm S}) \leq 0.07$ for at least one statistical distance. There are 89 PNe that satisfy these requirements and they are classified as case A in what follows.

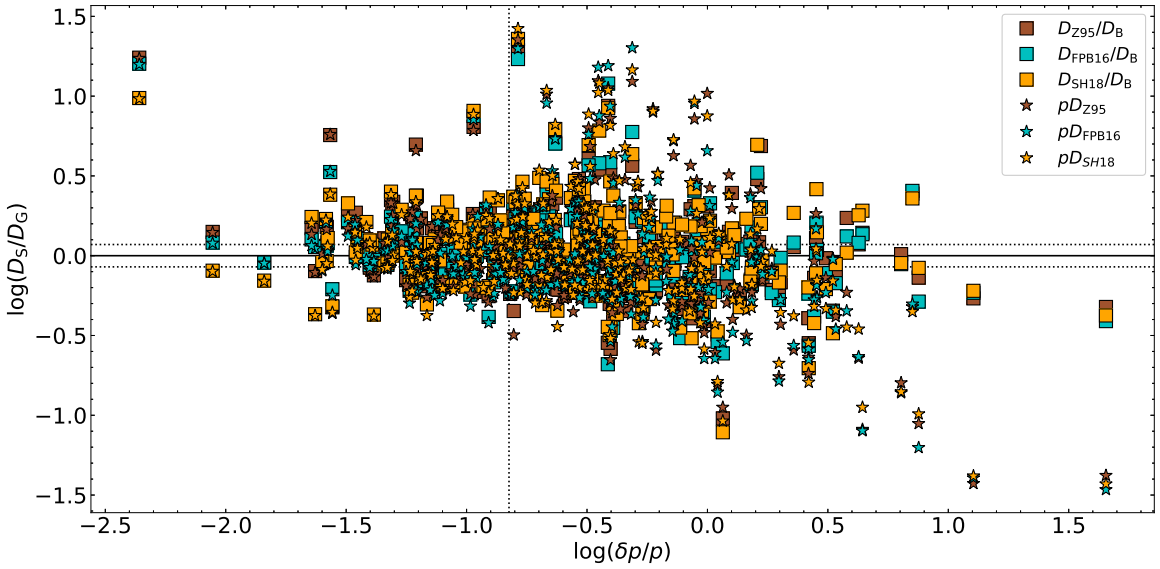

Fig. 1. Ratio of the statistical distances, D_S, and the distances derived from *Gaia* parallaxes, D_G, as a function of the relative error in the parallax, $\delta p/p$, for PNe that have statistical distances in the three catalogs that we are considering here: Frew et al. (2016, blue symbols, D_{FPB16}), Stanghellini & Haywood (2018, orange symbols, D_{SH18}), and Zhang (1995, brown symbols, D_{Z95}). Stars are used for the comparison with distances derived from the inverse of *Gaia* parallaxes and squares for the comparison with the Bayesian estimates D_B. The vertical dotted line indicates a parallax error of 15%, and the horizontal dotted lines correspond to differences of ± 0.07 dex. The color figure can be viewed online.

In order to assign uncertainties to those distances, we explored three different approaches: we studied the uncertainties implied by the parallax errors; those implied by the Bayesian method (Bailer-Jones et al. 2021); and those obtained by comparing the inverse of the parallax with the second-farthest statistical distance to the inverse of parallax. The first two approaches led to uncertainties smaller than 10% for 68% of the objects, whereas for the last approach the 68th percentile was equal to 40%. We decided to use the more conservative approach and assigned this last uncertainty to these distances. We have decided to use this approach because, even if the inverse of parallax shows some agreement with one statistical distance, the *Gaia* parallaxes might still be affected by all the problems discussed in §3.

5.2. *Median of the Available Distances*

We will use the median of the available distances when there is more than one distance estimate, but no parallax is available, or the parallax error is too large, or the inverse of the parallax implies a distance that is very different from all the statistical distances.

For the case of large parallax errors, we have to decide whether to include the Bayesian estimate D_B in our calculations. In order to use this estimate, we require it to fulfill the same condition imposed on the inverse of the parallax in § 5.1: $\log(D_S/D_B) \leq 0.07$ for at least one statistical distance. If this condition is met, our most reliable distance is given by the median of the statistical values and the Bayesian value (177 objects, case B in what follows). If not, our most reliable distance is given by the median of the statistical values (635 objects, case C in what follows). In order to minimize the effect of very anomalous distances on the final results, the median is calculated for the logarithmic distances.

We explored two possible ways to assign uncertainties to the median values: the Bayesian uncertainty and the uncertainty obtained by comparing the median of the distances with the most extreme distance. Both distributions are very similar, and the 68th percentile is at $\approx$ 40%. Hence we assign 40% uncertainties to these distance estimates. We do not use the Bayesian uncertainties because our estimate is not necessarily based on the Bayesian distance and this distance might still be affected by all the problems discussed in § 3.

5.3. *PNe with only One Distance Estimate*

Some PNe have a single distance estimate, either obtained from the *Gaia* parallax (the inverse of the parallax for errors below 15% and the Bayesian

estimate for larger errors) or from one statistical method. Besides, some PNe have just one statistical distance estimate and it disagrees with the results implied by the *Gaia* parallax; this implies that we only use the one statistical value to assign the distance to these objects. In total, there are 1310 PNe whose distances are based on a single distance estimate, which are labeled as case D in what follows.

In order to provide uncertainties for these distances, we explored the uncertainties assigned by Bailer-Jones et al. (2021) to their Bayesian estimates for those PNe where we use this distance estimate. These uncertainties are smaller than $\approx 60\%$. We also studied the distribution of distance differences for PNe that have only two distance estimates. We find that 68% of these differences are smaller than 60%. Since the results for PNe with only one distance estimate can be even less reliable, we decided to assign them a larger error. Hence, if the object has a single distance estimate, we assign a relative error of 70%.

5.4. *Final Results*

In Table 1 in Appendix A we present our final results for 2211 PNe. The table lists the distances provided in the three statistical catalogs we are using: Frew et al. (2016, $D_{\rm FPB16}$), Stanghellini & Haywood (2018, $D_{\rm SH18}$), and Zhang (1995, $D_{\rm Z95}$). Besides, Table 1 also shows the Bayesian distance of Bailer-Jones et al. (2021, $D_{\rm B}$), the distance implied by the *Gaia* parallax and its uncertainty, our final distance estimate, $D_{\rm tw}$, with its uncertainty, and the method used to determine this final estimate. The complete table can be found in the online version.

In the final results, we use some distances from *Gaia* for 959 objects (the inverse of the parallax or the Bayesian distance). We use the inverse of the parallax because it agrees, to within ± 0.07 dex, with some statistical distance in 89 cases. We use the median of statistical distances and Bayesian distances (because the latter agrees, to within ± 0.07 dex, with some statistical distance) in 177 cases. In 693 cases, the *Gaia* estimate is the only available distance estimate. Finally, for 1075 objects, the distances are based on one statistical distance or the median of the available statistical distances. Thus, the *Gaia* data are used in 43% of the cases and in some objects we only use statistical estimates even though the *Gaia* parallax is available.

In summary, we use the *Gaia* distances for 959 PNe, statistical distances for 1075 PNe, and the median of one Gaia distance and the statistical distances for 177 objects. In total, we have distances for 2211 PNe.

6. COMPARISON WITH INDIVIDUAL DISTANCE MEASUREMENTS

In this section, we compare our most reliable distances (those that are based on more than one distance estimate) with some individual distance estimates. We use the individual distance estimates for 48 PNe of the calibration sample of Frew et al. (2016); 9 PNe from Yang et al. (2016); 2 PNe from Schönberner et al. (2018); 2 PNe from Gómez-Gordillo et al. (2020); and 12 PNe from Dharmawardena et al. (2021). The results of Dharmawardena et al. (2021) are extinction distances based on optical and radio data. For some objects they provide two estimates of the extinction and these can be very different. Hence, we only use their results for PNe that have two estimates of the extinction that differ by less than 60%. The individual distance estimates that we are using are based on a variety of methods and we select only those distances that have uncertainties smaller than 25%. Some objects have two distance estimates and in this case we use the mean value. The final comparison sample has 65 PNe.

In Figure 2, we show the comparison between our final distances, $D_{\rm tw}$, and the individual distances, $D_{\rm ind}$, as a function of $D_{\rm ind}$. We also show this comparison for the three statistical distance estimates that we are using: $D_{\rm FPB16}$ (Frew et al. 2016)[4], $D_{\rm SH18}$ (Stanghellini & Haywood 2018), and $D_{\rm Z95}$ (Zhang 1995). Finally, the bottom panel compares the distances implied by the *Gaia* parallaxes (the inverse of the parallax for errors lower than 15% and the Bayesian estimate for larger errors) with the individual estimates for the 52 objects that had this information. All these parallaxes are positive and have RUWE values lower than 1.4. Three horizontal dotted lines at zero and 60% differences are plotted in Figure 2 for reference. Besides, the values of the median and mean absolute deviation of the plotted results are shown in each panel of Figure 2.

We can see in Figure 2 that our final distances, the three statistical distance estimates, and the results from *Gaia* broadly agree with the individual estimates for this sample of PNe, with our results and those of Frew et al. (2016) showing the best agreement. In fact, 68% of our results have agreements better than 40%, the uncertainty that we have assigned to the distances plotted in the top panel of Figure 2.

[4]Please note that in this case we are comparing the individual distances used by Frew et al. (2016) to calibrate their statistical method with the statistical distances they obtain for the same objects.

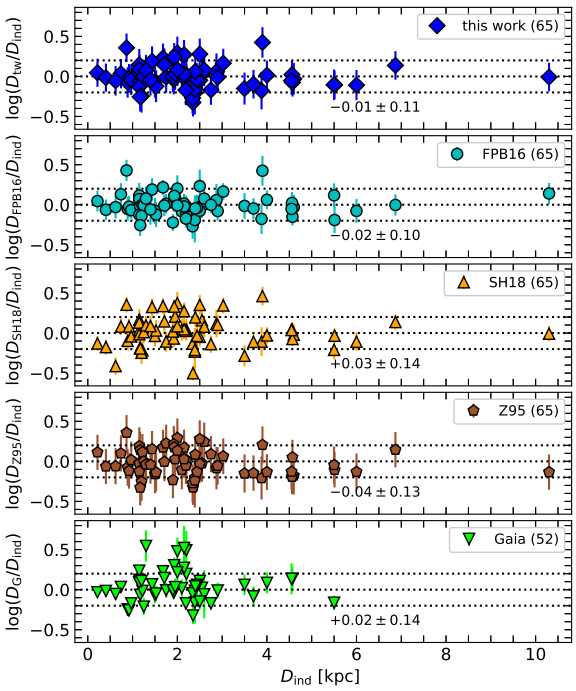

Fig. 2. Ratio of the distances derived in this work ($D_{\rm tw}$, top panel) and the statistical distances of Frew et al. (2016, $D_{\rm FPB16}$, second panel), Stanghellini & Haywood (2018, $D_{\rm SH18}$, third panel), and Zhang (1995, $D_{\rm Z95}$, fourth panel) to some individual distance estimates, $D_{\rm ind}$, as a function of $D_{\rm ind}$ for 65 PNe. The same comparison is performed for 52 of these PNe that have positive *Gaia* parallaxes and RUWE values lower than 1.4 (bottom panel). The horizontal dotted lines correspond to differences of zero and 60%. The median and the mean absolute deviation of the plotted values are shown in each panel. The color figure can be viewed online.

7. DISTANCES TO THE GALACTIC PLANE FOR H-RICH AND H-POOR CENTRAL STARS OF PNE

The spectral types of central stars of planetary nebulae (CSPNe) can give us information about the processes that they have undergone and about their evolutionary state. There are several types of CSPNe, and most of them can be grouped into two major groups: hydrogen-rich (HR) and hydrogen-poor (HP) CSPNe (Mendez 1991).

The origin of HP CSPNe is not entirely clear. It has been proposed that during their post-AGB phase, some stars experience a very late thermal pulse, which returns them to the AGB phase (Iben 1984), where the hydrogen is hidden or lost by winds. CSPNe that go through this event are known as *born-again* stars. This is the most studied origin, but so far only eight HP CSPNe have been proven to be *born-again* (Jacoby et al. 2020). Fang et al. (2014) and Górny & Tylenda (2000) mention that most CSPNe are unlikely to have a very late thermal pulse. Therefore, this phenomenon does not seem responsible for the known HP CSPNe, which amount to about 30% of the total CSPNe that have a well-defined spectral type (Weidmann et al. 2020).

Another possible scenario to explain the existence of HP stars is that they descend from a close binary system (see, e.g., Tylenda & Gorny 1993; De Marco et al. 2003). However, in many cases it is difficult to prove that the central star is part of a binary system, and as a result, it is not clear how many CSPNe could be converted to HP CSPNe in this way.

The origin of HP CSPNe could be related to the mass of the progenitor, either because a massive progenitor could solve some problems with the *born-again* phenomenon (Acker et al. 1996) or because of some undefined phenomena related to other possible scenarios. Heap (1982) propose that [WR] CSPNe, which are HP, come from a massive progenitor because they have higher luminosities than other types. This hypothesis has been explored using chemical abundances, in particular the N/O ratio. Gorny & Stasińska (1995) find no evidence that [WR] CSPNe come from massive progenitors, but García-Rojas et al. (2013) estimate that about half of their sample of [WC] CSPNe had initial masses larger than 4 $M_{\odot}$. However, determining the mass of the progenitor star using chemical abundances can be quite complicated due to the uncertainties involved in calculating abundances.

A better option is to study the distances to the Galactic plane, which should be smaller for massive progenitors. Some comparisons of the Galactic distributions of [WR] CSPNe (and other HP CSPNe) and HR CSPNe have been made. For example, Acker et al. (1996) compare the distribution of Galactic latitudes of 47 [WR] CSPNe with those of their total sample of 350 HR and HP ([WR] CSPNe included) CSPNe, and do not find significant differences. On the other hand, Weidmann & Gamen (2011) and Weidmann et al. (2020) use larger samples (397 and 443 CSPNe, respectively) to compare the distributions of Galactic latitude of HP (including [WR]) and HR CSPNe. Weidmann & Gamen (2011) have 205 HP objects (106 of them [WR]) and Weidmann et al. (2020) have 153 HP CSPNe (with 123 [WR]). Both works conclude that HP CSPNe are found at lower Galactic latitudes than HR CSPNe.

The different results found by the three studies might be due to the different sample sizes or could arise from the fact that Acker et al. (1996) make their comparison between [WR] and all CSPNe, and not between two different groups (such as HR and [WR] CSPNe). Nevertheless, a problem shared by the three works is that they do not consider the distributions of heliocentric distances of their objects. Górny et al. (2004) find that [WR] CSPNe are concentrated towards the Galactic center. This means that the different Galactic distributions of [WR] and HR objects could lead to differences in their distributions of Galactic latitudes.

Peña et al. (2013) compare distances to the Galactic plane of [WR] CSPNe and HR CSPNe using a total sample of 77 CSPNe (46 of them [WR]). They note that [WR] CSPNe are more concentrated towards the Galactic plane than HR CSPNe. Although Peña et al. (2013) consider distances, their sample is small.

We study here the distribution of distances to the Galactic plane ($z_{\rm G}$) using our distance catalog and the spectral types compiled by Weidmann et al. (2020). We only use CSPNe of this catalog that have well-defined spectral types and that can be clearly classified as HP or HR. We calculate $z_{\rm G}$ for 81 HP CSPNe and 187 HR CSPNe. In the HP CSPNe group, we distinguish between [WR] CSPNe and non-[WR] CSPNe, such as PG 1159 and DO white dwarfs.

Figure 3 shows the resulting distributions of $z_{\rm G}$ of [WR], HP non-[WR] and HR CSPNe. We can see in this figure that [WR] CSPNe are indeed closer to the Galactic plane than HR CSPNe, as previously found by Peña et al. (2013). A Kolmogorov-Smirnov test (Press et al. 2007) shows that the $z_{\rm G}$ distributions of [WR] CSPNe and HR CSPNe are significantly different, with a p-value of 0.008 (the probability of obtaining differences equal or greater than those observed if both distributions come from the same parent distribution). The $z_{\rm G}$ distribution of HP non-[WR] is also different from that of [WR] CSPNe (p-value equal to 0.01), but compatible with the distribution of HR CSPNe (p-value of 0.2).

However, most of our non-[WR] HP objects are close to the Sun, probably because of their lower brightness. Besides, as found by Górny et al. (2004), our [WR] CSPNe are more abundant towards the Galactic center. Therefore, we restricted our sample to objects with heliocentric distances smaller than 5 kpc in order to avoid as much as possible introducing biases in the distributions of $z_{\rm G}$. The [WR] CSPNe closer to the Galactic center are excluded with this

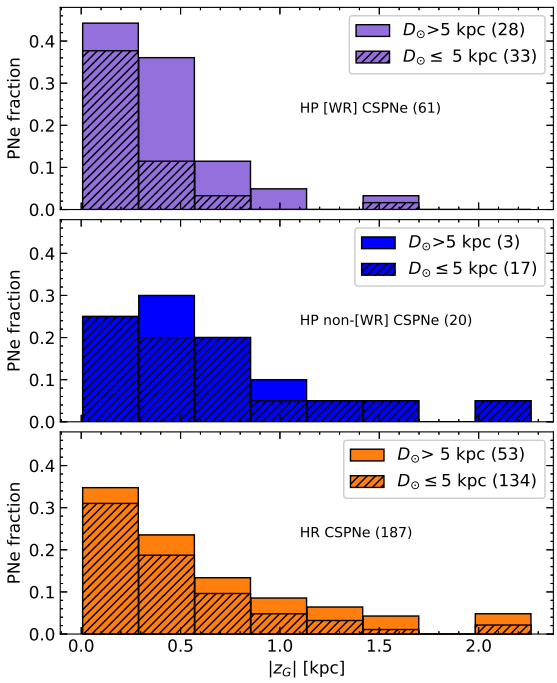

Fig. 3. Distributions of distances to the galactic plane ($z_{\rm G}$) for [WR] CSPNe (top panel), HP non-[WR] CSPNe (middle panel) and HR CSPNe (bottom panel) for objects at any heliocentric distance and for objects with heliocentric distances smaller than 5 kpc (hatched areas). The number of objects in each category is shown within parentheses. The color figure can be viewed online.

condition, but we still retain an acceptable amount of HP non-[WR] CSPNe. These objects are shown in Figure 3 with the hatched areas. The $z_{\rm G}$ for these PNe are shown in Table 2 in Appendix B. In the first column of this table the object is indicated, in the second column the group, in the third column the spectral type and in the last column, $z_{\rm G}$ and its uncertainty. The complete table is published in the online version.

In this restricted sample, there are 134 HR CSPNe, 17 HP non-[WR] CSPNe (including 12 PG 1159, one O(He) and four WD) and 33 [WR] CSPNe. Like the massive Pop. I WR stars, the [WR] stars are classified into two groups (Crowther et al. 1998): the early [WC] stars (types [WC 4] and [WO 4-1] and the late [WC] stars (types [WC 12-5]). In the sample with distances smaller than 5 kpc, there are 6 late [WC] and 24 early [WC] CSPNe.

A Kolmogorov-Smirnov test for the restricted sample shows that the difference in the $z_{\rm G}$ distributions of [WR] and HR CSPNe is even more significant (p-value of 0.0004); the differences between HP non-[WR] and [WR] CSPNe are still significant

(p-value of 0.025), and the distributions of HP non-[WR] and HR CSPNe are also significantly different (p-value of 0.048) instead of compatible, as found with the full sample. The median values of $|z_{\rm G}|$ are 0.55 kpc for HP non-[WR] objects, 0.34 kpc for HR CSPNe, and 0.19 kpc for [WR] CSPNe.

The different result obtained in the comparison between the distributions of $|z_{\rm G}|$ for HP non-[WR] and HR CSPNe for heliocentric distances below 5 kpc and for the full sample, is due to the effect of two HP non-[WR] with spectral type O(He) that have the largest Galactic heights in the HP non-[WR] group, $|z_{\rm G}| = 1.6$, 2.0 kpc. If we remove from this group the five non-PG 1159 objects and apply the Kolmogorov-Smirnov test, we find that the distributions of PG 1159 and HR CSPNe are again compatible (p-value of 0.98). On the other hand, the PG 1159 objects still have a significantly different distribution of $|z_{\rm G}|$ from the [WR] CSPNe (p-value of 0.012).

As Peña et al. (2013) did, we find that [WR] CSPNe seem to be related to massive progenitors. However, this is not true for the other HP CSPNe, like the PG 1159 objects. This result disagrees with the commonly assumed evolutionary sequence for HP CSPNe, in which late [WR] stars evolve to early [WR] stars and these, in turn, evolve to PG 1159 stars (Acker et al. 1996; Górny & Tylenda 2000; Werner & Herwig 2006; Weidmann et al. 2020). It seems clear from our results that the [WR] CSPNe are not the progenitors of the other HP CSPNe.

8. CONCLUSIONS

We have developed a method to determine the most reliable distance for 2211 PNe using the distances derived from *Gaia* data and three catalogs of statistical distances (Zhang 1995; Frew et al. 2016; Stanghellini & Haywood 2018). We show that the *Gaia* distances are not always reliable for CSPNe and they must be used with caution. We also assign uncertainties to our final distances using a homogeneous approach. We find that our distances and those of Frew et al. (2016) show the best agreements with individual distance estimates. With the next data releases from *Gaia*, we can expect to increase the number of PNe with well determined distances and to improve the reliability of our catalog.

We use our catalog to study the distributions of distances to the Galactic plane of HR and HP CSPNe. We find that there are differences between these distributions, arising from the lower heights above the Galactic plane of [WR] CSPNe. On the other hand, HP non-[WR] stars, especially the PG 1159 objects, have a distribution similar to the one followed by HR CSPNe. These results suggest that [WR] CSPNe have more massive progenitors and that there does not seem to exist an evolutionary sequence from [WR] CSPNe to PG 1159 stars, as commonly believed.

We thank the anonymous referee for her/his very useful comments. This work received financial support of Grant UNAM PAPIIT IN111423. DH-J acknowledges a scholarship from CONAHCYT, Mexico. This work has made use of data from the European Space Agency (ESA) mission *Gaia* (`https://www.cosmos.esa.int/gaia`), processed by the *Gaia* Data Processing and Analysis Consortium (DPAC, `https://www.cosmos.esa.int/web/gaia/dpac/consortium`). Funding for the DPAC has been provided by national institutions, in particular the institutions participating in the *Gaia* Multilateral Agreement.

APPENDICES

A. TABLE OF AVAILABLE DISTANCES AND OUR CHOSEN DISTANCES

TABLE 1

AVAILABLE DISTANCES AND OUR MOST RELIABLE DISTANCE (ALL IN KPC) FOR OUR SAMPLE ON PNE. THE COMPLETE TABLE IS PUBLISHED IN THE ONLINE VERSION*

PN G	$D_{\rm Z95}$	$D_{\rm FBP16}$	$D_{\rm SH18}$	$D_{\rm B}$	$1/p$	$\delta p/p$	$D_{\rm tw}$	Case[1]
000.0−01.0	···	···	···	8.20	1.22	0.48	8.2 ± 5.7	D
000.0−02.5	···	···	···	6.73	1.82	1.62	6.7 ± 4.7	D
000.0−06.8	···	6.97	···	8.39	21.28	0.72	7.0 ± 4.9	D
000.1+02.6	···	···	···	4.88	3.82	0.62	4.9 ± 3.4	D
000.1+17.2	8.87	9.46	14.51	7.82	34.56	2.28	9.2 ± 3.7	B
000.1−01.1	6.05	···	8.63	···	···	···	7.2 ± 2.9	C
000.1−01.7	···	6.95	···	···	···	···	7.0 ± 4.9	D
000.1−02.3	···	7.62	5.58	···	···	···	6.5 ± 2.6	C
000.1−05.6	···	6.19	7.92	5.66	2.94	0.79	6.2 ± 2.5	B
000.1−08.0	···	···	···	6.73	4.39	2.70	6.7 ± 4.7	D
000.2+01.7	···	8.50	···	···	···	···	8.5 ± 5.9	D
000.2+06.1	···	9.79	···	···	···	···	9.8 ± 6.9	D
000.2−01.9	6.77	4.89	8.80	9.03	6.10	0.68	6.8 ± 2.7	C
000.2−01.9a	···	···	···	6.40	5.77	0.49	6.4 ± 4.5	D
000.3+03.2	···	···	···	6.96	1.54	1.70	7.0 ± 4.9	D
000.3+04.2	···	···	···	6.61	5.57	1.34	6.6 ± 4.6	D
000.3+07.3	···	···	···	6.85	1.81	2.21	6.9 ± 4.8	D
000.3+12.2	3.49	2.35	3.97	2.46	3.07	0.13	3.1 ± 1.2	A
000.3−01.6	···	10.79	···	···	···	···	10.8 ± 7.6	D
000.3−02.8	···	6.63	···	···	···	···	6.6 ± 4.6	D
000.3−03.4	···	···	···	6.12	3.07	0.67	6.1 ± 4.3	D
000.3−04.2	···	···	···	5.68	6.54	0.29	5.7 ± 4.0	D
000.3−04.2	···	···	···	5.68	6.54	0.29	5.7 ± 4.0	D
000.3−04.6	7.54	5.80	9.65	···	···	···	7.5 ± 3.0	C
000.4+02.2	···	···	···	6.53	84.65	25.82	6.5 ± 4.6	D
000.4+04.4	···	5.57	···	6.17	5.59	2.21	5.6 ± 3.9	D
000.4−01.9	···	5.10	9.50	···	···	···	7.0 ± 2.8	C
000.4−02.9	7.36	4.96	7.96	7.63	2.72	0.51	7.5 ± 3.0	B
000.5+01.9	···	8.55	···	···	···	···	8.6 ± 6.0	D
000.5−03.1	···	6.39	9.08	7.69	0.28	0.20	7.6 ± 3.0	C
000.5−03.1	···	6.39	9.08	7.69	0.28	0.20	7.6 ± 3.0	C

[1]A: Inverse of parallax; B: Median of statistical estimate and Bayesian estimate; C: Median of statistical estimates; D: One useful distance estimate.

*The full table can be viewed online in `https://www.astroscu.unam.mx/rmaa/RMxAA..60-1/PDF/RMxAA..60-1_dhernandez-IV-Table1.pdf`.

B. TABLE OF DISTANCES TO THE GALACTIC PLANE FOR CSPNE WITH HELIOCENTRIC DISTANCES LOWER THAN 5 KPC.

TABLE 2

DISTANCES TO THE GALACTIC PLANE FOR CSPNE WITH HELIOCENTRIC DISTANCES SMALLER THAN 5 KPC. THE COMPLETE TABLE IS PUBLISHED IN THE ONLINE VERSION*

PN G	Type	Spectral Type	z_G (kpc)
002.2−09.4	[WR]	[WO 4]pec	-0.74 ± 0.30
002.4+05.8	[WR]	[WO 3]	0.116 ± 0.046
003.1+02.9	[WR]	[WO 3]	0.146 ± 0.058
011.9+04.2	[WR]	[WO 4]pec	0.26 ± 0.10
017.9−04.8	[WR]	[WO 2]	-0.40 ± 0.16
020.9−01.1	[WR]	[WO 4]pec	-0.044 ± 0.017
027.6+04.2	[WR]	[WC 7-8]	0.31 ± 0.13
029.2−05.9	[WR]	[WO 4]	-0.26 ± 0.10
048.7+01.9	[WR]	[WC 4]	0.147 ± 0.059
061.4−09.5	[WR]	[WO 2]	-0.29 ± 0.12
064.7+05.0	[WR]	[WC 9]	0.193 ± 0.077
089.0+00.3	[WR]	[WO 3]	0.0104 ± 0.0042
089.8−05.1	[WR]	[WR]	-0.44 ± 0.17
093.9−00.1	[WR]	[WC 11]	-0.0073 ± 0.0029
103.7+00.4	[WR]	[WR]	0.033 ± 0.013
120.0+09.8	[WR]	[WC 8]	0.214 ± 0.086
130.2+01.3	[WR]	[WO 4]	0.059 ± 0.023
189.1+19.8	[WR]	[WO 1]	0.61 ± 0.24
216.0+07.4	[WR]	[WC 4]:	0.44 ± 0.18
243.3−01.0	[WR]	[WO 1]	-0.052 ± 0.021
278.1−05.9	[WR]	[WO 2]	-0.229 ± 0.092
286.3+02.8	[WR]	[WO 3]	0.203 ± 0.081
300.7−02.0	[WR]	[WC 5-6]	-0.161 ± 0.064
306.4−00.6	[WR]	[WO 3]pec	-0.026 ± 0.010
307.2−03.4	[WR]	[WO 1]	-0.040 ± 0.016
309.0−04.2	[WR]	[WC 9]	-0.28 ± 0.11
309.1−04.3	[WR]	[WO 4]	-0.157 ± 0.063
319.6+15.7	[WR]	[WR]	0.49 ± 0.20
320.9+02.0	[WR]	[WC 5-6]	0.092 ± 0.037
327.1−02.2	[WR]	[WC 9]	-0.183 ± 0.073
346.2−08.2	[WR]	[WN 3]	-0.43 ± 0.17
350.1−03.9	[WR]	[WC 4-5]	-0.173 ± 0.069
358.3−21.6	[WR]	[WO 3]	-1.48 ± 0.59
042.5−14.5	HP non-[WR]	PG 1159	-0.78 ± 0.31

*The full table can be viewed online in `https://www.astroscu.unam.mx/rmaa/RMxAA..60-1/PDF/RMxAA..60-1_dhernandez-IV-Table2.pdf`.

REFERENCES

Acker, A., Gorny, S. K., & Cuisinier, F. 1996, A&A, 305, 944, https://doi.org/10.48550/arXiv.astro-ph/9505138

Ali, A., Algarni, E., Mindil, A., et al. 2022, RAA, 22, 085013, https://doi:10.1088/1674-4527/ac7545

Bailer-Jones, C. A. L., Rybizki, J., Fouesneau, M., et al. 2021, AJ, 161, 147, https://doi:10.3847/1538-3881/abd806

Buckley, D. & Schneider, S. E. 1995, ApJ, 446, 279, https://doi:10.1086/175787

Chornay, N. & Walton, N. A. 2020, A&A, 638, 103, https://doi.org/10.1051/0004-6361/202037554

Chornay, N. & Walton, N. A. 2021, A&A, 656, 110, https://doi:10.1051/0004-6361/202142008

Crowther, P. A., De Marco, O., & Barlow, M. J. 1998, MNRAS, 296, 367, https://doi:10.1046/j.1365-8711.1998.01360.x

Daub, C. T. 1982, ApJ, 260, 612, https://doi.org/10.1086/160283

De Marco, O., Sandquist, E. L., Mac Low, M.-M., et al. 2003, RMxAC, 18, 24

Dharmawardena, T. E., Barlow, M. J., Drew, J. E., et al. 2021, MNRAS, 501, 6156, https://doi.org/10.1093/mnras/staa3820

Fabricius, C., Luri, X., Arenou, F., et al. 2021, A&A, 649, 5, https://doi.org/10.1051/0004-6361/202039834

Fang, X., Guerrero, M. A., Marquez-Lugo, R. A., et al. 2014, ApJ, 797, 100, https://doi.org/10.1088/0004-637X/797/2/100

Frew, D. J., Parker, Q. A., & Bojičić, I. S. 2016, MNRAS, 455, 1459, https://doi.org/10.1093/mnras/stv1516

Gaia Collaboration, Brown, A. G. A., Vallenari, A., et al. 2021, A&A, 649, 1, https://doi:10.1051/0004-6361/202039657

Gaia Collaboration, Prusti, T., de Bruijne, J. H. J., et al. 2016, A&A, 595, 1, https://doi:10.1051/0004-6361/201629272

García-Rojas, J., Peña, M., Morisset, C., et al. 2013, A&A, 558, 122, https://doi:10.1051/0004-6361/201322354

Gómez-Gordillo, S., Akras, S., Gonçalves, D. R., et al. 2020, MNRAS, 492, 4097, https://doi.org/10.1093/mnras/staa060

González-Santamaría, I., Manteiga, M., Manchado, A., et al. 2021, A&A, 656, 51, https://doi.org/10.1051/0004-6361/202141916

Gorny, S. K. & Stasińska, G. 1995, A&A, 303, 893

Górny, S. K. & Tylenda, R. 2000, A&A, 362, 1008

Górny, S. K., Stasińska, G., Escudero, A. V., et al. 2004, A&A, 427, 231, https://doi.org/10.1051/0004-6361:20047064

Heap, S. R. 1982, IAUS 99, Subluminous Wolf-rayet stars: observations, 423

Hodgkin, S. T., Wyrzkowski, L., Blagorodnova, N., & Koposov, S. 2013, RSPTA, 371, 20120239, https://doi.org/10.1098/rsta.2012.0239

Iben, I. 1984, ApJ, 277, 333, doi.org/10.1086/161700

Jacoby, G. H., Hillwig, T. C., & Jones, D. 2020, MNRAS, 498, 114, https://doi.org/10.1093/mnrasl/slaa138

Kwitter, K. B. & Henry, R. B. C. 2022, PASP, 134, 022001, https://doi:10.1088/1538-3873/ac32b1

Lindegren, L., Hernández, J., Bombrun, A., et al. 2018, A&A, 616, 2, https://doi.org/10.1051/0004-6361/201832727

Lindegren, L., Klioner, S. A., Hernández, J., et al. 2021, A&A, 649, 2, https://doi:10.1051/0004-6361/202039709

Lindegren, L., Bastian, U., Biermann, M., et al. 2021, A&A, 649, 4, https://doi.org/10.1051/0004-6361/202039653

Mendez, R. H. 1991, IAUS 145, Evolution of Stars: the Photospheric Abundance Connection, ed. G. Michaud and A. V. Tutukov (Kluwer Academic Publishers, Dordrecht), 375

Oudmaijer, R. D., Jones, E. R. M., & Vioque, M. 2022, MNRAS, 516, 61, https://doi.org/10.1093/mnrasl/slac088

Peña, M., Rechy-García, J. S., & García-Rojas, J. 2013, RMxAA, 49, 87, https://doi:10.48550/arXiv.1301.3657

Press, W., Teukolsky, S. A., Vetterling, W. T., Flannery, B. P., 2007, Numerical recipes 3rd edition: The art of scientific computing (Cambridge, MA: CUP)

Rybizki, J., Demleitner, M., Bailer-Jones, C., et al. 2020, PASP, 132, 074501, https://doi.org/10.1088/1538-3873/ab8cb0

Schönberner, D., Balick, B., & Jacob, R. 2018, A&A, 609, 126, https://doi.org/10.1051/0004-6361/201731788

Shklovsky, I. S. 1956, AZh, 33, 222

Stanghellini, L. & Haywood, M. 2018, ApJ, 862, 45, https://doi.org/10.3847/1538-4357/aacaf8

Stanghellini, L., Shaw, R. A., & Villaver, E. 2008, ApJ, 689, 194, https://doi.org/10.1086/592395

Tylenda, R. & Gorny, S. K. 1993, AcA, 43, 389

van de Steene, G. C. & Zijlstra, A. A. 1995, A&A, 293, 541

Weidmann, W. A. & Gamen, R. 2011, A&A, 526, 6, https://doi.org/10.1051/0004-6361/200913984

Weidmann, W. A., Mari, M. B., Schmidt, E. O. et al. 2020, A&A, 640, 10, https://doi.org/10.1051/0004-6361/202037998

Werner, K. & Herwig, F. 2006, PASP, 118, 183, https://doi.org/10.1086/500443

Yang, A. Y., Tian, W. W., Zhu, H., et al. 2016, ApJS, 223, 6, https://doi.org/10.3847/0067-0049/223/1/6

Zhang, C. Y. 1993, ApJ, 410, 239, https://doi:10.1086/172740

_____. 1995, ApJS, 98, 659, https://doi.org/10.1086/192173

Diego Hernández-Juárez and Miriam Peña: Instituto de Astronomía, Universidad Nacional Autónoma de México, Apdo. Postal 70264, Ciudad de México, México.
Mónica Rodríguez: Instituto Nacional de Astrofísica, Óptica y Electrónica, Luis Enrique Erro 1, Tonantzintla 72840, Puebla, México.

Revista Mexicana de Astronomía y Astrofísica, **60**, 241–260 (2024)

https://doi.org/10.22201/ia.01851101p.2024.60.02.04

X-RAY ANALYSIS OF SEYFERT 1 GALAXIES WITH OPTICAL POLARIZATION: A TEST FOR UNIFICATION MODELS[5]

M. Gudiño[1], E. Jiménez-Bailón[1,2], A. L. Longinotti[1], M. Guainazzi[3], M. Cerviño[4], and A. C. Robleto-Orús[1]

Received November 3 2023; accepted March 7 2024

ABSTRACT

In accordance with the AGN Unified Model, observed polarization can be related to the orientation of the line of sight with respect to the torus. AGN X-ray emission arises from the central region and carries the imprints of the obscuring material. We aim to test a unified scheme based on optical polarization using X-ray absorption. Using the XMM-Newton data of 19, optically polarized Seyfert 1 sources, we develop a systematic analysis by fitting a baseline model to test the presence of X-ray neutral or ionized (warm) absorption. We find that 100% of the polar-polarized sources show the presence of absorption, with 70% favoring the presence of a warm absorber. In contrast, the equatorial-polarized sources show a fraction of absorbed spectra of 75%, with only 50% consistent with the presence of a warm absorber.

RESUMEN

De acuerdo con el Modelo Unificado AGN, la polarización observada se puede relacionar con la orientación de la línea de visión con respecto al toro. La emisión de rayos X de un AGN surge de la región central y lleva las huellas del material oscurecedor. Nuestro objetivo es probar un esquema unificado basado en polarización óptica mediante absorción de rayos X. Utilizando los datos XMM-Newton de 19 fuentes Seyfert 1 ópticamente polarizadas, desarrollamos un análisis sistemático para ajustar un modelo de referencia y probar la presencia de absorción neutra o ionizada. Encontramos que el 100% de las fuentes con polarización polar muestran la presencia de absorción, y el 70% favorece la presencia de un absorbedor tibio. Por el contrario, las fuentes con polarización ecuatorial muestran una fracción de espectros absorbidos del 75%, y sólo el 50% es consistente con la presencia de un absorbente tibio.

Key Words: galaxies: active — galaxies: nuclei — galaxies: Seyfert — X-rays: galaxies

1. INTRODUCTION

A galaxy is said to host an active nucleus (AGN) when it exhibits a highly luminous central region, comparable to, or even brighter than, the integrated light of the stars in the galaxy, with a luminosity extending throughout the entire electromagnetic spectrum. The AGN emission arises from a central compact region that consists of a supermassive black hole (SMBH) surrounded by an accretion disk. A characteristic feature present in some AGN spectra are optical broad emission lines, (full width half maximum (FWHM) $\approx 1000-20000$ km s^{-1}, Netzer 2015), from a high-density gas region that is excited and ionized by the central engine, located at $0.1-1$ pc from it, (Kaspi et al. 2005), the Broad Line Region (BLR). The observation of optical narrow lines (FWHM $\approx 300-1000$ km s^{-1}) indicates the presence of another gas region of lower density and ionization known as the Narrow Line Region (NLR); this region

[1]Instituto de Astronomía, Universidad Nacional Autónoma de México.
[2]Quasar Science Resource S.L. for the European Space Agency (ESA), European Space Astronomy Centre (ESAC).
[3]ESA, European Space Research and Technology Centre (ESTEC).
[4]Centro de Astrobiología (CAB), CSIC-INTA.
[5]Based on observations obtained with XMM-Newton, an ESA science mission with instruments and contributions directly funded by ESA Member States and NASA.

extends to a scale of $\approx$ 100 pc and up to 1000 pc, (Netzer 2015; Beckmann & Shrader 2012).

The absence of broad emission lines in some AGN spectra is explained by postulating that an optically thick toroidal structure made of neutral gas and dust extending up to $\approx$ 10 pc, surrounds the BLR and central engine, with the ultimate effect of obscuring the direct AGN emission from the observer view. The Unified Model, (Antonucci & Miller 1985; Antonucci 1993), states that different features observed in AGN spectra depend on the orientation of this obscuring torus relative to our line-of-sight. From this orientation effect, we distinguish two main AGN types. Type 1 are sighted directly into the central region, showing both narrow and broad optical emission lines. Type 2 are sighted through the torus, so the central region and BLR get obscured, and only narrow emission lines are detected. A more detailed classification is provided by looking to specific spectral lines, e.g. a Narrow Line Seyfert 1 (NLSy1) source shows a much narrower Hβ line compared to a classical type 1 AGN (FWHM < 2000 kms^{-1}) and an unusually strong Fe II line (Osterbrock & Pogge 1985; Komossa 2008), thus providing a wide range of AGN types. For this work, we will adopt the simplest classification with the aim to relate it to optical polarization.

We focus our work on optically polarized type 1 Seyfert galaxies (Sy). The findings of polarized broad emission lines in type 2 Sy, e.g. NGC 1068 (Miller et al. 1991), suggested that the BLR is present but obscured from the line-of sight, lending support to the Unification Model. In general, the polarization position angle (PA) of type 2 Sy is found to be perpendicular to the main axis of the system, i.e. the rotation axis of the accretion disk. In this case, the polar-polarization region, *PL-pol*, corresponds to the well-established AGN ionization cones that trace the kpc-scale NLR (Smith et al. 2002, 2004, hereafter S02, S04). In the framework envisaged by Smith, a second scattering region is postulated to account for the observations on polarized type 1 Sy, (Smith et al. 2005, hereafter S05); in this case the polarization position angle is parallel to the main axis of the system. This so-called equatorial-polarization region, *EQ-pol*, is co-planar to the accretion disk. However, we note that additional contributions from the nuclear components may determine the type of observed polarization, e.g. the accretion disk, as proposed by (Piotrovich et al. 2023), bringing more complexity to the original classification proposed by Smith. As an example, studies report that the optical lines from the *EQ-pol* region show the effects of the rotating motion of the scattering region emitting the gas, which are visible as a characteristically S-shaped profile detected in the polarization position angle, (Afanasiev & Popović 2015; Afanasiev et al. 2019).

Interestingly, Smith reported a list of type 1 sources with polarization properties similar to those of type 2, i.e. *PL-pol*, (S02,S05). Smith proposed a unified scheme addressed to relate these observations with the orientation of the torus: a Sy 1 with *PL-pol* represents an intermediate type between a Sy 2 with *PL-pol* and a Sy 1 with *EQ-pol*. This, in turn, would imprint different observing properties due to the absence (*EQ-pol* Sy 1) or presence (*PL-pol* Sy 1) of absorbing material co-spatial with the outer layers of the torus on the line of sight. In this framework, the X-ray regime is especially appropriate for assessing the role of the torus absorption effect.

X-ray emission in AGN arises from the upscattering of UV photons, emitted by the accretion disk, in a surrounding corona of hot electrons, (Haardt & Maraschi 1991). The primary feature of a Seyfert X-ray spectrum is a *power-law continuum*, extending up to $100 - 200$ keV and with photon indices varying between 1.4 and 2.3, (Piconcelli, E. et al. 2005; She et al. 2017). At 6.4 keV, we can observe the prominent *Kα Fe emission line*, (Ricci et al. 2014b), typically present in all Seyfert galaxies, produced via fluorescence mechanisms by reprocessing of the primary emission in circumnuclear neutral material. At energies < 2 keV, the spectrum may exhibit emission that exceeds the flux of the main continuum, called *soft-excess*, and sometimes interpreted as thermal radiation from the accretion disk, with black body temperatures in the range of $0.1 - 1.0$ keV, (Petrucci et al. 2018). Analogously to the optical, in the X-rays we can distinguish between type 1 and 2 through absorption. This distinction is mainly based on the detection of hydrogen column densities that can be as low as $N_H \approx 10^{19}$ cm^{-2}, for a type 1 and $N_H \approx 10^{23}$ cm^{-2} or higher in the case of type 2, the main dividing value being $N_H = 10^{22}$ cm^{-2}, (Beckmann & Shrader 2012). This refers only to absorption by neutral material, the so called *cold absorber*. Absorption by ionized material, the *warm absorber*, can also be present in the line-of-sight, and is generally observed as an outflow (100-2000 km s^{-1}) of gas with column densities of $N_H \approx 10^{21}$ to $10^{22.5}$ cm^{-2} and ionization parameter of $\log \xi = -1$ to 3 erg cm s^{-1}, (Laha et al. 2021).

The study of X-ray absorption can provide an independent test of the polarization unification scheme described above by comparing the X-ray absorption

properties, if present, to the known optical polarization characteristics. We remark that although our analysis is specifically addressed to test the presence and nature of X-ray absorption, for the time being, it provides a first approximation point of comparison with the polarization characteristics reported by S02, S04, S05. Further ideas on how to expand it are presented in the Discussion, § 5.

We carried out a systematic analysis of the X-ray spectra of 19 Sy 1 galaxies, classified in two subsamples according to their optical polarization, as detailed in § 2. This paper is structured as follows: the sample details are described in § 2, followed by a description of our analysis in § 3. In § 4 and § 5 we present our results and discussion, respectively, finalizing with conclusions in § 6. For our analysis we adopted the standard Λ CDM cosmology, with the parameters: $H_0 = 70$ km s^{-1} Mpc^{-1}, $\Omega\Lambda = 0.73$ and $\Omega M = 0.27$.

2. XMM-NEWTON SAMPLE AND DATA REDUCTION

Our sample consists of 19 sources, listed in Table 1, selected from the sample of 46 galaxies studied and classified by S02, S04, S05: polar polarization was reported for 11 sources (*PL-pol*) whereas 8 sources have equatorial polarization (*EQ-pol*). We obtained the *EPIC-pn* data at CCD resolution from the *XMM-Newton* archive[6]. For sources with more than one observation we selected the one with the longest exposure time regardless of the X-ray spectral state for the few sources in our sample with known prominent spectral changes (e.g. NGC 3227 and ESO 323-G077).

To process the data and extract the spectra, we utilized the *SAS v19.1*[7] software. The *EPIC-pn* data were reprocessed with the *epproc* task and were filtered for high background events using the standard procedure developed by the *XMM-Newton* Science Operations Center (SOC). Utilizing the SAO Image DS9 display (Joye & Mandel 2003), we selected a circular region that encloses the source, centered at the peak of X-ray emission, with radius ranging from 30 to 68 arcsec, depending on the target. With the *evselect* task, we selected the source region and extracted the corresponding spectrum. We used the same task to extract the background spectrum, selected from a circular region with no contribution from other sources in the CCD. The radius of the background regions varies from 50 to 96 arcsec, depending on the target. Response matrices were generated with the task *rmfgen* and *arfgen*. The resulting spectra were binned with the task *specgroup* in order to obtain 25 counts per energy bin, allowing us to use the χ^2 statistics. We corrected for out-of-time events that may occur due to the readout of the CCD as well as checked for possible pile-up. A moderate percentage of pile-up was found in the following sources: Fairall 51, Mrk 704, Mrk 766, NGC 3227, NGC 4593; they were corrected following the standard procedure suggested by the *XMM-Newton* Science Operation Centre (SOC)[8].

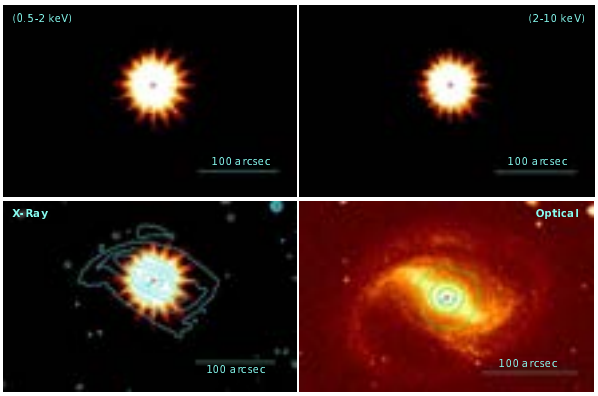

Fig. 1. Spatial analysis for NGC 4593. Top panel shows the X-ray images in two different energy ranges: soft X-ray from $0.5 - 2$ keV and hard X-ray from $2 - 10$ keV. The bottom panel shows a comparison between the X-ray emission ($0.5 - 10$ keV) with optical contours (in green) and an optical image from DSS with X-ray contours (in red). A red cross marks the maximum of the X-ray emission, and a cyan cross marks the maximum optical emission. The color figure can be viewed online.

3. X-RAY ANALYSIS

3.1. *Spatial Analysis*

The spatial analysis aims to give a general overview of each source. We used the filtered event files to generate X-ray images of the soft energy band ($0.5 - 2.0$ keV), and the hard energy band ($2.0 - 10$ keV). We also produced a full energy range image $0.5 - 10$ keV and combined it with the corresponding optical image, taken from the DSS (Digital Sky Survey). We produced combined images by plotting the optical contours in the X-ray image and vice versa. In Figure 1, we show as example the spatial analysis done for NGC 4593. In these images, we can see the point-like X-ray emission of the AGN and a more extended structure in the optical image. With

[6] `http://nxsa.esac.esa.int/nxsa-web/search`.

[7] User's Guide to the XMM-Newton Science Analysis System, Issue 16.0, 2021 (ESA: XMM-Newton SOC).

[8] `https://www.cosmos.esa.int/web/xmm-newton/sas-thread-epatplot`.

TABLE 1

SAMPLE OF POLARIZED SEYFERT 1 GALAXIES ORGANIZED ACCORDING TO THEIR POLARIZATION CHARACTERISTICS: POLAR AND EQUATORIAL.*

(1)	(2)	(3)	(4)	(5)	(6)	(7)	(8)
Object	RA	Dec	z	N_H^{Gal} $\times 10^{20}$ cm^{-2}	Type	Obs ID	Exp. ks
				Polar Polarization			
Mrk 1218	129.546	+24.8953	0.02862	3.1	Sy 1.8	0302260201	13.9
Mrk 704	139.608	+16.3053	0.02923	2.7	Sy 1.2	0502091601	98.2
Mrk 1239	148.080	-1.6121	0.01993	4.1	NLSy1	0891070101	105.0
NGC 3227	155.877	+19.8651	0.00386	1.9	Sy 1.5	0782520601	107.9
WAS 45	181.181	+31.1772	0.02500	1.4	Sy 1.9	0601780601	39.5
Mrk 766	184.611	+29.8129	0.01293	1.9	NLSy1/Sy 1.5	0109141301	129.9
Mrk 231	194.059	+56.8737	0.04217	0.9	Sy 1	0770580501	26.5
NGC 4593	189.914	-5.3443	0.00831	1.7	Sy 1	0784740101	142.1
ESO 323-G077	196.609	-40.4147	0.01501	7.7	Sy 1.2	0694170101	132.6
IRAS 15091-2107	227.999	-21.3171	0.04461	7.9	NLSy1	0300240201	23.0
Fairall 51	281.225	-62.3648	0.01418	6.3	Sy 1	0300240401	26.9
				Equatorial Polarization			
I Zw1	13.396	+12.6934	0.06117	4.6	NLSy1	0743050301	141.2
Akn 120	79.048	-0.1498	0.03271	9.9	Sy 1	0721600401	133.3
NGC 3783	174.757	-37.7387	0.00973	0.1	Sy 1.5	0112210201	137.8
Mrk 841	226.005	+10.4378	0.03642	2.0	Sy 1.5	0882130401	132.0
Mrk 876	243.488	+65.7193	0.12109	2.4	Sy 1	0102040601	12.8
KUV 18217+6419	275.489	+64.3434	0.29705	3.5	Sy 1.2	0506210101	14.3
Mrk 509	311.041	-10.7235	0.03440	3.9	Sy 1.5	0306090201	85.9
Mrk 304	334.301	+14.2391	0.06576	4.9	Sy 1	0103660301	47.3

*Columns 2 and 3 report coordinates (RA, Dec) in J2000, Column 4 indicates the redshift of each source, taken from the NASA/IPAC Extragalactic Database(NED). Column 5 corresponds to the column density of the Galaxy in the line-of-sight of the source from the HEASARC server. Column 6 indicates AGN classification, where NLSy1 refers to Narrow Line Seyfert 1, from NED. Columns 7 and 8 contain the *XMM-Newton* observation ID and the net exposure time.

this analysis, we can verify the general characteristic of point-like sources in the X-ray regime. The results of the spatial analysis are presented in § 4.1.

3.2. *Spectral Analysis*

For the fitting process, we used the *Xspec Spectral Fitting Package v 12.10.1n* in a *Python v 3.7.4.* environment: *PyXspec*, (Gordon & Arnaud 2021). We considered the Galactic absorption modelled by the Tuebingen-Boulder ISM absorption model, *TBabs*, with updated abundances, (Wilms et al. 2000). We used Galactic hydrogen column values from "nH Column Density Tool" from the HEASARC server, (HI4PI Collaboration et al. 2016), see Table 1. For all the models that include the redshift parameter, z, the value was fixed at the source redshift. Errors are quoted at 1σ confidence level or 90 percent for one free parameter.

In order to characterize the X-ray emission, we performed a systematic analysis of the spectra by adding components, either additive or multiplicative, to a baseline continuum model. As we build a nested model, we can calculate the F-test for additive components, where an F-test $> 95\%$ indicates that the new component significantly improves the fit. For multiplicative components, such as the absorption models, we used the Akaike Information Criterion (AIC, Akaike 1974). We first calculated the AIC value, equation 1, where k corresponds to the number of free parameters in each model. The comparison between both models is given by the factor $F_{\rm AIC}$, resulting from equation 2, where $\rm AIC_{NEW}$ refers to the model with the new component. The inverse, $1/F_{\rm AIC}$, indicates the improvement of the new and more complex model, (e. g. Krongold et al. 2021).

$$\rm AIC = 2k + \chi^2, \tag{1}$$

$$F_{\rm AIC} = \exp((\rm AIC_{NEW} - AIC_0)/2). \tag{2}$$

3.2.1. *The Hard Band (2-10 keV) Spectral Range*

The hard band corresponds to the energy range of $2 - 10$ keV. In this range, we fitted the main continuum component with a power law, using the model *zpowerlw*, reporting the resulting

photon index, Γ and normalization in units of photons keV^{-1} cm^{-2} s^{-1}. Subsequently, we tested for the presence of emission lines using the model *zgauss*. We only tested for narrow lines, with width fixed at $\sigma = 0.05$ keV. The most prominent X-ray emission line in AGN is the Fe Kα at 6.4 keV; if present, we reported the value of the normalization in units of photons cm^{-2} s^{-1}. We additionally tested for the presence of narrow emission lines corresponding to ionized Fe: Fe XXV at 6.697 keV and/or Fe XXVI at 6.966 keV (Bianchi et al. 2005). Lastly, we tested for a possible contribution from a cold absorber, fitted using the model *zTBabs*. If significant, we reported the column density in units of 10^{22} cm^{-2}. The results of the hard band fitting are shown in Table 2.

3.2.2. *The Full Band (0.5-10 keV) Spectral Range*

Extending our analysis to the full energy band, $(0.5-10$ keV), we first applied our hard band baseline model to the EPIC-pn data. This allowed us to verify the presence of additional spectral features such as a soft excess and absorption.

In order to fit the soft excess as thermal emission, we assumed a black body spectrum, modeled by the XSPEC component *zbbody*, (Singh et al. 2011; Scott et al. 2011; Petrucci et al. 2018). We report the black body temperature in keV, and the normalization in units of $L_{39}/[D_{10}(1+z)]^2$; where L_{39} is the luminosity of the source in units of 10^{39} erg s^{-1} and D_{10} is the distance of the source in units of 10 pc. The results of the baseline model with the addition of the black body fitted to the full energy band are reported in Table 3.

We now proceed with the absorption test. Absorption is referred to as cold or warm according to the state of the absorbing material, whether it is neutral or ionized. Our aim is to determine if absorption is in fact present in each spectrum and, if so, which component prevails: a cold absorber or a warm absorber. It is worth noting that ionized absorption typically requires a more complex modeling with several layers of gas in different ionization states and column densities, (e.g. Miniutti et al. 2014; Svoboda et al. 2015; Silva et al. 2018). All absorption models are multiplicative, so we calculate the AIC and use it to determine which component provides a better fit to the data.

For a cold absorber, we used the model *zTBabs*. The fit yields the amount of the line of sight equivalent hydrogen column in units of 10^{22} cm^{-2}. For warm absorption, we selected the model *zxipcf* [9], based on the XSTAR photoionization absorption models, and considered four parameters: the redshift of the source, the column density in units of 10^{22} cm^{-2}, the covering fraction, f, and the ionization parameter, $\log\xi$, where $\xi = L/nr^2$: L is the X-ray luminosity of the source, n is the electronic density of the ionized gas and r^2 is the squared distance of the ionized cloud to the source of ionizing radiation. The covering factor, f, is fixed to 1.0, so $1-f$ represents the portion of the source that is seen directly. As a final test, we explored the possibility that the fits for the sources with warm absorption could be further improved by adding a second warm absorber component, also with f fixed to 1.0. The absorption test results are reported in Table 4. All the spectral analysis results are detailed in § 4.2.

[9] https://heasarc.gsfc.nasa.gov/xanadu/xspec/models/zxipcf.html.

4. RESULTS

In this section, we present the results of the analysis of our sample that consists of 19 sources of which 11 sources with *PL-pol* and 8 with *EQ-pol*. We begin with the spatial analysis, that provides a general view of each source. We then detailed the results from the spectral analysis, organized according to the known polarization characteristics. In § 5, we discuss these results.

4.1. *Spatial Analysis*

We detailed the spatial analysis performed on the sources in the sample in § 3. The objects in the sample are all type-1 and intermediate type Seyfert galaxies, see Table 1. Consistently with their classification, they all appear as point-like sources in the X-ray energy range images. By tracing the optical contours onto the X-ray image, we verify that the X-ray emission is concentrated in the nuclear region, while the optical structure is extended, showing features such as the spiral arms with stellar formation activity. We can conclude that the sample displays general properties consistent with type 1 Sy galaxies.

While tracing the optical contours onto the X-ray image, we confirm that the optical structure is extended, displaying features such as spiral arms with stellar formation activity.

4.2. *Spectral Analysis*

In order to draw a first approximation description regarding the X-ray properties of our sample, we tested if the spectra could be satisfactorily fitted with our nested model, avoiding a source-by-source detailed modeling. To achieve a general good description of how these sources respond to a first-order broadband AGN emission model, we use the F-test

and the AIC for additive and multiplicative respectively. In particular, our aim is to determine if the fit is improved by adding an absorption component and, if significant, whether this absorption is cold or warm. The results of our analysis are listed in Tables 2, 3, and 4, corresponding to the hard band fits, the soft excess and the absorption test. In Table 4 we also include the source luminosity corresponding to the preferred model. The standard threshold for estimating parameter errors in our PyXspec script, and in Xspec in general, is $\chi^2_\nu > 2$; therefore, we do not report errors for fits with higher values of the χ^2 statistics.

We have organized the description of the results according to the optical polarization classification of the sources, – *PL-pol* and *EQ-pol* –. These results will be discussed in § 5. The fits of the entire sample in the full energy band are presented in Appendix A.

4.2.1. *Polar-Polarized Sources*

The photon index of the hard band power law continuum (see Table 2) ranges from the flatter 0.6 to the steeper 4.3. In particular, for 8 sources the photon index is in a range $1.4 < \Gamma < 2.1$ (mean=1.7). Also in the hard band, we tested the presence and significance of emission lines corresponding to Fe Kα, Fe XXV and Fe XXVI. We found significant emission of Fe Kα line in 9 of the sources, with only Mrk 1218 and Mrk 231 not showing any emission line. Additionally, NGC 4593 and ESO 323-G077 show the Fe XXVI line, and Mrk 766 shows both Fe XXV and Fe XXVI lines.

Extending to the full energy range, we find that soft excess is ubiquitous, see Table 3, and highly significant in all sources (F-test > 99%). For the black body component, we find temperatures of kT < 1 keV for 9 out of the 11 sources. Fairall 51 and ESO 323-G077 yield higher temperatures. However, these values decrease once we add absorption components.

Concerning the absorption test, according to the AIC, we determine the presence of absorption in all the *PL-pol* sources, see Table 4. Mrk 1218 and Mrk 231 favor the cold absorption scenario, resulting in column densities of the order of 10^{21} cm^{-2}. For NGC 4593, IRAS 15091-2107, Mrk 766 and ESO 323-G077, the AIC indicates that warm absorption is the best-fitting scenario. Figure 2 depicts the fits of NGC 4593 as an example of the baseline model, the addition of a soft excess and the absorption test, in which case the favored scenario corresponds to the warm absorption; see Appendix A for the fits of the entire sample. The fit

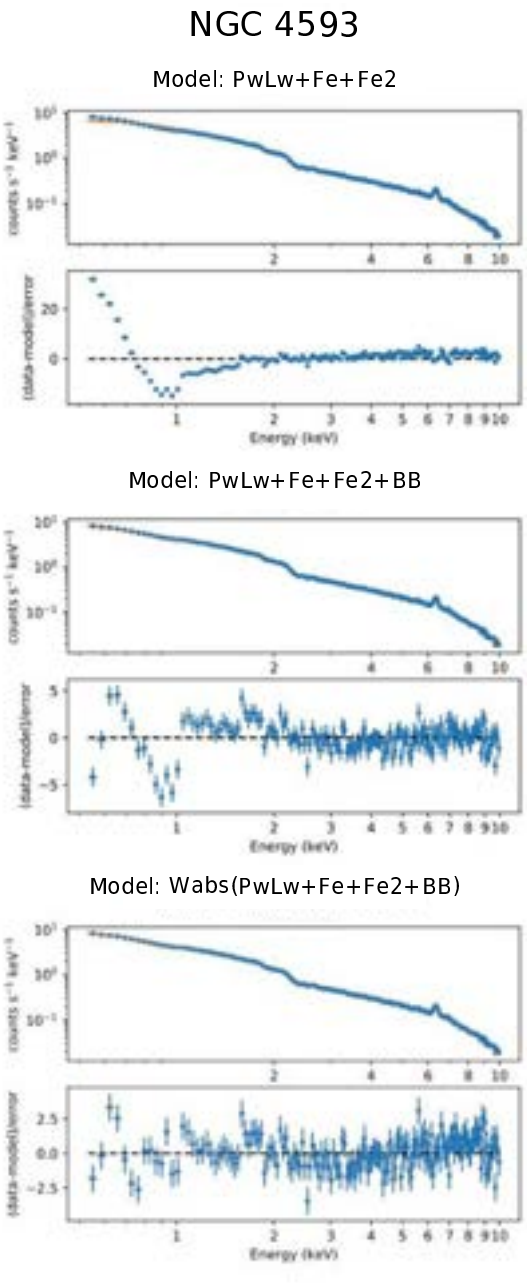

Fig. 2. *XMM-Newton EPIC-pn* spectrum of NGC 4593 fitted in the $0.5 - 10$ keV range. Top panel shows the fit of the baseline model reported in Table 2, middle panel depicts the fit with a soft excess added, as shown in Table 3. Last panel corresponds to the model resulting from the absorption test, a model with warm absorption, see Table 4. The color figure can be viewed online.

is further improved by adding a second warm absorption component for the cases of Fairall 51, Mrk 704, Was 45, and NGC 3227. For the warm absorbers, all the column densities are within the range

of $N_H \approx 10^{20} - 10^{22}$ cm^{-2}. We obtain a large range of values in the ionization parameters, from $-1.4 < \log\xi < 5.9$. In particular, for Mrk 1239 the results are inconclusive, with the AIC value indicating that the fit improves by adding an absorption component, but none of the two scenarios (cold vs warm) can be statistically favored.

4.2.2. *Equatorial-Polarized Sources*

In the hard band of the *EQ-pol* sources, one exhibits a flat spectrum with a power law index of ≈ 1.1, while the remaining 7 sources have a photon index in the range of $1.5 < \Gamma < 2.3$. The Fe Kα line is significantly detected in 4 sources: NGC 3783, Mrk 841, Mrk 509 and Akn 120. NGC 3783 also shows the Fe XXVI line, and Akn 120 shows both the Fe XXV and Fe XXVI lines.

In the full energy range, we again obtain a result that supports that the soft excess is ubiquitous, with F-tests $> 99\%$ for all the sources. The black body temperatures are all k$T < 1$ keV.

As for the absorption test, unlike the *PL-pol* sample, we do not find absorption in all the sources. In 6 out of 8 sources we can determine the presence of absorption. Mrk 876 and Mrk 509 are better fitted without any absorber, according to the small value of the AIC test. Mrk 304 favors the cold absorber scenario, with column density of the order of $N_{\rm H} \approx 10^{21}$ cm^{-2}. I Zw1, Mrk 841, KUV 18217+6419 and Akn 120 favor the scenario of warm absorption, yielding column densities of the order of $N_{\rm H} \approx 10^{20} - 10^{21}$ cm^{-2} and a range of ionization parameters of $-0.2 < \log\xi < 3.0$. None of the fits improved by the addition of a second warm absorption component. NGC 3783, similarly to the case of Mrk 1239, results in an AIC that indicates fit improvement by the addition of an absorption component. However, the test cannot conclusively indicate whether the favorable scenario consists of cold or warm absorption.

5. DISCUSSION

Our analysis on 19 Sy sources is intended to test the presence of absorption in the X-ray spectra in the context of the unification scheme based on optical polarization. Figure 3 shows the schematic view where we see both bi-conical and co-planar scattering regions and the line-of-sight orientation corresponding to the different observed scenarios.

We begin discussing the common X-ray properties of our Sy 1 sample, i.e. our baseline model, *PowerLaw + Fe + BB*. The main continuum component is well fitted in the hard band for the majority of the sample. A photon index in the range of $1.4 < \Gamma < 2.3$ is considered to be within the typical range for type Sy galaxies, (e.g. Piconcelli, E. et al. 2005; Cappi et al. 2006; Singh et al. 2011; Corral et al. 2011; She et al. 2017), and so is the case for 15 out of our 19 sources. Also consistently with studies on X-ray properties of Sy 1, we find the Fe Kα line in 13 out of the 19 observations, corresponding to the narrow component of the line, associated to the molecular torus, (Ricci et al. 2014a,b). We did not consider any broadening effect on the line, which would place the line emission mechanism closer to the accretion disk. Extending to the full energy band, we find the soft excess to be ubiquitous, resulting in an average temperature of 0.126 keV. While our sample can be fitted by considering these common characteristics of type 1 Sy, it is worth mentioning that a Seyfert Galaxy spectrum can be affected by additional complex processes, whose detailed description is beyond the scope of our analysis. The effects of Compton reflection, for example, might affect the shape of the continuum making it different from a simple power law. In the case of many sources in our sample, the spectra prove to be more complex, possibly requiring additional components. For this reason, we report in § 5.1 results of more detailed spectral analyses from the literature for each individual source. When available, we cite X-ray analysis carried out on the same XMM-Newton observation as the one used in our work.

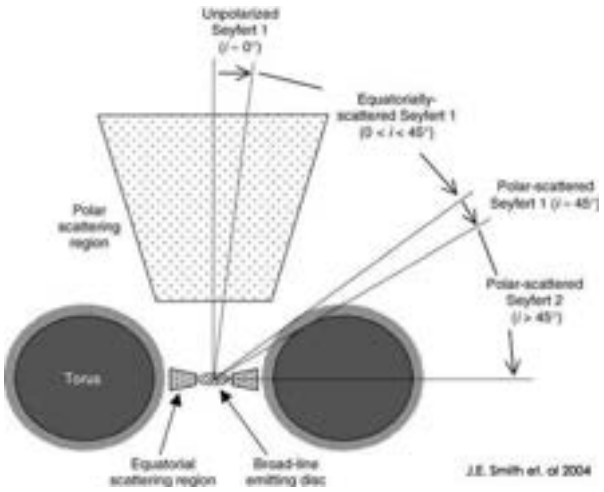

Fig. 3. The unification scheme, where both scattering regions are present in all Seyfert galaxies. According to this scheme, the observed optical polarization is due to the orientation of the AGN towards our line-of-sight, (Smith et al. 2004).

TABLE 2

HARD BAND FITS. BEST FIT PARAMETER VALUES AND GOODNESS OF FIT FOR THE HARD BAND ANALYSIS.*

(1)	(2)	(3)	(4)	(5)	(6)	(7)	(8)	(9)
Galaxy	Model	$N_{\rm H}$ $\times10^{22}$ cm^{-2}	Photon Index Γ	Norm $\times10^{-3}$ photons/keV/cm^2/s	Fe Norm $\times10^{-5}$ photons/cm^2/s	Fe$_{\rm XXV}$ Norm $\times10^{-5}$ photons/cm^2/s	Fe$_{\rm XXVI}$ Norm $\times10^{-5}$ photons/cm^2/s	χ^2_ν
			Polar Polarization					
Mrk 1218	**PwLw**	-	1.37 ±0.10	$0.4^{+0.3}_{-0.3}$	-	-	-	**0.94**
IRAS 15091-2107	**PwLw+Fe**	-	1.72 ±0.06	2.3 ±0.2	1.3 ±0.6	-	-	**1.10**
NGC 4593	**PwLw+Fe+Fe2**	-	$1.74^{+0.04}_{-0.07}$	$4.64^{+0.2}_{-0.14}$	2.8 ±0.2	-	$5.5^{+4.7}_{-4.3}$	**1.12**
Mrk 231	**N$_H$(PwLw)**	$2.4^{+1.8}_{-1.7}$	1.0 ±0.3	$0.006^{+0.004}_{-0.002}$	-	-	-	**1.13**
Fairall 51	**N$_H$(PwLw+Fe)**	2.3 ±0.2	1.89 ±0.04	8.8 ±0.7	2.6 ±0.5	-	-	**1.33**
Mrk 704	**PwLw+Fe**	-	1.82 ±0.02	2.69 ±0.06	1.1 ±0.2	-	-	**1.37**
NGC 3227	**N$_H$(PwLw+Fe)**	0.29 ±0.09	1.58 ±0.02	0.0062 ±0.0002	3.2 ±0.3	-	-	**1.49**
Was 45	**N$_H$(PwLw+Fe)**	$7.2^{+0.9}_{-1.0}$	1.56 ±0.13	$0.58^{+0.16}_{-0.12}$	1.0 ±0.2	-	-	**1.66**
Mrk 766	PwLw+Fe+Fe2+Fe3	-	2.11	8.0	1.0	0.9	0.6	2.10
ESO 323-G077	N$_H$(PwLw+Fe+Fe2)	5.5	0.6	0.11	2.0	-	0.9	5.54
Mrk 1239	N$_H$(PwLw+Fe)	57.7	4.3	186	1.6	-	-	6.0
			Equatorial Polarization					
Mrk 876	**PwLw**	-	1.62 0.11	1.7 ±0.3	-	-	-	**0.86**
NGC 3783	**N$_H$(PwLw+Fe+Fe2)**	0.6 ±0.2	1.50 ±0.03	$4.9^{+0.3}_{-0.2}$	4.5 ±0.4	-	1.3 ±0.4	**1.65**
Mrk 841	**N$_H$(PwLw+Fe)**	0.7 ±0.4	1.52 ±0.06	1.5 ±0.2	1.0 ±0.2	-	-	**1.75**
I Zw1	**PwLw**	-	2.33 ±0.05	2.7 ±0.2	-	-	-	**1.85**
Mrk 509	PwLw+Fe	-	1.86	8.4	1.7	-	-	2.30
Akn 120	PwLw+Fe+Fe2+Fe3	-	1.93	9.9	2.2	0.7	0.8	2.50
KUV 18217+6419	PwLw	-	1.14	5.8	-	-	-	2.53
Mrk 304	N$_H$*PwLw	5.99	1.74	1.14	-	-	-	3.0

*Column 2 indicates the resulting model. In Columns 3 to 8, we report the value of the model parameters: column density, (if significant), photon index and power law normalization, and normalization for the significant Fe emission lines. The resulting model statistics is shown in Column 9. Values in bold correspond to fits with $\chi^2_\nu < 2.0$ for which we can calculate parameter errors.

Regarding the absorption test, we first point out that the characteristics here reported on the warm absorbers, column density and ionization parameter, are consistent with the description provided by Laha et al. (2021): the column densities range is $N_{\rm H} \approx 10^{20}-10^{22}$ cm^2, and the ionization parameters range is $-1.0 < \log\xi < 3.0$. Only NGC 3227 yields a more highly ionized warm absorber, $\log\xi \approx 6.0$, a result that could be further improved by a more detailed modeling, (see notes on NGC 3227 in § 5.1). The sources that favor the cold absorption scenario yield column densities $N_{\rm H} \approx 10^{21}$ cm^2, consistent with type 1 sources that are not heavily absorbed. In general, the detected column density is always

TABLE 3

FULL ENERGY BAND FOR EACH SOURCE*

(1)	(2)	(3)	(4)	(5)	(6)	(7)	(8)
Galaxy	Model	Photon Index Γ	Norm $\times10^{-3}$ photons/keV/cm^2/s	kT keV	BBnorm $\times10^{-4}$ $L_{39}/[D_{10}(1+z)]^2$	χ^2_ν	F-test
Polar Polarization							
Mrk 1218	PwLw	0.95	0.2	-	-	2.24	
	PwLw+BB	$0.84^{+0.10}_{-0.11}$	0.13±0.02	$0.84\ ^{+0.11}_{-0.09}$	0.1±0.2	**1.18**	99.99%
Mrk 231	PwLw	0.91	0.04	-	-	4.30	
	PwLw+BB	0.46 ±0.08	0.023 ± 0.003	$0.169\ ^{+0.014}_{-0.012}$	0.0116 ± 0.0012	**1.68**	100%
IRAS 15091-2107	PwLw+Fe	1.44	1.4	-	-	6.47	
	PwLw+Fe+BB	1.31±0.03	0.93±0.04	0.52±0.02	0.24±0.02	**1.98**	100%
Mrk 704	PwLw+Fe	1.99	3.1	-	-	25.81	
	PwLw+Fe+BB	1.83	3.0	0.07	2.0	2.29	100%
NGC 4593	PwLw+Fe+Fe2	1.78	5.0	-	-	25.32	
	PwLw+Fe+Fe2+BB	1.69	4.0	0.07	1.3	2.60	100%
Was 45	PwLw+Fe	0.23	0.04	-	-	9.24	
	PwLw+Fe+BB	0.14	0.04	0.09	0.03	6.9	99.99%
ESO 323-G077	PwLw+Fe+Fe2	0.3	0.05	-	-	32.5	
	PwLw+Fe+Fe2+BB	0.3	0.07	3.4	0.7	8.10	100%
Mrk 766	PwLw+Fe+Fe2+Fe3	2.25	8.3	-	-	92.02	
	PwLw+Fe+Fe2+Fe3+BB	2.06	7.3	0.08	3.2	13.45	100%
NGC 3227	PwLw+Fe	1.37	5.0	-	-	40.28	
	PwLw+Fe+BB	1.41	4.0	0.87	0.49	27.53	99.99%
Fairall 51	PwLw+Fe	1.06	2.0	-	-	56.97	
	PwLw+Fe+BB	1.24	14.0	1.2	1.5	37.57	99.99%
Mrk 1239	PwLw+Fe	3.38	0.14	-	-	70.38	
	PwLw+Fe+BB	-0.14	0.013	0.06	0.15	31.41	100%
Equatorial Polarization							
Mrk 876	PwLw	1.99	2.5	-	-	2.55	
	PwLw+BB	1.73 ± 0.03	1.64 ± 0.06	0.102 ± 0.006	$0.48^{+0.6}_{-0.05}$	**1.09**	100%
I Zw1	PwLw	2.6	3.2	-	-	4.50	
	PwLw+BB	2.3	2.7	0.11	0.4	2.25	100%
Mrk 841	PwLw+Fe	1.81	1.8	-	-	24.81	
	PwLw+Fe+BB	1.46	1.3	0.101	0.6	2.36	100%
KUV 18217+6419	PwLw	1.55	10.1	-	-	18.50	
	PwLw+BB	1.15	5.9	0.2	1.7	2.63	100%
Akn 120	PwLw+Fe+Fe2+Fe3	2.11	12.0	-	-	21.43	
	PwLw+Fe+Fe2+Fe3+BB	1.97	10.5	0.14	0.8	4.20	100%
Mrk 509	PwLw+Fe	2.11	11.0	-	-	33.20	
	PwLw+Fe+BB	1.96	9.6	0.102	1.4	4.75	100%
Mrk 304	N_H*PwLw	0.54	0.11	-	-	12.16	
	N_H*PwLw+BB	0.46	0.10	0.07	0.2	8.43	99.99%
NGC 3783	PwLw+Fe+Fe2	1.28	3.4	-	-	40.38	
	PwLw+Fe+Fe2+BB	1.20	3.0	0.07	2.8	14.80	100%

*The first row shows the baseline model, the second row corresponds to the model with black body as soft excess. Columns 3 and 4 report the power law index and normalization. Columns 5 and 6 show the black body temperature and normalization. The following Columns, 7 and 8, correspond to the fit statistics. The last column indicates the F-test resulting from comparing models with and without soft excess. We highlight in bold the fits that yield $\chi^2_\nu < 2$.

consistent with that of type 1 AGN, with the dividing value between type 1 and type 2 sources being $N_H \approx 10^{22}$ cm^{-2}, (Beckmann & Shrader 2012).

Concerning the presence of absorption, our analysis shows that the absorption is present in 100% of the *PL-pol* sources. In particular ≈ 73% (8/11) of these sources favor the warm absorption scenario and only 18% (2/11) sources are affected by a cold absorber. The presence of warm absorption in the *PL-pol* sources can be put in the context of the scenario described by Smith et al. (2004) by interpreting it as the presence of the outer layer of the torus in the line-of-sight, which gets ionized by the central engine. Blustin et al. (2005) argue that warm absorbers in Seyfert galaxies are more likely to originate in outflows from a dusty torus, lending support

TABLE 4

ABSORPTION TEST[a]

(1)	(2)	(3)	(4)	(5)	(6)	(7)	(8)	(9)	(10)	(11)	(12)	(13)
Galaxy	Model	nH $\times10^{22}$cm^{-2}	$\log\xi$	N_{H2} $\times10^{22}$cm^{-2}	$\log\xi_2$	Photon Index Γ	kT keV	$\mathrm{Lum_{X-Ray}}$ $\times10^{43}$erg s^{-1}	χ^2_ν	AIC_{BB}	AIC	$1/F_{AIC}$
Polar Polarization												
Mrk 1218	**ColdAbs**	$0.47^{+0.14}_{-0.12}$	-	-	-	1.37±0.09	0.062±0.012	0.604	**1.17**	151.81	113.66	1.9×10^{8}
	WarmAbs	0.15 ± 0.10	$1.2^{+0.3}_{-1.6}$	-	-	$1.0^{+1.0}_{-0.3}$	$0.80^{+0.80}_{-0.10}$		1.21		118.18	2.01×10^{7}
Mrk 231	**ColdAbs**	0.6 ± 0.2	-	-	-	0.65 ± 0.10	$0.106^{+0.015}_{-0.012}$	0.324	**1.29**	140.41	110.78	2.7×10^{6}
	WarmAbs	0.05	0.4	-	-	$0.48^{+0.10}_{-0.07}$	0.168 ±0.013		1.82		152.41	0.002
NGC 4593	ColdAbs	0.060 ±0.010	-	-	-	1.735 ±0.009	$0.0782^{+0.0013}_{-0.0014}$		1.94	449.37	334.59	8.4×10^{24}
	WarmAbs	0.14±0.02	2.36±0.08	-	-	1.727 ±0.007	0.079 ±0.003	0.437	**1.40**		253.78	3.0×10^{42}
Fairall 51	ColdAbs	0.0	-	-	-	1.24	1.15		37.80	6095.58	6097.58	0.37
	WarmAbs	1.31	0.57	-	-	1.81	0.11		3.35		549.52	$>10^{90}$
	2WarmAbs	$2.50^{+1.03}_{-0.84}$	$2.5^{+0.5}_{-0.2}$	$1.0^{+0.4}_{-0.2}$	$0.46^{+0.05}_{-0.04}$	1.86 ±0.09	$0.113^{+0.006}_{-0.004}$	1.268	**1.60**		269.84	$>10^{90}$
IRAS 15091-2107	ColdAbs	0.08 ± 0.03	-	-	-	$1.51^{+0.06}_{-0.07}$	$0.51^{+0.04}_{-0.03}$		1.83	301.57	278.51	1.02×10^{5}
	WarmAbs	$0.12^{+0.05}_{-0.12}$	$-0.46^{+0.14}_{-0.23}$	-	-	$1.63^{+0.10}_{-0.07}$	$0.45^{+0.07}_{-0.11}$	4.562	**1.63**		251.32	8.2×10^{10}
Mrk 704	ColdAbs	0.05	-	-	-	1.88	0.07		2.05	382.46	344.67	1.6×10^{8}
	WarmAbs	$0.13^{+0.03}_{-0.04}$	$2.15^{+0.14}_{-0.15}$	-	-	$1.882^{+0.012}_{-0.013}$	0.076 ± 0.003		1.84		318.36	8.3×10^{13}
	2WarmAbs	$0.061^{+0.002}_{-0.009}$	$0.28^{+0.46}_{-0.13}$	$0.23^{+0.02}_{-0.14}$	$2.44^{+0.60}_{-0.11}$	1.9 ±0.9	$0.113^{+0.113}_{-0.003}$	2.919	**1.73**		293.35	2.2×10^{19}
Was 45	ColdAbs	1.4	-	-	-	0.6	0.05		4.54	858.41	565.55	$>10^{90}$
	WarmAbs	2.74	0.28	-	-	1.17	0.09		2.98		374.06	2.0×10^{62}
	2WarmAbs	0.013	2.04	2.5	0.3	1.30	0.09	0.325	3.67		454.79	4.4×10^{87}
Mrk 766	ColdAbs	0.09	-	-	-	2.13	0.08		11.72	2220.43	1926.75	5.9×10^{63}
	WarmAbs	0.4	0.9	-	-	2.18	0.12	0.128	2.87		480.05	$>10^{90}$
NGC 3227	ColdAbs	0.0	-	-	-	1.4	0.9		27.71	4635.78	4640.26	0.11
	WarmAbs	0.4	1.6	-	-	1.51	0.63		6.12		1023.29	$>10^{90}$
	2WarmAbs	0.6	0.3	0.02	5.9	1.59	0.07	0.144	3.72		627.24	$>10^{90}$
ESO 323-G077	ColdAbs	0.97	-	-	-	0.58	0.09		15.84	1259.63	2436.98	X
	WarmAbs	0.3	-1.4	-	-	0.14	0.12	0.230	6.64		1027.53	2.5×10^{50}
Mrk 1239 (*)	ColdAbs	0.02	-	-	-	-0.15	0.15		31.06	10495.39	4390.27	$>10^{90}$
	WarmAbs	0.05	5.96	-	-	-0.16	0.15	0.159	31.45		4415.32	$>10^{90}$
Equatorial Polarization												
Mrk 876	**Unabs**	-	-	-	-	1.73 ± 0.03	0.102 ± 0.006	0.341	**1.09**	106.95	-	-
	ColdAbs	0.0	-	-	-	$1.73^{+0.06}_{-0.05}$	$0.110^{+0.014}_{-0.015}$		1.10		108.96	0.37
	WarmAbs	0.04±0.04	$0.2^{+0.2}_{-1.4}$	-	-	$1.73^{+0.06}_{-0.05}$	$0.13^{+0.02}_{-0.03}$		1.19		117.70	0.005
1Zw 1	ColdAbs	0.0	-	-	-	2.80±0.03	$1.0^{+0.004}_{-1.0}$		3.02	307.83	409.14	X
	WarmAbs	$0.09^{+0.04}_{-0.09}$	$-0.2^{+0.6}_{-0.2}$	-	-	$2.3^{+0.3}_{-0.4}$	$0.12^{+0.011}_{-0.005}$	8.648	**1.91**		261.57	1.11×10^{10}
Mrk 841	ColdAbs	0.0	-	-	-	1.45	0.102		2.38	375.48	378.51	0.22
	WarmAbs	0.09	1.04	-	-	1.46	0.12	3.349	2.15		342.26	1.6×10^{7}
KUV 18217+6419	ColdAbs	0.0	-	-	-	1.15	0.2		2.65	445.24	447.61	0.3
	WarmAbs	1.0	3.28	-	-	1.15	0.2	1370.2	2.47		417.12	1.3×10^{6}
Akn 120	ColdAbs	0.0	-	-	-	1.98	0.14		3.66	617.45	619.45	0.4
	WarmAbs	0.30	0.27	-	-	1.98	0.15	11.419	3.49		587.54	3.1×10^{6}
Mrk 509	**Unabs**	-	-	-	-	1.96	0.102	12.454	4.75	802.98	-	-
	ColdAbs	0.0	-	-	-	1.95	0.103		4.78		805.77	0.3
	WarmAbs	0.014	4.6	-	-	1.99	0.11		6.29		1052.53	X
Mrk 304	**ColdAbs**	0.96	-	-	-	0.85	0.05	3.335	6.03	1146.04	817.48	2.2×10^{71}
	WarmAbs	0.05	0.02	-	-	0.51	0.08		7.92		1064.92	4.1×10^{17}
NGC 3783 (*)	ColdAbs	0.38	-	-	-	1.45	0.07		2.82	2453.57	477.19	$>10^{90}$
	WarmAbs	0.25	-0.43	-	-	1.42	0.09	0.688	7.13		1178.32	$>10^{90}$

[a]The model in bold corresponds to the preferred model. We indicate (Unabs) for unabsorbed sources and use (*) for cases where $1/F_{AIC}$ does not favor one particular model. In Columns 3 to 8, we report the corresponding model parameters in the following order: column densities and ionization parameter in the case of warm absorbers, power law index and black body temperature. In Column 9 we report the X-ray luminosity of the resulting model[10]. Column 10 indicates the fit statistics, Columns 11 and 12 correspond to the AIC, where AIC_{BB} corresponds to the model with absorption. Column 13 indicates the factor $1/F_{AIC}$, an indicator of the fit improvement.

to the hypothesis that the warm absorber gas could be located in its outer layers. The two *PL-pol* sources that resulted affected by cold absorption yield low column densities, $N_H \approx 10^{21}$ cm^{-2}; we can interpret this as a result of our line of sight passing through a colder section of the torus atmosphere but remaining in the type 1 regime.

In slight contrast, 75% (6/8) of the *EQ-pol* sources are affected by absorption, with 50% (4/8) favoring the warm absorption scenario. This fraction is consistent with previous studies on the spectra of type 1 Seyferts, (e.g. C. S. Reynolds & Fabian 1995; Laha et al. 2014), where they respectively report that 50% up to 65% of Sy 1 show the presence of warm absorbers. For two *EQ-pol* sources, 25% of the sample, our analysis does not find a significant absorption component, consistent with the expected description of a type 1 AGN, where our line-of-sight is looking directly into the central region.

In order to determine if the percentage of absorbed sources described above is significantly different, we conducted a Kolmogorov-Smirnov test (KS) at 95% confidence. The result of the test yields a p-value of ≈ 0.87. A p-value much greater than the significance level of 0.05 (95%) indicates that we reject the test's null hypothesis, i.e., that the samples

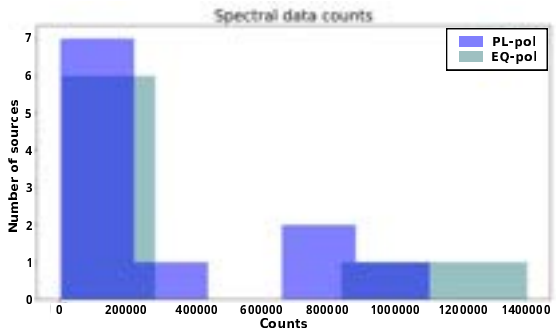

Fig. 4. Spectral data counts of each source. The color figure can be viewed online.

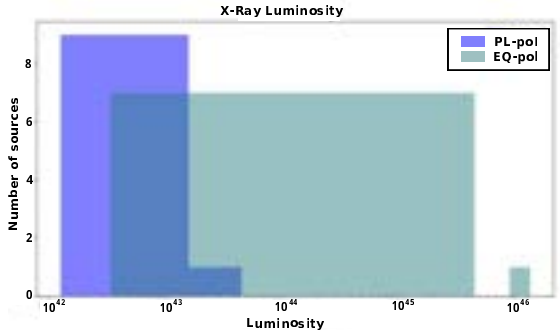

Fig. 5. X-ray Luminosity ($0.5 - 10$ keV) of each source. The value is shown in Table 4, referring to the luminosity of the preferred model after the absorption test. The color figure can be viewed online.

are drawn from the same distribution.. This means that the two sub-samples – *PL-pol* and *EQ-pol* – are statistically different from each other in terms of the incidence of absorption in these X-ray data.

We also considered the possible bias due to the data selected for this analysis. Our selection criterion was to choose the longest exposure time for each source, and this choice may introduce a bias related to the signal-to-noise of the X-ray spectra contained in each of the two sub-samples. Figure 4 is a histogram of the number of counts for each source, color-divided by sub-samples. We can see that there is no significant difference between the two sub-samples concerning the quality of the observation in terms of number of X-ray counts, which, if present, might have hindered the modeling of the spectrum. Regarding the X-ray luminosity of the sources, which may be intuitively associated to a higher frequency of the absorber due to the photoionization process, we show in Figure 5 a histogram of the X-ray luminosity calculated for the model resulting from the absorption test. This plot shows that the *EQ-pol* sources are actually more luminous than the *PL-pol*, therefore discarding the hypothesis that a higher luminosity is directly associated to the ubiquitous presence of an absorber.

A more recent study, Afanasiev et al. (2019), identifies 4 sources as *EQ-pol* that are instead listed as *PL-pol* in the studies by Smith, S04: Mrk 231, Mrk 704, NGC 3227, and NGC 4593. By assuming this new classification, the fraction of polar and equatorial polarized sources would shift to 7 and 12, respectively. For the former group, with all of them affected by absorption, only one favors the model with cold-absorption and 6, $\approx 86\%$, the warm-absorption scenario. For the sub-sample of *EQ-pol* sources, $\approx 83\%$ (10/12) of the sources are affected by absorption, with $\approx 58\%$ (7/12) favoring the presence of at least one warm absorber. This incidence of warm absorption is still within the threshold of the numbers reported by Laha, Sibasish and Guainazzi et al. (2014); therefore, we concluded that assuming an updated classification does not change the first-order conclusion of this analysis. For this reason and for consistency with the original criterion that defined our sample, we prefer to stick to the original classification proposed by Smith as a first test for the polarization unified scheme.

Considering now the sample of polarized sources as a whole, $\approx 90\%$ (17/19) of our sample shows presence of absorption and we can confirm the presence of at least one warm absorber in $\approx 63\%$ of the polarized Seyfert 1. This in itself is an interesting result on the incidence of X-ray absorption in polarized Seyfert galaxies, especially when compared to previous studies (e.g. C. S. Reynolds & Fabian 1995; Laha et al. 2014), where a very similar percentage of X-ray warm absorbers was reported (50% up to 65%, respectively).

From our review on previously published analysis of each source, reported in the following section, we find that the literature modeling is consistent with our analysis as a first approximation. In the majority of the sources, we see that best fit models include more components, e.g. reflection affecting the shape of the continuum, as in the cases of Mrk 1239, Mrk 766, ESO 323-G077. More specifically, we highlight that the modeling of absorption often requires more than one absorbing layer. In the majority of the sources, we see absorption modeled by two or even more components. In some cases, partial covering is the best way to reproduce the shape of the spectrum. We remark that the optical and X-ray data analyzed herein are far from being simultaneous, since the majority of the polarization data were obtained in 1996-1999, i.e. prior to XMM-Newton

launching. Although desirable, obtaining fully simultaneous data of this sample would require a considerable observational effort. We are confident that this analysis may serve to lay the basis for future observations.

These considerations motivate a more in-depth analysis addressed to characterize the absorber. For the time being, our analysis can serve as a first approximation model. Here, we describe the common components of a type 1 Seyfert spectrum and establish a point of reference for the presence of X-ray absorption in a sample of polarized Seyferts. This study would also benefit by the addition of a larger sample of Seyfert galaxies with well known and reported polarization.

5.1. *Notes on Individual Sources*

In this section, we briefly present properties taken from the available literature on each source of our sample. When possible, we report published results based on the analysis of the same data set used in our work.

5.1.1. *Polar-Polarized Sources*

Mrk 1218

Hernández-García et al. (2017) conclude that this source is best fitted by a power law with a cold absorber of $N_{\rm H} \approx 9 \times 10^{20}$ cm^{-2} in the soft energy range. This result is consistent with our analysis, (see Table 4).

Mrk 704

Our best fit for this source includes 2 warm absorbers. This result is consistent with that reported in Laha et al. (2011) & Matt et al. (2011), where the absorption is interpreted as the line of sight passing close to the torus. As an example of the complexity that these sources show, Matt et al. (2011) produced a best fit model including a second soft excess element and partial covering by a cold absorber.

Mrk 1239

Buhariwalla et al. (2020, 2023) report a very detailed analysis on this NLSy1. The hard band requires a relativistic blurred reflection component besides the power law which is partially covered by ionized material. This source has starburst activity, which affects and even dominates the soft band. Since we do not account for this features, our model fails to fit the continuum and the absorption test is inconclusive.

NGC 3227

In our analysis, the results favor the model with 2 warm absorbers. This result is consistent with the work by Markowitz et al. (2009), where the best fit model finds 2 warm absorbers, besides a strong soft excess also absorbed by cold gas. Moreover, by estimating a maximum distance, they place the ionized absorber outside the BLR. Newman et al. (2021) also find 2 warm absorbers, as well as a partially covered power law and a reflection component.

Was 45

Our results favor the presence of at least 2 warm absorbers. However, there are features in the spectra that are not accounted for by our model. A more detailed analysis will be reported in Gudiño et al. (in prep).

Mrk 766

We find a power law continuum on the steeper end of the typical Sy range, $\Gamma \approx 2.2$, as well as three different Fe emission lines and the presence of a warm absorber. This result is consistent with the studies made by Miller et al. (2006) & Turner et al. (2007), in particular, with the reports of a warm absorber with $\log \xi \approx 1$ and $N_{\rm H} \approx 10^{21}$ cm^{-2}, without considering any reflection or partial covering. In a variability study, Risaliti et al. (2011) also find warm absorption and estimate a lower limit for the location of the absorbing clouds, corresponding to the BLR.

Mrk 231

This is a well studied source and, among the many publications, Braito et al. (2004) argue that the resulting flat photon index suggests a heavily absorbed spectrum consisting of a scattered power law component and a reflected component, and even a reflection-dominated scenario. We do not consider any reflection components, but our results are consistent with a continuum well fitted by a power law with a flat slope and a column density of the order of $\approx 10^{22}$cm^{-2}.

NGC 4593

Our results for this source are consistent with previous analysis, such as Brenneman et al. (2007); Ebrero et al. (2013); Ursini et al. (2016). In particular, Ebrero et al. (2013), worked with grating spectra and found 4 warm absorbers of different ionization states with at least one of high-ionization ($\log \xi \approx 2.5$), and determined its distance from the source of around a few pc. This result is also consistent with the work of Ursini et al. (2016), where

they report two different warm absorbers, with the high-ionization one consistent with the column density and ionization parameter that we found; they determined this component to be at a distance of ≤ 3 pc from the central region.

ESO 323-G077

Our model does not accurately fit the continuum, possibly due to the omission of the reflection component and a soft excess that is modeled by more than one component. Miniutti et al. (2014) and Jiménez-Bailón et al. (2008) present a more detailed analysis. Both analyses find 2 warm absorbers as well as cold absorber that affects the power law in the hard band. Miniutti et al. (2014) present the idea that the variability observed in the warm absorber can be due to a clumpy torus or clouds in the BLR and propose this to be a source of intermediate type between 1 and 2, being observed at an angle of $\approx 45°$.

IRAS 15091-2107

Jimenez-Bailon et al. (2007) report a cold and a warm absorber in this source. We find our best fitted model to be the one with a warm absorption, since we do not consider a combination of both warm and cold absorption.

Fairall 51

This source shows significant improvement by adding a second warm absorber. Svoboda et al. (2015) present an in-depth analysis of this source, where the best fit model includes a cold absorber $N_{\rm H} \approx 4 \times 10^{22}$ cm^{-2} affecting the hard band and the need of a reflection component. One important point on the absorbers is that they find an improvement on the fit by allowing the covering factor of the *zxipcf* model to vary.

5.1.2. *Equatorial-Polarized Sources*

IZw 1

Gallo et al. (2007) and Costantini et al. (2007) report on the spectral details and variability between two observations. They find evidence of absorption of two different ionization states. Silva et al. (2018) worked on the same observation as we did and found a variable multi-phase ionized absorber by two gas components of similar column densities. The outflow velocity estimated for the low ionization component is ≈ 1900 km/s and for the high ionization is ≈ 2500 km/s. By assuming that the outflow velocity is greater than, or equal to, the escape velocity, they estimate the absorbers distance to the central source at $\approx 0.07, 0.04$ pc respectively, placing them on the scale of the accretion disk.

Akn 120

This source is referred to as a "bare-nucleus" AGN, and thus there are no reports of this source being affected by absorption. The spectra are characterized by a strong soft excess emission, as studied by Porquet et al. (2018) and Matt et al. (2014).

NGC 3783

According to the AIC, we are unable to determine whether the warm or cold absorber yield a better fit for this source. There are many previous publications on this AGN including reports on obscuring events. Based on RGS data, Blustin et al. (2002), reported the detection of a two-phase warm absorber. This result was confirmed by Mao et al. (2019).

Mrk 841

Our best fit for this source includes 2 warm absorbers of different ionization states, a result that is consistent with the in depth analysis made by Longinotti et al. (2010). In this work, they estimate the density of the absorbing gas to be below 10^3cm^{-3}, and a distance to the central source of a few tens of pc, placing the absorber on the scale of the BLR.

Mrk 876

We report this source as unabsorbed. This result is consistent with work reported in Bottacini (2022), using *NuSTAR* data, and Bottacini et al. (2015) with *XMM-Newton* and *Swift*. This unabsorbed scenario corresponds to a classical Seyfert 1.

KUV 18217+6419

The best fit from our analysis indicates the presence of a warm absorber. This source shows interesting features in the hard band, Jiménez-Bailón et al. (2007), but we found no studies on absorption in the soft band.

Mrk 509

This source has been much studied, in particular in a campaign lead by Kaastra et al. (2011), where we can find reports on the many components of the spectrum. In particular, Detmers et al. (2011) find multiple absorption systems, with three different velocity components. This is not consistent with our results, where this source appears unabsorbed, according to the AIC. This is an example of how an over-simplified model like ours does not recover the spectral complexity of the source.

Mrk 304

In our work, the AIC favors the cold absorption scenario. Our result differs from previous studies of the same observation. We find a cold absorber of $\approx 10^{21}$ cm^{-2} and our baseline model does not reproduce the convex shape of the continuum. Piconcelli et al. (2004) find that the convex shape of the spectrum corresponds to a heavily obscured source with column density up to $\approx 10^{23}$ cm^{-2}, and their final fit includes a multi-phase ionized absorber.

6. CONCLUSIONS

We presented the results of a systematic analysis of the X-ray spectra of 19 sources: 11 with *PL-pol* and 8 with *EQ-pol*. Our analysis consisted of fitting the main components of a typical Seyfert spectrum and testing the response when absorption was added to the model. We particularly tested whether cold or warm absorption was a preferred solution, as determined by the AIC statistical criterion.

- Concerning the common components of the spectral modeling, we find that the continuum is well-fitted by a power law, the Fe Kα is present in 13 out of the 19 observations, and the soft excess is ubiquitous. These components prove to be a good first approximation to model the typical type 1 Sy spectra. However, comparing our results to previously published work on these sources, we find that producing a more robust best fit model for the absorption components requires a more detailed analysis, to be complemented by high-resolution data. This suggests that our study can be further improved by the selection of a more complex model.

- From the absorption test, we find that 100% of the *PL-pol* and 75% of the *EQ-pol* sources are affected by absorption. This difference, which is corroborated by the statistical KS test, seems to indicate an intrinsic diversity of the scattering medium in the two groups of sources, lending support to the unification model proposed by Smith.

- "While we observe a distinction between subsamples, another interesting result emerges when examining the entire sample of polarized Sy 1. The incidence of absorption in 19 type 1 Sy is of $\approx$ 90%, with $\approx$ 75% confirmed to be warm absorption. In contrast with results where warm absorption is found in 65% of type 1 Sy, (Laha et al. 2014), this suggests a relationship between the presence of absorbing material in the line-of-sight and the region responsible for the scattering that yields the measured optical polarization.

- At first approximation, our work provides a promising test for the use of X-ray absorption as a tool for explaining the properties of the observed polarization and their interpretation in the context of the AGN unification model. It is desirable for further work to include more recent polarization measurements and a larger sample of X-ray sources with known polarization. The test of X-ray absorption can also be improved by considering more complex modeling of the absorbers, aiming at constraining the location of the absorbing gas with respect to the AGN torus. It is important to note that, while the model presented by Smith can be regarded as a first approximation to a unification scheme, the availability and quality of X-ray data and therefore our understanding of the X-ray emission of AGN has significantly improved since Smith's unification scheme was first proposed (2002-2005). This poses the interesting option of taking this systematic analysis further by considering a multi-layered absorber, a less homogeneous torus and a more detailed characterization of the absorbing gas.

This research has been founded by the project PID2019-107408GB-C41 and PID2022-136598NB-C33 by the Spanish Ministry of Science and Innovation/State Agency of Research MCIN/AEI/10.13039/501100011033 and by "ERDF A way of making Europe". MGY acknowledges "Programa de Apoyo a los Estudios de Posgrado (PAEP), UNAM". A.L.L. and MGY acknowledge support from DGAPA-PAPIIT grant IA101623. A.L.L. acknowledges the staff of the European Space Astronomy Centre (ESAC, Madrid) for hosting her visit during which this work was substantially discussed and advanced. Financial support is acknowledged from ESA through the Science Faculty - Funding reference ESA-SCI-SC-LE-123, and from project PID2019-107408GB-C41 by the Spanish Ministry of Science and Innovation/State Agency of Research MCIN/AEI/ 10.13039/501100011033.

APPENDIX

A. X-RAY SPECTRAL ANALYSIS

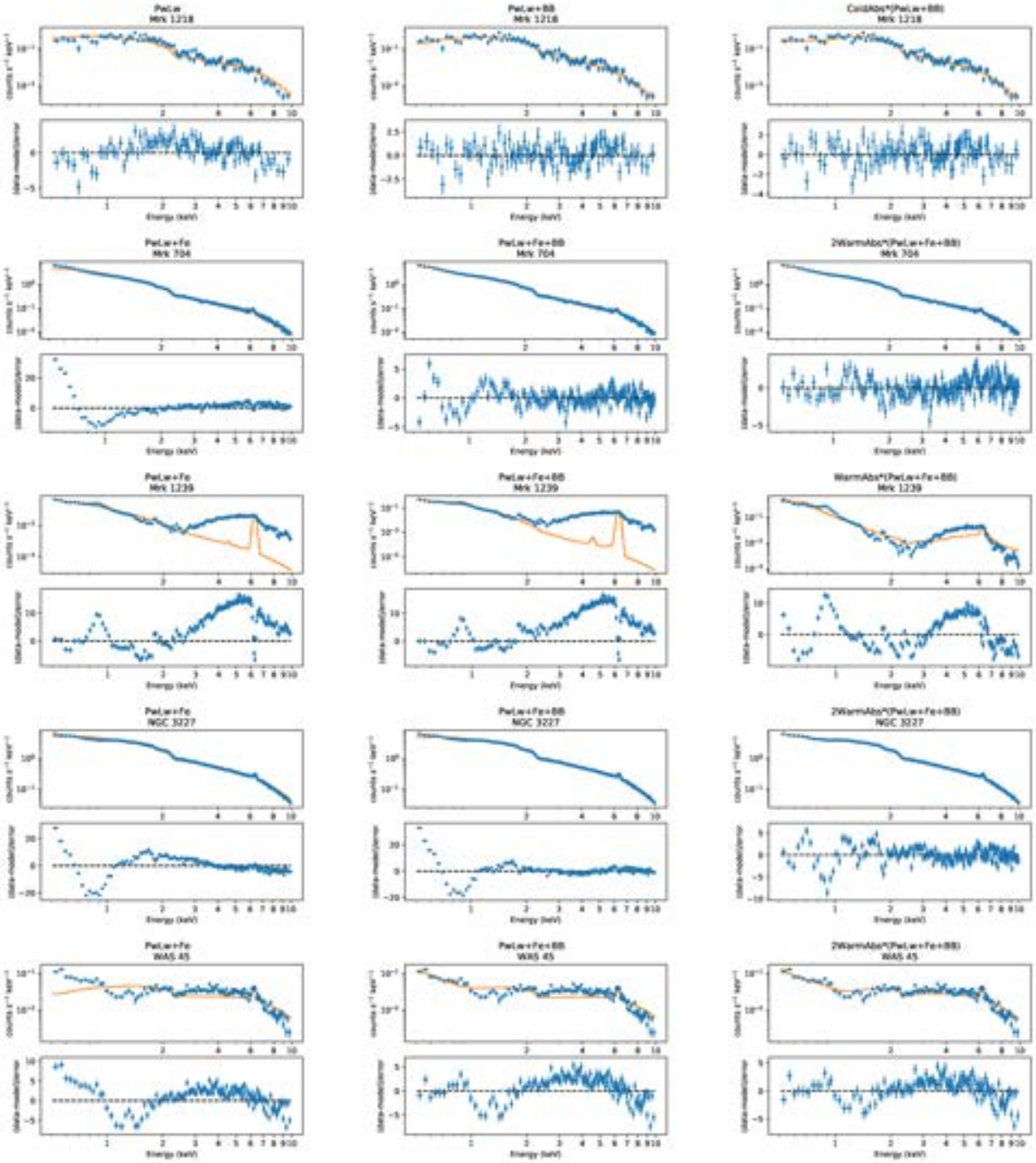

Fig. 6. **Polar polarized sources**. All the spectra are fitted in a range of 0.5-10 keV. The first column corresponds to the baseline model: power law + significant Fe emission lines. The second column contains fits with the addition of a soft excess as a black body. The third column shows the resulting model of the absorption test, either cold or warm.

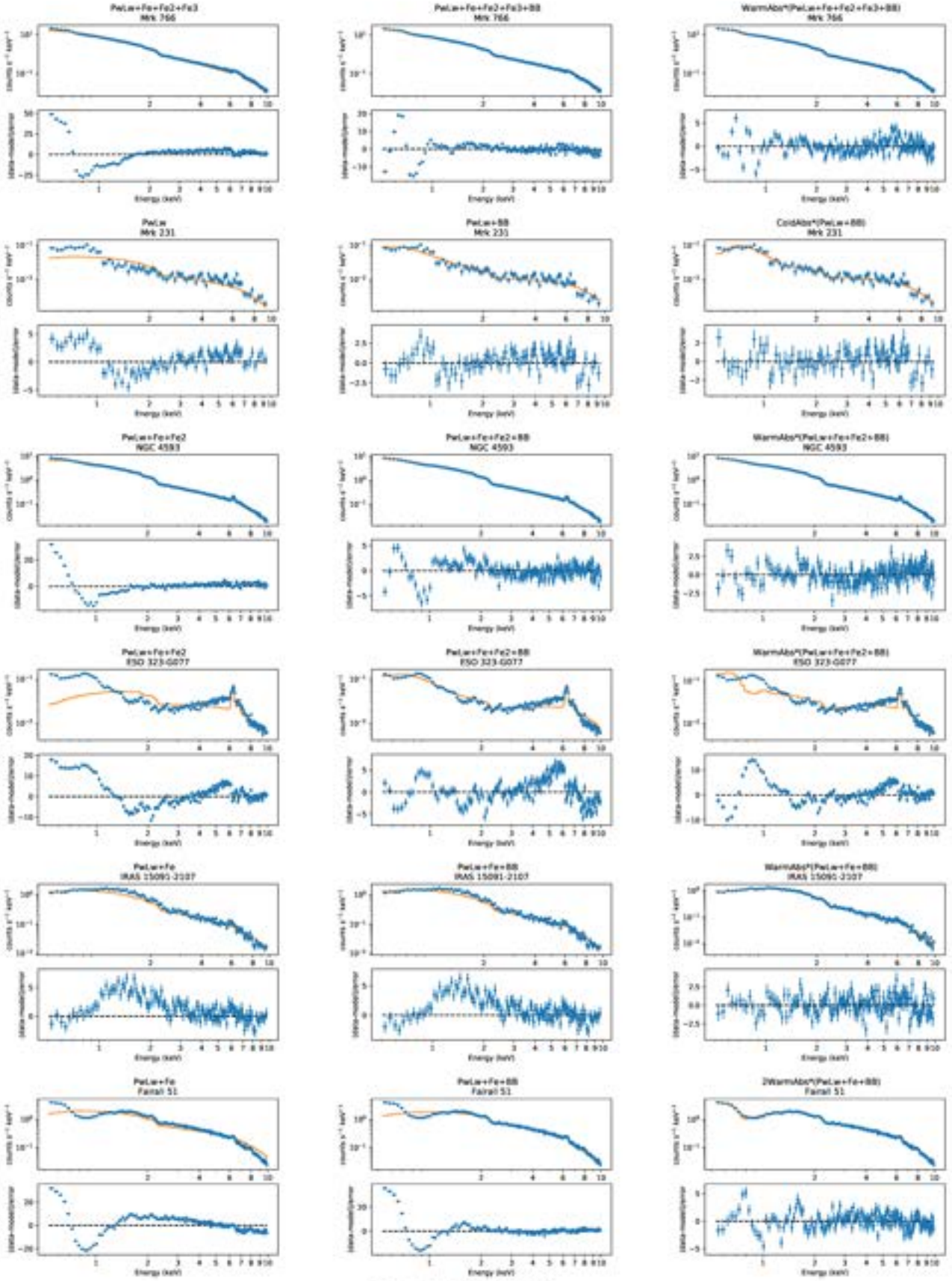

Fig. 6. CONTINUED

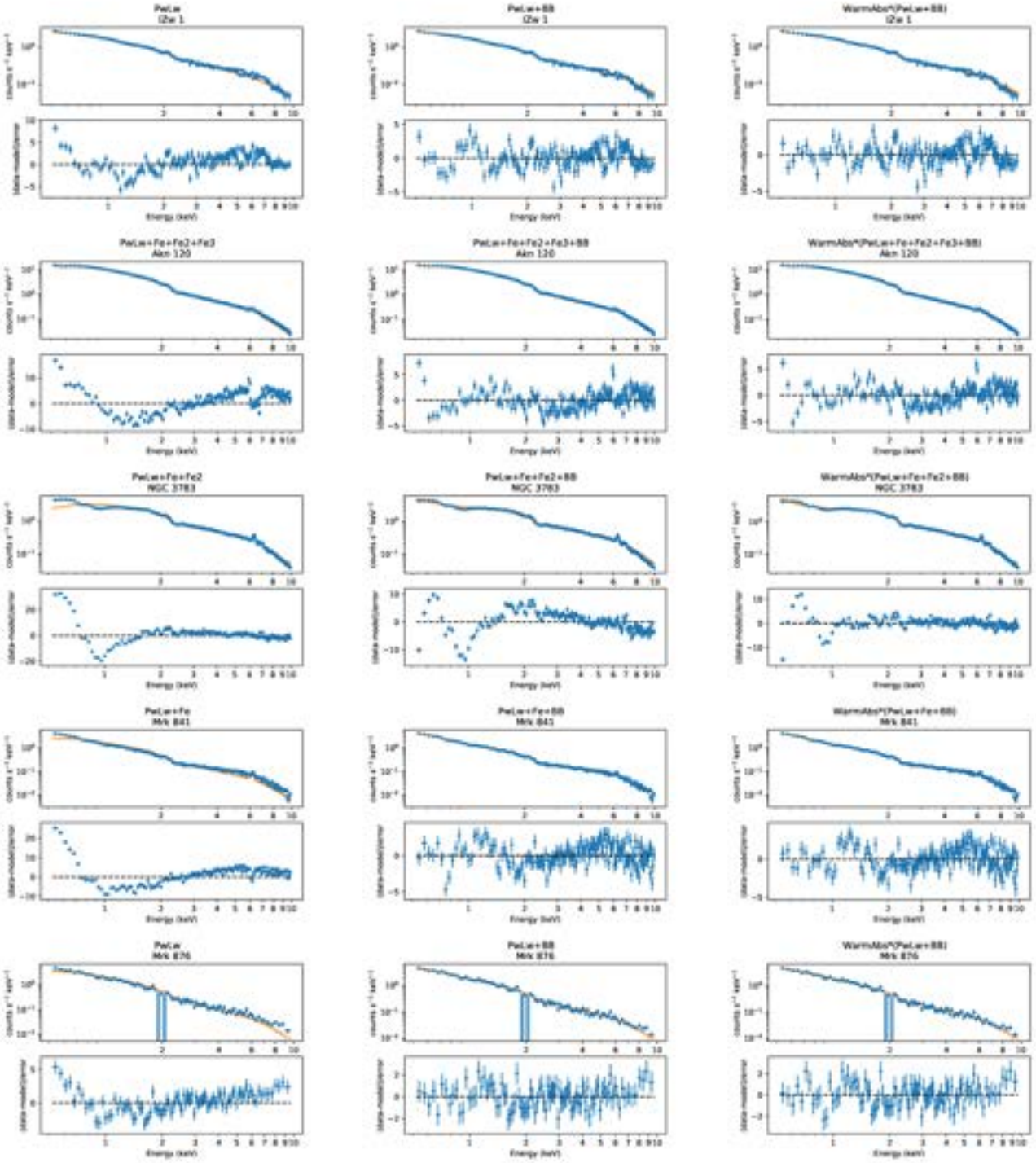

Fig. 7. **Equatorial Polarized sources**. All the spectra are fitted in a range of 0.5-10 keV. The first column corresponds to the baseline model: power law + significant Fe emission lines. The second column shows fits with the addition of soft excess as a black body. The third column shows the resulting model of the absorption test, either cold, warm or not absorbed.

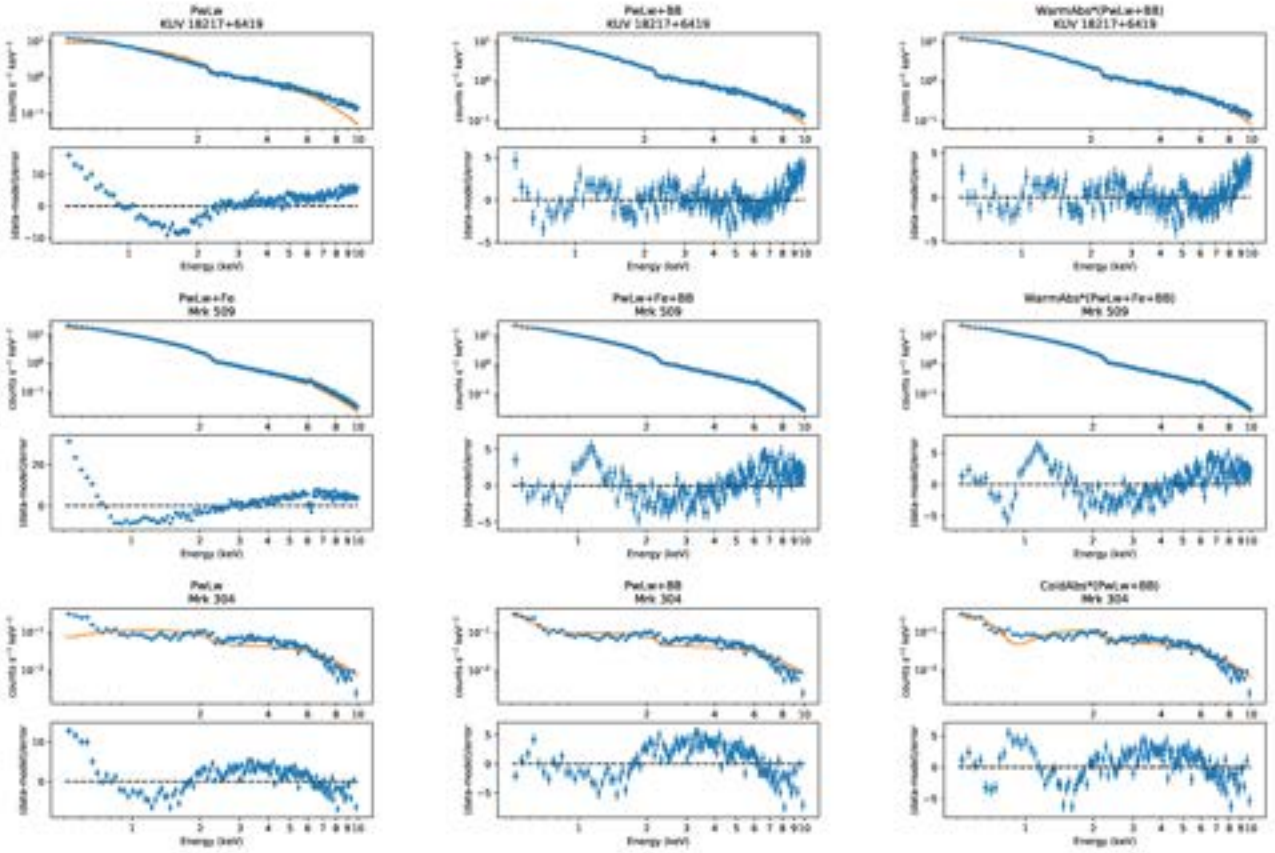

Fig. 7. CONTINUED

REFERENCES

Afanasiev, V. L. & Popović, L. Č. 2015, ApJ, 800, 35, https://doi.org/10.1088/2041-8205/800/2/L35

Afanasiev, V. L., Popović, L. Č., & Shapovalova, A. I. 2019, MNRAS, 482, 4985, https://doi.org/10.1093/mnras/sty2995

Akaike, H. 1974, IEEE Transactions on Automatic Control, 19, 716, https://doi.org/10.1109/TAC.1974.1100705

Antonucci, R. 1993, ARA&A, 31, 473, https://doi.org/10.1146/annureva.aa.31.090193.002353

Antonucci, R. R. J. & Miller, J. S. 1985, ApJ, 297, 621, https://doi.org/10.1086/163559

Beckmann, V. & Shrader, C. R. 2012, Active Galactic Nuclei (Wiley-VCH Verlag GmbH)

Bianchi, S., Matt, G., Nicastro, F., Porquet, D., & Dubau, J. 2005, MNRAS, 357, 599, https://doi.org/10.1111/j.1365-2966.2005.08661.x

Blustin, A. J., Branduardi-Raymont, G., Behar, E., et al. 2002, A&A, 392, 453, https://doi.org/10.1051/0004-6361:20020914

Blustin, A. J., Page, M. J., Fuerst, S. V., Branduardi-Raymont, G., & Ashton, C. E. 2005, A&A, 431, 111, https://doi.org/10.1051/0004-6361:20041775

Bottacini, E. 2022, MNRAS, 515, 3174, https://doi.org/10.1093/mnras/stac18890

Bottacini, E., Orlando, E., Greiner, J., et al. 2015, ApJ, 798, 14, https://doi.org/10.1088/2041-8205/798/1/L14

Braito, V., Ceca, R. D., Piconcelli, E., et al. 2004, A&A, 420, 79, https://doi.org/10.1051/0004-6361:20040061

Brenneman, L. W., Reynolds, C. S., Wilms, J., & Kaiser, M. E. 2007, ApJ, 666, 817, https://doi.org/10.1086/520763

Buhariwalla, M. Z., Gallo, L. C., Mao, J., et al. 2023, MNRAS, 521, 2378, https://doi.org/10.1093/mnras/stad265

Buhariwalla, M. Z., Waddell, S. G. H., Gallo, L. C., Grupe, D., & Komossa, S. 2020, ApJ, 901, 118, https://doi.org/10.3847/1538-4357/abb08a

C. S. Reynolds & Fabian, A. C. 1995, MNRAS, 273, 1167, https://doi.org/10.1093/mnras/273.4.1167

Cappi, M., Panessa, F., Bassani, L., et al. 2006, A&A, 446, 459, https://doi.org/10.1051/0004-6361:20053893

Corral, A., Ceca, R. D., Caccianiga, A., et al. 2011, A&A, 530, 42, https://doi.org/10.1051/0004-6361/201015227

Costantini, E., Gallo, L. C., Brandt, W. N., Fabian, A. C., & Boller, T. 2007, MNRAS, 378, 873, https://doi.org/10.1111/j.1365-2966.2007.11646.x

Detmers, R. G., Kaastra, J. S., Steenbrugge, K. C., et al. 2011, A&A, 534, 38, https://doi.org/10.1051/0004-6361/201116899

Ebrero, J., Kaastra, J. S., Kriss, G. A., de Vries, C. P., & Costantini, E. 2013, MNRAS, 435, 3028, https://doi.org/10.1093/mnras/stt1497

Gallo, L. C., Brandt, W. N., Costantini, E., et al. 2007, MNRAS, 377, 391, https://doi.org/10.1111/j.1365-2966.2007.11601.x

Gordon, C. & Arnaud, K. 2021, PyXspec: Python interface to XSPEC spectral- fitting program, Astrophysics Source Code Library, record ascl:2101.014

Haardt, F. & Maraschi, L. 1991, ApJ, 380, 51, https://doi.org/10.1086/186171

Hernández-García, L., Masegosa, J., González-Martín, O., et al. 2017, A&A, 602, 65, https://doi.org/10.1051/0004-6361/201730476

HI4PI Collaboration, Ben Bekhti, N., Flöer, L., et al. 2016, A&A, 594, 116, https://doi.org/10.1051/0004-6361/201629178

Jimenez-Bailon, E., Guainazzi, M., Matt, G., et al. 2008, RMxAC, 32, 131, https://doi.org/10.48550/arXiv.0710.1043

Jiménez-Bailón, E., Krongold, Y., Bianchi, S., Matt, G., Santos-Lleó, M., Piconcelli, E., & Schartel, N. 2008, MNRAS, 391, 1359, https://doi.org/10.1111/j.1365-2966.2008.13976.x

Jiménez-Bailón, E., Santos-Lleó, M., Piconcelli, E., et al. 2007, A&A, 461, 917, https://doi.org/10.1051/0004-6361:20065566

Joye, W. A. & Mandel, E. 2003, ASPC 295, Astronomical Data Analysis Software and Systems XII, ed. H. E. Payne, R. I. Jedrzejewski, and R. N. Hook, 489

Kaastra, J. S., Petrucci, P. O., Cappi, M., et al. 2011, A&A, 534, 36, https://doi.org/10.1051/0004-6361/201116869

Kaspi, S., Maoz, D., Netzer, H., et al. 2005, ApJ, 629, 61, https://doi.org/10.1086/431275

Komossa, S. 2008, RMxAC, 32, 86, https://doi.org/10.48550/arXiv.0710.3326

Krongold, Y., Longinotti, A. L., Santos-Lleó, M., et al. 2021, ApJ, 917, 39, https://doi.org/10.3847/1538-4357/ac0977

Laha, S., Dewangan, G. C., & Kembhavi, A. K. 2011, ApJ, 734, 75, https://doi.org/10.1088/0004-637X/734/2/75

Laha, S., Reynolds, C. S., Reeves, J., et al. 2021, NatAs, 5, 13, https://doi.org/10.1038/s41550-020-01255-2

Laha, S., Guainazzi, M., Dewangan, G. C., Chakravorty, S., & Kembhavi, A. K. 2014, MNRAS, 441, 2613, https://doi.org/10.1093/mnras/stu669

Longinotti, A. L., Costantini, E., Petrucci, P. O., et al. 2010, A&A, 510, 92, https://doi.org/10.1051/0004-6361/200912925

Mao, J., Mehdipour, M., Kaastra, J. S., et al. 2019, A&A, 621, 99, https://doi.org/10.1051/0004-6361/201833191

Markowitz, A., Reeves, J. N., George, I. M., et al. 2009, ApJ, 691, 922, https://doi.org/10.1088/0004-637X/691/2/922

Matt, G., Bianchi, S., Guainazzi, M., et al. 2011, A&A, 533, 1, https://doi.org/10.1051/0004-6361/201116443

Matt, G., Marinucci, A., Guainazzi, M., et al. 2014, MNRAS, 439, 3016, https://doi.org/10.1093/mnras/stu159

Miller, J. S., Goodrich, R. W., & Mathews, W. G. 1991, ApJ, 378, 47, https://doi.org/10.1086/170406

Miller, L., Turner, T. J., Reeves, J. N., et al. 2006, A&A, 453, 13, https://doi.org/10.1051/0004-6361:20065276

Miniutti, G., Sanfrutos, M., Beuchert, T., et al. 2014, MNRAS, 437, 1776, https://doi.org/10.1093/mnras/stt2005

Netzer, H. 2015, ARA&A, 53, 365, https://doi.org/10.1146/annurev-astro-082214-122302

Newman, J., Tsuruta, S., Liebmann, A. C., Kunieda, H., & Haba, Y. 2021, ApJ, 907, 45, https://doi.org/10.3847/1538-4357/abd1da

Osterbrock, D. E. & Pogge, R. W. 1985, ApJ, 297, 166, https://doi.org/10.1086/163513

Petrucci, P. O., Ursini, F., De Rosa, A., et al. 2018, A&A, 611, 59, https://doi.org/10.1051/0004-6361/201731580

Piconcelli, E., Jimenez-Bailón, E., Guainazzi, M., et al. 2004, MNRAS, 351, 161, https://doi.org/10.1111/j.1365-2966.2004.07764.x

Piconcelli, E., Jimenez-Bailón, E., Guainazzi, M., et al. 2005, A&A, 432, 15, https://doi.org/10.1051/0004-6361:20041621

Piotrovich, M. Y., Shablovinskaya, E. S., Malygin, E. A., Buliga, S. D., & Natsvlishvili, T. M. 2023, MNRAS, 526, 2596, https://doi.org/10.1093/mnras/stad2934

Porquet, D., Reeves, J. N., Matt, G., et al. 2018, A&A, 609, 42, https://doi.org/10.1051/0004-6361/201731290

Ricci, C., Ueda, Y., Ichikawa, K., et al. 2014a, A&A, 567, 142, https://doi.org/10.1051/0004-6361/201322701

Ricci, C., Ueda, Y., Paltani, S., et al. 2014b, MNRAS, 441, 3622, https://doi.org/10.1093/mnras/stu735

Risaliti, G., Nardini, E., Salvati, M., et al. 2011, MNRAS, 410, 1027, https://doi.org/10.1111/j.1365-2966.2010.17503.x

Scott, A. E., Stewart, G. C., Mateos, S., et al. 2011, MNRAS, 417, 992, https://doi.org/10.1111/j.1365-2966.2011.19325.x

She, R., Ho, L. C., & Feng, H. 2017, ApJ, 835, 223, https://doi.org/10.3847/1538-4357/835/2/223

Silva, C. V., Costantini, E., Giustini, M., et al. 2018, MNRAS, 480, 2334, https://doi.org/10.1093/mnras/sty1938

Singh, V., Shastri, P., & Risaliti, G. 2011, A&A, 532, 84, https://doi.org/10.1051/0004-6361/201016387

Smith, J. E., Robinson, A., Alexander, D. M., et al. 2004, MNRAS, 350, 140, https://doi.org/10.1111/j.1365-2966.2004.07610.x

Smith, J. E., Robinson, A., Young, S., Axon, D. J., & Corbett, E. A. 2005, MNRAS, 359, 846, https://doi.org/10.1111/j.1365-2966.2005.08895.x

Smith, J. E., Young, S., Robinson, A., et al. 2002, MNRAS, 335, 773, https://doi.org/10.1046/j.1365-8711.2022.05665.x

Svoboda, J., Beuchert, T., Guainazzi, M., Longinotti, A. L., Piconcelli, E., & Wilms, J. 2015, A&A, 578, 96, https://doi.org/10.1051/0004-6361/201425453

Turner, T. J., Miller, L., Reeves, J. N., & Kraemer, S. B. 2007, A&A, 475, 121, https://doi.org/10.1051/0004-6361:20077947

Ursini, F., Petrucci, P. O., Matt, G., 2016, MNRAS, 463, 382, https://doi.org/10.1093/mnras/stw2022

Wilms, J., Allen, A., & McCray, R. 2000, ApJ, 542, 914, https://doi.org/10.1086/317016

M. Cerviño: Centro de Astrobiología (CAB), CSIC-INTA, Campus ESAC, camino bajo del Castillo s/n, Villafranca del Castillo, Villanueva de la Cañada, 28692 Madrid, Spain.

M. Guainazzi: European Space Agency, European Space Research and Technology Centre (ESTEC), Keplerlaan 1, 2201 AZ Noordwijk, The Netherlands.

M. Gudiño, E. Jiménez-Bailón, A. L. Longinotti, and A. C. Robleto-Orús: Instituto de Astronomía, Universidad Nacional Autónoma de México, AP 70-264, Ciudad de México, CDMX 04510, México (megudino@astro.unam.mx).

E. Jiménez-Bailón: Quasar Science Resource S.L. for the European Space Agency (ESA), European Space Astronomy Centre (ESAC), Camino Bajo del Castillo s/n, 28692 Villanueva de la Cañada, Madrid, Spain.

Revista Mexicana de Astronomía y Astrofísica, **60**, 261–275 (2024)

https://doi.org/10.22201/ia.01851101p.2024.60.02.05

IDENTIFICATION OF PLANETARY AND PROTO-PLANETARY NEBULAE CANDIDATES THROUGH *AKARI* INFRARED PHOTOMETRY

R. A. Márquez-Lugo[1,2], S. N. Kemp[1,2], G. Ramos-Larios[1,2], A. Nigoche-Netro[1,2], S. G. Navarro[1,2], and L. J. Corral[1,2]

Received December 22 2023; accepted April 15 2024

ABSTRACT

We utilized photometric data from the space telescope *AKARI* to identify potential planetary nebulae (PNe) and proto-planetary nebulae (PPNe) candidates. Using the color-color diagram, we found a region with a high concentration of established PNe and PPNe, comprising about 95% of the objects. Based on this, we identified 67 objects within this region that lack definitive classification in existing literature, suggesting they are promising candidates. We conducted Spectral Energy Distribution (SED) analysis and morphological investigations using imagery from various observatories and satellites. Finally, we present a list of 65 potential PNe and PPNe candidates.

RESUMEN

Utilizamos datos fotométricos del telescopio espacial *AKARI* para identificar posibles candidatos a nebulosas planetarias (PNe) y proto-nebulosas planetarias (PPNe). Utilizando el diagrama de color-color, encontramos una región con una alta concentración de PNe y PPNe establecidas, que comprende aproximadamente el 95% de los objetos. Basados en esto, identificamos 67 objetos dentro de esta región que carecen de clasificación definitiva en la literatura existente, sugiriendo que son candidatos prometedores. Realizamos análisis de Distribución de Energía Espectral (SED) e investigaciones morfológicas utilizando imágenes de varios observatorios y satélites. Finalmente, presentamos una lista de 65 posibles candidatos a PNe y PPNe.

Key Words: infrared: ISM — planetary nebulae: general — stars: AGB and post-AGB

1. INTRODUCTION

The identification of extended planetary nebulae (PNe) has been carried out by morphological or spectral analysis (Pottasch 1984). However, in the case of unresolved sources, photometric methods, such as *IRAS* (Infrared Astronomical Satellite) color-color diagrams, have been employed (Pottasch et al. 1988; Preite-Martínez 1988; van de Steene & Pottasch 1993, 1995; Manchado et al. 1989; García-Lario et al. 1990; Ramos-Larios et al. 2009; Akras, Guzman-Ramirez, & Gonçalves 2019) or 2MASS (Two Micron All-Sky Survey) and *WISE* (Wide-Field Infrared Survey Explorer) for the identification and classification of symbiotic stars (Akras et al. 2019). The available data from the infrared astronomical mission *AKARI* (Murakami et al. 2007) have been shown to be useful in the study of known PNe and proto-planetary nebulae (PPNe) (Cox, et al. 2009 a,b, 2011; Phillips & Márquez-Lugo 2011; Pollo, Takeuchi & Rybka 2011; Ohsawa, et al. 2012, 2016; Ueta, et al. 2019), which is why we have used photometric data from the *AKARI* Point Source Catalog (*AKARI* PSC) to identify new PNe and PPNe candidates.

We utilized widely recognized catalogues encompassing planetary nebulae (PNe), galaxies, young stellar objects (YSOs), main sequence and pre-main sequence stars, symbiotic stars, OH/IR stars, Herbig-Haro objects (HH), and HII compact regions. The objective was to pinpoint the positions of these sources within an *AKARI* Point Source Catalogue (PSC) color-color diagram. Our focus was on iden-

[1]Instituto de Astronomía y Meteorología, Universidad de Guadalajara, Jalisco, México.
[2]Departamento de Física, Universidad de Guadalajara, Jalisco, México.

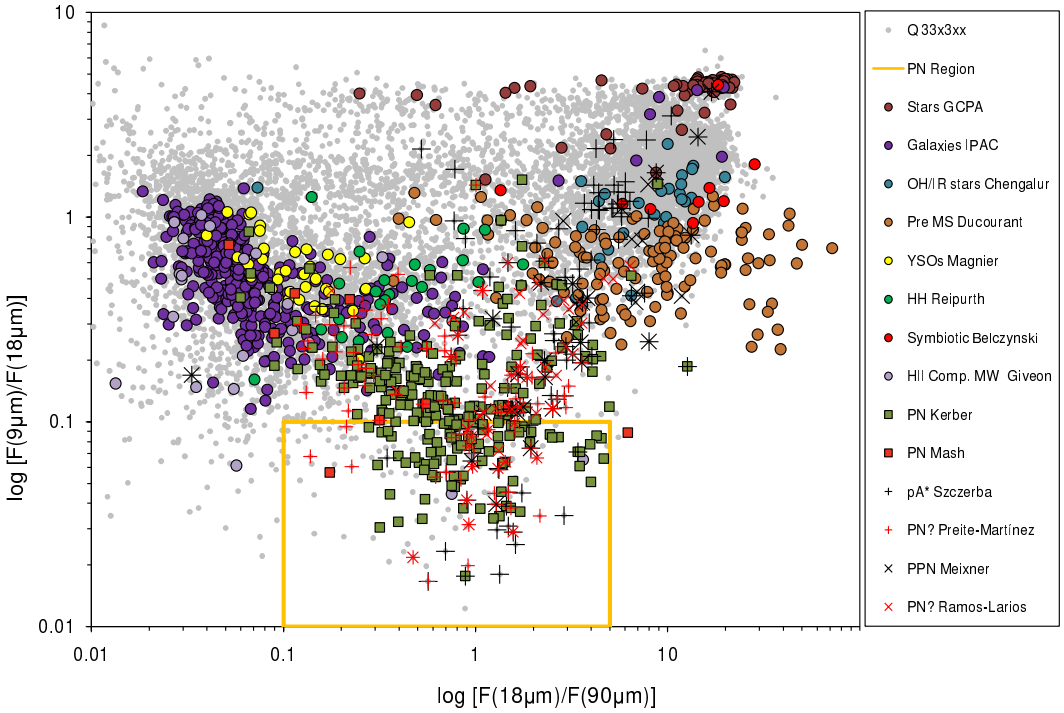

Fig. 1. *AKARI* PSC color-color diagram. The *AKARI* PSC sources with Q33x3xx are shown as grey points, and the right hand panel indicates other, superimposed symbols (see text for details). The area delineated in yellow contains a concentration of PNe, PPNe, post-AGB stars, and candidates for all these categories, and excludes an enormous proportion of other types of astronomical objects. The color figure can be viewed online.

tifying a distinct region where planetary nebulae (PNe) are prominently featured and relatively segregated from other categories of astronomical entities.

2. OBSERVATIONS

The *AKARI* PSC photometry has been accessible to the public since March 2010. In addition, mission image data have been released, starting with the *AKARI* far-infrared all-sky survey maps, available since December 2014, and subsequently the *AKARI*/IRC Pointed Observation Images from March 2015 (IRC, InfraRed Camera). However, owing to the suboptimal resolution of *AKARI* images for the present study, we employed image data from other infrared and optical projects such as the *Spitzer Space Telescope*, The INT Photometric Hα Survey of the Northern Galactic Plane (IPHAS), 2MASS, and *WISE*. These alternative datasets were utilized to examine the spatial emission profiles of PNe candidates and, as a preliminary step, to analyze their morphology (for detailed information, refer to § 6).

To generate the color-color diagram for distinguishing between various types of astronomical objects, we employed photometry data from the PSC of the *AKARI* space telescope (previously known as ASTRO-F or IRIS Infra Red Imaging Surveyor, launched on February 21, 2006). This dataset comprises two components: one obtained from the IRC featuring two bands centered at 9μm and 18μm (Ishihara et al. 2010), and the other from the Far-Infrared Surveyor (FIS) with four bands centered at 65μm, 90μm, 140μm, and 160μm (Kawada et al. 2007).

For constructing the spectral energy distributions (SEDs) we utilized data not only from *AKARI*, but also from: US Naval Observatory B catalogue (USNO-B), compiled from the digitalisation of various photographic sky surveys plates by the Precision Measuring Machine (PMM), located at the US Naval Observatory Flagstaff Station (NOFS), from 350 nm to 900 nm between 1949 and 2002 (Monet et al. 2003); 2MASS, with three bands J (1.25μm), H (1.65μm) and K (2.17μm) from the 1.3 m telescopes at Mount Hopkins and Cerro Tololo Inter-American Observatory (CTIO) Chile (Kleinmann 1992); the Deep Near Infrared Southern Sky Survey (DENIS) (Fouqué et al. 2000) with three bands i (0.802μm), J (1.248μm) and K_s (2.152μm); the Midcourse Space Experiment (MSX) (Egan & Price

1996), from the telescope SPIRIT III aboard the Ballistic Missile Defense Organization (BMDO) with the bands A (8.28μm), C (12.13μm), D (14.65μm) and E (21.3μm) and the Infrared Array Camera (IRAC) (Fazio et al. 2004) aboard the *Spitzer Space Telescope* with the bands I1 (3.6μm), I2 (4.5μm), I3 (5.8μm) and I4 (8.0μm).

The resolution of the images of the *AKARI* far-infrared all-sky survey maps, with pixel sizes of the detectors of $26.8'' \times 26.8''$ for the short wavelength bands N60 and WIDE-S, and $44.2'' \times 44.2''$ for the long wavelength bands N160 and WIDE-L (Doi, et al. 2015) is too poor to study the morphology and vicinity of the candidates; therefore *WISE* (Wide-Field Infrared Survey Explorer, Wright et al. 2010) images were used for this purpose. Furthermore, radial emission profiles of sources were derived from *Spitzer* IRAC, 2MASS and IPHAS data.

3. SEARCHING FOR CANDIDATES

3.1. *The* AKARI *Point Source Catalogue*

The *AKARI* PSC comprises two components: the *AKARI* FIS Bright Source Catalogue (Yamamura et al. 2010) and the *AKARI* IRC Point Source Catalogue (Ishihara et al. 2010). The AKARI IRC Catalogue encompasses data from two bands centered at 9μm and 18μm. The 9μm band includes information for 844,649 sources, while the 18μm band comprises data for 194,551 sources In total, there is information for 870,973 unique sources, with 168,227 sources appearing in both bands. On the other hand, the *AKARI* FIS Catalogue provides photometric data for 427,071 sources, each observed in at least one of the four bands centered at 65μm, 90μm, 140μm, and 160μm. Among these, the 90μm band, with data for 373,553 sources, emerges as the most crucial for subsequent analyses due to its heightened sensitivity.

In summary the *AKARI* PSC provides photometric information for six bands. Each datum comes with a quality indicator called Qualityflag (FQUAL). This indicator can take values from 0 to 3. FQUAL=3 is the highest quality, indicating a confirmed source. FQUAL=2 indicates a confirmed source with problems, a source with a very low flux level or a possible false detection, for example a "side-lobe" effect. FQUAL=1 implies that the source was not confirmed or that the flux value is unreliable. Finally FQUAL=0 is a non-detection. For our inquiry, we exclusively considered sources with a Qualityflag of FQUAL=3 in the 9μm, 18μm, and 90μm bands, and any Qualityflag in the 65μm, 140μm, and 160μm bands. We denote this specific combination of Qualityflag as Q33x3xx, representing the bands 9μm, 18μm, 65μm, 90μm, 140μm, and 160μm, respectively. This selection resulted in a total of 9,900 sources.

The *AKARI* photometric information was obtained from DARTS/Akari at ISAS/JAXA `http://darts.jaxa.jp/ir/akari/cas/tools/search/crossid.html` using *AKARI*-CAS (Yamauchi et al. 2011).

3.2. *Catalogues for Source Discrimination*

We have cross-referenced these 9,900 sources from the *AKARI* PSC, which report high-quality photometry, against catalogues of various types of astrophysical objects from VizieR and some bibliographic references to establish correspondences. The catalogues employed for this purpose were as follows:

General catalogue of stars with the system of photoelectric astrolabes (Working Group Of GCPA 1992), Catalogued galaxies and quasars observed in the *IRAS* survey, Version 2 (Fullmer & Lonsdale 1989), New OH/IR stars from color-selected *IRAS* sources. 3: A complete survey (Chengalur et al. 1996), Pre-main sequence star Proper Motion Catalogue (Ducourant et al. 2005), Transitional YSOs (Young Stellar Objects) candidates from flat-spectrum *IRAS* sources (Magnier et al. 2000), A General Catalogue of Herbig-Haro Objects, 2nd Edition (Reipurth 2000), A catalogue of symbiotic stars (Belczynski et al. 2001), A New Catalogue of Radio Compact H II Regions in the Milky Way. II. The 1.4 GHz Data (Giveon et al. 2005), Galactic Planetary Nebulae and their central stars. I. An accurate and homogeneous set of coordinates (Kerber et al. 2004), MASH (Macquarie/AAO/Strasbourg H_α) Catalogues of Planetary Nebulae (Parker et al. 2006), Torun catalogue of post-AGB (post-Asymtotic Giant Branch) and related objects (Szczerba et al. 2007), A Mid-Infrared Imaging Survey of Proto-Planetary Nebula Candidates (Meixner et al. 1999), Possible new planetary nebulae in the *IRAS* Point Source Catalogue (Preite-Martínez 1988) and *IRAS* identification of Post-AGB and PNe candidates (Ramos-Larios et al. 2009). The selection was carried out with the aim of encompassing a broad variety of astronomical objects, facilitating a comprehensive comparison of their infrared emissions and positions in color-color maps, in relation to the emission and position of PNe and PPNe.

3.3. *Color–Color Diagram*

After reviewing the work of García-Lario et al. (1990), taking into account the available AKARI

bands, and thoroughly exploring potential color combinations, we have chosen the following color definitions.:

$$x = \log \frac{F(18\mu m)}{F(90\mu m)},$$

and

$$y = \log \frac{F(9\mu m)}{F(18\mu m)}.$$

In Figure 1, we have plotted the values for log[F(18μm)/F(90μm)] against log[F(9μm)/F(18μm)] for the 9,900 sources in the *AKARI* PSC with photometry quality Q33x3xx. Superimposed symbols represent objects also present in the catalogues mentioned above (§ 3.2). The diagram delineates distinct areas corresponding to different types of objects. Notably, there is a defined region (marked by the yellow line) where known PNe and PNe candidates are concentrated. This region, referred to as the PNe region, is situated between:

$$0.1 \leq \log \frac{F(18\mu m)}{F(90\mu m)} \leq 5,$$

and

$$0.01 \leq \log \frac{F(9\mu m)}{F(18\mu m)} \leq 0.1.$$

In addition to the objects from the catalogues of known PNe and PNe candidates, only two objects from the 'New Catalog of Radio Compact H II Regions in the Milky Way' are located in the PNe region. No objects from any of the catalogues representing other types were identified in this region. The PNe region includes 215 sources from the *AKARI* PSC with Q33x3xx. Excluding the previously identified PNe, there are 67 sources that can in principle be regarded as potential PNe candidates (Table 1).

The selection of these limits is conservative. Confirming the proposed candidates in this study could warrant an extension of the PN region, particularly by increasing the value on the ordinate axis to 0.2 to encompass more potential candidates. However, this adjustment might introduce a risk of potential contamination of the PN region with galaxies.

4. SIMBAD SOURCES

We referred to the SIMBAD database to gather information about our 67 potential candidates, as

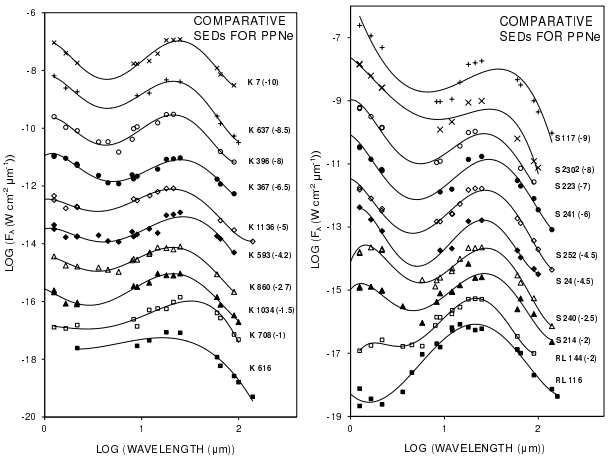

Fig. 2. SEDs of established PPNe. The double-component structure is clearly seen in the SEDs. Each PPN is identified by the initials of the authors of the corresponding catalogues: Kerber, Szczerba, and Ramos-Larios, followed by the corresponding identification number. In order to avoid overlaps between different SEDs, an offset has been applied; the value of the offset is given in brackets after the PPN name.

presented in Table 1. The search radius was set at 6 arcsec.

Out of the 67 potential candidates, 30 did not yield any identification, while in 37 cases at least one identification was obtained. Table 1 provides details such as the IRC identifier number, galactic coordinates, right ascension, declination, the SIMBAD identification, distance between the IRC source and the SIMBAD identification, and the concise SIMBAD object type (`http://simbad.u-strasbg.fr/simbad/sim-display?data=otypes`).

The total number of identifications is 50 (there may be more than one per object), of which 13 are infrared sources (IR), 7 maser sources (Mas), 7 possible PNe (PN?), 4 post-AGB candidates (pA?), 3 stars (*), 3 radio sources (Rad), 2 emission-line stars (Em*), 2 semi-regular pulsating stars (sr*) and 1 identification of each of the following types of objects: post-AGB-PPN (pA*), peculiar star (Pe*), variable star (V*), young stellar object candidate (Y*?), 'region defined in the sky' (reg), carbon star (C*), young stellar object (YSO), emission object (EmO) and high mass X-ray binary (HXB).

As a PN is an ionized circumstellar shell around a hot compact star, in the process of evolving between the AGB and white dwarf (WD) phase, it can be described in various ways depending on the particular characteristic under study. For example, it may be described as a transition object (pA* or pA?) while the central star is ionizing the envelope, the spec-

TABLE 1

AKARI PLANETARY NEBULAE CANDIDATES

No	IRC	G.C.	RA (2000) H M S	DEC (2000) D M S	IDENTIFICATION	DIST arcsec	TYPE
1	200475060	G001.30+04.07	17 33 13.13	-25 40 17.7	-	-	-
2	200557576	G006.43-01.92	18 07 31.86	-24 20 21.1	-	-	-
3	200455657	G008.55+11.49	17 23 11.65	-15 37 15.9	[M81] I-556	2.36	Em*
					IRAS 17203-1534	3.85	pA*
4	200535439	G008.85+01.69	17 59 05.08	-20 27 24.4	SCHB 258	0.61	Mas
5	200556938	G009.10-00.39	18 07 20.97	-21 16 11.2	SCHB 292	0.37	Mas
					IRAS 18043-2116	3.49	IR
6	200562588	G011.41+00.43	18 09 04.73	-18 50 42.6	*IRAS* 18061-1851	4.4	IR
7	200585006	G014.03-00.66	18 18 22.46	-17 04 00.6	-	-	-
8	200580061	G015.70+00.77	18 16 25.80	-14 55 13.0	-	-	-
9	200605366	G017.01-01.23	18 26 15.79	-14 42 26.5	OH 17.0 -1.2	2.46	Mas
					[TVH89] 301	2.46	Mas
					PN PM 1-232	5.17	PN?
10	200600445	G020.41+01.11	18 24 18.70	-10 36 30.2	*IRAS* 18215-1038	2.76	IR
11	200627833	G020.51-02.07	18 35 59.44	-11 59 39.1	-	-	-
12	200628891	G025.26+00.25	18 36 29.20	-06 42 46.7	GSC 05124-02611	1.18	*
13	200637610	G027.54+00.41	18 40 06.57	-04 36 41.9	-	-	-
14	200643853	G028.34+00.12	18 42 37.09	-04 02 04.7	-	-	-
15	200686203	G030.09-04.74	19 03 09.52	-04 41 08.4	-	-	-
16	200675903	G036.07-00.17	18 57 46.14	02 43 09.3	-	-	-
17	200700351	G036.41-03.68	19 10 54.42	01 24 41.6	2MASS J19105453+0124450	0.5	Pe*
18	200689042	G036.43-01.91	19 04 38.65	02 14 23.7	PK 036-01 3	2.4	PN?
19	200680582	G037.28-00.23	19 00 10.88	03 45 48.7	[WBH2005] G037.278-0.226	1.27	Rad
					V* V1672 Aql	1.61	V*
					2MASS J19001104+0345511	3.51	IR
20	200703532	G038.56-03.11	19 12 47.88	03 34 40.4	-	-	-
21	200704956	G042.90-01.08	19 13 37.89	08 21 47.9	-	-	-
22	200697923	G043.03+00.14	19 09 30.06	09 02 25.9	GPSR 043.028+0.140	0.75	Rad
					MSX6C G043.0281+00.1406	1.11	PN?
23	200754442	G052.24-06.42	19 51 00.78	13 58 20.4	V* TW Aql	5.44	sr*
24	200732448	G057.11+01.46	19 32 13.50	22 04 57.6	2MASS J19321348+2204566	0.99	Y*?
25	200734399	G057.81+01.46	19 33 41.50	22 42 02.8	PN PM 1-306	5.34	PN?
26	200765758	G068.20+00.24	20 01 59.87	31 03 09.9	*IRAS* 20000+3054	4.8	IR
27	200775563	G072.25+00.26	20 12 17.32	34 28 10.6	-	-	-
28	200500801	G077.13+30.87	17 44 55.03	50 02 40.2	V* V814 Her	4.25	sr*
29	200789311	G077.92+00.22	20 28 30.55	39 07 02.3	OH 2026+38	0.96	Rad
30	200796994	G080.94+00.02	20 38 49.61	41 25 22.0	-	-	-
31	200778777	G083.19+06.64	20 15 57.33	47 05 34.5	-	-	-
32	200808628	G083.61-02.20	20 57 03.78	42 06 26.6	-	-	-
33	200828078	G096.54+01.36	21 35 43.92	53 53 12.4	-	-	-
34	200862609	G111.71-02.13	23 23 13.49	58 48 05.0	[PF2007] R3	5.04	reg
35	200866080	G113.89-01.60	23 38 13.11	59 58 42.7	-	-	-
36	200865230	G115.21+04.32	23 34 21.97	66 01 56.5	*IRAS* 23321+6545	5.72	C*
37	200033305	G135.28+02.80	02 43 28.32	62 57 05.5	-	-	-
					MSX6C G200.0789-01.6323	5.19	Y*O

TABLE 1. CONTINUED

No	IRC	G.C.	RA (2000) H M S	DEC (2000) D M S	IDENTIFICATION	DIST arcsec	TYPE
38	200044584	G140.48+06.04	03 37 28.74	63 06 27.2	PN PM 1-8	2.44	PN?
					MSX6C G200.0789-01.6323	5.19	Y*O
39	200184830	G282.84-01.25	10 11 16.59	-57 44 10.6	-	-	-
40	200194383	G286.32-00.70	10 36 01.61	-59 07 44.6	*IRAS* 10341-5852	3.93	IR
					HD 303122	4.76	*
41	200193271	G286.60-01.92	10 33 05.11	-60 19 48.9	HD 305298	2.6	*
42	200200079	G289.36-02.65	10 50 20.48	-62 17 09.5	SPH 100	4.12	EmO
					IRAS 10484-6201	4.38	IR
43	200212827	G292.89-01.20	11 23 11.95	-62 20 25.8	-	-	-
44	200215868	G293.45+00.07	11 31 08.80	-61 19 07.0	-	-	-
45	200212510	G294.04-04.71	11 22 18.58	-66 01 46.8	*IRAS* 11201-6545	4.35	pA?
46	200235503	G299.54-00.02	12 21 45.12	-62 41 50.1	*IRAS* 12190-6225	2.71	IR
47	200246253	G302.55-02.74	12 47 46.78	-65 36 41.3	PN PM 1-69	2.43	PN?
48	200254043	G304.57+00.72	13 05 27.82	-62 06 37.4	-	-	-
49	200259071	G305.79+00.28	13 16 11.59	-62 27 14.2	*IRAS* 13129-6211	1.88	IR
50	200279625	G311.02+02.03	13 56 24.00	-59 48 59.3	*IRAS* 13529-5934	4.96	pA?
51	200285648	G311.68-00.63	14 07 35.16	-62 11 47.3	-	-	-
52	200302084	G313.87-04.08	14 36 34.50	-64 41 31.5	*IRAS* 14325-6428	0.89	pA?
53	200314558	G316.94-02.88	14 56 46.81	-62 17 29.9	-	-	-
54	200323862	G320.68+00.25	15 10 43.74	-57 44 47.7	*IRAS* 15068-5733	3.6	IR
55	200327862	G321.02-00.70	15 16 41.23	-58 22 28.6	*IRAS* 15127-5811	3.2	IR
56	200354340	G325.16-03.01	15 52 19.68	-57 50 52.5	*IRAS* 15482-5741	4.31	pA?
57	200366578	G331.16+00.78	16 06 40.62	-51 03 56.4	OH 331.16 +0.78	1.35	Mas
58	200365730	G332.29+02.28	16 05 41.23	-49 11 33.8	Caswell OH 332.295+02.280	5.79	Mas
					Caswell CH3OH 332.295+02.280	5.98	Mas
59	200392246	G335.06-01.16	16 32 39.87	-49 42 14.0	EM* VRMF 55	0.78	Em*
					IGR J16327-4940	0.78	HXB
					IRAS 16288-4935	4.69	IR
60	200397316	G335.95-01.36	16 37 14.40	-49 11 19.0	PN G335.9-01.3	3.67	PN?
61	200389424	G336.24+00.51	16 30 10.70	-47 42 37.8	-	-	-
62	200412657	G340.43-00.37	16 50 08.91	-45 09 26.4	-	-	-
63	200420643	G342.44-00.23	16 56 39.52	-43 30 49.6	-	-	-
64	200413826	G350.43+07.61	16 51 06.42	-32 23 00.5	-	-	-
65	200422895	G352.57+07.30	16 58 27.11	-30 55 06.3	2MASS J16582725-3055108	4.98	IR
66	200489617	G355.61-01.16	17 39 27.29	-33 16 41.2	-	-	-
67	200571327	G359.81-06.87	18 12 58.61	-32 30 04.1	-	-	-

trum of which shows strong emission lines (Em*) including those of ionized hydrogen (H II), the material expelled during the AGB mass-loss phase is heated by radiation or shocks, and therefore is an IR source (IR), and this material can contain large quantities of carbon, product of the triple-α reaction (C*). Besides, the central stars of PNe, which are terminating their AGB phase, can have brightness variations (sr* and V*). Also, the PPNe can show maser emission (Mas) due to the presence of water (Uscanga et al. 2019), and finally some rotational molecular transitions emit at radio wavelengths (Rad). So all these classifications do not rule out the possibility of the objects being PN or PPN candidates. Therefore, objects thus identified are not excluded from the potential candidate list.

On the other hand, classifications such as star (*), peculiar star (Pe*), region defined in the sky (reg) and emission object (EmO) are poorly defined and are not sufficient reasons to exclude sources with such classifications from the potential candidate list.

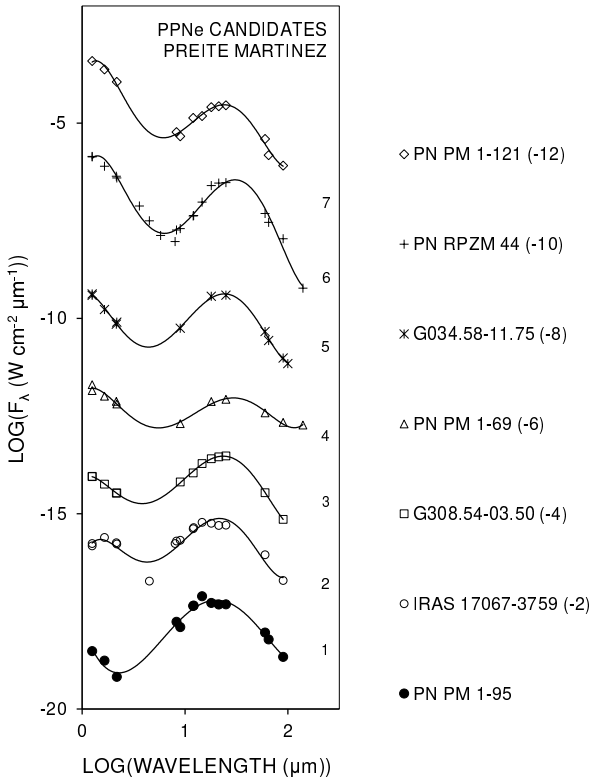

Fig. 3. SEDs of PPN candidates from Preite-Martínez (1988). The double-component structure is also clear in these candidates. In order to avoid overlaps between different spectra, an offset has been applied to the spectra. The value of the offset is given in brackets after the PPN name.

There are only three additional classifications corresponding to G057.11 +01.46, G140.48 +06.04 and G335.06 –01.16 (numbers 24, 38, and 59, respectively, in Table 1). The first source is designated as a candidate young stellar object (Y*?), but due to its unconfirmed status, we do not exclude it. The second source carries an additional classification as a PN candidate (PN?), which is why it remains in the list. The third is identified as a high-mass X-ray binary (HXB) and is also classified as an emission-line star (Em*) and an IR source (IR), the last two being consistent with PN candidacy.

Utilizing information from SIMBAD, there is no justification to exclude any of the 67 sources from the list of potential PNe candidates. Following this we present a thorough analysis of their spectral energy distributions (SEDs) to discern their posible evolutionary state, complemented by a morphological examination of the sources and an assessment of their environment using archival images.

5. SPECTRAL ENERGY DISTRIBUTIONS

It is anticipated that the 67 candidates identified as PN will exhibit a range of evolutionary states. We intend to explore these states through a comprehensive analysis of their SEDs. PNe in their formative stage, known as PPNe, possess an envelope that is still in the process of expansion. In the initial stages, the envelope exhibits a nearly uniform temperature, leading to emissions with a profile closely resembling that of a black body corresponding to a specific temperature. Furthermore, the central star of the planetary nebula (CSPN) emits with a black body profile corresponding to a distinct temperature. In this initial phase, the outcome is what Kwok (2000) refers to as a two-component SED. Here, the cooler component aligns with the envelope expelled during the asymptotic giant branch (AGB) phase, while the warmer component corresponds to the stellar photosphere. Following this, as the envelope expands, its temperature gradient will intensify. The overall emission will then be a cumulative effect of multiple layers, each at a distinct temperature, along with the emission from the star. The peak emission from the star will shift towards longer wavelengths (Hrivnak, Kwok, & Volk (1988), Hrivnak, Kwok, & Volk (1989)).

To characterize the potential candidates, we utilized photometry across various observational projects, encompassing wavelengths from the blue, at 0.44μm (USNO B1 + B2), to the far-infrared (FIR) at 160μm (*AKARI* FIS) (see Section 2: Observations, for details). It is crucial to highlight that the photometric data from the USNO frequently produced outcomes that displayed disparities with those acquired from other telescopes. Consequently, this specific dataset was omitted from the construction of the SEDs for the associated sources.

Furthermore, we produced comparable SEDs for well-established PNe and PPNe, serving as a control cohort. Figure 2 illustrates the SEDs of confirmed PPNe, displaying their distinctive two-component architecture. Likewise, Figure 3 showcases the SEDs of seven PPNe candidates identified by Preite-Martínez (1988).

Figures 4, 5, and 6 illustrate the SEDs of 49 candidates displaying a two-component structure. We shall refer to this ensemble of 49 candidates, whose SEDs align with those of known PPNe, as Group A. For presentation purposes, we have subdivided Group A into five sets, labelled A1 to A5. In A1 and A2 (Figure 4), the SEDs are primarily influenced by the emission peak at shorter wavelengths, signifying the hotter component, i.e., the central star. In A3

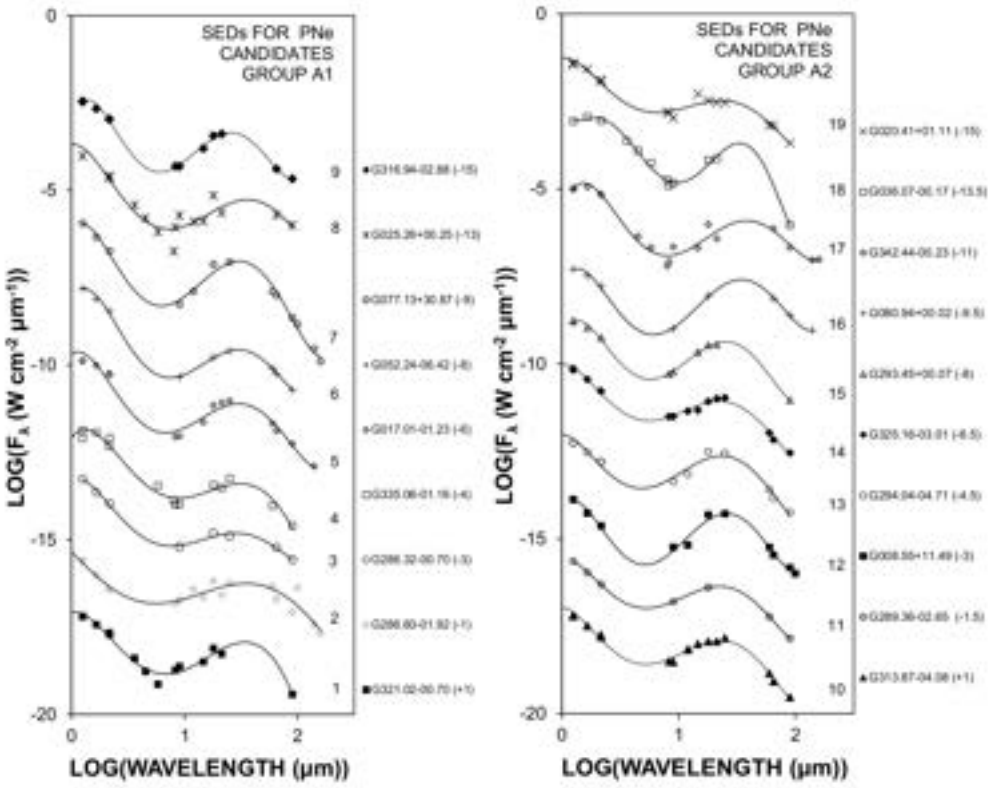

Fig. 4. SEDs of 19 candidates in PNe group A, which show the double-component structure characteristic of PPNe with a dominance of the hot component.

(Figure 5), the SEDs display a relatively balanced emission from both components, while A4 and A5 (Figure 6) predominantly exhibit emissions from the cooler component, i.e., the envelope.

On the contrary, a distinct subset of candidates presents a discernible SED pattern, reminiscent of more advanced PNe that do not exhibit distinct components. Instead, they exhibit collective emissions from multiple layers, each distinguished by its individual black-body radiation. Figure 7 illustrates the SEDs of three objects previously identified by Preite-Martínez (1988) as PNe showcasing this SED profile. In Figure 8, we depict the SEDs of potential PN candidates characterised by an SED featuring only one peak. This subset of candidates, referred to as Group B, represents the more evolved candidates for PNe.

6. MORPHOLOGY AND PROFILES

In our initial endeavor to verify the nature of potential candidates, we examined the images from the *AKARI* far-infrared all-sky survey maps. However, the pixel scale of the detectors, measuring $26.8'' \times 26.8''$ for the short wavelength bands N60 and WIDE-S, and $44.2'' \times 44.2''$ for the long wavelength bands N160 and WIDE-L (Doi, et al. 2015), proved insufficient for drawing definitive conclusions. Consequently, we turned to the observations from *WISE* (Wide-Field Infrared Survey Explorer, Wright et al. 2010), to conduct an initial morphological study. This approach aids us in reviewing the list of potential candidates.

Figures 9, 10 and 11 present RGB images of the 67 potential candidates combining the W1 (in blue), W2 (green) and W3 (red) bands. Upon close examination of the RGB images, a noteworthy observation is that the majority of objects exhibit significant obscuration in the W1 and W2 bands, in comparison to the W3 band. This characteristic is not observed in only two sources: G083.19+06.64 and G140.48+06.04 (Figure 10, Row 2, Column 3 and Row 4, Column 2 respectively). For the remaining sources, the prevalence of the W3 band is evident, ranging from subtle, in the case of G077.13+30.87, to remarkably pronounced, as observed in G352.57+07.30. Another common feature among the majority of these sources is their

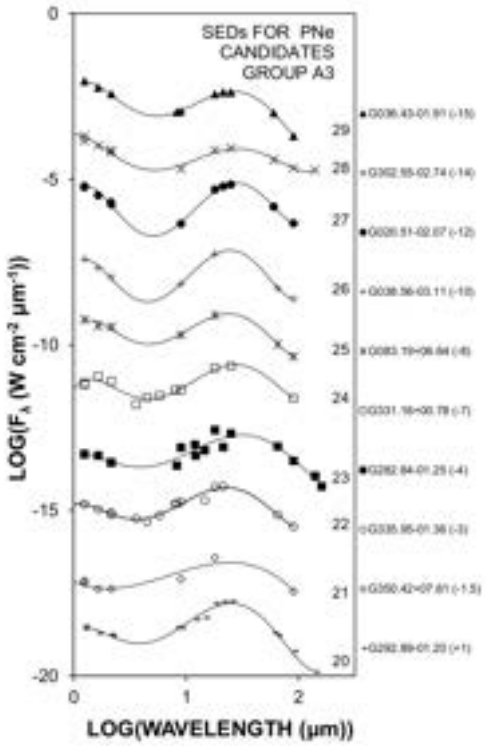

Fig. 5. SEDs of 10 candidates in PNe group A, which show the double-component structure characteristic of PPNe with a relative balance between the cold and hot components.

radial symmetry, with the sole exception being G342.44-00.23. Two sources warrant additional commentary, G111.71-02.13 and G113.89-01.60 (Figure 10, Row 3, Columns 2 and 3 respectively). G111.71-02.13 appears to be associated with a larger arc-like structure and does not exhibit a star-like appearance. In Figure 12 a broader section of the sky encompassing this source is depicted (FoV 3.2'), with the highlighted area inside the white square corresponding to the segment presented in Figure 10. It is evident that G111.71-02.17 effectively constitutes a component of a supernova remnant (SNR), precisely identified as the SNR G111.7-02.1, commonly referred to as Cassiopeia A (Cas A). This enables us to exclude this source from the ultimate candidate list. On the other hand G113.89-01.60 seems to represent an emission peak within an arc encircling the star LS I +59 10, documented in the literature as a B0.2III spectral type star (Negueruela & Marco 2003). It is plausible to categorize G113.89-01.60 as a component of the HII region LBN 113.05-04.51, associated with LS I +59 10, and thereby, we can remove it from our candidate list too.

Furthermore, we have examined potential instances using *Spitzer* IR images acquired with IRAC. In cases where IRAC images were unavailable, we turned to 2MASS images, aiming to identify morphologies consistent with extended emission of PNe, such as lobe structures, equatorial disks, or other PN-like configurations. Due to the limited resolution of 2MASS, we have opted to choose only certain cases of particular interest. Figure 13 shows RGB images of nine sources, five from *Spitzer* and four from 2MASS. For each instance, the orientation is set with North at the top and East to the left. The lower left corner of each image provides information about the data source, the lower right corner indicates the object name, and a scale bar is incorporated for reference.

In Figure 13, five sources-G083.61-02.20, G113.89-01.60, G332.29+02.28, G027.54+00.41, and G135.28+02.80-exhibit a notably dense envelope that prevails over the central emission. Regarding this, the first two are the most prominent, where the radiation from a possible central star is totally absorbed by a spherical-type envelope; but G113.89 –01.60 appears in Figure 10, Row 3, Column 3 to be an extended part of another source, while G083.61 –02.20 presents an E-W structure. In the other three cases mentioned above, we observe a clear bipolar structure with progressively more emission in the centre, but this central emission does not dominate the lobe emission. These five sources are part of our group B of the general candidate list.

On the other hand, the images of G304.57 +00.72, G311.68 –0.63, G025.26 +00.25 and G321.02 –00.70 show dominant central stars. In the first two cases we see spherical envelopes absorbing the emission of the central star. In both images we observe the envelope heated by the stellar radiation, although, as we can see in their respective SEDs (Figure 6, group A4, 38 and 37), the stellar emission is still important and its emission peak can be distinguished. Meanwhile, the image of G025.26 +00.25, although presenting an envelope similar to G304.57 +00.72 and G311.68 –00.63, has subtle differences which have important effects in its emission. The star is not situated in the center of the envelope, which allows part of the stellar emission to escape. In the corresponding SED (Figure 4, group A1, number 8) the dominant component is the high-temperature one (central star). Finally, the image of G321.02 –00.70 shows a structure clearly reminiscent of bipolar PNe. The emission from the central star dominates the combined emission from both lateral structures located to the NE and SW,

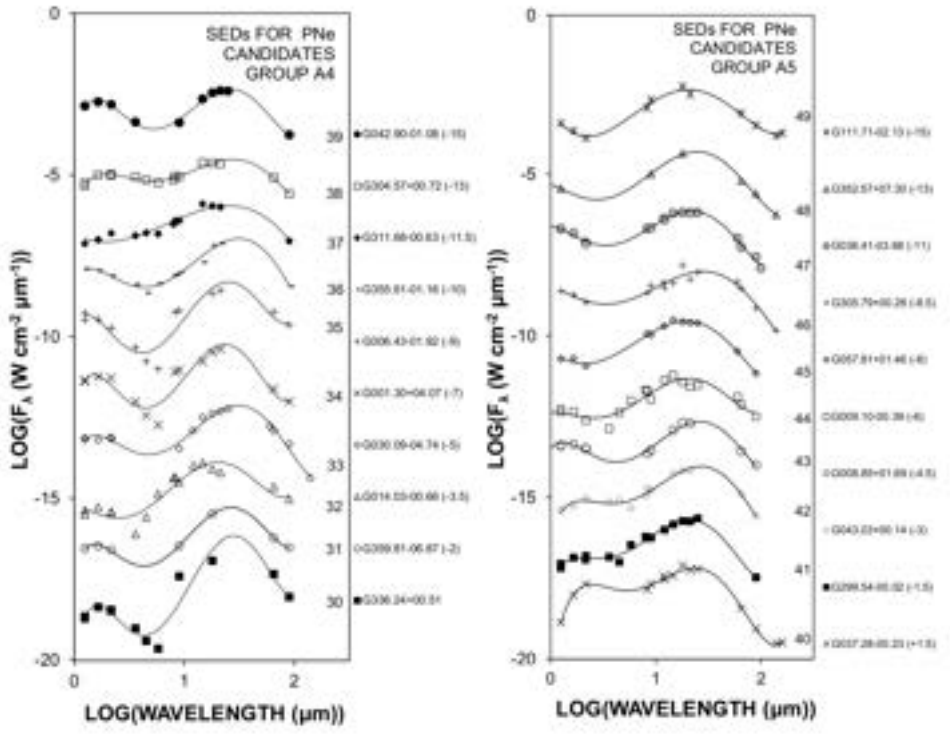

Fig. 6. SEDs of 20 candidates in PNe group A, which show the double-component structure characteristic of PPNe with a dominance of the cold component.

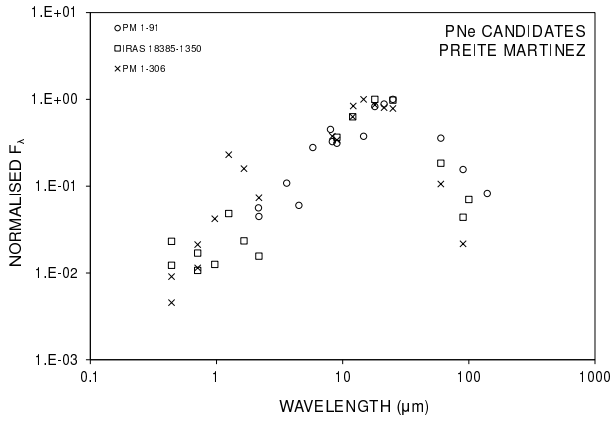

Fig. 7. SEDS of PN from Preite-Martínez (1988). More evolved PNe which do not have a SED of two components, but have layers with a continuous distribution of temperatures.

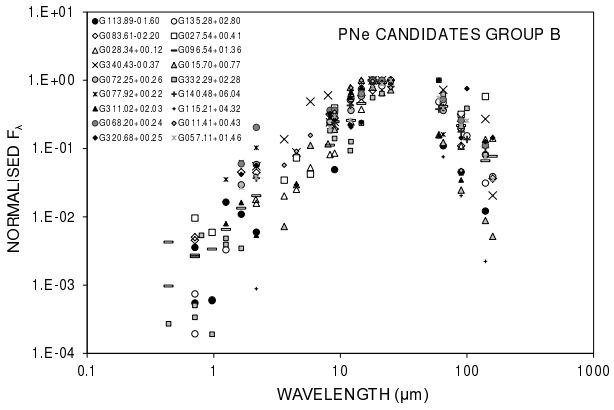

Fig. 8. SEDs of candidates in PNe group B, which have a more advanced evolutionary state.

as can be seen in its SED (Figure 4, A1, 1), which shows that the hot component clearly dominates the cold one.

We have conducted a comprehensive examination of the spatial distribution of the emission across multiple available bands for a subset of the candidates. The extracted profiles are depicted in Figure 14. The profiles of G113.89 –01.60 and G083.61 –02.20 show that these are extended sources. In particular the profile of G113.89 –01.60 has K-band emission with a width of ≈ 22 arcsec, but this emission appears in Figure 10, Row 3, Column 3 as an extended part of another source. G083.61 –02.20 has a width of ≈ 10 arcsec in the three 2MASS bands. G027.54 +00.41 and G332.29 +02.28 show an elongated emission profile, which is expected for PNe

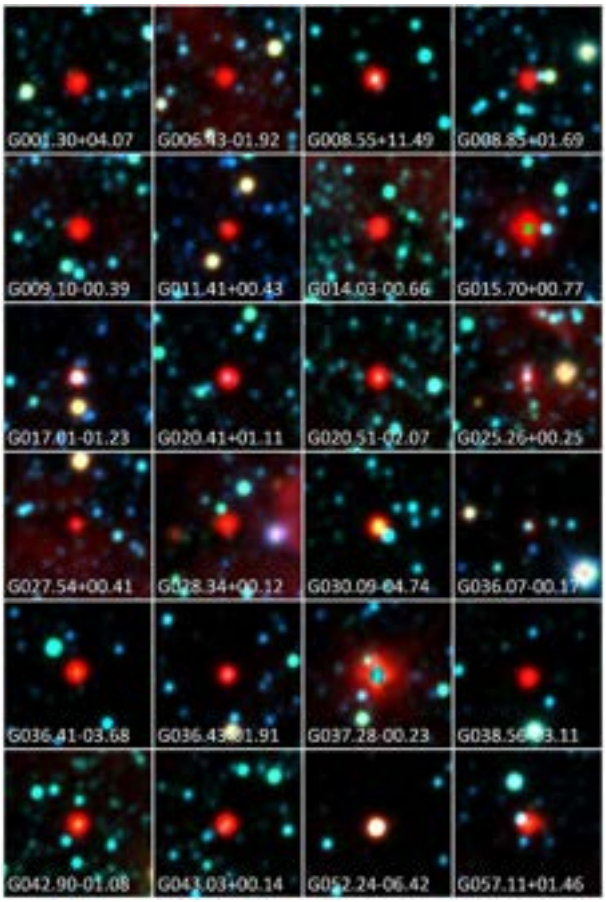

Fig. 9. RGB images of PNe candidates 1 to 24. RGBs constructed with *WISE* bands 3.4μm (blue), 4.6μm (green) and 12μm (red). In all images north is up, east to the left, and FoV 3.2'. The color figure can be viewed online.

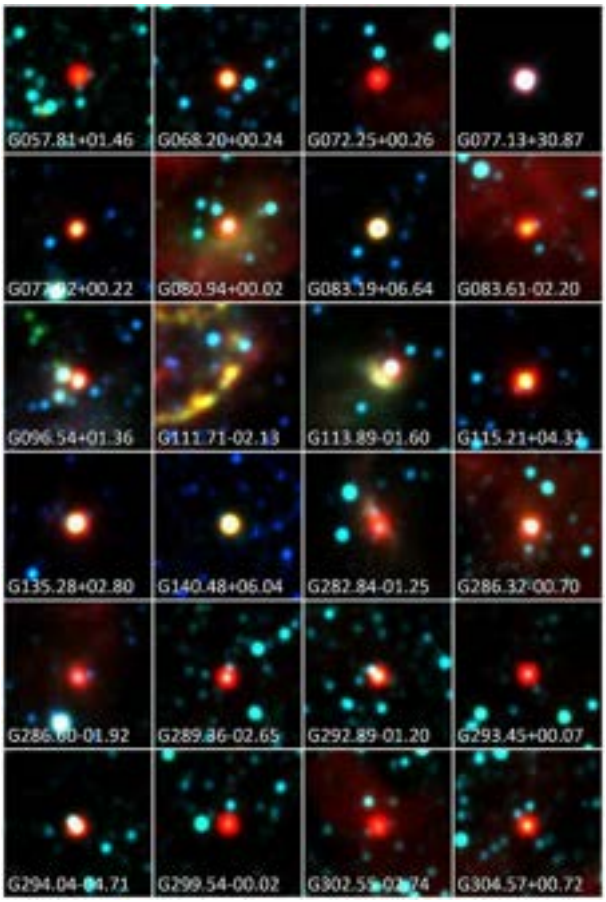

Fig. 10. RGB images of PNe candidates 25 to 48. RGBs constructed with *WISE* bands 3.4μm (blue), 4.6μm (green) and 12μm (red). In all images north is up, east to the left, and FoV 3.2'. The color figure can be viewed online.

with a certain degree of evolution, and this seems to be supported by the SEDs of both objects in Figure 8. In both cases the images also show the elongated structure characteristic of bipolar PNe.

G135.28 +02.80 and G025.26 +00.25 also show extended profiles, although with convex-shaped sides which appear to be layers expelled from the central region. In G135.28 +02.80 the convex-shaped sides are quite symmetric, which suggests that the central area is embedded in a dusty envelope, while in the case of G025.26 +00.25 this envelope is clearly asymmetric, permitting the emission of the possible CSPN to escape freely, which is confirmed by its SED (Figure 4, A1, 8). Finally the profiles of G311.68 –00.63 and G304.57 +00.72 show slightly extended emission in the four IRAC bands, especially at 5.8μm and 8.0μm. This can be explained by a layer of expelled dust, which can be confirmed using their SEDs (Figure 6, A4, 37 and 38 respectively), where two similar-strength components of thermal emission can be seen.

7. INDEPENDENT CONFIRMATION OF G050.48 –00-70

One of the sources within the PN region (Figure 1) that has been excluded from the current list of candidates is G050.48 -00.70. This object was previously identified as a PN by Urquhart et al. (2009), in a study on YSOs that is entirely independent of the analysis conducted here. To verify this classification, we present images (Figure 15) and emission profiles (Figure 16) of G050.48 –00.70 from *Spitzer*/IRAC, 2MASS and IPHAS. The Hα emission reveals significant extinction in its central region (Figure 15, above), with a pair of symmetric 'cones' of emission escaping from the high extinction region. This sug-

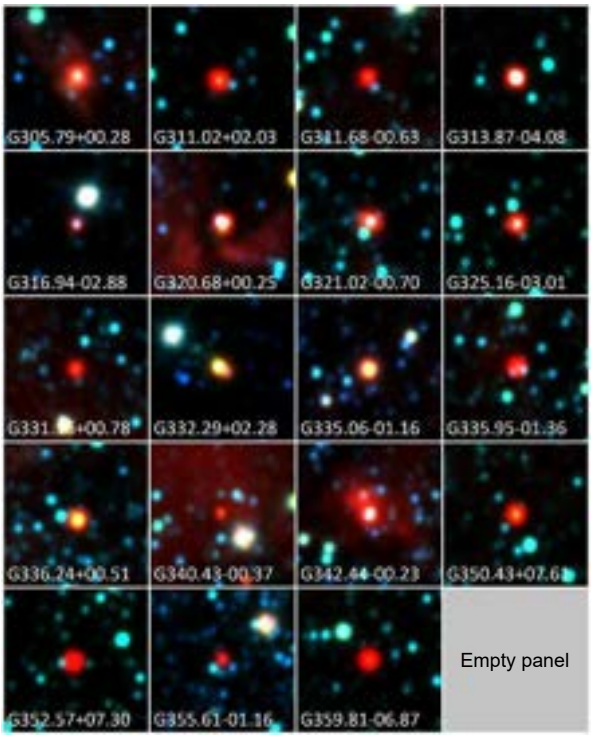

Fig. 11. RGB images of PNe candidates 49 to 67. RGBs constructed with *WISE* bands 3.4μm (blue), 4.6μm (green) and 12μm (red). In all images north is up, east to the left, and FoV 3.2'. The color figure can be viewed online.

gests the presence of dusty material in the center and ionized material in the cones. The color-composite image with J (blue), H (green) and K (red) from 2MASS (Figure 15, center) exhibits strong emission in the center of the cones and between them at shorter wavelengths, while K-band emission dominates at the edges. This indicates that the conical structures are being heated from the central region. Finally the color-composite image with bands 4.5μm (blue), 5.8μm (green) and 8.0μm (red) from *Spitzer*/IRAC (Figure 15, below) illustrates emission concentrated in the central region across all three bands.

In particular, the emission at 8.0μm indicates heated dust, which is the same material that causes the extinction in Hα, then re-emitting at 8.0μm. All the above can be seen in the graphical representation of the emission profiles in Figure 16, which contains the Hα profiles, the 3 bands of 2MASS and the four from *Spitzer*/IRAC. Therefore, from the PSC photometry of *AKARI*, and the morphology and emission profiles in the optical, NIR and FIR, we can conclude independently of Urquhart et al. (2009) that G050.48 +00.70 is a PN.

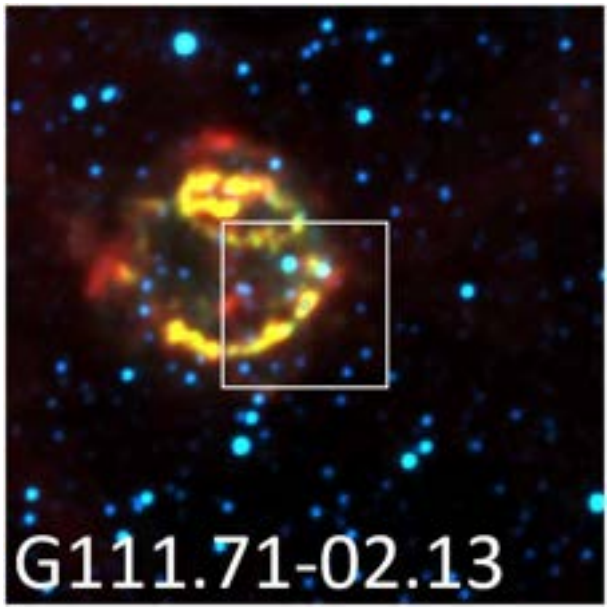

Fig. 12. Wide RGB images of PNe candidate G111.71-02.13. RGBs constructed with *WISE* bands 3.4μm (blue), 4.6μm (green) and 12μm (red). North is up, east to the left, and the total FoV is 12' while the white box encloses the frame shown in Figure 10 with FoV of 3.2'. The color figure can be viewed online.

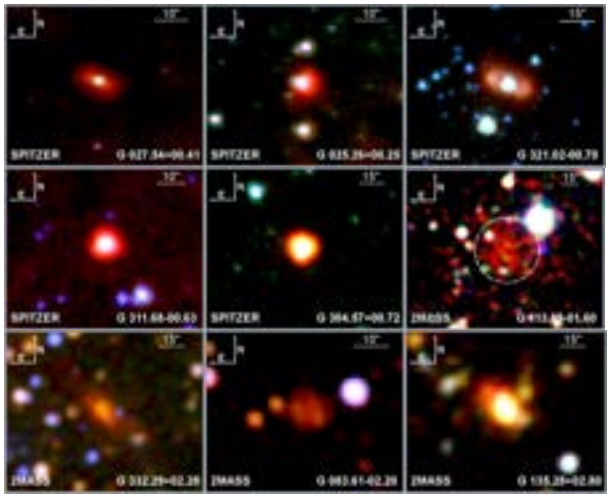

Fig. 13. RGB image of PNe candidates. The RGBs constructed from *Spitzer* images use the 4.5μm (blue), 5.8μm (green) and 8.0μm (red) bands, while those from 2MASS use the 1.25μm (blue), 1.65μm (green), and 2.17μm (red) bands. The color figure can be viewed online.

8. CONCLUSIONS

By analyzing the *AKARI* photometry and other instruments employed in this study, we can draw the following conclusions.

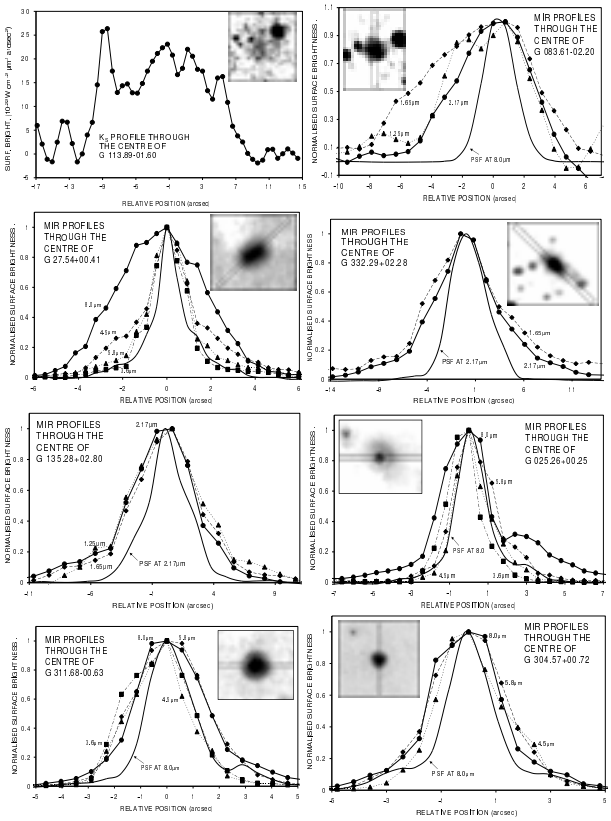

Fig. 14. Spatial profiles of selected candidates. We have extracted spatial profiles along an axis through the center of a sample of candidates, in order to study the spatial distribution of the emission and determine whether they are extended sources.

(i) The photometry in the 9μm, 18μm y 90μm *AKARI* bands enables the determination of color indices that are effective in discriminating between PNe-type sources, and other astronomical objects.

(ii) At least 67 sources from the *AKARI* PSC exhibit emission characteristics consistent with PNe or related objects, yet they haven't been definitively identified as such in the existing literature. We consider these as potential candidate PNe and/or PPNe.

(iii) Examination of the SEDs of the potential candidates facilitates their categorization into two groups based on their evolutionary stage, PPNe and PNe.

(iv) Visual inspection of images allows us to exclude two sources, G113.89-01.60, identified as part of a stellar envelope, and G111.71-02.13, associated with the Cassiopeia A SNR.

(v) Finally, after the elimination of two potential candidates, we propose 65 sources from the *AKARI* PSC as PNe or PPNe candidate.

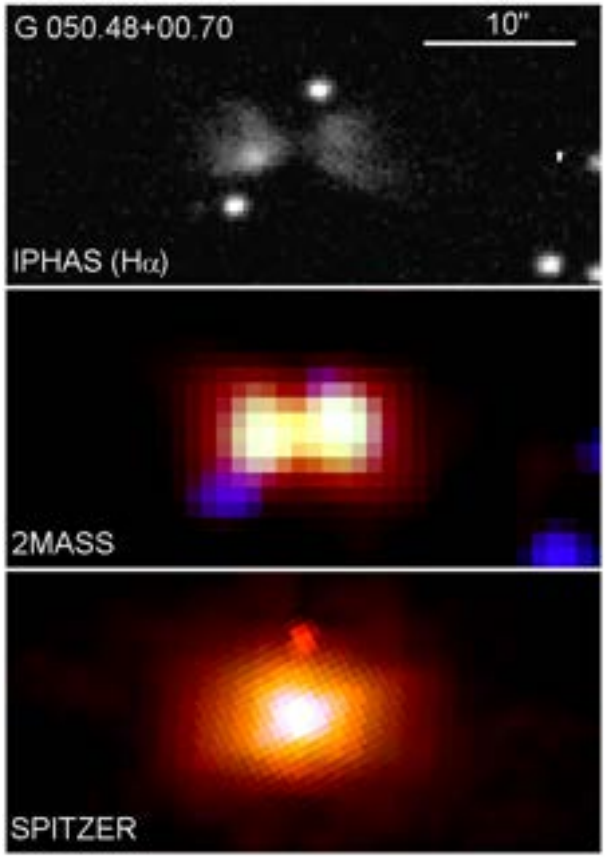

Fig. 15. Images of G050.48 +00.70. Above: Hα λ656.3nm from IPHAS. Center: Composite color image with J (blue), H (green), K (red) from 2MASS. Below: Composite color image using the 4.5μm (blue), 5.8μm (green) and 8.0μm (red) bands from *Spitzer*/IRAC. The color figure can be viewed online.

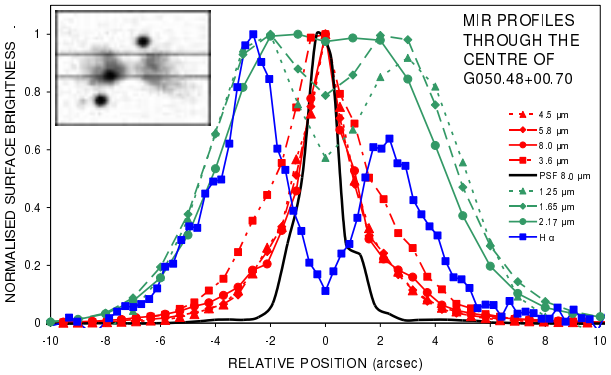

Fig. 16. Spatial profiles of G050.48 +00.70. The Hα emission profile is shown in blue, the three 2MASS bands in green and the four *Spitzer*/IRAC bands in red. Each 2MASS and *Spitzer*/IRAC band is identified by different geometric shapes. The color figure can be viewed online.

Additionally, we propose two avenues for future research. Firstly, a spectroscopic examination of the 65 final candidates to either validate or discard their candidacy. Secondly, a reconsideration of the limits used to define the planetary nebulae (PNe) region in our color-color diagram. If the majority of the 65 candidates presented here are substantiated, it would be valuable to expand the boundaries of the PN region, encompass more sources, categorize them, and subject them to thorough analysis of images and spectra for confirmation or rejection as candidates.

The authors express their gratitude to the Mexican National Council for Science and Technology (CONACyT) for financing this work. GR-L acknowledges support from CONACYT (Grant 263373) and PRODEP (Mexico). This research has made use of the NASA/IPAC Infrared Science Archive, which is operated by the Jet Propulsion Laboratory, California Institute of Technology, under contract with the National Aeronautics and Space Administration. This research has made use of the SIMBAD database, operated at CDS, Strasbourg, France. This research is based on observations with *AKARI*, a JAXA project with the participation of ESA. This work is based on observations made with the INT and WHT telescopes operated on the island of La Palma by the Isaac Newton Group (ING) in the Spanish Observatorio del Roque de los Muchachos.

REFERENCES

Akras S., Guzman-Ramirez L., & Gonçalves D. R., 2019, MNRAS, 488, 3238, https://doi.org/10.1093/mnras/stz1911

Akras S., Leal-Ferreira M. L., Guzman-Ramirez L., & Ramos-Larios G., 2019, MNRAS, 483, 5077, https://doi.org/10.1093/mnras/sty3359

Belczynski K., Mikolajewska J., Munari U., Ivison R. J., & Friedjung M., 2001, yCat, 4146, 60407

Chengalur J. N., Lewis B. M., Eder J., & Terzian Y., 1996, yCat, 2089, 90189, https://doi.org/10.26093/cds/vizier.20890189

Cox N., Manchado A., García-Lario P., & Szczerba R., 2009, ASPC, 418, 439, https://doi.org/10.48550/arXiv.0905.2903

Cox N., García-Lario P., García-Hernández D. A., & Manchado A., 2009, ASPC, 418, 137, https://doi.org/10.48550/arXiv.0905.2898

Cox N. L. J., García-Hernández D. A., García-Lario P., & Manchado A., 2011, AJ, 141, 111, https://doi.org/10.1088/0004-6256/141/4/111

Doi Y., Takita, S., Ootsubo, T., et al. 2015, PASJ, 67, 50, https://doi.org/10.1093/pasj/psv022

Drew J. E., Greimel, R., Irwin, M. J., et al. 2005, MNRAS, 362, 753, https://doi.org/10.1111/j.1365-2966.2005.09330.x

Ducourant C., Teixeira R., Perie J. P., Lecampion J. F., Guibert J., & Sartori M. J. 2005, yCat, 343880769, https://doi.org/10.26093/cds/vizier.34380769

Egan M. P. & Price S. D. 1996, AJ, 112, 2862, https://doi.org/10.1086/118227

Fazio G. G., Hora, J. L., Allen, L. E., et al. 2004, ApJS, 154, 10, https://doi.org/10.1086/422843

Fouqué P., Chevallier, L., Cohen, M. et al. 2000, A&AS, 141, 313, https://doi.org/10.1051/aas:2000123

Fullmer L. & Lonsdale C. J. 1989, IRASG, 0

García-Lario P., Manchado A., Suso S. R., Pottasch S. R., & Olling R. 1990, A&AS, 82, 497

Giveon U., Becker R. H., Helfand D. J., & White R. L. 2005, AJ, 129, 348, https://doi.org/10.1086/426360

Hrivnak B. J., Kwok S., & Volk K. M. 1988, ApJ, 331, 832, https://doi.org/10.1086/166603

Hrivnak B. J., Kwok S., & Volk K. M. 1989, ApJ, 346, 265, https://doi.org/10.1086/168007

Ishihara D., Onaka, T., Kataza, H., et al. 2010, A&A, 514, 1, https://doi.org/10.1051/0004-6361/200913811

Ishihara D., Onaka, T., Kataza, H., et al. 2010, yCat, 2297, 0

Kawada, M., Baba, H., Barthel, P. D., et al. 2007, PASJ, 59, 389, https://doi.org/10.1093/pasj/59.sp2.S389

Kerber F., Mignani R. P., Guglielmetti F., & Wicenec A. 2004, yCat, 340881029, https://doi.org/10.26093/cds/vizier.34081029

Kleinmann S. G. 1992, ASPC, 34, 203

Kwok S., 2000, The Origin and Evolution of Planetary Nebulae (Cambridge, UK: CUP)

Magnier E. A., Volp A. W., Laan K., van den Ancker M. E., & Waters L. B. F. M., 2000, yCat, 335220228, https://doi.org/10.26093/cds/vizier.33520228

Manchado, A., Pottasch S. R., Garcia-Lario P., Esteban C., & Mampaso A. 1989, A&A, 214, 139

Meixner, M., Ueta, T., Dayal, A. et al. 1999, ApJS, 122, 221, https://doi.org/10.1086/313215

Monet D. G., Levine, S. E., Canzian, B., et al. 2003, AJ, 125, 984, https://doi.org/10.1086/345888

Murakami, H., Baba, H., Barthel, P., et al. 2007, PASJ, 59, 369, https://doi.org/10.1093/pasj/59.sp2.S369

Negueruela, I. & Marco, A., 2003, A&A, 406, 119, https://doi.org/10.1051/0004-6361:20030605

Ohsawa, R., Onaka, T., Sakon, I. et al. 2012, PKAS, 27, 259, https://doi.org/10.5303/PKAS.2012.27.4.259

Ohsawa R., Onaka T., Sakon I., Matsuura M., & Kaneda H. 2016, AJ, 151, 93, https://doi.org/10.3847/0004-6256/151/4/93

Parker, Q. A., Acker, A., Free, D. J. et al. 2006, yCat, 5127, 0

Phillips, J. P. & Márquez-Lugo R. A. 2011, RMxAA, 47, 83
Pollo, A., Takeuchi, T. T., & Rybka P., 2011, EP&S, 63, 1051, https://doi.org/10.5047/eps.2011.04.005
Pottasch, S. R. 1984, ASSL, 107, https://doi.org/10.1007/978-94-009-7233-9
Pottasch, S. R., Bignell, C., Olling, R., & Zijlstra, A. A., 1988, A&A, 205, 248
Preite-Martínez, A. 1988, A&AS, 76, 317
Ramos-Larios, G., Guerrero, M. A., Suárez, O., Miranda, L. F., & Gómez, J. F., 2009, A&A, 501, 1207, https://doi.org/10.1051/0004-6361/200811552
Reipurth, B. 2000, yCat, 5104, 0
Szczerba, R., Siodmiak, N., Stasinska, G., & Borkowski J., 2007, yCat, 34690799, https://doi.org/10.26093/cds/vizier.34690799
Ueta, T., Szczerba, R., Fullard, A. G., & Takita, S., 2019, IAUS, 343, 522, https://doi.org/10.1017/S1743921318006452
Urquhart, J. S., Hoare, M. G., Lumsden, S. L., et al. 2009, A&A, 507, 795, https://doi.org/10.1051/0004-6361/200912608
Uscanga, L., Gómez, J. F., Yung, B. H. K., et al. 2019, IAUS 343, Why Galaxies Care About AGB Stars: A Continuing Challenge through Cosmic Time, 343, 527, https://doi.org/10.1017/S1743921318007354
Van de Steene, G. C. & Pottasch, S. R. 1993, IAUS Planetary nebulae: proceedings of the 155 Symposium of the International Astronomical Union, 155, 40
_____. 1995, A&A, 299, 238
Working Group Of GCPA, 1992, BICDS, 41, 7
Wright, E. L., Eisenhardt, P. R. M., Mainzer, A. K., et. al. 2010, AJ, 140, 1868, https://doi.org/10.1088/0004-6256/140/6/1868
Yamamura, I., Makiuti, S., Ikeda, N., 2010, yCat, 2298, 0
Yamauchi, C., Fujishima, S., Ikeda, N. et al. 2011, PASP, 123, 852, https://doi.org/10.1086/660926
Zhang, C. Y. & Kwok, S., 1991, A&A, 250, 179

L. J. Corral, S. N. Kemp, R. A. Márquez-Lugo, S. G. Navarro, A. Nigoche-Netro, and G. Ramos-Larios: Departamento de Física, Universidad de Guadalajara, Jalisco, México.
L. J. Corral, S. N. Kemp, R. A. Márquez-Lugo, S. G. Navarro, A. Nigoche-Netro, and G. Ramos-Larios: Instituto de Astronomía y Meteorología, Av. Vallarta 2602, C. P. 44130, Guadalajara, Jalisco, México (alejandro.marquez@academicos.udg.mx).

Revista Mexicana de Astronomía y Astrofísica, **60**, 277–292 (2024)

https://doi.org/10.22201/ia.01851101p.2024.60.02.06

LONG TERM CCD PHOTOMETRY OF THE DISTANT CLUSTER NGC2419: THE CMD REVISITED

A. Arellano Ferro[1], S. Muneer[2], Sunetra Giridhar[2], I. Bustos Fierro[3], M. A. Yepez[1,4], G. A. García Pérez[5], and G. Rios Segura[5]

Received March 3 2024; accepted May 1 2024

ABSTRACT

Employing *VI* images of NGC 2419 acquired over 17 years, light curves for most of the known variables in the field of the cluster are produced. A cluster membership analysis for about 3100 stars in the cluster field with proper motions from *Gaia*-DR3 revealed the presence of member stars as far as 140 pc from the cluster center and enabled the construction of a cleaner CMD free of field stars. It was found that RRab and RRc stars share the inter-order region in the instability strip, which is unusual for OoII clusters. Theoretical considerations confirm that Pop II cepheids are descendants of extreme ZAHB blue tail stars with very thin envelopes of about 10% of the total mass. Member RR Lyrae stars were employed to calculate independent estimates of the mean cluster metallicity and distance; we found $[\mathrm{Fe/H}]_{\mathrm{UV}} = -1.90 \pm 0.27$ and $D = 86.3 \pm 5.0$ kpc from the RRab and $[\mathrm{Fe/H}]_{\mathrm{UV}} = -1.88 \pm 0.30$ and $D = 83.1 \pm 8.1$ kpc from the RRc light curves.

RESUMEN

Con imágenes CCD *VI* del cúmulo globular NGC 2419, obtenidas durante 17 años, hemos construido curvas de luz de gran parte de las estrellas variables en el campo del cúmulo. A partir de un análisis de membresía basado en los movimientos propios de *Gaia*-DR3 de 3100 estrellas, detectamos miembros a distancias de 140 pc del centro del cúmulo, y construimos un diagrama color-magnitud libre de estrellas de campo. Encontramos que los dos modos de pulsación RRab y RRc comparten la región bimodal de la zona de inestabilidad, lo cual es inesperado en cúmulos Oo II. Nuestros modelos confirman que las estrellas cefeidas de Pob II provienen del extremo azul de la ZAHB con envolventes muy delgadas, de ≈10% de la masa total. A partir de estrellas RR Lyrae miembros calculamos la metalicidad y distancia medias del cúmulo $[\mathrm{Fe/H}]_{\mathrm{UV}} = -1.90 \pm 0.27$ y $D = 86.3 \pm 5.0$ kpc para estrellas RRab, y $[\mathrm{Fe/H}]_{\mathrm{UV}} = -1.88 \pm 0.30$ y $D = 83.1 \pm 8.1$ kpc para estrellas RRc.

Key Words: globular clusters: general — globular clusters: individual: NGC 2419 — stars: distances — stars: fundamental parameters — stars: horizontal branch — stars: variables: RR Lyrae

1. INTRODUCTION

NGC 2419 (C0734+390 in the IAU nomenclature) ($\alpha = 07^{\mathrm{h}}38^{\mathrm{m}}08.47^{\mathrm{s}}$, $\delta = +38°52'56.8''$, J2000; $l = 180.37°$, $b = +25.24°$) is a large and very luminous globular cluster at about 80 kpc from the Galactic center and hence it is among the most distant clusters in the outer halo of our Galaxy. It is noted for being a very loose or extended system given its brightness M_V and half-light radius, which led van den Bergh & Mackey (2004) to suggest its extra galactic origin, and the likelihood of it being a

[1]Instituto de Astronomía, Universidad Nacional Autónoma de México, Ciudad Universitaria, C.P. 04510, México.
[2]Indian Institute of Astrophysics, Bangalore, India.
[3]Observatorio Astronómico, Universidad Nacional de Córdoba, Córdoba C.P. 5000, Argentina.
[4]Instituto Nacional de Astrofísica, Óptica y Electrónica (INAOE), Luis Enrique Erro No.1, Tonantzintla, Pue., C.P. 72840, México.
[5]Facultad de Física, Universidad Veracruzana, Xalapa, México.

stripped core of a former spheroidal dwarf galaxy. These suggestions however have not been supported by Ripepi et al. (2007) on the ground of the following arguments: the cluster is of the Oo II type while extra galactic clusters and dwarf galaxies reside within the Oosterhoff gap (Catelan 2009); the lack of substructures in the main sequence bellow the TO (i.e. lack of multiple populations); the thinness of the red giant branch (ruling out multiple chemical compositions among cluster stars); and the apparent absence of extra-tidal structures. In Ripepi et al's opinion NGC 2419 is a normal metal-poor Galactic globular cluster.

The variable star population of NGC 2419 is quite rich. There are 101 variables registered in the Catalogue of Variable Stars in Globular Clusters (CVSGC) (Clement et al. 2001), 75 of which are RR Lyrae, 1 Pop II or CW star, 12 SX Phe, 5 long-period red giants, 3 eclipsing binaries, 2 δ Scuti stars and 3 non-classified. A thorough analysis of these variable stars, based on high-quality images from the HST, and from two large ground telescopes; the Galileo (TNG) 3.5 and the Subaru 8.2m, was carried out by Di Criscienzo et al. (2011).

Our team has obtained *VI* CCD images of NGC 2419 between 2005 and 2022 for a total of 405 and 327 in V and I respectively, using the 2m telescope of Indian Astronomical Observatory (IAO). Naturally the depth and accuracy of our photometry is not comparable to that used by Di Criscienzo et al. (2011), and due to crowding we were not able to recover the light curves for all known variables. It may seem pretentious to draw conclusions from RR Lyrae stars at $V \sim 20.5$, which nears the faint limit of our data. Nevertheless, we can use our photometry to provide a new discussion of the cluster membership of the stars in the field of our images, particularly those of variable nature, and provide independent estimates for the mean cluster reddening, average metallicity and distance.

Our approach to the determination of mean M_V and [Fe/H] of RRL stars, is the Fourier light curve decomposition, of both the fundamental mode and first overtone pulsators RRab and RRc respectively. This, and the employment of well established semi-empirical calibrations and their zero points between the Fourier parameters and the physical quantities, provide individual stellar estimations of the distance and [Fe/H]; hence, the average of these values for tested cluster member variables leads to proper average values for the parent cluster. The present paper is a report of our results.

TABLE 1

LOG OF OBSERVATIONS OF NGC 2419

Date	N_V	t_V(s)	N_I	t_I(s)	Mean seeing ($''$)
01/04/2005	7	600	-	-	1.9
02/04/2005	8	600	-	-	1.7
03/04/2005	11	600	-	-	1.9
19/01/2006	14	600	-	-	3.4
09/03/2007	8	600	-	-	2.0
10/03/2007	18	600	-	-	2.7
10/04/2007	10	600	-	-	2.0
11/04/2007	13	600	-	-	2.0
07/01/2009	5	300-600	2	300	1.7
08/01/2009	2	600	2	300	2.3
15/12/2011	3	450-500	4	100-150	3.5
16/12/2011	7	400-450	7	120-150	2.8
17/12/2011	2	380-420	4	110-120	2.7
05/02/2012	22	180-300	20	90	2.2
28/02/2012	32	180-200	35	80-100	2.1
29/02/2012	16	250-450	17	80-250	2.8
01/03/2012	11	180-300	12	80-150	2.7
19/01/2013	25	150-400	27	75-150	2.1
20/01/2013	41	170-210	44	80-100	2.2
21/01/2013	3	180	5	80	2.4
04/03/2013	6	125-150	6	65-85	1.8
01/02/2017	14	180	13	80	2.5
02/02/2017	14	180	13	80	2.7
16/02/2020	16	200	16	100	2.8
17/02/2020	8	200	8	100	2.4
19/03/2021	12	200	12	100	1.9
04/11/2021	27	200	28	100	2.6
12/02/2021	10	200	10	100	2.0
03/01/2022	8	200	8	100	2.9
31/01/2022	32	200	34	100	2.4
Total:	405		327		

Columns N_V and N_I give the number of images taken with the V and I filters respectively. Columns t_V and t_I provide the exposure time, or range of exposure times. In the last column the average seeing is listed.

2. OBSERVATIONS AND IMAGE REDUCTIONS

2.1. *Observations*

All observations were carried out with the Himalayan Chandra 2.0m Telescope of the Indian Astrophysical Observatory (IAO) at Hanle, in the Indian Himalayan range at about 4500 m above sea level. The detailed log of the observations is given in Table 1, where exposure times and estimations of the prevailing nightly average seeing are indicated. A total of 405 and 327 images in V and I were secured in a time span of seventeen years.

2.2. *Transformation to the Standard System*

The instrumental photometry was transformed to the standard Johnson-Kron-Cousins photometric system (Landolt 1992) *VI*, using local standard stars in the fields of the target clusters. These standard stars have been taken from the extensive collection of Stetson (2000)[6]. We found 554 standard stars

[6] `https://www.canfar.net/storage/list/STETSON/Standards`.

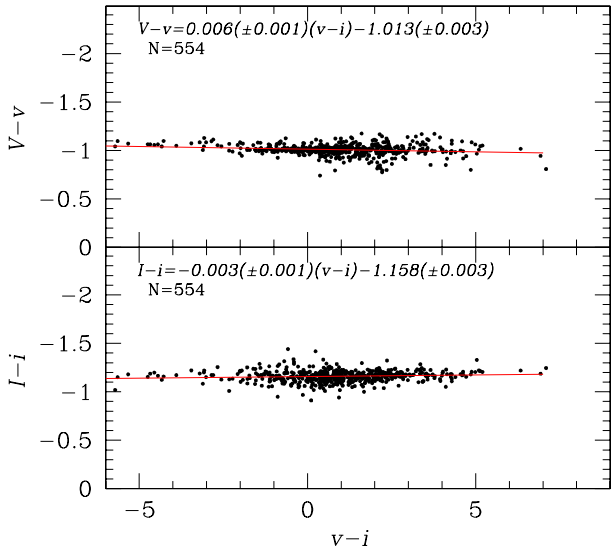

Fig. 1. Transformation relationship between instrumental and standard photometric systems. These equations were calculated using 554 local standard stars from the collection of Stetson (2000). The colour figure can be viewed online.

with instrumental light curves in the field of our images. The standard minus instrumental magnitudes and the light dependence with the $(v - i)$ colour is displayed in Figure 1. The corresponding transformation equations are also given in the figure.

2.3. *Difference Image Analysis*

All the image photometric treatment has been performed using the Difference Image Analysis using the *DanDIA* pipeline (Bramich 2008; Bramich et al. 2013, 2015). The approach and its caveats have been described in detailed by Bramich et al. (2011).

3. STELLAR MEMBERSHIP ANALYSIS

Distinguishing the true cluster members from the field stars projected on the field of view of a cluster is relevant since one is interested in a clean CMD that represents the structure of the system. Presently, this challenge is on reach given the high quality proper motions available in the *Gaia* mission (Gaia Collaboration et al. 2023).

The method developed by Bustos Fierro & Calderón (2019) to determine the stellar membership is based on a two step approach: (1) it finds groups of stars with similar characteristics in the four-dimensional space of the gnomonic coordinates (X_t,Y_t) and proper motions ($\mu_{\alpha*}$,μ_δ) employing the BIRCH clustering algorithm (Zhang et al. 1996) and (2) in order to extract likely members that were missed in the first stage, the analysis of the projected distribution of stars with different proper motions around the mean proper motion of the cluster is performed.

This method was applied to the stars within a radius of 15 arc minutes from the center of NGC 2419. This field contains 3965 *Gaia* sources but only 3129 have a measurement of the proper motion, 1584 of which were found to be likely cluster members. In Figure 2 the corresponding Vector Point Diagram (VPD) and colour-magnitude diagram (CMD) showing the cluster member and field stars are shown. The farthest member from the center is about 6 arc minutes away which, at a distance of 84.0 kpc (see our distance determination in § 7) corresponds to a distance of about 140 pc. In spite of its half-light radius at about 17.9 pc, comparable to other clusters in the halo (van den Bergh & Mackey 2004), these star members at such large distances are the indication of the extended halo that led van den Bergh & Mackey (2004) to suggest its extra galactic origin and presently being the remains of a former dwarf galaxy tidally stripped by the Milky Way. In Figure 3, the radial distance distribution of member stars in NGC 2419 is displayed and shows its extended nature. For comparison we included the similar distribution of large halo cluster NGC 1851. The membership analysis reveals the bound nature of a subtle cluster halo as large as 140 pc from the cluster center.

We have been able to obtain *VI* photometry for 1107 point sources in the field of our images. These light curves include 74 of the known variables in the cluster (Clement et al. 2001), and the general data for these variables is included in Table 2. A CMD with these variables identified has been produced and will be discussed in the following sections.

4. VARIABLE STARS MEASURED IN THE PRESENT STUDY

Given the size of our telescope and sky conditions at the time of the observations which limited the deepness and resolution of our imaging data, some of the well known variables remain blended and it was not possible to measure them well. It should be noted that the HB level of this distant cluster is fainter than 20th magnitude, which is close to the faint limit of our capabilities. Variables in Table 2 are mostly RR Lyrae (RRab and RRc), but also a sample of red giant branch variables (RGBs) is available, plus one W Vir (V18) and one double mode or RRd star (V39). The identifications of these variables are given in the charts of Figure 4. Their

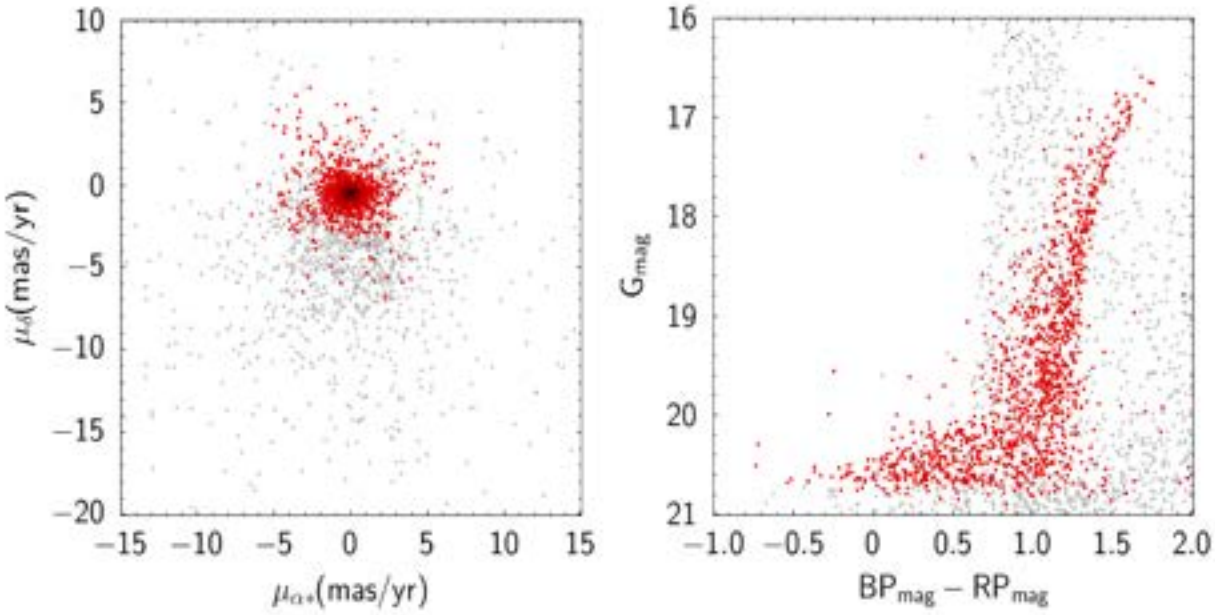

Fig. 2. *Gaia*-DR3 VPD (left panel) and CMD (right panel) of the cluster NGC 2419. Red and gray points correspond to likely cluster members and field stars respectively, determined as described in § 3. A total of 3965 *Gaia* point sources within 15 arc minutes are displayed, while 1584 were found to be cluster members. The colour figure can be viewed online.

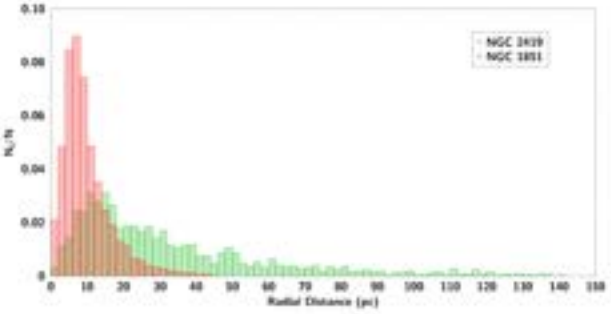

Fig. 3. Star members distribution of the extended cluster NGC 2419 compared with the large halo cluster NGC 1851. The horizontal axis represents the radial distance projected on the plane of the sky. The colour figure can be viewed online.

light curves are displayed in the Appendix, where we have distinguished the data from the several observing runs.

5. THE OOSTERHOFF TYPE OF NGC 2419

Given its low metallicity the cluster likely belongs to the Oo II type. This is in fact confirmed by the period average of its RRab and RRc stars of 0.665 d and 0.343 d respectively. The log P - Amplitude diagram (Bailey's diagram) is shown in Figure 5. It is clear that the distribution of stars, particularly that of the RRab, falls towards the sequences of evolved star (Cacciari et al. 2005) which is the characteristic of Oo II type clusters.

6. ON THE CLUSTER REDDENING

Given its Galactic location, NGC 2419 is not much affected by interstellar reddening. To estimate the colour excess of individual RRab stars, we have taken advantage of the fact that the $V - I$ colour curve of RRab stars is constant near its minimum, between the phases 0.5 and 0.8 (Sturch 1966). By employing the calibration of $(V - I)_{0,min} = 0.58 \pm 0.02$ (Guldenschuh et al. 2005), we calculated the average colour excess for 12 cluster member RRab and found $E(B - V) = 0.07 \pm 0.07$. This average is comparable with the predicted values from the calibrations of Schlafly & Finkbeiner (2011) and Schlegel et al. (1998), 0.052 ± 0.001 and 0.061 ± 0.001 respectively. In this work we adopted $E(B - V) = 0.06$ or $E(V - I) = 1.259 \times E(B - V)$, which leads to $E(V - I) = 0.08$.

7. PHYSICAL PARAMETERS OF THE RR LYRAE STARS FROM THE LIGHT CURVES FOURIER DECOMPOSITION

Our approach to the calculation of relevant stellar physical parameters for the RR Lyrae stars is

TABLE 2

GENERAL DATA OF THE VARIABLES OF THE FOV FOR NGC 2419

Variable	Type	$<V>$ (mag)	$<I>$ (mag)	A_V (mag)	A_I (mag)	Period (days)	HJD_{max} (d+2450000)	RA (J2000.0)	Dec. (J2000.0)	Membership (m/f/un)
					RRab					
V2	RRab	19.675	18.927	0.772	-	0.792335	4169.173	07:38:07.96	+38:52:33.7	m
V3	RRab	20.370	19.811	1.163	0.713	0.625995	9293.321	07:38:12.71	+38:52:27.4	m
V5	RRab	19.895	19.171	0.520	0.342	0.655855	9293.166	07:38:11.14	+38:53:38.8	m
V7	RRab	20.484	19.886	1.341	0.830	0.627353	6312.483	07:38:16.19	+38:54:18.8	m
V9	RRab	20.316	19.614	1.239	0.751	0.644727	4202.120	07:38:05.63	+38:54:21.2	m
V11	RRab	20.436	20.031	1.097	0.931	0.589179	4170.333	07:38:16.43	+38:52:42.3	m
V12	RRab	20.405	19.871	1.087	0.687	0.661853	9611.116	07:38:19.79	+38:54:41.0	m
V13	RRab	20.425	19.849	1.051	0.687	0.640	4169.334	07:38:16.93	+38:52:40.2	m
V14	RRab	20.257	19.777	1.310	1.003	0.741	9258.370	07:37:58.39	+38:52:42.3	m
V15	RRab	20.438	19.846	1.265	0.813	0.640	9293.166	07:38:13.66	+38:53:30.6	m
V16	RRab	20.202	-	1.139	-	0.666	4202.120	07:38:12.38	+38:54:03.4	m
V17	RRab	20.406	19.822	0.979	0.619	0.649	4201.162	07:38:17.74	+38:54:41.0	m
V19	RRab	20.434	19.890	1.303	0.866	0.703	9258.370	07:37:59.02	+38:52:15.0	m
V21	RRab	20.318	19.830	1.497	0.690	0.686	9293.166	07:38:03.58	+38:53:23.7	m
V22	RRab	20.404	-	1.123	-	0.577	6312.478	07:38:17.65	+38:52:44.4	m
V23	RRab	19.976	19.476	0.996	-	0.626	5988.205	07:38:10.70	+38:54:10.7	m
V24	RRab	20.427	19.743	0.869	0.799	0.653	4169.276	07:37:55.61	+38:52:45.7	m
V25	RRab	20.330	19.595	0.851	0.536	0.636	3464.280	07:38:03.28	+38:53:31.7	m
V26	RRab	19.609	18.958	0.580	0.373	0.664	4201.163	07:38:02.20	+38:52:03.2	m
V29	RRab	20.349	19.909	0.759	0.598	0.726	3464.173	07:38:03.26	+38:52:46.9	m
V30	RRab	20.600	-	1.152	-	0.584	4170.189	07:38:06.09	+38:53:16.2	m
V32	RRab	20.188	19.443	0.729	0.615	0.642	4170.230	07:38:06.70	+38:53:40.8	m
V35	RRab	20.797	-	1.627	-	0.677	4839.390	07:38:12.01	+38:52:59.9	m
V36	RRab	20.310	-	0.708	-	0.648	9611.423	07:38:10.30	+38:53:35.3	m
V37	RRab	19.361	18.467	0.184	0.226	0.661	4170.257	07:38:11.20	+38:53:09.1	un
V40	RRab	18.930	17.989	0.229	0.195	0.576	6312.400	07:38:13.09	+38:52:47.2	un
V42	RRab	19.787	-	0.277	-	0.775	5963.194	07:38:08.72	+38:52:45.7	un
V57	RRab	20.041	19.516	0.812	0.483	0.736	5963.078	07:38:06.00	+38:52:42.7	m
V59	RRab	20.258	-	0.585	-	0.829	5963.161	07:38:10.43	+38:53:09.5	m
V64	RRab	20.385	19.638	0.337	0.449	0.781	4170.333	07:38:10.29	+38:52:16.3	m
					RRc					
V4	RRc	20.420	19.917	0.403	0.380	0.392	6313.385	07:38:15.13	+38:52:35.1	m
V6	RRc	20.349	-	0.553	-	0.372	3463.242	07:38:12.89	+38:50:43.8	m
V27	RRc	20.454	-	0.311	-	0.342	9258.425	07:38:09.78	+38:51:09.0	m
V31	RRc	20.297	-	0.509	-	0.388	9293.285	07:38:21.24	+38:50:22.9	m
V33	RRc	20.604	-	0.427	-	0.303	5963.118	07:38:12.27	+38:52:33.9	m
V34	RRc	20.437	-	0.531	-	0.399	4170.119	07:38:10.34	+38:55:29.1	m
V38	RRc	18.748	17.819	0.134	0.162	0.364	5963.161	07:38:08.13	+38:52:03.9	un
V41	RRc	19.324	18.629	0.167	0.154	0.396	4202.187	07:38:07.20	+38:53:23.1	un
V48	RRc	19.452	18.241	0.218	0.219	0.375	6356.102	07:38:10.04	+38:52:41.2	un
V51	RRc	19.914	19.307	0.266	0.417	0.348	4839.375	07:38:06.19	+38:52:57.5	un
V55	RRc	20.392	-	0.409	-	0.378	4839.375	07:38:05.99	+38:52:59.6	m
V56	RRc	19.415	19.154	0.108	0.373	0.333	5963.117	07:38:07.99	+38:52:24.7	un
V60	RRc	20.376	-	0.362	-	0.390	6313.478	07:38:06.66	+38:53:18.8	m
V66	RRc	20.515	-	0.419	-	0.387	6313.156	07:38:11.60	+38:53:10.5	m
V67	RRc	19.978	-	0.305	-	0.348	5963.118	07:38:10.97	+38:53:23.5	m
V68	RRc	20.333	-	0.435	-	0.365	6313.454	07:38:12.15	+38:52:49.0	m
V69	RRc	20.109	19.441	0..335	0.386	0.344	5986.225	07:38:10.64	+38:53:37.7	un
V72	RRc	20.412	19.700	0.426	0.350	0.415	5912.464	07:38:09.92	+38:53:49.5	m

Columns 3 and 4 list mean magnitudes, Columns 5 and 6 show light curve amplitudes. Column 11 indicates the cluster membership status; m - members, f - field, un - unknown.

TABLE 2. CONTINUED

Variable	Type	$<V>$ (mag)	$<I>$ (mag)	A_V (mag)	A_I (mag)	Period (days)	HJD_{max} (d+2450000)	RA (J2000.0)	Dec. (J2000.0)	Memb (m/f/un)
V74	RRc	20.598	-	0.206	-	0.309	5963.118	07:38:13.78	+38:52:47.9	m
V75	RRc	20.288	-	0.429	-	0.324	4840.363	07:38:03.54	+38:52:16.9	m
V76	RRc	20.128	19.579	0.275	0.302	0.324	5986.267	07:38:12.11	+38:51:59.2	m
V77	RRc	20.298	-	0.332	-	0.381	5963.117	07:38:13.14	+38:52:08.2	m
V82	RRc	19.911	19.594	0.205	0.327	0.343	9293.289	07:38:13.85	+38:53:37.3	m
V84	RRc	20.046	19.165	0.287	0.301	0.329	5986.225	07:38:01.46	+38:53:12.0	m
V89	RRc	20.273	-	0.283	-	0.287	5963.118	07:38:19.78	+38:55:07.4	f
V90	RRc	20.354	-	0.328	-	0.391	5963.124	07:38:23.14	+38:54:11.6	m
					RRd					
V39	RRd	20.335	-	-	-	0.814	5963.181	07:38:10.72	+38:50:51.1	m
					RGBs					
V1	RGB	17.188	15.664	0.451	0.472	193.850	5963.161	07:38:11.61	+38:51:59.0	m
V8	RGB	17.301	15.887	0.603	0.613	16.350	9258.370	07:38:06.84	+38:53:34.1	m
V10	RGB	17.085	15.552	0.466	0.374	20.800	7786.166	07:38:09.89	+38:52:01.1	m
V20	RGB	17.425	16.680	0.427	0.528	48.980	5963.161	07:38:05.96	+38:53:38.2	m
V86	RGB	17.343	15.932	0.548	0.418	49.860	5963.161	07:38:19.62	+38:53:15.7	m
					V Vir					
V18	W VIR	18.837	18.207	0.412	0.725	1.579	4202.120	07:38:07.17	+38:54:46.8	m

Columns 3 and 4 list mean magnitudes, Columns 5 and 6 show light curve amplitudes. Column 11 indicates the cluster membership status; m - members, f - field, un - unknown.

via the Fourier decomposition of their V-band light curves. Of particular interest are the mean [Fe/H] and M_V of the RR Lyrae sample, as they are good representations of the mean cluster metallicity and distance.

The Fourier decomposition is performed by fitting the observed light curve with a Fourier series model of the form:

$$m(t) = A_0 + \sum_{k=1}^{N} A_k \cos\,(\frac{2\pi}{P}\ k\ (t-E) + \phi_k), \quad (1)$$

where $m(t)$ is the magnitude at time t, P is the period, and E is the epoch. A linear minimization routine is used to derive the best-fit values of the amplitudes A_k and phases ϕ_k of the sinusoidal components. From the amplitudes and phases of the harmonics in eq. 1, the Fourier parameters, defined as $\phi_{ij} = j\phi_i - i\phi_j$, and $R_{ij} = A_i/A_j$, are computed.

Subsequently, the low-order Fourier parameters can be used in combination with semi-empirical calibrations to calculate [Fe/H] and M_V. The employed calibrations for the mass, $T_{\rm eff}$, and radii are summarized in the papers by Arellano Ferro et al. (2010) and Arellano Ferro et al. (2011), while the calibrations for [Fe/H] and M_V and their zero points are most recently discussed by Arellano Ferro (2022) and Arellano Ferro (2024).

7.1. *Physical Parameters of RR Lyrae Stars*

The Fourier coefficients for the RRab and RRc stars were calculated for the stars that we were able to measure. For the sake of briefness these are not specifically given in this paper but they are available on request. These coefficients were then used in the cited calibrations to calculate the individual physical parameters, which are reported in Table 3. The average [Fe/H] and M_V (hence distance), should be representative of the parent cluster. It should be noted that the calibrations render the value $[{\rm Fe/H}]_{\rm ZW}$, i.e. in the metallicity scale of Zinn & West (1984) which can be transformed into the spectroscopic scale of Carretta et al. (2009), via the equation; $[{\rm Fe/H}]_{\rm UVES} = -0.413 + 0.130\ [{\rm Fe/H}]_{\rm ZW} - 0.356\ [{\rm Fe/H}]^2_{\rm ZW}$.

We found averages $[{\rm Fe/H}]_{\rm ZW} = -1.86 \pm 0.18$, $[{\rm Fe/H}]_{\rm UV} = -1.90 \pm 0.27$ and $D = 86.3 \pm 5.0$ kpc. from the RRab light curves, and $[{\rm Fe/H}]_{\rm ZW} = -1.84 \pm 0.21$, $[{\rm Fe/H}]_{\rm UV} = -1.88 \pm 0.30$ and $D = 83.1 \pm 8.1$ kpc from the RRc data. Emphasis should be made that, coming from independent calibrations with different calibrators, the results for the RRab and RRc stars are also fully independent. Still there is a very satisfactory agreement. These values can be compared with the value quoted $[{\rm Fe/H}]_{Spec} = -2.2$ in the spectroscopic scale (Carretta et al. 2009), and the critical literature mean distance $D = 88.47 \pm 2.40$ kpc estimated by Baumgardt & Vasiliev (2021). Thus, the agreement of our metallicity and distance determinations for NGC 2419 with this canonical values, cannot be better.

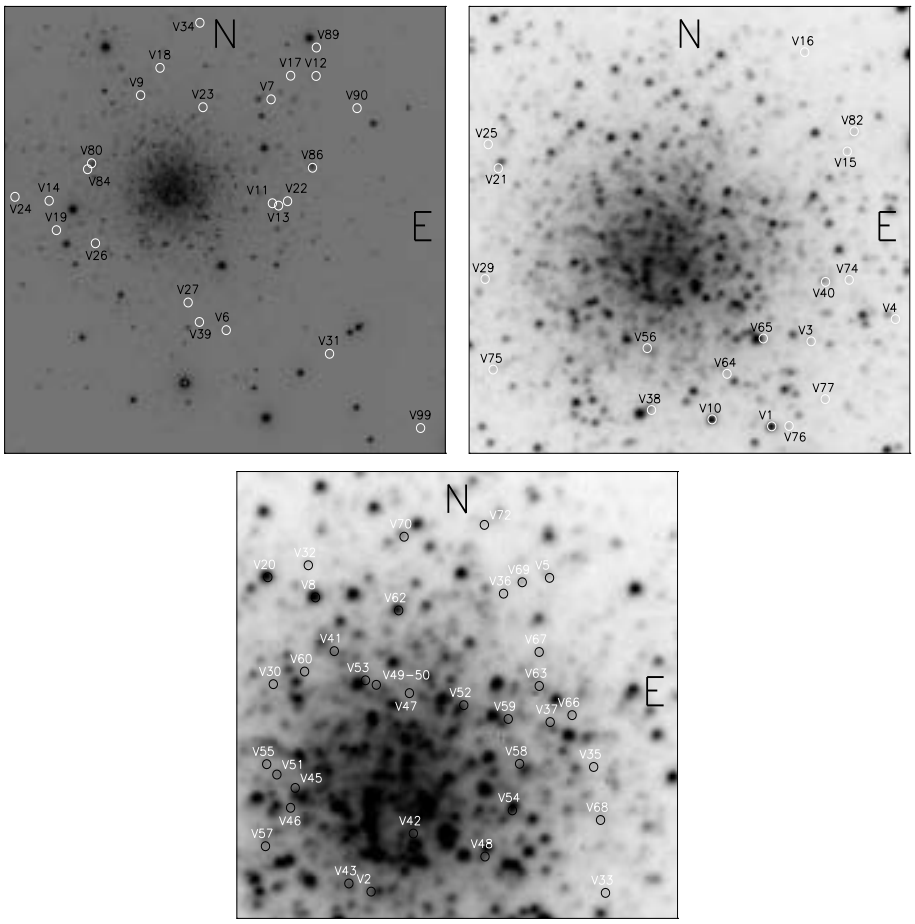

Fig. 4. Identification chart of variable stars in the field of NGC 2419. The approximate size of each images is 6.9×6.9, 2.5×2.5 and 1.6×1.6 square arc minutes.

8. DISCUSSION: THE COLOR MAGNITUDE DIAGRAM

In Figure 6 we display two versions of the observed CMD. The panel on the left shows the stellar distribution of every point source that we were able to measure in our collection of *VI* images. This includes cluster member stars as well as field stars. Through the membership analysis described in § 3, we could distinguish the most likely cluster members (red dots in the figure) from the field stars (small light blue dots). In the right panel, we have plotted only the cluster members and have dereddened the diagram by assuming $E(V-I) = 0.08$. The variable stars contained in Table 4 are plotted with colours according to their pulsational type, as coded in the figure caption. When a variable is found to be a cluster member, the colour symbol has a smaller red dot in the center, otherwise the star had no proper motion reported in *Gaia*-DR3, and hence its membership status is unknown, or it is likely a field star.

We also include in this dereddened diagram the two isochrones from VandenBerg et al. (2014) for ages of 12.5 Gyr (black) and 13.0 Gyr (turquoise) with [Fe/H]= -1.8 and -2.0, respectively. Red ZAHB is from the models built from the Eggleton code (Pols et al. 1997, 1998; Schröder et al. 1997), and calculated by Yepez et al. (2022). The black evolutionary track corresponds to a model with a central core mass of $0.50\,M_{\odot}$ and a thin envelope of $0.04\,M_{\odot}$ and it was selected as it best represents the position of the W Vir star V18 confirming the conclusions reached by Yepez et al. (2022), that type II Cepheids can be interpreted as products of post-HB evolution driven by burning of very low mass hydrogen and helium shells. According to Bono et al. (2020), W Vir stars may be post-early asymptotic giant branch stars (see also the case of the CWB star V81 in NGC 7006 (Arellano Ferro et al. 2023)), although the case of V18 seems more like that of a post-HB which according to the model has taken 114 million years from the HB to reach its present position.

TABLE 3

PHYSICAL PARAMETERS FROM THE MEMBER RR LYRAE FOURIER LIGHT CURVE DECOMPOSITION

ID	$[Fe/H]_{ZW}$	$[Fe/H]_{UVES}$	M_V	$\log T_{\rm eff}$	$\log(L/L_\odot)$	$M/M_\odot$	$D(kpc)$	$R/R_\odot$
				RRab				
V3	-1.78(9)	-1.77(11)	0.51(1)	3.80(2)	1.71(1)	0.73(14)	83.61(43)	6.01(3)
V9	-1.74(9)	-1.77(11)	0.46(1)	3.80(2)	1.73(1)	0.76(15)	83.41(48)	6.19(3)
V12	-2.09(10)	-2.24(15)	0.43(1)	3.80(2)	1.76(1)	0.83(16)	88.37(45)	6.54(3)
V13	-1.69(10)	-1.65(12)	0.50(1)	3.80(2)	1.72(1)	0.73(16)	86.13(44)	6.09(3)
V14	-2.23(10)	-2.47(17)	0.37(1)	3.79(2)	1.79(1)	0.86(20)	84.65(55)	7.06(4)
V15	-1.71(11)	-1.68(13)	0.46(1)	3.80(2)	1.73(1)	0.76(17)	88.41(52)	6.18(3)
V16	-2.05(18)	-2.17(27)	0.34(2)	3.80(3)	1.79(1)	0.89(31)	94.75(1.12)	6.75(7)
V17	-1.91(12)	-1.95(16)	0.45(1)	3.80(2)	1.74(1)	0.78(19)	87.28(62)	6.30(4)
V19	-1.88(12)	-1.92(15)	0.35(1)	3.80(2)	1.78(1)	0.80(19)	92.56(55)	6.65(4)
V21	-1.91(10)	-1.95(13)	0.39(1)	3.80(2)	1.77(1)	0.80(19)	86.50(51)	6.58(3)
V22	-1.79(10)	-1.79(13)	0.47(1)	3.81(3)	1.73(1)	0.80(26)	93.55(68)	5.94(4)
V24	-1.57(15)	-1.50(17)	0.49(1)	3.80(3)	1.72(1)	0.68(24)	86.77(63)	5.99(4)
V25	-1.74(7)	-1.72(8)	0.51(1)	3.80(1)	1.72(1)	0.72(12)	82.27(29)	6.03(2)
V29	-2.12(12)	-2.28(18)	0.40(01)	3.79(1)	1.77(1)	0.84(18)	87.01(46)	6.90(3)
V32	-1.67(9)	-1.62(10)	0.50(1)	3.80(1)	1.72(1)	0.72(15)	77.43(29)	6.04(2)
V57	-1.91(12)	-1.97(16)	0.46(1)	3.79(2)	1.74(1)	0.74(20)	75.11(33)	6.64(3)
V59	-2.51(62)[1]	-2.79(1.11)[1]	0.39(02)	3.78(6)	1.79(1)	0.82(60)	89.19(88)	7.27(6)
Mean	-1.86	-1.90	0.44	3.80	1.75	0.78	86.3	6.42
σ	±0.18	±0.27	±0.5	±0.01	±0.03	±0.03	±5.0	±0.40
				RRc				
V4	-1.71(11)	-1.68(13)	0.51(4)	3.83(1)	1.69(1)	0.46(2)	85.43(14)	4.54(7)
V6	-2.06(7)	-2.19(11)	0.51(4)	4.12(1)	1.70(1)	0.53(2)	85.70(16)	4.63(8)
V27	-1.54(14)	-1.45(16)	0.75(4)	3.84(1)	1.60(2)	0.53(2)	81.09(16)	4.42(8)
V31	-1.61(20)	-1.55(23)	0.48(3)	3.86(1)	1.71(1)	0.48(2)	85.60(14)	4.59(8)
V33	-1.75(39)	-1.74(48)	0.55(8)	3.84(1)	1.68(3)	0.53(5)	92.40(35)	4.91(18)
V34	-1.70(8)	-1.66(10)	0.42(4)	3.86(1)	1.73(2)	0.50(3)	92.44(1.92)	4.78(10)
V55	-1.06(20)[1]	-0.95(15)[1]	0.52(5)	3.87(1)	1.69(2)	0.45(3)	85.79(1.67)	4.39(10)
V60	-1.60(3)	-1.53(3)	0.58(4)	3.86(1)	1.67(2)	0.42(2)	81.37(1.53)	4.37(8)
V66	-1.79(11)	-1.79(14)	0.54(4)	3.86(1)	1.69(2)	0.46(2)	91.17(1.89)	4.51(9)
V67	-1.96(5)	-2.04(7)	0.56(3)	3.86(1)	1.68(1)	0.52(2)	70.60(1.03)	4.46(6)
V68	-2.12(9)	-2.28(14)	0.48(2)	3.85(1)	1.71(1)	0.58(2)	85.95(1.07)	4.74(6)
V72	-2.12(10)	-2.29(15)	0.49(4)	3.85(1)	1.70(2)	0.51(2)	86.02(1.61)	4.87(9)
V74	-2.05(8)	-2.17(12)	0.62(4)	3.85(1)	1.65(1)	0.61(3)	90.07(1.50)	4.40(7)
V75	-1.36(6)[1]	-1.25(6)[1]	0.56(3)	3.87(1)	1.68(1)	0.53(2)	81.04(1.04)	4.27(5)
V76	-1.49(11)	-1.39(12)	0.39(4)	3.86(1)	1.74(1)	0.45(2)	79.03(1.31)	4.85(8)
V77	-1.94(15)	-2.00(21)	0.44(4)	3.84(1)	1.72(1)	0.61(3)	86.16(1.43)	5.09(8)
V84	-2.05(15)	-2.19(22)	0.56(3)	3.86(1)	1.68(1)	0.58(2)	70.47(92)	4.48(6)
V82	-1.77(12)	-1.75(15)	0.77(3)	3.84(1)	1.59(1)	0.49(1)	60.06(75)	4.36(5)
V90	-2.085(24)	-2.23(35)	0.42(4)	3.85(1)	1.73(2)	0.56(3)	88.57(1.83)	4.88(10)
Mean	-1.84	-1.88	0.53	3.86	1.69	0.52	83.1	4.61
σ	±0.21	±0.30	±0.10	±0.01	±0.04	±0.05	±8.1	±0.23

[1]Value not included in the calculation of the mean.

A qualitative comparison of our limited CMD with the deep and detailed CMD, Figure 2 of Di Criscienzo et al. (2011) (hereinafter diC11), leads to the following instructive observations. First, NGC 2419 has a well developed HB blue tail from where V18 has most likely evolved.

Our photometry does not reach these faint regions of the CMD. If we consider the variable star distribution near the HB in diC11 CMD, we may conclude that all RR Lyrae in their study are cluster members. However, diC11 did not perform a membership analysis. In our CMD of Figure 6, sev-

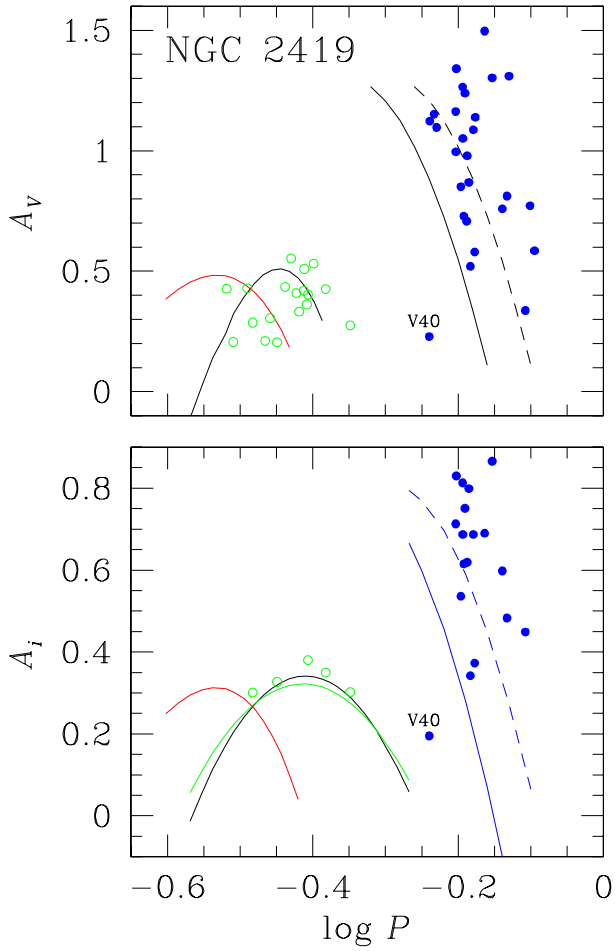

Fig. 5. Period-Amplitude diagram for the RR Lyrae in NGC 2419. Blue and green symbols represent RRab and RRc stars respectively. The star V40 is not a cluster member. In the top panel, the curves to the right are the locy for RRab stars (unevolved continuous and evolved segmented) in M3 according to Cacciari et al. (2005). The black parabola for the RRc stars was calculated by Kunder et al. (2013b) from 14 OoII clusters and Arellano Ferro et al. (2015) calculated the red parabolas from a sample of RRc stars in five OoI clusters. In the bottom panel, the continuous and segmented blue lines were constructed by Kunder et al. (2013a). The black and green parabolas were calculated by Yepez et al. (2020) and Deras et al. (2019) respectively, using 35 RRc stars from eight OoII clusters. The colour figure can be viewed online.

eral RR Lyrae appear noticeably brighter than the HB (e.g. V37, V38, V40, V41, V48, V51, V56 and V69). It is not difficult to corroborate from the identification chart of Figure 4, that these stars are tenants of the cluster central regions and hence are most likely blended, making our photometry further limited and hence producing spurious positions in our CMD. These conditions may have also limited the possibilities of the *Gaia* mission to measure them, as none of them have proper motions reported in *Gaia*-DR3; thus, we have assigned them the unknown (UN) membership status in Table 2. The membership of these variables in NGC 2419 should be corroborated in the future. The rest of the variables in Table 2, all likely members, are distributed closer to the HB with some scatter. This scatter is comparable to that observed in Figure 2 of diC11 if plotted at the same scale; therefore, the RR Lyrae population shows signs of evolution off the ZAHB.

The mass distribution along the ZAHB is determined by the amount of mass lost during the He-flash events at RGB, as it is clearly demonstrated by the models of Silva Aguirre et al. (2008). The more mass is lost, the less massive the star is when settling towards the bluer regions of the ZAHB. This is consistent, for instance, with the fact that bluer (hotter) RRc stars are less massive than redder (cooler) RRab stars. The two modes are in principle separated by the first overtone red edge (FORE) of the instability strip. Depending upon the exact total mass at exhaustion of core-Helium, RRc and RRab stars can either be neatly separated by the FORE or can share the inter-order or bimodal instability strip (i.e. the intersection of the first overtone and fundamental mode instability strips). These concepts are graphically illustrated in Figure 3 of Caputo et al. (1978).

The empirical position of the FORE (Arellano Ferro et al. 2015, 2016) is shown in Figure 6 by two black vertical lines. Also shown are the theoretical borders of the instability strip for the first overtone and fundamental modes from Bono et al. (1994). Note that the theoretical and empirical FORE match very well. It was found by Arellano Ferro et al. (2019) that in all OoII type clusters studied by them, RR Lyrae pulsating modes are well segregated by the FORE, whereas such clear segregation happens only in some OoI clusters, while in others the two modes share the inter-order or "either-or" region. This was interpreted by these authors as indicating that in OoII clusters the RR Lyrae stars always start their ZAHB evolution from less massive bluer stars, while in OoI clusters they exhibit a wider mass distribution, and hence segregation may or may not occur. It remains unclear what physics constrain these two options but it is likely connected with the mass-loss processes during the RGB.

In the case of NGC 2419, the RRc and RRab stars are all mixed across the HB. This can be seen in the CMD of Figure 6, but also in the CMD in Figure 2 of

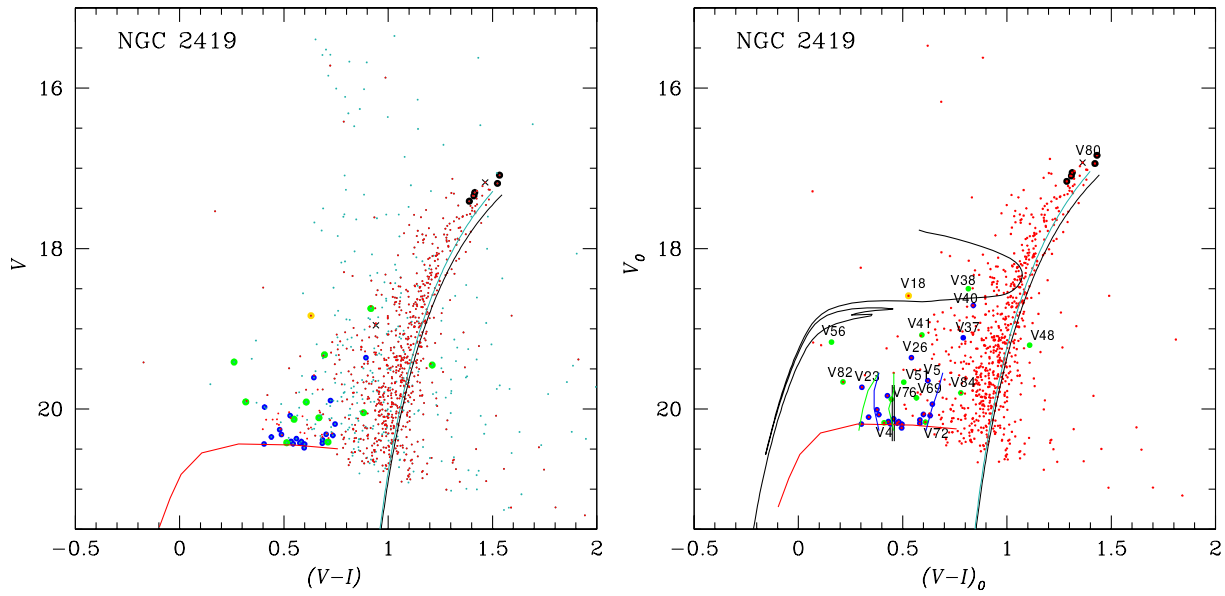

Fig. 6. Observed CMD of NGC 2419. The left panel shows the field stars (small blue dots) and likely cluster member stars (red dots), according to our membership analysis. The right panel shows only the member stars in the dereddened plane. We use $E(B-V) = 0.08$. Blue and green circles represent RRab and RRc stars, respectively. Black circles are used for SR stars. The only CW star is the yellow circle. Black X corresponds to V80, whose variability we could not confirm. The vertical black lines at the ZAHB mark the empirical red edge of the first overtone instability strip (Arellano Ferro et al. 2015, 2016). Also shown are the theoretical fundamental (blue lines) and first overtone (green lines) instability strip borders from Bono et al. (1994). Isochrones are from VandenBerg et al. (2014) for an age of 12.5 Gyr (black) and 13.0 Gyr (turquoise) with [Fe/H]= -1.8 and -2.0, respectively. Red ZAHB is from the models built from the Eggleton code (Pols et al. 1997, 1998; Schröder et al. 1997), and was calculated by Yepez et al. (2022). The black evolutionary track corresponds to a model of total mass 0.54 $M_\odot$ and a core of 0.50 $M_\odot$. These very thin envelope models explain well type II Cepheids such as V18 (Yepez et al. 2022). The colour figure can be viewed online.

diC11. For a Oo II cluster, the location of RRab stars in the inter-order region is contrary to the argument given in the earlier paragraph. Hence, NGC 2419 is an unconventional Oo II cluster exhibiting mixing of the modes in the instability strip.

9. CONCLUSIONS

Using the *Gaia*-DR3 proper motions of stars in the field of NGC 2419, we have been able to confirm the membership of most of the variables known in the cluster. Several of the known variables are in crowded environments and, due to blending with neighbours, we were not able to resolve them; thus, they may appear in odd positions in the CMD. These stars also lack *Gaia*-DR3 proper motion data; thus, we cannot confirm their membership status (e.g. V38, V41, V48, V51, V56, V69). V89, with a proper motion measurement, was found to be a likely field star.

The radial distribution of member stars, clearly demonstrates the extended reach of the cluster to distances of about 140 pc, making of NGC 2419 one of the largest clusters in the Galaxy.

From the Fourier light curve decomposition of clearly resolved RR Lyrae stars, we determined the average metallicity and distance $[\mathrm{Fe/H}]_{\mathrm{UV}} = -1.90 \pm 0.27$ and $D = 86.3 \pm 5.0$ kpc from the RRab light curves and $[\mathrm{Fe/H}]_{\mathrm{UV}} = -1.88 \pm 0.30$ and $D = 83.1 \pm 8.1$ kpc from the RRc stars. These determinations are in excellent agreement with the well established results $[\mathrm{Fe/H}]_{Spec} = -2.2$ (Carretta et al. 2009), and $D = 88.47 \pm 2.40$ kpc (Baumgardt & Vasiliev 2021).

Our post He-flash models show that the W Virginis star V18 has evolved from a ZAHB blue tail progenitor with a very thin shell; this progenitor has a total mass of 0.54 $M_\odot$ but a shell of only 0.04 $M_\odot$. These results confirm the conclusions from Deras et al. (2022) for the Pop II cepheids of M56 or from Yepez et al. (2022) for M14, that thin shells are a required condition for the generation of Pop II cepheid pulsations.

AAF is grateful to the Indian Institute of Astrophysics, for warm hospitality during the writing of

this work. AAF also thankfully acknowledges the sabbatical support granted by the program PASPA of the DGAPA-UNAM. The present project has benefited from the support of DGAPA-UNAM through projects IG100620 and IN103024. The permanent help received from the IA-UNAM librarian, Beatriz Juárez Santamaría, with the bibliographical material needed for this work is fully acknowledged. We are thankful to the IAO TACs for the telescope time allocations over 17 years and to the supporting staff at the Hanle (IAO) and Hosakote (CREST) observing stations. The facilities at IAO and CREST are operated by the Indian Institute of Astrophysics, Bangalore.

A. APPENDIX

A.1. *Light Curves of Measured Variable Stars*

The light curves of all variables resolved in our photometry are displayed in Figures 7, 8, 9 and 10 for the RRab, RRc, RGBs and CW respectively.

A.2. *Comments on Individual Stars*

V37, V49 and V42. These three stars display a very low amplitude in V. This has also been noted by diC11 and Clement et al. (2001). These stars are in the central regions of the cluster and therefore are very likely blended with near neighbours, so that their amplitudes appear diminished. None of them have proper motions reported in *Gaia*-DR3; thus, we cannot confirm their cluster membership.

V38, V41, V48, V51, V56, V69. These RRc variables are all blended in our images. They have no proper motions reported in *Gaia*-DR3, hence no membership status could be assigned.

V39. This double mode star was first found by Clement & Nemec (1990) with the periods $P_1 = 0.40704$ and $P_0 = 0.5465$. The fitting of our data with a model of these two periods is shown in Figure 11 and looks quite satisfactory given the intrinsic noise of our observations.

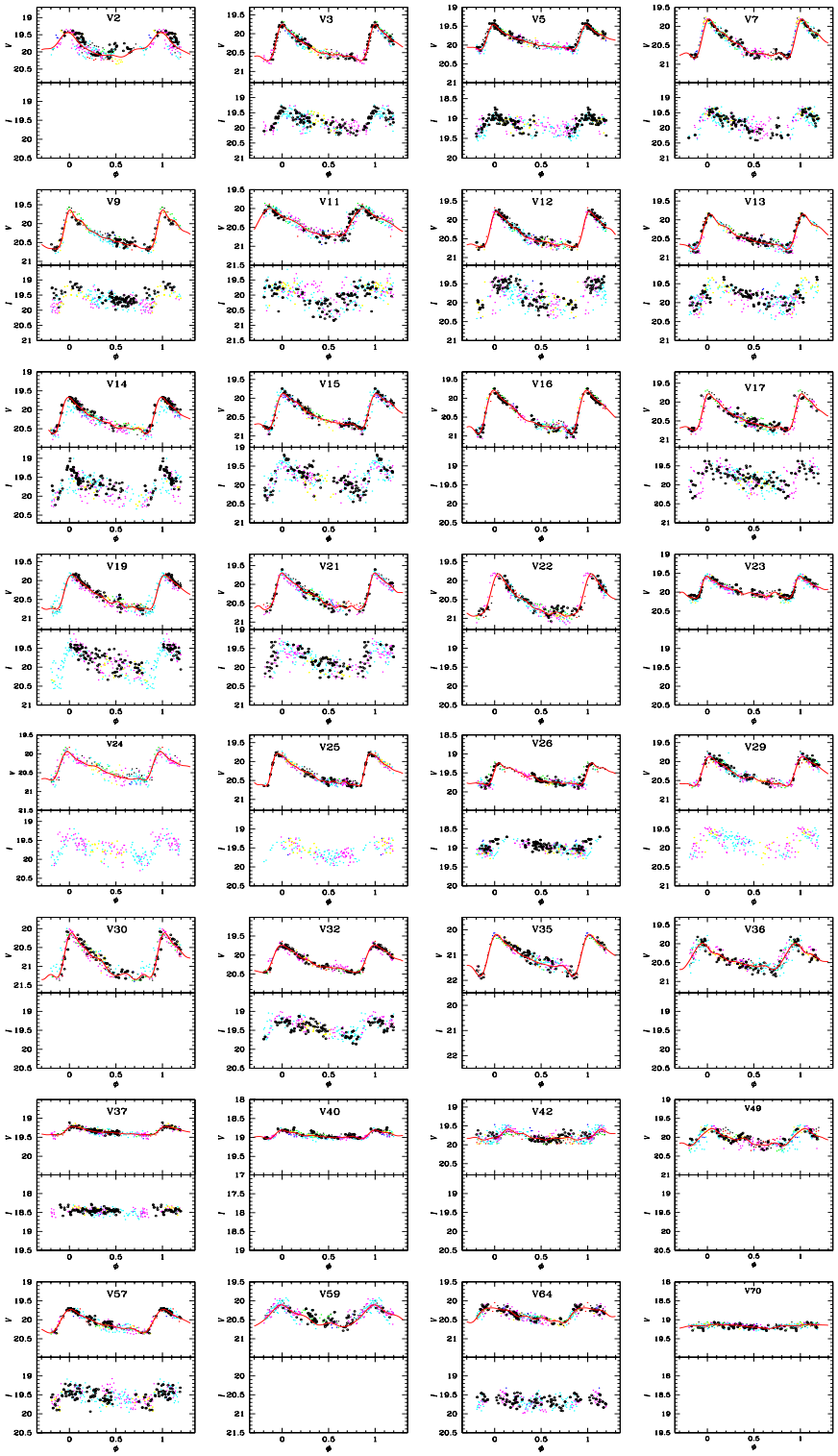

Fig. 7. Light curves of the RRab stars. Color code is as follows: black, red, green, blue, turquoise, lilac, yellow and empty circles for 2005, March 2007, April 2007, 2009, 2011-2012, 2013, 2017 and 2021-2022 seasons, respectively. The colour figure can be viewed online.

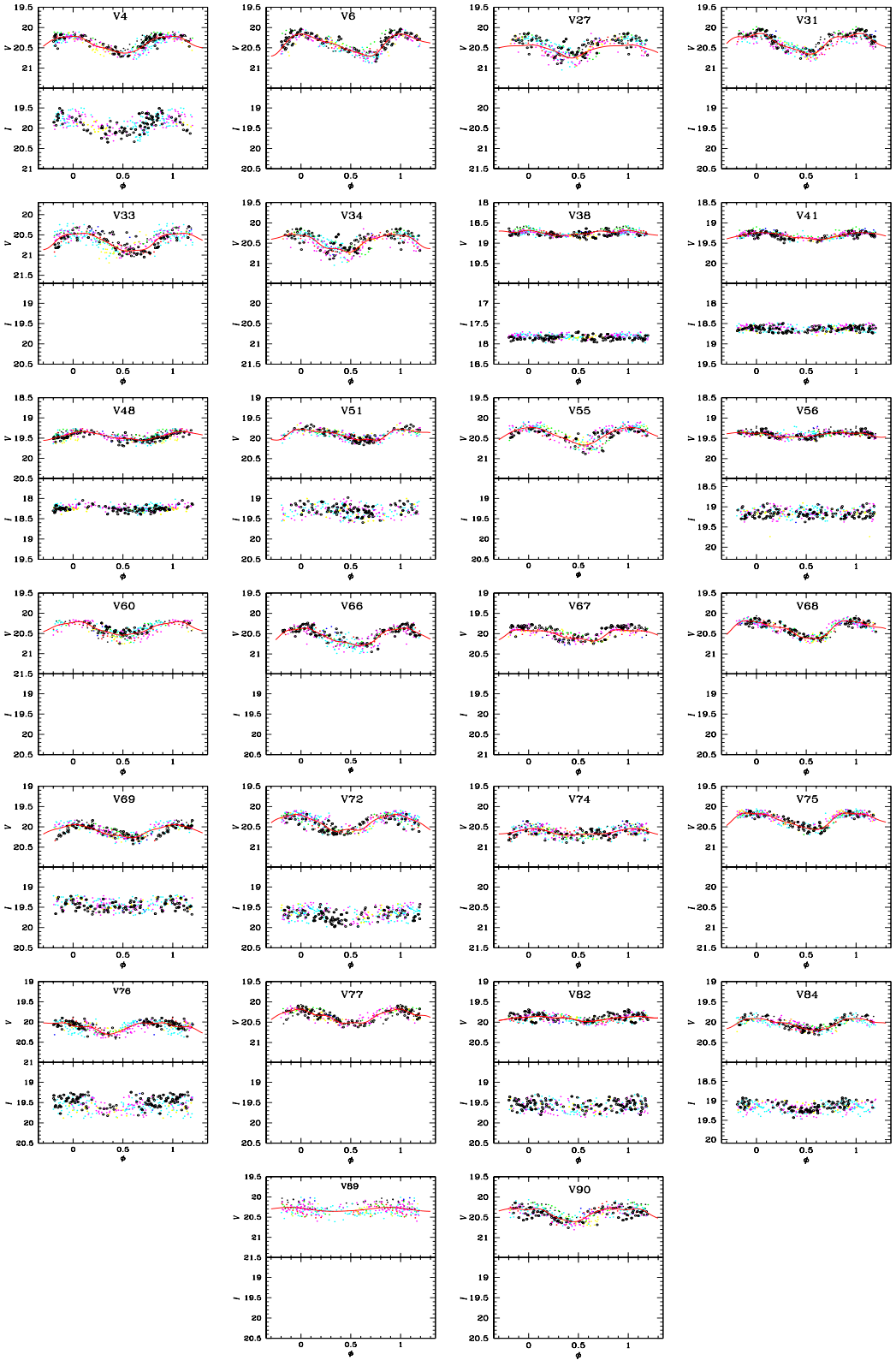

Fig. 8. Light curves of the RRc stars. Color code is as Figure 7. The colour figure can be viewed online.

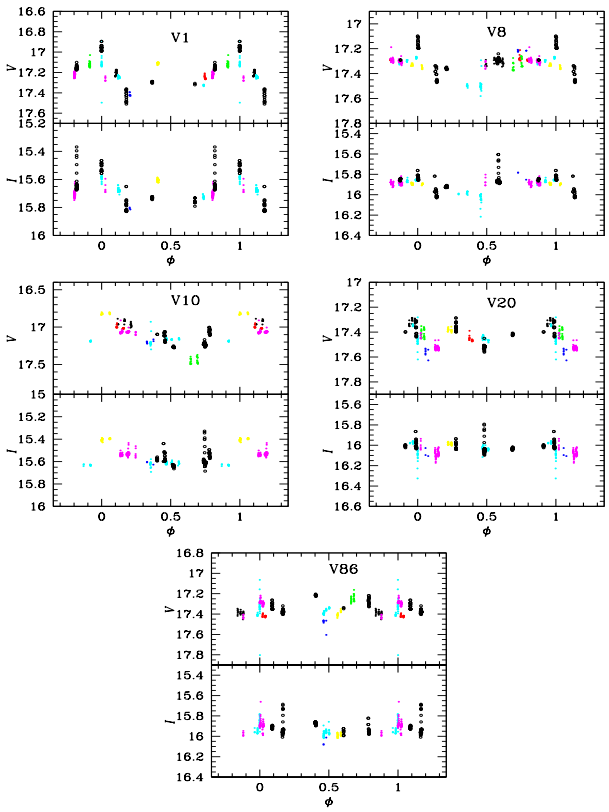

Fig. 9. Light curves of Long period variables in NGC 2419 phased with the periods of Table 2. Color code is as Figure 7. The colour figure can be viewed online.

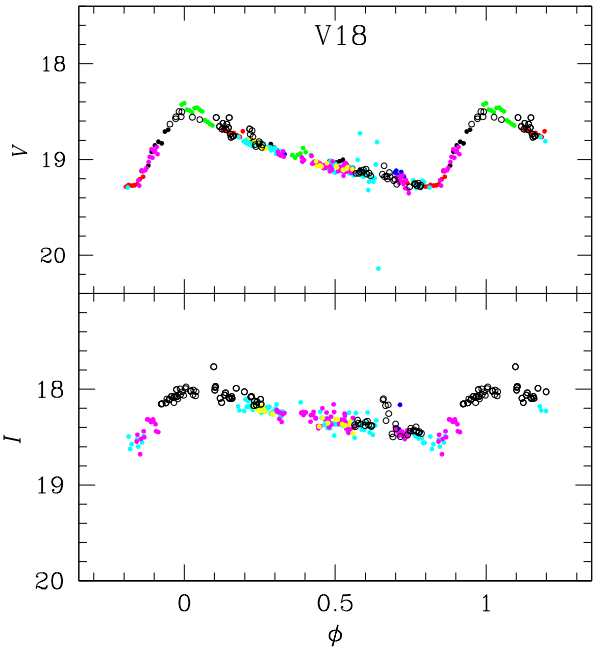

Fig. 10. Light curve of the CW star V18. The colour figure can be viewed online.

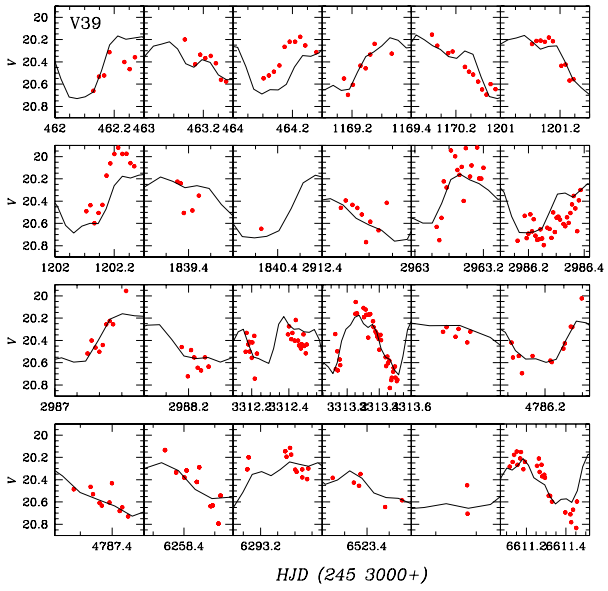

Fig. 11. Light curve of V39 with a two-period model fit with $P_0 = 0.54650$ and $P_1 = 0.40704$. The colour figure can be viewed online.

REFERENCES

Arellano Ferro, A. 2022, RMxAA, 58, 257, https://doi.org/10.22201/ia.01851101p.2022.58.02.08

_____. 2024, IAU Symposium, 376, At the crossroads of astrophysics and cosmology: Period-luminosity relations in the 2020s, ed. R. De Grijs, P. A. Whitelock, and M. Catelan, (CUP), 222, https://doi.org/10.1017/S1743921323002880

Arellano Ferro, A., Bustos Fierro, I. H., Calderón, J. H., & Ahumada, J. A. 2019, RMxAA, 55, 337, https://doi.org/10.22201/ia.01851101p.2019.55.02.18

Arellano Ferro, A., Figuera Jaimes, R., Giridhar, S., et al. 2011, MNRAS, 416, 2265, https://doi.org/10.1111/j.1365-2966.2011.19201.x

Arellano Ferro, A., Giridhar, S., & Bramich, D. M. 2010, MNRAS, 402, 226, https://doi.org/10.1111/j.1365-2966.2009.15931.x

Arellano Ferro, A., Luna, A., Bramich, D. M., et al. 2016, Ap&SS, 361, 175, https://doi.org/10.1007/s10509-016-2757-5

Arellano Ferro, A., Mancera Piña, P. E., Bramich, D. M., et al. 2015, MNRAS, 452, 727, https://doi.org/10.1093/mnras/stv1299

Arellano Ferro, A., Rojas Galindo, F. C., Bustos Fierro, I. H., et al. 2023, MNRAS, 519, 2451, https://doi.org/10.1093/mnras/stac3650

Baumgardt, H. & Vasiliev, E. 2021, MNRAS, 505, 5957, https://doi.org/10.1093/mnras/stab1474

Bono, G., Braga, V. F., Fiorentino, G., et al. 2020, A&A, 644, 96, https://doi.org/10.1051/0004-6361/202038191

Bono, G., Caputo, F., & Stellingwerf, R. F. 1994, ApJ, 423, 294, https://doi.org/10.1086/173806

Bramich, D. M. 2008, MNRAS, 386, 77, https://doi.org/10.1111/j.1745-3933.2008.00464.x

Bramich, D. M., Bachelet, E., Alsubai, K. A., Mislis, D., & Parley, N. 2015, A&A, 577, 108, https://doi.org/10.1051/0004-6361/201526025

Bramich, D. M., Figuera Jaimes, R., Giridhar, S., & Arellano Ferro, A. 2011, MNRAS, 413, 1275, https://doi.org/10.1111/j.1365-2966.2011.18213.x

Bramich, D. M., Horne, K., Albrow, M. D., et al. 2013, MNRAS, 428, 2275, https://doi.org/10.1093/mnras/sts184

Bustos Fierro, I. H. & Calderón, J. H. 2019, MNRAS, 488, 3024, https://doi.org/10.1093/mnras/stz1879

Cacciari, C., Corwin, T. M., & Carney, B. W. 2005, AJ, 129, 267, https://doi.org/10.1086/426325

Caputo, F., Castellani, V., & Tornambe, A. 1978, A&A, 67, 107

Carretta, E., Bragaglia, A., Gratton, R., D'Orazi, V., & Lucatello, S. 2009, A&A, 508, 695, https://doi.org/10.1051/0004-6361/200913003

Catelan, M. 2009, Ap&SS, 320, 261, https://doi.org/10.1007/s10509-009-9987-8

Clement, C. & Nemec, J. 1990, JRASC, 84, 434

Clement, C. M., Muzzin, A., Dufton, Q., et al. 2001, AJ, 122, 2587, https://doi.org/10.1086/323719

Deras, D., Arellano Ferro, A., Lázaro, C., et al. 2019, MNRAS, 486, 2791, https://doi.org/10.1093/mnras/stz642

Deras, D., Arellano Ferro, A., Bustos Fierro, I., & Yepez, M. A. 2022, RMxAA, 58, 121, https://doi.org/10.22201/ia.01851101p.2022.58.01.10

Di Criscienzo, M., Greco, C., Ripepi, V., et al. 2011, AJ, 141, 81, https://doi.org/10.1088/0004-6256/141/3/81

Gaia Collaboration, Vallenari, A., Brown, A. G. A., et al. 2023, A&A, 674, 1, https://doi.org/10.1051/0004-6361/202243940

Guldenschuh, K. A., Layden, A. C., Wan, Y., et al. 2005, PASP, 117, 721, https://doi.org/10.1086/431178

Kunder, A., Stetson, P. B., Cassisi, S., et al. 2013a, AJ, 146, 119, https://doi.org/10.1088/0004-6256/146/5/119

Kunder, A., Stetson, P. B., Catelan, M., Walker, A. R., & Amigo, P. 2013b, AJ, 145, 33, https://doi.org/10.1088/0004-6256/145/2/33

Landolt, A. U. 1992, AJ, 104, 340, https://doi.org/10.1086/116242

Pols, O. R., Schröder, K.-P., Hurley, J. R., Tout, C. A., & Eggleton, P. P. 1998, MNRAS, 298, 525, https://doi.org/10.1046/j.1365-8711.1998.01658.x

Pols, O. R., Tout, C. A., Schroder, K.-P., Eggleton, P. P., & Manners, J. 1997, MNRAS, 289, 869, https://doi.org/10.1093/mnras/289.4.869

Ripepi, V., Clementini, G., Di Criscienzo, M., et al. 2007, ApJ, 667, 61, https://doi.org/10.1086/522000

Schlafly, E. F. & Finkbeiner, D. P. 2011, ApJ, 737, 103, https://doi.org/10.1088/0004-637X/737/2/103

Schlegel, D. J., Finkbeiner, D. P., & Davis, M. 1998, ApJ, 500, 525, https://doi.org/10.1086/305772

Schröder, K.-P., Pols, O. R., & Eggleton, P. P. 1997, MNRAS, 285, 696, https://doi.org/10.1093/mnras/285.4.696

Silva Aguirre, V., Catelan, M., Weiss, A., & Valcarce, A. A. R. 2008, A&A, 489, 1201, https://doi.org/10.1051/0004-6361:200810047

Stetson, P. B. 2000, PASP, 112, 925, https://doi.org/10.1086/316595

Sturch, C. 1966, ApJ, 143, 774, https://doi.org/10.1086/148557

van den Bergh, S. & Mackey, A. D. 2004, MNRAS, 354, 713, https://doi.org/10.1111/j.1365-2966.2004.08228.x

VandenBerg, D. A., Bergbusch, P. A., Ferguson, J. W., & Edvardsson, B. 2014, ApJ, 794, 72, https://doi.org/10.1088/0004-637X/794/1/72

Yepez, M. A., Arellano Ferro, A., & Deras, D. 2020, MNRAS, 494, 3212, https://doi.org/10.1093/mnras/staa637

Yepez, M. A., Arellano Ferro, A., Deras, D., et al. 2022, MNRAS, 511, 1285, https://doi.org/10.1093/mnras/stac054

Zhang, T., Ramakrishnan, R., & Livny, M. 1996, ACM SIGMOD Rec., 25, 103, https://doi.org/10.1145/235968.233324

Zinn, R. & West, M. J. 1984, ApJS, 55, 45, https://doi.org/10.1086/190947

A. Arellano Ferro and M. A. Yepez: Instituto de Astronomía, Universidad Nacional Autónoma de México, Ciudad Universitaria, C.P. 04510, México.

I. Bustos Fierro: Observatorio Astronómico, Universidad Nacional de Córdoba, Córdoba C.P. 5000, Argentina.

G. A. García Pérez and G. Rios Segura: Facultad de Física, Universidad Veracruzana, Xalapa, México.

Sunetra Giridhar and S. Muneer: Indian Institute of Astrophysics, Bangalore, India.

M. A. Yepez: Instituto Nacional de Astrofísica, Óptica y Electrónica (INAOE), Luis Enrique Erro No.1, Tonantzintla, Pue., C.P. 72840, México.

Revista Mexicana de Astronomía y Astrofísica, **60**, 293–304 (2024)

https://doi.org/10.22201/ia.01851101p.2024.60.02.07

SUPERNOVAE PHOTOMETRY AT OAUNI[1]

M. Espinoza[2] and A. Pereyra[3,2]

Received February 17 2024; accepted June 4 2024

ABSTRACT

We analyse photometric data of nine supernovae (SNe) in filters V, R and I obtained during observational campaigns at the OAUNI site in 2016, 2017 and 2023. The calibrated magnitudes of the observed SNe were compared with their respective light curves available in the literature to study their evolution after their maximum brightness. In some cases, the supernova color-color diagnostic diagram was used to determine our observation date and correctly locate our magnitudes on the light curves. For this purpose, the use of supernova light curve templates, as well as reference supernovae, was also helpful. This work allowed us to verify the feasibility of performing precision astronomical photometry at the OAUNI.

RESUMEN

Analizamos los datos fotométricos de nueve supernovas en los filtros V, R e I que se obtuvieron durante las campañas observacionales de OAUNI en 2016, 2017 y 2023. Para investigar la evolución posterior a su punto máximo de brillo, se compararon las magnitudes calibradas de las supernovas observadas con sus respectivas curvas de luz disponibles en la literatura. En algunos casos, se usó el diagrama de diagnóstico color-color de supernovas para determinar nuestras fechas de observación y ubicarlas correctamente en las curvas de luz. Para este propósito también fueron de ayuda la utilización de plantillas de curvas de luz de supernovas, así como supernovas de referencia. Este trabajo permitió verificar la factibilidad de realizar fotometría astronómica de precisión en el OAUNI.

Key Words: supernovae: general — techniques: photometric

1. INTRODUCTION

The Astronomical Observatory of the National University of Engineering (OAUNI in Spanish) began operations in 2015 (Pereyra et al. 2015). This facility is situated in Huancayo, 3300 meters above sea level, in the heart of the Peruvian Andes. One of the main scientific programs proposed was the supernovae photometric follow-up with several detections since then. This work presents the main SNe events observed at OAUNI site in the last years since 2016. Special care was taken for the photometric calibration process in order to contribute with useful data to the supernovae light curves of the analyzed events. Previous efforts of SNe observations in Perú include the detection of the famous SN 1987 by M. Ishitsuka and H. Trigoso (private communication) at the same site of these observations, and SN 2003gt (Carlos Reyes et al. 2013) observed at the southern Peruvian Andes.

In the following, we describe the observed SNe (§ 2), and the reduction process (§ 3), including the different methods used for the calibration data. The analysis and comparison of OAUNI data with template light curves, diagnostic color-color diagrams, and data available in the literature for each event is shown in § 4. Finally, our conclusions are drawn in § 5.

2. DETECTED OAUNI SUPERNOVAE EVENTS

The OAUNI SNe sample is indicated in Table 1 and Figure 1. A total of nine events were detected including four SNe Type Ia, four Type II, and one Type Ib. All the analyzed SNe are at a redshift lower than 0.04 (see Table 1). Below is listed the relevant information about each event.

[1]Observations obtained at the Astronomical Observatory of the National University of Engineering (OAUNI) in Huancayo, Perú.

[2]National University of Engineering, Lima, Perú.

[3]Geophysical Institute of Perú, Astronomy Area, Lima, Perú.

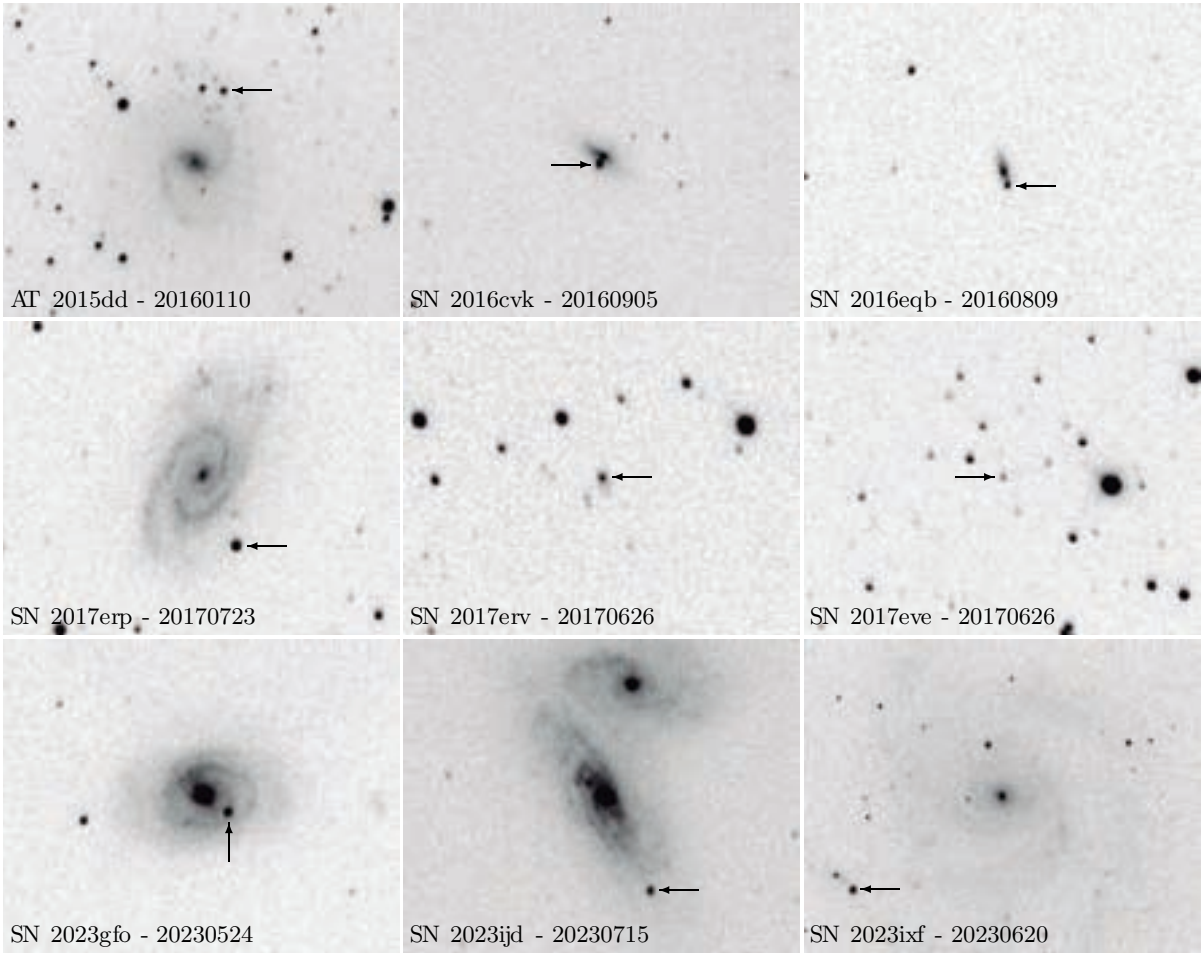

Fig. 1. OAUNI SNe sample in the R filter. Each frame indicates the observed SN (arrow) and the observation date. The individual FOV is $4\farcm1\times3\farcm2$, except for SN 2023ixf with $9\farcm6\times7\farcm7$. North is top and East is left.

2.1. *AT 2015dd*

On December 15, 2015, AT 2015dd was found in the center of the galaxy NGC 5483 (z = 0.006) by the MASTER-SAAO[4] (Gress et al. 2015). Using the SOAR telescope, three days later, it was identified as a Type Ib SN, and 2015-12-08 was determined to be the day of maximum brightness (Foley, Hounsell & Miller 2015).

2.2. *SN 2016cvk*

On June 12, 2016, the BOSS group[5] discovered SN 2016cvk. The SN was situated east of the host galaxy ESO 344-G 021 (z=0.010783, Parker 2016), and had a very low brightness of ≈17 mag in the V filter. With a behavior very similar to SN 2009ip, the *ASASSN* group[6] classified this SN as Type IIn. The PESSTO group (Parker 2016) further confirmed this classification.

2.3. *AT 2016eqb*

On August 1, 2016, the *ASASSN* group (Brimacombe et al. 2016) identified AT 2016eqb in the host galaxy 2MASX J23154564-0120135 (z=0.025308). KOSMOS[7] classified it as a Type Ia SN, with the day of maximum brightness being 2016-08-07 (Pan et al. 2016).

2.4. *SN 2017erp*

K. Itagaki discovered SN 2017erp on June 13, 2017 (Itagaki 2017). SALT[8] (Jha et al. 2017) classified it as an extremely young Type Ia SN, located in the arm of NGC 5861

[4]Mobile Astronomical System of Telescope-Robots at the South African Astronomical Observatory, a self-detection system.
[5]Backyard Observatory Supernova Search.
[6]All-Sky Automated Survey for SNe.
[7]The Cosmic Evolution Survey (COSMOS).
[8]The Southern African Large Telescope.

($z = 0.006174 \pm 0.000003$, Theureau et al. 2020). This SN was of special interest because of the relationship between its non-homogeneous composition and its light curve, as well as the peculiar reddening of its spectral lines in the near-ultraviolet range.

2.5. *AT 2017erv and AT 2017eve*

The *ASASSN* group found AT 2017erv on 2017-06-13 in AM 1904-844 (z=0.017035). A few days later, on June 19, 2017, AT 2017eve was also found on the same images in GALEXASC J184352.21-562927.7 (z=0.031, Nicholls, Brimacombe & Cacella 2017). On June 20, 2017, Uddin et al. (2017) categorized both SNe as Type Ia SNe, with a phase from maximum brightness of −2 days for AT 2017erv and +2 days for AT 2017eve.

2.6. *SN 2023gfo*

On 2023-04-19, SN 2023gfo was detected in NGC 4995 (z=0.0058) by the ATLAS[9] system. Additionally, the same field was observed four days prior to this detection, but no sign of the SN was found. According to Moore et al. (2023), this event would suggest that the SN was in its growth phase. Lick Observatory classified it as a SN Type IIP with a spectrum remarkably similar to SN 1999gi (Fulton et al. 2023b).

2.7. *SN 2023ijd*

The *ASASSN* group found SN 2023ijd in NGC 4568 (z = 0.007446, Stanek 2023) on 2023-05-14. It was classified as a Type II SN (Perley 2023).

2.8. *SN 2023ixf*

SN 2023ixf was classified as a Type II SN in its early stages of life (Perley & Gal-Yam 2023) after K. Itagaki discovered it on May 19, 2023, in M101 (z=0.000804, Itagaki 2023). Over the past few decades, SN 2023ixf has been considered the nearest Type II SN. Subsequent reports of earlier sightings, following the discovery, helped narrow down the explosion date (Fulton et al. 2023a; Filippenko, Zheng & Yang 2003) to a 20-hour window between May 18 and 19. SN 2023ixf was later reclassified as Type II-L (Bianciardi et al. 2023).

3. OBSERVATIONS, REDUCTIONS AND CALIBRATIONS

All observations mentioned here were collected using the OAUNI telescope (Pereyra et al. 2015) during the 2016, 2017, and 2023 observation campaigns. These observational runs typically take place in the months of May through September. In only one instance (AT 2015dd), a single observation was made in January. The OAUNI telescope has a Cassegrain type optical tube with Ritchey-Chrétien design and a primary mirror with a diameter of 0.51 m and f/8.2. A front-illuminated CCD STXL-6303E with 3072×2048 pixels^2 and 9μm/pixel served as the detector. A field-of-view of $\approx 23' \times 15'$ and a plate scale of 0.45″/pixel are produced by this detector and the optical system's focal ratio. For the scientific objects, multicolor photometry was made possible via a $UBVRI$ filter wheel. The record of observations made during the campaigns is displayed in Table 2. Column 1 shows the name of the SN, Column 2 presents the local observation date, Column 3 indicates the filters used, Column 4 displays the number of images obtained in each filter, and Column 5 shows the total integration time for each case. Column 6 presents the mean air mass during each sequence. In total, data from nine SNe are presented, with three different SNe observed each year. The individual integration time for one measurement is 20 seconds, and the total time for stacking images (N×20s) ranges from 600 to 1400 seconds.

With standard corrections for dark current and flat field, we used IRAF[10] for image reduction. Aperture photometry was extensively used with a typical instrumental magnitude error of tens of milimagnitude for the magnitude range of our sample (typically, between 11.3 to 17.1 mag). The first step in the calibration process was to find stars in each stellar field that matched both our images and the UCAC4 photometric catalog (Zacharias et al. 2013). These stars, listed in Table 3, were then used as comparison stars for every SN analyzed. We utilized two methods to determine the corrected value of the SN brightness using this data. The first method (m_1), involving equations 1, 2, and 3, was used to represent the transformation of the instrumental magnitudes (v, i, and r) to the calibrated magnitudes (V, I, and R) by obtaining a single zero point (v_0, i_0, and r_0). This method is useful when only one filter is available for measurements and was used for all the objects in our sample.

$$V = v_0 + v, \tag{1}$$

$$R = r_0 + r, \tag{2}$$

$$I = i_0 + i. \tag{3}$$

Using the transformation equations, the second method (m_2) involves the zero points (v_0, r_0, and i_0), the linear dependence (v_1, r_1, and i_1), and the

[9] Asteroid Terrestrial-Impact Last Alert System.

[10] Image Reduction and Analysis Facility hosted by the National Optical Astronomy Observatories in Tucson, Arizona.

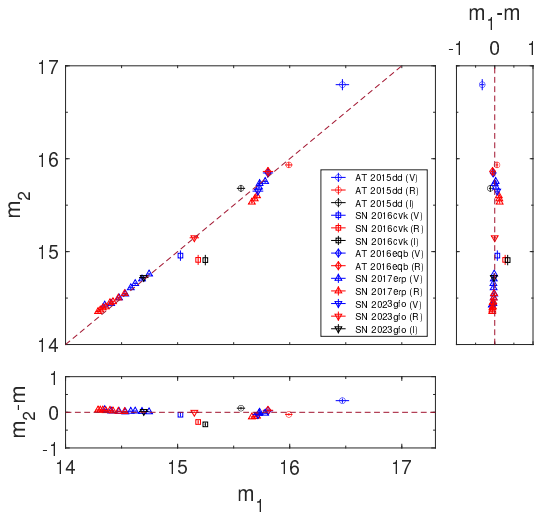

Fig. 2. Point-to-point correlation between m_1 and m_2 calibration methods for OAUNI SNe sample. Instrumental magnitudes in the V (blue dots), R (red dots) and I filters (black dots) are shown with different symbols for each supernova. The residuals for each calibration with respect to the perfect positive correlation (dashed line) are indicated below and on the right. The color figure can be viewed online.

coefficients (v_2, r_2, and i_2) for the color terms ($v-r$ or $v-i$) of the objects under consideration. The equations 4, 5, and 6 illustrate these transformations. This calibration method is more robust, but multicolor photometry is necessary for its applicability. It was used on five of the sample's objects.

$$V = v_0 + v_1 \times v + v_2 \times (v - r), \quad (4)$$

$$R = r_0 + r_1 \times r + r_2 \times (v - r), \quad (5)$$

$$I = i_0 + i_1 \times i + i_2 \times (v - i). \quad (6)$$

Our findings for the calibrations of the SNe magnitude of our sample, m_1 (Column 7) and m_2 (Column 8), are displayed in Table 2.

4. ANALYSES

Figure 2 displays m_1 and m_2 for any scenario in which both calibrations are provided for the same object so that the two calibration techniques can be compared. With the exception of 2016cvk, all examples have a high point-to-point correlation, and the typical residual between m_1 and m_2 is 0.096 ± 0.064 mag. When two calibrations are available, we will utilize m_2 for the analyses in the following; in other circumstances, we will use m_1.

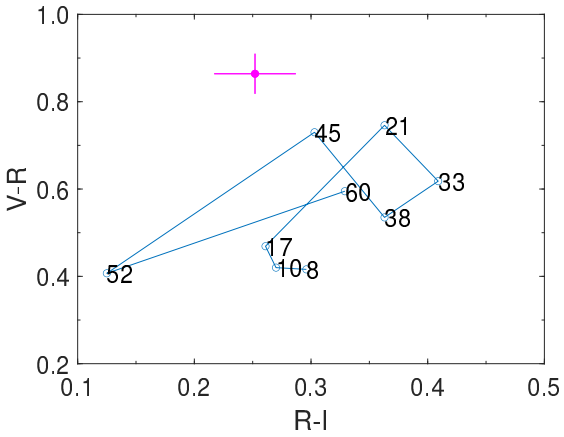

Fig. 3. $V-R$ vs. $R-I$ color diagram of Type Ib SN with $z = 0$ (blue line), adapted from Poznanski et al. (2002). Numbers indicate days after maximum light. OAUNI colors for AT 2015dd using the m_2 calibration are also indicated (magenta dot). The color figure can be viewed online.

4.1. *AT 2015dd*

When a SN reaches its maximum brightness, color-color diagnostic diagrams can be used to confirm how old it is (Poznanski et al. 2002). Based on the Type Ib SN classification of AT 2015dd and the near-zero redshift of the host galaxy (see to Table 1), Figure 3 illustrates the temporal behavior of a well-studied Type Ib SN at various stages of its life for $z = 0$. Using the m_2 calibration (Table 2), we computed the colors $V-R$ and $R-I$ for AT 2015dd. The values $V - R = 0.864 \pm 0.047$ and $R - I = 0.252 \pm 0.035$ are also displayed in Figure 3. The location of AT 2015dd on the diagram indicates a period of 20-40 days after the maximum of brightness, although it is not sufficient to explicitly validate the age of the supernova. Nevertheless, our observations are ≈32 days after the maximum, taking into account the day of the explosion on 2015-12-08 (Foley, Hounsell & Miller 2015).

4.2. *2016cvk*

Based on the information found in Table 2, we calculated the m_2 colors for SN 2016cvk, which are $V - R$=0.045 ± 0.004 and $R - I$=0.002 ± 0.005 on the Type IIn SN's $z = 0$ diagnostic diagram (refer to Figure 4). This SN 2016cvk is located almost exactly on the line that the diagram's days 3 through 13 encompass. It implies that when OAUNI observed this SN, it was still very young. On the other hand, we used a template (Nugent, Kim & Perlmutter 2002), literature data (see Table 4), and OAUNI m_2 data

TABLE 1

OAUNI SUPERNOVAE SAMPLE

SN	Other name	Type	RA (2000)	DEC (2000)	Discovery date (UT)	Host galaxy	z[a]
AT 2015dd	PSN J141[b]	Ib	14:10:23.42	-43:18:43.70	2015-12-15	NGC 5483	0.005921
SN 2016cvk	ASASSN-16jt	IIn-pec	22:19:49.43	-40:40:05.50	2016-06-12	ESO 344-G21	0.010842
AT 2016eqb	ASASSN-16hz	Ia	23:15:45.48	-01:20:22.73	2016-08-01	2MASX[c]	0.02531(15)
SN 2017erp		Ia	15:09:14.90	-11:20:03.00	2017-06-13	NGC 5861	0.006303
AT 2017erv	ASASSN-17ho	Ia	19:18:47.10	-84:41:50.03	2017-06-13	AM 1904-844	0.017035
AT 2017eve	ASASSN-17hq	Ia	18:43:53.51	-56:29:29.04	2017-06-19	GALEXASC[d]	0.031
SN 2023gfo		IIP	13:09:39.68	-07:50:11.75	2023-04-20	NGC 4995	0.005834
SN 2023ijd	ASASSN-23du	II	12:36:32.47	+11:13:19.71	2023-05-14	NGC 4568	0.00744(10)
SN 2023ixf		IIL	14:03:38.56	+54:18:41.94	2023-05-19	M101	0.000811(16)

[a] Of host galaxy from SIMBAD, except for AT 2016erv (Nicholls, Brimacombe & Cacella 2017) and AT 2017eve (Uddin et al. 2017).
[b] PSN J14102342-4318437.
[c] 2MASX J23154564-0120135.
[d] GALEXASC J184352.21-562927.7.

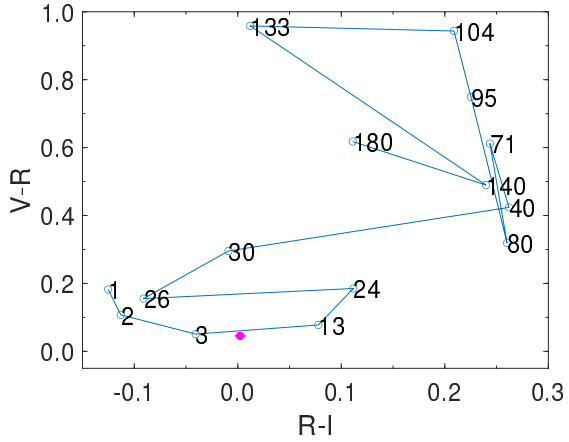

Fig. 4. $V - R$ vs. $R - I$ color diagram of Type IIn SN with $z = 0$ (blue line, adapted from Poznanski et al. 2002). Numbers indicate days after maximum light. OAUNI colors for SN 2016cvk using m_2 calibration are also indicated (magenta dot). The color figure can be viewed online.

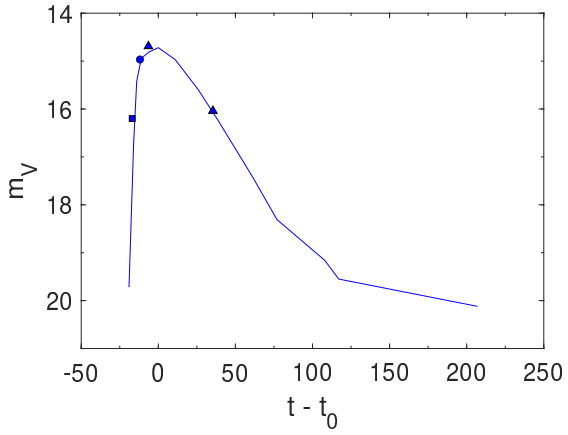

Fig. 5. SN 2016cvk light curve in the V filter. Template light curve for Type IIn SN with $z = 0$ (blue line, Nugent, Kim & Perlmutter 2002) with *ASASSN* data (blue square, Brimacombe et al. 2016), Kato's data (blue triangle, `http://ooruri.kusastro.kyoto-u.ac.jp/mailarchive/vsnet-recent-sn/6612`) and OAUNI m_2 data (blue dot, Table 2). Time offset is $t_0 = 2457648.5$ days. The color figure can be viewed online.

(see Table 2) to generate the light curve in the V filter for this SN. To determine whether the brightness of this SN behaves similarly to the average brightness of SNe of the same type, the Nugent's template is shown. In order to compare the data, we must fit all of the data to the same reference system because Nugent's template plots the peak of brightness in the B filter of the time coordinate. First, we use equation 7 to convert the numbers at the template's peak to a polynomial.

$$m(t) = \sum_{i=0}^{6} m_i \times (t - t_0)^i. \qquad (7)$$

Using data from the SN close to the peak, we modify m_0 and t_0 in this polynomial to determine the values that present the least residual. We divide the duration of the data by $1+z$ to subtract the z contribution of the host galaxy (see Table 1) before substituting this data. In order to modify the template to fit the displayed data, we acquired the final vector (t_0; m_0) after changing the SN data (see Table 5). Since the maximum brightness date is unknown, we set the beginning t_0 value for the fitting using the information provided by the diagnostic diagram (Figure 4). The ultimate outcome of the development of the light curve, where the data follows the template, is shown in Figure 5. The diagnostic diagram places this event around day 10 after the peak; however, the OAUNI data is situated around day ≈ -12 before the peak.

TABLE 2

OAUNI SUPERNOVAE OBSERVATION LOG

SN	Date (UTC)	Filter	N	IT (s)	X	m_1	m_2
(1)	(2)	(3)	(4)	(5)	(6)	(7)	(8)
AT 2015dd	2016/01/10.385	V	30	600	1.467	16.470 ± 0.060	16.797 ± 0.060
	2016/01/10.396	R	30	600	1.402	15.992 ± 0.033	15.933 ± 0.033
	2016/01/10.410	I	30	600	1.336	15.565 ± 0.037	15.681 ± 0.037
SN 2016cvk	2016/09/05.084	V	90	1800	1.375	15.025 ± 0.079	14.957 ± 0.052
	2016/09/05.099	R	90	1800	1.305	15.183 ± 0.076	14.911 ± 0.050
	2016/09/05.113	I	90	1800	1.250	15.247 ± 0.079	14.909 ± 0.065
AT 2016eqb	2016/08/09.405	V	45	900	1.310	15.806 ± 0.046	15.847 ± 0.046
	2016/08/09.390	R	45	900	1.243	15.806 ± 0.046	15.863 ± 0.046
SN 2017erp	2017/07/23.087	V	45	900	1.064	14.349 ± 0.014	14.424 ± 0.019
	2017/07/23.055	R	45	900	1.167	14.289 ± 0.015	14.355 ± 0.022
	2017/07/24.066	V	45	900	1.156	14.406 ± 0.011	14.442 ± 0.018
	2017/07/24.050	R	45	900	1.100	14.309 ± 0.015	14.372 ± 0.019
	2017/07/25.103	V	45	900	1.195	14.476 ± 0.011	14.502 ± 0.016
	2017/07/25.087	R	45	900	1.280	14.332 ± 0.016	14.395 ± 0.022
	2017/07/26.200	V	45	900	2.756	14.533 ± 0.013	14.544 ± 0.017
	2017/07/26.186	R	45	900	3.614	14.359 ± 0.014	14.405 ± 0.016
	2017/07/27.059	V	45	900	1.041	14.581 ± 0.018	14.611 ± 0.020
	2017/07/27.034	R	45	900	1.104	14.396 ± 0.017	14.450 ± 0.013
	2017/07/28.042	V	45	900	1.035	14.621 ± 0.014	14.656 ± 0.016
	2017/07/28.027	R	45	900	1.065	14.423 ± 0.014	14.461 ± 0.016
	2017/07/29.053	V	45	900	1.064	14.682 ± 0.012	14.706 ± 0.016
	2017/07/29.039	R	45	900	1.105	14.471 ± 0.012	14.501 ± 0.015
	2017/07/30.044	V	45	900	1.049	14.745 ± 0.011	14.759 ± 0.016
	2017/07/30.029	R	45	900	1.085	14.527 ± 0.012	14.548 ± 0.015
	2017/08/21.041	V	45	900	1.255	15.725 ± 0.014	15.695 ± 0.013
	2017/08/21.025	R	45	900	1.362	15.662 ± 0.016	15.532 ± 0.010
	2017/08/22.064	V	20	400	1.350	15.731 ± 0.026	15.733 ± 0.016
	2017/08/22.036	R	15	300	1.617	15.680 ± 0.019	15.568 ± 0.014
	2017/08/23.090	V	60	1200	1.747	15.780 ± 0.016	15.755 ± 0.018
	2017/08/23.070	R	60	1200	2.145	15.707 ± 0.026	15.601 ± 0.010
AT 2017erv	2017/06/26.354	R	45	900	3.535	15.423 ± 0.030	
	2017/06/27.085	R	45	900	3.907	15.372 ± 0.018	
AT 2017eve	2017/06/26.386	R	45	900	2.138	17.010 ± 0.032	
	2017/06/27.156	R	45	900	1.503	17.077 ± 0.033	
	2017/06/28.158	R	90	1800	1.485	17.145 ± 0.028	
SN 2023gfo	2023/05/24.228	V	45	900	1.637	15.716 ± 0.025	15.651 ± 0.048
	2023/05/24.242	R	45	900	1.866	15.149 ± 0.022	15.149 ± 0.042
	2023/05/24.212	I	45	900	1.457	14.698 ± 0.021	14.721 ± 0.042
	2023/06/20.079	R	60	1200	1.108	15.417 ± 0.025	
	2023/06/21.091	R	80	1600	1.162	15.507 ± 0.025	
	2023/07/14.022	R	70	1400	1.144	15.720 ± 0.025	
	2023/07/15.045	R	70	1400	1.275	15.616 ± 0.025	
	2023/07/16.084	R	70	1400	1.663	15.592 ± 0.023	
	2023/07/17.079	R	70	1400	1.633	15.680 ± 0.025	
	2023/07/18.105	R	70	1400	2.153	15.431 ± 0.023	
	2023/07/20.102	R	70	1400	2.231	15.604 ± 0.026	
	2023/07/21.107	R	70	1400	2.465	15.540 ± 0.024	
	2023/08/16.057	R	70	1400	3.761	16.131 ± 0.032	
	2023/08/17.039	R	90	1400	2.801	16.636 ± 0.038	
	2023/08/18.038	R	90	1400	2.903	16.706 ± 0.038	
	2023/08/19.038	R	90	1400	2.768	16.391 ± 0.034	
SN 2023ijd	2023/07/15.070	R	70	1400	2.554	15.571 ± 0.022	
	2023/07/16.054	R	70	1400	2.174	15.613 ± 0.018	
	2023/07/17.050	R	70	1400	2.135	15.557 ± 0.018	
	2023/07/18.071	R	70	1400	2.908	15.621 ± 0.022	
	2023/07/20.070	R	70	1400	3.200	15.568 ± 0.013	
	2023/07/21.079	R	70	1400	4.045	15.591 ± 0.018	
SN 2023ixf	2023/06/20.021	R	54	1080	2.499	11.285 ± 0.025	
	2023/06/21.022	R	50	1000	2.483	11.301 ± 0.023	
	2023/07/14.050	R	53	1060	2.804	11.635 ± 0.024	
	2023/07/16.025	R	50	1000	2.615	11.606 ± 0.024	
	2023/07/17.018	R	50	1000	2.585	11.600 ± 0.029	
	2023/07/18.031	R	50	1000	2.715	11.690 ± 0.023	
	2023/07/20.038	R	53	1060	2.856	11.704 ± 0.026	
	2023/07/21.052	R	50	1000	3.131	11.714 ± 0.027	

4.3. *AT 2016eqb*

Since the maximum brightness date for AT 2016eqb is known (Pan et al. 2016), we have plotted it alongside the OAUNI m_2 data (see Table 2) and the available literature data (see Table 4) using the least residual method to determine m_0 only and fit the type Ia SN Nugent's template in the V filter. Since the host galaxy's z value is known in this instance as well (see Table 1), we used all of the data points that are near the peak to calculate the value of m_0. Nugent's template in the V filter with the appropriate t_0 and m_0 adjustments, as well as the OAUNI photometry of AT 2016eqb, are displayed in Figure 6 (see Table 5).

4.4. *2017erp*

We utilized values close to the peak of the light curves (15 days before and after the maximum) in both filters (V and R) to fit the type Ia SN Nugent's

TABLE 3

UCAC4 COMPARISON STARS

UCAC4 name	V_{cat} (mag) (1)	R_{cat} (mag) (2)	I_{cat} (mag) (3)
AT 2015dd			
235-072564	11.356	10.968	10.607
235-072546	12.711	12.394	12.108
234-070894	9.800	9.879	9.879
234-070931	10.706	10.353	9.965
234-070956	12.923	12.591	12.292
SN 2016cvk			
247-183586	12.291	12.176	12.060
247-183587	15.491	15.333	15.205
247-183594	14.920	14.771	14.651
247-183606	14.646	14.477	14.352
247-183607	13.416	13.317	13.222
247-183608	14.249	14.099	13.966
248-191420	12.131	11.962	11.834
248-191421	15.182	15.036	14.954
AT 2016eqb			
444-131450	16.501	15.924	-
444-131442	15.745	15.506	-
445-136436	16.153	16.061	-
445-136441	16.506	16.386	-
445-136458	15.839	15.539	-
445-136465	16.083	15.858	-
SN 2017erp			
394-058196	14.691	14.464	-
394-058202	14.800	14.535	-
394-058177	14.867	14.717	-
393-061368	15.085	14.916	-
394-058204	15.196	14.986	-
394-058168	15.204	14.870	-
AT 2017erv			
027-009815	-	12.024	-
027-009769	-	12.309	-
027-009780	-	12.704	-
027-009785	-	12.884	-
027-009751	-	12.937	-
027-009784	-	12.985	-
027-009787	-	13.197	-
027-009792	-	13.255	-
027-009754	-	13.413	-
027-009747	-	13.431	-
027-009800	-	13.443	-
027-009768	-	13.487	-
027-009794	-	13.543	-
027-009807	-	13.547	-
027-009809	-	13.754	-
027-009755	-	13.775	-
AT 2017eve			
168-205741	-	12.147	-
168-205790	-	12.191	-
168-205740	-	12.395	-
168-205715	-	12.493	-
168-205795	-	12.778	-
168-205776	-	13.051	-
168-205727	-	13.226	-
168-205789	-	13.628	-
168-205806	-	13.716	-
169-196343	-	13.748	-
168-205754	-	13.781	-
169-196291	-	13.947	-
168-205770	-	13.952	-
168-205798	-	13.996	-
169-196333	-	14.000	-
SN 2023gfo			
412-054666	14.292	14.114	14.018
412-054667	14.279	14.121	14.030
412-054681	15.068	14.674	14.433
411-055301	15.112	14.930	14.793
411-055298	14.656	14.203	13.907
411-055299	15.053	14.781	14.604

TABLE 3. CONTINUED

UCAC4 name	V_{cat} (mag) (1)	R_{cat} (mag) (2)	I_{cat} (mag) (3)
SN 2023ijd			
506-053220	-	15.925	-
506-053224	-	15.901	-
506-054413	-	16.161	-
506-054416	-	15.760	-
506-054417	-	15.790	-
506-054418	-	16.008	-
SN 2023ixf			
723-053563	-	15.400	-
723-053565	-	14.719	-
723-053569	-	14.582	-
722-053112	-	15.410	-
722-053102	-	14.245	-
722-053103	-	15.298	-

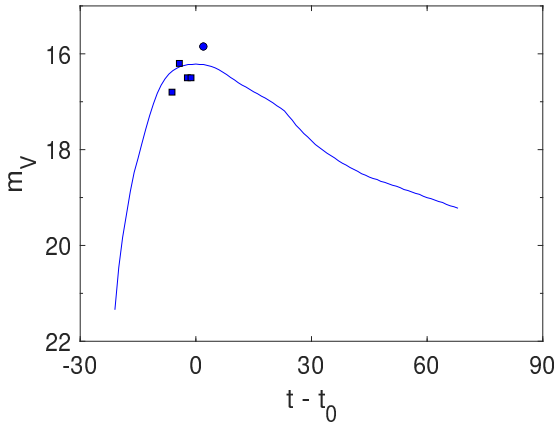

Fig. 6. AT 2016eqb light curve in the V filter. Template light curve for Type Ia SN with $z = 0$ (blue line, Nugent, Kim & Perlmutter 2002) with *ASASSN* data (blue squares, Brimacombe et al. 2016) and OAUNI m_2 data (blue dot, Table 2). Time offset is $t_0 = 2457607.5$ days. The color figure can be viewed online.

template because of the large amount of available literature data. The least residual approach was used to compute m_0, similar to the last supernova, since the date of the maximum brightness is known ($t_0 =$ 2457934.9 JD, Brown et al. 2016). We got distinct values of m_0 (see Table 5) for each filter, accounting for z from its host galaxy (see Table 1). Using the OAUNI m_2 data (see Table 2) and the available literature data for SN 2017erp (Brown et al. 2016), Figures 7 and 8 display the light curves in the V and R filters with their corresponding templates. Both charts demonstrate how well the OAUNI data match the data from UVOT, LCO, and AZT[11]. Even while the V filter's light curve up to day ≈30 follows the template's trend, as the days pass, the discrepancy becomes larger. The R filter's light curve, on the

[11]Shamakhi Astrophysical Observatory.

TABLE 4

AVAILABLE LITERATURE LIGHT CURVE DATA

SN	Date (UT)	G	V	R	Reference
SN 2016cvk	2016-08-31.09	-	16.2	-	(a)
	2016-09-10.60	-	14.69	-	(b)
	2016-10-22.42	-	16.04	-	(b)
AT 2016eqb	2016-08-01.35	-	16.8	-	(a)
	2016-08-03.27	-	16.2	-	(a)
	2016-08-05.31	-	16.5	-	(a)
	2016-08-06.18	-	16.5	-	(a)
AT 2017erv	2017-06-11.23	-	16.6	-	(c)
	2017-06-13.31	-	16.2	-	(c)
	2017-06-13.38	-	16.1	-	(c)
	2017-06-19.25	-	15.8	-	(c)
	2017-07-13.04	16.67	-	-	(d)
	2017-07-13.08	16.66	-	-	(d)
	2017-08-10.08	17.75	-	-	(d)
	2017-08-10.29	17.77	-	-	(d)
	2017-09-14.33	18.74	-	-	(d)
	2017-10-19.25	19.41	-	-	(d)
	2017-10-19.29	19.43	-	-	(d)
	2017-11-09.96	19.81	-	-	(d)
	2017-11-10.04	19.86	-	-	(d)
	2017-12-19.67	20.22	-	-	(d)
AT 2017eve	2017-06-11.18	-	16.6	-	(c)
	2017-06-13.26	-	16.9	-	(c)
	2017-06-19.14	-	16.5	-	(c)
	2017-08-01.29	18.45	-	-	(e)
	2017-08-01.54	18.41	-	-	(e)
	2017-08-01.63	18.43	-	-	(e)
	2017-08-01.88	18.47	-	-	(e)
	2017-08-01.88	18.47	-	-	(e)
	2017-08-02.13	18.48	-	-	(e)
	2017-08-02.29	18.49	-	-	(e)
	2017-08-02.38	18.47	-	-	(e)
	2017-08-02.54	18.48	-	-	(e)
	2017-08-02.63	18.48	-	-	(e)
	2017-08-02.79	18.50	-	-	(e)
	2017-08-02.88	18.51	-	-	(e)
	2017-08-03.04	18.50	-	-	(e)
	2017-08-03.13	18.50	-	-	(e)
	2017-08-03.29	18.55	-	-	(e)
	2017-08-03.63	18.54	-	-	(e)
	2017-08-03.88	18.51	-	-	(e)
	2017-08-04.13	18.53	-	-	(e)
	2017-08-05.29	18.58	-	-	(e)
	2017-08-05.38	18.63	-	-	(e)
	2017-08-05.54	18.58	-	-	(e)
	2017-08-05.63	18.58	-	-	(e)
	2017-08-05.79	18.61	-	-	(e)
	2017-08-05.88	18.60	-	-	(e)
	2017-08-06.04	18.64	-	-	(e)
	2017-08-06.29	18.62	-	-	(e)
	2017-08-06.38	18.61	-	-	(e)
	2017-08-06.54	18.58	-	-	(e)
	2017-08-06.79	18.62	-	-	(e)
	2017-09-20.54	19.88	-	-	(e)
	2017-10-25.08	20.59	-	-	(e)
SN 2023ijd	2023-07-01.21	-	-	15.649±0.031	(f)
	2023-06-29.17	-	-	15.661±0.030	(f)
	2023-06-21.21	-	-	15.701±0.034	(f)
	2023-06-14.17	-	-	15.689±0.041	(f)
	2023-06-06.29	-	-	15.667±0.026	(f)
	2023-06-04.21	-	-	15.601±0.029	(f)
	2023-06-02.21	-	-	15.606±0.031	(f)
	2023-05-17.21	-	-	15.796±0.033	(f)
	2023-05-15.29	-	-	16.121±0.039	(f)

[a] Brimacombe et al. (2016)
[b] http://ooruri.kusastro.kyoto-u.ac.jp/mailarchive/vsnet-recent-sn/6612.
[c] Nicholls, Brimacombe & Cacella (2017)
[d] http://gsaweb.ast.cam.ac.uk/alerts/alert/Gaia17bto/.
[e] http://gsaweb.ast.cam.ac.uk/alerts/alert/Gaia17byi/.
[f] https://lasair-ztf.lsst.ac.uk/objects/ZTF23aajrmfh/.

other hand, traces the trend both before and after the maximum brightness.

4.5. *AT 2017erv*

The AT 2017erv light curve in V and R filters, together with the type Ia SN Nugent's templates, is displayed in Figure 9 using OAUNI m_1 data (see Table 2) and the available literature data (see Table 4). In order to fit template in filter R, we used the host galaxy redshift information (see Table 1) and the date of the maximum brightness (Uddin et al. 2017). Since OAUNI data are in the R filter, the template for this filter was used as a reference to plot the template in the V filter. This is a feature of Nugent's template, as each template was created using a correlation filter-to-filter. To do this, we found m_0 with the least residual by substituting OAUNI m_1 data in the polynomial fit for the template in filter R (see Table 5). Next, we used Nugent's SN Ia template light curve to compare the OAUNI findings in the R filter (Table 2) with the values found by $GAIA$ and $ASASSN$ for the V and G filters, since this SN was categorized as a Type Ia (Uddin et al. 2017). The outcome of fitting Nugent's template to OAUNI R filter data is displayed in Figure 9. Furthermore, we can see that, in contrast to the template in the V fil-

TABLE 5

OAUNI SUPERNOVAE PARAMETERS

SN	Filter	Peak date (JD)	m_0 (mag)	Residual (mag) (x10^{-4})
AT 2015dd	-	2457374.5	-	-
SN 2016cvk	R	2457648.5	14.7197	1.0569
AT 2016eqb	V	2457607.5	16.2130	2.1325
SN 2017erp	R	2457934.9	13.5922	3.0811
	V	2457934.9	13.4813	2.6995
AT 2017erv	R	2457926.5	15.2615	2.8972
AT 2017eve	R	2457922.5	16.6213	3.5673
SN 2023gfo	R	2460049.7	15.1622*	2.8806
SN 2023ijd	R	2460088.9	15.6157*	2.7022
SN 2023ixf	R	2460094.0	-	-

*SN 2004et was used as a template

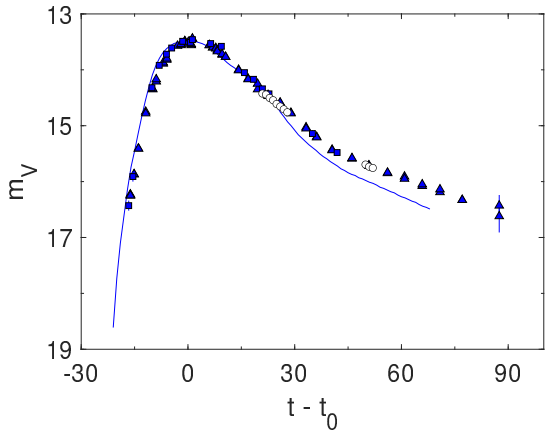

Fig. 7. SN 2017erp light curve in the V filter. Template light curve for Type Ia SN with $z = 0$ (blue line, Nugent, Kim & Perlmutter 2002) with UVOT data (blue squares, Brown et al. 2016), LCO data (blue triangles, Brown et al. 2016) and OAUNI m_2 data (white dots, Table 2). Time offset is $t_0 = 2457934.9$ days. The color figure can be viewed online.

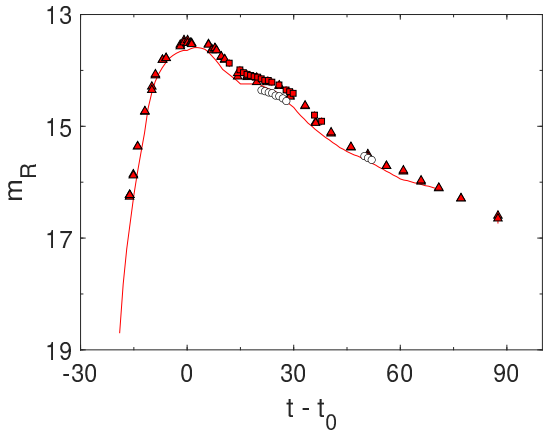

Fig. 8. SN 2017erp light curve in R filter. Template light curve for Type Ia SN with $z = 0$ (red line, Nugent, Kim & Perlmutter 2002) with AZT data (red squares, Brown et al. 2016), LCO data (red triangles, Brown et al. 2016) and OAUNI m_2 data (white dots, Table 2). Time offset is $t_0 = 2457934.9$ days. The color figure can be viewed online.

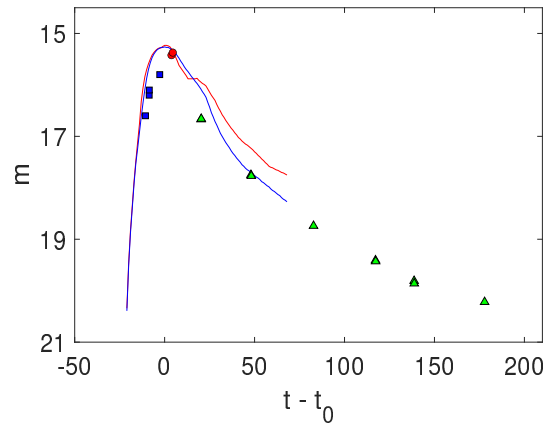

Fig. 9. AT 2017erv light curve. Template light curve for Type Ia SN in V (blue line) and R (red line) filters with $z = 0$ (Nugent, Kim & Perlmutter 2002), with $ASASSN$ data (V filter, blue squares, Nicholls, Brimacombe & Cacella 2017), GAIA data (G filter, green triangles, `http://gsaweb.ast.cam.ac.uk/alerts/alert/Gaia17bto/`) and OAUNI data (R filter, red dots, Table 2). Time offset is $t_0 = 2457926.5$ days. The color figure can be viewed online.

ter, the $ASASSN$ data exhibit a continuous rise in brightness before the peak, whereas the $GAIA$ data have a faster fall rate.

4.6. *AT 2017eve*

We have used Nugent's templates in the R and V filters, like for the previous SN. We employed OAUNI

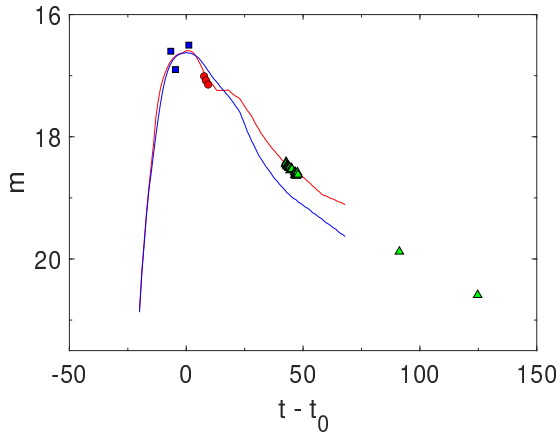

Fig. 10. AT 2017eve light curve. Template light curve for Type Ia SN in V (blue line) and R (red line) filters with $z = 0$ (Nugent, Kim & Perlmutter 2002), with $ASASSN$ data (V filter, blue squares, Nicholls, Brimacombe & Cacella 2017), GAIA data (G filter, green triangles, `http://gsaweb.ast.cam.ac.uk/alerts/alert/Gaia17byi/`) and OAUNI data (R filter, red dots, Table 2). Time offset is $t_0 = 2457922.5$ days. The color figure can be viewed online.

m_1 data (see Table 2) in the least residual technique to obtain the value m_0 solely (see Table 5), taking into account its categorization as a Type Ia SN, the date of the peak, and the host galaxy z (see Table 1). This fitting enables us to see the $ASASSN$ data dispersion around the maximum brightness date in Figure 10. However, $GAIA$ data show a behavior different from the preceding SN, with a smaller fall rate than the template.

4.7. *SN 2023gfo*

The V-R and R-I colors for the single OAUNI multicolor photometry data (see to Table 2) of SN 2023gfo have been computed and are shown in Figure 11. Although its location on the diagnostic diagram is not precise enough to determine the observational period, it indicates that this SN may have occurred between days 34 and 42 following the maximum brightness. The telegram of its discovery (Moore et al. 2023), which highlights the fact that the ATLAS system found no evidence of this event three days earlier in the same area, despite the SN being discovered on May 19, supports this view. The type IIp SN 2004et data (Sahu 2006) and the OAUNI m_1 data (see Table 2) of four consecutive months in filter R are plotted together in Figure 12. Since SN 2004et's data have already been adjusted for its peak brightness time, it can be used as a kind of template. Thus, in order to obtain the offset vec-

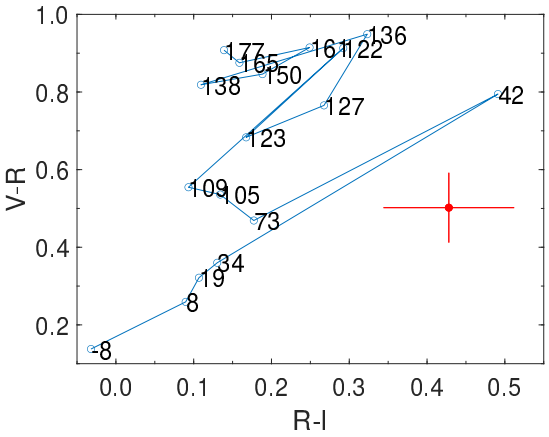

Fig. 11. $V - R$ vs. $R - I$ color diagram of a Type IIp SN with $z = 0$ (blue lines, adapted from Poznanski et al. 2002). Numbers indicate days after maximum light. OAUNI colors for SN 2023gfo using m_2 calibration are also indicated (red point). The color figure can be viewed online.

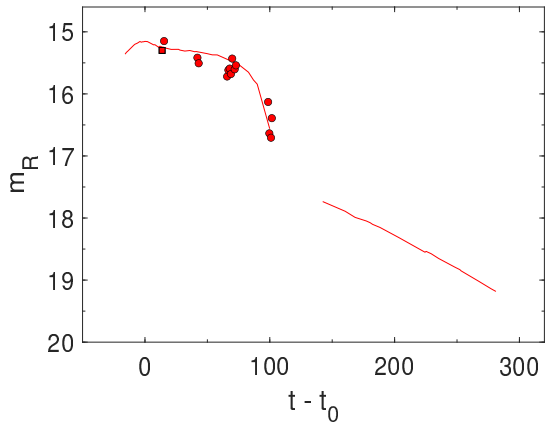

Fig. 12. SN 2023gfo light curve in the R filter. SN 2004et Type IIp light curve with $z = 0.0002$ (red squares, Sahu 2006), with OAUNI data (red dots, Table 2). Time offsets is $t_0 = 2460049.7$. The color figure can be viewed online.

tor $(t_0; m_0)$, we fitted the SN 2004et light curve to a polynomial. Next, we obtained its equivalent vector (see Table 5) from the least residual approach after substituting the OAUNI m_1 data in the SN 2004et polynomial fitting. During the initial three months, OAUNI detected a 0.6 mag decline in magnitude while SN 2004et remained within the same range. In the last month, data could set SN 2023gfo at the end of the plateau phase. The OAUNI data indicate a higher fall rate compared to prior months, which is consistent with SN 2004et. Because the

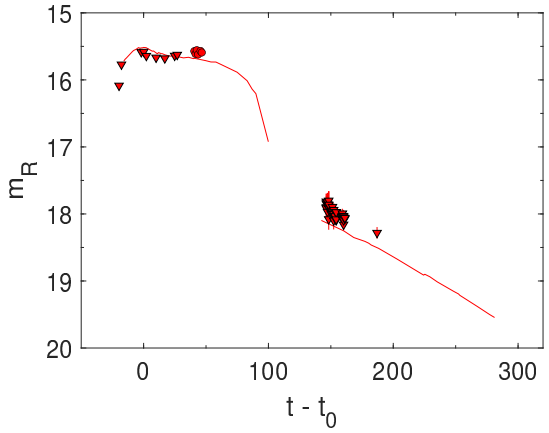

Fig. 13. SN 2023ijd light curve in the R filter. SN 2004et Type IIp light curve with $z = 0.0002$ (red squares, Sahu 2006), with ZTF data (red triangles, `https://lasair-ztf.lsst.ac.uk/objects/ZTF23aajrmfh/`), and OAUNI data (red dots, Table 2). Time offsets is $t_0 = 2460088.9$ days. The color figure can be viewed online.

first night of observation was on day 39 using the approach of least residual, this result supports the information provided by the diagnostic diagram.

4.8. *SN 2023ijd*

We used OAUNI m_1 data (see Table 2) and ZTF (The Zwicky Transient Facility, Bellm et al. 2016) data[12] to plot the light curve of SN 2023ijd in Figure 13. We show OAUNI and ZTF data with the SN 2004et light curve in filter R with $z = 0.0002$ (type IIp), just as for the previous SN with a similar type. We plot the SN 2004et light curve against the SN 2023ijd data following the same procedures as in the prior case. In this instance, we used ZTF data close to the peak to estimate the vector $(t_0; m_0)$ with the least residual because the date of the maximum brightness is unknown (see Table 5). The data show a steady phase of decrease with a magnitude variation of $\pm$ 0.1 mag from +10 to +60 days following the peak. This light curve phase may represent the plateau onset phase of SN 2004et.

4.9. *SN 2023ixf*

The last SN studied was the nearest and brilliant SN2023ixf. This fact is reflected in the wide available literature data up to +225 days from AAVSO[13]. As usual, we corrected the temporal values using z

[12] `https://lasair-ztf.lsst.ac.uk/objects/ZTF23aajrmfh/`.

[13] The American Association of Variable Star Observers (AAVSO).

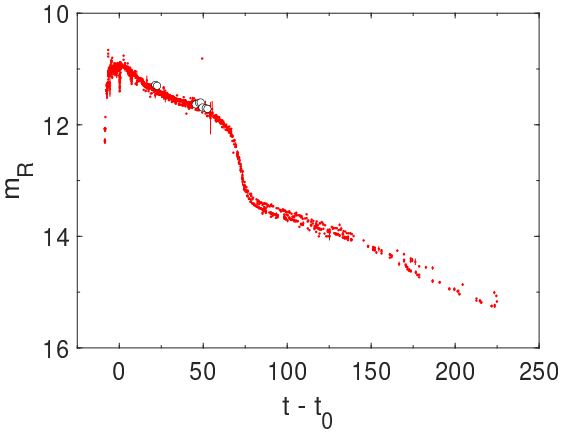

Fig. 14. SN 2023ixf light curve in R filter. AAVSO data (red points, `www.aavso.org`) and OAUNI data (white dots, Table 2). Time offset t_0 = 2460094.0. The color figure can be viewed online.

of its host galaxy (see Table 1), and we interpolated the peak date t_0 = 2460094.0 JD. This fact is supported by Filippenko, Zheng & Yang (2003), where they set t_0 = 2460094.2 JD. The OAUNI m_1 data (see Table 2) for the eight nights of observation of SN 2023ixf match the trend of the light curve between days +0 and +50, as can be observed in Figure 14. Following these days, the brightness shows an increase in slope, declining in 20 days from 12 mag to 13.5 mag. At last, the SN resumes its gradual decline phase.

5. CONCLUSIONS

Using the equipment available at OAUNI, the reduction of images from different SNe was accomplished effectively. These nine SNe were observed in the V, R, and I filters over a total of 43 nights, confirming the good quality of the images. This was made possible by the fact that on several observation nights, we were able to maintain an uncertainty of less than 0.09 mag despite the presence of high air masses.

Data calibration for m_1 and m_2 method was carefully examined for each filter. As a result, the agreement between both methods has an average precision of 0.096 ± 0.064. Diagnostic diagrams were used to evaluate the position of three supernovae after the maximum brightness date. The position of the supernovae found on this diagram was corroborated by different sources that recorded the date on which these events reached their peak magnitude. Through the construction of light curves using several templates and a comparison of literature and OAUNI data, we were able to study the brightness behavior of each SN. The fitting of these templates (for SNe Types Ia and IIn) and SN2004et light curve (for Type IIp) was carried out carefully using the available data close to the peak and seeking to ensure that the residual was as small as possible (> 0.001). The viability of conducting precise astronomical photometric programs at the OAUNI site is validated by this work.

The authors are grateful for economic support from Concytec (Contrato N^o PE501081907-2022-PROCIENCIA, Contrato 133-2020 Fondecyt). Special thanks to the Huancayo Observatory staff for the logistic support and to J, Tello, M. Zevallos, J. Ricra, R. Santacruz, D. Alvarado and E. Torre for their collaboration with the observations.

REFERENCES

Bellm, E. C., Kulkarni, Sh. R., Graham, M. J., et al. 2019, PASP, 131, 018002, `https://doi.org/10.1088/1538-3873/aaecbe`

Bersier, D., Smartt, S., & Yaron, O. 2016, NSCR, 650, 1

Bianciardi, G., Ciccarelli, A. M., Conzo, G., et al. 2023, TNSAN, 213, 1, `https://doi.org/10.48550/arXiv.2307.05612`

Brimacombe, J., Brown, J. S., Stanek, K. Z., et al. 2016, ATeL, 9439

Brimacombe, J., Post, R. S., Kiyota, S., et al. 2016, ATeL, 9332

Brown, J. S., Prieto, J. L., Shappee, B. J., et al. 2016, ATeL, 9445

Brown, P. J., Hosseinzadeh, G., Jha, S. W., et al. 2019, AJ, 877, 152, `https://doi.org/10.3847/1538-4357/ab1a3f`

Carlos Reyes, R., Ferrero, G., Navarro, F. A. R., & Meléndez, J. 2013, RMxAA, 49, 357

Filippenko, A. V., Zheng, W., & Yang, Y. 2003, TNSAN, 123

Foley, R. J., Hounsell, R., & Miller, J. A. et al. 2015, ATeL, 8434

Fulton, M., Nicholl, M., Smith, K. W. et al. 2023a, TNSAN, 124

Fulton, M., Srivastav, S., Nicholl, M., et al. 2023b, TNSCR, 871

Gress, O., Lipunov, V., Gorbovskoy, E., et al. 2015, ATeL, 8415

Itagaki, K. 2017, TNSTR, 647

_____. 2023, TNSTR, 1158

Jha, S. W., Camacho, Y., Dettman, K., et al. 2017, Anel, 10490

Krisciunas, K., Contreras, C., Burns, C. R., et al. 2017, AJ, 154, 211, `https://doi.org/10.3847/1538-3881/aa8df0`

Moore, T., Smith, K. W., Srivastav, S., et al. 2023, TNSAN, 92

Nicholls, B., Brimacombe, J., & Cacella, P., 2017, ATeL, 10509

Nugent, P., Kim, A., & Perlmutter, S. 2002, PASP, 114, 803, https://doi.org/10.1086/341707

Pan, Y. -C., Kilpatrick, C. D., Siebert, M. R., et al. 2016, Anel, 9333

Parker, S. 2016, TNSTR, 422

Pereyra, A., Tello, J., Meza, E., et al. 2015, arXiv151203104, https://doi.org/10.48550/arXiv.1512.03104

Perley, D. 2023, TNSCR, 1112

Perley, D. & Gal-Yam, A. 2023, TNSCR, 1164

Phillips, M. M. 1993, ApJ, 413, 105, https://doi.org/10.1086/186970

Phillips, M. M., Lira, P., Suntzeff, N. B., et al. 1999, AJ, 118, 1766, https://doi.org/10.1086/301032

Poznanski, D., Gal-Yam, A., Maoz, D., et al. 2002, PASP, 114, 833, https://doi.org/10.1086/341741

Sahu, D. K., Anupama, G. C., Srividya, S., et al. 2006, MNRAS, 372, 1315, https://doi.org/10.1111/j.1365-2966.2006.10937.x

Smith, K. W., Williams, R. D., Young, D. R., et al. 2019, RNAAS, 3, 26, https://doi.org/10.3847/2515-5172/ab020f

Stanek, K. Z. 2023, TNSTR, 1092

Theureau, G., Coudreau, N., Hallet, N., et al. 2005, A&A, 430, 373, https://doi.org/0.1051/0004-6361:20047152

Uddin, S., Mould, J., Zhang, J. -J., et al. 2017, ATeL, 10517

Zacharias, N., Finch, C. T., Girard, T. M., et al. 2013, AJ, 145, 44, https://doi.org/10.1088/0004-6256/145/2/44

M. Espinoza and A. Pereyra: National University of Engineering, Lima, Perú.
A. Pereyra: Geophysical Institute of Perú, Astronomy Area, Lima, Perú.

Revista Mexicana de Astronomía y Astrofísica, **60**, 305–316 (2024)

https://doi.org/10.22201/ia.01851101p.2024.60.02.08

RELATIONSHIP BETWEEN PHOTOMETRIC PERIOD AND SURFACE DIFFERENTIAL ROTATION IN CHROMOSPHERICALLY ACTIVE STARS

O. Özdarcan[1], H. A. Dal[1], E. Sipahi Kılıç[1], and E. Yoldaş[1]

Received April 18 2024; accepted June 5 2024

ABSTRACT

We present a quantitative investigation of the relationship between the photometric periods of late-type chromospherically active stars showing spot activity and their photometric period variation interval as the proxy of the surface differential rotation. The results show that as the photometric period increases, the magnitude of the surface differential rotation also increases. However, there is a noticeable distinction between main sequence and evolved stars. Comparing a main sequence star and an evolved star with the same photometric period, it turns out that the magnitude of the surface differential rotation of the main sequence star appears greater than that of the evolved star. The distinction is apparent around short photometric periods but tends to disappear towards longer photometric periods.

RESUMEN

Presentamos una investigación cuantitativa de la relación entre los períodos fotométricos de estrellas tardías con actividad cromosférica y manchas y el intervalo de variación del período fotométrico, como indicador de la rotación diferencial superficial. Los resultados muestran que al aumentar el período fotométrico aumenta también la magnitud de la rotación diferencial superficial. Sin embargo, hay una diferencia notable entre estrellas de la secuencia principal y estrellas evolucionadas. Al comparar ambas, encontramos que la magnitud de la rotación diferencial superficial es mayor en las estrellas de la secuencia principal que en las evolucionadas, para períodos fotométricos iguales. Esta diferencia es notable para los períodos fotométricos cortos pero tiende a desaparecer hacia períodos mayores.

Key Words: stars: activity — stars: late-type — stars: rotation

1. INTRODUCTION

The most comprehensive and long-term study to investigate chromospheric activity in stars is the Mount Wilson HK project, which started in 1966 and continued for almost 40 years until 2003 (Wilson 1978; Vaughan et al. 1978; Duncan et al. 1991; Baliunas et al. 1995). The HK project aimed to examine the chromospheric activity and its change in stars by measuring the resonance doublet of singly ionized calcium (Ca II H& K), which is a good indicator of chromospheric activity. From the long-term Ca II H& K measurements, it was found that 60% of the observed stars exhibited periodic and cyclical changes similar to the solar activity cycle (Baliunas et al. 1998). Donahue et al. (1996) applied period analysis to the 12-year HK measurements of 37 main sequence stars observed within the scope of the HK project and determined the largest (P_{max}) and the smallest (P_{min}) values of the observed photometric periods of each star. They also calculated the $\Delta P = P_{max} - P_{min}$ values and the average photometric period of each star determined over 12 years and adopted this value as the average rotation period ($\overline{P}$) of the relevant star. When they plotted the calculated ΔP and $\overline{P}$ against each other on a logarithmic scale, they found a linear relationship showing that as the $\overline{P}$ increased, the ΔP also increased. A similar study was conducted by Messina & Guinan (2003), who analysed the long-term photometry of 14 main sequence stars, and they found the linear relationship between ΔP and the $\overline{P}$. The advent of unprecedented $KEPLER$ photometry enabled scientists to focus on the relationship between ΔP and $\overline{P}$ over a very large sample. Based on the ex-

[1]Department of Astronomy and Space Sciences, Faculty of Science, Ege University, 35100, İzmir, Turkey.

tremely precise *KEPLER* data, Reinhold & Gizon (2015) analysed four years of continuous photometry of 12 319 stars and confirmed the linear relationship between the aforementioned quantities. The only restriction of their study is that the observations span over only four years. In chromospherically active stars, cool surface spots may emerge from different latitudes at different times; therefore, long-term continuous photometric observations become crucial to increase the detection chance of surface spots emerging from a wider latitude range. Taking this into consideration, Özdarcan (2021) conducted a comprehensive spectroscopic and photometric review of 21 chromospherically active stars. They adopted $\Delta P/P_{min}$ as a measure of the surface differential rotation (SDR), instead of ΔP. They established a quantitative linear relationship between $\Delta P/P_{min}$ and P_{min}. They implicitly assumed that the target stars possess solar-type differential rotation and hence P_{min} practically corresponds to the equatorial rotation period. Moreover, they noticed a suspicious separation between main sequence stars and giant stars. According to this separation, it was concluded that the photometric period of giant stars is closely related to the SDR, but in main sequence stars, this relationship is slightly weaker than what is observed in giants. Kővári et al. (2017) showed that binarity may play a critical role in the observed strength of SDR and hence might be responsible for the observed photometric period – relative shear distribution.

Rechecking the results given in Özdarcan (2021) with a larger sample group will provide information about the reliability of the separation and enable the relationship between the rotation period and the SDR to be determined more reliably over a broader range of photometric periods. For this purpose, thirty-five stars that were determined to show chromospheric activity and have never been studied before, were selected. In the next section, we describe new observations and collected data of the target stars. In the third section, we estimate the astrophysical properties of the target stars from new UBV observations and determine seasonal photometric periods from long-term photometry to estimate the magnitude of the surface differential rotation. In the final section, we summarize our findings and give a comparison with theoretical predictions.

2. DATA

2.1. *Observations*

We carry out Johnson UBV observations of the target stars with a 0.35m Schmidt-Cassegrain telescope equipped with Optec SSP-5 photometer located at Ege University Observatory Application and Research Center (EUOARC). The photometer includes an R6358 photomultiplier tube, which is sensitive to the longer wavelengths at the optical part of the electromagnetic spectrum. We use a circular diaphragm with an angular size of $53''$ and we adopt ten seconds of integration time for all observations. A typical observing sequence for a selected target is like sky-sky-VAR-VAR-VAR-VAR-sky-sky, where sky and VAR denote measurements from the sky and the variable star, respectively. We list the target stars in Table 1.

We follow the procedure described in Hardie (1964) to obtain reduced instrumental magnitudes. Moreover, we observe a set of standard stars selected from Landolt (2009) and Landolt (2013) along with each target. Hence, we transform all reduced instrumental magnitudes of the target stars into the standard system. Since RA coordinates of the target stars are distributed homogeneously around the celestial equator, we carried out standard star observations on two nights with an almost six-month time difference. These are 27th December 2022 and 13th July 2023 nights. We give computed transformation coefficients in the Appendix section.

Preliminary analysis of the EUOARC observations shows that signal-to-noise ratios of TYC 5275-00646-1, V1330 Sco, TYC 5610-00066-1, TYC 5050-00802-1, TYC 01572-00794-1 and GSC 00140-01925 are not sufficient for reliable colour and magnitude measurements. Increasing the integration time or gain, or using another EUOARC telescope (0.4m Schmidt-Cassegrain with a CCD camera and standard Johnson–Bessell filters) does not change the situation. Therefore, we take $B-V$ colours and V magnitudes of these stars from The AAVSO Photometric All-Sky Survey for analysis (APASS; Henden et al. 2015). We tabulate standard colours and magnitudes of the target systems in Table 2.

2.2. *Long-Term Photometry*

Besides EUOARC observations, we collect long-term V photometry of target stars from The All Sky Automated Survey (ASAS, Pojmanski 1997, 2002; Pojmanski et al. 2005) and All-Sky Automated Survey for Supernovae Sky Patrol (ASAS-SN, Shappee et al. 2014; Kochanek et al. 2017). The time range of the collected data usually spans over 15 or 18 years, depending on the beginning and the end of the observations. However, there is a significant time gap (3 or 4 years) between ASAS and ASAS-SN data, where no observation is available. This prevents us from precise tracing of the long-term photometric behaviour of our target systems. These time gaps are

TABLE 1

LIST OF TARGET STARS

Target Star	GCVS Identifier	RA (2000) (h m s)	Dec (2000) (° ′ ″)	V (mag)	$B-V$ (mag)	Ref.
TYC 05275-00646-1	IM Cet	01 01 45.3	−12 08 02.4	9.67	1.042	3
TYC 04688-02015-1	IR Cet	01 46 51.7	−05 47 15.1	11.29	1.37	7
TYC 05282-02210-1	IZ Cet	02 19 47.3	−10 25 40.6	10.72	1.076	2
TYC 00648-01252-1	HW Cet	03 12 34.2	+09 44 57.1	10.39	1.089	1
TYC 04723-00878-1	LN Eri	03 48 36.2	−05 20 30.4	11.713	0.971	5
TYC 04734-00020-1	OP Eri	04 36 12.5	−01 50 24.9	10.17	0.961	7
TYC 00083-00788-1	V1330 Tau	04 42 18.5	+01 17 39.8	11.88	1.042	1
V1339 Tau	V1339 Tau	04 48 57.9	+19 14 56.1	11.8	1.141	1
TYC 01281-01672-1	V1841 Ori	05 00 49.2	+15 27 00.6	10.83	1.218	1
TYC 00099-00166-1	V1854 Ori	05 13 19.0	+01 34 47.0	10.28	0.907	1
TYC 04767-00071-1	V2814 Ori	05 39 45.6	−00 55 51.0	11.33	1.212	7
GSC 00140-01925	V2826 Ori	06 15 18.6	+03 47 01.0	11.64	1.483	7
TYC 04806-03158-1	V969 Mon	06 36 56.3	−05 21 03.6	11.71	0.66	2
TYC 01358-01303-1	V424 Gem	07 16 50.4	+21 45 00.1	10	1.074	1
TYC 01942-00318-1	KU Cnc	08 35 26.8	+24 15 39.4	11.48	1.201	1
TYC 00840-00219-1	EQ Leo	10 13 23.8	+12 08 45.7	9.345	1.091	1
TYC 00845-00981-1	IN Leo	10 39 59.0	+13 27 22.0	10.326	0.901	1
TYC 00856-01223-1	OS Leo	11 33 36.9	+07 51 28.9	11.369	1.344	6
TYC 00865-01164-1	V358 Vir	11 56 51.6	+08 27 21.3	11.37	1.347	1
TYC 00881-00657-1	PW Com	12 35 57.4	+13 29 25.2	10.27	1.044	2
TYC 05003-00309-1	V436 Ser	15 23 46.1	−00 44 24.7	11.13	1.214	1
TYC 05003-00138-1	V561 Ser	15 26 52.7	−00 53 11.7	11.39	1.201	7
TYC 05610-00066-1	V354 Lib	15 54 44.9	−07 52 04.5	11.34	1.229	1
V1330 Sco	V1330 Sco	16 23 07.8	−23 00 59.9	11.85	1.263	1
TYC 05050-00802-1	V2700 Oph	16 51 22.1	−00 50 01.2	11.7	1.007	5
TYC 00990-02029-1	V1404 Her	17 16 29.7	+13 23 14.5	11.41	0.758	7
GSC 00978-01306	V2723 Oph	17 17 11.4	+08 15 24.6	12	1	4
TYC 01572-00794-1	V1445 Her	18 16 52.7	+17 57 03.1	11.22	0.726	7
TYC 01062-01972-1	V1848 Aql	19 54 03.1	+10 41 45.4	10.16	0.965	6
TYC 05165-00365-1	V1890 Aql	20 11 39.5	−02 35 25.7	11.15	0.975	7
TYC 05183-00044-1	V365 Aqr	20 54 09.2	−02 45 33.7	10.74	0.964	7
GSC 00563-00384	V641 Peg	22 28 36.1	+03 05 25.6	11.89	1.165	7
TYC 02221-00759-1	V543 Peg	22 47 22.7	+23 13 16.6	11.48	1.197	7
TYC 01712-00736-1	V580 Peg	23 12 29.0	+17 09 21.7	11.107	1.467	1
TYC 00583-00566-1	KZ Psc	23 16 45.0	+06 18 57.4	10.77	1.027	7

References are 1: Berdnikov & Pastukhova (2008), 2: Bernhard & Otero (2011), 3: Bernhard et al. (2009), 4: Bernhard & Lloyd (2008b), 5: Bernhard & Lloyd (2008a), 6: Bernhard et al. (2010), 7: Schirmer et al. (2009). V and $B-V$ magnitudes are from Tycho catalogue (Høg et al. 2000).

filled with unpublished observations obtained in the scope of the extension of the ASAS project (ASAS3-N and ASAS4; Pojmanski, 2022; priv. comm.). Therefore, we are able to collect photometric data of the target stars without a significant time gap. We plot the collected data of each target in Figure 1.

3. ANALYSIS

3.1. *Photometric Properties*

In the first step of our analysis, we plot measured standard $U-B$ and $B-V$ colours of the target systems in a colour – colour diagram (Figure 2). More than half of the target stars appear systematically shifted from the predicted positions of the unreddened main sequence stars. This could be interpreted as the effect of interstellar reddening, which means a kind of systematic interstellar reddening is valid for most of our target stars. However, these stars are located at different positions in the celestial sphere. If one applied a reddening correction suggested by Figure 2, then many of the target stars would become early-type stars. This is contradictory to the reported properties of our tar-

TABLE 2

JOHNSON UBV STANDARD MAGNITUDES AND COLOURS OF THE TARGET SYSTEMS

Star	V (mag)	σ_V (mag)	$B-V$ (mag)	σ_{B-V} (mag)	$U-B$ (mag)	σ_{U-B} (mag)	$E(B-V)$ (mag)	$(B-V)_0$ (mag)
IM Cet *	10.38	0.05	1.10	0.10	—	—	0.0275	1.16
IR Cet	11.39	0.06	1.09	0.09	0.54	0.29	0.0228	1.16
IZ Cet	10.25	0.06	1.01	0.06	0.77	0.19	0.0242	1.08
HW Cet	10.77	0.05	0.99	0.02	0.81	0.15	0.3132	0.77
LN Eri	11.79	0.05	1.02	0.05	−0.06	0.13	0.0787	1.03
OP Eri	10.13	0.06	1.05	0.04	0.58	0.14	0.0422	1.10
V1330 Tau	11.71	0.06	1.16	0.13	0.51	0.20	0.1144	1.14
V1339 Tau	11.99	0.07	1.02	0.07	1.11	0.30	0.4134	0.70
V1841 Ori	11.06	0.06	1.24	0.04	1.19	0.45	0.3542	0.98
V1854 Ori	10.37	0.05	0.92	0.04	0.27	0.16	0.1111	0.90
V2814 Ori	11.19	0.08	1.52	0.07	1.81	0.17	0.3338	1.28
V2826 Ori *	11.64	0.05	1.48	0.08	—	—	0.6493	0.92
V969 Mon	11.53	0.08	1.37	0.09	1.03	0.39	0.3963	1.06
V424 Gem	10.38	0.06	1.19	0.02	1.08	0.18	0.0559	1.22
KU Cnc	11.59	0.11	1.38	0.11	1.96	0.38	0.0276	1.44
EQ Leo	9.56	0.06	1.19	0.03	0.79	0.17	0.0326	1.25
IN Leo	10.55	0.06	1.01	0.07	0.41	0.17	0.0339	1.07
OS Leo	11.71	0.06	0.98	0.06	0.00	0.19	0.0380	1.03
V358 Vir	11.58	0.06	1.00	0.04	0.73	0.35	0.0165	1.07
PW Com	10.55	0.05	0.79	0.06	0.09	0.17	0.0308	0.85
V436 Ser	11.32	0.15	1.12	0.19	0.53	0.61	0.0485	1.16
V561 Ser	11.35	0.16	1.17	0.19	0.57	0.48	0.0557	1.20
V354 Lib *	11.38	0.06	1.16	0.10	—	—	0.1607	1.09
V1330 Sco *	11.85	0.04	1.26	0.07	—	—	1.8802	1.35
V2700 Oph *	11.72	0.17	1.28	0.22	—	—	0.1014	1.27
V1404 Her	11.78	0.20	0.91	0.25	0.64	0.31	0.1403	0.86
V2723 Oph	12.24	0.20	1.10	0.28	0.32	0.29	0.1047	1.09
V1445 Her *	11.18	0.12	0.98	0.15	—	—	0.1865	0.88
V1848 Aql	10.07	0.10	0.97	0.08	0.35	0.24	0.2900	0.77
V1890 Aql	11.17	0.12	1.26	0.18	0.08	0.27	0.1631	1.19
V365 Aqr	10.91	0.23	0.82	0.26	0.83	0.34	0.0783	0.83
V641 Peg	11.69	0.08	1.07	0.14	−0.15	0.23	0.0824	1.08
V543 Peg	11.38	0.07	0.88	0.14	0.67	0.36	0.0847	0.89
V580 Peg	11.05	0.08	1.27	0.12	0.91	0.25	0.1112	1.25
KZ Psc	10.59	0.09	1.17	0.14	0.48	0.23	0.0773	1.18

Note: V and $B-V$ measurements of the target stars (marked by * sign) are from Henden et al. (2015). These targets do not have reliable U measurement. In the last two columns, we list the estimated interstellar reddening values and corrected $B-V$ colour indexes. See text for the details.

get stars, such as detected X-ray emission, photometric colours and light curve properties (see references mentioned in Table 1). In this case, interstellar reddening cannot be a satisfactory explanation for the disagreement between observed and predicted colours seen in Figure 2. An alternative explanation is colour excess due to the chromospheric activity of the target stars. Since their chromospheric activity was confirmed by their properties in the references mentioned above, we may expect average colour excesses of $0\overset{\mathrm{m}}{.}09$ and $0\overset{\mathrm{m}}{.}35$ for $B-V$ and $U-B$ colours, respectively (Amado 2003). Due to these colour excesses, the observed $U-B$ and $B-V$ colours become bluer than their predicted values from standard stellar atmosphere models. An observational test of the suggested colour excess was done for the observed colours of HD 208472, an RS CVn variable, and corrected colours indicated an effective temperature, which was in agreement with spectroscopically estimated one (Özdarcan et al. 2010). To calculate reliable astrophysical parameters of the target stars, we aim to remove the effects of both interstellar reddening and activity-originated colour excess from the observed $B-V$ colours. Regarding interstellar red-

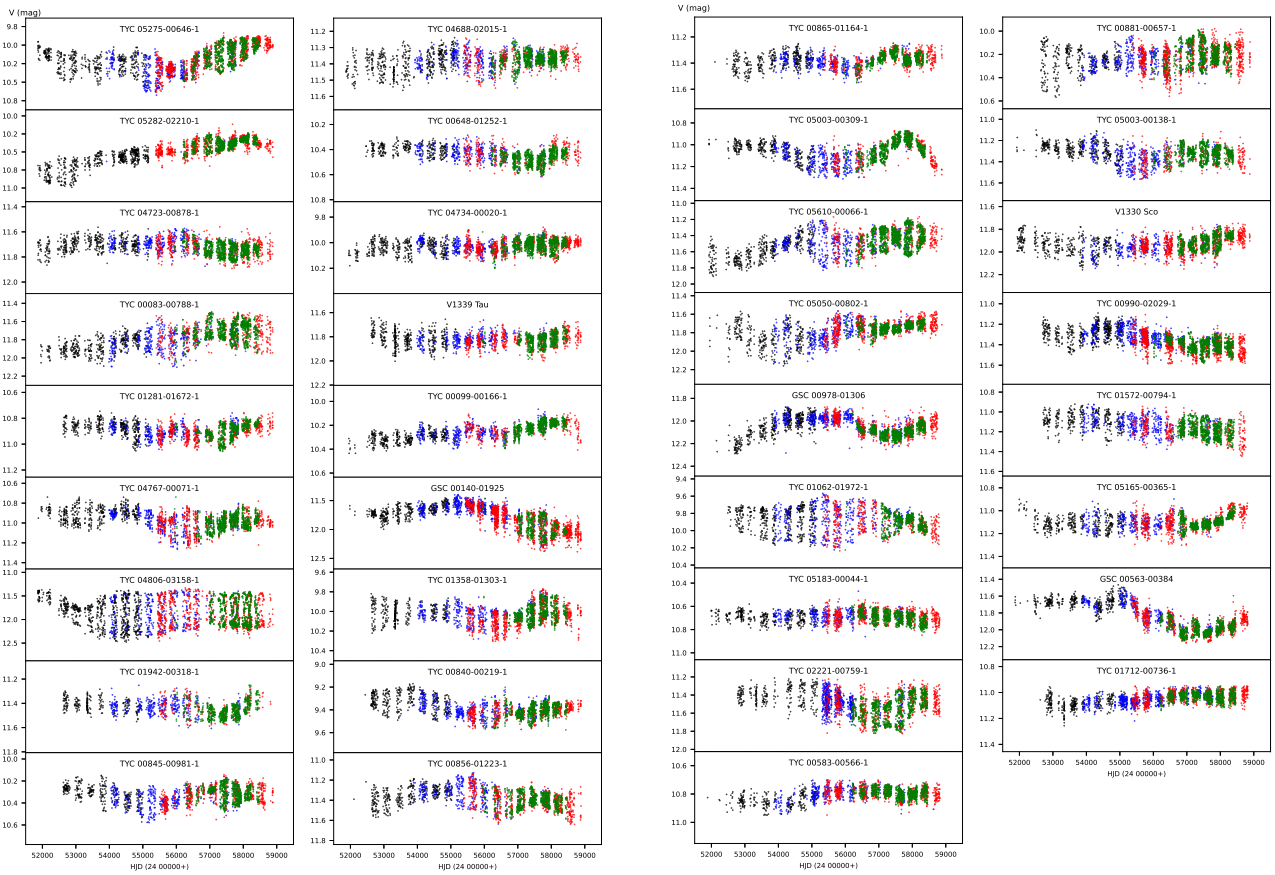

Fig. 1. Compiled ASAS3 (black), ASAS3-N (blue), ASAS4 (red) and and ASAS-SN (green) photometry of target stars. The colour figure can be viewed online.

dening, we adopt the estimated mean $E(B-V)$ colour excess (Schlafly & Finkbeiner 2011) for the precise equatorial coordinates of each target. Then, we subtract the estimated $E(B-V)$ excess from the observed $B-V$ colour (fourth column in Table 2). For correction of activity-originated average blue excess in $B-V$ colour, we add $0\overset{\mathrm{m}}{.}09$ to each reddening corrected $B-V$ colour and obtain the final $B-V$ colour index of each target. We list the estimated $E(B-V)$ values and corrected $B-V_0$ colour index of each target in the last two columns of the Table 2. Here, we note that we find unreasonably large reddening for V1330 Sco ($E(B-V) \approx 1\overset{\mathrm{m}}{.}88$) from Schlafly & Finkbeiner (2011). Using this correction, we find a hot (≈ 25000 K) main sequence star. This finding is not consistent with the previously reported properties of the star (see reference given in Table 1). Therefore, we omit the effect of interstellar reddening for this star and only apply the activity-related $0\overset{\mathrm{m}}{.}09$ colour excess correction to the observed $B-V$ colour index.

3.2. *Astrophysical Properties*

By using the corrected $B-V$ colours, we first determine the effective temperatures (T_{eff}) and bolometric corrections (BC) of the target stars according to the empirical colour – temperature and colour – bolometric correction relations given in Gray (2005). Then, we determine the distance of each target depending on its parallax measurement taken from the third GAIA data release (Gaia Collaboration et al. 2016, 2023). In the third step, we use the measured V magnitudes (in Table 2) and the calculated distances (d) of each target in the distance modulus formula and find the absolute V magnitude (M_V). After that, we apply estimated bolometric corrections to the calculated M_V magnitudes and obtain the bolometric absolute magnitude (M_{bol}) of each star. In the final step, we use the calculated M_{bol} of each star with the solar M_{bol} value of $4\overset{\mathrm{m}}{.}74$ in Stefan-Boltzmann law and calculate the luminosity ($L/L_{\odot}$) of the target stars. We estimate the spectral clas-

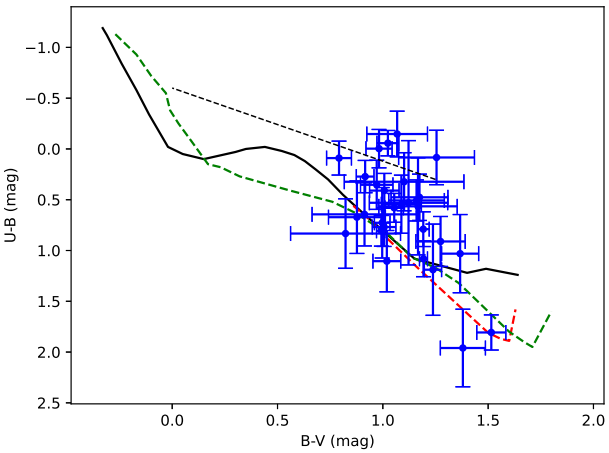

Fig. 2. Positions of the target systems on the UBV colour – colour diagram. Six targets that do not have reliable measurements are not plotted in the figure. The continuous curve (black) shows the theoretically expected positions of the unreddened main sequence stars, while the dashed curves show the positions of unreddened giant (shorter curve) and supergiant stars (longer curve), respectively. The dashed (black) line denotes the reddening vector. Theoretical data are from Drilling & Landolt (2000). The colour figure can be viewed online.

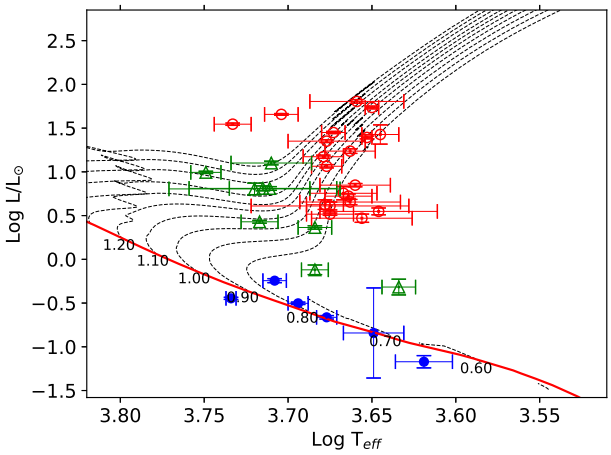

Fig. 3. Positions of the target systems on the HR diagram. Theoretical evolutionary tracks (dashed lines) for solar abundance ($Y = 0.279$ and $Z = 0.017$) are from Bressan et al. (2012). Each track is labelled with its corresponding mass in solar units. Continuous (red) curve denotes the zero-age main sequence. Filled (blue) circles are for main sequence stars, open triangles (green) denote sub-giant stars and open (red) circles show giant stars. The colour figure can be viewed online.

sification of each star by comparing estimated effective temperatures and calculated luminosities with the calibrations given in Gray (2005). Following the outlined procedure, we calculate the results listed in Table 3.

Now, we are in a position to determine the location of each target on the Hertzsprung – Russell (HR) diagram (Figure 3). In the figure, one may notice that there is no available evolutionary track for the positions of a few targets located at the redder part of the diagram. These targets may be pre-main sequence stars, which still evolve towards the zero-age main sequence. LN Eri, V1330 Sco, V2700 Oph and KZ Psc might be pre-main sequence stars with their remarkably short photometric periods ($P < 8$ day) and a light curve amplitude between $0\overset{\mathrm{m}}{.}1$ or $0\overset{\mathrm{m}}{.}2$ in the V filter (see Table 5 in the Appendix). Optical spectroscopic observations of these particular targets are required to arrive at a conclusive result.

3.3. *Analysis of Seasonal Light Curves*

We use long-term photometry of each star (Figure 1) to determine seasonal light curve properties, which are photometric period (P_{phot}), peak-to-peak light curve amplitude (A) and minimum (V_{min}), maximum (V_{max}) and mean (V_{mean}) brightnesses. For that purpose, we first divide the photometric data of a given target into subsets, where each one covers an observing season. Then, we check each season by eye for any dramatic change in light curve amplitudes. If there is a significant amplitude change in a season, we further divide the corresponding subset into parts so that each part possesses a fairly constant amplitude.

Among photometric period determination methods, we employ Analysis of Variance (ANOVA, Schwarzenberg-Czerny 1996), which is a hybrid method that combines the power of Fourier analysis and ANOVA statistics. The method is capable of determining the best-fitting period for a given light curve independently of the shape of the light curve and is very effective to damp the amplitudes of the alias periods[2]. To estimate the uncertainty of the computed photometric periods, we follow the method proposed by Schwarzenberg-Czerny (1991). The method provides more accurate uncertainties compared to the least-squares correlation matrix or Rayleigh resolution criteria.

Before proceeding with the ANOVA method, we apply a linear fit to the corresponding subset light curve to remove any long-term brightness variation, because such a variation may alter the photomet-

[2]Practical application of the method is done by computer codes/scripts located at `https://users.camk.edu.pl/alex/\#software`

TABLE 3

ESTIMATED ASTROPHYSICAL PROPERTIES OF THE TARGET STARS

Star	T_{eff} (K)	$\sigma_{T_{eff}}$ (K)	BC (mag)	d (pc)	σ_d (pc)	M_V (mag)	σ_{M_V} (mag)	M_{bol} (mag)	$\sigma_{M_{bol}}$ (mag)	$L/L_\odot$	$\sigma_{L/L_\odot}$	Sp.
IM Cet	4602	161	-0.495	427	7	2.14	0.19	1.65	0.10	17	1	K2 III
IR Cet	4610	150	-0.492	379	2	3.43	0.10	2.93	0.06	5.3	0.3	K2 III
IZ Cet	4752	99	-0.430	341	3	2.51	0.10	2.08	0.05	11.6	0.5	K1 III
HW Cet	5415	41	-0.149	57.4	0.1	6.00	0.05	5.86	0.07	0.36	0.01	G9 V
LN Eri	4834	91	-0.391	167	4	5.43	0.31	5.04	0.15	0.76	0.09	K0 IV
OP Eri	4713	75	-0.448	486.62	0.09	1.56	0.06	1.11	0.03	28.2	0.8	K1 III
V1330 Tau	4647	212	-0.477	403	14	3.33	0.41	2.85	0.23	5.7	0.9	K1 III
V1339 Tau	5608	116	-0.103	468	5	2.36	0.14	2.25	0.07	9.9	0.3	G1 IV
V1841 Ori	4941	63	-0.339	53.09	0.04	6.34	0.06	6.00	0.08	0.31	0.01	K3 V
V1854 Ori	5101	81	-0.264	76.3	0.8	5.61	0.13	5.35	0.08	0.57	0.03	K2 V
V2814 Ori	4417	106	-0.563	483	5	1.74	0.14	1.17	0.23	27	6	K3 III
V2826 Ori	5054	118	-0.285	561	1	0.88	0.06	0.60	0.08	45	1	G6 III
V969 Mon	4774	133	-0.420	412	3	2.23	0.11	1.81	0.10	14.9	0.6	K0 III
V424 Gem	4500	30	-0.533	482	2	1.79	0.07	1.26	0.04	24.7	0.9	K2 III
KU Cnc	4163	162	-0.760	41.27	0.03	8.43	0.11	7.67	0.12	0.07	0.01	M1 V
EQ Leo	4463	44	-0.546	504	3	0.95	0.09	0.40	0.05	54	2	K3 III
IN Leo	4769	124	-0.422	234	6	3.60	0.31	3.18	0.14	4.2	0.5	K1 III
OS Leo	4832	112	-0.392	298	2	4.22	0.09	3.83	0.06	2.3	0.1	K0 IV
V358 Vir	4756	66	-0.429	87.2	0.2	6.83	0.06	6.40	0.07	0.22	0.01	K4 V
PW Com	5213	132	-0.217	206	1	3.89	0.09	3.67	0.05	2.7	0.1	G4 IV
V436 Ser	4603	307	-0.495	326.9	0.4	3.60	0.15	3.10	0.09	4.5	0.3	K2 III
V561 Ser	4532	299	-0.521	262	2	4.09	0.18	3.56	0.11	3.0	0.3	K2 III
V354 Lib	4728	155	-0.442	250.1	0.4	3.89	0.07	3.45	0.06	3.3	0.1	K1 III
V1330 Sco	4303	101	-0.619	138	4	6.15	0.31	5.53	0.20	0.48	0.09	K4 IV
V2700 Oph	4429	342	-0.559	313	1	3.93	0.17	3.37	0.12	3.5	0.3	K3 III
V1404 Her	5188	497	-0.227	480	2	2.94	0.20	2.71	0.08	6.5	0.4	G4 IV
V2723 Oph	4735	485	-0.438	449	4	3.65	0.22	3.22	0.12	4.1	0.4	K1 III
V1445 Her	5135	276	-0.249	337	2	2.96	0.13	2.71	0.07	6.5	0.3	G5 IV
V1848 Aql	5407	141	-0.151	425	5	1.03	0.16	0.88	0.07	35	1	G2 III
V1890 Aql	4561	280	-0.511	967	4	0.74	0.13	0.23	0.08	64	3	K2 III
V365 Aqr	5254	580	-0.202	353	18	2.93	0.63	2.73	0.18	6.4	0.9	G4 IV
V641 Peg	4749	245	-0.432	847	2	1.80	0.08	1.36	0.05	22.4	0.8	K1 III
V543 Peg	5131	274	-0.251	597	8	2.24	0.16	1.99	0.06	12.6	0.6	G5 III
V580 Peg	4461	180	-0.547	46	6	7.39	1.53	6.84	0.97	0.1	0.1	K6 V
KZ Psc	4568	215	-0.508	278.22	0.05	3.13	0.09	2.62	0.06	7.0	0.3	K2 III

ric period artificially. After the linear correction, we apply the ANOVA method to the residuals from the linear fit and determine the best-fitting period and the light curve properties mentioned above. After we find the final photometric period for a given subset, we make a phase-folded light curve of this subset concerning the final photometric period and fit a cubic spline polynomial to the phase-folded data. Here, the purpose is to determine the minimum and the maximum values of the spline function, which correspond to the brightnesses of the light curve maximum and minimum, respectively. The amplitude and the mean brightness can be calculated straightforwardly from these values. Otherwise, fitted spline polynomials do not have any physical meaning. We list the analysis results in the Appendix (Table 5).

3.4. *Photometric Periods and Surface Differential Rotation*

In this section, we use the advantage of having long-term photometry to estimate the magnitude of the SDR. It is clear that determining the latitude of the cool surface spots from photometry is a well-known ill-posed problem. This prevents the type of differential rotation (solar type or anti-solar type) from being clearly determined in this study. However, the range in which the photometric period takes value for a particular star can set a lower limit for

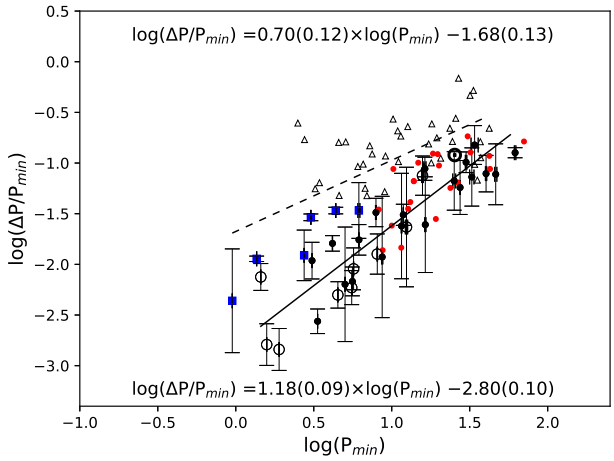

Fig. 4. Relation between the observed minimum period P_{min} and the calculated relative shear. Black filled circles show giant stars listed in Table 5, while blue filled square and open circle symbols denote main sequence stars and sub-giant stars, respectively. Open triangles show stars taken from Donahue et al. (1996), small (red) dots (without error bars) show RS CVn stars analysed in Özdarcan (2021) and five other stars mentioned in the text. We also show the position of our Sun in the figure. Dashed and straight lines show linear fits to the distribution of main sequence and giant stars, respectively. The corresponding coefficients and their statistical errors are given inside the plot window (upper one for the main sequence stars, lower one for the giant stars). The colour figure can be viewed online.

the magnitude of the SDR. Given the brief discussion above, we implicitly assume that all target stars possess solar-type SDR (i.e., the equator rotates faster than the poles). Therefore, we consider the observed minimum value of the photometric period as the equatorial rotation period. The observed maximum value, then, corresponds to the highest latitude at which spots could emerge during the time interval of the photometric data. We make a quantitative estimation of the magnitude of the SDR by relative shear defined in terms of periods (equation 1),

$$\frac{\Delta P}{P_{min}} = \frac{(P_{max} - P_{min})}{P_{min}}. \qquad (1)$$

We take P_{max} and P_{min} values of each target star from Table 5 and compute the relative shear via equation 1. We plot the P_{min} – relative shear pair of each star in Figure 4. We also tabulate these pairs along with the estimated spectral types in Table 4.

For comparison, we also show the positions of the 37 main sequence stars analysed in Donahue et al. (1996) and 21 giant stars analysed in Özdarcan (2021). Five more giant stars are also plotted in the figure (with red dots), which are HD 208472 (Özdarcan et al. 2010), FG UMa (HD 89546, Özdarcan et al. 2012) and BD+13 50000, TYC 5163-1764-1 and BD+11 3024 (Özdarcan & Dal 2018). We note that analysis of all these stars was done in a similar way as described above. The only difference could be that Donahue et al. (1996) used the S index based on Ca II H& K measurements, which is a spectroscopic indicator of the chromospheric activity. For the remaining stars, pure V photometry, which is a photometric indicator of the same phenomenon, was used.

A linear fit to the positions of all main sequence stars plotted in Figure 4 gives the coefficients shown in the upper part of the figure with a correlation coefficient of 0.67 and a p value of 6.9×10^{-7}. In the figure, sub-giants and giants appear as aligned on the same slope. Thus, we apply a similar linear fit to the positions of all giant and sub-giant stars. The fit results in the coefficients shown in the bottom part of the figure with a correlation coefficient of 0.88 and a p value of 3.2×10^{-19}.

4. SUMMARY AND DISCUSSION

Johnson UBV photometry of 35 target stars suggests a significant colour excess, particularly in the $U - B$ colour, for most of the targets. We interpret this excess as the effect of intense chromospheric activity in the UBV colours. Neglecting the interstellar reddening, adopting average $B - V$ colour excess reported in Amado (2003) and using GAIA parallaxes, we estimate astrophysical properties of the target stars via colour-temperature calibrations. At that point, we stress that we remove an average excess value from our observations, which apparently reduces the reliability of the estimated astrophysical properties. Therefore, we believe that a re-determination of colour excesses in $U - B$ and $B - V$ colours with a more comprehensive study based on a larger sample size deserves effort. In the current case, the positions of the target stars on the HR diagram indicate that six of our target stars are main-sequence star, while nine of them appear as sub-giant, and the remaining 20 stars are located in the region of giant stars.

Analysis of long-term V photometry of the target stars enables us to investigate possible variability of the photometric period, which indicates SDR. We determine seasonal photometric periods of each star and calculate the relative shear via observed minimum and maximum photometric periods in the time span of the available photometric data. However, among stars which we classify as giant, we find

TABLE 4

CALCULATED PERIODS AND RELATIVE SHEAR VALUES OF THE TARGET STARS ALONG WITH THEIR SPECTRAL TYPES

Star	Sp.	P_{min} (day)	$\sigma_{P_{min}}$ (day)	P_{max} (day)	$\sigma_{P_{max}}$ (day)	$\Delta P/P_{min}$	$\sigma_{\Delta P/P_{min}}$
IM Cet	K2 III	27.4	0.2	29.0	0.7	0.06	0.03
IR Cet	K2 III	16.3	0.3	17.7	0.2	0.09	0.02
IZ Cet	K1 III	7.92	0.06	8.18	0.04	0.032	0.009
HW Cet	G9 V	6.15	0.09	6.36	0.03	0.03	0.02
LN Eri	K0 IV	1.4467	0.0009	1.458	0.003	0.008	0.002
OP Eri	K1 III	46.4	0.8	50	2	0.08	0.04
V1330 Tau	K1 III	8.68	0.08	8.787	0.005	0.012	0.009
V1339 Tau	G1 IV	15.7	0.2	16.9	0.4	0.08	0.03
V1841 Ori	K3 V	2.743	0.009	2.78	0.01	0.012	0.005
V1854 Ori	K2 V	1.3609	0.0007	1.3764	0.0006	0.0113	0.0007
V2814 Ori	K3 III	61.8	0.7	69.6	0.5	0.13	0.01
V2826 Ori	G6 III	25.2	0.5	26.8	0.6	0.07	0.03
V969 Mon	K0 III	5.018	0.006	5.05	0.02	0.006	0.005
V424 Gem	K2 III	40.2	0.4	43	1	0.08	0.03
KU Cnc	M1 V	0.950	0.001	0.954	0.005	0.004	0.006
EQ Leo	K3 III	33	1	35.0	0.5	0.07	0.04
IN Leo	K1 III	6.161	0.009	6.27	0.03	0.017	0.005
OS Leo	K0 IV	5.69	0.01	5.74	0.01	0.009	0.003
V358 Vir	K4 V	4.376	0.007	4.525	0.009	0.034	0.002
PW Com	G4 IV	4.514	0.004	4.537	0.004	0.005	0.001
V436 Ser	K2 III	11.55	0.06	11.8	0.4	0.02	0.03
V561 Ser	K2 III	11.86	0.01	12.22	0.08	0.031	0.007
V354 Lib	K1 III	5.594	0.002	5.63	0.01	0.007	0.002
V1330 Sco	K4 IV	8.08	0.04	8.18	0.01	0.013	0.005
V2700 Oph	K3 III	3.347	0.002	3.356	0.001	0.003	0.001
V1404 Her	G4 IV	12.4	0.2	12.72	0.04	0.02	0.02
V2723 Oph	K1 III	3.08	0.01	3.116	0.003	0.011	0.004
V1445 Her	G5 IV	1.896	0.001	1.8986	0.0002	0.001	0.001
V1848 Aql	G2 III	16.4	0.2	16.8	0.2	0.02	0.02
V1890 Aql	K2 III	34	2	39.1	0.5	0.15	0.05
V365 Aqr	G4 IV	1.5789	0.0004	1.5814	0.0009	0.002	0.001
V641 Peg	K1 III	30.0	0.3	33.0	0.5	0.10	0.02
V543 Peg	G5 III	5.538	0.005	5.571	0.009	0.006	0.002
V580 Peg	K6 V	3.030	0.006	3.119	0.003	0.029	0.002
KZ Psc	K2 III	4.168	0.009	4.235	0.006	0.016	0.003

very short rotation periods. V2723 Oph, V2700 Oph, KZ Psc and V969 Mon are such stars. Since these stars appear in giant region on the HR diagram and giant stars often tend to have much longer periods, finding such short periods is not expected. One possible explanation is that these stars are likely members of a binary system. IZ Cet and V1330 Tau are such stars among our sample, which are reported as SB2 binaries (Torres et al. 2002). On the other hand, we carried out a quick inspection of space photometry provided by the *TESS* satellite (Ricker et al. 2014) and did not notice any eclipse event for any star in our sample. Unfortunately, we have no high-resolution spectra to check if these stars exhibit an orbital motion in their radial velocities. Another possible explanation is that, if these giants are single, then they might be FK Com variables. These systems deserve additional attention by further spectroscopic studies.

Computing photometric periods and relative shear values for each star enables us to investigate the relation between the photometric period and the relative shear (i.e., differential rotation, Figure 4) via a more extended sample compared to Özdarcan (2021). In the figure, the distribution of the main sequence and giant stars shows a significant distinction

in the shorter periods, while the distinction tends to disappear towards long periods. The slopes of the best-fitting linear fits in Figure 4 indicate that the relative shear is more sensitive to the photometric period in giant stars compared to main-sequence stars. That picture confirms the distinction reported in Özdarcan (2021). Yet, the number of main sequence stars still requires to be increased, particularly for the shorter photometric periods for more reliable results. On the other hand, the distinction between giant and main sequence stars appears to be lost towards the longer photometric periods. Increasing the sample size of main sequence stars having long term continuous photometry is crucial for revealing the true form of the observed distinction between main sequence and giant stars. It is also desirable to observe main sequence stars with short photometric periods that appear below the dashed line in Figure 4). We may argue that these stars show less shear than the relation for longer period MS stars would predict.

In Figure 4, plotting the main sequence stars mentioned in Donahue et al. (1996) together with the target stars analysed in this study might be questionable because Donahue et al. (1996) obtained periods via the S index, which is a chromospheric indicator of the stellar activity, while we use pure V photometry (a photospheric indicator of the same phenomenon) to obtain periods. If the differential rotations of the photosphere and the chromosphere are significantly different from each other, then it is a reasonable concern. Since there are no long-term and simultaneous period measurements of the photosphere and the chromosphere of any star, we can only inspect the rotational behaviour of the solar photosphere and chromosphere and make interpretations in the scope of a solar-stellar connection. In a recent study, Xu et al. (2020) found that rotation periods indicated by chromospheric and photospheric indices vary in the same period range in the Sun (see Figure 6 in their study). This means that the differential rotation of the chromosphere of the Sun is not significantly different from the photosphere. A very recent study by Mishra et al. (2024) reported a 1.59% difference between the equatorial periods found from differential rotations of the solar photosphere and the chromosphere, which indicates a little difference between their rotations. Considering these findings, we may expect a similar behaviour for the chromospherically active stars in the scope of the Solar-Stellar connection. Then, it is reasonable to expect very little difference for SDR values computed from the S index (chromospheric indicator) and broadband V photometry (photospheric indicator). The difference would likely be within our observational errors.

We note that photometric periods are computed by tracing the rotational modulation signal observed in light curves. These signals are produced by cool surface spots. Rotation periods of these spots may be different depending on their latitudinal position on the surface of the star. This is the basic idea in our analysis. However, it was reported that any change in the area of a surface spot, vanishing and emerging of spots in short time scales at various locations on the surface of the star may alter the measured photometric period (Fekel et al. 2002). Such events show themselves as dramatic changes in the peak-to-peak light curve amplitude over short time scales (days). Even if these effects are in progress, we do not expect a significant change in our results because we determine photometric periods from stable parts of the light curves where the amplitude can be fairly accepted as constant.

Upon comparing the summarized findings with the theoretical computations of Kitchatinov & Rüdiger (1999), we observe that our results support the predicted relation between period and differential rotation. However, the observed distinction between giants and main sequence stars appears to be opposite to the theoretical predictions. According to calculations by Kitchatinov & Rüdiger (1999), giant stars should have stronger differential rotation compared to main-sequence stars. However, Figure 4 suggests the opposite, where the main-sequence stars appear to have stronger differential rotation than the giant stars. Further observational and theoretical studies may be conducted to investigate the source of this contradiction.

Kővári et al. (2017) investigated the relation between the rotation period and SDR in the scope of single and binary stars. They found that SDR weakly depends on the rotation period for of a binary system compared to a single star. We are not in a position to test this finding here since we do not consider single/binary distinction in our study. However, a further detailed investigation, which considers binarity and evolutionary status, might yield results that would provide a more comprehensive view of the relation between the SDR and the photometric period for chromospherically active stars.

We are indebted to Dr. Grzegorz Pojmański for providing reduced and unpublished photometric data of target stars from the ASAS3-N and ASAS4 surveys. These data significantly increased the reliability of the results obtained in this study. We also

TABLE 5

ANALYSIS RESULTS OF SEASONAL LIGHT CURVES*

TYC 05275-00646-1 — IM Cet								
HJD begin (24 00000+)	HJD end (24 00000+)	HJD mean (24 00000+)	P_{phot} (day)	σ_P (day)	V_{max} (mag)	V_{min} (mag)	V_{mean} (mag)	N
51868.5706	51931.5318	51900.0512	28.54	0.960	9.995	10.209	10.102	17
52039.9296	52262.5831	52151.2564	28.14	0.200	10.054	10.188	10.121	62
52439.8937	52563.679	52501.7864	28.58	0.210	10.106	10.430	10.268	35
52623.5446	52677.5206	52650.5326	27.96	1.380	10.106	10.474	10.290	17
52787.9123	53035.5455	52911.7289	28.55	0.130	10.098	10.438	10.268	62
53512.9328	53765.5344	53639.2336	28.06	0.100	10.151	10.487	10.319	59
53900.9278	54146.7157	54023.8218	27.97	0.120	10.086	10.344	10.215	52
54246.9291	54498.5336	54372.7314	27.43	0.160	10.172	10.413	10.292	72
54632.9086	54875.7108	54754.3097	28.46	0.140	10.107	10.437	10.272	60
54969.9312	55239.7217	55104.8265	28.19	0.130	10.142	10.584	10.363	99
55367.108	55601.7162	55484.4121	27.83	0.140	10.166	10.599	10.383	165
55696.9278	55969.7267	55833.3273	27.66	0.170	10.264	10.429	10.347	190
56127.0973	56328.7437	56227.9205	28.26	0.300	10.219	10.461	10.340	90
56427.9281	56676.756	56552.3421	28.01	0.130	10.140	10.437	10.289	194
56816.1142	57060.5301	56938.3222	28.08	0.100	10.038	10.290	10.164	211
57154.9277	57424.5312	57289.7295	28.15	0.050	9.955	10.357	10.156	272
57523.9064	57788.7204	57656.3134	28.06	0.090	9.953	10.300	10.127	347
57907.9044	58151.5406	58029.7225	28.36	0.150	9.910	10.194	10.052	264
58256.9314	58511.5387	58384.2351	28.98	0.300	9.910	10.057	9.983	243
58617.9279	58818.5378	58718.2329	29.00	0.700	9.903	10.056	9.979	72
52054.9387	52214.7281	52134.8334	16.91	0.150	11.327	11.527	11.427	28
52453.8408	52578.7414	52516.2911	16.99	0.440	11.324	11.448	11.386	22
52629.5971	52688.5164	52659.0568	17.00	0.320	11.301	11.452	11.376	21
52805.9047	53054.5124	52930.2086	17.19	0.060	11.339	11.508	11.424	70
53525.9300	53780.5195	53653.2248	17.26	0.060	11.307	11.499	11.403	60
53930.1083	54153.7105	54041.9094	16.68	0.130	11.352	11.429	11.391	45
54270.1206	54387.8141	54328.9674	17.27	0.300	11.347	11.473	11.410	46
54399.6743	54509.5175	54454.5959	17.31	0.190	11.304	11.453	11.378	37

*The full table can be viewed online in `https://www.astroscu.unam.mx/rmaa/RMxAA..60-2/PDF/RMxAA..60-2_oozdarcan-VIII-Table5.pdf`.

thank the anonymous referee for thoughtful comments and a critically reading that improved the quality of the manuscript. We acknowledge the Unit of Scientific Research Projects (BAP) at Ege University, for supporting this work through Grant No. 24150.

APPENDICES

A. TRANSFORMATION COEFFICIENTS FOR THE EUOARC OBSERVING SETUP

Equations A1 and A2 are for the EUOARC Johnson measurements for 27th December, 2022 and 13th July, 2023 nights, respectively. $(u-b)_0$, $(b-v)_0$, and v_0 denote reduced instrumental colours and magnitudes.

$$\begin{aligned} V-v_0 &= -0.017(\pm0.045)\times(B-V)+18.648(\pm0.033) \\ B-V &= 1.149(\pm0.016)\times(b-v)_0+0.537(\pm0.006) \\ U-B &= 0.995(\pm0.023)\times(u-b)_0-2.048(\pm0.056) \end{aligned} \tag{A1}$$

$$\begin{aligned} V-v_0 &= -0.059(\pm0.068)\times(B-V)+17.850(\pm0.055) \\ B-V &= 1.020(\pm0.046)\times(b-v)_0+0.533(\pm0.022) \\ U-B &= 1.022(\pm0.074)\times(u-b)_0-1.174(\pm0.121) \end{aligned} \tag{A2}$$

B. SEASONAL LIGHT CURVE ANALYSIS RESULTS

In this section, we tabulate analysis results of seasonal light curves. In the first three columns, begin, end and mean times of each subset are given in heliocentric Julian date. The last column shows the number of data for the corresponding subset.

REFERENCES

Amado, P. J. 2003, A&A, 404, 631, https://doi.org/10.1051/0004-6361:20030494

Baliunas, S. L., Donahue, R. A., Soon, W., & Henry, G. W. 1998, ASPC 154, The Tenth Cambridge Workshop on Cool Stars, Stellar Systems and the Sun, ed. R. A. Donahue & J. A. Bookbinder, 153

Baliunas, S. L., Donahue, R. A., Soon, W. H., et al. 1995, ApJ, 438, 269, https://doi.org/10.1086/175072

Berdnikov, L. N. & Pastukhova, E. N. 2008, PZ, 28, 9

Bernhard, K., Bernhard, C., & Bernhard, M. 2009, OEJV, 98, 1

Bernhard, K. & Lloyd, C. 2008a, OEJV, 92, 1

_____. 2008b, OEJV, 82, 1

Bernhard, K., Lloyd, C., & Frank, P. 2010, OEJV, 123, 1

Bernhard, K. & Otero, S. 2011, PZP, 11, 15

Bressan, A., Marigo, P., Girardi, L., et al. 2012, MNRAS, 427, 127, https://doi.org/10.1111/j.1365-2966.2012.21948.x

Donahue, R. A., Saar, S. H., & Baliunas, S. L. 1996, ApJ, 466, 384, https://doi.org/10.1086/177517

Drilling, J. S. & Landolt, A. U. 2000, in Allen's Astrophysical Quantities, ed. A. N. Cox, 381

Duncan, D. K., Vaughan, A. H., Wilson, O. C., et al. 1991, ApJS, 76, 383, https://doi.org/10.1086/191572

Fekel, F. C., Henry, G. W., Eaton, J. A., Sperauskas, J., & Hall, D. S. 2002, AJ, 124, 1064, https://doi.org/10.1086/341612

Gaia Collaboration, Prusti, T., de Bruijne, J. H. J., et al. 2016, A&A, 595, 1, https://doi.org/10.1051/0004-6361/201629272

Gaia Collaboration, Vallenari, A., Brown, A. G. A., et al. 2023, A&A, 674, 1, https://doi.org/10.1051/0004-6361/202243940

Gray, D. F. 2005, The Observation and Analysis of Stellar Photospheres (CUP), https://doi.org/10.1017/CBO9781316036570

Hardie, R. H. 1964, in Astronomical techniques, ed. W. A. Hiltner, 178

Henden, A. A., Levine, S., Terrell, D., & Welch, D. L. 2015, AAS, 225, 336.16

Høg, E., Fabricius, C., Makarov, V. V., et al. 2000, A&A, 355, 27

Kitchatinov, L. L. & Rüdiger, G. 1999, A&A, 344, 911

Kochanek, C. S., Shappee, B. J., Stanek, K. Z., et al. 2017, PASP, 129, 4502, https://doi.org/10.1088/1538-3873/aa80d9

Kővári, Z., Oláh, K., Kriskovics, L., et al. 2017, AN, 338, 903, https://doi.org/10.1002/asna.201713400

Landolt, A. U. 2009, AJ, 137, 4186, https://doi.org/10.1088/0004-6256/137/5/4186

_____. 2013, AJ, 146, 131, https://doi.org/10.1088/0004-6256/146/5/131

Messina, S. & Guinan, E. F. 2003, A&A, 409, 1017, https://doi.org/10.1051/0004-6361:20031161

Mishra, D. K., Routh, S., Jha, B. K., et al. 2024, ApJ, 961, 40, https://doi.org/10.3847/1538-4357/ad1188

Özdarcan, O. 2021, PASA, 38, 27, https://doi.org/10.1017/pasa.2021.21

Özdarcan, O. & Dal, H. A. 2018, AN, 339, 277, https://doi.org/10.1002/asna.201813391

Özdarcan, O., Evren, S., & Henry, G. W. 2012, AN, 333, 138, https://doi.org/10.1002/asna.201111646

Özdarcan, O., Evren, S., Strassmeier, K. G., Granzer, T., & Henry, G. W. 2010, AN, 331, 794, https://doi.org/10.1002/asna.201011413

Pojmanski, G. 1997, AcA, 47, 467, https://doi.org/10.48550/arXiv.astro-ph/9712146

_____. 2002, AcA, 52, 397, https://doi.org/10.48550/arXiv.astro-ph/0210283

Pojmanski, G., Pilecki, B., & Szczygiel, D. 2005, AcA, 55, 275, https://doi.org/10.48550/arXiv.astro-ph/0508017

Reinhold, T. & Gizon, L. 2015, A&A, 583, 65, https://doi.org/10.1051/0004-6361/201526216

Ricker, G. R., Winn, J. N., Vanderspek, R., et al. 2014, JATIS, 1, 014003, https://doi.org/10.1117/1.JATIS.1.1.014003

Schirmer, J., Bernhard, K., & Lloyd, C. 2009, OEJV, 105, 1

Schlafly, E. F. & Finkbeiner, D. P. 2011, ApJ, 737, 103, https://doi.org/10.1088/0004-637X/737/2/103

Schwarzenberg-Czerny, A. 1991, MNRAS, 253, 198, https://doi.org/10.1093/mnras/253.2.198

_____. 1996, ApJ, 460, 107, https://doi.org/10.1086/309985

Shappee, B. J., Prieto, J. L., Grupe, D., et al. 2014, ApJ, 788, 48, https://doi.org/10.1088/0004-637X/788/1/48

Torres, G., Neuhäuser, R., & Guenther, E. W. 2002, AJ, 123, 1701, https://doi.org/10.1086/3391778

Vaughan, A. H., Preston, G. W., & Wilson, O. C. 1978, PASP, 90, 267, https://doi.org/10.1086/130324

Wilson, O. C. 1978, ApJ, 226, 379, https://doi.org/10.1086/156618

Xu, J.-C., Gao, P.-X., & Shi, X.-J. 2020, ApJ, 902, 64, https://doi.org/10.3847/1538-4357/abb5b7

O. Özdarcan, H. A. Dal, E. Sipahi Kılıç, and E. Yoldaş: Ege University, Faculty of Sciences, Department of Astronomy and Space Sciences, 35100 Bornova, İzmir, Turkey.

Revista Mexicana de Astronomía y Astrofísica, **60**, 317–322 (2024)

https://doi.org/10.22201/ia.01851101p.2024.60.02.09

INSTRUMENTAL BROADENING OF THE SPOL SPECTROPOLARIMETER AT THE UNIVERSITY OF ARIZONA

Alfredo Amador-Portes[1], Vahram Chavushyan[1], and Victor M. Patiño-Alvarez[1,2]

Received March 3 2024; accepted June 7 2024

ABSTRACT

The Ground-based Observational Support of the Fermi Gamma-ray Space Telescope is conducted by the University of Arizona using the 2.3m Bok and 1.54m Kuiper telescopes operated by the Steward Observatory (SO). This program monitors blazar sources with spectroscopic observations. Yet, the instrumental broadenings for the different slit widths used in the spectra are unavailable (the widths range from 2.″0 to 12.″7). Using quasi-simultaneous spectroscopic observations of the blazar 3C 273 between the SO, Observatorio Astrofísico Guillermo Haro, and Observatorio Astronómico Nacional San Pedro Mártir, we can provide an estimation of the instrumental profile for two of the slit widths. Since the instrumental broadening and the slit width are directly proportional, we are able to estimate the instrumental broadening for all six slit widths used at the SO.

RESUMEN

El soporte de observaciones terrestres del telescopio espacial Fermi de rayos gamma, se realiza por la Universidad de Arizona con los telescopios Bok de 2.3m y Kuiper de 1.54m, operado por el Observatorio Steward (SO). Este programa monitorea fuentes blazares con observaciones espectroscópicas. Sin embargo, la información del perfil instrumental para diferentes anchos de rendija usados en los espectros ópticos no está disponible (los anchos van desde 2.″0 a 12.″7). Por ello, utilizando observaciones de espectros cuasi-simultáneos del blazar 3C 273 entre el SO, el Observatorio Astrofísico Guillermo Haro y el Observatorio Astronómico Nacional San Pedro Mártir, determinamos el perfil instrumental para dos anchos de rendija. Ya que el ancho instrumental y el ancho de rendija son directamente proporcionales, fue posible estimar el perfil instrumental para los seis anchos de rendija usados en el SO.

Key Words: galaxies: active — instrumentation: spectrographs — methods: observational — quasars: individual: 3C 273

1. INTRODUCTION

Since the launch of the Fermi Gamma-Ray Space Telescope, there have been counterpart supporting monitoring programs in the entire electromagnetic spectrum, from radio waves to X-rays (e.g. SMA, Gurwell et al. 2007; OVRO, Richards et al. 2011, SMARTS; Bonning et al. 2012, Swift; Stroh & Falcone 2013). In particular, we focus on the Ground-based Observational Support of the Fermi Gamma-ray Space Telescope carried out at the University of Arizona using the 2.3m Bok (Kitt Peak) and 1.54m Kuiper (Mt. Bigelow) telescopes operated by the Steward Observatory (SO) (Smith et al. 2009)[3]. This is one of the most important monitoring programs because it is the most complete public database of optical spectroscopy, photometry, and polarimetry, for blazars, with the largest number of sources and best cadence of observation[4]. In this program, the spectroscopic observations are conducted with the SPOL spectropolarimeter, which uses up to 6 configurations (apertures) corresponding to six different slit widths (1=2.″0, 2=3.″0, 3=4.″1, 4=5.″1, 5=7.″6,

[1]Instituto Nacional de Astrofísica, Óptica y Electrónica, Luis Enrique Erro #1, Tonantzintla, Puebla, México, C.P. 72840.
[2]Max-Planck-Institut für Radioastronomie, Auf dem Hügel 69, D-53121 Bonn, Germany.

[3]2009 Fermi Symposium, eConf Proceedings C091122.
[4]`http://james.as.arizona.edu/~psmith/Fermi/`.

and 6=12.″7). Smith et al. (2009) also provide a spectral resolution range of $15 - 25$ Å, depending on the slit width chosen for the observation.

Unfortunately, the instrumental broadening for each slit width is not publicly available; this has prevented us from studying the variability of the FWHM of the broad emission lines present in flat-spectrum radio quasars (FSRQ), unlike the study of flux variability previously done in various works for the Mg II λ2798 (León-Tavares et al. 2013; Chavushyan et al. 2020; Amaya-Almazán et al. 2021), Hβ (Fernandes et al. 2020), and C IV λ1549 (Amaya-Almazán et al. 2022) emission lines.

FSRQ are a sub-type of blazars (Urry & Padovani 1995) characterized by their high variability across the entire electromagnetic spectrum (e.g. Aharonian et al. 2007; Amaya-Almazán et al. 2021), with variations on very different time scales, even in the same wavelength range (e.g. Fan et al. 2018; Gupta 2018). When there is a flux increase in a very short time and well above the average emission we call this phenomenon a flare. Among AGNs, flares are mostly found in blazars. There is observational evidence that the emission line flares in some blazars can be driven by non-thermal emission from the jet (e.g. León-Tavares et al. 2013; Chavushyan et al. 2020; Amaya-Almazán et al. 2021, 2022); so it is interesting to study if the emission line profile also changes during these flares. Such a study could involve a detailed analysis of emission lines during both quiescent and flaring states, aiming to characterize any changes in emission line profiles, including shifts in peak wavelength, changes in line width (FWHM), and alterations in profile asymmetry.

The importance of monitoring the FWHM is that the emission lines provide information about the kinematics and dynamics of the gas in the broad-line region (BLR) surrounding the central supermassive black hole (SMBH). Therefore, understanding the characteristics of the BLR contributes to the knowledge of accretion processes and gravitational potential. For example, SMBH mass estimation techniques like reverberation mapping (Blandford & McKee 1982; Peterson 1993), and single-epoch spectra (Greene & Ho 2005; Kong et al. 2006; Vestergaard & Peterson 2006; Shaw et al. 2012), directly use this parameter.

It is clear that obtaining and understanding the instrumental line profile is a fundamental step for studying emission line variability in AGNs and other astronomical sources, as it enables the separation of the intrinsic characteristics of the source from instrumental effects, leading to more accurate scientific conclusions. The observed profile (FWHM_{obs}) is a convolution of both, the intrinsic profile of the source (FWHM_{corr}) and the instrumental profile (FWHM_{inst}, also known as the spectral resolution). This convolution is typically represented mathematically as a quadratic sum, shown in equation 1.

$$\mathrm{FWHM}^2_{obs} = \mathrm{FWHM}^2_{corr} + \mathrm{FWHM}^2_{inst}. \quad (1)$$

Nalewajko et al. (2019) studied line width behavior without performing a correction for instrumental broadening, which yielded an inconclusive result. This fact led to the establishment of techniques to counteract the lack of knowledge of instrumental broadening for SO spectroscopic data. Zhang et al. (2019) used a single value for FWHM_{inst} estimated from other spectroscopic observations (not quasi-simultaneous) to apply it to observations with different slit widths. Rakshit (2020) used the same value and applied it to the SO spectra with different slit widths. The latter can lead to an underestimation or an overestimation of intrinsic emission line widths in a set of spectra with different slit widths. Even using only spectra taken with a single slit width as in Pandey et al. (2022), FWHM measurements of emission lines will be overestimated without an instrumental broadening correction. However, studies of the relative line width behavior can still be done in this case.

A proper approach to this problem would be to use calibration lamps or night sky lines to measure the instrumental profile. Unfortunately, as these original data were not available, we had to use instead a different method. We use spectra from the same source from an observatory with known instrumental widths, selecting only observations quasi-simultaneous to the SO data (within 24 hours of each other), and taking into account the possible intra-day variability (IDV) that Blazars can show (Gupta 2018). Assuming that the corresponding intrinsic line profile is the same in the spectra from both observatories, we can use the quasi-simultaneous data to estimate the SO instrumental profile. This procedure must be performed for each slit width because they have different instrumental broadenings.

The spectrograph resolution depends on a series of factors that we assume remain unchanged in the observations made in the SO, with the exception of the slit width. Hence, the spectral resolution (instrumental broadening) should be proportional to this slit width[5] ($\mathrm{FWHM}_{inst} \propto \mathrm{SW}$, e.g. Schroeder 1974).

[5] http://james.as.arizona.edu/~psmith/SPOL/gratings.html.

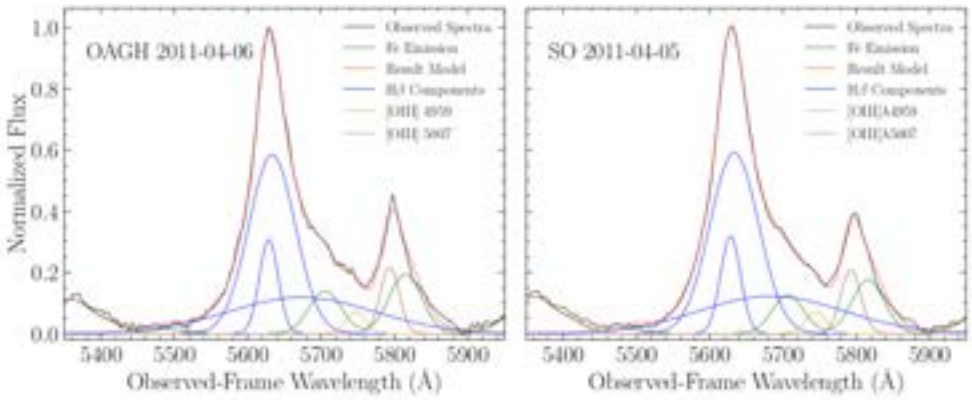

Fig. 1. Example of spectral decomposition for the Hβ region in the 3C 273 data (observed frame) Left Panel: Spectra from the SO database. Right Panel: Spectra from OAGH. The spectra were taken within 24 hours of each other. The color figure can be viewed online.

Also, the ratio between the widths of the slits will reflect the expected difference in instrumental broadening.

2. OBSERVATIONAL DATA

We search for quasi-simultaneous observations between the SO, the OAGH operated by the Instituto Nacional de Astrofísica, Óptica y Electrónica[6] (INAOE) and the OAN-SPM operated by the Universidad Nacional Autónoma de México[7] (UNAM), in which for the last two we have knowledge of the instrumental profile used in every observation. The instrument used in the OAGH and OAN-SPM observations is the Boller & Chivens spectrograph. The best candidate for this analysis was the FSRQ blazar 3C 273, due to the large number of observations, the high S/N ratio in the spectral range between 4000-7000Å, the absence of telluric absorption lines around the emission lines of interest, and finally, the fact that its redshift (0.158) allows for the presence of a narrow emission line ([O III] λ5007 Å), which in AGNs is not expected to vary significantly over a long period of time (e.g. Shapovalova et al. 2001).

We made a further filter in the spectra set for all observatories by removing spectra with a low S/N ratio. We end up with 5 spectra taken with a slit width of 5.1 arcsec (SO), in which we have quasi-simultaneous data in the OAGH or OAN-SPM, while there are 19 spectra taken with a slit width of 7.6 arcsec (SO), with quasi-simultaneous data.

3. DATA ANALYSIS

As mentioned before, for the OAGH and OAN-SPM spectra the instrumental broadening is known, because for each object spectra, we take a comparison lamp of He-Ar (OAGH) and Cu-Ne-He-Ar (OAN-SPM) that is used for wavelength calibration. Therefore the spectrum of the comparison lamp uses the same setup and light path as the spectrum of the blazar; this justifies using the width of the lines in the comparison lamp as the instrumental broadening for the object spectra correction. Hence, for each lamp spectrum, the FWHM of the non-blended lines was measured. We estimated a mean value, with its error as the quadratic sum of the standard deviation of the measurements and the dispersion of the spectrum (Å/pixel).

We left all the spectra in the observed frame because the instrumental broadening is geometrical, i.e. a fixed value in pixels. We then fitted a local continuum and subtracted it from the spectra. The spectral features were fitted with Gaussian functions in the range from 5500 − 5900Å which corresponds to the Hβ region in the observed frame, and consequently, the emission lines fitted were Hβ (with narrow, broad, and very-broad components), [O III]$\lambda\lambda$4959, 5007Å (with one Gaussian each), and the Fe II emission. The same multi-Gaussian model was used for each pair of spectra, allowing to vary only the FWHM and amplitude. An example can be seen in Figure 1, where the pair of spectra are normalized to the maximum flux of the Hβ emission.

All measurements in this paper were made using the [O III] λ5007 Å emission line, in the observed frame; at the redshift of 3C 273, the line is at 5798 Å. This line is produced in the narrow-line region (NLR), and due to its large size, it is not expected to change over large periods of time, because the ionizing radiation will respond more slowly (Shapovalova et al. 2001, and references therein).

[6] https://astro.inaoep.mx/observatorios/oagh/.
[7] https://www.astrossp.unam.mx/es/.

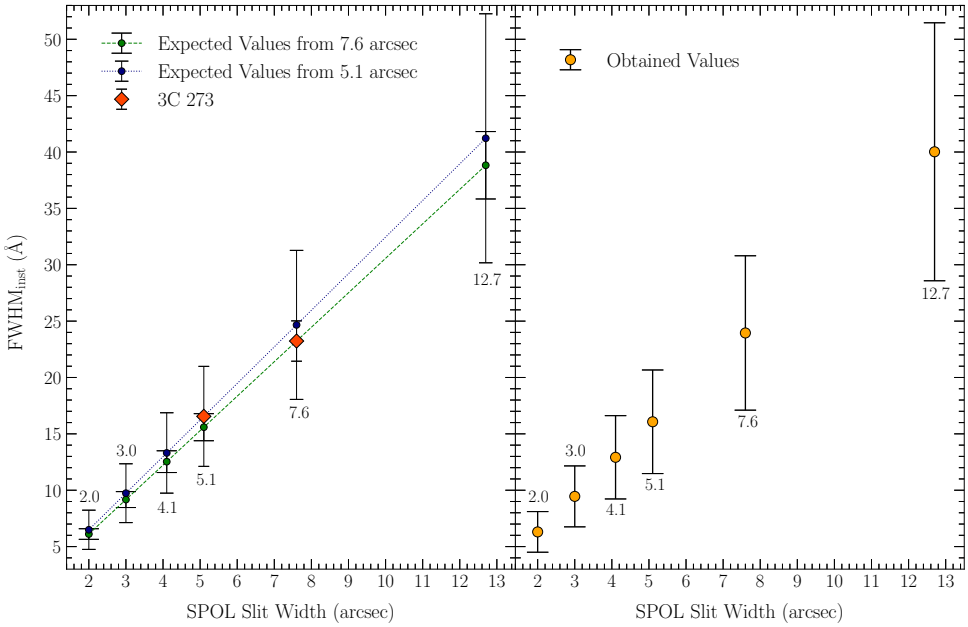

Fig. 2. Left panel: Expected sets of instrumental profiles with their uncertainties, measured using a 5.1 arcsec (navy blue squares and dotted line), and a 7.6 arcsec (orange dots and dashed line) slit width as a reference point. Observational measurements of instrumental broadening are also shown (red diamonds). Right panel: Instrumental broadening estimations for all 6 slit widths based upon the mean of the two expected values for each slit width. The color figure can be viewed online.

Previous studies of IDV on 3C 273 mainly focus on the high-energy and optical bands and have not been reported for narrow lines. However, as mentioned earlier we do not expect such fast variations in narrow emission lines. An example of the low expected variations in these lines is presented in Yuan et al. (2022), where they calculate the [O III] λ5007 Å emission line flux. The variation between each day was always less than the uncertainties that could be obtained from the spectra. Additionally, for each pair of spectra, if the multi-Gaussian model was not fitted with similar amplitudes (taking into account that the width changes), then the spectra pair was discarded to avoid possible IDV.

From all the measurements obtained, we estimate the intrinsic profile and their uncertainty with error propagation for each quasi-simultaneous observation. Assuming that the intrinsic profiles for each date on the spectra of both observatories are the same (since they are quasi-simultaneous), we were able to estimate the instrumental broadening of the SO spectra, using the intrinsic profile widths obtained from OAGH and OAN-SPM, and the observed profile widths measured in the SO spectra. We estimated a weighted mean for the instrumental broadening measurements of the two slit widths available and calculated the standard error of the weighted mean.

4. RESULTS

This analysis shows us that the instrumental profile for the SO spectra for the slit widths of 5.1, and 7.6 arcsec are 16.55 ± 4.43, and 23.23 ± 1.79Å, respectively. Given that the instrumental broadening should be proportional to the slit width, we can take any of the instrumental broadening measurements we have and obtain expected values for the instrumental profiles of the other slit widths. This means that for any two slit widths (e.g. a and b) these values must satisfy $\mathrm{FWHM}_{inst}(a)/\mathrm{FWHM}_{inst}(b) = \mathrm{SW}(a)/\mathrm{SW}(b)$. For example, for the slit width of 4.1 (that we do not measure) and 7.6 (that we do measure), the instrumental broadening for the former is calculated as $\mathrm{FWHM}_{4.1} = \mathrm{FWHM}_{7.6} \times 4.1/7.6$.

Since we have two measurements of the instrumental broadening, we obtained two sets of expected instrumental profiles, with their uncertainties, for all the slit widths. The difference between the values obtained for each slit width is most likely due to the uncertainties. We then calculated the mean of these two values for each slit width as well as their errors. These different values of instrumental broadening for each slit width are presented in Table 1.

TABLE 1

INSTRUMENTAL BROADENING FOR EACH SLIT WIDTH OF THE SPOL AT THE SO

Slit Width (arcsec)	Instrumental Broadening (Å)		
	Expected Values		Final Values
	From 5.1 arcsec	From 7.6 arcsec	
2.0	6.49 ± 1.74	6.11 ± 0.47	6.30 ± 1.80
3.0	9.74 ± 2.61	9.17 ± 0.71	9.45 ± 2.70
4.1	13.31 ± 3.57	12.53 ± 0.97	12.92 ± 3.69
5.1	16.55 ± 4.44	15.59 ± 1.20	16.07 ± 4.59
7.6	24.67 ± 6.61	23.23 ± 1.79	23.95 ± 6.85
12.7	41.22 ± 11.04	38.82 ± 2.99	40.02 ± 11.44

In Figure 2, left panel we present the instrumental broadening obtained through this analysis for the spectra taken with slit widths of 5.1 and 7.6 (red diamonds), and the expected values estimated with both measurements (blue squares and orange circles respectively). The final instrumental broadening values for all the slit widths (green circles) are presented in Figure 2 right panel.

5. CONCLUSIONS

We have estimated the instrumental broadening for the six different slit widths used in the spectroscopic observations carried out by the Steward Observatory[8], and the results are presented in Table 1. Notably, there is a significant difference in instrumental broadening across the different slit widths (which is expected), with the ratio between the maximum and minimum broadening being approximately 6.35 times. This highlights the importance of considering distinct instrumental broadening values for each slit width. Using a fixed or mean instrumental broadening for all slit widths will lead to an overestimation for smaller slit widths and an underestimation for the larger ones. Even when using mean and root mean square (rms) spectra with multiple slit widths, it is not correct to use a single instrumental broadening value, because the resulting spectra would still retain broadening information from all the slit widths, and they are strongly dependent on the most used setup.

We thank the anonymous referee for the constructive comments that helped to improve the manuscript. A.A.-P. acknowledges support from the CONAHCYT (Consejo Nacional de Humanidades, Ciencia y Tecnología) program for Ph.D. studies. This work was supported by CONAHCYT research Grants 280789 and 320987. In addition, this work was supported by the Max Plank Institute for Radioastronomy (MPIfR) - Mexico Max Planck Partner Group led by V.M.P.-A. Data from the Steward Observatory spectropolarimetric monitoring project were used. This program is supported by Fermi Guest Investigator Grants NNX08AW56G, NNX09AU10G, NNX12AO93G, and NNX15AU81G. This publication is based on data collected at the Observatorio Astrofísico Guillermo Haro (OAGH), Cananea, Sonora, Mexico, operated by the Instituto Nacional de Astrofísica, Óptica y Electrónica (INAOE). Funding for the OAGH has been provided by CONAHCYT. This paper is based upon observations carried out at the Observatorio Astronómico Nacional on the Sierra San Pedro Mártir (OAN-SPM), Baja California, México.

[8] http://james.as.arizona.edu/~psmith/Fermi/

REFERENCES

Aharonian, F., Akhperjanian, A. G., Bazer-Bachi, A. R., et al. 2007, ApJ, 664, 71, https://doi.org/10.1086/520635

Amaya-Almazán, R. A., Chavushyan, V., & Patiño-Álvarez, V. M. 2021, ApJ, 906, 5, https://doi.org/10.3847/1538-4357/abc689

_____. 2022, ApJ, 929, 14, https://doi.org/10.3847/1538-4357/ac5741

Blandford, R. D. & McKee, C. F. 1982, ApJ, 255, 419, https://doi.org/10.1086/159843

Bonning, E., Urry, C. M., Bailyn, C., et al. 2012, ApJ, 756, 13, https://doi.org/10.1088/0004-637X/756/1/13

Chavushyan, V., Patiño-Álvarez, V. M., Amaya-Almazán, R. A., & Carrasco, L., 2020, ApJ, 891, 68, https://doi.org/10.3847/1538-4357/ab6ef6

Fan, J. H., Tao, J., Liu, Y., et al. 2018, AJ, 155, 90, https://doi.org/10.3847/1538-3881/aaa547

Fernandes, S., Patiño-Álvarez, V. M., Chavushyan, V., et al. 2020, MNRAS, 497, 2066, https://doi.org/10.1093/mnras/staa2013

Greene, J. E. & Ho, L. C. 2005, ApJ, 630, 122, https://doi.org/10.1086/431897

Gupta, A. 2018, Galaxies, 6, 1, https://doi.org/10.3390/galaxies6010001

Gurwell, M. A., Peck, A. B., Hostler, S. R., Farrah, M. R., & Katz, C. A. 2007, ASPC 375, From Z-Machines to ALMA: (Sub)Millimeter Spectroscopy of Galaxies, ed. A, J. Baker, J. Glenn, A. I. Harris, J. G. Mangum, & M. S. Yun, 234

Kong, M.-Z., Wu, X.-B., Wang, R., et al. 2006, ChJAA, 6, 396, https://doi.org/10.1088/1009-9271/6/4/02

León-Tavares, J., Chavushyan, V., Patiño-Álvarez, V., et al. 2013, ApJ, 763, 36, https://doi.org/10.1088/2041-8205/763/2/L36

Nalewajko, K., Gupta, A. C., Liao, M., et al. 2019, A&A, 631, 4, https://doi.org/10.1051/0004-6361/201935904

Pandey, S., Rakshit, S., Woo, J.-H., et al. 2022, MNRAS, 516, 2671, https://doi.org/10.1093/mnras/stac2418

Patiño Álvarez, V., Torrealba, J., Chavushyan, V., et al. 2016, FrASS, 3, 19, https://doi.org/10.3389/fspas.2016.00019

Peterson, B. M. 1993, PASP, 105, 247, https://doi.org/10.1086/133140

Rakshit, S. 2020, A&A, 642, 59, https://doi.org/10.1051/0004-6361/202038324

Richards, J. L., Max-Moerbeck, W., Pavlidou, V., et al. 2011, arXiv:1111.0318, https://doi.org/10.48550/arXiv.1111.0318

Schroeder, D. J. 1974, Astrophysics. Part A: Optical and infrared, 463

Shapovalova, A. I., Burenkov, A. N., Carrasco, L., et al. 2001, A&A, 376, 775, https://doi.org/10.1051/0004-6361:20011011

Shaw, M. S., Romani, R. W., Cotter, G., et al. 2012, ApJ, 748, 49, https://doi.org/10.1088/0004-637X/748/1/49

Smith, P. S., Montiel, E., Rightley, S., et al. 2009, arXiv:0912.3621, https://doi.org/10.48550/arXiv.0912.3621

Stroh, M. C. & Falcone, A. D. 2013, ApJS, 207, 28, https://doi.org/10.1088/0067-0049/207/2/28

Urry, C. M. & Padovani, P. 1995, PASP, 107, 803, https://doi.org/10.1086/133630

Vestergaard, M. & Peterson, B. M. 2006, ApJ, 641, 689, https://doi.org/10.1086/500572

Yuan, Y. H., Zheng, Y. G., Fan, J. H., et al. 2022, PASP, 134, 044102, https://doi.org/10.1088/1538-3873/ac5b88

Zhang, Z.-X., Du, P., Smith, P. S., et al. 2019, ApJ, 876, 49, https://doi.org/10.3847/1538-4357/ab1099

Alfredo Amador-Portes, Vahram Chavushyan, and Victor M. Patiño-Alvarez: Instituto Nacional de Astrofísica, Óptica y Electrónica, Luis Enrique Erro #1, Tonantzintla, Puebla, México, C.P. 72840 (aamador, vahram, victorp@inaoep.mx).

Victor M. Patiño-Alvarez: Max-Planck-Institut für Radioastronomie, Auf dem Hügel 69, D-53121 Bonn, Germany.

Revista Mexicana de Astronomía y Astrofísica, **60**, 323–341 (2024)

https://doi.org/10.22201/ia.01851101p.2024.60.02.10

THE CAVITY PROJECT: SPATIALLY-RESOLVED AND CHARACTERISTICS PROPERTIES OF GALAXIES DERIVED USING `pyPipe3D`

S. F. Sánchez[1,2], R. García-Benito[3], R. González Delgado[3], A. Conrado[3], I. Perez[4,5], A. Z. Lugo-Aranda[1], L. Sánchez-Menguiano[4,5], T. Ruiz-Lara[4,5], A. Jiménez[4], S. Duarte Puertas[4,5,6], J. Domínguez-Gómez[4,5], G. Torres-Ríos[4], M. Argudo-Fernández[4,5], G. Blázquez-Calero[3], Manuel Alcázar-Laynez[4], S. Verley[4,5], D. Espada[4,5], U. Lisenfeld[4,5], A. Zurita[4,5], E. Florido[4,5], B. Bidaran[4,5], P. Villalba-González[7], A. Ferré-Mateu[2,8], P. M. Sánchez Alarcón[2,8], J. Román[2,8], I. del Moral-Castro[9], and F. Agüi[10]

Received April 30 2024; accepted June 12 2024

ABSTRACT

We present the analysis using `pyPipe3D` of a sample of 208 galaxies from the CAVITY project (Pérez et al. 2024), that includes: (i) a description of the processes performed by this pipeline, (ii) the data model adopted to store the spatially resolved properties, and (iii) a catalog comprising integrated and characteristics properties, and the slope of radial gradients for various observational and physical parameters determined for each galaxy. We elucidate the analysis outcomes by (i) presenting the spatial distribution of various derived parameters for a representative galaxy, CAVITY66239, and (ii) exploring the integrated extensive and intensive scaling relations that rule star-formation for this galaxy sample, comparing with results from the literature. The individual galaxy data products for the galaxies featured in the inaugural data release of the CAVITY project, along with the catalog described in this article, are available at the 1st Data Release web page.

RESUMEN

Presentamos el análisis utilizando pyPipe3D en una muestra de 208 galaxias del proyecto CAVITY (Pérez et al. 2024), que incluye: (i) una descripción de los procesos realizados por este dataducto, (ii) el modelo de datos adoptado para almacenar las propiedades espacialmente resueltas, y (iii) un catálogo que comprende propiedades integradas y características, y la pendiente de gradientes radiales para varios parámetros observacionales y físicos determinados para cada galaxia. Ilustramos los resultados del análisis (i) presentando la distribución espacial de varios parámetros derivados para una galaxia representativa, CAVITY66239, y (ii) explorando las relaciones de escala integradas extensivas e intensivas que regulan la formación estelar para esta muestra de galaxias, comparadas con resultados de la literatura. Los productos de datos individuales para las galaxias incluidas en el lanzamiento inaugural de datos del proyecto CAVITY, junto con el catálogo descrito en este artículo, están disponibles en la página web del 1st Data Release.

Key Words: galaxies: evolution — galaxies: fundamental parameters — galaxies: resolved properties — galaxies: star formation — techniques: imaging spectroscopy

1. INTRODUCTION

The Calar Alto Void Integral-field Treasury Survey (CAVITY Pérez et al. 2024) is an ongoing legacy

[1]Universidad Nacional Autónoma de México, Instituto de Astronomía, AP 106, Ensenada 22800, BC, México.

[2]Instituto de Astrofísica de Canarias, Vía Láctea s/n, 38205, La Laguna, Tenerife, Spain.

[3]Instituto de Astrofísica de Andalucía (IAA/CSIC).

[4]Facultad de Ciencias (Edificio Mecenas), Departmento de Física Teórica y del Cosmos, Universidad de Granada, E-18071 Granada, Spain.

[5]Instituto Carlos I de Física Teórica y computacional, Universidad de Granada, E-18071 Granada, Spain.

[6]Département de Physique, de Génie Physique et d'Optique, Université Laval, and Centre de Recherche en Astrophysique du Québec (CRAQ), Québec, QC, G1V 0A6, Canada.

[7]Department of Physics and Astronomy, University of British Columbia, Vancouver, BC V6T 1Z1, Canada.

[8]Departamento de Astrofísica, Universidad de La Laguna, E-38206, La Laguna, Tenerife, Spain.

[9]Instituto de Astrofísica, Facultad de Física, Pontificia Universidad Católica de Chile, Campus San Joaquín, Av. Vicuña Mackenna 4860, Macul, 7820436, Santiago, Chile.

[10]Centro Astronómico Hispano en Andalucía, Observatorio de Calar Alto, Sierra de los Filabres, 04550 Gérgal, Almería, Spain.

project by the Calar Alto Observatory. Its goal is to collect detailed observations of ≈300 galaxies found in empty spaces of the Universe, known as voids, using the PMAS/PPaK instrument located on the 3.5m telescope at Calar Alto, the same used by the CALIFA project (e.g. Sánchez et al. 2012). CAVITY aims to understand how galaxies grow and what their stars and gas are like in these lonely parts of space, helping to estimate how being in such an empty environment affects the birth and growth of a galaxy.

The CAVITY project has already observed a total of 208 galaxies during the last three years, completing ≈70% of the foreseen sample. Early exploration using SDSS single spectroscopy (York et al. 2000) of the entire parent sample from which this observed sub-sample was drawn has already provided some interesting results. Domínguez-Gómez et al. (2023b) managed to trace back the history of star formation in galaxies living in different environments, like clusters, filaments and walls of galaxies, and the voids. They found that galaxies in voids take longer to build up their mass. In Domínguez-Gómez et al. (2023a) it was explored how the stellar metallicity of galaxies changes depending on their location. They discovered that galaxies in voids tend to have slightly less metals compared to those in denser areas, especially the smaller galaxies. In particular, they found a noticeable difference in metal content between void galaxies and those in clusters.

More recently, Conrado et al. (2024) delved deeper into the characteristics of galaxies in voids by exploring, for the first time, the spatially resolved properties of the stellar populations in a sub-sample of the CAVITY dataset, including the mass, age, star formation rate (SFR), and specific star formation rate (sSFR), both overall and relative to their distance from the center of the galaxy. They compared their results to similar analyses of galaxies located in denser environments, like filaments and walls, using data from the CALIFA survey. They found that galaxies in voids tend to have lower stellar mass surface density, younger ages, and higher values of SFR and sSFR. Many of these differences appear in the outer parts of spiral galaxies ($R > 1R$e), which are younger and have higher sSFR than galaxies in filaments and walls, indicating that their disks are less evolved. Large variations also occur for early-type spirals, which points to a slower transition from star-forming to quiescent galaxies in voids.

Following a similar approach adopted in previous Integral Field Spectroscopy (IFS) galaxy surveys (e.g. Sánchez et al. 2022), we describe in this paper the data products of the analysis for the CAVITY IFS dataset using the `pyPipe3D` pipeline (Lacerda et al. 2022). `pyPipe3D` is a recently updated version of `Pipe3D` fully coded in `Python`. The `Pipe3D` pipeline makes use of the routines and algorithms included in the `FIT3D` package (Sánchez et al. 2016c), with the main goal of extracting the properties of the ionized gas and the stellar component of an observed galaxy using its IFS data in the optical range. `Pipe3D` has been extensively used to explore the data from different surveys: e.g., CALIFA (Sánchez-Menguiano et al. 2016; Espinosa-Ponce et al. 2020), SAMI (Sánchez et al. 2019b), AMUSING++ (Sánchez-Menguiano et al. 2018; López-Cobá et al. 2020) and MaNGA (Sánchez et al. 2018, 2022).

This article is organized as follows: § 2 provides an overview of the dataset under investigation, including a brief summary of the observations and data reduction process; § 3 outlines the selection criteria and the main properties of the sample; the analysis performed on the data is described in § 4, including a summary of the main procedures included in the adopted Pipeline (§ 4.1), a description of the procedures to derive the provided physical quantities (§ 4.3), and how the integrated and characteristics properties are estimated (§ 4.4); the results of this analysis are presented in § 5, including a description of the data model adopted for the final delivered data products (§ 5.1), and the catalog of parameters extracted for each galaxy (§ 5.2); an example of the use of the derived parameters, exploring the global intensive and extensive relations that rule star-formation in galaxies, is included in § 5.3; finally, the summary and conclusions of this study are presented in § 6.

Throughout this study, when necessary, we assumed a standard Λ Cold Dark Matter cosmology with the following parameters: H_0=71 km/s/Mpc, Ω_M=0.27, Ω_Λ=0.73.

2. OBSERVATIONS AND DATA REDUCTION

Observational data were acquired using the 3.5m telescope located at the Calar Alto Observatory, employing the Potsdam Multi-Aperture Spectrometer (PMAS) in its PPaK configuration, as detailed by Roth et al. (2005) and Kelz et al. (2006), respectively. The PPaK configuration incorporates a 382 fiber bundle, effectively covering a field of view measuring 74″ by 64″. Each fiber, positioned in an hexagonal layout, possesses a diameter of 2.7″ on the sky, achieving a filling factor of 60%. This configuration is augmented by six peripheral bundles, each comprising six fibers, dedicated to sampling the sky background at the edges of the field of view. Through the application of a three-position dithering pattern, the filling factor is enhanced to 100%, resulting in data cubes with dimensions of 78 by 73 pixels, where each pixel corresponds to a spatial area of 1″ by 1″. These observations were conducted in the V500 low-resolution mode, yielding a resolution of approximately R ≈850 at 5000 Å with a full width at half maximum (FWHM) of roughly 6 Å.

The wavelength span for this observational mode extends from 3745 to 7500 Å, with a spectral sampling interval of 2 Å.

The data reduction pipeline of the CAVITY project is built on the techniques and procedures developed to reduce the data from the IFS observations (Sánchez 2006) and, in particular, those implemented to handle the data from the CALIFA survey (Sánchez et al. 2016a), introducing the required modifications to meet the particular needs of the CAVITY project. The pivotal steps included in the pipeline are summarized here: (i) pre-processing of the raw data to consolidate reads from different amplifiers into a single frame, removing bias, adjusting for gain, and cleaning cosmic rays; (ii) identification and tracing of spectra from various fibers on the CCD, determining the FWHM of the projected spectra along both dispersion and cross-dispersion axes; (iii) spectra extraction using the previously estimated trace and widths, with a removal of stray-light effects; (iv) wavelength calibration and resampling to achieve a linear wavelength scale (2Å per spectral pixel); (v) homogenization of spectral resolution across wavelengths, setting a final resolution of FWHM = 6Å; (vi) correction for differential fiber-to-fiber transmission; (vii) flux calibration of the spectra; (viii) separation of science fibers (covering the central hexagonal area) from sky-sampling fibers, and subtraction of a night-sky spectrum for each dither point; (ix) combining the three dither points into a single spectral frame with an associated position table; (x) generation of a final data cube using the image reconstruction procedure described in García-Benito et al. (2015), in which the X and Y coordinates correspond to the location in the sky and the Z coordinate to the wavelength. Pérez et al. and García-Benito et al. are preparing a more comprehensive discussion of this pipeline, which will be detailed in the upcoming CAVITY presentation paper and DR1 paper.

3. SAMPLE

The CAVITY project mother sample includes 4866 galaxies located within 15 specifically chosen voids, as identified in the comprehensive void galaxy catalog by Pan et al. (2012), which catalogued 79,947 galaxies across 1,055 voids. These 15 voids were intentionally selected to represent a variety of sizes and dynamical states. The galaxies within this primary sample are part of the nearby Universe, with redshift values between 0.005 and 0.05, and cover a broad spectrum of masses, ranging from $10^{8.5}$ to 10^{11} $M_{\odot}$. The mass estimates for these galaxies were derived using the mass-to-light ratio from the color technique, as detailed by McGaugh & Schombert (2014). To be included in the sample, galaxies had to meet specific criteria: they must be located within 80% of the effective radius of their respective void; each void should have at least 20 galaxies along its radius for adequate sampling; and the galaxies' distribution in right ascension must facilitate year-round observability.

This sample is far too large to be observable in a reasonable time. Like in the case of other IFS (e.g. CALIFA, MaNGA Sánchez et al. 2012), we used that sample as a pool of possible targets from which the actual galaxies to be observed were picked randomly according to their visibility on the allocated nights. In this way the observed sample should be a randomly selected sub-sample of the mother sample, being completely representative of the sample from which it was selected. This statement should be checked *a posteriori*, characterizing the possible deviations introduced during the object picking and observing process. Based on the range of parameters to be sampled it was estimated that observing ≈20 galaxies per void should be enough to achieve the goals of the project. Thus, the final observed sample is foreseen to comprise a total of ≈300 galaxies. The full procedure and the details of the properties for the foreseen observed sample was described in detail in the CAVITY presentation article (Pérez et al. 2024).

The sample analyzed in this study comprises 208 galaxies (i.e., ≈2/3 of the finally foreseen sample). Of them, 199 correspond to all the galaxies observed by the CAVITY project up to November 2023. Nine additional galaxies were extracted from the Voids Galaxy Survey (VGS) by Kreckel et al. (2011). These galaxies were observed using an identical instrument and settings as the CAVITY project during 2019 and 2020, effectively acting as a preliminary study. Of them, four targets already fulfill the CAVITY selection criteria, being part of the mother sample. On the contrary, the remaining five are not directly associated with any of the voids identified in the CAVITY project. Nevertheless, they were all included in our analysis. Finally, we should highlight that we are not distributing the full analyzed dataset, but only those galaxies included in the CAVITY DR1. The remaining data products will be liberated in the successive data releases of the project.

To illustrate which kind of galaxies are explored by the CAVITY project we compare their properties with those of galaxies covered by previous surveys, in particular their absolute magnitudes, colors and morphology. To do so we derive the synthetic magnitudes in the rest-frame directly from the reduced data cubes by convolving the redshifted SDSS-filters (Gunn et al. 2006) with the data cubes and applying the zero-point corresponding to the AB-photometric system. Then, using the standard cosmology, and without any K-correction, we derive the corresponding absolute magnitudes. Finally, following Conrado et al. (2024) we adopted the morphologi-

cal classification provided by Domínguez Sánchez et al. (2018). To assign a Hubble classification, we utilized the T-Type parameter described by de Vaucouleurs (1963), separating between E and S0 following the prescriptions described in Domínguez Sánchez et al. (2018, 2022).

Figure 1 presents the color-magnitude diagram (CMD), $g-r$ color against the r-band absolute magnitude, for the analyzed sub-sample. For comparison purposes we include the same distibution for the extended CALIFA sample (eCALIFA, Sánchez et al. 2023b) and a sub-sample of galaxies extracted from the NASA Sloan Atlas (SDSS-NSA, Blanton et al. 2017) that resembles a diameter selected sub-sample at the redshift footprint of eCALIFA (Sánchez et al. 2023b). It is evident that while the eCALIFA sample effectively spans through the CMD, covering a similar range of magnitudes and colors as a diameter selected sample at a similar redshift, the CAVITY sub-sample covers a much narrower range of magnitudes and colors. Low-luminosity (M_r >-18 mag) and extremely red objects ($g-r$ >0.8 mag), are practically absent in the analyzed sub-sample. If we compare these distributions with those shown in Conrado et al. (2024), comparing with the CAVITY mother sample, it seems that the origin of the bias is in the observed sub-sample, not in the original selection.

Additional differences are found in the morphological distribution, included as an inset in Figure 1. As already noticed by Conrado et al. (2024) for the CAVITY project, and in previous explorations of the properties of galaxies in Voids (e.g. Rojas et al. 2004; Kreckel et al. 2011), there is an excess of late-type spirals, in particular Sc, when comparing to field galaxies. This is true, even considering that eCALIFA has an over-representation of earlier type spirals, Sb-type (e.g. Sánchez et al. 2023b). Another difference is the apparent lack of Sd galaxies in the CAVITY sample. However, we should be cautious before drawing a clear conclusion in this regard, as a possible bias against this particular morphological type in the classification presented by Domínguez Sánchez et al. (2018) has been reported.

4. ANALYSIS

Following the methodologies outlined by Sánchez et al. (2022, 2024a), we embarked on a detailed examination of our dataset to uncover the core features and overall properties of each galaxy within it. By leveraging the `pyPipe3D` pipeline on every data cube, we were able to discern the spatially resolved characteristics as well as the integrated aspects of these cosmic structures. This process involved the careful analysis of the outputs of the pipeline to distill a variety of physical measurements.

In this summary, we briefly outline the essence of our analytical process and the main findings derived from it.

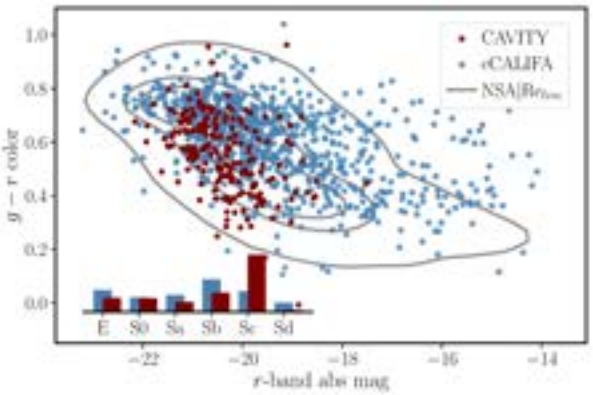

Fig. 1. Distribution in the $g-r$ vs. $r-$band absolute magnitude diagram of the CAVITY galaxies (maroon solid-circles), compared to the same distribution for eCALIFA galaxies (blue solid-circles) and a sub-sample of SDSS-NSA galaxies selected using the same diameter, magnitude and redshift range as the eCALIFA compilation (grey contours). Each successive contour encircles a 95%, 65% and 40% of the SDSS-NSA galaxies. The bottom-left inset shows the morphological distribution of the CAVITY and eCALIFA galaxies. The color figure can be viewed online.

For a more detailed discussion and to avoid redundancy, we refer readers to our earlier works, particularly those by Sánchez et al. (2016b, 2022, 2024a), where we explore these topics in greater depth.

4.1. `pyPipe3D` *Analysis*

In our analysis, we employ `pyPipe3D` (Lacerda et al. 2022), an updated version of the `Pipe3D` pipeline (Sánchez et al. 2016b). This version has been re-coded in Python, leveraging the advanced computational capabilities of this programming language to enhance performance, streamline the analysis sequence, and address any bugs identified in previous versions. `Pipe3D` is a robust and well-established tool, extensively applied in the analysis of Integral Field Spectroscopy (IFS) data across a wide array of data sets. Notably, it has contributed to significant insights within the CALIFA survey (e.g., Cano-Díaz et al. 2016a; Espinosa-Ponce et al. 2020), the MaNGA project (e.g., Ibarra-Medel et al. 2016; Barrera-Ballesteros et al. 2018; Sánchez et al. 2019a; Bluck et al. 2019; Sánchez-Menguiano et al. 2019), the SAMI Galaxy Survey (e.g., Sánchez et al. 2019b), and the AMUSING++ compilation (Sánchez-Menguiano et al. 2018; López-Cobá et al. 2020).

Furthermore, the efficiency and accuracy of the pipeline have been rigorously vetted through analyses involving mock data sets and specialized simulations designed around hydrodynamical models (Guidi et al. 2018; Ibarra-Medel et al. 2019; Sarmiento et al. 2023). Here,

we provide only a concise summary of the functionality of the code to prevent duplicate content.

4.1.1. *Spatial Binning/Tessellation*

The `pyPipe3D` pipeline uses the `pyFIT3D` package to automatically analyze each data cube. To get accurate results for the stellar population analysis, it is important to increase the signal-to-noise ratio (S/N). This is done by grouping nearby pixels together in a process called spatial binning, which `pyPipe3D` does in a way that keeps the original light pattern of the galaxy as intact as possible (see Sánchez et al. 2016c; Lacerda et al. 2022, for more details). After binning, the software analyzes these grouped pixels to learn about the properties of the stellar population and the ionized gas in each region of the galaxy.

4.1.2. *Stellar Population Analysis*

As we mentioned before, each grouped (or binned) spectrum is analyzed by `pyFIT3D`. This part of the process separates the light coming from stars from the light coming from ionized gas in each part of the galaxy. To estimate the spectra corresponding to the stellar population, `pyFIT3D` creates a model using a mix of different single stellar populations (SSP) templates from the MaStar_sLOG library. This library has 273 templates, covering 39 different ages of stars (from 1 Myr to 13.5 Gyr, following a logarithm scale) and 7 values of metallicity ($Z/Z_{\odot}$ = 0.006, 0.029, 0.118, 0.471, 1, 1.764, 2.353). This library was selected from a large set of SSP templates created with an updated version the GALAXEV stellar population synthesis code (Bruzual & Charlot 2003), adopting a Salpeter initial mass function (Salpeter 1955) and using the `PARSEC` isochrones (Bressan et al. 2012) and the MaStar empirical stellar library (Yan et al. 2019) as basic ingredients. For more details on how we picked these particular sub-set of templates, see Appendix A, in Sánchez et al. (2022).

Before making the model, the SSP templates are adjusted to match the speed at which the galaxy is moving towards or away from us (systemic velocity) and how spread out the speeds of the stars in the galaxy are (velocity dispersion). We also consider how dust in the galaxy might be dimming the star light (dust attenuation) using the formula from Cardelli et al. (1989).

After adjusting the SSPs for kinematics, spread, and dust effects, we fit them to the spectra of the galaxy. This is done through a step-by-step process, as described in Sánchez et al. (2016c) and Lacerda et al. (2022), where we keep adding or removing templates to get the best match. To do so we perform a linear combination of the adjusted templates, starting with all the templates in the library. Then, from each iteration all those templates that contribute with a negative coefficient are removed from the library. The goal is to mix only those templates that contribute with a positive coefficient. The procedure stops once this goal is reached. Several iterations are performed perturbing the original spectrum by the error, ending up with several (different) realizations of the fitting.

This iterative procedure is performed twice. First, a limited SSP library is adopted with just 12 templates selected to avoid degenerancies between the stellar parameters (age and metallicity) and non-linear parameters that describe the kinematics (velocity and velocity dispersion) and dust attenuation. This template is adopted in the exploration of these three non-linear parameters, performing a brute-force exploration of the space of parameters. Then, we fix these three parameters, readjust the full library according to them, and re-analyze the spectrum.

The average (standard-deviation) of the positive coefficients derived in each iteration described before weights the (error of the) contribution of each SSP to the observed spectrum. The sum of all the SSPs in the library weighted by those coefficients is the final model. This spectral model is then matched to the flux intensity in a specific part of the spectrum (5450-5550Å, which is in the range of what we call the V-band). In this procedure the strongest emission lines are first masked. Then, once their contribution is estimated as we will describe in the next section, it is removed from the original spectrum and the derivation of the stellar model is repeated. This procedure could be iterated several times until converging to a stable solution.

Finally `pyFIT3D` derives the luminosity- and mass-weighted parameters of the stellar population (LW and MW) using the coefficients of the stellar decomposition, following equation (2) in Sánchez et al. (2024a). In essence an average of the logarithm values of the considered parameters is performed; that is, a geometrical average, weighted by the fraction of light (or mass) that each SSP contributes to the observed spectrum, multiplied by the corresponding value for the considered template. Also, the stellar mass across the considered aperture, using equation (3) in Sánchez et al. (2024a), is estimated by co-adding the mass in each analyzed spatial bin (§ 4.1.1). For each bin the stellar mass is derived by multiplying the dust corrected luminosity assigned to each SSP by the decomposition by its mass-to-light ratio (Υ_{SSP}), and then coadding for all the templates in the adopted library.

4.1.3. *Emission Line Analysis*

To estimate the observational properties of the ionized gas in the galaxy, the software first removes the light coming from the stars, using the best stellar spectrum

model we described in the previous section. What is left is mostly light from the ionized gas. The code then looks at a particular emission line from the ionized gas[11]. Each of these emission lines gets fitted with a Gaussian function, in order to describe their shape, and to derive their velocity dispersion, systemic velocity and integrated flux.

This whole process, working out the stellar and ionized gas component, is iterated, refining each time both models. We use the best guess of the ionized gas spectrum to decontaminate the original spectrum and to create a spectrum that contains only light from the stars, and then we update our emission line model. We improve each model based on how well they fit the actual data we observe, judging the accuracy of the model by the best χ^2.

The described process helps us understand the gas emission lines for each tessella or spatial bin. To dig deeper and learn about these emissions for individual pixels (spaxels), we have an extra step. We start by adjusting the best star model we found for each group of pixels to fit each individual pixel inside that group. This adjustment uses a special scaling factor (DZ, Cid Fernandes et al. 2013). Then, we subtract this adjusted star model from the original galaxy data to get a new data set that mainly includes gas emissions, along with some noise and residuals from the stellar model fitting.

Next, to estimate the properties of the gas emissions from this cleaned-up data, we use two approaches. (i) We fit Gaussian models to the brightest and more detectable emissions, as done before. (ii) We use a method that weighs different parts of the emissions to study both the strong and the faint ones, giving us a fuller picture. This second method not only tells us about the flux intensity (F_{el}), velocity (v_{el}), and velocity dispersion (σ_{el}) of these emissions but also measures how much light they emit compared to the background stellar component (i.e, the equivalent width, EW_{el}). The complete list of emission lines we looked at with this method were already published in Table 7 of Sánchez et al. (2024a).

4.1.4. *Stellar Indices*

Moreover, `pyPipe3D` calculates various stellar indices for each pixel group (voxel/tessella) in the data. First, it creates a stellar spectrum that is cleaned of any effect from gas emissions. This is done by removing the best gas emission model found earlier. Then, for each stellar index (which is a way of measuring specific features in the stellar spectrum), it looks at three different sections of the spectrum: (i) the main part where the stellar index is defined, and (ii) two side sections that help estimate the background light level. The list of stellar indices we specifically looked at in this study is included in Table 4 of Sánchez et al. (2024a).

4.1.5. *Error Estimation*

To make sure we know how accurate our findings are, we used the Monte Carlo (MC) method to estimate the errors for all the measured parameters. We take the original spectra for each spaxel (or each group of spaxels that have been binned together) and add random noise based on the uncertainties estimated during the data reduction. This gives us a set of 50 slightly altered versions of our original data.

Next, we go through the whole analysis process again for each of these tweaked versions. By looking at how the results vary across these different runs, we can get a good idea of how reliable our original measurements are. We say that the spread of these results (technically, their standard deviation) represents the error of our measurements.

It is important to note that whenever we remove the effects of gas emissions or stellar spectrum from our data to get a clearer look at either one, we also adjust our error estimates. This takes into account any extra uncertainty that might be added by our models of gas emissions or starlight. For a deeper dive into how we estimate these errors, refer to Lacerda et al. (2022).

4.2. *Data Masks*

For each measurement described before we derive the corresponding errors. In particular, the error of the flux intensity help us to decide which parts of the galaxy data present reliable information and which ones do not. Before we group pixels together (a process described in § 4.1.1), we pick out the parts of the data where the flux intensity is stronger than the noise by at least a factor one. This helps us create a "selection mask" that guides us on where to focus our analysis of the properties in the galaxy.

We also make another mask to cover areas that might be messed up by foreground stars. We find these intrusive stars using the catalog of stars from Gaia DR3[12], that has mapped the positions and movements of billions of stars with unprecedented precision. We only consider stars from this catalog that have precise positions, meaning that their position is known five times more precisely than the uncertainty. Around each of these stars, we mask a circle with a radius of 2.5″, avoiding the use of data within those circles.

4.3. *Physical Quantities*

The observational data extracted by `pyPipe3D` for each spaxel or tessella within the data cubes, encompassing both stellar populations and ionized gas emission

[11] For this study, we are looking at [O II]λ3727, Hδ, Hγ, Hβ, [O III]$\lambda\lambda$4959,5007, Hα, [N II]$\lambda\lambda$6548,84 and [S II]$\lambda\lambda$6717,31

[12] `https://www.cosmos.esa.int/web/gaia/dr3`.

lines, serve as the foundation for deriving more physical parameters. The methodologies employed to derive those parameters from the primary observational properties have been thoroughly elucidated in previous articles. For an in-depth understanding of these procedures, readers are encouraged to consult the extensive discussions presented in Sánchez et al. (2021b, 2022, 2024a).

We show here the list of derived parameters and properties to avoid unnecessary repetition: (i) stellar masses ($M_\star$) and stellar mass surface density ($\Sigma_\star$), integrated along the look-back time (i.e., the current values), the value for stellar populations of a particular age, $\mathcal{A}_\star$ (or metallicity, $\mathcal{Z}_\star$), of the integrated up to a certain age of the Universe (i.e. the mass assembly history, MAH); (ii) star-formation at a certain time ($SFR_{ssp,t}$), obtained as the numerical derivative of the MAH, thus based on the stellar population analysis; (iii) chemical enrichment history, i.e., the cummulative metallicity evaluated up to a certain cosmological time ($[Z/H]_t$); (iv) the timescales at which a certain amount of the current accumulated mass is formed (`T%` e.g., T80, time at which 80% of the stellar mass was formed); (v) the metallicity at those time scales (`a_ZH_T%`); (vi) line ratios that are commonly utilized to ascertain the characteristics of the ionizing sources and to understand the physical properties of the ionized gas, including [O II]/Hβ, [O III]/Hβ, [O I]/Hα, [N II]/Hα, [S II]/Hα, and Hα/Hβ; (vii) the ionized gas dust attenuation ($A_{V,gas}$) derived from the Hα/Hβ-line ratio; (viii) oxygen and nitrogen abundances and ionization parameter; a total of 28 oxygen abundances, 3 nitrogen abundances and 4 ionization parameter estimations have been included using different calibrators (the complete list is included in Appendix D and Table 15 of Sánchez et al. 2022); (ix) ionized gas electron density n_e; (x) star-formation rate derived from the dust-corrected Hα luminosity (SFR), and the corresponding SFR surface density (Σ_{SFR}); (xi) molecular gas mass (M_{mol}) derived from the dust attenuation (based on the Hα/Hβ ratio, i.e., $A_{V,gas}$), following Barrera-Ballesteros et al. (2020) and Barrera-Ballesteros et al. (2021), and the corresponding surface density (Σ_{mol}); and finally (xii) velocity to velocity dispersion ratio $\left(\frac{v}{\sigma}_R\right)$ for both the stellar and ionized gas components, and the apparent stellar angular momentum parameter (λ_R) at different deprojected galactocentric distances (R) following Falcón-Barroso et al. (2017). It is important to mention that the spectral resolution of our current data, which has an instrumental broadening of about $\sigma_{inst} \approx 150$ km s^{-1}, is not ideal for determining these kinematic parameters, especially when the velocity dispersion is low.

We should note that, when required the Salpeter (1955) initial mass function is assumed through all the calculations.

4.4. *Integrated, Aperture Limited and Characteristic Properties*

The analysis we have conducted provides a range of parameters for every individual spaxel, tessella, or at a certain distance from the galaxy center. Using these data, we calculate the values of various extensive properties (like stellar mass, $M_\star$, or SFR) at different sizes of areas: the whole galaxy, within 1 effective radius (Re), or in a central region (1.5″ in diameter). For properties that do not depend on the size of the area (intensive properties), such as star density ($\Sigma_\star$), oxygen abundance, or the explored stellar indices, we estimate the azimuthal average values at various distances from the galaxy center. This method follows the approach outlined in previous research by Sánchez (2020), Sánchez et al. (2021b), and Barrera-Ballesteros et al. (2023), which involves drawing elliptical rings around the galaxy center, following the position angle and ellipticity of the galaxy, each one 0.15 Re wide, stretching from the center out to 3.5 Re (or as far as our data go).

For each of these elliptical areas, we calculate the average value of the parameter we are interested in (P_R) along with the standard deviation (e_P_R). We then use these radial profiles to do a linear fit, helping us to understand how these properties change as we move outward from the center. From this fit, we can deduce the value of the parameter at the effective radius of the galaxy (P_{Re}) and how steeply this value changes with radius ($slope\_P$). Previous studies have shown that for many galaxy properties, the value at the effective radius provides a good estimate of the property across the entire galaxy. Additionally, for some intensive properties, we also calculate the values at a central aperture (5″ diameter) of the galaxy and the average across the whole galaxy for a comprehensive view.

5. RESULTS

In this section, we present the findings from the analysis detailed in the previous section. This includes an overview of the data products generated by the analysis, accompanied by illustrative examples that showcase their potential applications in scientific research.

5.1. *Pipe3D Data Model*

The analysis outlined in § 4.1 yields a variety of parameters for each individual spaxel or grouped area (tessella), along with their associated errors. Consequently, for every analyzed data cube, this process generates a collection of maps or 2D arrays for each parameter. These maps are aligned with the astrometry and dimensions of the original data cube . In agreement with the methodologies described in Sánchez et al. (2016b, 2018, 2022), we organize these maps based on the specific analysis that

TABLE 1

DESCRIPTION OF THE PIPE3D FILE

HDU	EXTENSION	Dimensions
0	ORG_HDR	()
1	SSP	(NX, NY, 25)
2	SFH	(NX, NY, 319)
3	INDICES	(NX, NY, 70)
4	ELINES	(NX, NY, 11)
5	FLUX_ELINES	(NX, NY, 432)
6	FLUX_ELINES_LONG	(NX, NY, 1040)
7	GAIA_MASK	(NX, NY)
8	SELECT_REG	(NX, NY)

generated them and store them in a series of 3D arrays or cubes of data products. In this structure, each channel along the z-axis of a cube represents the spatial distribution of a distinct parameter. To facilitate distribution, each of these pyPipe3D data cubes is then saved as an extension within the same FITS file.

For the data examined in this study, the Pipe3D-generated FITS files include nine distinct extensions for each derived file, as described in Table 1. The content of each extension is the following one:

ORG_HDR: An initial extension without data, containing all metadata of the analyzed data cube, especially the astrometric solution (World coordinate system).

SSP: Contains the spatial distributions of the average stellar properties derived from the stellar population fitting (§ 4.1.2): (i) average properties of stellar populations based on SSP template decomposition (like light-weighted and mass-weighted ages and metallicities), (ii) stellar mass and mass-to-light ratio ($\Upsilon_\star$), (iii) non-linear parameters such as velocity ($v_\star$), velocity dispersion ($\sigma_\star$), and dust attenuation ($A_{V,\star}$), and (iv) details on light distribution, binning pattern, and scaling adjustments made during the fitting. Since these analyses are conducted on spatially-binned data cubes, the parameters within each tessella are consistent, except for the original light distribution and scaling factors. An example of the content of this extension of the galaxy CAVITY 662369 is shown in Figure 2. More details are listed in Table 2 of Sánchez et al. (2024a).

SFH: Includes the spatial distribution of the coefficients $w_{\star,L}$ from the fitting of the stellar population with the templates from the adopted SSP library. The first 273 channels of the data cube cover the full spectrum of ages (39) and metallicities (7) outlined in the MaStar_sLOG SSP template. Additionally, the cube includes 39 channels dedicated to the weights associated with each age ($w_{\star,L}$(age)), calculated by summing all $w_{\star,L}$ across the seven metallicities for each age (channels 273 to 311). Moreover, there are 7 channels that capture the weights for each metallicity ($w_{\star,L}$(met)), derived by aggregating all $w_{\star,L}$ for each metallicity across the 39 ages (channels 311 to 318). A description of the content of this extension is included in Table 3 in Sánchez et al. (2024a). Figure 3 visualizes the content of each extension by displaying the spatial distribution of age-related weights, $w_{\star,L}$(age), organized into 10 age categories, for the galaxy CAVITY 66239.

INDICES: Contains the spatial distribution of the stellar indices and their corresponding errors. A total of 33 indices is analyzed. A detailed description of the adopted wavelength to define the indices (and the adjacent continuum) and the procedures is given in detail in Lacerda et al. (2022) and in Sánchez et al. (2024a). An example of the content of this extension is included in Figure 4, showing the stellar indices derived for the galaxy CAVITY 66239.

ELINES: Comprises the properties of the strong emission lines derived by fitting them with a set of Gaussian functions (§ 4.1.3). The extension comprises the velocity and velocity dispersion maps for Hα (usually the strongest emission line in the considered wavelength range), and the flux intensities for the [O II], [O III] 4959,5007, Hβ, Hα, [N II] 6458,6583 [S II]6713,6717, and their corresponding errors. Figure 5 illustrates the content of this extension for the galaxy CAVITY 66239. We should stress that the velocity dispersion is provided in the observed units (Å), without subtracting the value of the instrumental resolution corresponding to the σ of the fitted Gaussian function.

FLUX_ELINES and **FLUX_ELINES_LONG**: These contain the parameters of the emission lines derived using a weighted-moment analysis (§ 4.1.3), for two subsets of emission lines. The first case includes a list of 54 emission lines previously analyzed with Pipe3D for CALIFA data (Sánchez et al. 2016b). The second case uses a larger list of emission lines, with updated rest-frame wavelengths as included in Sánchez et al. (2022), adjusted for the narrower wavelength range of the current data (totaling 130 emission lines). The extension includes four distinct parameters: flux intensity, velocity, velocity dispersion, and equivalent width, along with their corresponding errors. Therefore, there are eight channels designated from I to I + 7N for the N different parameters calculated for the same I emission line. Here, $0 \leq N < 8$ and I ranges from 0 to 53 (for the FLUX_ELINES extension) or up to 130 (for the FLUX_ELINES_LONG extension). Figure 6 provides an illustration of what these extensions encompass, showcasing the four parameters determined for the Hα emission line, along with their respective errors, within the FLUX_ELINES extension, for the galaxy

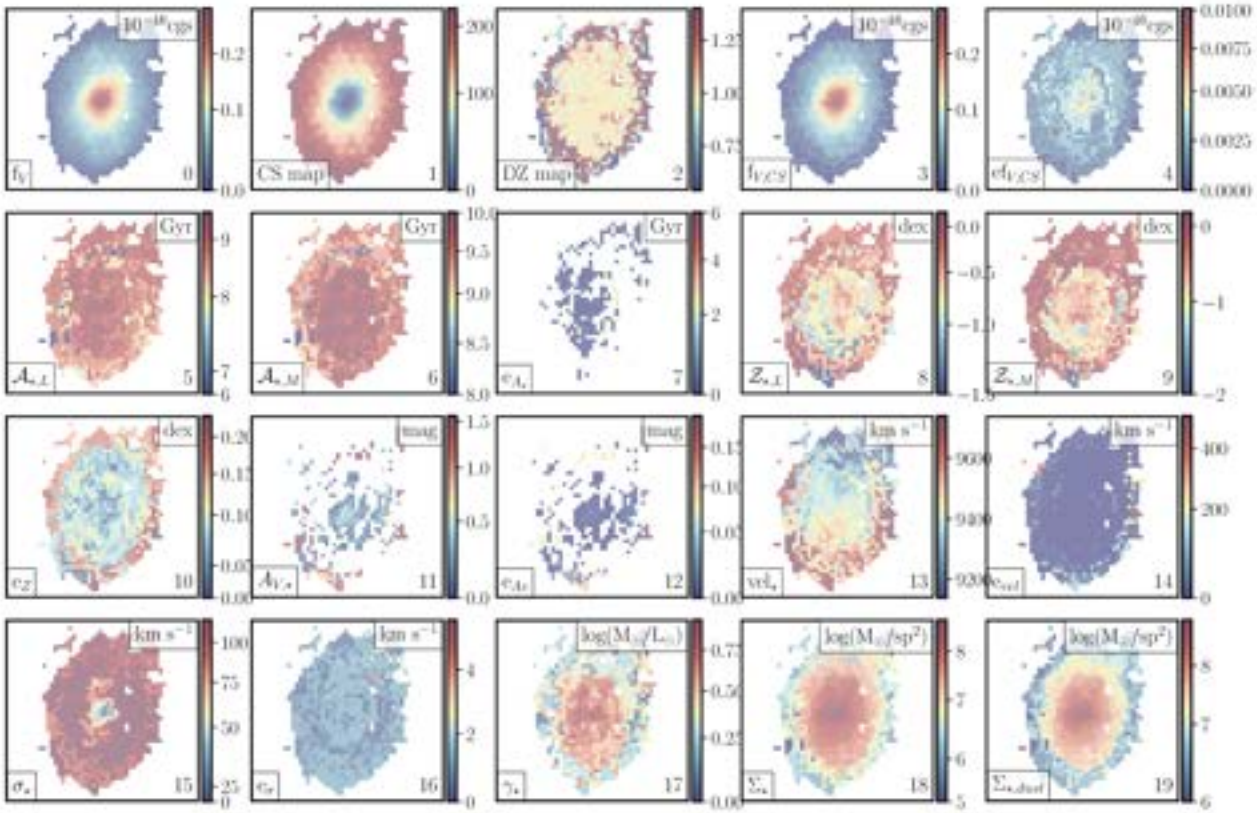

Fig. 2. Example of the content of the SSP extension in the Pipe3D FITS file, corresponding to the galaxy CAVITY66239. Each panel shows a color image with the property stored in the corresponding channel of the data cube, including, from top-left to bottom-right: (i) the flux intensity in the pseudo V-bandv(f_V); (ii) the identification index of each voxel/tessella at which each spaxel is assigned in the binning process (CS map); (iii) the dezonification map, i.e., the ratio between the flux intensity in the V-band at each particular pixel and the average flux intensity within the voxel to which this pixel is assigned (DZ map); (iv) flux-intensity in the V-band after binning the cube spatially (f_{VCS}); (v) standard deviation of the flux-intensity along the wavelength considered to derive the pseudo V-band image, adopted as upper limit of the noise level (ef_{VCS}); (vi) luminosity-weighted age ($\mathcal{A}_{\star,L}$); (vii) mass-weighted age ($\mathcal{A}_{\star,M}$); (viii) error estimated for the LW and MW ages (e$\mathcal{A}_\star$); (ix) luminosity-weighted metallicity ($\mathcal{Z}_{\star,L}$); (x) mass-weighted metallicity ($\mathcal{Z}_{\star,M}$); (xi) error estimated for the LW and MW metallicities (e$\mathcal{Z}_\star$); (xii) dust attenuation derived for the stellar populations ($A_{V,\star}$); (xiii) error estimated for the dust attenuation (e$A_{V,\star}$); (xiv) stellar velocity ($vel_\star$); (xv) error estimated for the stellar velocity (e_{vel}; (xvi) stellar velocity dispersion ($\sigma_\star$); (xvii) error estimated for the velocity dispersion (e_σ; (xviii) average mass-to-light ratio ($\Upsilon_\star$); (xix) stellar mass density ($\Sigma_\star$); (xx) stellar mass density corrected by dust attenuation ($\Sigma_{\star,dust}$). The index, corresponding property, and units, are indicated in each panel as a label at the bottom-right, bottom-left and top-right of the figure. The color figure can be viewed online.

CAVITY 66239. Like in the case of the ELINES extension, the velocity dispersion is provided in the observed units (Å), without subtracting the value corresponding to the instrumental resolution. In the case of the FLUX_ELINES and FLUX_ELINES_LONG the reported quantity corresponds to the FWHM.

GAIA_MASK: A mask of field stars derived from the Gaia catalog as described in § 4.2.

SELECT_REG: A mask of regions with a signal-to-noise ratio greater than 3 in the stellar continuum (V-band), i.e., areas where the analysis of the stellar population is considered reliable.

For each analyzed galaxy (CUBENAME.*V500.rscube.fits.gz*), we provide one of these files, adopting the nomenclature CUBENAME.*Pipe3D.cube.fits.gz*.

5.2. *Catalog of Individual Parameters*

As outlined in § 4.4, guided by the methodologies of Sánchez et al. (2022, 2024a), we calculate a variety of specific parameters for each galaxy. These encompass integrated and aperture-limited values, as well as characteristic parameters (such as those at the effective radius). Additionally, for some parameters, we also determine the slopes of their radial gradients. This process utilizes the

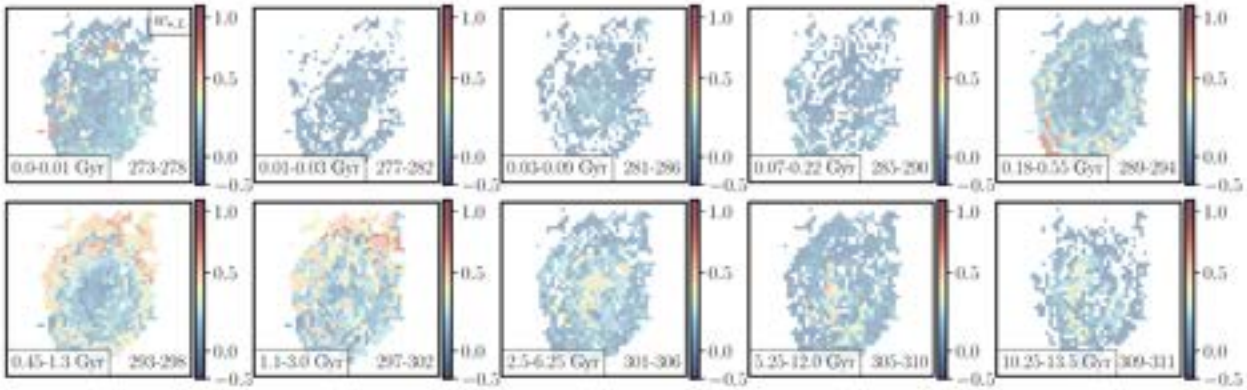

Fig. 3. Example of the content of the SFH extension in the `Pipe3D` fitsfile, corresponding to the galaxy CAVITY66239. Each panel shows a color image with the fraction of light at the normalization wavelength ($w_{\star,\lambda}$) for different ranges of age included in the SSP library. The range of age is indicated in the bottom-left inbox, and the corresponding indices of the co-added channels in the SFH extension are shown in the bottom-right legend. For clarity we do not show the individual $w_{\star,\lambda}$ maps included in the SFH extension. The color figure can be viewed online.

TABLE 2

INTEGRATED AND CHARACTERISTIC PARAMETERS FOR EACH DATA CUBE

#	Param	Units	Description
0	ID	–	Running index
1	cubename	–	CAVITY galaxy (cube) name
2	ra	deg	Right Ascension of the object
3	dec	deg	Declination of the object
4	void	–	Void location of the galaxy
5	TType	–	Hubble Type number
...	...	...	...

For the remaining parameters we refer the reader to Table 2 of Sánchez et al. (2024a).

data contained within each individual `pyPipe3D` file, as detailed in § 5.1, and employs the calculation methods described in Sánchez et al. (2024a). The final catalog, included in the `CAVITY.pyPipe3D.fits` FITs file, comprises 559 parameters. Table 2 lists the first 5 of them; the details of the remaining parameters were already included in Table 2 of Sánchez et al. (2024a). We include here just the first rows that contain the only differences between both tables to avoid repetition. Nevertheless an electronic format of the description of the complete table is provided in the CALIFA 1st DR web page.

5.3. *The Relations that Rule SF*

An example of the use of the content of the delivered data products to explore the global extensive and intensive relations that rule star-formation (SF) in galaxies (Sánchez 2020, for a review on the topic).

5.3.1. *A Brief Introduction to the SF Scaling Relations*

Schmidt (1959) initially proposed a theoretical relation between the star formation rate (SFR) and the gas density within a specific volume. This relation was further examined in Schmidt (1968), but it wasn't until Kennicutt (1998b) that it was articulated in its modern form: a log-log (or power-law) relationship between the SFR surface density ($\Sigma_{\rm SFR}$) and the gas surface density ($\Sigma_{\rm gas}$), representing two intensive parameters independent of galaxy size. Kennicutt (1998a) predicted a slope of approximately 1.4 for this relationship, based on considerations of the free-fall time for a self-collapsing cloud. While originally derived for global intensive parameters, it is now understood to be applicable above the typical scale of large molecular clouds ($\approx$ 500 pc), characterizing spatially resolved sub-galactic structures as well (e.g., the rSK-law; Wong & Blitz 2002; Kennicutt et al. 2007). Both the global and resolved relations exhibit a similar dispersion, around $\approx$ 0.2 dex (Bigiel et al. 2008; Leroy et al. 2013). However, discrepancies in the slope have been observed when compared to theoretical predictions, with contemporary estimations leaning towards a slope of $\approx$ 1 (e.g., Sánchez 2020; Sánchez et al. 2021b).

The relationship between SFR and $\mathbf{M_\star}$ has been more recently uncovered, following analyses of extensive galaxy surveys like the Sloan Digital Sky Survey (SDSS; York et al. (2000)). Known as the star-formation main sequence (SFMS), this tight correlation (dispersion $\approx$ 0.25 dex) between the logarithms of these two quantities, with a slope close to one, is observed exclusively in star-forming galaxies, where ionization is predominantly influenced by young, massive OB stars. It has

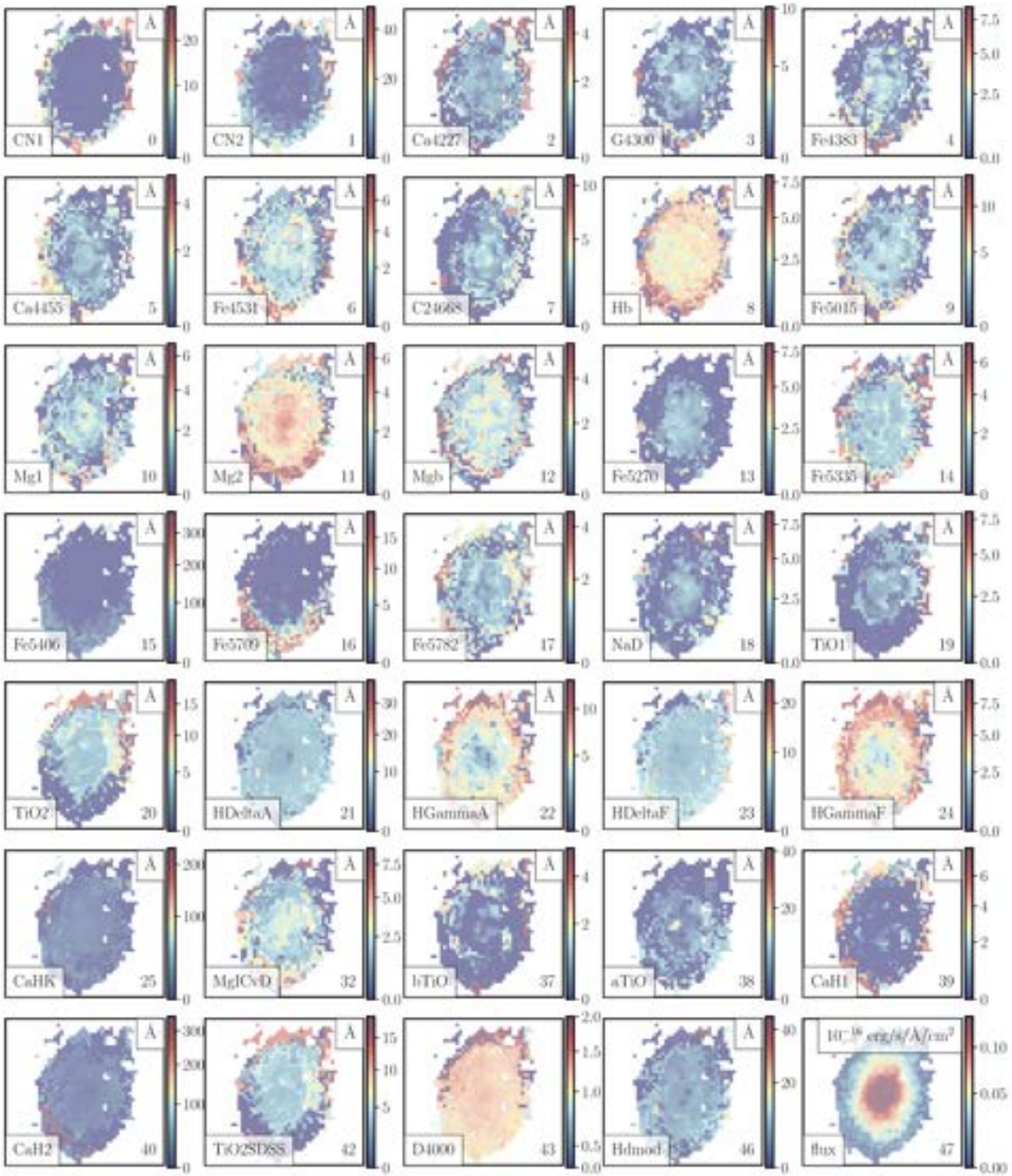

Fig. 4. Example of the content of the INDICES extension in the `Pipe3D` file, corresponding to the galaxy CAVITY66239. Each panel shows a color image with the content of a channel in this data cube. The actual content is indicated for each panel in the lower-left, the channel in the lower-right and the units of the represented quantity in the upper-right legend. The color figure can be viewed online.

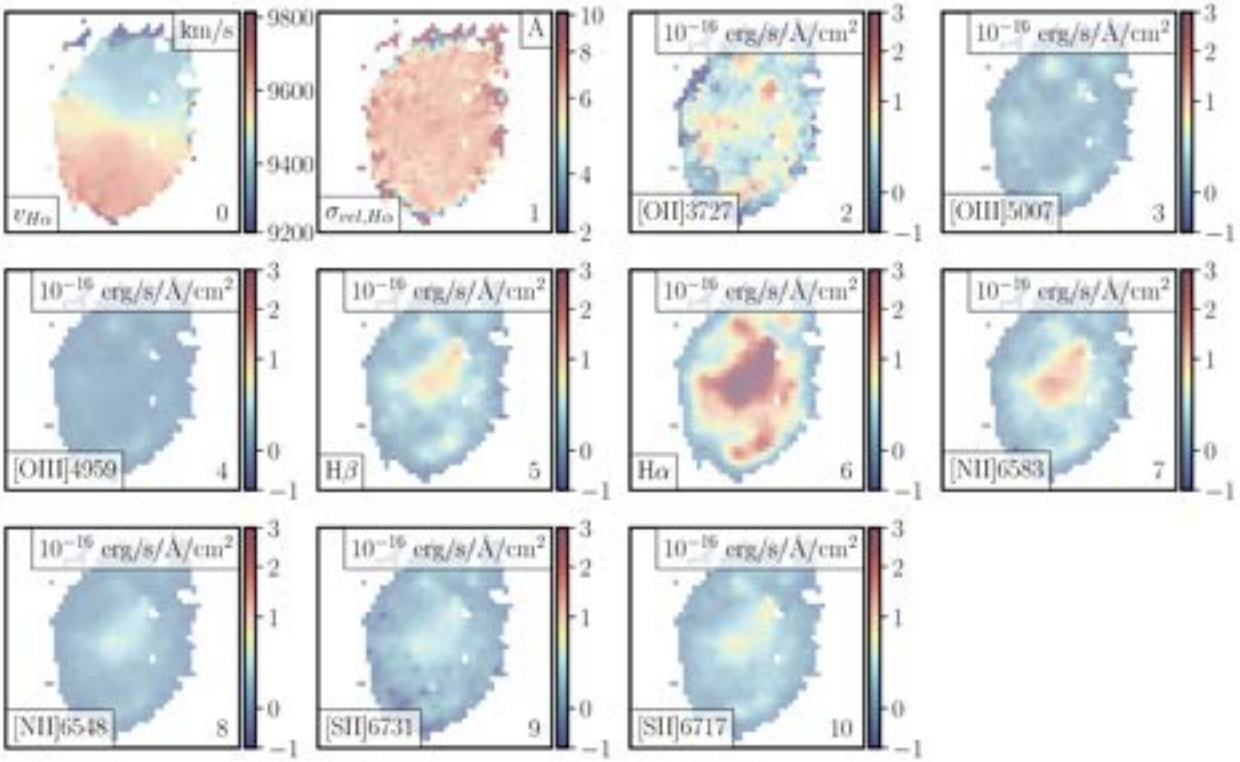

Fig. 5. Example of the content of the ELINES extension in the `Pipe3D` file, corresponding to the galaxy CAVITY66239. Each panel shows a color image with the content of a channel in this data cube. The 1st panel corresponds to the velocity, in km/s, and the 2nd panel to the velocity dispersion, in Å (to transform to km/s, it is required to subtract the instrumental dispersion). The remaining panels represent the distribution of the flux intensities for the different analyzed emission lines (lower-left legend). The color figure can be viewed online.

been detected across a broad spectrum of redshifts in detail particularly in the nearby Universe ($z \approx 0$), but is evident up to redshifts of 1-2 (e.g., Speagle et al. (2014), Rodríguez-Puebla et al. (2016)). The relation demonstrates noticeable evolution, particularly in its zero-point, reflecting the increase in stellar masses and decrease in SFR from early cosmological times to the present. Two nearly simultaneous studies, Sánchez et al. (2013) and Wuyts et al. (2013), introduced the concept of a resolved version of this relation, applicable down to ≈ 1kpc scales, the rSFMS, noted for its tight correlation between the logarithms of Σ_{SFR} and Σ_*. Further investigations, such as that by Cano-Díaz et al. (2016a), utilizing data from the CALIFA survey (Sánchez et al. 2012), have definitively established its characteristics and form. The potential dependency of this relation on other galactic properties, like morphology, has been probed by various authors, (e.g., González Delgado et al. 2016; Catalán-Torrecilla et al. 2017; Cano-Díaz et al. 2019; Méndez-Abreu et al. 2019).

A third correlation, this time between molecular gas and stellar masses in star-forming galaxies (SFGs), has also been delineated (e.g. Saintonge et al. 2016; Calette et al. 2018). Similar to the preceding two, this relationship, dubbed the molecular gas main sequence (MGMS), features a tight correlation with a slope close to one. Its resolved counterpart at the kiloparsec scale, the rMGMS, has been explored more recently (Lin et al. 2019), relating the corresponding intensive parameters: Σ_{gas} versus Σ_*, using a combination of IFS data from the MaNGA survey (Bundy et al. 2015) and CO mapping from the ALMAQUEST compilation (Lin et al. 2020).

Bolatto et al. (2017) first demonstrated that a simple parametrization of the global intensive Schmidt-Kennicutt relation mirrors the distribution observed in the resolved rSK between Σ_{SFR} and Σ_{gas}. Subsequent detailed studies have confirmed this correspondence between the global extensive SFMS and the local/resolved rSFMS (Pan et al. 2018; Cano-Díaz et al. 2019). Finally, it has been established that the global intensive relations (where Σ_{SFR}, Σ_{gas}, and Σ_* are measured as average quantities galaxy-wide) and the local/resolved relations (where these parameters are measured in star-forming regions at

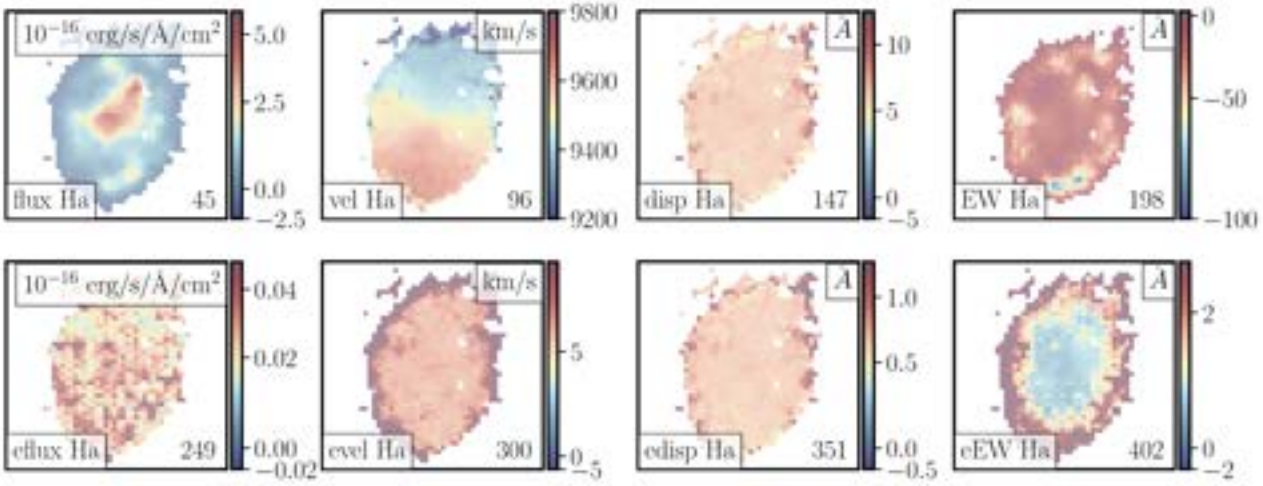

Fig. 6. Example of the content of the FLUX_ELINES extension in the `Pipe3D` file, corresponding to the galaxy CAVITY66239 for one particular emission line (Hα). From top-left to bottom-right the figure shows the flux intensity [10^{-16} erg/s/Å/cm^2], the velocity [km/s], the velocity dispersion, FWHM [Å], the EW Hα [Å], and the corresponding errors. The color figure can be viewed online.

a kpc-scale) exhibit the same distributions, slopes, and similar zero points (e.g. Sánchez et al. 2021b,a, 2023c).

5.3.2. *Selecting SF-Galaxies Using the WHaD Diagram*

We explore here those relations for the analyzed CAVITY sub-sample. To do so we first need to select the star-forming galaxies among them. We depart from the classical approach, frequently adopted in the literature, that uses the classical diagnostic-diagrams that compare pairs of collisionally excited versus Balmer photoionized emission lines (e.g., the BPT diagram that compares [O III]/Hβ vs. [N II]/Hα, Baldwin et al. 1981). Instead, we select the SF galaxies using the recently introduced WHaD diagram, that makes use of the EW and the velocity dispersion of a single emission line, Hα (Sánchez et al. 2024). In this way we illustrate the quality (and useability) of the kinematics analysis performed by `pyPipe3D`.

Following Sánchez (2020); Sánchez et al. (2021b), we consider that a galaxy is actively forming stars if its ionization is dominated by OB-stars at the effective radius, assuming that the values at this galactocentric distance are characteristic of the average properties in a galaxy (González Delgado et al. 2014, 2015). In this way, we extract the following parameters from the delivered catalog, all estimated at 1 effective radius: (i) the flux intensities of [O III], Hβ, [N II] and Hα; (ii) the EW(Hα), and (iii) the velocity dispersion of Ha ($\sigma_{\rm H\alpha}$).

Figure 7 shows the distribution of the analyzed galaxies in the WHaD diagram, color-coded by the [N II]/Hα line ratio. As expected, due to the predominance of late-type (Sc) galaxies in the CAVITY observed sample, most of the galaxies are located in the region associated with star-formation in this diagram. This region corresponds to galaxies with an EW(Hα)>3Å and a $\sigma_{H\alpha}$>57 km s^{-1}, comprising a total of 122 galaxies. These are the SF galaxies (SFGs) that we will use to explore the relations described in the previous section. It can be noticed that most of them present low-values of [N II]/Hα. On the contrary, outside this region, in areas of the WHaD diagram assigned to ionizations due to strong or weak AGNs, the galaxies present larger values of this line ratio, in agreement with the expectations using other more classical diagnostic diagrams such as the WHaN diagram (Cid Fernandes et al. 2010) or the already mentioned BPT diagram. This is illustrated in Figure 7, right panels, which showns the distribution of the full sample (central panel) and SF-sub-sample (right panel) in the BPT diagram. It is evident that the galaxies selected using the WHaD diagram are found in the classical location of HII-regions, dominated by photoinization by OB-stars (e.g. Osterbrock 1989). After applying these criteria we end up with 122 star forming galaxies out of the 208 galaxies analysed.

5.3.3. *Extensive and Intensive Scaling Relations*

Once the SFGs were selected, we followed the methodology outlined by Cano-Díaz et al. (2019) to examine the global extensive relationships among the three extracted parameters (SFR, M_*, and $M_{\rm gas}$), analyzing the distribution and relationship between SFR-M_* (SFMS), $M_{\rm gas}$-M_* (MGMS), and SFR-$M_{\rm gas}$ (SK). Those parameters were derived as described in § 4.3 and are included in the catalog described in § 5.2. Figure 8, top panels,

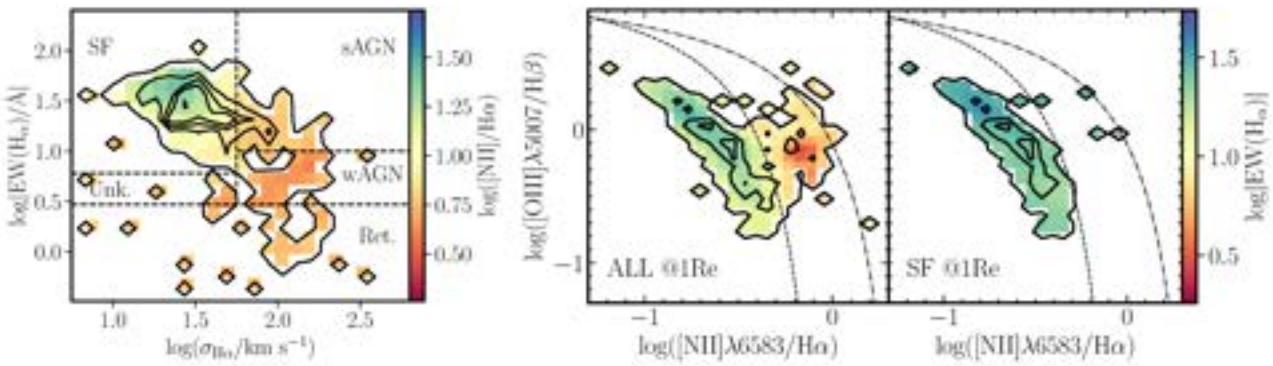

Fig. 7. Diagnostic-diagrams for the analyzed CAVITY sample using emission line values estimated at one effective radius. *Left-panel*: WHaD diagram ($\sigma_{\rm H\alpha}$ vs. EW(Hα)) for the full sample. *Right-panels*: BPT diagram ([O III]/Hβ vs. [N II]/Hα, Baldwin et al. 1981), for the full sample (left) and the SF sub-sample selected using the WHaD diagram (right). In each panel contours represent the density points (encircling 5%, 45% and 85% of the points, respectively), and colors represent the average value of a particular emission line property: [N II]/Hα, in the WHaD diagram, and EW(Hα), in the BPT diagrams. The dashed line in the WHaD diagram represents the boundaries between different ionizations proposed for this diagram, with the different ionizations labeled in each regime. The dotted and dash-dotted lines in the BPT diagram correspond to the demarcation lines usually adopted to distinguish between SF and AGNs, proposed by Kauffmann et al. (2003) and Kewley et al. (2001), respectively. The color figure can be viewed online.

TABLE 3

RESULTS OF THE ANALYSIS OF GLOBAL SF-RELATIONS

Relation	β	α	r_c	$\sigma_{\rm obs}$	$\sigma_{\rm exp}$
SFMS	-9.38±1.36	0.92±0.39	0.73	0.25	0.17
SK	-11.88±1.40	1.26±0.46	0.66	0.26	0.16
MGMS	-1.97±1.62	1.12±0.63	0.66	0.25	0.18
rSFMS	-10.13±0.59	0.97±0.41	0.82	0.31	0.18
rSK	-9.50±0.50	1.02±0.45	0.72	0.31	0.26
rMGMS	-0.81±0.43	1.05±0.32	0.62	0.35	0.28

Zero-point (β) and slope (α) of the three extensive global relations (SFMS, SK and MGMS), and the corresponding intensive ones (rSFMS, rSK, rMGMS) shown in Figure 8. In addition, we include the correlation coefficient (r_c), the standard deviation of the distribution of data before ($\sigma_{\rm obs}$) and after applying the best fitted linear relation ($\sigma_{\rm exp}$).

displays these distributions for the selected SFGs, which show clear linear trends in all three cases, delineating the well-established relations. To parameterize these relationships, we employ a binning strategy on the x-axis and y-axis data, calculating the mean and standard deviation within bins of 0.25 dex. From these two bins the code selects the values that are closer to the peak density. The locations of the final binned data are also illustrated in the respective panels. Subsequently, we conducted a simple linear regression on the binned data to ascertain the best-fitting relation between each pair of parameters. Error estimations were obtained through a Monte-Carlo iteration applied to the original data set, thereby facilitating the propagation of errors for each derived parameter.

Table 3 show the results of this analysis, including the zero-point (β) and slope (α) of the three relations, with their corresponding errors, together with the correlation coefficient (r_c), and the standard deviation of the dependent parameter before ($\sigma_{\rm obs}$) and after applying the best fitted linear relation ($\sigma_{\rm exp}$). In all instances, the slopes approximate unity, being compatible within approximately 1σ with this value. The Schmidt-Kennicutt law (SK-law) exhibits the most significant deviation from this norm.

Following the derivation of the extensive relations, we conducted a subsequent analysis focusing on the global intensive relations ($\Sigma_{\rm SFR}$, Σ_*, and $\Sigma_{\rm gas}$). To calculate these parameters, we adhered to the methodology outlined by Sánchez et al. (2021b) and Sánchez et al. (2023c), involving the division of the respective extensive parameter by the effective area encompassed by each galaxy (defined as $4\pi R_e^2$, that is, the area within two effective radii). Then, we repeated the same binning and fitting procedure. The results are shown in Figure 8, bottom panels, and the derived parameters from the linear regression are included in Table 3. As anticipated, the distributions reveal a clear and tight relationship between the two parameters, displaying correlations that are as strong and almost as tight as those of the extensive ones, accompanied by similar errors for both slopes and zero-points. Moreover, in all instances, the slopes are closer to one, within less than 1σ for the all the relations.

Despite the limited number of galaxies explored in this analysis (≈122 SF-galaxies), and the smaller range of stellar masses sampled, current results agree with the most recent explorations on the topic. For instance, the compilation of values reported by Sánchez et al. (2023c) indicates that the slope of the differ-

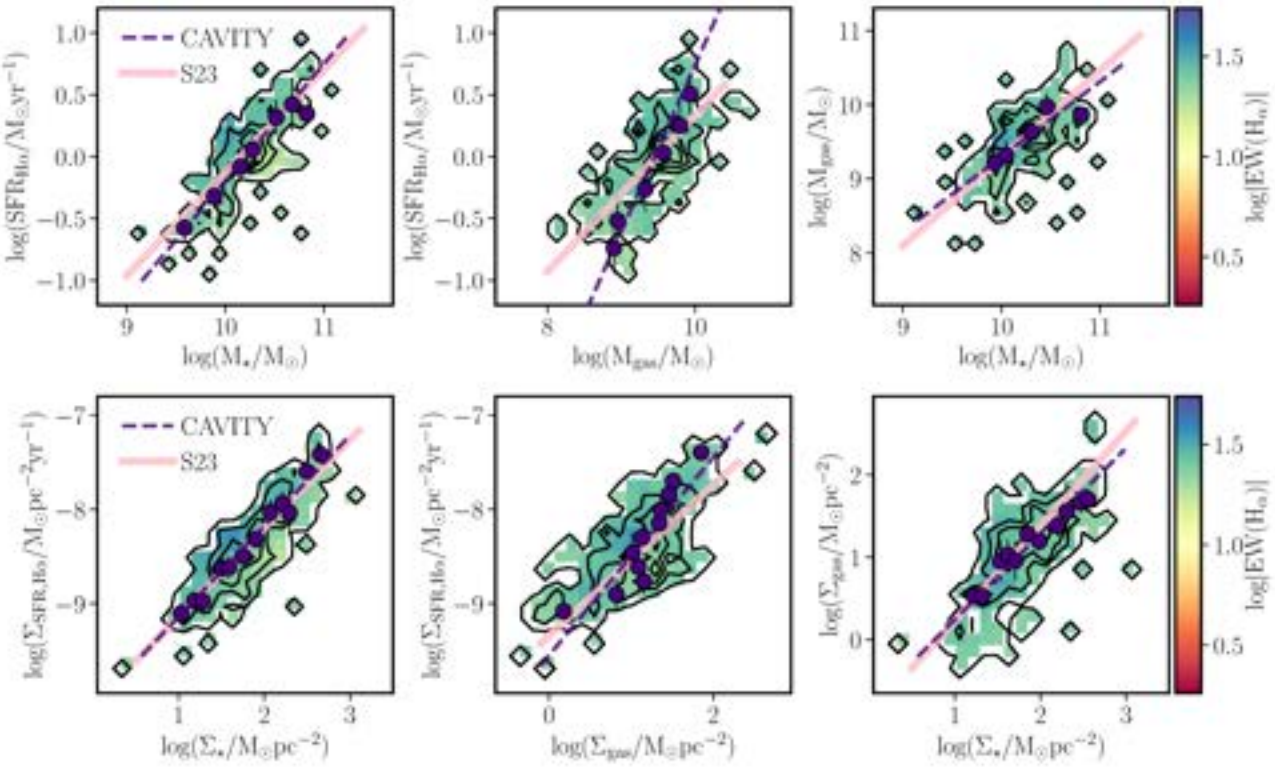

Fig. 8. Global/Integrated extensive (top-panels) and intensive (bottom-panels) relations that rule SF in galaxies. From top-left to bottom-right is shown the distribution of (i) SFR vs. $M_\star$, (ii) SFR vs. M_{gas}, (iii) M_{gas} vs. $M_\star$, (iv) Σ_{SFR} vs. $\Sigma_\star$, (v) Σ_{SFR} vs. Σ_{gas} and (vi) Σ_{gas} vs. $\Sigma_\star$. In each panel contours represent the density points (encircling 5%, 45% and 85% of the points, respectively), and colors represent the average value of EW(Hα). We adopted the same scale range used in Figure 7, to clearly see that all selected galaxies are indeed SFGs. Finally, dark purple circles correspond to a binning that traces the peaks of the density. The dark purple dashed-line represents the best linear relation found for the binned values (labelled as CAVITY), and the pink solid line corresponds to the values reported by Sánchez et al. (2023c) (labelled as S23). The color figure can be viewed online.

ent global intensive relations covers a range of values of (i) 0.74-1.02 (rSFMS), (ii) 0.76-0.98 (rSK) and (iii) 0.73-1.15 (rMGMS), with a typical error of ≈0.11-0.27. Indeed, the zero-points and slopes estimated for the intensive relations match better the values reported in the literature than those estimated for the extensive relation, as appreciated in the comparison included in Figure 8 (in particular for the SK-relation). That is also expected as the dynamical range of the extensive quantities in the observed CAVITY sample is shorter than that covered by other less focused surveys (see Figure 1, for instance), and the derivation of this kind of extensive relation is less accurate. Furthermore, the values reported for the slopes and zero-points are also compatible with the corresponding resolved intensive relations (see Sánchez et al. 2023c, Table 1), in agreement with the results presented by Sánchez et al. (2021a).

6. SUMMARY AND CONCLUSIONS

Throughout this article, we present the spatially resolved spectroscopic properties of galaxies obtained using integral field spectroscopy (IFS) data for the currently observed CAVITY project. When compared with the most recent distributions of similar products, such as the results from the analysis using `pyPipe3D` on the final data release (DR) of the MaNGA IFS galaxy survey (Sánchez et al. 2022) or the eCALIFA survey (Sánchez et al. 2024a), we recognize that both distributions encompass a much larger number of galaxies (≈10,000 and ≈900, respectively). However, none of the surveys sample galaxies directly selected to be located in voids. Therefore, while they may be representative of the bulk population, they lack the ability to determine the potential differences in the evolution and properties of galaxies in these low populated regions of the Universe.

This article details the analysis conducted on this data set. For each galaxy, we provide a single FITS file containing different extensions, each of which includes the spatial distributions of various physical and observational quantities derived from the analysis. We offer a detailed description of each of these extensions, exemplifying their content with the results for the galaxy

CAVITY 66239 as a case study. Additionally, we extract a set of integrated and/or characteristic parameters for each galaxy and, when necessary, the slopes of their radial gradients. In this way, a catalog containing over 550 derived quantities for each object in the dataset is also provided. The delivered data set is restricted to the galaxies distributed in the 1st CAVITY data release, and would be incremented in successive distributions along the life-time of the survey.

The utility of this new set of data products is demonstrated using as examples the global extensive and intensive relations that rule SF galaxy wide, i.e., the (r)SFMS, (r)SK and (r)MGMS relations. To do so we select SFGs using the recently presented WHaD diagram, a novelty that allows us to illustrate the quality of our analysis, not only to recover the flux intensities of the emission lines but also their kinematics properties. Once the SFGs is selected, we examine the described relation characterizing them with a linear relation (between the logarithm of the involved quantities). We find a remarkable agreement with the most recent results in the literature, in particular for the global intensive relations, that exhibit similar shape (slope), strength (correlation coefficients) and tightness (dispersion of the residuals), despite the fact of the nature of the sample (void galaxies) and its limited number (≈122 SFGs).

The comprehensive suite of data products and the catalog of individual quantities are freely available for community use as part of the CAVITY data release for the subset of analyzed galaxies part of the CAVITY DR1.

SFS thanks the PAPIIT-DGAPA AG100622 project and CONACYT Grant CF19-39578. RGB acknowledges financial support from the Grants CEX2021-001131-S funded by MCIN/AEI/10.13039/501100011033, SEV-2017-0709, and to PID2019-109067-GB100. We acknowledge financial support by the research projects AYA2017-84897-P, PID2020-113689GB-I00, and PID2020-114414GB-I00, financed by MCIN/AEI/10.13039/501100011033, the project A-FQM-510-UGR20 financed from FEDER/Junta de Andalucía-Consejería de Transformación Económica, Industria, Conocimiento y Universidades and by the Grants P20_00334 and FQM108, financed by the Junta de Andalucía (Spain). L.S.M. acknowledges support from Juan de la Cierva fellowship (IJC2019-041527-I). TRL acknowledges support from Juan de la Cierva fellowship (IJC2020-043742-I). DE acknowledges support from a Beatriz Galindo senior fellowship (BG20/00224) from the Spanish Ministry of Science and Innovation. PVG acknowledges that the project that gave rise to these results received the support of a fellowship from "la Caixa" Foundation (ID 100010434). The fellowship code is B005800. BB acknowledges financial support from Grant AST22_4.4, funded by Consejería de Universidad, Investigación e Innovación and Gobierno de España and Unión Europea - NextGenerationEU, and by the research project PID2020-113689GB-I00 financed by MCIN/AEI/10.13039/501100011033. SDP acknowledges financial support from Juan de la Cierva Formación fellowship (FJC2021-047523-I) financed by MCIN/AEI/10.13039/501100011033 and by the European Union 'NextGenerationEU'/PRTR, Ministerio de Economía y Competitividad under Grants PID2019-107408GB-C44, PID2020-113689GB-I00, PID2020-114414GB-I00, and PID2022-136598NB-C32, and is grateful to the Natural Sciences and Engineering Research Council of Canada, the Fonds de Recherche du Québec, and the Canada Foundation for Innovation for funding. JR acknowledges funding from University of La Laguna through the Margarita Salas Program from the Spanish Ministry of Universities ref. UNI/551/2021-May 26, and under the EU Next Generation. M.A-F acknowledges support from the Emergia program (EMERGIA20_38888) from Consejería de Universidad, Investigación e Innovación de la Junta de Andalucía. IMC acknowledges funding from ANID programme FONDECYT Postdoctorado 3230653. AFM acknowledges support from RYC2021-031099-I and PID2021-123313NA-I00 of MICIN/AEI/10.13039/501100011033/FEDER, UE, NextGenerationEU/PRT. GTR acknowledges financial support from the research project PRE2021-098736, funded by MCIN/AEI/10.13039/501100011033 and FSE+. PMSA acknowledges Grants PID2019-105602GBI00 and PID2022-136505NB-I00 funded by MCIN/AEI/10.13039/501100011033 and EU, ERDF.

Paper based on observations collected at Centro Astronómico Hispano en Andalucía (CAHA) at Calar Alto, operated jointly by Instituto de Astrofísica de Andalucía (CSIC) and Junta de Andalucía. This paper is based on data obtained by the CAVITY project, funded by the Spanish Ministery of Science and Innovation under Grant PID2020-113689GB-I00.

This paper is (partially) based on data obtained by the CAVITY Survey, funded by the Spanish Ministery of Science and Innovation under Grant PID2020-113689GB-I00.

This research made use of Astropy,[13] a community-developed core Python package for Astronomy (Astropy Collaboration et al. 2013, 2018).

[13] http://www.astropy.org.

REFERENCES

Astropy Collaboration, Price-Whelan, A. M., SipHocz, B. M., et al. 2018, AJ, 156, 123, https://doi.org/10.3847/1538-3881/aabc4f

Astropy Collaboration, Robitaille, T. P., Tollerud, E. J., et al. 2013, A&A, 558, 33, https://doi.org/10.1051/0004-6361/201322068

Baldwin, J. A., Phillips, M. M., & Terlevich, R. 1981, PASP, 93, 5, https://doi.org/10.1086/130766

Barrera-Ballesteros, J. K., Heckman, T., Sánchez, S. F., et al. 2018, ApJ, 852, 74, https://doi.org/10.3847/1538-4357/aa9b31

Barrera-Ballesteros, J. K., Sánchez, S. F., Espinosa-Ponce, C., et al. 2023, RMxAA, 59, 213, https://doi.org/10.22201/ia.01851101p.2023.59.02.06

Barrera-Ballesteros, J. K., Sánchez, S. F., Heckman, T., et al. 2021, arXiv e-prints, arXiv:2101.04683, https://doi.org/10.48550/arXiv.2101.04683

Barrera-Ballesteros, J. K., Utomo, D., Bolatto, A. D., et al. 2020, MNRAS, 492, 2651, https://doi.org/10.1093/mnras/stz3553

Bigiel, F., Leroy, A., Walter, F., et al. 2008, AJ, 136, 2846, https://doi.org/10.1088/0004-6256/136/6/2846

Blanton, M. R., Bershady, M. A., Abolfathi, B., et al. 2017, AJ, 154, 28, https://doi.org/10.3847/1538-3881/aa7567

Bluck, A. F. L., Maiolino, R., Sanchez, S., et al. 2019, arXiv e-prints, arXiv:1911.08857, https://doi.org/10.48550/arXiv.1911.08857

Bolatto, A. D., Wong, T., Utomo, D., et al. 2017, ApJ, 846, 159, https://doi.org/10.3847/1538-4357/aa86aa

Bressan, A., Marigo, P., Girardi, L., et al. 2012, MNRAS, 427, 127, https://doi.org/10.1111/j.1365-2966.2012.21948.x

Bruzual, G. & Charlot, S. 2003, MNRAS, 344, 1000https://doi.org/10.1046/j.1365-8711.2003.06897.x

Bundy, K., Bershady, M. A., Law, D. R., et al. 2015, ApJ, 798, 7, https://doi.org/10.1088/0004-637X/798/1/7

Calette, A. R., Avila-Reese, V., Rodríguez-Puebla, A., Hernández-Toledo, H., & Papastergis, E. 2018, RMxAA, 54, 443

Cano-Díaz, M., Ávila-Reese, V., Sánchez, S. F., et al. et al. 2019, MNRAS, 488, 3929, https://doi.org/10.1093/mnras/stz1894

Cano-Díaz, M., Sánchez, S. F., Zibetti, S., et al. 2016a, ApJ, 821, 26, https://doi.org/10.3847/2041-8205/821/2/L26

Cardelli, J. A., Clayton, G. C., & Mathis, J. S. 1989, ApJ, 345, 245, https://doi.org/10.1086/167900

Catalán-Torrecilla, C., Gil de Paz, A., Castillo-Morales, A., et al. 2017, ApJ, 848, 87, https://doi.org/10.3847/1538-4357/aa8a6d

Cid Fernandes, R., Pérez, E., García Benito, R., et al. 2013, A&A, 557, 86, https://doi.org/10.1051/0004-6361/201220616

Cid Fernandes, R., Stasińska, G., Schlickmann, M. S., et al. 2010, MNRAS, 403, 1036, https://doi.org/10.1111/j.1365-2966.2009.16185.x

Conrado, A. M., González Delgado, R. M., García-Benito, R., et al. 2024, arXiv e-prints, arXiv:2404.10823, https://doi.org/10.48550/arXiv.2404.10823

de Vaucouleurs, G. 1963, ApJS, 8, 31, https://doi.org/10.1086/190084

Domínguez-Gómez, J., Pérez, I., Ruiz-Lara, T., et al. 2023a, A&A, 680, 111, https://doi.org/10.1051/0004-6361/202346884

Domínguez-Gómez, J., Pérez, I., Ruiz-Lara, T., et al. 2023b, Natur, 619, 269, https://doi.org/10.1038/s41586-023-06109-1

Domínguez Sánchez, H., Huertas-Company, M., Bernardi, M., Tuccillo, D., & Fischer, J. L. 2018, MNRAS, 476, 3661, https://doi.org/10.1093/mnras/sty338

Domínguez Sánchez, H., Margalef, B., Bernardi, M., & Huertas-Company, M. 2022, MNRAS, 509, 4024, https://doi.org/10.1093/mnras/stab3089

Espinosa-Ponce, C., Sánchez, S. F., Morisset, C., et al. 2020, MNRAS, 494, 1622, https://doi.org/10.1093/mnras/staa782

Falcón-Barroso, J., Lyubenova, M., van de Ven, G., et al. 2017, A&A, 597, 48, https://doi.org/10.1051/0004-6361/201628625

García-Benito, R., Zibetti, S., Sánchez, S. F., et al. 2015, A&A, 576, 135, https://doi.org/10.1051/0004-6361/201425080

González Delgado, R. M., Cid Fernandes, R., García-Benito, R., et al. 2014, ApJ, 791, 16, https://doi.org/10.1088/2041-8205/791/1/L16

González Delgado, R. M., Cid Fernandes, R., Pérez, E., et al. 2016, A&A, 590, 44, https://doi.org/10.1051/0004-6361/201628174

González Delgado, R. M., García-Benito, R., Pérez, E., et al. 2015, A&A, 581, 103, https://doi.org/10.1051/0004-6361/201525938

Guidi, G., Casado, J., Ascasibar, Y., et al. 2018, MNRAS, 479, 917, https://doi.org/10.1093/mnras/sty1480

Gunn, J. E., Siegmund, W. A., Mannery, E. J., et al. 2006, AJ, 131, 2332, https://doi.org/10.1086/500975

Ibarra-Medel, H. J., Avila-Reese, V., Sánchez, S. F., González-Samaniego, A., & Rodríguez-Puebla, A. 2019, MNRAS, 483, 4525, https://doi.org/10.1093/mnras/sty3256

Ibarra-Medel, H. J., Sánchez, S. F., Avila-Reese, V., et al. 2016, MNRAS, 463, 2799, https://doi.org/10.1093/mnras/stw2126

Kauffmann, G., Heckman, T. M., Tremonti, C., et al. 2003, MNRAS, 346, 1055, https://doi.org/10.1111/j.1365-2966.2003.07154.x

Kelz, A., Verheijen, M. A. W., Roth, M. M., et al. 2006, PASP, 118, 129, https://doi.org/10.1086/497455

Kennicutt, Jr., R. C. 1998a, ARA&A, 36, 189, https://doi.org/10.1146/annurev.astro.36.1.189

_____. 1998b, ApJ, 498, 541, https://doi.org/10.1086/305588

Kennicutt, Jr., R. C., Calzetti, D., Walter, F., et al. 2007, ApJ, 671, 333, https://doi.org/10.1086/522300

Kewley, L. J., Dopita, M. A., Sutherland, R. S., Heisler, C. A., & Trevena, J. 2001, ApJ, 556, 121, https://doi.org/10.1086/321545

Kreckel, K., Platen, E., Aragón-Calvo, M. A., et al. 2011, AJ, 141, 4, https://doi.org/10.1088/0004-6256/141/1/4

Lacerda, E. A. D., Sánchez, S. F., Mejía-Narváez, A., et al. 2022, arXiv:2202.08027, https://doi.org/10.48550/arXiv2202.08027

Leroy, A. K., Walter, F., Sandstrom, K., et al. 2013, AJ, 146, 19, https://doi.org/10.1088/0004-6256/146/2/19

Lin, L., Ellison, S. L., Pan, H.-A., et al. 2020, arXiv:2010.01751, https://doi.org/10.48550/arXiv.2010.01751

Lin, L., Pan, H.-A., Ellison, S. L., et al. 2019, arXiv:1909.11243, https://doi.org/10.48550/arXiv.1909.11243

López-Cobá, C., Sánchez, S. F., Anderson, J. P., et al. 2020, arXiv:2002.09328, https://doi.org/10.48550/arXiv.2002.09328

McGaugh, S. S. & Schombert, J. M. 2014, AJ, 148, 77, https://doi.org/10.1088/0004-6256/148/5/77

Méndez-Abreu, J., Sánchez, S. F., & de Lorenzo-Cáceres, A. 2019, MNRAS, 488, 80, https://doi.org/10.1093/mnrasl/slz103

Osterbrock, D. E. 1989, Astrophysics of gaseous nebulae and active galactic nuclei, (University Science Books)

Pan, D. C., Vogeley, M. S., Hoyle, F., Choi, Y.-Y., & Park, C. 2012, MNRAS, 421, 926, https://doi.org/10.1111/j.1365-2966.2011.20197.x

Pan, H.-A., Lin, L., Hsieh, B.-C., et al. 2018, ApJ, 854, 159, https://doi.org/10.3847/1538-4357/aaa9bc

Pérez, I., Verley, S., Sánchez-Menguiano, L., et al. 2024, arXiv:2405.04217, https://doi.org/10.48550/arXiv.2405.04217

Rodríguez-Puebla, A., Primack, J. R., Behroozi, P., & Faber, S. M. 2016, MNRAS, 455, 2592, https://doi.org/10.1093/mnras/stv2513

Rojas, R. R., Vogeley, M. S., Hoyle, F., & Brinkmann, J. 2004, ApJ, 617, 50, https://doi.org/10.1086/425225

Roth, M. M., Kelz, A., Fechner, T., et al. 2005, PASP, 117, 620, https://doi.org/10.1086/429877

Saintonge, A., Catinella, B., Cortese, L., et al. 2016, MNRAS, 462, 1749, https://doi.org/10.1093/mnras/stw1715

Salpeter, E. E. 1955, ApJ, 121, 161, https://doi.org/10.1086/145971

Sánchez, S. F. 2006, AN, 327, 850, https://doi.org/10.1002/asna.200610643

_____. 2020, ARA&A, 58, 99, https://doi.org/10.1146/annurev-astro-012120-013326

Sánchez, S. F., Avila-Reese, V., Hernandez-Toledo, H., et al. 2018, RMxAA, 54, 217, https://doi.org/10.48550/arXiv.1709.05438

Sánchez, S. F., Avila-Reese, V., Rodríguez-Puebla, A., et al. 2019a, MNRAS, 482, 1557, https://doi.org/10.1093/mnras/sty2730

Sánchez, S. F., Barrera-Ballesteros, J. K., Colombo, D., et al. 2021a, MNRAS, 503, 1615, https://doi.org/10.1093/mnras/stab442

Sánchez, S. F., Barrera-Ballesteros, J. K., Galbany, L., et al. 2024a, RMxAA, 60, 41, https://doi.org/10.22201/ia.01851101p.2024.60.01.04

Sánchez, S. F., Barrera-Ballesteros, J. K., Lacerda, E., et al. 2022, ApJS, 262, 36, https://doi.org/10.3847/1538-4365/ac7b8f

Sánchez, S. F., Barrera-Ballesteros, J. K., López-Cobá, C., et al. 2019b, MNRAS, 484, 3042, https://doi.org/10.1093/mnras/stz019

Sánchez, S. F., Galbany, L., Walcher, C. J., García-Benito, R., & Barrera-Ballesteros, J. K. 2023b, MNRAS, 526, 5555, https://doi.org/10.1093/mnras/stad3119

Sánchez, S. F., García-Benito, R., Zibetti, S., et al. 2016a, A&A, 594, 36, https://doi.org/10.1051/0004-6361/201628661

Sánchez, S. F., Gómez Medina, D. C., Barrera-Ballesteros, J. K., et al. 2023, IAUS 373, Resolving the Rise and Fall of Star Formation in Galaxies, 3, https://doi.org/10.107/S1743921322003830

Sánchez, S. F., Kennicutt, R. C., Gil de Paz, A., et al. 2012, A&A, 538, 8, https://doi.org/10.1051/0004-6361/201117353

Sánchez, S. F., Lugo-Aranda, A. Z., Sánchez Almeida, J., et al. 2024, A&A, 682, 71, https://doi.org/10.1051/0004-6361/202347711

Sánchez, S. F., Pérez, E., Sánchez-Blázquez, P., et al. 2016b, RMxAA, 52, 171

Sánchez, S. F., Pérez, E., Sánchez-Blázquez, P., et al. 2016c, RMxAA, 52, 21

Sánchez, S. F., Rosales-Ortega, F. F., Jungwiert, B., et al. 2013, A&A, 554, 58, https://doi.org/10.1051/0004-6361/201220669

Sánchez, S. F., Walcher, C. J., Lopez-Cobá, C., et al. 2021b, RMxAA, 57, 3, https://doi.org/10.22201/ia.01851101p.2021.57.01.01

Sánchez-Menguiano, L., Sánchez, S. F., Pérez, I., et al. 2016, A&A, 587, 70, https://doi.org/10.1051/0004-6361/201527450

Sánchez-Menguiano, L., Sánchez, S. F., Pérez, I., et al. 2018, A&A, 609, 119, https://doi.org/10.1051/0004-6361/201731486

Sánchez-Menguiano, L., Sánchez Almeida, J., Muñoz-Tuñón, C., et al. 2019, ApJ, 882, 9, https://doi.org/10.3847/1538-4357/ab3044

Sarmiento, R., Huertas-Company, M., Knapen, J. H., et al. 2023, A&A, 673, 23, https://doi.org/10.1051/0004-6361/202245509

Schmidt, M. 1959, ApJ, 129, 243, https://doi.org/10.1086/146614

_____. 1968, ApJ, 151, 393, https://doi.org/10.1086/149446

Speagle, J. S., Steinhardt, C. L., Capak, P. L., & Silverman, J. D. 2014, ApJS, 214, 15, https://doi.org/10.1088/0067-0049/214/2/15

Wong, T. & Blitz, L. 2002, ApJ, 569, 157, https://doi.org/10.1086/339287

Wuyts, S., Förster Schreiber, N. M., Nelson, E. J., et al. 2013 al. 2013, ApJ, 779, 135, https://doi.org/10.1088/0004-637X/779/2/135

Yan, R., Chen, Y., Lazarz, D., et al. 2019, ApJ, 883, 175, https://doi.org/10.3847/1538-4357/ab3ebc

York, D. G., Adelman, J., Anderson, Jr., J. E., et al. 2000, AJ, 120, 1579, https://doi.org/10.1086/301513

F. Agüi: Centro Astronómico Hispano en Andalucía, Observatorio de Calar Alto, Sierra de los Filabres, 04550 Gérgal, Almería, Spain.

M. Alcázar-Laynez, M. Argudo-Fernández, B. Bidaran, J. Domínguez-Gómez, S. Duarte Puertas, D. Espada, E. Florido, A. Jiménez, U. Lisenfeld, I. Perez, T. Ruiz-Lara, L. Sánchez-Menguiano, G. Torres-Ríos, S. Verley, and A. Zurita: Facultad de Ciencias (Edificio Mecenas), Departmento de Física Teórica y del Cosmos, Universidad de Granada, E-18071 Granada, Spain.

M. Argudo-Fernández, B. Bidaran, J. Domínguez-Gómez, S. Duarte Puertas, D. Espada, E. Florido, U. Lisenfeld, I. Perez, T. Ruiz-Lara, L. Sánchez-Menguiano, S. Verley, and A. Zurita: Instituto Carlos I de Física Teórica y computacional, Universidad de Granada, E-18071 Granada, Spain.

G. Blázquez-Calero, A. Conrado, R. García-Benito, and R. González Delgado: Instituto de Astrofísica de Andalucía (IAA/CSIC).

I. del Moral-Castro: Instituto de Astrofísica, Facultad de Física, Pontificia Universidad Católica de Chile, Campus San Joaquín, Av. Vicuña Mackenna 4860, Macul, 7820436, Santiago, Chile.

S. Duarte Puertas: Department of Physics and Astronomy, University of British Columbia, Vancouver, BC V6T 1Z1, Canada.

A. Ferré-Mateu, J. Román, and P. M. Sánchez Alarcón: Departamento de Astrofísica, Universidad de La Laguna, E-38206, La Laguna, Tenerife, Spain.

A. Ferré-Mateu, S. F. Sánchez, P. M. Sánchez Alarcón, and J. Román: Instituto de Astrofísica de Canarias, Vá Láctea s/n, 38205, La Laguna, Tenerife, Spain.

A. Z. Lugo-Aranda and S. F. Sánchez: Universidad Nacional Autónoma de México, Instituto de Astronomía, AP 106, Ensenada 22800, BC, México.

P. Villalba-González: Département de Physique, de Génie Physique et d'Optique, Université Laval, and Centre de Recherche en Astrophysique du Québec (CRAQ), Québec, QC, G1V 0A6, Canada.

Revista Mexicana de Astronomía y Astrofísica, **60**, 343–354 (2024)

https://doi.org/10.22201/ia.01851101p.2024.60.02.11

FEED-FORWARD NEURAL NETWORKS TO ESTIMATE STOKES PROFILES

Joan Manuel Raygoza-Romero[1], Irvin Hussein Lopez Nava[1], and Julio Cesar Ramírez-Vélez[2]

Received December 22 2023; accepted June 27 2024

ABSTRACT

Magnetic fields are believed to play a crucial role in stellar evolution. To better understand this evolution, it is essential to measure the magnetic fields on the stellar surface. These measurements can be achieved through spectropolarimetric observations, using the polarized radiative transfer equation. Magnetic field properties are inferred by adjusting the Stokes profiles. In this study, we propose a deep learning approach using a feed-forward neural network to estimate the Stokes profiles based on eight input parameters that describe the magnetic field configuration. To achieve this, we conducted scaling experiments on the data, explored different configurations of the FNN architecture, and compared two approaches. A model capable of accurately estimating the Stokes profiles I, Q and V was obtained. However, we encountered difficulties in estimating Stokes profiles Q and U when they have low amplitudes.

RESUMEN

Los campos magnéticos desempeñan un papel crucial en la evolución estelar. Para comprender mejor esta evolución, es esencial medirlos en la superficie estelar. Estas mediciones se logran mediante observaciones espectropolarimétricas, utilizando la ecuación de transferencia radiativa polarizada. Las propiedades del campo magnético se infieren ajustando los perfiles de Stokes. Este estudio propone un enfoque de aprendizaje profundo mediante una red neuronal *feed-forward* para estimar los perfiles de Stokes a partir de ocho parámetros que describen la configuración del campo magnético. Se realizaron experimentos de escalado, de diversas configuraciones de la arquitectura y se compararon dos enfoques. Se obtuvo un modelo que logra una estimación precisa de los perfiles de Stokes I, Q y V. Sin embargo, hubo dificultades para estimar los perfiles de Stokes Q y U cuando estos tienen una amplitud baja.

Key Words: methods: data analysis — polarization — stars: magnetic field

1. INTRODUCTION

Magnetic fields are the origin of solar and stellar activity, and it is widely accepted that they can play a very important role in stellar evolution: from young stars to compact objects. Furthermore, the strength and topology of the magnetic field vary depending on the evolutionary stage, i.e., the age of the star. Therefore, it is crucial to understand how stellar magnetic fields evolve (Ramírez-Vélez, J. C. et al. 2018).

Mapping and measuring stellar magnetic fields present several challenges due to the invisible nature of these fields and the complex interactions occurring within stars. However, over the years, different techniques and tools have been developed to address this task. One of the most used observational techniques is spectropolarimetry, which consists of obtaining simultaneously the intensity and the degree of polarization in spectral lines. This technique exploits the polarization state of the light emitted by a star to infer the presence and properties of the magnetic field. It is through the analysis of spectropolarimetric data that magnetic fields can be properly characterized (Degl'Innocenti & Landolfi 2006).

[1]Centro de Investigación Científica y Educación Superior de Ensenada (CICESE), Departamento de Ciencias de la Computación.
[2]Universidad Nacional Autónoma de México (UNAM), Instituto de Astronomía - Ensenada.

Therefore, the reliability of astronomical inferences largely depends on the accuracy of light measurements. In this sense, spectropolarimetry analyzes light based on its two fundamental characteristics: intensity and polarization degree (del Toro Iniesta 2003). The polarization of light is described through the Stokes profiles. These emerged from the mathematical theory of light polarization and were proposed in the 19th century by the British physicist George Gabriel Stokes. They consist of four numerical values that provide a complete description of the polarization state of light. These profiles are commonly identified as I, Q, U, and V. The profile I represents the intensity of the light, while the profiles Q and U represent linear polarization, and the profile V represents circular polarization. These profiles vary in response to the presence and properties of the magnetic field in the star.

To fit spectropolarimetric observations, theoretical codes are required. These codes solve the polarized radiative transfer equation (RTE) to synthesize the Stokes profiles from a given magnetic field configuration on the star. In this work, a generalized off-centered dipolar magnetic configuration will be considered, and atmospheric parameters such as effective temperature ($T_{\rm eff}$), rotational speed (v_r), gravity ($\log g$), among others, are fixed. To obtain synthetic spectra, the code COSSAM is employed (Stift 2000). Note that by using a dipolar configuration the magnetic field is not uniform over the surface. In our case, the star's surface is divided into 284 areas, and in each area, COSSAM calculates the so-called local Stokes profiles using the eight attributes that describe the magnetic geometry of the dipolar configuration. The local Stokes profiles are then integrated over the entire surface to obtain the resulting Stokes profiles that will be compared with the observations.

This process requires significant computational time for modeling. Using COSSAM implies a comprehensive theoretical approach based on RTE, and it also allows generating a broad data set. For this reason, in this work a deep learning-based model was developed to provide a reliable tool for synthesizing a large number of magnetic configurations for the Stokes profiles in an affordable manner.

2. RELATED WORK

Currently, studies on stellar magnetism are based on the analysis of Stokes profiles observed in stars. Through the RTE, it is theoretically possible to model different configurations of the stellar magnetic field. By fitting the observed profiles with those obtained using RTE, it becomes possible to recover the magnetic field configuration and/or atmospheric characteristics of the star. However, the process of fitting theoretically calculated Stokes profiles is computationally expensive (Gafeira et al. 2021), due to the time required by resolution methods to solve the differential equations of RTE to simulate a given magnetic model, specially if many spectral lines have to be considered simultaneously.

Faced with this challenge, the use of machine learning (ML) algorithms, particularly deep learning, has emerged as a possible solution. Initially, all the efforts were applied in studies of the solar magnetism: In the pioneer work in this field (Carroll & Staude 2001), the authors trained a multilayer perceptron (MLP) neural network to demonstrate the possibility to infer the magnetic and atmospheric model from a given set of Stokes profiles. Later, in Carroll & Kopf (2008), the authors used snapshots of magnetohydrodinamycs (MHD) simulations to produce synthetic Stokes profiles, which were used for training to study the depth stratification of the magnetic and atmospheric models and to identify magnetic flux tube structures.

In general, in the scientific literature, most of the ML models were focused on performing regressions of physical properties, or magnetic configuration, of the solar atmosphere (Asensio & Díaz 2019; Gafeira et al. 2021; Knyazeva et al. 2022). In these studies, local Stokes profiles were analyzed from a very small region of the solar disk, allowing for detailed spatial resolution. In contrast, some articles focused on stars beyond the Sun, and the Stokes profiles were obtained from the entire (integrated) disk, resulting in a lack of spatial resolution in these observations, as all stars were considered point sources in telescopes (Carroll et al. 2008; Ramírez-Vélez, J. C. et al. 2018; Córdova, J. P. et al. 2018).

In the stellar domain, two studies (Córdova, J. P. et al. 2018; Ramírez-Vélez, J. C. et al. 2018) employ a regressor model to predict the effective magnetic field of a star. The first one uses the mean Stokes V profile, whereas the other one also utilizes Stokes Q and U profiles. In the cited works, the Stokes profiles were used to train ML algorithms to use the model as regressor, and consequently, to infer the physical atmospheric properties (including the magnetic field). In this sense, and to our knowledge, only the work of Carroll et al. (2008) has focused on training a ML algorithm to obtain as output the Stokes profiles given a set of 5 free parameters of the atmospheric and magnetic model. Prior to the training, the authors applied a decomposition using principal component analysis (PCA) of the Stokes profiles, finding very

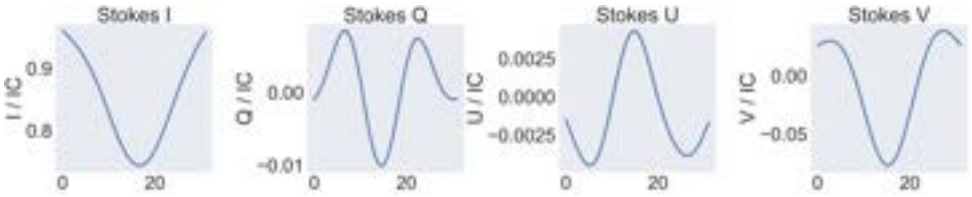

Fig. 1. Example of the four Stokes profiles. The color figure can be viewed online.

good results. The work we present here has a similar goal, to train a ML model to obtain the Stokes profiles given 8 free parameters of the magnetic configuration.

3. DATA SET

A synthetic data set generated by COSSAM was used to estimate Stokes profiles. Remembering that COSSAM employs the RTE to produce Stokes profiles (Stift 2000), a corpus of 1.3M data instances was generated in a spectral line at 6311.5 Å, with each instance having 8 attributes, namely the dipolar moment strength (m), the magnetic dipole position inside the star described by two coordinates (X_2, X_3), the rotation phase (p), three attributes describing the magnetic geometry of the dipolar configuration (α, β, γ), and the inclination angle (i) of the stellar rotation axis with respect to the line of sight. Each instance, with these eight input attributes, is associated with an output signal of 128 points, corresponding to the Stokes profiles, 32 points for each. Figure 1 shows an example of a signal generated with the following attribute values: $m = 1493.9, i = 35.7, \alpha = -58.4, \beta = 51.4, \gamma = -24.5, X_2 = 0.15, X_3 = 0.10, p = 0.64$; it was segmented into the four Stokes profiles that will be the output of our model.

This example highlights an important property in the Stokes profiles, which is the difference in amplitudes of each profile, with Stokes I being much larger than Stokes V, and Stokes V being larger than Stokes Q and U. Therefore, it is necessary to preprocess and scale the input and output data so that the prediction model will be able to estimate different magnitudes. Each instance was generated by selecting a random value from a uniform distribution for each input attribute ($m, i, \alpha, \beta, \gamma, X_2, X_3, p$) in the range shown in Table 1.

4. METHODS

The use of deep learning was motivated by the need to regress each point of the profile of each Stokes profile, thus requiring a multi-output model, and a feed-forward neural network (FNN) is suitable for this problem. In this study, two different metrics, namely the mean squared error (MSE) and the weighted mean absolute percentage error (WMAPE), were employed to evaluate the model's performance among several configurations. The following are the equations for each metric:

TABLE 1

RANGE FOR 8 INPUT ATTRIBUTES

Attribute	Min Value	Max Value
m	100.0	5010.0
X_2	0.00	0.20
X_3	0.00	0.20
p	0.0	1.0
α	-180.0	180.0
β	0.0	180.0
γ	-180.0	180.0
i	0.0	180.0

$$MSE = \frac{1}{n}\sum_{i=1}^{n}(Y_i - \hat{Y}_i)^2, \quad \text{and}$$
$$WMAPE = \frac{\sum_{i=1}^{n}|Y_i - \hat{Y}_i|}{\sum_{i=1}^{n}|Y_i|}, \tag{1}$$

where n is the number of points or sample, Y_i is the ground truth value, and $\hat{Y}_i$ is the model prediction for each point i.

MSE allows the comparison of different model configurations of the same data set. However, MSE penalizes larger errors more, as the differences between predicted and actual values are squared. On the other hand, WMAPE is a useful metric for comparing model predictions independently of the magnitude of the values being compared. As a percentage-based metric, WMAPE will be used to compare the accuracy of predicted values and true values between Stokes profiles. A good WMAPE is defined as being below 5%. It is important to emphasize that calculating the mean of this metric involves dividing the sum of WMAPE of each Stokes profile by the total number of Stokes profiles. This ensures that scale changes do not have a disproportionate impact and that all profiles are considered with equal weight.

Through the COSSAM code, combinations of values for the 8 attributes of the magnetic field (X_{cossam}) are provided, and in return, the four Stokes profiles (I, Q, U, V) denoted by (Y) are obtained. The FNN is responsible for estimating the Stokes profiles ($\hat{Y}$), and the error between Y and $\hat{Y}$ is calculated using the previously described metrics to evaluate the estimations. For all the work, the data set was split into 75% training, 15% validation, and 10% test, each of them having the same distribution among instances.

4.1. *Feed-forward Neural Network*

Feed-forward neural networks are a fundamental building block of deep learning architectures and have proven to be highly effective in many real-world applications (Paliwal & Kumar 2009). They consist of an input layer, one or more hidden layers, and an output layer, with the data flowing in a single direction from input to output. Each neuron in the network receives input from the previous layer, processes it using a set of weights and biases, and passes the result to the next layer. The hidden layers of the network are responsible for extracting complex features from the raw input data and transforming them into a representation suitable for the task at hand. The output layer provides the final prediction or decision.

The training of FNN is an optimization problem, where the objective is to find the set of weights and biases that minimize the prediction error on a training data set. This is typically achieved using an optimization algorithm, such as stochastic gradient descent or a variant thereof, and the back-propagation algorithm is used to compute the gradients of the error with respect to the weights and biases (Svozil et al. 1997).

4.2. *Selection of Neural Network Parameters*

The parameters for the following experiments are listed in Table 2. These parameters apply to all experiments, with some exceptions noted at the bottom of the table. In order to perform a wide range of experiments within a restricted timeframe, only a sample of the entire data set (50,000 instances) was considered.

These parameters were selected with some empirical experiments to determine them. The ReLU activation function was used in all layers except for the output layer, where no activation function was used. Based on the results of these preliminary experiments, a dynamic weight decay approach was applied. It consists of varying the weight decay as a function of the data set size, as weight decay plays a crucial role in the training process.

TABLE 2

FIXED PARAMETERS FOR FNN TRAINING

Attribute	Value
Data set Size	50,000
Momentum	0.95
Activation Function	ReLU
Epochs	1000
Optimizer	Stochastic gradient descent
Early Stopping	25
Learning Rate*	1
Batch Size	1024
Weight Decay	$1/(2 * dataset\_size)$
Loss Function	MSE

*Learning rates are variable in the scaling experiments.

This approach consists of varying the learning rate according to the number of epochs. A dynamic approach enables the adaptation of this parameter to the specific characteristics of the data set (Smith 2018). These neural network parameters are expected to enhance the overall effectiveness of the training process and improve the generalization capability of the network.

In this experiment, the Standard, Min-Max, Max-Abs and Quantile scalers were evaluated for both input (dipole moment strength, three Euler angles, inclination angle, two dipole position coordinates, and rotation phase) and output (32 points for each Stokes profile). This resulted in a total of 16 different models. As mentioned before, these models were trained and evaluated using a subset of the data, with the purpose of determining the optimal scaling method for both input and output of the model. The hyperparameters used in the FNN of this experiment were those listed in Table 2.

Figure 2 displays the results of combining different scaling methods using a baseline estimation model. Outliers were removed for improved analysis and visualization. On the X-axis, the scaling methods are grouped for the output scaler, while the color series correspond to the scaler on the input data.

4.3. *Scaling Selection*

In this visual representation, it is highlighted that the standard scaling method for output out-performs the others in terms of the mean WMAPE of all Stokes profiles (left of Figure 2). Regarding input scaling, no significant difference is observed among the different methods. However, to supplement this

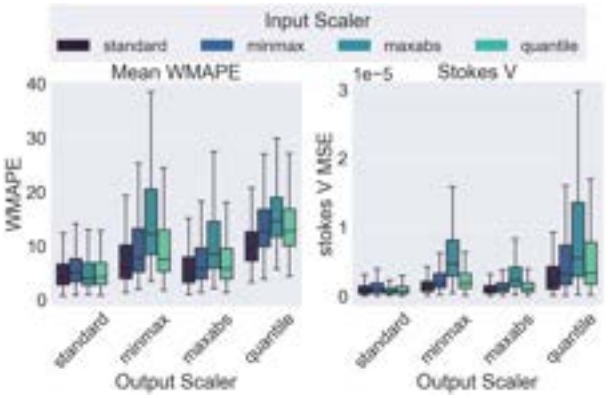

Fig. 2. Mean WMAPE of the Stokes profiles and the MSE of Stokes V for the different combinations of input and output scaling methods. The color figure can be viewed online.

information, the right graph in Figure 2 shows the MSE for the Stokes V, which is the most relevant profile in our research. Once again, a similar improvement is seen with the standard method for output. However, in the case of input scaling, a more noticeable difference is observed with the Max-Abs method.

By analyzing in detail each Stokes profile in Table 3, it can be noticed that the model using Max-Abs scaling for input along with standard scaling for output achieves better performance in terms of the MSE for each profile. Based on the results, it is recommended to select the Max-Abs scaling method for input and the standard scaling method for output.

4.4. *Architecture Selection*

A crucial aspect to consider is the choice of FNN architecture. Determining the optimal number of hidden layers and neurons per layer is essential for achieving the best performance. In our experiment, we tested different configurations, including 2, 3, 4, 5, 6, and 7 hidden layers with 512, 1024, 2048, and 4096 neurons per layer, resulting in a total of 24 models. This experiment was conducted using the input and output scaling previously selected (Max-Abs for input and standard for output).

In Figure 3, outlier data and results from the models with two layers are omitted to better visualize these outcomes. In the left side of Figure 3, the mean WMAPE of the Stokes profiles for these models is displayed, and it is evident that as we increase the number of hidden layers and the number of neurons per hidden layer, the model's performance improves. Furthermore, by looking at the right side of Figure 3, which presents the Stokes V MSE, we can see the same trend, with more improvement occur-

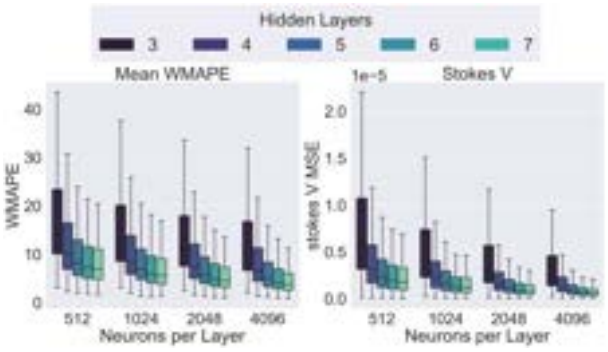

Fig. 3. Mean WMAPE of the Stokes profiles and the MSE of Stokes V for the different architectures of FNN grouped by the number of neurons per layer. The color figure can be viewed online.

ring with the number of hidden layers and neurons per layer.

In Table 4, the best-found architectures are presented. The largest model, with 7 hidden layers and 4096 neurons per hidden layer, scores lower MSE in each Stokes profile, as well as lower mean WMAPE. Based on the results of this experiment, the architecture with 7 hidden layers and 4096 neurons per hidden layer is selected. It is important to note that due to hardware limitations, experiments with more neurons and hidden layers cannot be conducted.

4.5. *General vs Specialized Models*

In the quest for the best model, we encountered two approaches. One of them involves creating a model to estimate each Stokes profile individually, resulting in a specialized model for each of them, named from now on "specialized models". On the other hand, we could employ a single model capable of predicting all four Stokes profiles simultaneously, i.e., a "general model". This leads us to the following question: Is it better to construct a specialized model for each Stokes profile or to use a single model capable of predicting all four profiles simultaneously?

In Figure 4 and Table 5, we present the results that showcase the comparative performance of these approaches. There is a notable difference between them, with the general model standing out in terms of performance. Both the general model and the specialized models contain the same input parameters, but somehow the general model benefits from containing the values of all Stokes profiles and therefore performs better than the specialized models in the experiments we performed.

In contrast, specialized models for each Stokes profile lack access to these values, as their aim is limited to predicting a specific profile. While these

TABLE 3

MEAN MSE PER STOKES PROFILE AND MEAN WMAPE OF THE STOKES PROFILES OF INPUT AND OUTPUT SCALING

Input Scaler	Output Scaler	S_I MSE	S_Q MSE	S_U MSE	S_V MSE	Mean WMAPE
Standard	Standard	1.2e-06	2.3e-07	1.6e-07	1.2e-06	**6.41**
Standard	Max-Abs	1.2e-05	2.4e-07	1.9e-07	1.2e-06	9.52
Max-Abs	Standard	**1.0e-06**	**1.7e-07**	**1.5e-07**	**1.0e-06**	8.33
Quantile	Standard	1.1e-06	2.1e-07	**1.5e-07**	1.1e-06	6.85

TABLE 4

MEAN MSE PER STOKES AND MEAN WMAPE OF THE STOKES BY NUMBER OF HIDDEN LAYERS AND NEURONS PER LAYER

Hidden Layers	Neurons	S_I MSE	S_Q MSE	S_U MSE	S_V MSE	Mean WMAPE
5	4096	1.3e-06	2.5e-07	2.1e-07	1.3e-06	11.03
6	4096	1.0e-06	1.7e-07	1.5e-07	1.0e-06	8.33
7	2048	1.2e-06	1.9e-07	1.5e-07	1.2e-06	8.39
7	4096	**9.3e-07**	**1.5e-07**	**1.2e-07**	**8.8e-07**	**7.09**

TABLE 5

MEAN MSE PER STOKES PROFILE AND MEAN WMAPE OF THE STOKES PROFILES FOR GENERAL AND SPECIALIZED MODELS

Model	S_I MSE	S_Q MSE	S_U MSE	S_V MSE	Mean WMAPE
Specialized	5.8e-06	4.4e-07	4.8e-07	1.5e-06	10.25
General	**9.3e-07**	**1.5e-07**	**1.2e-07**	**8.8e-07**	**7.09**

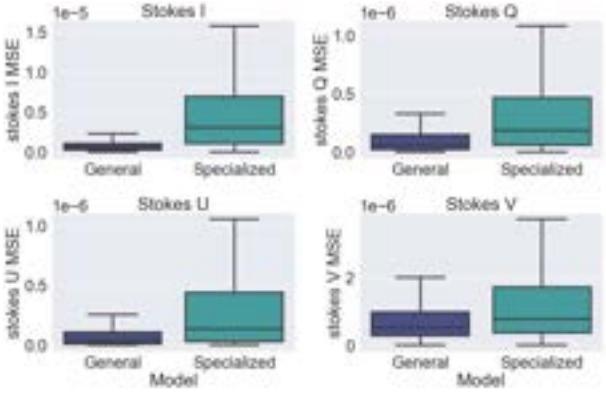

Fig. 4. MSE of each Stokes profile for general and specialized models. The color figure can be viewed online.

models can capture the unique characteristics of each individual Stokes profile; they cannot leverage the connections with neurons predicting the other Stokes profiles.

This limitation can lead to lower accuracy in predicting the Stokes profiles in isolation. As a result, the general model, by benefiting from the interaction among the Stokes profiles, out-performs the specialized models in terms of precision and predictive capability. These findings support the notion of using the general model to predict the Stokes profiles.

5. RESULTS

Based on previous experiments, we proceeded to evaluate the performance of the best model using the complete dataset (1.3M instances). In Table 6, we can observe the WMAPE for each Stokes profile as well as the mean WMAPE; along with the value for the third quartile as a measure of dispersion.

In summary, the model achieves good performance for Stokes I, Q, and V (lower than 2.79% of mean WMAPE), and a satisfactory performance for Stokes U (6.62%). The results demonstrate that the model is quite robust and reliable for all Stokes profiles.

TABLE 6

MEAN MSE PER STOKES PROFILE AND THE MEAN WMAPE OF THE STOKES PROFILES, ALONG WITH THE THIRD QUARTILE

S_I WMAPE (Q3)	S_Q WMAPE (Q3)	S_U WMAPE (Q3)	S_V WMAPE (Q3)	Mean WMAPE (Q3)
0.0279 (0.0348)	2.79 (2.35)	6.62 (4.76)	1.37 (1.59)	2.70 (2.13)

5.1. *Analysis of Error Based on Stokes profile Amplitude*

Next, a comprehensive analysis of WMAPE about the amplitude of the Stokes profile profile was conducted. However, before delving into the details, it is necessary to define the calculation of amplitude for each Stokes profile. The amplitude of the Stokes profiles is defined as follows:

$$Amplitude_{StokesI} = \min(Y_I), \tag{2}$$

$$Amplitude_{Stokes\lambda} = \max(\mid Y_\lambda \mid), \tag{3}$$

where Y_I is the Stokes I profile, λ is any Stokes profile of Q, U and V. Since the Stokes Q, U, and V profiles cross zero, the maximum value of absolute values belonging to the Stokes profile is taken.

Using these definitions of Stokes profile amplitudes, an analysis of error was conducted, as the amplitude changes in each profile. Bar graphs were generated, where each bar represents a range of amplitude. The height of the bar corresponds to the mean WMAPE of the test cases within that amplitude range, and a number is displayed above each bar representing the percentage of test cases found within that amplitude range. Additionally, vertical lines were plotted within each bar to represent the standard deviation.

In Figure 5, we observe the WMAPE of each Stokes profile across its amplitude range. The 100%, 94.1%, 90.3% and 97.2% of the data are shown for the Stokes profiles I, Q, U and V, respectively. This is in order to better visualize most of the instances. As the amplitude of Stokes I increases, we also observe an increase in the error.

In general, the amplitude of any of the Stokes profiles varies as function of the intensity of the magnetic field (the stronger the field, the larger the amplitude). In particular, for the case of Stokes I, this amplitude variation is not significant. Due to this, the FNN prediction of the Stokes I can be considered successful, since even in the worst cases, the WMAPE remains below 0.06%.

A smaller amplitude in the three polarized Stokes profiles (U, Q, V) signifies lower polarized light intensity, which is attributed to a weakly magnetized star or a large inclination angle of the star with respect to the line-of-sight (for Stokes V) or that the transverse component of the field is weak (for Stokes Q and U).

For the Stokes Q profile, it is found that as its amplitude decreases, the WMAPE increases. However, in 94.1% of the cases, the mean of WMAPE is less than 4.5%. This suggests that the model performs well to estimate the Stokes Q profile in the majority of cases.

The Stokes U profile also exhibits a similar trend to the Stokes Q profile. The WMAPE increases as the amplitude decreases. Additionally, it's noted that in 90.3% of the test data, the mean of WMAPE is less than 10%. Given that Stokes Q and U are linear polarizations, there is a notable difference in the predictive capability between Stokes Q and U, with the latter being slightly more challenging for the model to estimate. Nonetheless, in most cases, the model provides a good estimation of the Stokes U profile.

In order to explain why the FNN model reproduces the Stokes Q profiles better than the U profiles is necessary to compare their amplitudes.

We are using in COSSAM the de-centered dipolar model, in which the position of the dipole in the stellar interior is determined by two coordinates. Even if the use of two coordinates, instead of three, to determine the position of the dipole combined with the ranges of variation of the Eulerian and inclination angles is a general approach for all possible magnetic configurations (Stift 1975), it results in an imbalance in the amplitudes of the linear Stokes profiles: the amplitudes of the Stokes Q are greater than those of Stokes U. In consequence, the FNN model performs better for the Stokes Q profiles –with higher amplitudes– than for the Stokes U profiles. See the Appendix for a more details.

Finally, for the Stokes V profile, a situation similar to that of the Stokes Q and U profiles is observed. As the amplitude decreases, the WMPAE increases. However, it is found that in 97.2% of the test data, the WMAPE is below 2.6%, indicating that the model is quite robust in estimating it with a very low WMAPE.

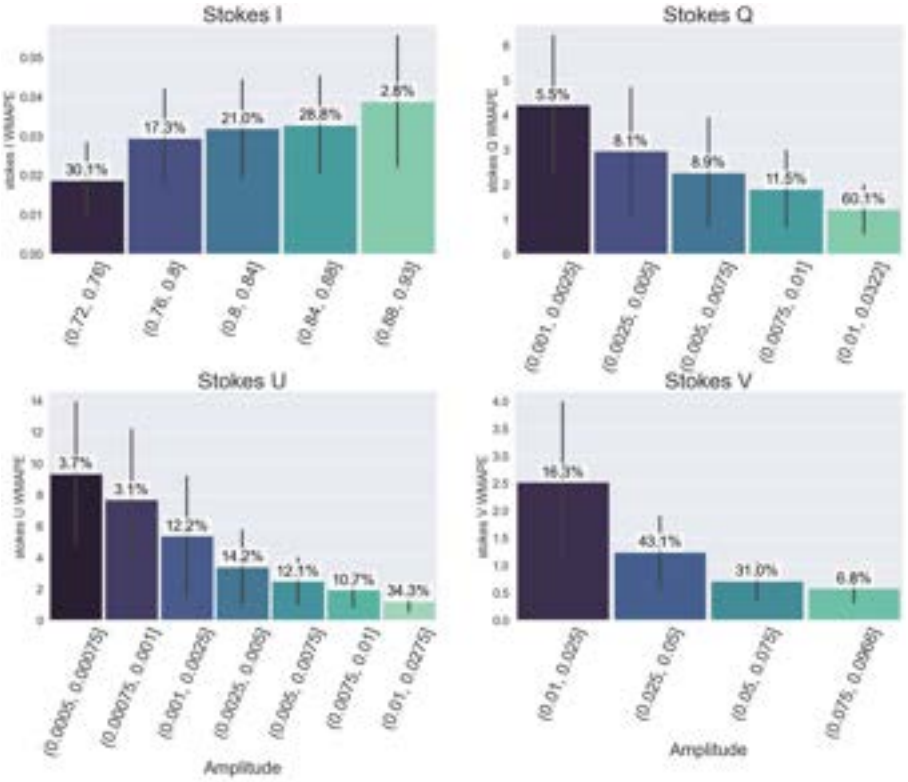

Fig. 5. WMAPE of each Stokes profile from the model for Stokes profile estimation grouped by amplitude ranges. The color figure can be viewed online.

5.2. *Percentile Analysis*

Finally, in Figure 6, we present the visualization of the 20th, 40th, 60th, 80th, 90th and 99th percentiles of the Stokes profile estimates based on the mean WMAPE of each Stokes profile. We can observe that in percentile 80th and below the model achieves a good performance in WMAPE on every Stokes profile. The results indicate that in 80% of cases the model performs well. At the 90th percentile, the mean WMAPE increases from 2.5% to 4.2%; the Stokes U profile proves to be the most challenging to estimate, with an error over 13%, but for the other Stokes profiles we obtain a good performance.

In the 99th percentile, representing one of the worst-case scenarios, the mean WMAPE is nearly 30%. The magnetic field configuration of this case has the following attribute values: $m = 127.4, i = 176.7, \alpha = 65.8, \beta = 57.1, \gamma = 156.5, X_2 = 0.139, X_3 = 0.057$ and $p = 0.70$. In this scenario, the Stokes U profile has an error of almost 70% (amplitude $\approx 5 \times 10^{-5}$), and the Stokes Q profile also exhibits a significant error, nearly 42% (amplitude $\approx 1 \times 10^{-4}$). Hence, in certain cases, the model does not respond adequately, specially if the amplitudes of the linear Stokes profiles are very low. Nonetheless, the Stokes V profile has an error of 7.1%, indicating that even in the worst cases, the estimation of the Stokes V profile remains with acceptable performance. Across all cases, the Stokes I profile is consistently well estimated by the model. We then conclude that in those magnetic configurations which produces a low amplitude of the Stokes profiles Q and U, the model has difficulties in their estimation, while for V and I Stokes profiles the performance of the model is quite acceptable for all magnetic configurations.

6. CONCLUSION AND FUTURE WORK

Through our research, deep learning models were implemented and evaluated to estimate Stokes profiles. We employed a feed-forward neural network due to its multi-output capability and adaptability to the problem. Additionally, experiments were conducted to determine the appropriate FNN architecture. The obtained results were highly satisfactory. When estimating Stokes profiles I and V, we

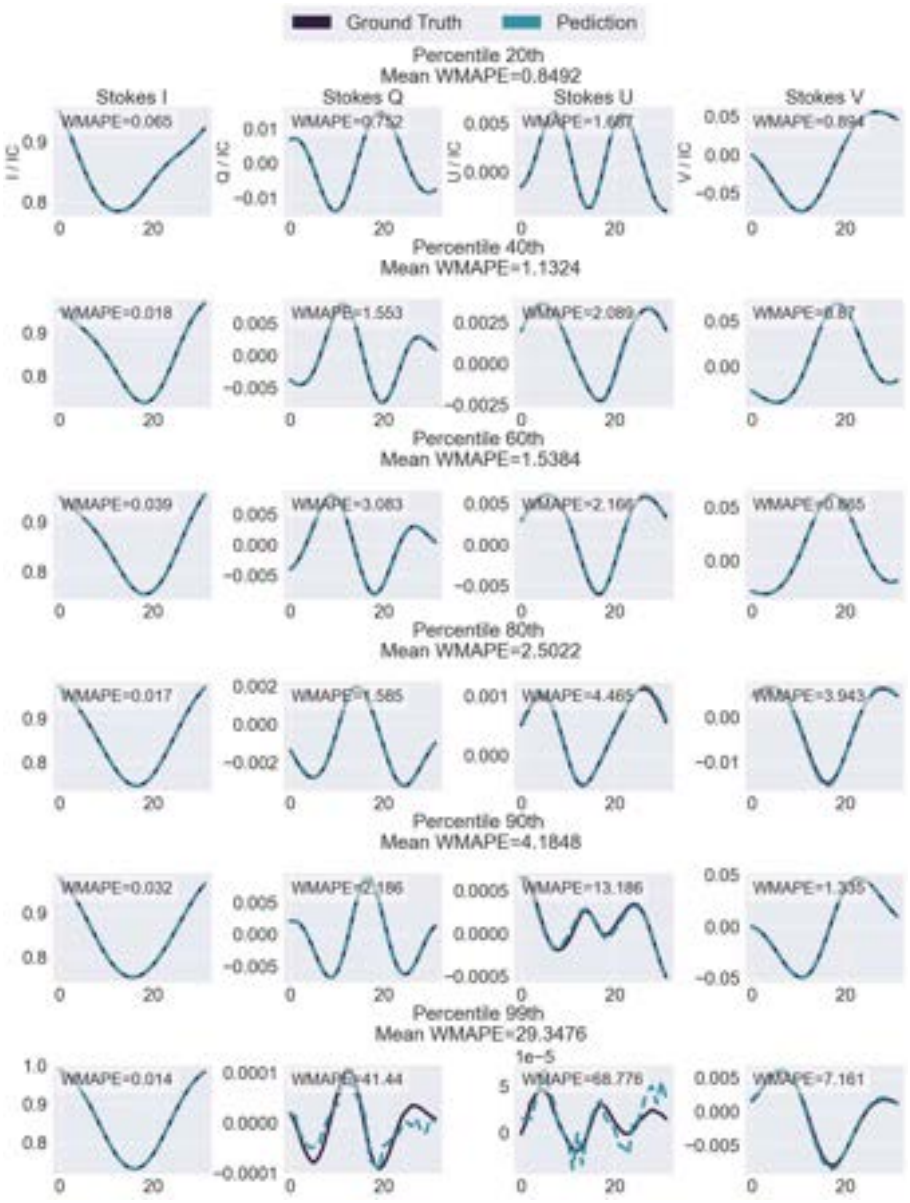

Fig. 6. Estimation of the Stokes profiles for the 20th, 40th, 60th, 80th, 90th and 99th percentile. The color figure can be viewed online.

achieved an MSE of 1.0e-07 and 9.1e-08, respectively. In terms of WMAPE, we obtained 0.02% and 1.37% for Stokes profiles I and V.

However, for Stokes profiles Q and U, the model struggled to accurately estimate these two Stokes profiles, obtaining 2.79% and 6.62% of WMAPE respectively. Our findings reveal a correlation between the amplitude of the Stokes profiles and the corresponding estimation errors. Specifically, as the amplitude decreases, the errors exhibit an upward trend. Notably, the estimation is better for Stokes I, followed sequentially by Stokes V, Q, and U, mirroring the decreasing amplitude order of these profiles. In some cases where the Stokes amplitudes Q and U are very small, we find that the model has difficulties in estimating them.

A potential avenue for future research involves utilizing the trained model to conduct inversions. This process entails optimizing the input attributes to adjust an observed Stokes profile to a synthesized profile generated by the model, with the ultimate goal of recovering the magnetic configuration of a

star and applying the developed methodology to real data obtained from astronomical observations. In this sense, our goal is to use the trained FNN to analyze the observed Stokes profiles and consequently recover the magnetic field configuration of real stars.

It is important to emphasize that this study does not consider noise of the Stokes profiles, but evaluating its impact on model performance is crucial. This strategy would simulate more realistic situations, as astronomical data in practice often contain noise.

Furthermore, it is interesting to experiment with other architectures of deep neural networks, such as recurrent networks, convolutional networks, or transformers. These architectures could offer additional advantages in terms of capturing temporal patterns, extracting spatial features, or modeling long-range relationships. Exploring these alternatives could provide new insights and further enhance the model performance.

Finally, the model presented here can be used as a basis for training other neuronal models through the so-called *transfer technique* (Zhuang et al. 2021). This approach has the great advantage for training new neuronal models with fewer instances, since a pre-trained model for a similar task is used. In other words, we can use the presented model for training other models dedicated to the synthesis of polarized spectral lines at different wavelengths, or the synthesis of multi-line profiles as the LSD profiles with fewer data in a shorter time and with a similar performance.

This work is funded by the Mexican National Council for Science and Technology (CONACYT), under Grant number 806073. We would like to thank the UNAM- PAPIIT Grant IN118023.

APPENDIX

In Figure 7 we show from top to bottom the distribution of the amplitudes of Stokes Q, U and V profiles using the dipolar de-centred approach. The left column corresponds to the training sample (1.3 million instances), while in the right column, and for consistence purposes, are included the amplitudes of another spectral line, namely Fe at 4503 Å for a smaller sample of 50,000 instances.

We remark that the distributions of both columns follow a similar tendency, where the amplitudes of Stokes V are the largest (as they should be), while the amplitudes of the Stokes Q are larger than those of Stokes U. As we mention, this is due to the fact that in COSSAM the position of the dipole is given by two coordinates instead of three, inducing an amplitude difference in the lines Stokes profiles. This in turn is the reason why the FNN perform better for Stokes Q than for Stokes U profiles.

Finally, in Figure 8 we show the same as in Figure 7 but for the centered dipolar model. In this case we can notice that the amplitudes of the linear Stokes profiles cover the same ranges; it should be expected that the FNN could perform equally well for both, Stokes Q and Stokes U.

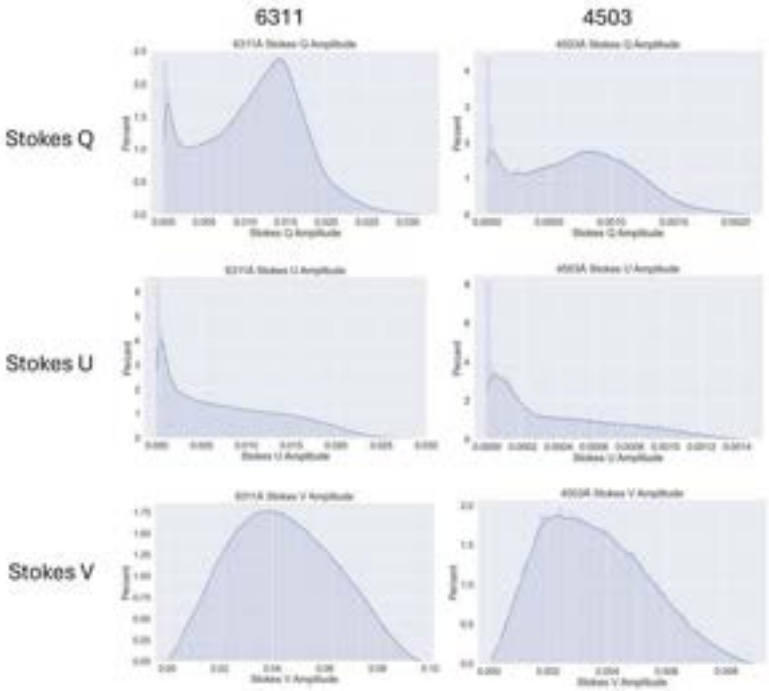

Fig. 7. Percent distribution of amplitudes of the polarized Stokes parameters. The left column corresponds to the total sample used for training (1.3 M instances), while the right column corresponds to the Fe line at 4503 Å (sample of 50 k instances). The color figure can be viewed online.

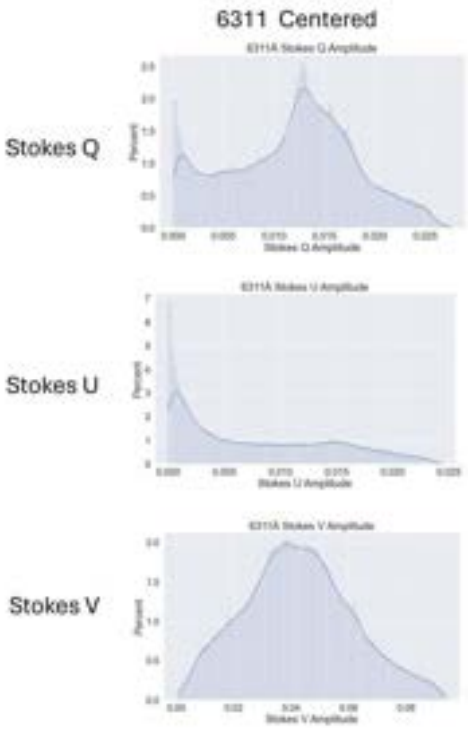

Fig. 8. Similar to Figure 7 but for a centered dipolar model (the dipole is in the center of the star). The amplitudes correspond to a sample of 50,000 instances for the Fe 6311 Å line. In this case, the amplitudes of the linear Stokes profiles cover the same range of amplitudes. The color figure can be viewed online.

REFERENCES

Asensio, A. & Díaz, C. J. 2019, A&A, 626, 102, https://doi.org/10.1051/0004-6361/201935628

Carroll, T. A. & Kopf, M. 2008, A&A, 481, 37, https://doi.org/10.1051/0004-6361:20079197

Carroll, T. A., Kopf, M., & Strassmeier, K. G. 2008, A&A, 488, 781, https://doi.org/10.1051/0004-6361:200809981

Carroll, T. A. & Staude, J. 2001, A&A, 378, 316, https://doi.org/10.1051/0004-6361:20011167

Córdova, J. P., Navarro, S. G., & Ramírez-Vélez, J. C. 2018, International Journal of Computational Intelligence Systems, 11, 608, https://doi.org/10.2991/ijcis.11.1.46

Degl'Innocenti, M. L. & Landolfi, M. 2006, Polarization in spectral lines, Vol. 307 (Springer Science & Business Media), https://doi.org/10.1007/1-4020-2415-0

del Toro Iniesta, J. C. 2003, Introduction to spectropolarimetry (CUP), https://doi.org/10.1017/CBO9780511536250

Gafeira, R., Orozco, D., Milić, I., et al. 2021, A&A, 651, 31, https://doi.org/10.1051/0004-6361/201936910

Knyazeva, I., Plotnikov, A., Medvedeva, T., & Makarenko, N. in Advances in Neural Computation, Machine Learning, and Cognitive Research V, 2021, ed. B. Kryzhanovsky, W. Dunin-Barkowski, V. Redko, Y. Tiumentsev, and V. V. Klimov, 299, Springer, Cham, https://doi.org/10.1007/978-3-030-91581-0_40

Paliwal, M. & Kumar, U. A. 2009, Expert systems with applications, 36, 2, https://doi.org/10.1016/j.eswa.2007.10.005

Ramírez-Vélez, J. C., Yáñez, C., & Córdova, J. P. 2018, A&A, 619, 22, https://doi.org/10.1051/0004-6361/201833016

Smith, L. N. 2018, arXiv:1803.09820, https://doi.org/10.48550/arXiv.1803.09820

Stift, M. J. 1975, MNRAS, 172, 133, https://doi.org/10.1093/mnras/172.1.133

Stift, M. J. & Leone, F. 2003, A&A, 388, 411, https://doi.org/10.1051/0004-6361:20021605

Svozil, D., Kvasnicka, V., & Pospichal, J. 1997, Chemometrics and Intelligent Laboratory Systems, 39, 43, https://doi.org/10.1016/S0169-7439(97)00061-0

Zhuang, F., Qi, Z., Duan, K., et al. 2021, Proceedings of the IEEE, 109, 43, https://doi.org/10.1109/JPROC.2020.3004555

Irvin Hussein Lopez Nava and Joan Manuel Raygoza-Romero: Ciencias de la Computación, Centro de Investigación Científica y de Educación Superior de Ensenada, Carr. Tijuana-Ensenada km107, 22860 Ensenada, Baja California, México (jraygoza, hussein@cicese.edu.mx).

Julio Cesar Ramírez-Vélez: Instituto de Astronomía, Universidad Nacional Autónoma de México, Carr. Tijuana-Ensenada km107, 22860 Ensenada, Baja California, México (jramirez@astro.unam.mx).

Revista Mexicana de Astronomía y Astrofísica, **60**, 355–359 (2024)

https://doi.org/10.22201/ia.01851101p.2024.60.02.12

THE RADIO CONTINUUM SOURCE PROJECTED NEAR HR 8799

L. F. Rodríguez[1,2] and L. A. Zapata[1]

Received February 17 2024; accepted July 3 2024

ABSTRACT

HR 8799 is an A5/F0 V star where exoplanets were first directly imaged. Four exoplanets were found within $\simeq 2\farcs0$ from the star. Here we report the VLA detection of a faint (19.1±2.7 μJy) radio continuum (3.0 GHz) source projected at $\simeq 2\farcs2$ from the star. The *a priori* probability of finding a background source with this flux density within a radius of $2\farcs2$ is only 0.0046. However, the astrometry made with the VLA and ALMA images, separated by 5.5 years, indicates no significant proper motions and rules out the association of the radio source with the HR 8799 system and suggests it is a background millimeter galaxy with dust emission in the millimeter and partially thick synchrotron emission in the centimeter.

RESUMEN

HR 8799 es una estrella A5/F0 V en la cual se detectaron por primera vez exoplanetas con la técnica de imágenes directas. Se encontraron cuatro exoplanetas dentro de $\simeq 2\farcs0$ de la estrella. Aquí reportamos la detección con el VLA de una fuente débil de radio continuo (19.1±2.7 μJy) a una frecuencia de 3.0 GHz proyectada a $\simeq 2\farcs2$ de la estrella. La probabilidad *a priori* de encontrar una fuente de fondo con esta densidad de flujo dentro de un radio de $2\farcs2$ es sólo 0.0046. Sin embargo, la astrometría realizada con las imágenes del VLA y ALMA, separadas por 5.5 años, indica que no hay movimientos propios significativos, descarta la asociación de la fuente de radio con el sistema HR 8799 y sugiere que se trata de una galaxia milimétrica de fondo con emisión de polvo en el milimétrico y emisión sincrotrón parcialmente ópticamente gruesa en el centimétrico.

Key Words: astrometry — proper motions — radio continuum: general — stars: individual: HR 8799

1. INTRODUCTION

More than 100 exoplanets have been discovered with the technique of direct imaging, as listed in the NASA Exoplanet Archive (Akeson et al. 2013). HR 8799 is the star where exoplanets were first directly imaged. Four exoplanets were found within ≈80 au (≈ $2''$ at the distance of 40.85 pc) in the plane of the sky from the star (Marois et al. 2008; 2010). The observed proper motions of the exoplanets around the star confirmed the association (Close & Males 2010). In addition to the four exoplanets, HR 8799 exhibits a debris disk (Booth et al. 2016; Wilner et al. 2018), extending from $\simeq 2''$ ($\simeq$80 au) to $\simeq 7''$ ($\simeq$280 au) in radius, with a clear central cavity, and detectable in the sub-millimeter (Faramaz et al. 2021). In addition, these authors report the presence of an 880 μm point source associated with the star.

In this paper we present sensitive VLA observations of the HR 8799 region obtained with the purpose of searching for emission from the star or from one of its four exoplanets. In § 2 we discuss the observations, while in § 3 we interpret the data. Finally, our conclusions are presented in § 4.

2. OBSERVATIONS

2.1. *VLA*

The data of project 12B-188 were obtained from the archives of the Karl G. Jansky Very Large Array (VLA) of NRAO[3]. These observations were made with the highest angular resolution **A** configuration

[1]Instituto de Radioastronomía y Astrofísica, UNAM, México.
[2]Mesoamerican Center for Theoretical Physics, UNACH, México.

[3]The National Radio Astronomy Observatory is a facility of the National Science Foundation operated under cooperative agreement by Associated Universities, Inc.

TABLE 1

PARAMETERS OF THE VLA AND ALMA OBSERVATIONS OF THE HR 8799 REGION

Project	Mean Epoch	Telescope	Frequency/ Bandwidth	Deconvolved Dimensions	Total Flux Density	Position[a] RA(J2000)[b]	DEC(J2000)[c]
12B-188	2012.88	VLA	3/2 GHz	$0\farcs5\pm0\farcs2\times0\farcs2\pm0\farcs2;+71^\circ\pm35^\circ$	19.1±2.7 μJy	$28\fs763\pm0\fs003$	$04\farcm71\pm0\farcs03$
2016.1.00907.S	2018.38	ALMA	340/8 GHz	$0\farcs5\pm0\farcs1\times0\farcs5\pm0\farcs1;+160^\circ\pm91^\circ$	207±10 μJy	$28\fs764\pm0\fs003$	$04\farcm68\pm0\farcs05$

[a]For the epoch of the observations.
[b]23^h07^m.
[c]$+21^\circ08'$.

during six epochs between 2012 October 31 and 2012 November 26. The observations were made in the S-band continuum (2-4 GHz), with 16 spectral windows of 128 MHz each. These spectral windows were divided into 64 channels of 2 MHz individual width. The amplitude calibrator was J0137+3309 (3C48) and the gain calibrator was J2254+2445. The data were calibrated in the standard manner using the version 5.6.2-3 of the CASA (Common Astronomy Software Applications; McMullin et al. 2007) package of NRAO and the pipeline provided for VLA[4] observations. The data of the six epochs were concatenated in a single file to increase the signal-to-noise ratio. The images were made using a robust weighting of 2 (Briggs 1995), to optimize the sensitivity at the expense of losing some angular resolution.

2.2. *ALMA*

The sub-millimeter continuum data (at 340 GHz) were obtained from the ALMA data archive. The project was conducted under the program 2016.1.00907.S (PI: V. Faramaz). For this study, we only used the 12 m array observations carried out from 2018 May 13 to June 1. The data were taken using baselines ranging from 15 to 314 m (18 to 392 kλ). The ALMA digital correlator was configured with four spectral windows (SPWs), each one 2 GHz wide. Three of these SPWs were used for the continuum, and one for the detection of the CO(3−2) molecular line at a rest frequency of 345.79598990 GHz. Bright quasars J2148+0657, J2253+1608, and J2253+1608 were used as flux, bandpass, and gain phase calibrators. The total time on-source was 4.5 hrs. The raw data were calibrated, and then imaged using the Common Astronomy Software Applications (CASA) version 5.1.1. The digital correlator was set up with three spectral windows with a bandwidth of 2 GHz (divided into 128 channels resulting in a channel width of 15.625 MHz) and one spectral window with a bandwidth of 1.875 GHz (divided into 3840 channels resulting in a channel width of 488.281 kHz). The CO(3−2) line was the only spectral line excluded during the process of the continuum construction. We obtained an image rms noise for the continuum at 0.8 mm of 10 μJy beam^{-1} at an angular resolution of $0\farcs88\times0\farcs76$; 14°. This angular resolution is very similar to that obtained in the VLA image (see caption of Figure 1). We used a robust parameter equal to 0.5 in the TCLEAN task, an adequate compromise between angular resolution and sensitivity. The parameters of the sub-millimeter source detected are given in Table 1. The ALMA observations were not configured to detect any polarized emission. For both the VLA and the ALMA observations we fitted the data in the image plane with the task IMFIT of CASA. The results of such fittings are given in Table 1. Our derived value for ALMA, 207±10 μJy is lower than the value of 316±20 μJy obtained by Faramaz et al. (2021). This difference is probably due to the fact that Faramaz et al. (2021) included in their analysis data from the Atacama Compact Array, recovering more extended flux.

3. INTERPRETATION

3.1. *VLA data*

The final image (Figure 1) reveals the presence of a 3.0 GHz source about $2\farcs2$ to the north of HR 8799. This radio source does not coincide in position with the star or with any of its exoplanets and appears to be located at the inner edge of the debris disk of HR 8799. In Figure 1 we show the radio continuum source as well as the positions of HR 8799 and its four exoplanets for epoch 2012.88, corrected for the proper motions of the star from Gaia DR3 (Gaia collaboration et al. 2023) and an interpolation of the orbital motions of the exoplanets with respect to the star taken from Konopacky et al. (2016). In Figure 1 we also show the approximate position of the inner radius of the debris disk. The best-fit model for this parameter given by Faramaz et al. (2021) is 135±4 au, that at the distance of 40.85 pc derived from the Gaia DR3 parallax equals 3.3±0.1 arcsec.

The parameters of the radio source are given in Table 1. No circular polarization was detected at an

[4]https://science.nrao.edu/facilities/vla/data-processing/pipeline.

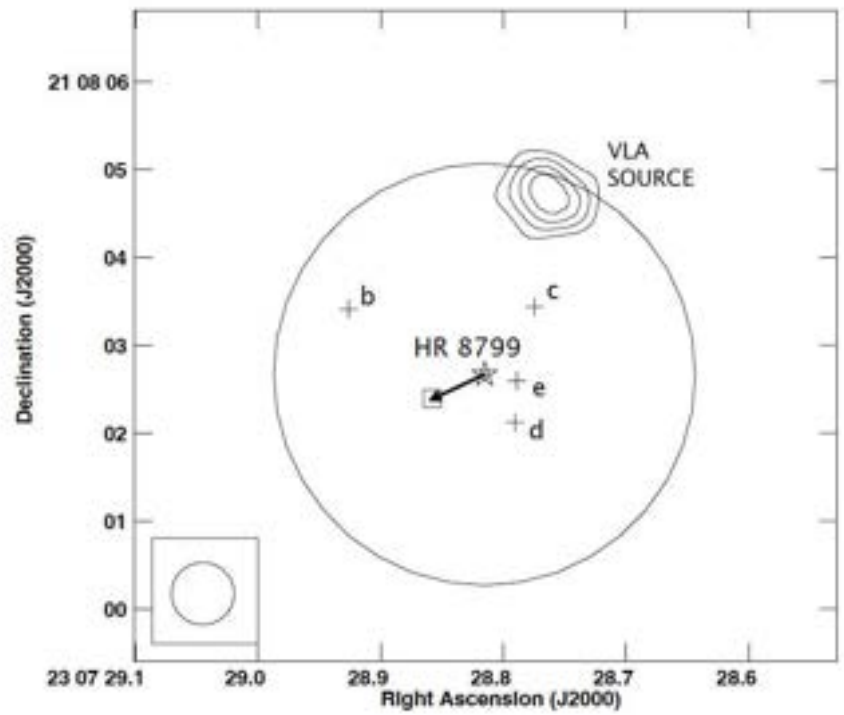

Fig. 1. Objects in the vicinity of HR 8799. The contours show the Very Large Array source observed at 3.0 GHz for epoch 2012.88. Contours are -4, 4, 6, 8 and 10 times 1.28 μJy beam^{-1}, the rms noise in this region of the image. The synthesized beam ($0\overset{''}{.}71 \times 0\overset{''}{.}71; -85\overset{\circ}{.}6$) is shown in the bottom left corner of the image. The positions of HR 8799 (star) and its four exoplanets b, c, d, and e (crosses) have been corrected for proper motions and the orbital motions of the exoplanets to the epoch of the VLA observations (2012.88). The large circle marks the inner edge of the debris disk and shows that all four exoplanets as weLl as the VLA source fall inside this inner edge. The arrow gives the proper motion of HR 8799 between the epoch of the VLA observations (star) and that of the ALMA observations (2018.38), with the position of HR 8799 for this epoch indicated with a square.

absolute upper limit of 19%. What is the *a priori* probability of finding a 3.0 GHz source with a flux density of 19.1 μJy in a circle with radius of $2\overset{''}{.}2$? To estimate this probability we have used the 3.0 GHz source catalog of Smolčić et al. (2017) to produce a plot of the expected number of background sources as a function of flux density (Figure 2). From this figure we find that the expected number of sources with a flux density equal or larger than 19.1 μJy is 1.1 per square arcmin. Since a circle with radius of $2\overset{''}{.}2$ has a solid angle of 0.0042 square arcmin, the *a priori* probability is 0.0046, or 1 in 215. This probability is small, but not stringently improbable.

Another characteristic that may help understand the nature of the radio source is its spectral index. Dividing the data in two windows of 1 GHz wide each centered at 2.5 and 3.5 GHz, we obtain flux densities of 16.5±4.1 and 25.3±2.9 μJy, respectively. These flux densities give a spectral index of $\alpha = 1.3 \pm 0.9$ ($S_\nu \propto \nu^\alpha$). The uncertainty is large but the value certainly favors a positive spectral index. This is somewhat unusual for 3.0 GHz background sources since only $\simeq$11% of them have spectral indices $\geq$0.4 (Smolčić et al. 2017), the 1-σ lower limit of our estimate. Finally, we searched for time variability determining the flux density of the source for each of the individual six epochs. We found that all individual six flux densities coincided at the 1-2σ level with the average value given in Table 1, suggesting no variability in a timescale of days to one month.

3.2. *ALMA Data*

In the same way that at 3.0 GHz, we can ask how probable it is that a background source with 0.49 mJy at 338 GHz falls inside the circle with a radius of $2\overset{''}{.}2$ centered on HR 8799. From the results of Zavala et al. (2017) we estimate that the number of background sources with a flux density of 0.49 mJy or higher at 850 μm is about 4.9 per square arcmin. Then, the *a priori* probability that such a source falls inside the circle with a solid angle of 0.0042 square arcmin is 0.021. Considering that a large number of

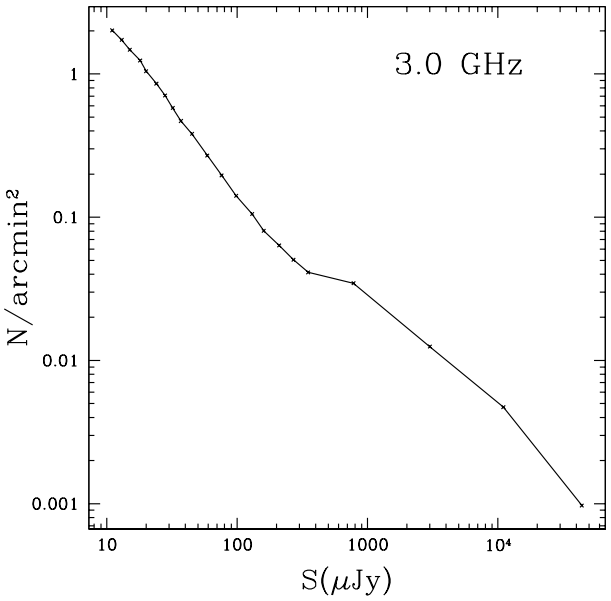

Fig. 2. Expected number of 3.0 GHz sources per square arcmin as function of the flux density lower limit. Derived from Smolčić et al. (2017).

protoplanetary disks is known, this apparent association is not unexpected. Just in Orion, several hundred protoplanetary disks have been detected (van Terwisga et al. 2022). As in the case of the VLA data, we searched for time variability determining the flux density of the source for each of the individual six epochs. We found that all six individual flux densities coincided at the 1-2σ level with the average value given in Table 1, suggesting no variability in a timescale of days to one month.

3.3. *Comparison Between the VLA and the ALMA Data*

Our first conclusion is that despite the low probability of finding a centimeter source so close to HR 8799, the coincidence of positions between the VLA and ALMA data (separated by 5.5 years) rules out the association of the radio source with the HR 8799 system. The two positions coincide within $\leq 0\farcs03$. HR 8799 has large proper motions, of order $0\farcs1$ per year ($\mu_\alpha \cos\delta = 108.284 \pm 0.056$ mas yr^{-1}; $\mu_\delta = -50.040 \pm 0.059$ mas yr^{-1}; Gaia collaboration et al. 2023). In the time interval between the two data sets, we expect a total displacement of $\simeq 0\farcs6$, twenty times larger than our upper limit. This rules out a possible true association between the radio source and the HR 8799 system.

The deconvolved dimensions of the VLA and ALMA sources are consistent within the noise. The spectral index between the 3.0 and 340.0 GHz flux densities is 0.69±0.03. This spectral index and the lack of a proper motion suggest that the radio source is a background millimeter galaxy.

We also note that the data points of Faramaz et al. (2021) have flux densities of 316±20 and 58±18 μJy, at 340 and 230 GHz, respectively. These two points give a spectral index of 4.0±0.9. As noted by Faramaz et al. (2021), this value is too steep to be consistent with the typical millimeter spectral index expected from debris disks (2.5±0.4; MacGregor et al. 2016) and is more consistent with typical values expected for extragalactic dust emission (3.6±0.4; Casey 2012). This source is thus likely to be a background millimeter galaxy. Our 3 GHz flux density (19.1±2.7 μJy) far exceeds the extrapolation of the mm fit to 3 GHz, and at this frequency has a spectral index of 1.3±0.9, suggesting this emission is partially thick synchrotron emission from the galaxy. Recent reviews on protoplanetary disks and debris disks are given by Andrews (2020) and Hughes et al. (2018), respectively.

3.4. *The Arp Effect*

These unlikely associations between sources in the plane of the sky can be called the Arp Effect. Alton Arp (1927-2013) was a distinguished astronomer that studied interacting and apparently interacting galaxies. In some cases, he found that two apparently interacting galaxies close in the sky had different redshifts, leading him to question the cosmological interpretation of redshifts. Several of these apparently interacting sources are described in his Atlas of Peculiar Galaxies (Arp 1966). An example of this type of sources is Stephan's Quintet, that more properly should be called Stephan's Quartet because one of the galaxies is much closer to us than the other four. Arp's Effect can be summarized as follows: if you study a sufficiently large number of sources, you will find some with unlikely apparent associations. Nevertheless, the topic deserves more research.

4. CONCLUSIONS

We analyzed VLA observations of the A5/F0 V star HR 8799, detecting a source at $2\farcs2$ to the north of HR 8799. The *a priori* probability of finding such a source is 0.0042. Despite this low probability, which suggests a true association, the lack of proper motions, obtained by comparing the VLA data with ALMA data taken 5.5 years after, favors the radio source being a background millimeter galaxy unrelated to the HR 8799 system.

As more protoplanetary and debris disks are studied, other apparent associations are expected to

emerge. Another case is HD 95086, where a millimeter source was found projected on its debris disk (Zapata et al. 2018). In this case the lack of a proper motion also favors the source being a background millimeter galaxy. Another example is the source dubbed the "Great Dust Cloud" (Gáspár et al. 2023) apparently associated with Fomalhaut, that has also been interpreted as a background millimeter galaxy (Kennedy et al. 2023).

This research has made use of the NASA Exoplanet Archive, which is operated by the California Institute of Technology, under contract with the National Aeronautics and Space Administration under the Exoplanet Exploration Program. This research has made use of data obtained from or tools provided by the portal exoplanet.eu of The Extrasolar Planets Encyclopaedia. This work also made use of data from the European Space Agency (ESA) mission *Gaia* (https://www.cosmos.esa.int/gaia), processed by the *Gaia* Data Processing and Analysis Consortium (DPAC, https://www.cosmos.esa.int/web/gaia/dpac/consortium). Funding for the DPAC has been provided by national institutions, in particular the institutions participating in the *Gaia* Multilateral Agreement. L.A.Z. acknowledges financial support from CONACyT-280775 and UNAM-PAPIIT IN110618, and IN112323 grants, México. L.F.R. acknowledges the financial support of DGAPA (UNAM) IN105617, IN101418, IN110618 and IN112417 and CONACyT 238631 and 280775-CF Grant 263356.

REFERENCES

Akeson, R. L., Chen, X., Ciardi, D., et al. 2013, PASP, 125, 989, https://doi.org/10.1086/672273

Andrews, S. M. 2020, ARA&A, 58, 483, https://doi.org/10.1146/annurev-astro-031220-010302

Arp, H. 1966, ApJS, 14, 1, https://doi.org/10.1086/190147

Booth, M., Jordán, A., Casassus, S., et al. 2016, MNRAS, 460, 10, https://doi.org/10.1093/mnrasl/slw040

Briggs, D. S. 1995, High Fidelity Deconvolution of Moderately Resolved Sources, Ph.D. Thesis, The New Mexico Institute of Mining and Technology

Casey, C. M. 2012, MNRAS, 425, 3094, https://doi.org/10.1111/j.1365-2966.2012.21455.x

Close, L. M. & Males, J. R. 2010, ApJ, 709, 342, https://doi.org/10.1088/0004-637X/709/1/342

Faramaz, V., Marino, S., Booth, M., et al. 2021, AJ, 161, 271, https://doi.org/10.3847/1538-3881/abf4e0

Gaia Collaboration, Vallenari, A., Brown, A. G. A., et al. 2023, A&A, 674, 1, https://doi.org/10.1051/0004-6361/202243940

Gáspár, A., Wolff, S. G., Rieke, G. H., et al. 2023, NatAs, 7, 790, https://doi.org/10.1038/s41550-023-01962-6

Hughes, A. M., Duchêne, G., & Matthews, B. C. 2018, ARA&A, 56, 541, https://doi.org/10.1146/annurev-astro-081817-052035

Kennedy, G. M., Lovell, J. B., Kalas, P., et al. 2023, MNRAS, 524, 2698, https://doi.org/10.1093/mnras/stad2058

Konopacky, Q. M., Marois, C., Macintosh, B. A., et al. 2016, AJ, 152, 28, https://doi.org/10.3847/0004-6256/152/2/28

MacGregor, M. A., Wilner, D. J., Chandler, C., et al. 2016, ApJ, 823, 79, https://doi.org/10.3847/0004-637X/823/2/79

Marois, C., Macintosh, B., Barman, T., et al. 2008, Sci, 322, 1348, https://doi.org/10.1126/science.1166585

Marois, C., Zuckerman, B., Konopacky, Q. M., et al. 2010, Natur, 468, 1080, https://doi.org/10.1038/nature09684

McMullin, J. P., Waters, B., Schiebel, D., et al. 2007, ASPC 376, Astronomical Data Analysis Software and Systems XVI, ed. R. A. Shaw, F. Hill and J. Bell, 127

Smolčić, V., Novak, M., Bondi, M., et al. 2017,A&A, 602, 1, https://doi.org/10.1051/0004-6361/201628704

van Terwisga, S. E., Hacar, A., van Dishoeck, E. F., et al. 2022, A&A, 661, 53, https://doi.org/10.1051/0004-6361/202141913

Wilner, D. J., MacGregor, M. A., Andrews, S. M., et al. 2018, ApJ, 855, 56, https://doi.org/10.3847/1538-4357/aaacd7

Zapata, L. A., Ho, P. T. P., & Rodríguez, L. F. 2018, MNRAS, 476, 5382, https://doi.org/10.1093/mnras/sty420

Zavala, J. A., Aretxaga, I., Geach, J. E., et al. 2017, MNRAS, 464, 3369, https://doi.org/10.1093/mnras/stw2630

Luis F. Rodríguez and Luis A. Zapata: Instituto de Radioastronomía y Astrofísica, Universidad Nacional Autónoma de México, Apartado Postal 3–72, 58090 Morelia, Michoacán, México (l.rodriguez@irya.unam.mx).

Luis F. Rodríguez: Mesoamerican Center for Theoretical Physics, UNACH, México.

Revista Mexicana de Astronomía y Astrofísica, **60**, 361–365 (2024)

https://doi.org/10.22201/ia.01851101p.2024.60.02.13

ALP-PHOTON INTERACTION IN THE STELLAR ENVIRONMENT

Ankur Chaubey[1] and Avijit K. Ganguly[2]

Received February 24 2024; accepted July 22 2024

ABSTRACT

The spin zero, very light bosons, like the pseudoscalar axion, are collectively grouped into the term axion-like particle (ALP). These elusive particles qualify as candidates for dark matter. ALPs also show their presence in higher dimensional theories, as K.K. particles in Kaluza Klein theory, moduli in string theory and chameleons in cosmology. They can interact with the photon via dimension-five coupling. In this text we provide an alternative method for investigating the signatures of the dark matter candidate particles (i.e., ALP) by estimating the expressions of the probabilities of conversion between different degrees of freedom of interacting photons into ALP and into each other in presence of a stellar magnetized background. We have also tried to explain the contribution of pseudoscalar ALP-photon mixing to the luminosity function of stars like red giants, supergiants, white dwarfs, etc.

RESUMEN

Los bosones ligeros de espín cero, como el axión seudoescalar, se agrupan con el término "partículas similares al axión (ALP)". Estas partículas son candidatos para explicar la materia oscura. Los ALP muestran su presencia en teorías de muchas dimensiones, como partículas K.K. en la teoría de Kaluza-Klein, como módulos en la teoría de cuerdas o como camaleones en cosmología. Pueden interactuar con los fotones mediante un acoplamiento de dimensión 5. Presentamos un método alternativo para investigar las señales de los ALP como candidatos a materia oscura, estimando las expresiones para la probabilidad de conversión entre varios grados de libertad de un fotón en interacción con un ALP o de fotones entre sí, en presencia de un fondo interestelar magnetizado. Intentamos explicar la contribución de la mezcla seudoescalar ALP-fotón a la función de luminosidad de las gigantes rojas, supergigantes, o enanas blancas.

Key Words: galaxies: photometry — methods: numerical — white dwarfs

1. INTRODUCTION

For quite some time now the evidences in favour of the existence of dark matter (DM) have been mounting from astrophysical and cosmological observations (e.g. flatness of galaxy rotation curves or the light spectrum from bullet clusters etc.). According to the current understanding, nearly twenty two percent of the matter content of the universe is in the form of DM, that needs proper identification. There are many candidate particles to explain it, like neutrino, millicharge particles, dark photons, to name a few. However, compared to them axions are more appealing because they were the ones initially postulated to cure the strong CP and the $U_A(1)$ problem of quantum chromodynamics (QCD). Owing to their origin and connection to theories of unification, as well as particle physics (Conlon & David 2013-Sikivie 2021), confirmation of their existence has remained a sought after activity in laboratories, based as well on astrophysics experiments.

Owing to their anomaly-related origin, the structure of the axion (ϕ') and the photon (γ interaction Lagrangian) when expressed in terms of the coupling constant $g_{\phi'\gamma\gamma}$ and the field strength tensor $F^{\mu\nu}$, turns out to be of the form,

$$L_{int} = \frac{1}{4} g_{\phi'\gamma\gamma} \phi' F_{\mu\nu} \tilde{F}^{\mu\nu}.$$

[1]Awdhoot Bhagwan Ram PG. College, Anpara, Sonebhadra 231225, India.

[2]Institute of Science, Department of Physics, Banaras Hindu University, Varanasi 221005, India.

For L_{int} to remain invariant under charge C conjugation, parity P and time T reversal symmetry transformations, the axion field turns out to be CP violating ($\not{C}\not{P}$) and PT preserving. As a result, in a magnetized vacuum (i.e. vacuum with an external magnetic field B), or in an unmagnetized medium, only those photons having their polarization plane parallel ($\gamma_\parallel$) to B interact with ϕ' and the rest, i.e., photons having a polarization plane orthogonal ($\gamma_\perp$) to B remain free. Therefore, in a magnetized vacuum or in an unmagnetized medium, only the $\gamma_\parallel$ and ϕ' undergo conversion into each other and back. Once converted, the axions residing in the medium stream out almost freely due to their extremely small cross section $\sigma \propto g^2_{\phi' e}$ (i.e., due to smallness of the $e\phi'$ coupling constant $g_{\phi' e} < 10^{-13}$ GeV^{-1} and the $\gamma\ \phi'$ coupling constant $g_{\phi'\gamma\gamma} \sim 10^{-11}$ GeV^{-1}). Thus they turn out to be ideal candidates as astrophysical cooling agents next to neutrinos ($\bar{\nu}_e$) or other agents mentioned already. Therefore, studies of axion-aided cooling physics for multiple astrophysical sources were initiated to vindicate their existence.

Sources like giants, supergiants, red giants, horizontal branch stars or white-dwarfs (WD) have shown a statistically significant amount of extra energy loss, which is difficult to explain using standard physics arguments. Their existence has been inferred from various phenomena, e.g., from the excess spin-down rate of the WDs, from their luminosity function (Gianotti et al. 2016) ($L_\gamma = C_\gamma L_{sun} T_7^{3.5}$) or from the ratio of the number of stars in the horizontal branch (HB) and the red giant branch (RGB) existing in globular clusters (Gianotti et al. 2016-Cho & Lee 2005). Labelling the ratio of these two numbers as R, it was realised that its observed value is smaller than the expected range, that is supposed to lie between 1.44 to 1.5. So these observations initiated a need to look for some extra cooling mechanisms operating in the stellar interior, so that extra channels of energy transport open up that could, in principle, compensate the mismatch between various theoretical and observational estimates.

Independently of this cooling anomaly, it was noted in earlier studies (Chaubey et al. 2024-Ganguly et al. 2009) that the standard picture of single channel $\gamma_\parallel \to \phi'$ oscillation undergoes a paradigm shift once the parity violating correction to the photon self-energy tensor (PSET) is incorporated in the effective axion-photon Lagrangian. With the incorporation of the parity violating piece, all the existing degrees of freedom of the system (i.e. photon's $\parallel$, $\perp$ and longitudinally (L) polarized states represented by $\gamma_\parallel, \gamma_\perp$ and γ_L - and axion ϕ') would get coupled with each other and hence they would be oscillating into each other. Thus, these oscillations would initiate a new ($\gamma_\perp - \phi'$) channel of energy loss. The goal of this study is to explore the role of this extra energy loss channel to explain the required anomalous cooling of these stars.

2. EFFECTIVE LAGRANGIAN WITH MAGNETIZED MEDIUM EFFECTS

In the interior of a compact star, pseudoscalar axions are produced abundantly due to Compton, Bremsstrahlung and Primakoff processes. The presence of a non-zero electron fraction ($Y_e > 5$), a magnetic field B and a core temperature of the order of 10^{7o} K, make an ideal physical situation for the production of axion-like particles. The extent of this magnetized medium introduces a parity violating part to the PSET that was estimated in Ganguly et al. (1999).

The pseudoscalar ALP (ϕ')-photon(γ) mixing dynamics can now be studied by employing the effective Lagrangian provided below:

$$L_{eff,\phi'} = \frac{1}{2}\phi'[k^2 - m^2_{\phi'}]\phi' - \frac{1}{4} f_{\mu\nu} f^{\mu\nu} + \frac{1}{2} A_\mu \Pi^{\mu\nu}(k, \mu, T, eB) A_\nu - \frac{1}{4} g_{\phi'\gamma\gamma}\phi' \tilde{\bar{F}}^{\mu\nu} f_{\mu\nu}, \quad (1)$$

where the term defined as $A_\mu \Pi^{\mu\nu}(k, \mu, T, eB) A_\nu$ corresponds to the photon self energy correction to the effective Lagrangian of the pseudoscalar ALP-photon system, $g_{\phi'\gamma\gamma}$ is the coupling constant of pseudoscalar ALP-photon mixing. The other terms have their usual meanings as found in the literature.

3. EQUATIONS OF MOTION

The equations of motion of an ALP-photon interacting system are obtained by using the standard variational principle. They can be expressed in terms of the form factors ($\gamma_\parallel, \gamma_\perp, \gamma_L$) of the gauge potential A_μ in the orthonormal basis vectors $\hat{b}^{(1)\nu} = k_\mu \bar{F}^{\mu\nu}, \hat{I}^\nu = (b^{2\nu} - \frac{\tilde{u} b^{(2)}}{\tilde{u}^2}\tilde{u}^\nu)$, $\hat{\tilde{u}}^\nu = (g^{\mu\nu} - \frac{k^\mu k^\nu}{k^2}) u_\mu$, $b^{(2)\nu} = k_\mu \tilde{\bar{F}}^{\mu\nu}$ constructed out of the available four vectors and tensors of the system. In matrix form, they can be written as:

$$\left[(\omega^2 + \partial_z^2)\mathrm{I} - \mathrm{M}\right] \begin{bmatrix} \gamma_\parallel(\omega, z) \\ \gamma_\perp(\omega, z) \\ \phi'(\omega, z) \\ \gamma_L(\omega, z) \end{bmatrix} = 0, \quad (2)$$

where I is an identity matrix and matrix M is the 4×4 mixing matrix. The symbols ∥ and ⊥ correspond to plane parallel and perpendicular to the direction of the magnetic field.

The mixing matrix M in terms of the newly defined variables $\Pi_L = \omega_p^2\left(1-\frac{\omega_p^2}{\omega^2}\right)$, $G = g_{\phi'\gamma\gamma}\omega B\sin(\pi/4)$, $F = \omega_B\omega_p^2\cos(\pi/4)/\omega$ and $L = g_{\phi'\gamma\gamma}\omega_p B\sin(\pi/4)$ can be cast in the following form:

$$\mathrm{M} = \begin{bmatrix} \omega_p^2 & -iF & 0 & 0 \\ iF & \omega_p^2 & iG & 0 \\ 0 & -iG & m_{\phi'}^2 & -iL \\ 0 & 0 & iL & \Pi_L \end{bmatrix}. \tag{3}$$

Here ω_p is the plasma frequency of the medium. In order to get the dynamics of the available degrees of freedom of the system, the mixing matrix M has been diagonalized by a unitary transformation $\mathbf{U}^\dagger\mathrm{M}\mathbf{U} = M_D$ (see Chaubey et al. 2024). The matrix M_D is the diagonalized matrix that contains four eigenvalues λ_1, λ_2, λ_3, and λ_4 of the mixing matrix M. Matrix $\mathbf{U}$, given by:

$$\mathbf{U} = \begin{bmatrix} \hat{u}_1 & \hat{u}_2 & \hat{u}_3 & \hat{u}_4 \\ \hat{v}_1 & \hat{v}_2 & \hat{v}_3 & \hat{v}_4 \\ \hat{w}_1 & \hat{w}_2 & \hat{w}_3 & \hat{w}_4 \\ \hat{x}_1 & \hat{x}_2 & \hat{x}_3 & \hat{x}_4 \end{bmatrix}, \tag{4}$$

is the unitary matrix constructed from the eigenvectors of matrix M. The elements (for $i = 1, 2, 3, 4$) are as follows:

$$\hat{u}_i = \big[(\omega_P^2-\lambda_i)(m_{\phi'}^2-\lambda_i)(\Pi_L-\lambda_i) - (\omega_P^2-\lambda_i)(L)^2 - (\Pi_L-\lambda_i)(G)^2\big]\times N_i, \tag{5}$$

$$\hat{v}_i = \big[(\omega_P^2-\lambda_i)[(m_{\phi'}^2-\lambda_i)(\Pi_L-\lambda_i) - (L)^2]\big]\times N_i, \tag{6}$$

$$\hat{w}_i = \big[(\Pi_L-\lambda_i)[(\omega_P^2-\lambda_i)(\omega_P^2-\lambda_i) - (F)^2]\big]\times N_i, \tag{7}$$

$$\hat{x}_i = \big[(\omega_P^2-\lambda_1)(\omega_P^2-\lambda_i)(m_{\phi'}^2-\lambda_i) - (\omega_P^2-\lambda_i)(G)^2 - (m_{\phi'}^2-\lambda_i)(F)^2\big]\times N_i. \tag{8}$$

Here N_i's are the normalization constants, which can be obtained by the expression $N_i = \frac{1}{\sqrt{u_i^2+v_i^2+w_i^2+x_i^2}}$.

The mixing pattern that leads to the mixing matrix M obtained in eq. (3) from the effective Lagrangian given in eq. (1) can be understood in the following way. Due to the presence of PSET in L_{eff}, the two transverse degrees of freedom of the photon (i.e., $\gamma_\parallel$ and $\gamma_\perp$) would mix with each other. Next, due to the presence of the tree level interaction Lagrangian L_{int}(in an external magnetic field) the ⊥ component of photons and the one due to the unmagnetized medium effect: the longitudinal component of photon mix with ϕ'. Thus, all four degrees of freedom of the ALP-photon system mix with each other. These mixings are represented by: $\gamma_\parallel \to \phi'$, $\gamma_\perp \to \phi'$, $\gamma_L \to \phi'$, $\gamma_\perp \to \gamma_L$, $\gamma_\parallel \to \gamma_\perp$ and $\gamma_\perp \to \gamma_L$. The evaluation of probabilities of these mixings is provided in the following section.

4. PROBABILITIES OF CONVERSIONS

The amplitude of the evolution of a state corresponding to one degree of freedom [say $|\gamma_\perp(\omega,0)\rangle$] of an ALP-photon system into another (say $|\phi'(\omega,z)\rangle$) with respect to the photon path length z is obtained by $\langle\gamma_\perp(\omega,0)|\phi'(\omega,z)\rangle$. The probability of this evolution is estimated from the square of the modulus of the obtained amplitude, that is given by:

$$P_{\gamma_\perp\to\phi'} = |\langle\gamma_\perp(\omega,0)|\phi'(\omega,z)\rangle|^2. \tag{9}$$

Since due to the photon self-energy correction introduced in the effective Lagrangian, the pseudoscalar ALP-photon system has four physical degrees of freedom (i.e., $\gamma_\perp$, $\gamma_\parallel$, γ_L and ϕ') that can produce C $\binom{4}{2=6}$ number of combinations of such evolution amplitudes, and hence the corresponding oscillation probabilities represented by: $P_{\gamma_\perp\to\phi'}$ for oscillation between perpendicularly polarized photon to ALP, $P_{\gamma_\parallel\to\phi'}$ for oscillation between parallel polarized photon to ALP, $P_{\gamma_L\to\phi'}$ for oscillation between longitudinally polarized photon to ALP, $P_{\gamma_\parallel\to\perp}$ for oscillation between parallel polarized photon to perpendicularly polarized photon, $P_{\gamma_\perp\to\gamma_L}$ for oscillation between perpendicularly polarized photon to longitudinally polarized photon and lastly $P_{\gamma_\parallel\to\gamma_L}$ for oscillation between parallel polarized photon to longitudinally polarized photon - are generated.

Using the exact solutions of the equations of motion for an ALP-photon system, the full expressions of the probabilities of conversion can be written as follows.

Defining the variables $A = |\hat{v}_1|\hat{w}_1|$, $B = |\hat{v}_2|\hat{w}_2|$, $C = |\hat{v}_3|\hat{w}_3|$ and $D = |\hat{v}_4|\hat{w}_4|$ from eqns. (5)-(8), the probability of conversion of the perpendicular polarization state of the photon $\gamma_\perp$ into the pseudoscalar axion ϕ' turns out to be:

$$\begin{aligned} P_{\gamma_\perp\to\phi'} = {} & (A^2+B^2+C^2+D^2) + 2AB\cos((\Omega_\parallel-\Omega_\perp)z) \\ & + 2BC\cos((\Omega_\perp-\Omega_{\phi'})z) + 2CD\cos((\Omega_{\phi'}-\Omega_L)z) \\ & + 2AC\cos((\Omega_\parallel-\Omega_{\phi'})z) + 2BD\cos((\Omega_\perp-\Omega_L)z) \\ & + 2AD\cos((\Omega_\parallel-\Omega_L)z), \end{aligned} \tag{10}$$

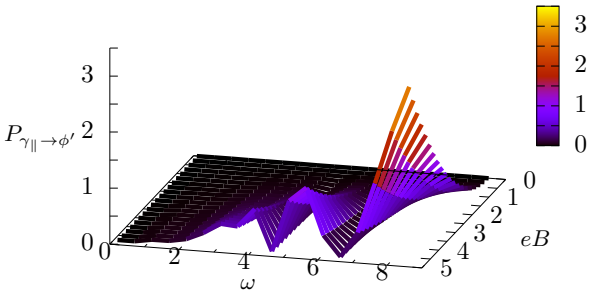

Fig. 1. Plot of oscillation probability $P_{\gamma_\parallel \to \phi'}$ versus photon energy ω (in units of 10^{-5} GeV) and magnetic field eB (in units of 10^{11} Gauss). The probability $P_{\gamma_\parallel \to \phi'}$ has been scaled by the factor 10^{+7}. Plasma frequency ω_p is taken to be $\approx 10^{-10}$ GeV, mass of axion $m_{\phi'} \approx 10^{-11}$ GeV and coupling constant $g_{\phi'\gamma\gamma} \approx 10^{-11}$ GeV^{-1}. The colour figure can be viewed online.

where the variables $\Omega_\parallel$, $\Omega_\perp$, Ω_L and $\Omega_{\phi'}$ in terms of photon energy ω are defined as:

$$\Omega_\parallel = \left(\omega - \frac{\lambda_1}{2\omega}\right),\ \Omega_\perp = \left(\omega - \frac{\lambda_2}{2\omega}\right),$$
$$\Omega_{\phi'} = \left(\omega - \frac{\lambda_3}{2\omega}\right) \text{ and } \Omega_L = \left(\omega - \frac{\lambda_4}{2\omega}\right). \quad (11)$$

It is to be noted that $P_{\gamma_\perp \to \phi'}$ is the only probability (out of six) that survives in absence of any background medium. The other probabilities would vanish.

The oscillation between the parallel polarization state of photon into the pseudoscalar ALP is possible due to the presence of PSET introduced due to magnetized medium effects in the effective Lagrangian. We have numerically evaluated and show in Figure 1 the dependence of it on the magnetic field strength eB and photon frequency ω in the $1-10$KeV range.

Defining a new set of variables, $E = |\hat{u}_1|\hat{w}_1|$, $F = |\hat{u}_2|\hat{w}_2|$, $G = |\hat{u}_3|\hat{w}_3|$ and $H = |\hat{u}_4|\hat{w}_4|$ the probability of finding the ALP ϕ' evolved from the parallel polarization state of photon $\gamma_\parallel$ after travelling a distance z turns out to be:

$$P_{\gamma_\parallel \to \phi'} = (E^2+F^2+G^2+H^2)+2EF\cos((\Omega_\parallel-\Omega_\perp)z) + 2FG\cos((\Omega_\perp-\Omega_{\phi'})z) + 2GH\cos((\Omega_{\phi'}-\Omega_L)z) + 2EG\cos((\Omega_\parallel-\Omega_{\phi'})z) + 2FH\cos((\Omega_\perp-\Omega_L)z) + 2EH\cos((\Omega_\parallel-\Omega_L)z). \quad (12)$$

The unique feature of the presence of a medium is the activation of the longitudinal component of the photon. This interacts directly with the pseudoscalar ALP at the tree level of the effective Lagrangian. Defining the variables $I = |\hat{x}_1|\hat{w}_1|$, $J = |\hat{x}_2|\hat{w}_2|$, $K = |\hat{x}_3|\hat{w}_3|$ and $L = |\hat{x}_4|\hat{w}_4|$, the probability of conversion of the longitudinal polarization state of photon into an axion or pseudoscalar ALP can be written in terms of the variables defined above as:

$$P_{\gamma_L \to \phi'} = (I^2+J^2+K^2+L^2)+2IJ\cos((\Omega_\parallel-\Omega_\perp)z) + 2JK\cos((\Omega_\perp-\Omega_{\phi'})z) + 2KL\cos((\Omega_{\phi'}-\Omega_L)z) + 2IK\cos((\Omega_\parallel-\Omega_{\phi'})z) + 2JL\cos((\Omega_\perp-\Omega_L)z) + 2IL\cos((\Omega_\parallel-\Omega_L)z). \quad (13)$$

It needs to be emphasised here that this probability of conversion is absent in the case of scalar ALP-photon interaction, and when the mixing background of ALP(scalar or pseudoscalar)-photon is a vacuum.

The other three oscillations happening between the photon (which is initially in a particular polarization state) and the photon of a different polarization state after travelling a path of length z, denoted by $\gamma_\parallel \to \gamma_\perp$, $\gamma_\parallel \to \gamma_L$ and $\gamma_\perp \to \gamma_L$ - imply a transformation in the plane of the photon's polarization state. The expressions of their oscillation probabilities turn out to be:

$$P_{\gamma_\parallel \to \gamma_\perp} = (M^2+N^2+O^2+P^2)+2MN\cos((\Omega_\parallel-\Omega_\perp)z) + 2NO\cos((\Omega_\perp-\Omega_{\phi'})z) + 2OP\cos((\Omega_{\phi'}-\Omega_L)z) + 2MO\cos((\Omega_\parallel-\Omega_{\phi'})z) + 2NP\cos((\Omega_\perp-\Omega_L)z) + 2MP\cos((\Omega_\parallel-\Omega_L)z), \quad (14)$$

$$P_{\gamma_\parallel \to \gamma_L} = (Q^2+R^2+S^2+T^2)+2QR\cos((\Omega_\parallel-\Omega_\perp)z) + 2RS\cos((\Omega_\perp-\Omega_{\phi'})z) + 2ST\cos((\Omega_{\phi'}-\Omega_L)z) + 2QS\cos((\Omega_\parallel-\Omega_{\phi'})z) + 2RT\cos((\Omega_\perp-\Omega_L)z) + 2QT\cos((\Omega_\parallel-\Omega_L)z), \quad (15)$$

$$P_{\gamma_\perp \to \gamma_L} = (U^2+V^2+W^2+X^2)+2UV\cos((\Omega_\parallel-\Omega_\perp)z) + 2VW\cos((\Omega_\perp-\Omega_{\phi'})z) + 2WX\cos((\Omega_{\phi'}-\Omega_L)z) + 2UW\cos((\Omega_\parallel-\Omega_{\phi'})z) + 2VX\cos((\Omega_\perp-\Omega_L)z) + 2UX\cos((\Omega_\parallel-\Omega_L)z), \quad (16)$$

where we have defined the variables (in terms of variables present in eqns. 5-8) as follows $M = |\hat{u}_1|\hat{v}_1|$, $N = |\hat{u}_2|\hat{v}_2|$, $O = |\hat{u}_3|\hat{v}_3|$ and $P = |\hat{u}_4|\hat{v}_4|$, $Q = |\hat{u}_1|\hat{x}_1|$, $R = |\hat{u}_2|\hat{x}_2|$, $S = |\hat{u}_3|\hat{x}_3|$ and $T = |\hat{u}_4|\hat{x}_4|$, $U = |\hat{v}_1|\hat{x}_1|$, $V = |\hat{v}_2|\hat{x}_2|$, $W = |\hat{v}_3|\hat{x}_3|$ and $X =$

$|\hat{v}_4|\hat{x}_4|$. The nonzero magnitudes of the last three probabilities verify the prominent contributions of magnetized medium effects on the ALP-photon oscillation.

5. ASTROPHYSICAL APPLICATIONS AND CONCLUSION

To conclude, in this work we noted that the hot dense core of WDs is capable of providing a suitable environment for the photon axion conversion due to the presence of a non-zero fraction of charged fermions and He ions. Axions produced in this environment, would stream out from the core of the WDs carrying a non-trivial amount of energy from the WD interior.

These streaming axion-flux from the core of WDs would contribute not only to the cooling of the star but in turn may also affect the same in two ways. First, by a reduction of mass, hence increasing the extent of the radius (since they are connected by the mass radius relationship). Hence the star period is likely to slow down. G117-B15A, a WD, has been noted to spin down at a rather fast rate, $\dot{P} \approx (12.0 \pm 3.5) \times 10^{-15}$sec. (sec.)$^{-1}$ (c.f. Gianotti et al. 2016 and references therein). If the same happens due to axionic energy loss, it would leave open possibilities of explaining other phenomena (like the electromagnetic torque decay) due to axion physics.

Second. A change in the effective surface temperature of the star, because the total luminosity ($L_{tot} = L_{photon} + L_{neutrinos}$) would undergo a modification through axion luminosity (L_{axion}). As a result, the characteristic cooling time ($\tau_{chr} \propto L_{tot}^{-1}$) of the star would be modified. Therefore one may expect to see changes in the luminosity distribution curve obtained from the expressions provided in Isern et al. (2018).

In this work we have presented some of the possible ways that the magnetized media present in the environment of any compact star can render some observable effects, prominently due to axion mediated interactions, those predicted in the past. We have numerically shown that the presence of magnetized media causes oscillations between the axion and the parallel component of the photon, which are absent when the effect of a magnetized medium is not considered. The amplitude of the probability of this oscillation increases with an increase in eB and ω (see Figure 1).

We expect that, with the availability of more observational data, the significance level of some of the past predictions can be improved.

REFERENCES

Caputo, F., Martinez Roger, C., & Paez, E. 1987, A&A, 183, 228

Chaubey, A., Jaiswal, M. K., & Ganguly, A. K. 2020, PhRvD, 102, 123029, https://doi.org/10.1103/PhysRevD.102.123029

Chaubey, A., Jaiswal, M. K., Ganguly, A. K. 2023, PhRVD, 107, 023008, https://doi.org/10.1103/PhysRevD.107.023008

Chaubey, A., Jaiswal, M. K., Singh, D., Singh, V., & Ganguly, A. K. 2024, EPJC, 84, 627, https://doi.org/10.1140/epjc/s10052-024-12851-1

Cho, D. -H., Lee, S.-G., Jeon, Y -B., & Sim, K. J. 2005, AJ, 129, 1922, https://doi.org/10.1086/428369

Conlon, J. P. & David, M. C. D. 2013, PhRVL 111, 151301, https://doi.org/10.1103/PhysRevLett.111.151301

Craig, N. J. & Raby, S. 2009, arXiv0908, https://doi.org/10.48550/arXiv.0908.1842

Ganguly, A. K., Jain, P., & Mandal, S. 2009, PhRvD, 79, 115014, https://doi.org/10.1103/PhysRevD.79.115014

Ganguly, A. K., Konar, S., & Pal, P. B. 1999, PhRvD, 60, 105014, https://doi.org/10.1103/PhysRevD.60.105014

Gianotti, M., Irastorza, I., Redondo, J., & Ringwald, A. 2016, JCAP, 05, 057, https://doi.org/10.1088/1475-7516/2016/05/057

Isern, J., Gracia-Berro, E., Torres, S., Cojocaru, R., & Catalan, S. 2018, MNRAS,478, 2569, https://doi.org/10.1093/mnras/sty1162

Maiani, L., Petronzio, R., & Zavattini, E. 1986, PhLB, 175, 359, https://doi.org/10.1016/0370-2639(86)90869-5

Raffelt, G. & Stodolsky, L. 1988, PhRvD, 37, 1237, https://doi.org/10.1103/PhysRevD.37.1237

Raffelt, G. 1990, ApJ, 365, 559, https://doi.org/10.1086/169510

Sikivie, P. 2021, RvMP, 93, 015004, https://doi.org/10.1103/RevModPhys.93.015004

Ankur Chaubey: Awdhoot Bhagwan Ram PG. College, Anpara, Sonebhadra 231225, India (ankurchaubey@hotmail.com).

Avijit K. Ganguly: Institute of Science, Department of Physics, Banaras Hindu University, Varanasi 221005, India (avijitk@hotmail.com).

Revista Mexicana de Astronomía y Astrofísica, **60**, 367–371 (2024)

https://doi.org/10.22201/ia.01851101p.2024.60.02.14

PRELIMINARY RESULTS FROM 5 YEARS' SPECTRAL MONITORING OF ANTARES

B. Oostra[1] and M. G. Batista[1]

Received June 25 2024; accepted July 30 2024

ABSTRACT

We present preliminary results of 5 years' monitoring of the radial velocity of Alpha Sco, performed at the Astronomical Observatory of the Universidad de Los Andes in Bogotá, Colombia. The data include 580 spectra acquired on 153 nights between March 2015 and March 2020. The aim of this study is to probe the dynamics of the star's atmosphere on all possible time-scales through the variations of the observed radial velocity. At present, our findings are consistent with previous results from other observers, and the combination of older and new data make it possible to assess several periodicities. A detailed study of these results, including the convective motions in the photosphere, is still in progress.

RESUMEN

Presentamos resultados preliminares de 5 años de monitoreo de la velocidad radial de Alpha Sco, realizado en el Observatorio Astronómico de la Universidad de Los Andes en Bogotá, Colombia. Los datos incluyen 580 espectros adquiridos en 153 noches entre marzo de 2015 y marzo de 2020. El objetivo de este estudio es investigar la dinámica de la atmósfera de la estrella en todas las escalas de tiempo posibles a través de las variaciones en la velocidad radial observada. En la actualidad, nuestros hallazgos son consistentes con resultados previos de otros observadores, y la combinación de datos antiguos y nuevos hace posible evaluar las diversas periodicidades. Un estudio detallado de estos resultados, que incluye los movimientos convectivos en la fotósfera, aún está en progreso.

Key Words: stars: atmospheres — supergiant — techniques: imaging spectroscopy — techniques: radial velocities

1. INTRODUCTION

More than a century ago Wright (1906), at Lick Observatory, noted the variability of Antares' radial velocity (RV). Further studies were conducted by Halm (1909), Lunt (1916), Spencer-Jones (1928), Evans (1961), Smith et al. (1989) and Pugh & Gray (2013a).

These studies revealed a six-year oscillation with a semi-amplitude of about 3 km/s around a mean velocity of -3 km/s. Additional to the 6-year period, several observers have noted the existence of faster oscillations with a period of a few months. Other red supergiant (RSG) stars such as Betelgeuse and Alpha Herculis exhibit a similar behavior (Smith et al. 1989).

The importance of these observations lies in the fact that the cause or excitation mechanism of RV oscillations in RSG is still not fully understood. Early observers considered the possibility of binary-star orbital motion (i.e. Halm 1909, Lunt 1916), but it has already become clear that we are seeing single-star radial pulsations (i.e. Evans 1961, Smith et al. 1989). Spencer-Jones (1928) proposed that the variations were δ Cephei-like; however, RSG are definitely outside the instability strip on the HR diagram.

There seems to be no report of a series of observations of Antares covering densely and consistently a complete 6-year period with the same instrumentation. This is what we attempted to do, taking advantage of our equatorial location which gives us longer observing seasons than previous observers at more northern latitudes. Additional goals included:

[1]Universidad de los Andes, Departamento de Física, Bogotá, Colombia.

TABLE 1

SUMMARY OF OBSERVATIONS

Year	Nights	Spectra
2015	27	53
2016	33	204
2017	13	49
2018	35	142
2019	37	106
2020	8	26

improve the time-coverage and cadence of previous work; combine new observations with published results to construct a longer time baseline; compare new and old data to detect eventual changes; take account of convection effects; search for variability in the granulation pattern; and search for fast (day- or hour-scale) variations.

We could not reach the 6-year goal due to the closing of our campus from March 2020 till end 2021. New observations began in September 2023 using an improved spectrograph. Neither have we completed the study of convection effects: the velocities presented in this initial report are simple averages of 15 selected spectral lines (Table 2). A simplistic approach would assume that the effect of convection would just introduce an additive constant; but this is not the case, because we observed the granulation pattern to be variable, a fact also reported by Gray and Pugh (2012).

In the next section we present details of the instruments and observations; in § 3 we summarize our results, compare them with previously published data and highlight some notable findings; and § 4 gives some plans and expectations for future work.

2. OBSERVATIONS

We secured a total of 580 spectra on 153 nights from March 2015 to March 2020 (Table 1).

From our location in Bogotá, Colombia, at 4.6° northern latitude, Antares can be studied, in principle, from mid-January to the first days of November, the limits being imposed by the mountains to the East and the city buildings to the West of the observatory. Observing dates were not planned systematically; they are the result of the star's visibility, the observers' available time, and the weather. Additionally, observations were impossible during the best part of 2017 because the camera failed and a new one had to be purchased and installed.

Some details of the instrumentation:

- Telescope: Meade LX200 (40 cm).

TABLE 2

SPECTRAL LINES USED FOR VELOCITY MEASUREMENTS [a]

Line	λ	Line	λ
Zr I	6143.2	Sc I	6210.658
Fe I	6151.6169	V I	6216.3643
Na I	6154.2255	Fe I	6219.2801
Fe I	6157.7275	V I	6251.8231
Ca I	6162.173	Fe I	6252.5546
Fe I	6173.3339	Fe I	6254.2573
Fe I	6180.2018	Ti I	6261.0988
Fe I	6200.3121		

[a]The wavelengths are from the VALD server (Ryabchikova et al. 2015).

- Spectrograph: Espartaco (Oostra & Ramirez 2011).
- Spectral resolution: 31000.
- Calibration: Hollow-cathode Th-Ar lamp on separate exposures, and a neon spectrum on all exposures.
- Exposure time: 20 minutes.
- S/N ratio: ≈ 100.
- Uncertainty: ≈ 0.1 km/s judged from the dispersion of the results.

The wavelength range was selected between 6140 and 6265 Å to avoid strong telluric lines and to include strong Th-Ar and neon lines (three neon lines, at 6143, 6164 and 6217 Angstrom, were present in all spectra through a second fiber and made it possible to monitor the instrument's shifts between the stellar and calibration spectra). Unfortunately, this spectral range coincides with a strong TiO band which affects line depth measurements.

For the conversion from the observatory reference to the heliocentric reference we used the tool included in the ISIS software (ISIS, 1997).

3. RESULTS AND DISCUSSION

Figure 1 shows our results as blue dots; the numerical data are available in machine-readable format[2]. Each dot represents the average of the velocities from one night, weighted by the amount of signal present in each individual spectrum. The mean heliocentric velocity of our measurements is

[2]Observational data are available in the repository: `https://github.com/MGBatista1/Antares_Uniandes.git`.

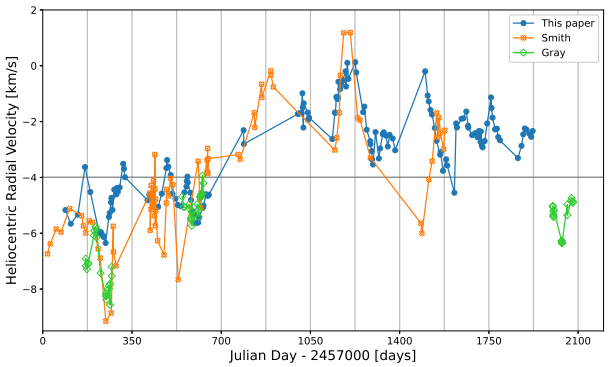

Fig. 1. Nightly averages of our measured velocities (blue dots), compared with results from Smith et al. (1989) (orange dots) and Pugh & Gray (2013) (green dots). The uncertainty of a typical average is about 0.1 km/s. Vertical lines mark steps of 175 days, where the secondary peak of the combined periodogram was found. The color figure can be viewed online.

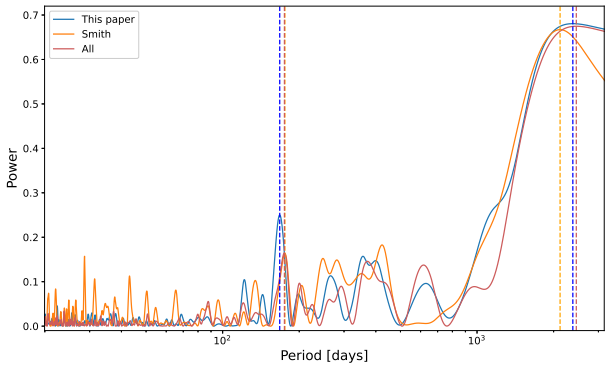

Fig. 2. Lomb-Scargle periodogram of our data (blue line), Smith data (orange) and combined data (light red). Vertical lines show periods close to the two highest powers of our data. The color figure can be viewed online.

−3.14 km/s, with an amplitude of ± 3 km/s. This result is consistent with previous reports from Smith et al. (1989) and Pugh & Gray (2013a). We also combined these three studies in order to find a global oscillation behavior and the mean heliocentric velocity obtained is −3.99 km/s, where several smaller oscillations with shorter periods are also evident.

Superimposed on our results are Smith's and Gray's data, shifted forward by time-intervals determined using a cross-correlation method in order to ensure the best fit. For this comparison we shifted Smith's data forward by 10946 days; assuming 5 cycles to have elapsed between Smith's and our observations; this gives a mean period of 2189 days. Gray's first-season data are advanced by two periods, and his other two seasons by only one period.

We calibrated the spectra directly with calibration lamps, and the same was done by Pugh & Gray (2013a); however, Smith et al. (1989) did it by comparing some metal lines of Antares with the same lines in a spectrum of Arcturus recorded on the same night, and using a known or reported value of Arcturus' velocity. The difference in methods may introduce a small discrepancy in the radial velocity zero point. For now, we have not considered this detail.

We note that some short-period oscillations are similar in the three mentioned data sets. The highest peak observed by Smith et al. (1989) (plotted here at Day ≈1200) was also reported by Wright (1906), but appears lower and broader in our data. Around Day 500 we see an 80-day periodic variation which resembles the 100-day oscillation reported by Pugh and Gray (2013b).

As to the six-year oscillation, Figure 2 shows a Lomb-Scargle periodogram of our data, including a broad peak around 2380 ± 11 days. A periodogram of Smith's results is similar; it peaks at 2120.5 ± 1.7 days. The three data sets combined give us a narrow peak at 2455.8 ± 7.4 days. Errors are estimated by applying a Monte Carlo method. For comparison, Pugh and Gray (2013a) combined their data with all available previous results and report a period of 2167 ± 5 days. The exact value of the six-year period needs not be unique nor constant.

Our periodogram (Figure 2) also shows a conspicuous secondary peak at 167.6 ± 0.08 days. Smith's and the combined data shows a peak at 175.6 ± 0.16 days and 174.9 ± 0.05 days, respectively, which are close to the theoretical value of 180 days computed by Stothers, R. (1969) for the fundamental mode radial pulsation of Antares. Likewise, this is close to the double of the 80-day period mentioned above; but the graph shows no sign at 80 days, nor at 100 days as given by Pugh and Gray (2013b). Vertical lines in Figure 1 show steps of 175 days, and several peaks tend to occur close to them.

In Figure 1, around Day 200 where the minimum radial velocity occurs, Smith's and Gray's results show a larger negative velocity than ours; between Day 500 and 600 all results seem to match; and around Day 1200, where the maximum RV occurs, Smith's measurements are higher than ours. This suggests the amplitude has decreased during the last years. Smith et al. (1989) has commented on the varying amplitude of Alpha Ori. More observations will help to confirm and characterize such a behavior.

A decreasing amplitude is to be expected when no valve mechanism is available to pump energy into

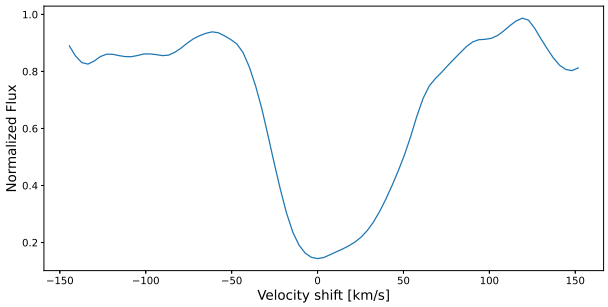

Fig. 3. Profile of the H-alpha absorption line in Antares. The asymmetrical shape does not change appreciably between observations. The color figure can be viewed online.

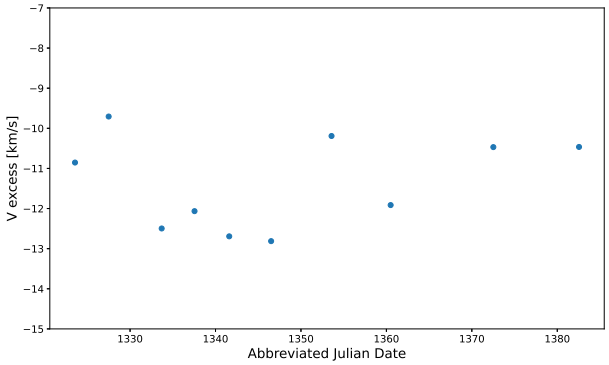

Fig. 4. Velocity excess of the deepest core of the H-alpha line, with respect to the metallic lines, measured during August and September 2018. The color figure can be viewed online.

the pulsation as occurs in Cepheids. This suggests a damped oscillation, excited irregularly by sporadic or stochastic events. Our observations around Days 1500 and 1600 might have witnessed such an event, because after the maximum, instead of declining towards Gray's data set, the RV rises sharply and remains above the expected behavior. Smith et al. (1989) also report a "missing half-cycle" which may be related to this non-periodical driving force. The resulting phase shifts will be a limitation when comparing or combining several data sets.

Some of our data sets acquired during single nights seem to indicate significant variations of the radial velocity ($\approx$ 0.5 km/s) in about an hour. Our 20-minute integration time didn't allow us to confirm this, but presently we are using a faster spectrograph (Oostra & Batista in prep.), allowing 5-minute exposures, to gather more evidence on this aspect.

Smith et al. (1989) showed that the core of the H-alpha line gives a velocity up to 15 km/s more negative than metallic lines; they report a large scatter of this excess, but also a systematic variation which might be in phase with the 6-year oscillation. Moreover, the hydrogen line is quite asymmetrical; the barycenter of the whole profile gives a velocity similar to the metallic lines, but the deepest core is notably shifted blueward; this may be related to an H-rich stellar wind. In 2018 we took some additional spectra around H-alpha to check these facts; we found the hydrogen line profile evidently asymmetrical (Figure 3) and the inner core shifted blueward by some 12 km/s (Figure 4). These details warrant more investigation.

4. CONCLUSIONS AND FUTURE WORK

As to our observatory we may conclude that, despite the adverse environmental conditions, it has proven possible to obtain a meaningful set of observed data on stellar radial velocities.

Our findings are consistent with previous results from other observers, including a 6-year main pulsation and several shorter periods, the most prominent being an oscillation of roughly 175 days, around a mean velocity of -4 km/s.

A comparison of our results with previous observations hints at a variable amplitude.

For the near future we are planning to acquire new data and compare them with our previous results, in order to conclude more about possible changes in the amplitude of the oscillations. Also, our new spectrograph enables us to take 10 spectra per hour, which makes it possible to confirm or reject the fast variations. As our observations span a greater time interval, more will be known about the several oscillation periods.

A better understanding of the (changing) granulation pattern will give us better estimates of the velocity of the outer layers of the star, and, by the way, also for some deeper layers. Also, as has been shown elsewhere (Oostra & Vargas 2022), due to convection effects it is convenient to limit the analysis to a single chemical species; preferably neutral iron (Dravins et al. 1981). These facts justify a complete reevaluation of the measured velocities. A study along this line has been initiated by Luisa Rodríguez (2018) using the first three years of observation.

The hydrogen alpha line profile and differential blueshift will also demand more attention. Finally, comparisons with other similar stars will be useful.

This work has made use of the VALD database, operated at Uppsala University, the Institute of As-

tronomy RAS in Moscow, and the University of Vienna.

REFERENCES

D'Odorico, S., Ghigo, M., & Ponz, D. 1987, ESO Scientific Report, 6, https://spectroscopy.wordpress.com/wp-content/uploads/2010/05/an_atlas_of_the_thorium-argon-spectrum-3900-9000.pdf.

Dravins, D., Lindegren, L., & Nordlund, A. 1981, A&A, 96, 345, https://ui.adsabs.harvard.edu/abs/1981A&A....96..345D

Evans, D. 1961, Royal Observatory bulletins, Series E, 44, 351

Gray, D. F. & Pugh, T. 2012, AJ, 143, 92, https://doi.org/10.1088/0004-6256/143/4/92

Halm, F. 1961, AnCap, 10, 56

ISIS software, 1997, https://ui.adsabs.harvard.edu/abs/1997LPI....28.1443T

Lunt, J. 1916, ApJ, 44, 250, https://doi.org/10.1086/142291

Oostra, B. & Ramírez Casallas, D. A. 2011, Revista Colombiana de Física, 43, 2

Oostra, B. & Vargas, P. 2022, RMxAA, 58, 173, https://doi.org/10.22201/ia.01851101p.2022.58.02.01

Pugh, T. & Gray, D. F. 2013a, AJ, 145, 38, https://doi.org/10.1088/0004-6256/145/2/38

_____. 2013b, AJ, 777, 10, https://doi.org/10.1088/0004-637X/777/1/10

Rodríguez, L. 2018, Bachelor Thesis, https://repositorio.uniandes.edu.co/handle/1992/40018

Ryabchikova, T., Piskunov, N., Kurucz, R. L., et al. 2015, PhyS, 90, 054005, https://doi.org/10.1088/0031-8949/90/5/054005

Smith, M. A., Patten, B. M., & Goldberg, L. 1989, AJ, 98, 2233, https://doi.org/10.1086/115293

Spencer-Jones, H. 1928, MNRAS, 88, 660, https://doi.org/10.1093/mnras/88.8.660

Stothers, R. 1969, ApJ, 156, 541, https://doi.org/10.1086/149987

Wright, H. 1906, Lick Observatory Bulletin, https://doi.org/10.1086/141419

M. G. Batista and B. Oostra: Universidad de los Andes, Departamento de Física, Carrera 1 #18a - 12, 111711, Bogotá, Colombia (mg.batistar, boostra@uniandes.edu.co).

Revista Mexicana de Astronomía y Astrofísica, **60**, 373–379 (2024)

https://doi.org/10.22201/ia.01851101p.2024.60.02.15

RECENT UPDATE OF GAS-PHASE CHEMICAL REACTIONS AND MOLECULAR LINES OF TiO IN CLOUDY

Gargi Shaw[1], Gary J. Ferland[2], Phillip Stancil[3], and Ryan Porter[4]

Received July 2 2024; accepted July 26 2024

ABSTRACT

We present our current update on the gas-phase chemical reactions and spectral lines of TiO in the spectral synthesis code CLOUDY. For this purpose, we have added 229 Ti-related reactions in the chemical network. In addition, we consider 230 fine-structure energy levels, the corresponding 223 radiative transitions, and 444 collisional transitions with ortho and para H_2, and predict 66 TiO lines. We perform spectroscopic simulations of TiO emission from the circumstellar region of the oxygen-rich red supergiant VY Canis Majoris to validate our update. Our model reproduces the observed TiO column density. This update is helpful in modeling dust-free astrophysical environments where Ti is in the gas phase and TiO can form.

RESUMEN

Presentamos nuestra actualización de las reacciones químicas en fase gaseosa y líneas espectrales de TiO en el código de síntesis espectral CLOUDY. Para ello, hemos añadido 229 reacciones relacionadas con el Ti en la red química. Además, consideramos 230 niveles de energía de estructura fina, las correspondientes 223 transiciones radiativas, y 444 transiciones colisionales con orto- y para- H_2 y predecimos 66 líneas de TiO. Realizamos simulaciones espectroscópicas de la emisión de TiO de la región circunestelar de la supergigante roja rica en oxígeno VY Canis Majoris para validar nuestra actualización. Nuestro modelo reproduce la densidad de la columna de TiO observada. Esta actualización es útil para modelar entornos astrofísicos libres de polvo donde el Ti está en fase gaseosa y se puede formar TiO.

Key Words: astrochemistry — methods: numerical — molecular data — software: simulations

1. INTRODUCTION

The spectroscopic simulation code CLOUDY simulates the conditions in a non-equilibrium astrophysical plasma and predicts the resulting spectrum and column densities of various ions, neutrals, and molecules (Chatzikos et al. 2023; Gunasekera et al. 2023; Ferland et al. 2017, 2013). Our aim is to predict more molecular lines with better precision. Hence, we regularly update our chemical network and incorporate improved chemical reactions and internal structures for our existing chemistry whenever new or better data are available (Shaw et al. 2017, 2020, 2023, 2022) and add new molecules as the astrophysical need arises. One such molecule is TiO, a possible precursor of inorganic dust (Danilovich et al. 2020).

TiO is the dominant source of opacity in the atmosphere of cool stars (Lodders 2002) and is observed in the atmosphere of giant M stars (Jorgensen 1994; Kamiński et al. 2013b). Kamiński et al. (2013a) observed pure rotational lines of TiO in the circumstellar envelope of the red supergiant VY Canis Majoris (VY CMa). The observed column density of TiO in VY CMa is $(6.7 \pm 0.8) \times 10^{15}$ cm^{-2}. They also observed TiO_2. In an oxygen-rich circumstellar envelope, nearly all carbon is locked into CO, and hence, TiO forms and can act as an important seed for inorganic dust formation (Gail & Sedlmayr 1998). Kamiński et al. (2013b) showed that for

[1]Department of Astronomy and Astrophysics, Tata Institute of Fundamental Research, Mumbai 400005, India.
[2]Physics & Astronomy, University of Kentucky, Lexington, Kentucky, USA.
[3]Physics & Astronomy, University of Georgia, Georgia, USA.
[4]Stellar Science, 6565 Americas Pkwy 925, Albuquerque, NM 87110, USA.

VY CMa, the dust and TiO emission come from different regions. Their formation regions are separated by about $0''.15$ corresponding to 2.7×10^{13}cm assuming the distance of VY CMa to be 1.20 kpc (Zhang et al. 2012). This confirms that TiO is present in the dust-free region of VY CMa.

The solar abundance of Ti is 8.91×10^{-8} (Grevesse et al. 2010). However, TiO is not observed in the ISM due to the high depletion of Ti (Welsh et al. 1997). In dust-free environments, Ti is in the gas phase and TiO can form.

Here, we aim to include the gas-phase chemical reactions and spectral lines of TiO in the spectral synthesis code CLOUDY (Chatzikos et al. 2023; Gunasekera et al. 2023) which will be useful in modeling dust-free astrophysical environments where TiO is in the gas phase. These updates will be part of the next release of CLOUDY.

2. CALCULATIONS AND RESULTS

2.1. *Updated Ti-Chemistry in* CLOUDY

There is a scarcity of reaction rates for Ti-chemistry due to its very low abundance in the ISM. It is not included in the UMIST Database for Astrochemistry (UDfA) (McElroy et al. 2013) or in Kinetic Database for Astrochemistry (KIDA) (Wakelam et al. 2012). We incorporate available reactions(Tsai et al. 2021; Churchwell et al. 1980; Ramírez et al. 2020), but these are small in number.

We adopted a Si-based chemistry as a proxy for the missing Ti chemistry. Both Ti and Si are important refractory elements (Gilli et al. 2006). In addition, Ti-oxides and Si-oxides are precursors of inorganic dust, and Si-chemistry is well-studied and documented. Hence, for the rest of the Ti-related reactions, we copied analogous reactions involving Si from UDfA. All the reactions in our new network are given in the Appendix.

A large number of models covering diverse astrophysical environments are publicly available with the CLOUDY download under the directory `tsuite`. We compare `tsuite` model predictions every day to monitor the changes in species abundances and line intensities as a result of changes in the source code and atomic and molecular data. The CLOUDY test suite is extensive and includes simulations at very low and very high temperatures, CMB to 10^{10} K. The chemistry must work for all conditions. Often we encounter problems with the extrapolation of simple fits to the temperature range we need for chemical rate coefficients. To overcome this problem, we apply a temperature cap, T_{cap}, for $\beta > 0$ (See Appendix). For $T > T_{cap}$, the rate coefficients retain the same values as at T_{cap}. Though ad-hoc, we choose T_{cap}=2500 K (Shaw et al. 2023). The chemical network is very sensitive to small changes in rate coefficients. Hence, for any chemical update to pass through all the `tsuite` models simultaneously is hard and time-consuming. We critically examine each update if it results in a relative change of greater than ± 30% in column density or line intensity.

In this work, some updates produce a relative change greater than ± 90% in column density.

We find that the two reactions, $H_3O^+ + SiO \rightarrow SiOH^+ + H2O$ and $H_3+ SiO \rightarrow SiOH^+ + H_2$, produce significant changes in $SiOH^+$ column densities with the updated UDfA2012 rate coefficients. The UDfA2012 rate coefficients for the reactions, $HSiO_2^+ + e \rightarrow SiO_2 + H$ and $OH + SiO \rightarrow SiO_2 + H$ result in convergence problem for high density ($> 10^{17}$ cm^{-3}) and low radiation models. Hence, we retain the UDfA2006 rate coefficients for these two reactions.

We calculate the line luminosities/intensities from energy levels and radiative and collisional rate coefficients in the Leiden Atomic and Molecular Database (LAMDA) format (Schöier et al. 2005). TiO energy levels and radiative rate coefficients are taken from the Cologne Database for Molecular Spectroscopy (CDMS) (https://cdms.astro.uni-koeln.de/). The ground state of TiO is triplet-delta with lambda splitting. We consider 230 energy levels, and the corresponding 223 radiative transitions. In addition, we consider 444 collisional transitions with ortho and para H_2. The collisional transitions of CO with ortho and para H_2 are modified from Yang et al. (2010) as a proxy for ortho and para H_2 collisions with TiO. In cases with J_{low}=3 there are four possible transitions, so the CO rates were divided by 4. For J_{low}=2 and J_{low}=1, CO rates were divided by 3 and 2, respectively. Otherwise, each CO rate was divided by 5. The temperature range for collisional rates varies from 2 to 3000 K. These were compiled and converted to LAMDA format. This will be part of the next release of CLOUDY. In the future, we will replace these collisional rates with actual data when they become available. We will also add collisional rate coefficients for other colliders, H and He, when data becomes available.

2.2. *Modelling TiO from VY Canis Majoris*

We present a model for the circumstellar envelope of the red supergiant VY CMa to validate our Ti-chemical network. All calculations are done using the development version of CLOUDY (Chatzikos et al. 2023; Gunasekera et al. 2023). VY CMa has a rich inventory of various molecules (Kamiński et al.

2013b). However, here we concentrate mainly on TiO.

We consider a spherical model with the ionizing source (star) at the center. CLOUDY requires basic input parameters, such as the radiation field, density at the inner radius which is illuminated by the starlight, chemical abundances, etc. Observations reveal that the effective temperature of the central star is 3650 K (Massey et al. 2006) with a luminosity of $(3\pm0.5) \times 10^5$ L$\odot$ (Choi et al. 2008). We use this observed value to set the SED of the radiation field.

VY CMa is a large star with $R\star = 1420 \pm 120$R$\odot$ (Wittkowski et al. 2012). We consider the inner radius of the circumstellar envelope to be at $R\star$. TiO is expected to form nearer the star, where the temperature is high, above the sublimation temperature of dust. Decin et al. (2016) have observed that NaCl forms at $R < 250R\star$ from the central star. Kamiński et al. (2013a) also noticed that the main component of the TiO emission covers the same velocity range as the NaCl profile, but is confined within $R = 28 \times R\star$. The dissociation energy of TiO is much higher than NaCl, so in the gas phase it is expected to peak closer to the central star than NaCl. Since our main focus is TiO, we further confine our model to $R = 28 \times R\star$ from the central star.

For an oxygen-rich environment, nearly all carbon is locked up in CO. Thus, formation of silicate dusts is more favorable than the formation of graphite dust, when physical conditions permit. The sublimation temperature of silicate dusts is ≈ 1400 K. Furthermore, Kamiński et al. (2013a) estimated $T_{rot} = 1010 \pm 870$ K. So, we further constrain our model to have a temperature above > 1400 K.

The density, in general, depends on the distance from the central source of ionization. We consider the density to be proportional to r^{-2}, consistent with a $v \propto r$ wind (Keady et al. 1988; Ziurys 2006). In addition, it is known that the density of the circumstellar envelope can vary over a wide range. Hence, in our grid models, we vary the density $n_H(r_{in})$ (the density at the inner radius (r_{in}) of the circumstellar envelope) from 10^9 to $10^{12.5}$ cm^{-3} in steps of 0.25 dex. We consider solar abundances of elements as reported in Grevesse et al. (2010), and we do not include dust in our model. Finally, we include a background cosmic ray ionization rate (important for the ion balance in molecular regions) of 2×10^{-16} s^{-1} s^{-1} in our grid models (Shaw et al. 2008; Shaw & Ferland 2021).

Figure 1 shows our model's predicted TiO column density as a function of hydrogen number density, $n_H(r_{in})$. The solid horizontal lines represent the observed column density range (Kamiński et al. 2013a). From the plot, we conclude that the observed TiO column density comes from a region with $n_H(r_{in})$=$10^{12.06}$ to $10^{12.08}$ cm^{-3}.

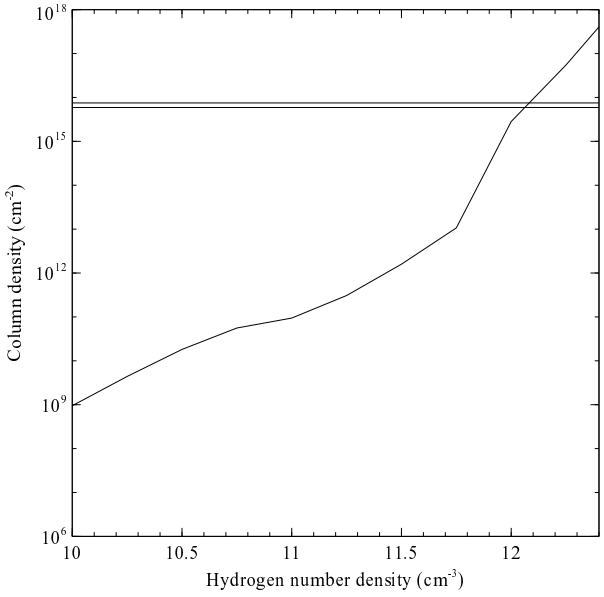

Fig. 1. Column density of TiO as a function of $n_H(r_{in})$. The horizontal lines represent the observed column density range.

Next, we consider a single model with $n_H(r_{in}) = 10^{12.07}$ cm^{-3}, holding other parameters constant. Figure 2 shows the variation of TiO, TiO$^+$, TiO$_2$, Ti, Ti$^+$ as a function of the depth of the cloud from the illuminated surface. The temperature varies from 3431 K to 1400 K across the region considered. We find that Ti is mostly ionic, and the dominant oxide form of Ti is TiO.

Our model's predicted neutral hydrogen column density is $\approx 8\times10^{25}$ cm^{-2}. Although our model does not include dust, it predicts a high H$_2$ column density $\approx 10^{18}$ cm^{-2}. This is due to the presence of a significant H$^-$ abundance, which helps to form H$_2$ in dust-free environments (Shaw et al. 2005). However, this single model predicts a TiO$_2$ column density, 7.16×10^{12} cm^{-2}, much below the observed value.

Figure 3 shows the line intensity of TiO lines for this single model assuming the distance of VY CMa to be 1.20 kpc (Zhang et al. 2012).

Earlier, Gail & Sedlmayr (1998) showed that TiO$_2$ forms at a much lower temperature than TiO. So, we recomputed the same single model but removing the 1400 K temperature limit. The predicted TiO and TiO$_2$ column densities are 7.5×10^{15} and 8.7×10^{15} cm^{-2}, respectively. The observed

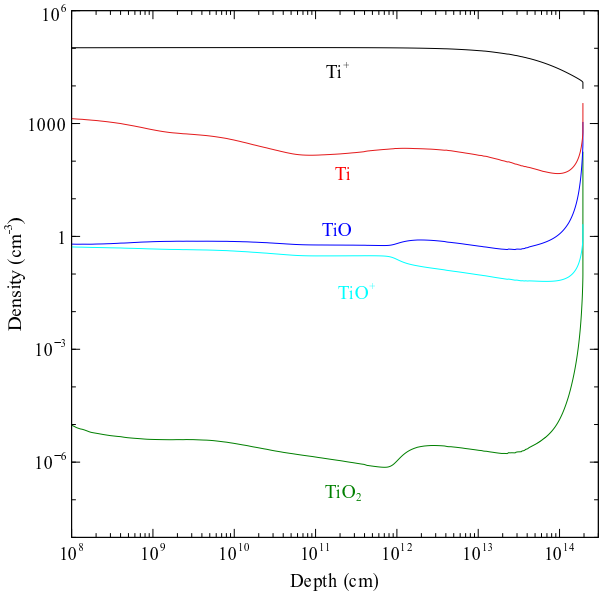

Fig. 2. Variation of TiO, TiO^+, TiO_2, Ti, Ti^+ as a function of cloud depth. The gas temperature is > 1400 K. The color figure can be viewed online.

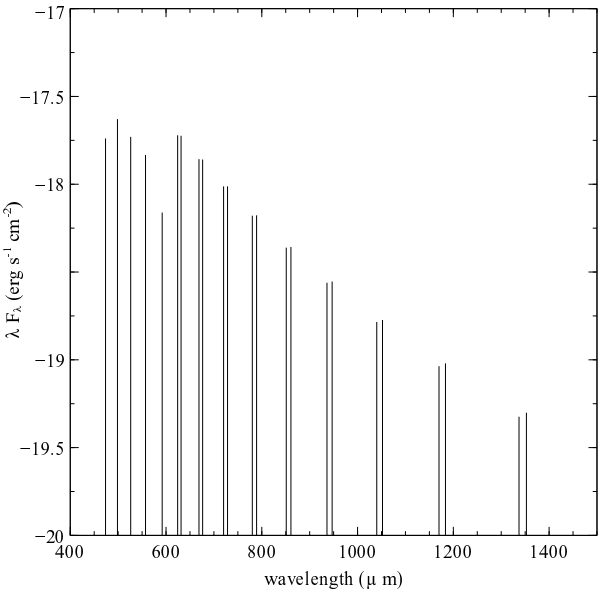

Fig. 3. Intensity of TiO lines

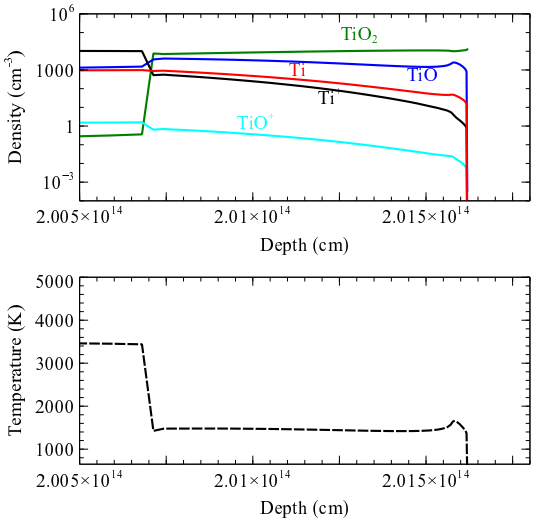

Fig. 4. Variation of TiO, TiO^+, TiO_2, Ti, Ti^+, and temperature as a function of cloud depth. The color figure can be viewed online.

TiO_2 column density is (5.65 ± 1.33) $\times 10^{15}$ cm^{-2} (De Beck et al. 2015). Both these molecules are confined within $R = 28 \times R\star$. The corresponding ionization structure is shown in Figure 4. We notice that as the temperature decreases below 1400 K, more TiO_2 is formed. We conclude that Ti is locked in TiO above 1400 K, and in TiO_2 at a lower temperature. Since silicate dust can form below 1400K, we conclude that TiO_2 remains in the gas phase outside the dust-formation zone, and might play only a minor role in the dust-condensation process around VY CMa. The same conclusion was made by De Beck et al. (2015).

2.3. *Effects of Input Parameters*

There is a debate regarding the luminosity and radius of the star VY CMa. Massey et al. (2006) have estimated the luminosity and radius to be 6×10^4 L$\odot$ and 600 R$\odot$, respectively. However, Wittkowski et al. (2012) have estimated these to be 5×10^5 L$\odot$ and $R\star$ = 1420 $\pm$ 120 R$\odot$, respectively. Here, we show the effects of various input parameters on the predicted hydrogen number density, column densities of TiO and TiO_2 for the above-mentioned model of VY CMa.

Firstly, we consider a value, 1.0 $\times$ 10^5 L$\odot$, instead of 2.5$\times$ 10^5 L$\odot$ considered in § 2.2. We run a similar grid of models varying $n_H(r_{in})$ from 10^9 to $10^{12.5}$ cm^{-3} in steps of 0.25 dex, keeping all the other parameters the same. For this case, the observed TiO column density comes from a region with $n_H(r_{in}) = 10^{11.79}$ to $10^{11.80}$ cm^{-3}. This is lower by $\approx$ 0.3 dex from the value derived in § 2.2.

Next, we consider a lower value of $R\star$ =770 R$\odot$ compared to the earlier value of $R\star$=1540 R$\odot$ for VY CMa, and run a similar grid model keeping other parameters fixed. For this case, the observed TiO column density comes from a region with $n_H(r_{in}) =$

$10^{12.66}$ to $10^{12.67}$ cm^{-3}. This is higher by ≈ 0.6 dex than the value derived in § 2.2.

Further, we change the density to be proportional to r^{-3}, and run a similar grid model keeping other parameters fixed as described in § 2.2. We find that with the new density law, the observed TiO column density comes from a region with $n_H(r_{in}) = 10^{12.28}$ to $10^{12.31}$ cm^{-3}. This is higher by ≈ 0.2 dex than the value derived in § 2.2.

We notice that the value of $n_H(r_{in})$ is more dependent on the inner radius r_{in} of the envelope. However, for all these cases, as the temperature decreases below 1400 K, more TiO_2 is formed. Similarly, both TiO and TiO_2 are confined within $R = 28 \times R\star$.

2.4. *Model Limitations*

Like every astrophysical model, our model also has some limitations. The main limitations are listed below.

Firstly, most of our Ti-related gas-phase chemical reaction rate coefficients involving Ti are copied from analogous Si-related reactions. Secondly, we have considered only ortho- and para- H_2 collisional excitation and deexcitation. Thirdly, we have assumed a spherical geometry. However, observations suggest that the geometry is not perfectly spherical. Despite these limitations, our model predicts the observed column density of TiO and TiO_2.

3. DISCUSSIONS AND CONCLUSIONS

In this work, we updated gas-phase chemical reaction rates and molecular lines arising from TiO in the spectral synthesis code CLOUDY. We added 229 reactions in the chemical network. In addition, we considered 230 energy levels, corresponding radiative transitions, and 444 collisional transitions with ortho- and para- H_2. These molecular lines can be observed using ALMA and JWST. These updates will be part of the next release of CLOUDY.

Our main conclusions from this work are:

1. In the gas-phase, Ti is mainly in TiO for temperatures above 1400 K, whereas TiO_2 dominates at a lower temperature.

2. Our model predicts the observed column densities of TiO and TiO_2 around the oxygen rich red super giant VY CMa. Both of these molecules are confined within $R = 28 \times R\star$. However, TiO forms closer to the central star when the temperatures are above 1400K.

3. Few ISM-appropriate Ti molecular reaction networks exist due to its low gas-phase abundance in the ISM. Most of our Ti-related gas-phase chemical reaction rate coefficients are copied from analogous Si-related reactions. Our model does predict observed TiO and TiO_2 column density around VY CMa. However, we look forward to actual rate coefficients for these reactions.

In the future, we hope to incorporate another important precursor of inorganic dust, AlO, into CLOUDY's chemical network.

We thank Peter van-hoof, Kyle Walker, and Krishal Patel for their valuable help. GS acknowledges support from DST/WOS-A/PM-2/2021.

APPENDIX

Here we list the rate coefficients used for various Ti-related reactions in Table 1. Ti-related reactions are mainly copied from the analogous Si-related reactions from UDfA2006 and UDfA2012. For example, in the column Si5209 refers to a copied reaction from the Si reaction of UDfA2012 with the reaction number 5209. Ref 1, 2, and 3 refer to Churchwell et al. (1980), Ramírez et al. (2020), and Tsai et al. (2021), respectively. The rate coefficient for the reaction, $Ti^+ + H^- \rightarrow Ti + H$, is taken from Dalgarno & McCray (1973).

The format for the two-body rate coefficients is given in an Arrhenius-type equation,

$$k = \alpha \left(\frac{T}{300}\right)^{\beta} \exp(-\gamma/T). \quad (1)$$

where T is the temperature of the gas, whereas the photoreaction rate coefficients are given by

$$k = \alpha \exp(-\gamma A_V)\,. \quad (2)$$

where A_V is the extinction at visible wavelengths. Details can be found in McElroy et al. (2013). For the two-body reactions and photoreactions, γ depends on the activation energy of the reaction and the increased dust extinction at ultraviolet wavelengths, respectively. It is to be noted that we do not use UDfA cosmic ray ionization rates. Our cosmic-ray ionization rates are normalised to a total rate for electron production from cosmic-ray ionization. We adopt a mean cosmic-ray ionization rate of 2×10^{-16} s^{-1} for atomic hydrogen as the default background value (Indriolo et al. 2007; Shaw et al. 2008). Shaw & Ferland (2021) showed that this rate is dependent on the presence of PAHs as well. For details, see Shaw et al. (2022).

TABLE 1

LIST OF Ti RELATED CHEMICAL REACTIONS*

Reactions	α	β	γ	Ref
C + TiH → TiC + H	6.59e-11	0	0	Si5209
C + TiH_2 → HCTi + H	1.e-10	0	0	Si5207
N + TiH → TiN + H	1.66e-10	-0.09	0	Si5513
N + TiH_2 → HNTi + H	8.0e-11	0.17	0	Si5511
N + TiC → Ti + CN	5.0e-11	0	0	Si5509
N + TiC → TiN + C	5.e-11	0	0	Si5510
CH_2 + Ti → HCTi + H	1.e-10	0	0	Si5241
O + TiH → TiO + H	1.e-10	0	0	Si5665
O + TiH_2 → TiO + H_2	8.e-11	0	0	Si5661
O + TiH_2 → TiO + H + H	1.2e-10	0	0	Si5662
O + TiC → TiO + C	5.e-11	0	0	Si5660
O + TiC → Ti + CO	5.e-11	0	0	Si5659
O + HCTi → TiO + CH	2.e-11	0	0	Si5626
O + TiN → NO + Ti	5.e-11	0	0	Si5666
O + TiN → TiO + N	5.75e-11	0.1	200	Si5667
O + TiNC → TiN + CO	1.e-11	0	0	Si5668
O + TiC_2 → TiC + CO	4.e-11	0	0	Si5656
OH + Ti → TiO + H	1.e-10	0	0	Si5698
OH + TiO → TiO_2 + H	2.e-12	0	0	Si5699
C_2H_2 + Ti → TiC_2 + H_2	1.30e-10	-0.71	29	Si5100
Ti + O_2 → TiO + O	1.72e-10	-0.53	17	Si5710

*The full table can be viewed online in `https://www.astroscu.unam.mx/rmaa/RMxAA..60-2/PDF/RMxAA..60-2_gshaw-XV-Table1.pdf`.

REFERENCES

Chatzikos, M., Bianchi, S., Camilloni, F., et al. 2023, RMxAA, 59, 327, https://doi.org/10.22201/ia.01851101p.2023.59.02.12

Choi, Y. K., Hirota, T., Honma, M., et al. 2008, PASJ, 60, 1007, https://doi.org/10.1093/pasj/60.5.1007

Churchwell, E., Hocking, W. H., Merer, A. J., & Gerry, M. C. L. 1980, AJ, 85, 1382, https://doi.org/10.1086/112810

Dalgarno, A. & McCray, R. A. 1973, ApJ, 181, 95, https://doi.org/10.1086/152032

Danilovich, T., Gottlieb, C. A., Decin, L., et al. 2020, ApJ, 904, 110, https://doi.org/10.3847/1538-4357/abc079

De Beck, E., Vlemmings, W., Muller, S., et al. 2015, A&A, 580, 36, https://doi.org/10.1051/0004-6361/201525990

Decin, L., Richards, A. M. S., Millar, T. J., et al. 2016, A&A, 592, 76, https://doi.org/10.1051/0004-6361/201527934

Ferland, G. J., Chatzikos, M., Guzmán, F., et al. 2017, RMxAA, 53, 385

Ferland, G. J., Porter, R. L., van Hoof, P. A. M., et al. 2013, RMxAA, 49, 137

Gail, H. P. & Sedlmayr, E. 1998, FaDi, 109, 303, https://doi.org/10.1039/a709290c

Gilli, G., Israelian, G., Ecuvillon, A., Santos, N. C., & Mayor, M. 2006, A&A, 449, 723, https://doi.org/10.1051/0004-6361:20053850

Grevesse, N., Asplund, M., Sauval, A. J., & Scott, P. 2010, Ap&SS, 328, 179, https://doi.org/10.1007/s10509-010-0288-z

Gunasekera, C. M., van Hoof, P. A. M., Chatzikos, M., & Ferland, G. J. 2023, RNAAS, 7, 246, https://doi.org/10.3847/2515-5172/ad0e75

Indriolo, N., Geballe, T. R., Oka, T., & McCall, B. J. 2007, ApJ, 671, 1736, https://doi.org/10.1086/523036

Jorgensen, U. G. 1994, A&A, 284, 179

Kamiński, T., Gottlieb, C. A., Menten, K. M., et al. 2013a, A&A, 551, 113, https://doi.org/10.1051/0004-6361/201220290

Kamiński, T., Gottlieb, C. A., Young, K. H., Menten, K. M., & Patel, N. A. 2013b, ApJS, 209, 38, https://doi.org/10.1088/0067-0049/209/2/38

Keady, J. J., Hall, D. N. B., & Ridgway, S. T. 1988, ApJ, 326, 832, https://doi.org/10.1086/166141

Lodders, K. 2002, ApJ, 577, 974, https://doi.org/10.1086/342241

Massey, P., Levesque, E. M., & Plez, B. 2006, ApJ, 646, 1203, https://doi.org/10.1086/505025

McElroy, D., Walsh, C., Markwick, A. J., et al. 2013, A&A, 550, 36, https://doi.org/10.1051/0004-6361/201220465

Ramírez, V., Cridland, A. J., & Mollière, P. 2020, A&A, 641, 87, https://doi.org/10.1051/0004-6361/202038186

Schöier, F. L., van der Tak, F. F. S., van Dishoeck, E. F., & Black, J. H. 2005, A&A, 432, 369, https://doi.org/10.1051/0004-6361:20041729

Shaw, G., Ferland, G., & Chatzikos, M. 2023, Research Notes of the American Astronomical Society, 7, 45, https://doi.org/10.3847/2515-5172/acc1ea

Shaw, G., Ferland, G., & Chatzikos, M. 2023, Research Notes of the AAS, 7, 153, https://dx.doi.org/10.3847/2515-5172/ace9b5

Shaw, G. & Ferland, G. J. 2021, ApJ, 908, 138, https://doi.org/10.3847/1538-4357/abdab2

Shaw, G., Ferland, G. J., Abel, N. P., Stancil, P. C., & van Hoof, P. A. M. 2005, ApJ, 624, 794, https://doi.org/10.1086/429215

Shaw, G., Ferland, G. J., & Chatzikos, M. 2022, ApJ, 934, 53, https://doi.org/10.3847/1538-4357/ac7789

Shaw, G., Ferland, G. J., & Ploeckinger, S. 2020, Research Notes of the American Astronomical Society, 4, 78, https://doi.org/10.3847/2515-5172/ab97ae

Shaw, G., Ferland, G. J., Srianand, R., et al. 2008, ApJ, 675, 405, https://doi.org/10.1086/526395

Shaw, G., Ferland, G. J., & Hubeny, I. 2017, ApJ, 843, 149, https://doi.org/10.3847/1538-4357/aa7747

Tsai, S.-M., Malik, M., Kitzmann, D., et al. 2021, ApJ, 923, 264, https://doi.org/10.3847/1538-4357/ac29bc

Wakelam, V., Herbst, E., Loison, J. C., et al. 2012, ApJS, 199, 21, https://doi.org/10.1088/0067-0049/199/1/21

Welsh, B. Y., Sasseen, T., Craig, N., Jelinsky, S., & Albert, C. E. 1997, ApJS, 112, 507, https://doi.org/10.1086/313044

Wittkowski, M., Hauschildt, P. H., Arroyo-Torres, B., & Marcaide, J. M. 2012, A&A, 540, 12, https://doi.org/10.1051/0004-6361/201219126

Yang, B., Stancil, P. C., Balakrishnan, N., & Forrey, R. C. 2010, ApJ, 718, 1062, https://doi.org/10.1088/0004-637X/718/2/1062

Zhang, B., Reid, M. J., Menten, K. M., & Zheng, X. W. 2012, ApJ, 744, 23, https://doi.org/10.1088/0004-637X/744/1/23

Ziurys, L. M. 2006, Proceedings of the National Academy of Science, 103, 12274, https://doi.org/10.1073/pnas.0602277103

G. Ferland: Physics & Astronomy, University of Kentucky, Lexington KY 40506, USA (gary@uky.edu).

R. Porter: Stellar Science, 6565 Americas Pkwy 925, Albuquerque, NM 87110, USA.

G. Shaw: Department of Astronomy and Astrophysics, Tata Institute of Fundamental Research, Mumbai 400005, India (gargishaw@gmail.com).

P. Stancil: Department of Physics and Astronomy and Center for Simulational Physics, University of Georgia, USA.

Revista Mexicana de Astronomía y Astrofísica, **60**, 381–396 (2024)

https://doi.org/10.22201/ia.01851101p.2024.60.02.16

THE VARIABLE STARS POPULATION OF THE EXTENDED YOUNG GLOBULAR CLUSTER NGC 1851

A. Arellano Ferro[1], C. E. Pérez Parra[2,3], M. A. Yepez[4,5], I. Bustos Fierro[6], Z. Prudil[7], and L. J. Zerpa Guillen[2,3]

Received July 15 2024; accepted August 15 2024

ABSTRACT

We report *VI* CCD photometry of the globular cluster NGC 1851. We aim to study the membership of the variable stars detected in the field of the cluster as listed in the *Catalogue of Variable stars in Globular Clusters* (CVSGC; Clement et al. 2001) and reported by the *Gaia* mission. We cross match the two sets of variables to produce light curves that lead to the estimation of physical parameters. The resulting colour-magnitude diagram (CMD), free of likely field stars, enables us to confirm from the position of the variables their type and evolutionary stage. We provide new estimations of the period using data acquired on a long time-base. The Fourier decomposition of cluster member RR Lyrae light curves lead to a mean metallicity and distance of $[Fe/H]_{ZW} = -1.35 \pm 0.22$ dex and 11.9 ± 0.6 kpc. The variability and membership of stars reported by *Gaia*-DR3 as variables in the field of the cluster is discussed.

RESUMEN

Reportamos fotometría *VI* del cúmulo globular NGC 1851. La finalidad es hacer un análisis de membresía de las variables detectadas en el campo del cúmulo y reportadas en el *Catalogue of Variable stars in Globular Clusters* (CVSGC, Clement et al. 2001) y por la misión *Gaia*. Los dos conjuntos de datos permitieron la producción de curvas de luz y la estimación de parámetros físicos estelares. El diagrama color-magnitud resultante, sin estrellas de campo, permite confirmar el tipo de cada estrella variable y su estado evolutivo. Reportamos nuevas estimaciones de los periodos de pulsación. La descomposición de Fourier de las curvas de luz de estrellas RR Lyrae miembros del cúmulo conduce a los valores medios de la metalicidad y la distancia del cúmulo; $[Fe/H]_{ZW} = -1.35 \pm 0.22$ dex y 11.9 ± 0.6 kpc. Se discute la variabilidad y la membresía de las estrellas reportadas como variables por *Gaia*-DR3 en el campo del cúmulo.

Key Words: globular clusters: general — globular clusters: individual: NGC 1851 — stars: distances — stars: fundamental parameters — stars: horizontal branch — stars: variables: RR Lyrae

1. INTRODUCTION

The southern globular cluster NGC 1851 is a remarkably bright system located in the constellation Columba, and in the outer region of the Milky Way, at a distance of about 12.0 kpc from the Sun ($\alpha = 5^h14^m06.76^s$, $\delta = -40^o02'47.6''$, J2000; $l = 244.51^o$, $b = -35.03^o$). It is a highly concentrated system (Kuzma et al. 2018) characterized by a diffuse halo extending to more than 10 times the tidal radius, although according to Marino et al. (2014), stars dynamically linked to the cluster are present to at least 2.5 tidal radii. The Galactic orbit of

[1]Instituto de Astronomía, Universidad Nacional Autónoma de México, México.
[2]Universidad de Los Andes, Facultad de Ciencias, Dpto. Física, Grupo de Astrofísica Teórica, Mérida, Venezuela.
[3]Fundación Centro de Investigaciones de Astronomía Francisco, J. Duarte (CIDA), Mérida, Venezuela.
[4]Instituto Nacional de Astrofísica, Óptica y Electrónica, Tonantzintla, Puebla, México.
[5]Consejo Nacional de Humanidades, Ciencias y Tecnologías, Ciudad de México, México.
[6]Observatorio Astronómico, Universidad Nacional de Córdoba, Córdoba, Argentina.
[7]European Southern Observatory, Garching, Germany.

the cluster is very eccentric, $e = 0.7$, and the lack of a tidal tail has triggered the suggestion that the cluster may be a stripped dwarf galaxy nucleus accreted by the Milky Way (Kuzma et al. 2018). However, a tail that seems to emerge from NGC 1851 was detected by Carballo-Bello et al. (2018), which may be interpreted as a tidal remnant of a tentative progenitor dwarf galaxy host of NGC 1851. Its rather young age, 9.2 Gyr according to Koleva et al. (2008) or 11.0 Gyr according to VandenBerg et al. (2013), seems to support the hypothesis of an extra Galactic origin. From a chemo-dynamical analysis, Callingham et al. (2022) associated NGC 1851 to the ancient major merger event of the Milky Way Gaia-Enceladus-Sausage (Belokurov et al. 2018; Helmi et al. 2018).

The horizontal branch (HB) of NGC 1851 possesses a moderate population of hot blue tail stars and a dense red clump nearly twice as populated; hence its HB structural parameter $L = -0.36$ (Arellano Ferro 2024) is consistent with its Oosterhoff type Oo I and metallicity [Fe/H]=-1.3, following the trend defined by other Galactic clusters of the same Oo-type and similar metallicity.

NGC 1851 harbours a large number of RR Lyrae stars, 48 according the the 2020 edition of the *Catalogue of Variable Stars in Globular Clusters* (CVSGC, Clement et al. 2001). It may also contain 4-5 long period variables near the tip of the red giant branch (RGB). One of our goals in this paper is to employ the variable stars as indicators of the mean metallicity and distance of the parental cluster; hence it is of relevance to ask whether all the variables reported in the CVSGC are cluster members, since the large majority of them were discovered before a detailed membership analysis was a feasible possibility. In the present paper we propose a membership analysis based on the *Gaia*-DR3 proper motions before we produce a cleaner colour-magnitude diagram (CMD) and then to study the distribution of the variables and their physical properties.

2. OBSERVATIONS AND IMAGE REDUCTIONS

2.1. *Observations*

The *VI* CCD images were obtained with the 1.54m telescope of the Estación Astrofísica Bosque Alegre del Observatorio de Córdoba, Universidad Nacional de Córdoba, Argentina (EABA), during December 14, 15 and 16, 2018 and during five nights between April 6-28 2019. We shall refer to these seasons as BA18 and BA19 respectively. During the BA18 season we used the camera Alta F16M, equipped with a KAF-16803 chip of 4096×4096 square pixels of 9 microns, binned 2×2. This produced a scale of 0.496 arc seconds per pixel and resulted in a field of view of 16.9×16.9 square arc minutes. During the BA19 season the camera was an Alta U9 with a KAF-6303E CCD detector of 3072×2048 square pixels of 9 microns, also binned 2×2. The scale is 0.496 arc seconds per pixel for a field of view of 12.7×8.5 square arc minutes.

TABLE 1

LOG OF OBSERVATIONS OF NGC 1851

Date	N_V	t_V(s)	N_I	t_I(s)	Mean seeing ($''$)
2018-12-14	53	100	61	50	3.3
2018-12-15	72	100	80	50	2.3
2018-12-16	62	100	63	50	2.7
2019-04-06	13	100	13	50	3.4
2019-04-07	24	100	29	50	2.4
2019-04-12	23	100	24	50	2.5
2019-04-13	23	100	24	50	2.7
2019-04-28	23	100	24	50	2.6
Total:	293		318		

Columns N_V and N_I give the number of images taken with the V and I filters respectively. Columns t_V and t_I provide the exposure time. In the last column the prevailing nightly average seeing is listed.

The log of the observations is given in Table 1, where the employed exposure times and the nightly seeing conditions are indicated. The goal of these observations is to extract accurate photometry of all point sources in the field of our images, and to build their corresponding light curves. For this purpose we employed the difference imaging analysis (DIA) and the DanDIA pipeline (Bramich 2008; Bramich et al. 2013, 2015).

2.2. *Locking Our Photometry to the Standard System*

For the BA18 season we were able to produce light curves for 4623 point sources in the V-band and 1578 in the I-band. For the BA19 season we measured 2305 light curves in the V-band and 1949 in the I-band. These instrumental light curves were transformed to the standard Johnson-Kron-Cousins system defined by Landolt (1992), by employing the local standard stars in the field of NGC 1851 provided in the catalogue of Stetson (2000)[8]. We identified 179 and 101 standards in BA18 and BA19 respectively for which we have *VI* photometry. Figure 1 shows the dependence of the standard minus instrumental magnitudes with the instrumental colour $(v-i)$, from which the transformation equations, inscribed in the figure legend, were calculated. These

[8] https://www.canfar.net/storage/list/STETSON/Standards.

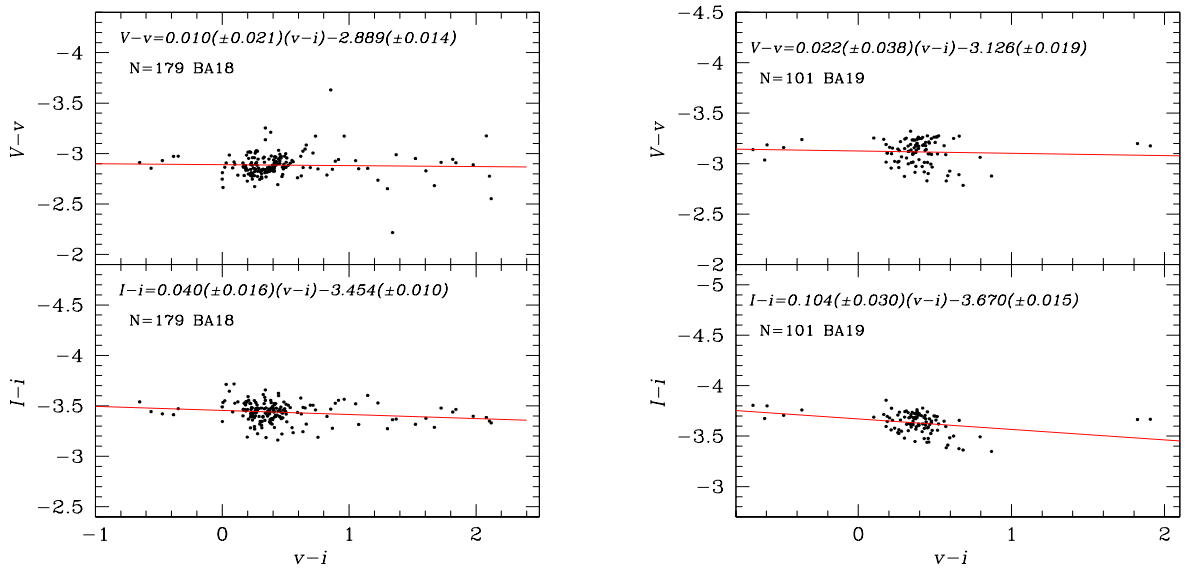

Fig. 1. Transformation relationship between *VI* instrumental and standard photometric systems, calculated for the BA18 and BA19 seasons with 179 and 101 standards respectively, taken from the collection of Stetson (2000).

equations were employed to convert all instrumental light curves into the standard system.

Table 2 displays a small portion of the time-series *VI* photometry obtained in this work. The full table will be made available in electronic form in the Centre de Donnés Astronomiques de Strasbourg database (CDS).

3. VARIABLE STARS IN THIS STUDY

We were able to measure *VI* magnitudes for 1434 stars identified as cluster members in the field of our images. These cluster members will be used to produce the CMD diagram. We could measure 47 of the 55 variables in the cluster listed by Clement et al. (2001) in the CVSGC. As can be seen in Table 1, the observations were carried out under limited seeing conditions, and as a result our DIA analysis was unable to retrieve useful data for stars that are very faint, stars near the cluster center, or stars blended with a brighter neighbour. We could not measure the RRab stars V30, V36, V39, V40, V41, V43 and V44.

From an independent exploration we detected clear variability of three faint stars that we temporarily call F1, F2 and F3.

The *Gaia*-DR3 lists 22 variable stars in the field of the cluster that do not match any of the V55 already known in the CVSGC. *Gaia* photometry is available for 21 of these stars. For the sake of clarity we list these 21 stars in Table 3 along with their *Gaia* source identification and equatorial coordinates. We arbitrarily number these variables with a prefix 'G'. We explore their light curves from our own photometry and from *Gaia* data, and can confirm with confidence the variability and nature for only five of them.

All the reported variables in field of NGC 1851 are listed in Table 4, along with their variable types,

TABLE 2

TIME-SERIES *VI* PHOTOMETRY FOR THE VARIABLE STARS OBSERVED*

Variable Star ID	Filter	HJD (d)	$M_{\rm std}$ (mag)	$m_{\rm ins}$ (mag)	σ_m (mag)
V1	*V*	2458467.53771	16.000	18.889	0.014
V1	*V*	2458467.55788	16.097	18.985	0.009
⋮	⋮	⋮	⋮	⋮	⋮
V1	*I*	2458467.53148	15.433	18.884	0.020
V1	*I*	2458467.53416	15.525	18.976	0.012
⋮	⋮	⋮	⋮	⋮	⋮
V3	*V*	2458467.53771	16.264	19.155	0.019
V3	*V*	2458467.55788	16.206	19.097	0.012
⋮	⋮	⋮	⋮	⋮	⋮
V3	*I*	2458467.53148	15.719	19.179	0.026
V3	*I*	2458467.53416	15.775	19.235	0.018
⋮	⋮	⋮	⋮	⋮	⋮

*The standard and instrumental magnitudes are listed in Columns 4 and 5, respectively, corresponding to the variable stars in Column 1. Filter and epoch of mid-exposure are listed in Columns 2 and 3, respectively. The uncertainty in $m_{\rm ins}$, which also corresponds to the uncertainty in $M_{\rm std}$, is listed in Column 6. A full version of this table is available at the CDS database.

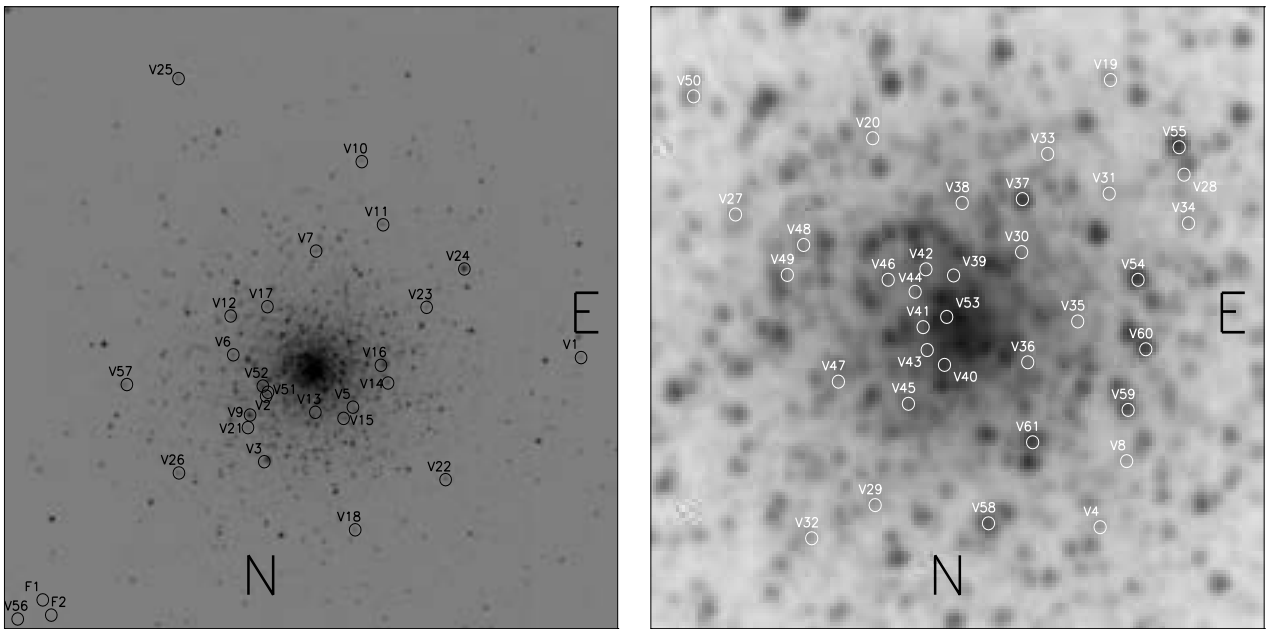

Fig. 2. Identification chart of variable stars in the field of NGC 1851. The approximate size of the images is 9.7×9.7 and 1.6×1.6 square arc minutes.

mean magnitudes, amplitudes and ephemerides whenever possible. Included in the table are also the stars that we were unable to measure and the non-confirmed *Gaia* variables, since we are providing their equatorial coordinates and a proper field identification.

The cluster membership status of all these variables is discussed in the following section.

We offer a finding chart of all the variables in Figure 2. Their light curves are displayed in the Appendix, where we shall distinguish the data from different seasons. In the Appendix we also discuss individual peculiar or outstanding variables.

4. STELLAR MEMBERSHIP ANALYSIS

In current times, the membership analysis of large numbers of stars in the field of a given globular cluster is possible thanks to the high quality of proper motions available in the *Gaia* mission (Gaia Collaboration et al. 2023). Sieving the likely cluster members and the field stars, enables the production of cleaner CMDs, and hence a better perspective of the stellar distributions and evolutionary properties. This is of particular interest for specific groups of variable stars, e.g. RR Lyrae stars in the horizontal branch (HB).

The method developed by Bustos Fierro & Calderón (2019) to determine the stellar membership is based on a two step approach: (1) it finds groups of stars with similar characteristics in the four-dimensional space of the gnomonic coordinates ($X_{\rm t}$,$Y_{\rm t}$) and proper motions ($\mu_{\alpha*}$,μ_{δ}) employing the Balanced Iterative Reducing and Clustering using Hierarchies (BIRCH) clustering algorithm (Zhang et al. 1996); and (2) in order to extract likely members that were missed in the first stage, the analysis of the projected distribution of stars with different proper motions around the mean proper motion of the cluster is performed.

Figure 3 shows the corresponding vector point diagram (VPD) and CMD, distinguishing the likely cluster members from the field stars. We considered a 30 arc minute radius field from the cluster center, which contains 25238 *Gaia* point sources out of which 11220 were found to be likely cluster members.

An independent membership analysis for a large number of globular clusters, based on the proper motions of *Gaia*-DR3, was performed by Vasiliev & Baumgardt (2021). These authors provided membership probabilities for each star in the cluster field. In Columns 9 and 10 of Table 4 we list the membership status according the method from Bustos Fierro & Calderón (2019) (B&C) and the probabilities from Vasiliev & Baumgardt (2021) (V&B). With a few exceptions, the match is good. The exceptions that call for attention are V8, V25, V37, V42, V44, V45 and V48, and their membership status deserves a few comments. We should note that the coordi-

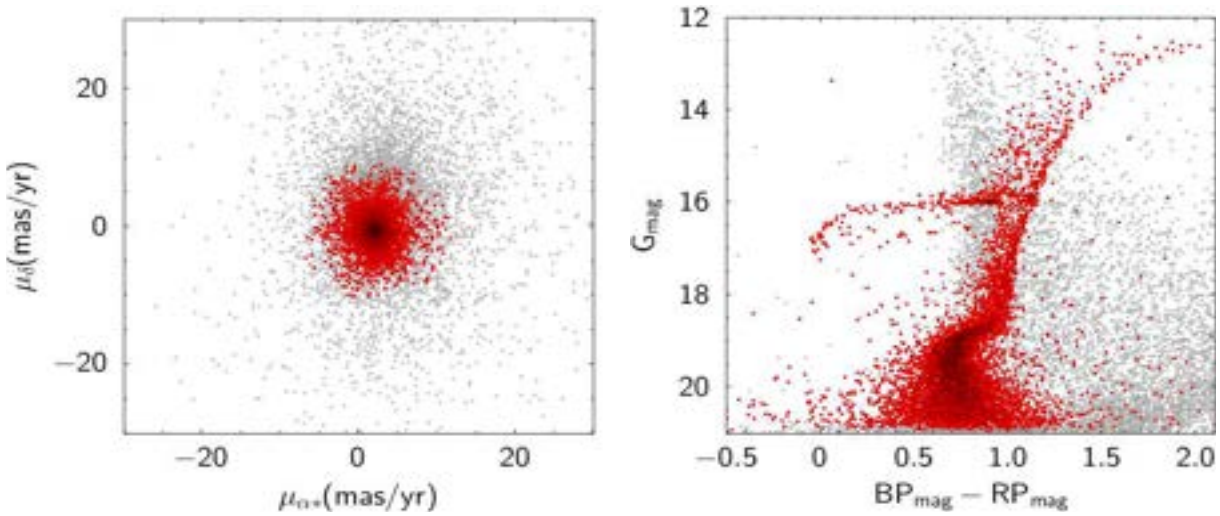

Fig. 3. *Gaia*-DR3 VPD (left panel) and CMD (right panel) of the cluster NGC 1851. Red and gray points correspond to likely cluster members and field stars, respectively, determined as described in § 4. A total of 25238 *Gaia* point sources within 30 arc minutes are displayed, while 11220 were found to be cluster members. The colour figure can be viewed online.

TABLE 3

VARIABLE STARS IN THE FIELD OF NGC 1851 REPORTED IN *GAIA*-DR3

Var Id	*Gaia* Source	R.A.	DEC
G1	4819198634647024512	05:14:02.32	-40:00:01.0
G2	4819198187968154496	05:13:52.49	-40:01:04.3
G3	4819198089187642112	05:13:51.14	-40:02:37.2
G4	4819197779947169152	05:14:02.37	-40:01:41.9
G5	4819197779945787392	05:14:00.84	-40:01:38.4
G6	4819197711229437952	05:14:05.02	-40:01:51.9
G7	4819197676868199168	05:14:01.50	-40:02:37.9
G8	4819197608151761152	05:14:08.52	-40:01:55.8
G9	4819197608147820032	05:14:11.79	-40:02:09.2
G10	4819197505072742912	05:14:07.05	-40:02:18.2
G11	4819197505072715264	05:14:08.96	-40:02:35.0
G12	4819197505072513152	05:14:05.82	-40:02:46.2
G13	4819197500774037376	05:14:09.21	-40:02:44.2
G14	4819197500774029312	05:14:07.67	-40:02:30.3
G15	4819197500774029056	05:14:07.64	-40:02:27.0
G16	4819197470714194304	05:14:02.92	-40:03:30.8
G17	4819197436349844992	05:14:08.95	-40:03:40.1
G18	4819197401991836544	05:14:06.29	-40:03:59.8
G19	4819197092756042496	05:14:01.95	-40:04:41.6
G20	4819185822760255616	05:14:19.10	-40:02:26.4
G21	4819185685319251456	05:14:13.34	-40:04:12.9

nates given in the CVSGC are the starting point for a match with *Gaia* and that for stars V37, V38, V42, V45, V46 and V48 only X,Y coordinates are listed; hence the matching is sometimes more dubious. In the present work we provide equatorial coordinates for these six stars

We should consider the fact that at the reported coordinates in Table 4, we recover in our photometry the light curve of a variable star of the expected type, period and light curve morphology, and that their position in the CMD also becomes a sound membership indicator tool. Therefore, we conclude that V8 is a cluster member, whereas V25, based on its accurate parallax is a field star, much closer than the cluster. For RR Lyrae stars V37, V42, V45, V47, V48, V50 and V53 there are good matches with *Gaia* sources with good proper motions, but in all cases the corresponding stars are much brighter than the HB, as can be appreciated in the CMD; hence they are all foreground field RR Lyrae stars. Given that at least one of the two membership identification methods indicate that they are field stars, we opted for labeling them as such. Similarly off the HB there are the RR Lyrae V14, V33, and V51. However in these cases both B&C and V&B approaches identify them as very likely cluster members. Since these are located near the central region of the cluster, we cannot rule out contamination of our photometry by close unresolved neighbours and we opted for considering them likely cluster members. We were unable to reliably measure the star V44 in the central region of the cluster, and hence its membership status remains unknown (UN).

Regarding the variable stars reported by *Gaia*-DR3, listed in Table 3, all but G17, G18 and G21 were found to be cluster members by both B&C and V&B. All stars marked with 'UN' by B&C lack proper motion in the *Gaia* database; hence its membership cannot be assessed from that information. In

Column 11 of Table 4 we list our final membership assessment.

4.1. *The New Variables in the Field of NGC 1851*

Of the three newly detected variables in the field of NGC 1851, F1, F2 and F3, only F3 is a likely cluster member; hence we assigned to it the variable number V56 and we tentatively classified it as SX Phe star. These three stars are contained in Table 4, and their light curves are displayed in the Appendix.

5. THE OOSTERHOFF TYPE OF NGC 1851

The period averages for the RRab and RRc stars in NGC 1851 are $<P\mathrm{ab}> = 0.57 \pm 0.06$ days and $<P\mathrm{c}> = 0.31 \pm 0.04$ days. These numbers point to an Oosterhoff type Oo I for this cluster. In the $\log P$ - amplitude plane, or Bailey's diagram, of Figure 4 we plot amplitudes and periods for all RR Lyrae stars measured in the this work (Table 4). The distribution of star on this plane clearly favours the unevolved sequences and the Oo I type of this cluster, in agreement with the average periods and the metallicity of the cluster of about $[\mathrm{Fe/H}]_{\mathrm{UV}} = -1.25$, (see § 7).

6. ON THE CLUSTER REDDENING

Given its Galactic location, the reddening of NGC 1851 is relatively low compared to other globular clusters closer to the Galactic plane, where the density of dust and gas is higher. Independent estimates of the cluster reddening consistently report low values of $E(B-V)$; for example, Harris (1996) and Walker (1998) give a value of $E(B-V) = 0.02$. The latter stresses that there are no compelling evidences for values too different from this estimation. The calibrations of Schlegel et al. (1998), and Schlafly & Finkbeiner (2011) give values of 0.037 and 0.032, respectively. We have not attempted a reddening determination from the colour $(V-I)$ being constant between phases 0.5−0.8 for RRab stars (Sturch 1966) and the subsequent calibration of Guldenschuh et al. (2005), since our I light curves are scanty and phase gaps are present. Hence we adopted the value of $E(B-V) = 0.032 \pm 0.002$ from the calibration by Schlafly & Finkbeiner (2011).

7. PHYSICAL PARAMETERS OF THE RR LYRAE STARS FROM THE LIGHT CURVES FOURIER DECOMPOSITION

The Fourier decomposition of the light curves of RR Lyrae stars, both RRab and RRc, is a well established approach towards the determination of some

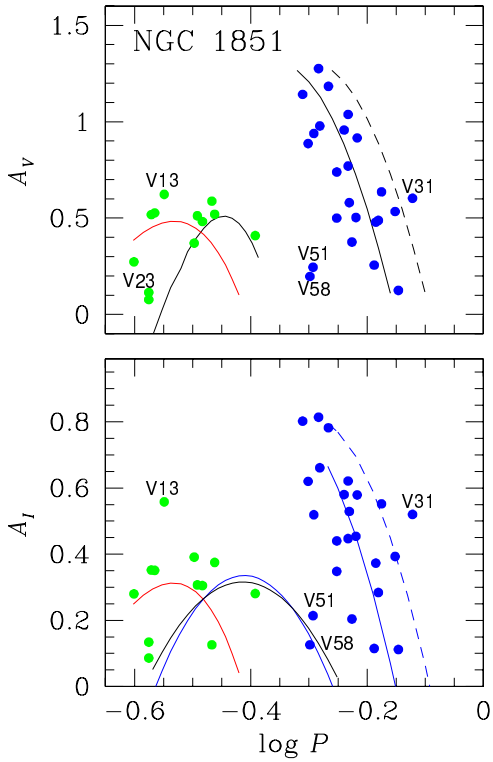

Fig. 4. Period-amplitude diagram for RR Lyrae stars in NGC 1851. Blue and green circles represent RRab and RRc stars, respectively. The colour figure can be viewed online.

physical parameters, mainly the metallicity [Fe/H], the luminosity (or absolute magnitude M_{V} and hence the distance), as well as the mass and mean stellar radius. The Fourier decomposition technique, as well as the semi-empirical calibrations and their zero points leading to the physical parameters, have been presented and discussed in detail in the papers by Arellano Ferro et al. (2010). A summary of the results for 40 clusters calculated homogeneously for over more than a decade can be found in Arellano Ferro (2024). The interested reader is referred to those works for the the involved details.

In the present paper we have limited the calculation of physical parameters to those stars that have proven to be likely cluster members, according to the discussion offered in §4 and summarized in Table 4.

7.1. *Physical Parameters of RR Lyrae Stars*

In Table 5 are given the values of [Fe/H] in the scales of Zinn & West (1984) and in the spectroscopic scale of Carretta et al. (2009) for the member RRab and RRc stars. Also listed are the individual values of $\log T_{\mathrm{eff}}$, $\log(L/L_{\odot})$, $M/M_{\odot}$, $R/R_{\odot}$ and distance. All the reported mean values in this table have been weighted by the inner uncertainties,

TABLE 4

GENERAL DATA OF VARIABLES IN THE FIELD OF NGC 1851[1]

Variable	Type	$<V>$ (mag)	$<I>$ (mag)	A_V (mag)	A_I (mag)	Period (days)	HJD_{max} (d+2450000)	B&C (M/F)	V&B %	Memb. (m/f/?)	RA (J2000.0)	Dec. (J2000.0)
V1	RRab	16.161	15.617	1.276	0.814	0.520583	8581.4671	M1	0.99	m	05:14:28.94	−40:02:56.5
V2	CST	—	—	—	—	—	—	M1	0.99	m	05:14:02.75	−40:02:24.5
V3	RRc	16.068	15.627	0.512	0.307	0.322103	8665.7971	M1	1.00	m	05:14:02.46	−40:01:20.7
V4	RRab	16.197	15.617	0.770	0.447	0.585438	8602.4723	M1	0.99	m	05:14:08.56	−40:02:17.2
V5	RRab	16.015	15.490	0.580	0.529	0.587831	7596.6515	M1	0.99	m	05:14:09.90	−40:02:12.1
V6	RRab	16.094	15.537	0.916	0.579	0.606628	8468.5608	M1	1.00	m	05:14:00.02	−40:03:04.4
V7	RRab	16.151	15.393	1.038	0.621	0.585186	8581.4660	M1	0.99	m	05:14:07.04	−40:04:43.4
V8	RRab	16.154	15.566	0.939	0.519	0.510979	8469.8129	M1	0.16	m	05:14:08.93	−40:02:27.2
V9	L/SR	—	—	—	—	—	—	M1	1.00	m	05:14:01.34	−40:02:06.0
V10	RRab	16.304	15.709	0.887	0.620	0.499528	8468.6287	M1	1.00	m	05:14:10.96	−40:06:09.1
V11	RRab	15.908	15.411	0.636	0.552	0.667919	8581.5263	M1	1.00	m	05:14:12.65	−40:05:07.8
V12	RRab	16.223	15.684	0.957	0.580	0.575942	8586.5057	M1	0.99	m	05:13:59.85	−40:03:41.9
V13	RRc	16.170	16.172	0.623	0.558	0.282543	8580.5020	M1	0.61	?	05:14:06.77	−40:02:07.7
V14	RRab	15.413	14.697	0.376	0.204	0.594038	8469.7261	M1	0.89	m	05:14:12.85	−40:02:34.9
V15	RRab	16.140	15.353	1.184	0.782	0.541344	7002.5754	M1	0.99	m	05:14:09.11	−40:02:01.4
V16	RRab	16.111	15.711	1.142	0.802	0.488699	7380.6230	M1	1.00	m	05:14:12.28	−40:02:52.1
V17	RRab	16.073	15.594	0.534	0.393	0.704841	8467.5715	M1	0.99	m	05:14:02.92	−40:03:50.4
V18	RRc	16.078	15.704	0.527	0.351	0.272094	8467.5579	M1	1.00	m	05:14:09.93	−40:00:13.6
V19	RRc	15.852	15.392	0.409	0.281	0.405181	8602.4853	M1	0.99	m	05:14:08.79	−40:03:25.3
V19	RRc	15.852	15.392	0.409	0.281	0.405181	8602.4853	M1	0.99	m	05:14:08.79	−40:03:25.3
V20	RRab	16.161	15.583	0.739	0.440	0.559460	8467.6636	M1	0.00	m	05:14:05.58	−40:03:17.0
V21	RRc	16.107	15.804	0.518	0.352	0.268520	8581.4671	M1	0.99	m	05:14:01.15	−40:01:53.9
V22	RRab	15.804	15.350	0.500	0.348	0.559401	8602.4613	M1	0.99	m	05:14:17.51	−40:01:00.7
V23	RRc	16.187	15.823	0.114	0.134	0.265835	8469.7203	M1	1.00	m	05:14:16.16	−40:03:47.4
V24	Lb/S	13.161	11.528	—	—	—	—	M1	1.00	m	05:14:19.35	−40:04:23.9
V25	EC	15.706	14.823	0.461	0.445	0.173673	8587.5103	M2	0.00	f	05:13:55.81	−40:07:32.0
V26	RRc	16.149	15.732	0.482	0.305	0.328669	8469.7001	M1	0.99	m	05:13:55.36	−40:01:11.1
V27	RRab	16.063	15.532	0.978	0.661	0.523208	7440.3531	M1	0.99	m	05:14:03.72	−40:03:05.7
V28	RRab	—	—	—	—	—	—	M1	0.99	m	05:14:09.76	−40:03:10.7
V29	RRab	15.671	15.073	0.503	0.454	0.603592	8469.7120	M1	0.55	m	05:14:05.54	−40:02:21.1
V30	RRab	—	—	—	—	—	—	M2	0.90	m	05:14:07.56	−40:02:59.3
V31	RRab	15.973	15.404	0.603	0.520	0.755159	7873.3458	M1	0.99	m	05:14:08.75	−40:03:08.0
V32	RRab	15.909	15.073	0.488	0.284	0.659681	8602.4747	M1	0.99	m	05:14:04.68	−40:02:16.2
V33	RRc	15.680	14.818	0.588	0.126	0.341202	8468.5790	M1	0.99	m	05:14:07.93	−40:03:14.2
V34	RRc	15.989	15.620	0.520	0.375	0.345033	8468.6727	M1	0.83	m	05:14:09.81	−40:03:03.3
V35	RRc	16.137	15.655	0.370	0.391	0.318175	7380.6231	M1	0.99	m	05:14:08.30	−40:02:48.6
V36	RRab	—	—	—	—	—	—	UN	U	?	05:14:07.62	−40:02:42.5
V37	RRc	13.217	11.769	0.066	0.046	0.351040	8469.6989	UN	1.00	f	05:14:07.56	−40:03:07.4
V38	RRab	15.885	0	0.479	0.373	0.653044	8468.7343	M1	0.99	m	05:14:06.77	−40:03:07.0
V39	RRab	—	—	—	—	—	—	M1	0.83	m	05:14:06.64	−40:02:55.9
V40	RRab	—	—	—	—	—	—	M1	0.84	m	05:14:06.50	−40:02:42.3
V41	RRab	—	—	—	—	—	—	UN	U	?	05:14:06.22	−40:02:48.1
V42	RRc	14.648	13.638	0.360	0.163	0.309567	8580.5193	M1	0.20	f	05:14:06.27	−40:02:56.9
V43	RRab	—	—	—	—	—	—	M2	0.99	m	05:14:06.27	−40:02:44.6
V44	RRab	—	—	—	—	—	—	UN	0.13	?	05:14:06.12	−40:02:53.5
V45	RRc	14.640	13.283	0.179	0.123	0.256363	8581.4970	UN	0.94	f	05:14:06.00	−40:02:36.5
V46	RRc	14.637	14.386	0.141	0.303	0.289664	8469.6989	M2	0.98	f	05:14:05.76	−40:02:55.4
V47	RRc	15.629	14.703	0.369	0.148	0.280101	8602.4680	M2	0.59	?	05:14:05.07	−40:02:40.0
V48	RRab	15.176	15.177	0.547	0.220	0.520895	8586.5101	M2	0.15	f	05:14:04.63	−40:03:00.9
V49	RRc	14.174	0	0.077	0.086	0.265827	8468.5790	M1	0.99	m	05:14:04.41	−40:02:56.5
V50	RRc	15.462	14.787	0.231	0.135	0.325064	8581.5275	M1	0.00	f	05:14:03.18	−40:03:23.8
V51	RRab	14.805	13.899	0.245	0.214	0.509389	8580.5303	M1	1.00	m/f?	05:14:02.75	−40:02:24.5
V52	RRab	16.120	15.327	0.256	0.115	0.648831	8468.6052	M1	0.99	m	05:14:02.44	−40:02:33.8
V53	RRc	12.617	11.260	0.260	0.257	0.325140	8581.4789	UN	0.99	f	05:14:06.54	−40:02:49.6
V54	L	—	—	—	—	—	—	M1	0.99	m	05:14:09.12	−40:02:54.8
V55	L	—	—	—	—	—	—	M1	1.00	m	05:14:09.70	−40:03:14.9

which are given between parentheses as described in the notes at the bottom of the table. The average [Fe/H] and distances are considered good representations of the metallicity and distance of the parental cluster. We find $[\mathrm{Fe/H}]_{\mathrm{ZW}} = -1.35 \pm 0.22$, or in the spectroscopic scale of Carretta et al. (2009) $[\mathrm{Fe/H}]_{\mathrm{UV}} = -1.16 \pm 0.25$ and a distance to the cluster of 11.9 ± 0.6 kpc.

TABLE 4. CONTINUED

Variable	Type	$<V>$ (mag)	$<I>$ (mag)	A_V (mag)	A_I (mag)	Period (days)	HJD_{max} (d+2450000)	B&C (M/F)	V&B %	Memb. (m/f/?)	RA (J2000.0)	Dec. (J2000.0)
New Stars Identified in the NGC1851 Field.												
V56	SX Phe?	18.381	17.842	0.273	0.28	0.250666	8468.5802	M1	1.00	m	05:13:41.80	−39:58:52.3
F1	RRc	18.419	17.282	0.236	0.455	0.337433	8467.5760	FS	0.00	f	05:13:43.90	−39:59:10.4
F2	RRc	17.843	16.100	0.236	0.296	0.257364	8467.5660	FS	0.00	f	05:13:44.59	−39:58:55.6
Variables in *Gaia*-DR3 confirmed in the present work												
V57(G3)	RRab	16.106	15.509	0.141	0.122	0.714154	8468.6053	M1	1.00	m	05:13:51.14	−40:02:37.2
V58(G10)	RRab	14.352	13.211	0.197	0.126	0.503017	7063.5570	M1	1.00	m	05:14:07.05	−40:02:18.2
V59(G11)	L	13.55	12.03	0.40	0.21	——	——	M1	1.00	m	05:14:08.96	−40:02:35.0
V60(G13)	L	13.42	11.63	0.37	0.20	——	——	M1	1.00	m	05:14:09.21	−40:02:44.2
V61(G14)	L	13.27	11.62	0.43	0.19	——	——	M1	1.00	m	05:14:07.67	−40:02:30.3
Variables in *Gaia*-DR3 not confirmed in the present work												
		$\overline{V}$	$\overline{I}$									
G1	——	19.129	18.268	——	——	——	——	M1	1.00	m	05:14:02.32	−40:00:01.0
G2	——	18.952	18.593	——	——	——	——	M1	1.00	m	05:13:52.49	−40:01:04.3
G4	——	17.452	16.467	——	——	——	——	M1	1.00	m	05:14:02.37	−40:01:41.9
G5	——	*19.461*	*18.610*	——	——	——	——	M1	1.00	m	05:14:00.84	−40:01:38.4
G6	——	*19.406*	*18.756*	——	——	——	——	M1	1.00	m	05:14:05.02	−40:01:51.9
G7	——	*19.299*	*18.644*	——	——	——	——	M1	1.00	m	05:14:01.50	−40:02:37.9
G8	——	17.027	16.138	——	——	——	——	M1	1.00	m	05:14:08.52	− 40:01:55.8
G9	——	18.585	18.118	——	——	——	——	M2	0.00	f	05:14:11.79	−40:02:09.2
G12	——	13.442	11.815	——	——	——	——	M1	1.00	m	05:14:05.82	−40:02:46.2
G15	——	13.230	11.513	——	——	—-	—-	M1	1.00	m	05:14:07.64	−40:02:27.0
G16	——	*19.629*	*18.943*	——	——	——	——	M2	0.99	m	05:14:02.92	−40:03:30.8
G17	——	16.672	15.754	——	——	——	——	UN	0.89	?	05:14:08.95	−40:03:40.1
G18	——	*19.601*	*18.926*	——	——	——	——	M2	0.01	?	05:14:06.29	−40:03:59.8
G19	——	15.472	14.510	——	——	——	——	M1	1.00	m	05:14:01.95	−40:04:41.6
G20	——	*20.219*	*19.732*	——	——	——	——	M1	1.00	m	05:14:19.10	−40:02:26.4
G21	——	17.363	16.544	——	——	——	——	M2	0.00	?	05:14:13.34	−40:04:12.9

[1]Columns 3 and 4 contain intensity weighted means, except for the LPV stars and for the G-group in the bottom section, which are magnitude weighted means. Numbers in italics are averages exclusively from *Gaia* data transformed into *VI*. Columns 5 and 6 list light curve amplitudes. Column 9 indicates the membership status found in this work from the method of Bustos Fierro & Calderón (2019) (M1 or M2 for likely members, UN for unknown and FS for field stars). Column 10 contains the membership probability assigned by Vasiliev & Baumgardt (2021).

8. THE COLOUR MAGNITUDE DIAGRAM

The observed CMD of NGC 1851 built from our *VI* photometry with only likely cluster member stars was dereddened assuming $E(B-V) = 0.03$ mag. The resulting intrinsic CMD is displayed in Figure 5. All variable stars are plotted with the colours and symbols code in the caption. This diagram helps to confirm the non-membership of many stars, as discussed in previous sections, since their positions are at odds with their variable type in many cases. We remind the reader that our final membership assessment is given Column 11 of Table 4.

We call attention to the distribution of RRab and RRc stars on the HB. Considering exclusively the stars that are clear cluster members, we see that some RRab are located in the bimodal region of the instability strip, i.e. in the intersection of the fundamental and first overtone instability strips. The theoretical bounds of these strips are indicated by the green and blue borders calculated by Bono et al. (1994). The empirical border of the first overtone red edge (FORE) is indicated by the two vertical black lines in the HB (Arellano Ferro et al. 2015, 2016) and matches well with the theoretical FORE. RRab stars crossing to the blue of the FORE are a characteristic of some Oo I type clusters, like NGC 1851, but this does not happen in Oo II clusters, where the RRab remain to the red of the FORE, i.e. off the bimodal region (see Yepez et al. 2022 and references there in for a discussion). This characteristic of Oo II clusters is probably a consequence of the more advanced stage of their evolution to the red, towards the AGB.

Of the 21 stars in the field of NGC 1851 marked in *Gaia*-DR3 as variables, we found a counterpart measured in our photometry for 15 of them. The others, were either too faint or unresolved, given the spatial resolution of our images. For a proper comparison we transformed the *Gaia* photometric data into *VI* using the transformation equations of Riello et al. (2021). We could confirm the variability and variable type of 5 of them; V57-V61 in Table 4. The remaining 10 are plotted in the DCM with purple open triangles and are distributed all across the diagram. The *Gaia* cadence is not designed for the iden-

TABLE 5

PHYSICAL PARAMETERS FROM THE MEMBER RR LYRAE FOURIER LIGHT CURVE DECOMPOSITION

ID	$[Fe/H]_{ZW}$	$[Fe/H]_{UVES}$	M_V	log T_{eff}	$\log(L/L_\odot)$	$M/M_\odot$	D(kpc)	$R/R_\odot$
				RRab				
V1	-1.49(3)[1]	-1.40(3)	0.57(1)	3.82(1)	1.68(1)	0.74(7)	12.55(3)	5.42(1)
V6	-1.25(5)	-1.14(4)	0.54(1)	3.81(1)	1.69(1)	0.67(8)	12.35(3)	5.69(1)
V7	-1.40(4)	-1.29(4)	0.53(1)	3.81(1)	1.69(1)	0.68(7)	12.73(3)	5.63(1)
V11	-1.32(34)[2]	-1.20(32)[2]	0.52(1)	3.80(1)	1.70(1)	0.62(11)	11.44(1)	5.85(1)
V12	-1.47(6)	-1.38(7)	0.55(1)	3.81(1)	1.69(1)	0.70(11)	13.00(4)	5.61(2)
V15	-1.43(9)	-1.33(9)	0.61(1)	3.82(2)	1.66(1)	0.68(12)	12.22(6)	5.35(2)
V16	-1.05(6)	-0.94(5)	0.60(1)	3.82(1)	1.66(1)	0.68(9)	12.42(4)	5.07(2)
V38	-1.41(12)	-1.31(12)	0.55(1)	3.84(3)	1.69(1)	0.40(15)	11.34(3)	4.87(1)
Mean	-1.38	-1.25	0.54	3.81	1.68	0.67	11.92	5.52
σ	±0.15	±0.15	±0.03	±0.01	±0.02	±0.11	±0.68	±0.33
				RRc				
V3	-1.56(22)	-1.49(24)	0.57(1)	3.83(1)	1.67(1)	0.78(1)	12.06(3)	4.96(1)
V9	-1.81(29)	-1.82(38)	0.51(1)	3.83(1)	1.70(1)	0.63(1)	11.21(5)	5.23(3)
V21	-0.96(16)	-0.87(11)	0.63(1)	3.88(1)	1.65(1)	0.59(1)	11.95(6)	4.00(1)
V23	-1.45(47)	-1.35(48)	0.75(2)	3.86(1)	1.60(1)	0.63(2)	11.70(12)	4.09(4)
V26	-1.36(21)	-1.25(21)	0.54(1)	3.84(1)	1.68(1)	0.71(1)	12.67(6)	4.85(2)
V34	-1.07(79)	-0.96(61)	0.49(1)	3.86(1)	1.70(1)	0.59(2)	12.04 (8)	4.64(3)
Mean	-1.29	-1.07	0.59	3.85	1.65	0.64	11.96	4.42
σ	±0.31	±0.35	±0.10	±0.02	±0.04	±0.08	±0.48	±0.49

[1]Numbers in parentheses indicate the internal uncertainty expressed to the last digit; e.g. -1.49(3) is equivalent to -1.49±0.03.
[2]Value not included in the mean.

tification of some variables; therefore, the authenticity of these variables will have to be confirmed with proper time-series observations on images of resolution higher than ours.

The theoretical ZAHB shown in the figure as a red continuous locus was calculated by Yepez et al. (2022) using the models built with the Eggleton code (Pols et al. 1997, 1998; Schröder et al. 1997) for a metallicity of z=0.001, a core mass of 0.5 $M/M_\odot$, and a range of total masses of 0.59-0.68 $M/M_\odot$. The isochrone is from VandenBerg et al. (2014) for [Fe/H]=−1.35 and an age of 12.0 Gyr.

All the above loci have been drifted to a distance of 11.95 kpc and represent well the observed distribution of the cluster member stars.

9. CONCLUSIONS

The presence of variable field stars projected against a Galactic globular cluster is very common, and while such contamination by field stars in the Galactic bulge globular clusters can be remarkably high (e.g. see the case of NGC 6558 Arellano Ferro et al. 2024) due to the richness of the bulge of field variable stars, particularly of RR Lyrae, it can also be noticeable in more isolated globular clusters in the outer regions of the Milky Way. Such is the case of NGC 1851, as we have demonstrated in the present work. An *ad hoc* membership analysis based on the proper motions and parallaxes available in *Gaia*-DR3, complemented with mean magnitudes and colours in the $V-(V-I)$ CMD, has shown that of the 55 variables originally listed in the CVSGC, 8 have been found to be clearly field stars, and for 6 more the membership cannot be solidly assessed due to the lack of proper motion data or to blending with bright neighbours, particularly in the central regions of the cluster.

Three variables not detected before were identified, but only one turned out to be a cluster member. We named it V56 and classified it tentatively as an SX Phe star. Among the 21 variables reported by *Gaia* not included in the CVSGC, we confirmed the variability of two RRab and three long term L variables. Since they turned out to be cluster members we assign to them variable names V57-V61.

Identifying variable cluster members is rewarding, since they can be used with confidence, as indicators of average physical quantities representative of the parental cluster. Here we estimated the mean

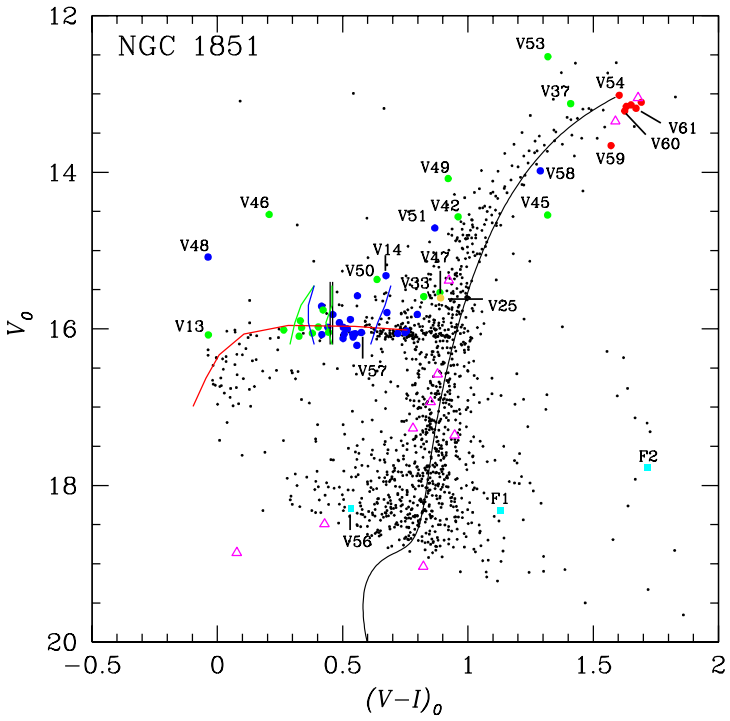

Fig. 5. Color-Magnitude Diagram (CMD) of NGC 1851. Variables stars in the field of the cluster are plotted with colour symbols according to the following code:solid blue and green circles represent RRab and RRc star respectively; red circles are for SR/L variables near the tip of the RGB. The star V25, classified as an eclipsing binary, is shown with a yellow circle. Turquoise colour is use for three newly identified variables, and purple open triangles for variables reported in *Gaia* that were not identified in our photometry or were not confirmed as variables. The Red ZAHB was constructed by Yepez et al. (2022) using the models built from with the Eggleton (Pols et al. 1997, 1998; Schröder et al. 1997). The green and blue vertical nearly vertical lines on the HB are the theoretical first overtone and fundamental mode instability strips respectively (Bono et al. 1994).en The isochrone is from VandenBerg et al. (2014) for [Fe/H]=-1.35 and an age of 12.0 Gyrs. The vertical black lines at the ZAHB mark the empirical red edge of the first overtone instability strip (Arellano Ferro et al. 2015, 2016). The colour figure can be viewed online.

metallicity and distance of NGC 1851 via the Fourier decomposition of RR Lyrae light curves, to find $[\mathrm{Fe/H}]_{\mathrm{ZW}} = -1.35 \pm 0.22$ dex and $d = 11.9 \pm 0.6$ kpc.

A few comments on the position of NGC 1851 relative to the Oosterhoff gap are in order, since the cluster has been associated with an CMa dwarf galaxy (Martin et al. 2004). We noted before that the average period of the member RRab stars is $<P\mathrm{ab}> = 0.57 \pm 0.06$ d, which with the metallicity $[\mathrm{Fe/H}]_{\mathrm{ZW}} = -1.35$ places the cluster among the Oo I clusters and slightly off the Oosterhoff gap marked by Catelan (2009, see his Figure 5). On the other hand, let us consider the structural, or horizontal branch type parameter, defined as $HBt = (B - R)/(B + V + R)$, Lee et al. (1994), where B and R are the number of stars to the blue and to the red of the instability strip respectively, and V represents the number of RR Lyrae in the instability strip (Lee et al. 1994; Demarque et al. 2000). In the [Fe/H]-HBt plane Catelan (2009, his Figure 7) identified a region devoid of Galactic globular clusters, but populated otherwise by clusters associated with neighbouring galaxies, and termed this region as "forbidden" or as the "Oosterhoff gap". We should recall here that the Oo I clusters NGC 1851 and NGC 2808, as well as the Oo II clusters NGC 2298 and NGC 1904, have been suggested by Martin et al. (2004) to be associated to the Canis Major dwarf galaxy accreted by the Milky Way. More recently, Callingham et al. (2022) have associated the first three to the Gaia-Enceladus-Sausage merger event and to the Helmi merger (Helmi et al. 2018) for the case of NGC 1904.

NGC 1851 and NGC 2808 have well developed HB blue tails but prominent red clumps; hence their HBt values are very red, i.e. negative, whereas NGC 1904 and NGC 2298 have massive blue tails

but lack a red clump. Therefore, their HBt values are very blue, hence large and positive.

Considering the updated version of the [Fe/H]-HBt plane (Yepez et al. 2022, see their Figure 11), and plotting these four clusters with the coordinates ([Fe/H],HBt); NGC 1851 (−1.35,−0.36, this work), NGC 2808 (−1.15, −0.49, Catelan 2009), NGC 1904 (−1.68,+0.74, Arellano Ferro 2024) and NGC 2298 (−1.96,+0.96, Torelli et al. 2019), it is evident that none of these four clusters occupy the Oosterhoff gap.

We are faced with two possible conclusions; these clusters are not associated to external galaxy mergers of the MW beyond the spatial coincidence, or else the globular clusters of extragalactic origin can occupy regions in the [Fe/H]-HBt or [Fe/H]-$< P_{\rm ab} >$ planes other than the Oosterhoff gap defined by Catelan (2009), as in fact some are seen in his Figures 5 and 7. This reinforces the view that the Oosterhoff gap retains its meaning only in Galactic terms. Hence, we do not find compelling evidence, from these arguments, for an association of NGC 1851 (and perhaps neither of NGC 2808, NGC 1904 and NGC 2298) to the large accretion events that seem to have sculpted the Galactic halo.

AAF is grateful to the European Southern Observatory (Garching), for warm hospitality during the writing of this work. The permanent support from the IA-UNAM librarian, Beatriz Juárez Santamaría, with the bibliographical material needed for this work is fully acknowledged. AAF also thankfully acknowledges the sabbatical support granted by the program PASPA of DGAPA-UNAM. We have benefited from the support of DGAPA-UNAM through Projects IG100620 and IN103024.

APPENDICES

A. LIGHT CURVES OF THE MEASURED VARIABLE STARS

The light curves of all variables resolved in our photometry are displayed in Figures 6, 7, 8, 9 and 10 for the RRab, RRc, RGBs, newly detected variables and confirmed *Gaia* variables, respectively.

B. COMMENTS ON INDIVIDUAL STARS

V13. This RRc star falls too far to the blue of the HB. Its membership to the the cluster is controversial. The assignment by the B&C membership method and the membership probability assigned by V&B is contradictory. In the period-amplitude diagram the star has too large an amplitude for its period.

V25. In spite of being an eclipsing binary EC, its light curve is included in Figure 7. The only difference with other RRc stars is that its period is much shorter, 0.173673 d, and it is brighter than the HB by about half a magnitude (see CMD of Figure 5), The V light curve exhibits a small flattening near maximum which may be a suggestion of an incipient secondary eclipse. This is also seen in the I-band light curve from the BA19 season.

V34. This variable was first reported by Sumerel et al. (2004) as an RRab star with a period of 0.515 d, which in fact produces a well phased light curve. However, at the coordinates given in the CVSGC we in fact find a variable star, but we find a period of 0.345033 d that displays a clear and complete RRc-like light curve (see Figure 7). The only reason we find for this discrepancy is that the data of Sumerel et al. (2004) cover only about half a cycle, and then their period and type may be spurious. We classified the star as RRc.

V51. It was reported as variable by Sumerel et al. (2004), and the light curve obtained by these authors (labeled NV18), although incomplete, clearly suggests the RRab nature of the star. It was noticed by Layden et al. (2010) that the star is in fact an RR Lyrae stars badly blended with a non-variable star previously identified as V2 by Sawyer (1939). The light curve measured by Layden (2010) was not published, but it was said to be noisy, likely due to the contamination of the brighter V2. Our light curve in Figure 6 is fairly complete, and confirms the RRab nature of the star nicely phased with a period of 0.509389 days. The mean VI magnitude level of our curve is spurious due to the light contamination of V2 and its position in the CMD of Figure 5.

V52. This star is not classified in the present edition of the CVSGC, where only its X-Y coordinates are listed. We have identified the star and found it to be a cluster member RRab star. It sits on the HB and its light curve is properly phased with a period of 0.648831 d.

V56. This is a newly identified variable in this work. Its light curve shape and position on the CMD diagram remind us of an SX Phe-type star. However a period of 0.25 d. is perhaps a little too long for an SX Phe. We have retained it in our general Table 4 as SX Phe? awaiting a confirmation in the future.

V58. Its light curve is that of an RRab; however, it appears about two magnitudes above the HB near the RGB. Both membership approaches, B&C and V&B, based on its proper motion, identify the star as a cluster member. In the identification chart we see that evidently the star is blended with at least

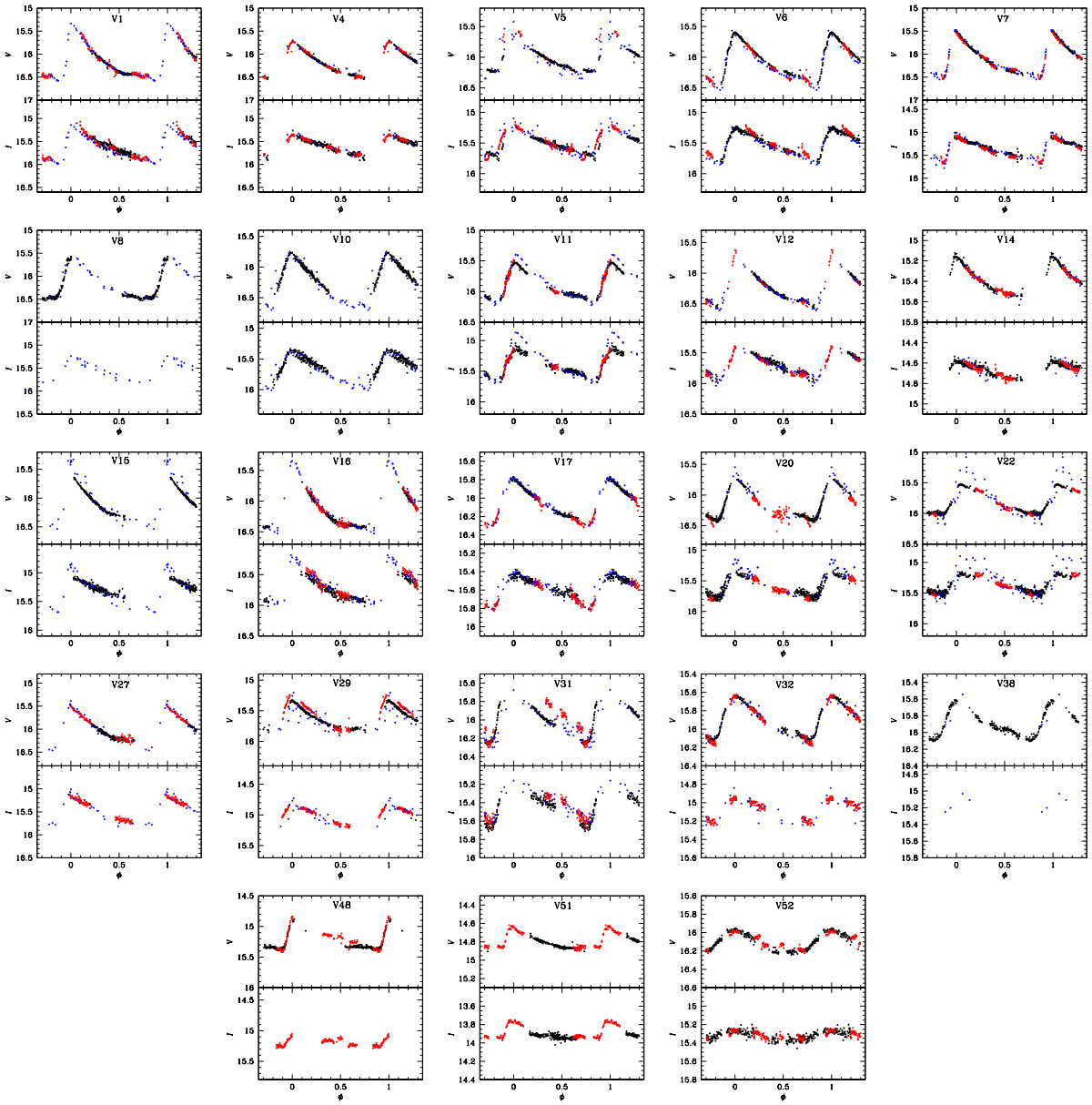

Fig. 6. NGC 1851 RR Lyrae stars *VI* light curves. The colour code is: black: BA18; red: BA19; blue: *Gaia*-DR3. The colour figure can be viewed online.

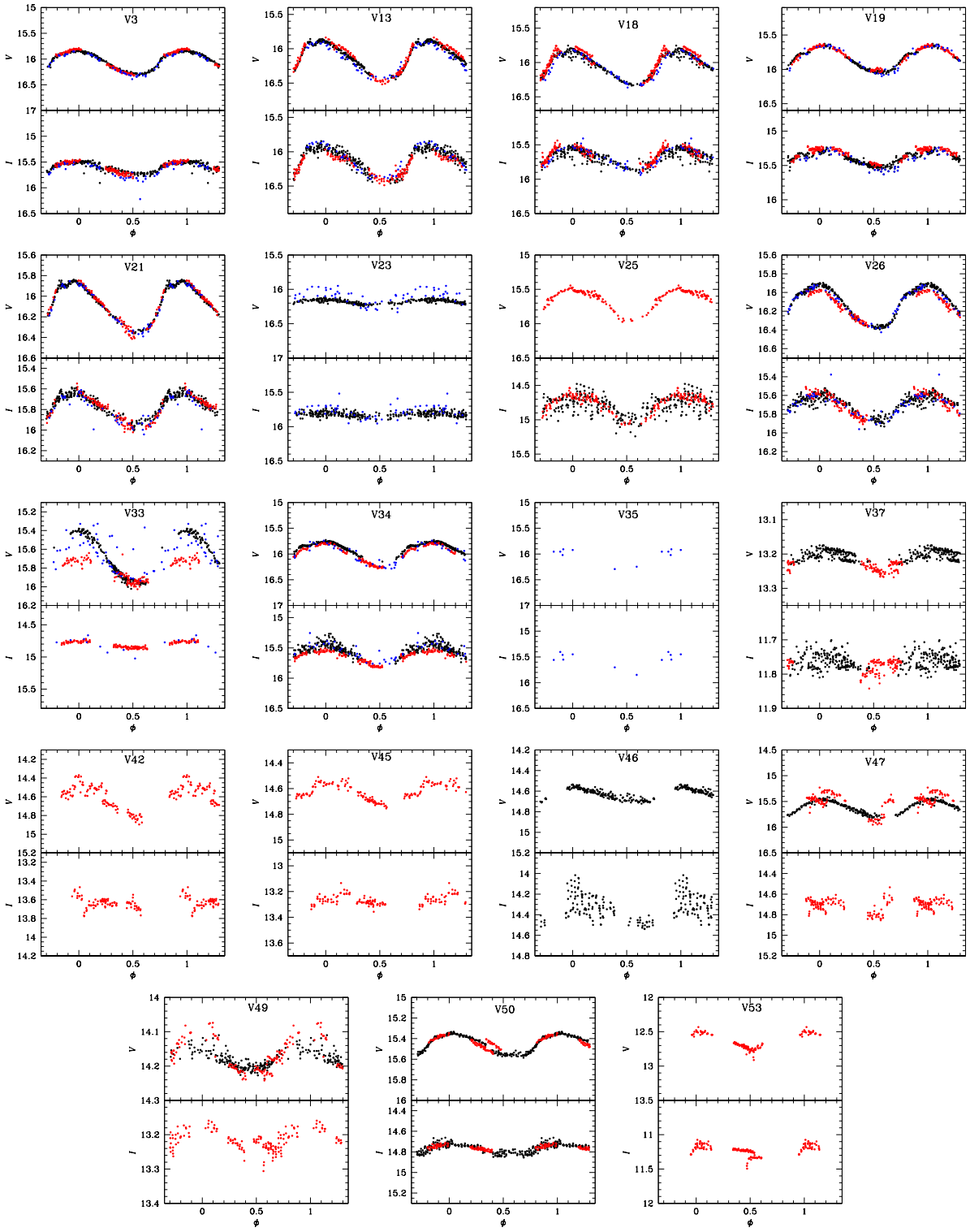

Fig. 7. Light curves of the RRc stars in the field of NGC 1851. The colour code is as in Figure 6. The colour figure can be viewed online.

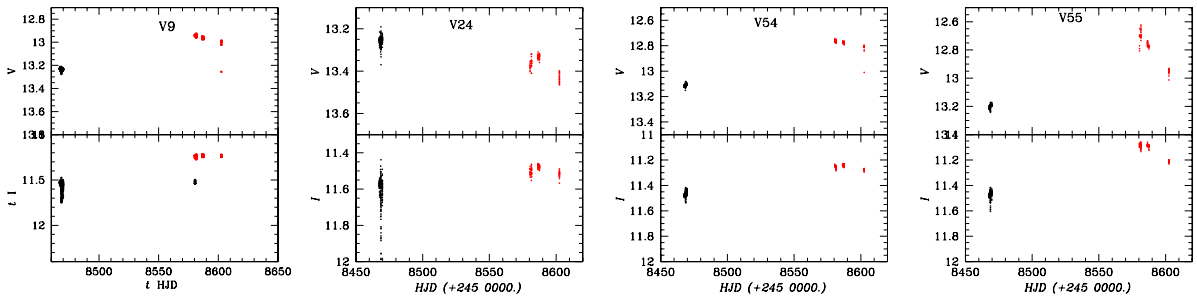

Fig. 8. Light curves of long-period variables in NGC 1851 plotted as a function of heliocentric Julian date (HJD). Colour coding follows that of Figure 6. The colour figure can be viewed online.

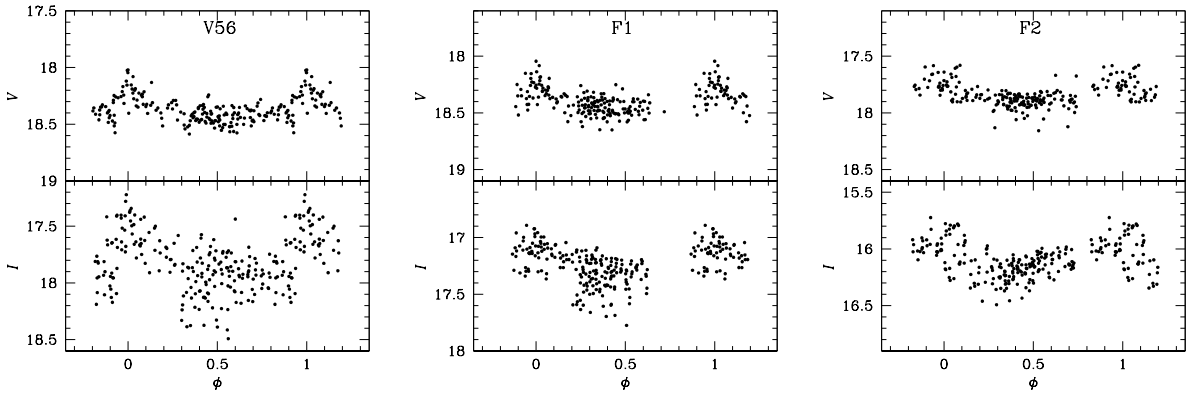

Fig. 9. Newly identified variable stars not previously recorded.They have been phased with the periods in Table 4.

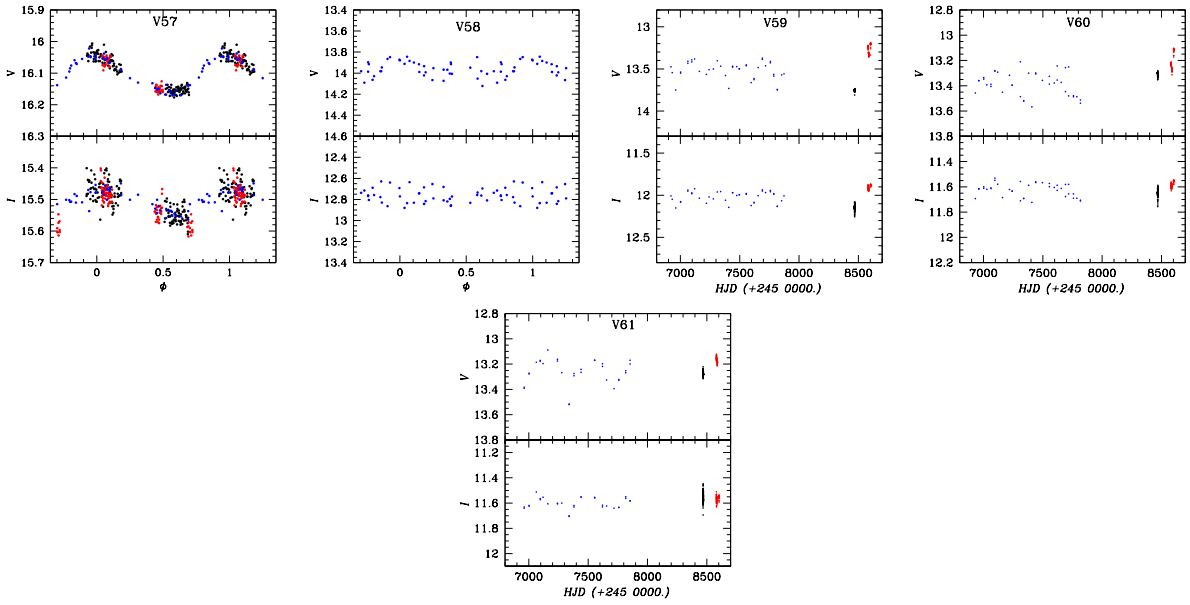

Fig. 10. Light curves of the confirmed variables reported in *Gaia*-DR3. Colour code as in Figure 6. The colour figure can be viewed online.

a brighter star, which explains its mean magnitude being spuriously too bright. We have considered the star to be a cluster member and assigned to it the variable name V58.

REFERENCES

Arellano Ferro, A. 2024, IAUS 376, At the crossroads of astrophysics and cosmology: Period-luminosity relations in the 2020s, ed. R. De Grijs, P. A. Whitelock, and M. Catelan (CUP), 222, https://doi.org/10.1017/S1743921323002880

Arellano Ferro, A., Giridhar, S., & Bramich, D. M. 2010, MNRAS, 402, 226, https://doi.org/10.1111/j.1365-2966.2009.15931.x

Arellano Ferro, A., Luna, A., Bramich, D. M., et al. 2016, Ap&SS, 361, 175, https://doi.org/10.1007/s10509-016-2757-5

Arellano Ferro, A., Mancera Piña, P. E., Bramich, D. M., et al. 2015, MNRAS, 452, 727, https://doi.org/10.1093/mnras/stv1299

Arellano Ferro, A., Zerpa Guillen, L. J., Yepez, M. A., et al. 2024, MNRAS, 532, 2159, https://doi.org/10.1093/mnras/stae1609

Belokurov, V., Erkal, D., Evans, N. W., Koposov, S. E., & Deason, A. J. 2018, MNRAS, 478, 611, https://doi.org/10.1093/mnras/sty982

Bono, G., Caputo, F., & Stellingwerf, R. F. 1994, ApJ, 423, 294, https://doi.org/10.1086/173806

Bramich, D. M. 2008, MNRAS, 386, 77, https://doi.org/10.111/j.1745-3933.2008.00464.x

Bramich, D. M., Bachelet, E., Alsubai, K. A., Mislis, D., & Parley, N. 2015, A&A, 577, 108, https://doi.org/10.1051/0004-6361/201526025

Bramich, D. M., Horne, K., Albrow, M. D., et al. 2013, MNRAS, 428, 2275, https://doi.org/10.1093/mnras/sts184

Bustos Fierro, I. H. & Calderón, J. H. 2019, MNRAS, 488, 3024, https://doi.org/10.1093/mnras/stz1879

Callingham, T. M., Cautun, M., Deason, A. J., et al. Frenk, C. S., Grand, R. J. J., & Marinacci, F. 2022, MNRAS, 513, 4107, https://doi.org/10.1093/mnras/stac1145

Carballo-Bello, J. A., Martínez-Delgado, D., Navarrete, C., et al. 2018, MNRAS, 474, 683, https://doi.org/10.1093/mnras/stx2767

Carretta, E., Bragaglia, A., Gratton, R., D'Orazi, V., & Lucatello, S. 2009, A&A, 508, 695, https://doi.org/10.1051/0004-6361/200913003

Catelan, M. 2009, Ap&SS, 320, 261, https://doi.org/10.1077/s10509-009-9987-8

Clement, C. M., Muzzin, A., Dufton, Q., et al. 2001, AJ, 122, 2587, https://doi.org/10.1086/323719

Demarque, P., Zinn, R., Lee, Y.-W., & Yi, S. 2000, AJ, 119, 1398, https://doi.org/10.1086/301261

Gaia Collaboration, Vallenari, A., Brown, A. G. A., et al. 2023, A&A, 674, 1, https://doi.org/10.1051/0004-6361/202243940

Guldenschuh, K. A., Layden, A. C., Wan, Y., et al. 2005, PASP, 117, 721, https://doi.org/10.1086/431178

Harris, W. E. 1996, AJ, 112, 1487, https://doi.org/10.1086/118116

Helmi, A., Babusiaux, C., Koppelman, H. H., et al. 2018, Nature, 563, 85, https://doi.org/10.1038/s41586-018-0625-x

Koleva, M., Prugniel, P., Ocvirk, P., Le Borgne, D., & Soubiran, C. 2008, MNRAS, 385, 1998, https://doi.org/10.1111/j.1365-2966.2008.12908.x

Kuzma, P. B., Da Costa, G. S., & Mackey, A. D. 2018, MNRAS, 473, 2881, https://doi.org/10.1093/mnras/stx2353

Landolt, A. U. 1992, AJ, 104, 340, https://doi.org/10.1086/116242

Layden, A. C., Broderick, A. J., Pohl, B. L., et al. 2010, PASP, 122, 1000, https://doi.org/10.1086/656018

Lee, Y.-W., Demarque, P., & Zinn, R. 1994, ApJ, 423, 248, https://doi.org/10.1086/173803

Marino, A. F., Milone, A. P., Yong, D., et al. 2014, MNRAS, 442, 3044, https://doi.org/10.1093/mnras/stu1099

Martin, N. F., Ibata, R. A., Bellazzini, M., et al. 2004, MNRAS, 348, 12, https://doi.org/10.1111/j.1365-2966.2004.07331.x

Pols, O. R., Schröder, K.-P., Hurley, J. R., Tout, C. A., & Eggleton, P. P. 1998, MNRAS, 298, 525, https://doi.org/10.1046/j.1365-8711.1998.01658.x

Pols, O. R., Tout, C. A., Schroder, K.-P., Eggleton, P. P., & Manners, J. 1997, MNRAS, 289, 869, https://doi.org/10.1093/mnras/289.4.869

Riello, M., De Angeli, F., Evans, D. W., et al. 2021, A&A, 649, 3, https://doi.org/10.1051/0004-6361/202039587

Sawyer, H. B. 1939, PDDO, 1, 125

Schlafly, E. F. & Finkbeiner, D. P. 2011, ApJ, 737, 103, https://doi.org/10.1088/0004-637X/737/2/103

Schlegel, D. J., Finkbeiner, D. P., & Davis, M. 1998, ApJ, 500, 525, https://doi.org/10.1086/305772

Schröder, K.-P., Pols, O. R., & Eggleton, P. P. 1997, MNRAS, 285, 696, https://doi.org/10.1093/mnras/285.4.696

Stetson, P. B. 2000, PASP, 112, 925, https://doi.org/10.1086/316595

Sturch, C. 1966, ApJ, 143, 774, https://doi.org/10.1086/148557

Sumerel, A. N., Corwin, T. M., Catelan, M., Borissova, J., & Smith, H. A. 2004, IBVS, 5533, 1

Torelli, M., Iannicola, G., Stetson, P. B., et al. 2019, A&A, 629, 53, https://doi.org/10.1051/0004-6361/201935995

VandenBerg, D. A., Brogaard, K., Leaman, R., & Casagrande, L. 2013, ApJ, 775, 134, https://doi.org/10.1088/0004-637X/775/2/134

Vasiliev, E. & Baumgardt, H. 2021, MNRAS, 505, 5978, https://doi.org/10.1093/mnras/stab1475

Walker, A. R. 1998, AJ, 116, 220, https://doi.org/10.1986/300432
Yepez, M. A., Arellano Ferro, A., Deras, D., et al. 2022, MNRAS, 511, 1285, https://doi.org/10.1093/mnras/stac054
Zhang, T., Ramakrishnan, R., & Livny, M. 1996, ACM SIGMOD Recoed, 25, 103, https://doi.org/10.1145/235968.233324
Zinn, R. & West, M. J. 1984, ApJS, 55, 45, https://doi.org/10.1086/190947

A. Arellano Ferro: Instituto de Astronomía, Universidad Nacional Autónoma de México, Ciudad Universitaria, C.P. 04510, México.
C. E. Pérez Parra and L. J. Zerpa Guillen: Universidad de Los Andes, Facultad de Ciencias, Dpto. Física, Grupo de Astrofísica Teórica, Mérida, Venezuela.
C. E. Pérez Parra and L. J. Zerpa Guillen: Fundación Centro de Investigaciones de Astronomía Francisco, J. Duarte (CIDA), Mérida, Venezuela.
I. Bustos Fierro: Observatorio Astronómico, Universidad Nacional de Córdoba, Córdoba C.P. 5000, Argentina.
Z. Prudil: European Southern Observatory, , Karl-Schwarzschild-Strasse 2, 85748, Garching, Germany.
M. A. Yepez: Instituto Nacional de Astrofísica, Óptica y Electrónica (INAOE), Luis Enrique Erro No.1, Tonantzintla, Puebla, C.P. 72840, México.
M. A. Yepez: Consejo Nacional de Humanidades, Ciencias y Tecnologías, Av. Insurgentes Sur 1582, 03940, Ciudad de México, México.

Revista Mexicana de Astronomía y Astrofísica, **60**, 397–402 (2024)

https://doi.org/10.22201/ia.01851101p.2024.60.02.17

RADIO PROPER MOTIONS AND A SEARCH FOR THE ORIGIN OF PSR B1849+00

L. F. Rodríguez[1,2], S. A. Dzib[3], L. A. Zapata[1], and L. Loinard[1]

Received July 13 2024; accepted August 15 2024

ABSTRACT

Until now it has not been possible to obtain the proper motion of PSR B1849+00 with timing techniques or VLBI imaging, given the enhanced interstellar scattering along its line of sight. We present an analysis of archive Very Large Array observations at epochs from 2012 to 2022 that indicates a total proper motion of 23.9±5.5 mas yr^{-1} toward the southwest. After correction for the proper motions produced by galactic rotation, we find a peculiar transverse velocity of ≃740 km s^{-1}. We searched unsuccessfully along the past trajectory of the pulsar for an associated supernova remnant. In particular, W44 is in this trajectory but its distance is different from that of PSR B1849+00.

RESUMEN

Hasta ahora no ha sido posible obtener el movimiento propio de PSR B1849+00 con técnicas de sincronización o imágenes de VLBI debido a la fuerte dispersión en su línea de visión. Presentamos un análisis de datos del archivo del Very Large Array en épocas de 2012 a 2022 que indican un movimiento propio total de 23.9±5.5 mas año^{-1} hacia el suroeste. Después de corregir por el movimiento propio producido por la rotación galáctica encontramos una velocidad transversal peculiar de ≃740 km s^{-1}. Buscamos infructuosamente en la trayectoria pasada del pulsar una remanente de supernova asociada. En particular, W44 está en esta trayectoria pero su distancia es diferente a la de PSR B1849+00.

Key Words: astrometry — proper motions — pulsars: general

1. INTRODUCTION

The positions and proper motions of hundreds of pulsars have been determined using the analysis of pulsar timing residuals (e.g. Hobbs et al. 2004) and very long baseline interferometry (VLBI) imaging (e.g. Deller et al. 2019). However, in some cases, the pulsar suffers strong scattering effects from plasma along the line of sight. This condition scatters the radio image of the pulsar up to arcsec angular dimensions, ruling out the possibility of VLBI imaging. For some sources it has been possible to make images with connected interferometers (i.e. the Very Large Array), since these observations do not resolve out the scattered emission (e.g. Dzib et al. 2018). Multiple examples of pulsars whose proper motions have been determined with the Very Large Array are given by Brisken et al. (2003). The presence of inhomogeneous plasma in the line of sight also limits the timing method by broadening the pulses to a level that makes timing experiments difficult or impossible.

PSR B1849+00 (PSR J1852+00) is a pulsar that has a period of 2.18 s and a characteristic age of $10^{5.55}$ yr (Taylor et al. 1993). It is located in a region of enhanced line-of-sight interstellar scattering (Lazio 2004) that makes it one of the most heavily scattered pulsar known, with a pulse broadening time of 0.22 seconds at 1.4 GHz (Löhmer et al. 2001). It has a large dispersion measure, DM = 787 cm^{-3} pc (Han et al. 2016). Only seven of the 228 pulsars studied by these authors have larger dispersion measures.

In this paper we present an analysis of archive Very Large Array data with the goal of determining the proper motion of PSR B1849+00 and possibly

[1]Instituto de Radioastronomía y Astrofísica, UNAM, México.
[2]Mesoamerican Center for Theoretical Physics, UNACH, México.
[3]Max-Planck-Institut fur Radioastronomie, Germany.

TABLE 1

PARAMETERS OF THE JANSKY VLA OBSERVATIONS

Project	Mean Epoch	ν (GHz)	Synthesized Beam	Flux Density (mJy)	Position of PSR B1849+00 RA(J2000)[a]	DEC(J2000)[b]
12B-225	2012.779	1.50	$1\farcs47\times1\farcs21$; $+20\fdg6$	3.51±0.33	$27\fs499\pm0\fs002$	$01\farcs91\pm0\farcs03$
14A-404	2014.362	1.52	$2\farcs25\times1\farcs60$; $-44\fdg4$	4.74±0.20	$27\fs502\pm0\fs002$	$01\farcs83\pm0\farcs02$
15A-301	2015.630	1.50	$2\farcs05\times1\farcs35$; $-48\fdg4$	6.04±1.00	$27\fs507\pm0\fs007$	$01\farcs80\pm0\farcs05$
19A-386	2019.647	1.57	$1\farcs39\times1\farcs21$; $+24\fdg8$	3.92±0.32	$27\fs494\pm0\fs004$	$01\farcs80\pm0\farcs03$
22A-097	2022.474	1.52	$2\farcs29\times1\farcs32$; $+65\fdg3$	2.42±0.21	$27\fs486\pm0\fs004$	$01\farcs72\pm0\farcs02$

[a]Offset from RA(J2000) = $18^h52^m00^s$.

[b]Offset from DEC(J2000) = $+00^\circ32'00''$.

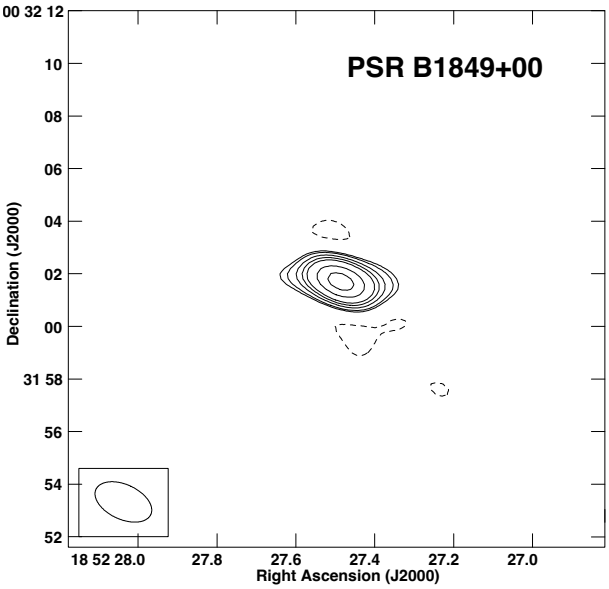

Fig. 1. Very Large Array contour image of PSR B1849+00 at 1.52 GHz for epoch 2022.474. Contours are −3, 3, 4, 6, 8, 10, 15, and 20 times 100 μJy beam^{-1}, the rms noise in this region of the image. The synthesized beam ($2\farcs29\times1\farcs32;+65\fdg3$) is shown in the bottom left corner of the image.

advance in our understanding of the supernova that created this pulsar.

2. VLA OBSERVATIONS

We searched unsuccessfully in the archives of the Karl G. Jansky VLA of NRAO[4] for observations made with the highest angular resolution A configuration pointing toward PSR B1849+00. We found, however, several good quality A configuration observations made in the L-band (1-2 GHz) with the phase center at the position of the gain calibrator J1851+0035. Although J1851+0035 is located at $\approx 11'$ from PSR B1849+00 we could obtain images of good quality over the full extent of the primary beam ($\approx 30'$). This was possible because the Jansky VLA records the continuum data in narrow channels (2 MHz), that do not produce significant bandwidth smearing. For all observations the position of J1851+0035 used was the updated position given in the VLA Calibrator Manual, RA(J2000) = $18^h51^m46\fs7217$; DEC(J2000) = $00^\circ35'32\farcs414$. The data were calibrated in the standard manner using the CASA (Common Astronomy Software Applications; McMullin et al. 2007) package of NRAO and the pipeline provided for VLA[5] observations. We obtained images using a robust weighting (Briggs 1995) of 0 to optimize the compromise between angular resolution and sensitivity. All images were also corrected for the primary beam response. Finally, the images were also corrected for wide-field effects using the gridding option *widefield* with 10×10 subregions in the task TCLEAN (Rodriguez et al. 2023).

3. DISCUSSION

In Table 1 we list the five projects found, indicating the name of the project, its mean epoch, frequency, synthesized beam, and flux density. We finally give the position of PSR B1949+00 for each epoch. In Figure 1 we show a contour image of the source from project 22A-097. In Figure 2 we present the positions as a function of time for PSR B1949+00. In Table 2 we give the equatorial proper motions obtained from a least-squares fit to the positions shown in Figure 2. In this table we can see that PSR B1949+00 has a statistically significant equatorial total proper motion (4.3σ).

The weighted mean flux density and weighted mean standard deviation at 1.5 GHz over the five epochs are 3.7±1.1 mJy for PSR B1949+00. The spectral index can be used to further define the nature of the radio source. Kijak et al. (2011) report a spectral index of $\alpha = -2.4$ for this source, a steep value characteristic of pulsars (e.g. Taylor et al. 1993; Maron et al. 2000).

[4]The National Radio Astronomy Observatory is a facility of the National Science Foundation operated under cooperative agreement by Associated Universities, Inc.

[5]`https://science.nrao.edu/facilities/vla/data-processing/pipeline`.

TABLE 2

POSITION AND PROPER MOTIONS OF PSR B1849+00

Position[a]		Equatorial Proper Motions[d]				Corrected Galactic Proper Motions[d]			
RA(J2000)[b]	DEC(J2000)[c]	$\mu_{RA}\cos(\mathrm{DEC})$	μ_{DEC}	μ_{TOTAL}	PA[e]	$\mu_l cos(b)$	μ_b	μ_{TOTAL}	PA[e]
$27^s.518\pm0^s.007$	$02''.06\pm0''.06$	-19.1±6.4	-14.4±3.2	23.9±5.5	$233^\circ \pm 9^\circ$	-14.6±5.8	+10.4±4.2	17.9±5.3	$305^\circ \pm 15^\circ$

[a]For epoch 2000.0.
[b]Offset from RA(J2000) = $18^h52^m00^s$.
[c]Offset from DEC(J2000) = $+00^\circ32'00''$.
[d]In mas yr^{-1}.
[e]Position angle of the proper motion vector in the respective coordinates.

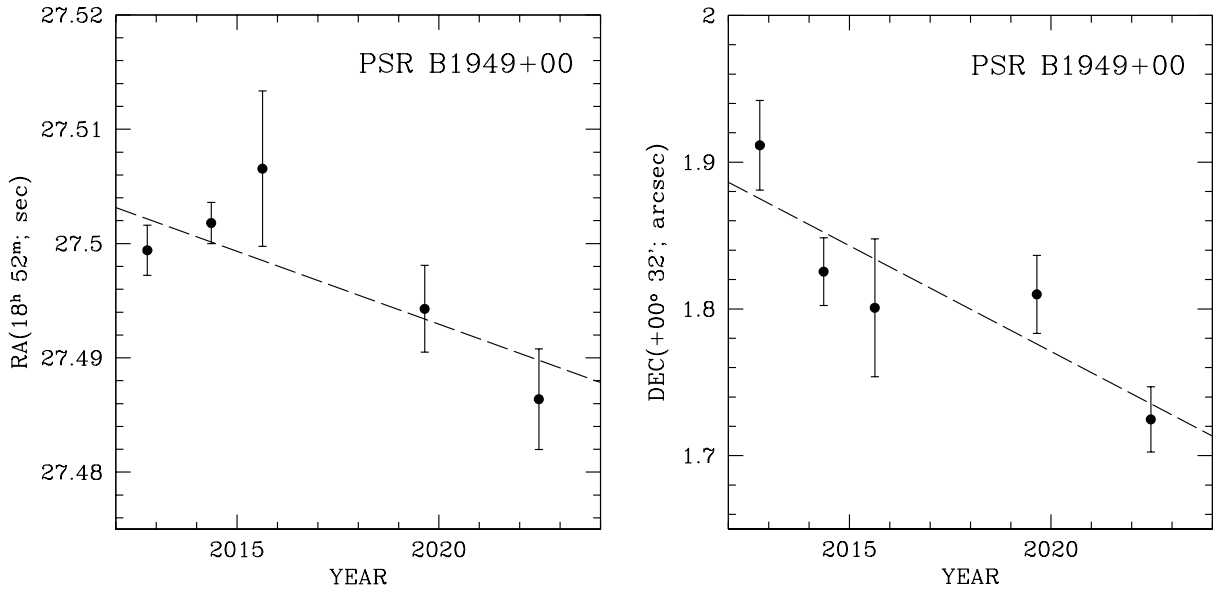

Fig. 2. Right ascension (left) and declination (right) of PSR B1849+00 as a function of time. The dashed lines indicate the least squares fit for each parameter. The resulting proper motions are given in Table 2.

4. THE TRANSVERSE VELOCITY OF PSR B1849+00

The distance of PSR B1849+00 has been estimated by several groups. We weight-averaged the results of Cordes & Lazio (2003), Verbiest et al. (2012), Yao et al. (2017), Pynzar (2020) and Kütükcü et al. (2022), listed in Table 3, to obtain a value of 8.6±1.7 kpc.

The total proper motion of PSR B1949+00 has to be corrected for the proper motion contribution due to the kinematics of the Galaxy in order to obtain the peculiar proper motion. We use a distance from the Sun to the center of the Galaxy of 8.15 kpc and a circular rotation velocity at the Sun of 236 km s^{-1} (Reid et al. 2019). We also assume a flat rotation curve outside the tangent point (with a galactocentric distance of 4.6 kpc in the direction of the pulsar) and that the H I disk of the Galaxy has an outer radius of 13.4 kpc (Goodwin, Gribbin, & Hendry 1998). In Figure 3 we show the proper motion in galactic longitude for a circular Galactic orbit as a function of distance in the direction of PSR B1949+00. At the distance of the pulsar, 8.6 kpc, a galactic longitude proper motion of -6.9 mas yr^{-1} is expected. We have corrected the galactic proper motion of PSR B1949+00 for this effect to obtain the values given in Table 2. This correction reduces the total proper motion from 23.9 mas yr^{-1} to 17.9 mas yr^{-1}. This is the peculiar proper motion of the pulsar.

At the distance of 8.6 kpc the corrected total proper motion implies a peculiar velocity of 740±220 km s^{-1} in the plane of the sky. The large error comes from propagating the errors in the proper motion and in the distance. The Australia Telescope National Facility Pulsar Catalogue (Manchester et al. 2005) lists a total of 294 pulsars with reported transverse velocities. Of these pulsars, 15 (5%) equal or exceed 740 km s^{-1}.

TABLE 3

DISTANCE ESTIMATES TO PSR B1849+00

Distance(kpc)	Method	Reference
8.4±1.7	Dispersion measure model	Cordes & Lazio (2003)
8.0±2.0	HI absorption	Verbiest et al. (2012)
7.0±1.0	HI absorption	Yao et al. (2017)
10.7± 0.9	Dispersion measure model	Pynzar et al. (2020)
7.0±1.5	Dispersion measure model	Kütükcü et al. (2022)

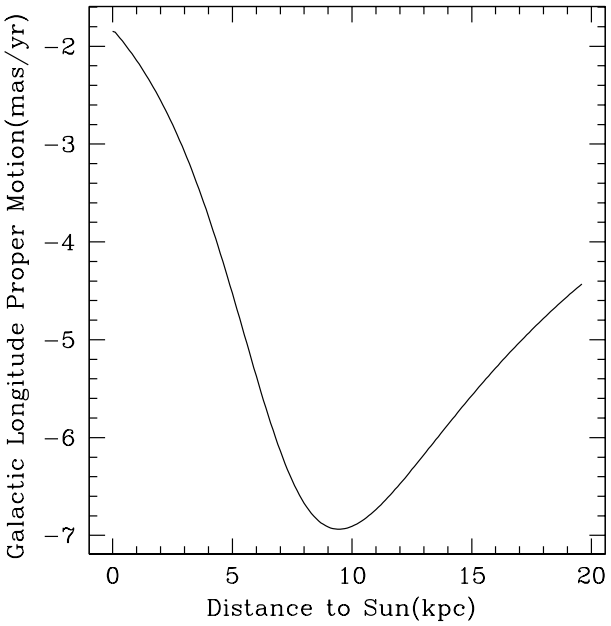

Fig. 3. Galactic longitude proper motion in the direction of PSRB1849+00 as a function of distance to the Sun. This theoretical curve is based on the Galactic model for circular motion described in the text.

5. THE POSSIBLE ORIGIN OF PSR B1849+00

In Figure 4 we plot the position and proper motion of PSR B1849+00, superposed on a GLOSTAR image at 5.8 GHz (Medina et al. 2019; Brunthaler et al. 2021; Medina et al. 2024). In this image we also mark with circles supernova remnants and candidate supernova remnants in the region.

The sources best aligned with the past trajectory of PSR B1849+00 are the W44 remnant and the supernova remnant candidate G34.524-0.761. Taking the characteristic age of $10^{5.55}$ yr and the corrected total proper motion given in Table 2, we find that assuming a ballistic motion the origin would be located at $\approx 1.^{\circ}77$ to the NE of its present position. The supernova W44 is located at $1.^{\circ}16$ to the NE of PSR B1849+00 and appears to be an interesting possibility since pulsar characteristic ages could depart importantly from the true age of the pulsar (Suzuki et al. 2021).

However, the distance of W44 appears to be well established at ≃3 kpc (Radhakrishnan et al. 1972; Caswell et al. 1975; Cox et al. 1999; Su et al. 2014; Wang et al. 2020). The first four groups used HI absorption observations and a model of the Galactic kinematics, while the last one used the extinction to red clump stars (Paczyński & Stanek 1998) probably associated with the supernova. This significantly different distance seems to rule out an association of W44 with PSR B1849+00. In any case, it would be valuable to estimate the distance to W44 by parallax measurements of the OH 1720 MHz masers associated with it. Also W44, whose age is estimated to be ≃20,000 yr (Smith et al. 1985; Cox et al. 1999; Giuliani et al. 2011), seems to be much younger that the pulsar and this result also gravitates against an association. The supernova age is estimated from observations of its size, expansion rate, and the properties of the surrounding interstellar medium.

The distance to G34.524-0.761 is not yet determined. This source has a spectral index of -0.9 and exhibits a 10% degree of linear polarization (Dokara et al. 2023), supporting the supernova remnant interpretation. However, as noted by these authors, its filamentary morphology suggests that it is probably a fragment of a much larger faint remnant. We conclude that we cannot clearly associate a supernova remnant with PSR B1849+00. It is probable that the related supernova remnant has mixed with the interstellar medium and is no longer detectable.

The Next Generation VLA (Murphy et al. 2018), with its unprecedented sensitivity and high angular resolution will be the ideal instrument for the study of the proper motions of pulsars whose images and pulses are scattered by inhomogeneous plasma in the line of sight.

6. CONCLUSIONS

(1) We analyzed archive VLA observations of the pulsar PSR B1849+00 to obtain its radio proper mo-

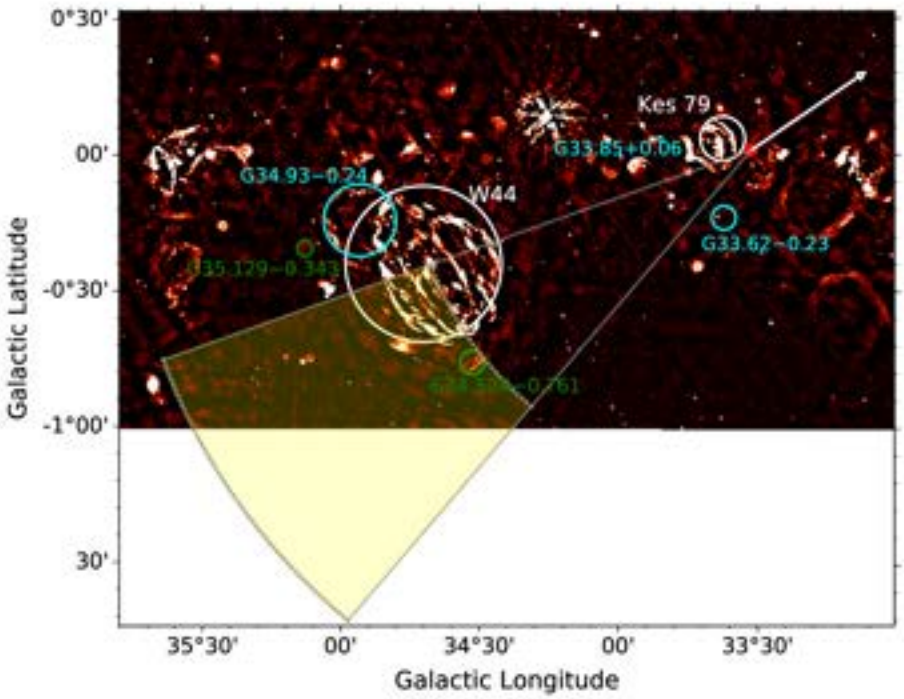

Fig. 4. Position (red dot) and proper motion of PSR B1849+00 for a period of 10^5 yr (white arrow) in galactic coordinates and superposed on a GLOSTAR image. The dashed lines indicate the ± 1-σ angular range for the past trajectory of the pulsar. The dashed curved lines indicate the ± 1-σ distance range for the origin of the pulsar assuming an age of $10^{5.55}$ yr, the characteristic age of the pulsar. These dashed lines define the most likely area in the sky for the origin of the pulsar, shown in yellow. The white circles indicate the position and extent of confirmed supernova remnants (Green 2022), while the green and cyan circles indicate candidate supernova remnants from Dokara et al. (2021) and Anderson et al. (2017), respectively.

tions. At a distance of 8.6 kpc the resulting peculiar velocity in the plane of the sky is $\simeq$740 km s^{-1}.

(2) We searched unsuccessfully along the past trajectory of PSR B1849+00 for a supernova remnant that could be associated with this pulsar. The bright supernova remnant W44 is in the past trajectory of the pulsar, but its distance is different.We suggest that the remnant that originated PSR B1849+00 has dissipated and is no longer detectable.

L.A.Z. acknowledges financial support from CONACyT-280775 and UNAM-PAPIIT IN110618, and IN112323 Grants, México. L.L. acknowledges the support of DGAPA PAPIIT Grant IN108324. L.F.R. acknowledges the financial support of DGAPA (UNAM) IN105617, IN101418, IN110618 and IN112417 and CONACyT 238631 and 280775-CF Grant 263356. S.A.D. acknowledges the M2FINDERS project from the European Research Council (ERC) under the European Union's Horizon 2020 research and innovation programme (Grant No 101018682).

REFERENCES

Anderson, L. D., Wang, Y., Bihr, S., et al. 2017, A&A, 605, 58, https://doi.org/10.1051/0004-6361/201731019

Briggs, D. S. 1995, AAS, 27, 1444

Brisken, W. F., Fruchter, A. S., Goss, W. M., et al. 2003, AJ, 126, 3090, https://doi.org/10.1086/379559

Brunthaler, A., Menten, K. M., Dzib, S. A., et al. 2021, A&A, 651, 85, https://doi.org/10.1051/0004-6361/202039856

Caswell, J. L., Murray, J. D., Roger, R. S., Cole, D. J., & Cooke, D. J. 1975, A&A, 45, 239

Cordes, J. M. & Lazio, T. J. W. 2003, astro-ph/0301598, https://doi.org/10.48550/arXiv.astro-ph/0301598

Cox, D. P., Shelton, R. L., Maciejewski, W., et al. 1999, ApJ, 524, 179, https://doi.org/10.1086/307781

Deller, A. T., Goss, W. M., Brisken, W. F., et al. 2019, ApJ, 875, 100, https://doi.org/10.3847/1538-4357/ab11c7

Dokara, R., Brunthaler, A., Menten, K. M., et al. 2021, A&A, 651, 86, https://doi.org/10.1051/0004-6361/202039873

Dokara, R., Gong, Y., Reich, W., et al. 2023, A&A, 671, 145, https://doi.org/10.1051/0004-6361/

202245339
Dzib, S. A., Rodríguez, L. F., Karuppusamy, R., Loinard, L., & Medina, S-N. X. 2018, ApJ, 866, 100, https://doi.org/10.3847/1538-4357/aada07
Goodwin, S. P., Gribbin, J., & Hendry, M. A. 1998, The Observatory, 118, 201
Green, D. A., 2022, 'A Catalogue of Galactic Supernova Remnants (2022 December version)', Cavendish Laboratory, Cambridge, United Kingdom (available at "http://www.mrao.cam.ac.uk/surveys/snrs/")
Han, J., Wang, C., Xu, J., et al. 2016, RAA, 16, 159, https://doi.org/10.1088/1674-4527/16/10/159
Hobbs, G., Lyne, A. G., Kramer, M., Martin, C. E., & Jordan, C. 2004, MNRAS, 353, 1311, https://doi.org/10.1111/j.1365-2966.2004.08157.x
Kijak, J., Lewandowski, W., Maron, O., Gupta, Y., & Jessner, A. 2011, A&A, 531, 16, https://doi.org/10.1051/0004-6361/201014274
Kütükcü, P., Ankay, A., Yazgan, E., & Bozkurt, K. 2022, MNRAS, 511, 4669, https://doi.org/10.1093/mnras/stac346
Lazio, T. J. W. 2004, ApJ, 613, 1023, https://doi.org/10.1086/423261
Löhmer, O., Kramer, M., Mitra, D., Lorimer, D. R., & Lyne, G. 2001, ApJ, 562, 157, https://doi.org/10.1086/338324
Manchester, R. N., Hobbs, G. B., Teoh, A., & Hobbs, M. 2005, AJ, 129, 1993, https://doi.org/10.1086/428488
Maron, O., Kijak, J., Kramer, M., et al. 2000, A&AS, 147, 195, https://doi.org/10.1051/aas:2000298
Medina, S.-N. X., Urquhart, J. S., Dzib, S. A., et al. 2019, A&A, 627, 175, https://doi.org/10.1051/0004-6361/201935249
Medina, S.-N. X., Dzib, S. A., Urquhart, J. S., et al. 2024, arXiv:2407.12585, https://doi.org/10.48550/arXiv.2407.12585
Murphy, E. J., Bolatto, A. & Chatterjee, S., et al. 2018, ASPC 517, Science with a Next Generation Very Large Array, 3, https://doi.org/10.48550/arXiv.1810.07524
Paczyński, B. & Stanek, K. Z. 1998, ApJ, 494, 219, https://doi.org/10.1086/311181
Pynzar, A. V. 2020, ARep, 64, 681, https://doi.org/10.1134/S1063772920090036
Radhakrishnan, V., Goss, W. M., Murray, J. D., & Brooks, J. W. 1972, ApJS, 24, 49, https://doi.org/10.1086/190249
Reid, M. J., Menten, K. M., Brunthaler, A., et al. 2019, ApJ, 885, 131, https://doi.org/10.3847/1538-4357/ab4a11
Rodriguez, L. F., Yanza, V., & Dzib, S. A. 2023, arXiv:2311.14296, https://doi.org/10.48550/arXiv.2311.14296
Smith, A., Jones, L. R., Watson, M. G., et al. 1985, MNRAS, 217, 99, https://doi.org/10.1093/mnras/217.1.99
Su, H., Tian, W., Zhu, H., et al. 2014, IAUS 296, Supernova Environmental Impacts, 372, https://doi.org/10.1017/S1743921313009885
Suzuki, H., Bamba, A., & Shibata, S. 2021, ApJ, 914, 103, https://doi.org/10.3847/1538-4357/abfb02
Taylor, J. H., Manchester, R. N., & Lyne, A. G. 1993, ApJS, 88, 529, https://doi.org/10.1086/191832
Verbiest, J. P. W., Weisberg, J. M., Chael, A. A., Lee, K. J., & Lorimer, D. R. 2012, ApJ, 755, 39, https://doi.org/10.1088/0004-637X/755/1/39
Wang, S., Zhang, C., Jiang, B., et al. 2020, A&A, 639, 72, https://doi.org/doi:10.1051/0004-6361/201936868
Yao, J. M., Manchester, R. N. & Wang, N. 2017, ApJ, 835, 29, https://doi.org/10.3847/1538-4357/835/1/29

Sergio A. Dzib: Max-Planck-Institut für Radioastronomie, Auf dem Hügel 69, D-53121 Bonn, Germany.
Laurent Loinard, Luis F. Rodríguez, and Luis A. Zapata: Instituto de Radioastronomía y Astrofísica, Universidad Nacional Autónoma de México, Apartado Postal 3–72, 58090 Morelia, Michoacán, México (l.rodriguez@irya.unam.mx).
Luis F. Rodríguez: Mesoamerican Center for Theoretical Physics, UNACH, México.

Revista Mexicana de Astronomía y Astrofísica, **60**, 403–412 (2024)

https://doi.org/10.22201/ia.01851101p.2024.60.02.18

X-RAY OBSERVATIONS OF THE VERY-FAINT X-RAY TRANSIENT XMMSL1 J171900.4–353217: A NEW CANDIDATE NEUTRON STAR LOW-MASS X-RAY BINARY

O. Ahmed[1,2], N. Degenaar[3], R. Wijnands[3], and M. Armas Padilla[4,5]

Received November 14 2023; accepted August 15 2024

ABSTRACT

XMMSL1 J171900.4–353217 is a very-faint X-ray transient that was discovered in 2010 March when it exhibited an outburst. We report on 7 observations, obtained with the X-Ray Telescope (XRT) aboard the Neil Gehrels *Swift* Observatory between 2010 May and October. By fitting a single absorbed power-law model to the XRT spectra, we infer power-law indices of $\Gamma = 1.8 - 2.7$ and an absorption column density of $N_{\rm H} = (4.6 - 7.9) \times 10^{22}$ cm^{-2}. The inferred $0.5 - 10$ keV luminosity fluctuated irregularly and peaked at $L_{\rm X} \simeq 10^{35} - 10^{36}$ erg s^{-1} for a distance of $4 - 12$ kpc. Based on the evolution of the power-law index with varying luminosity, we propose that the source most likely is a transient neutron star low-mass X-ray binary located at several kpc. If true, it would be a good candidate to search for coherent millisecond pulsations when it enters a new accretion outburst.

RESUMEN

XMMSL1 J171900.4-353217 es una binaria de rayos-X transitoria poco luminosa descubierta en marzo de 2010 durante una erupción. Presentamos 7 observaciones obtenidas entre mayo y octubre de 2010 con el Telescopio de Rayos-X (XRT) a bordo del Observatorio Neil Gehrels Swift. Mediante el ajuste de los espectros del XRT con un modelo de ley de potencias absorbido, obtenemos un índice fotónico de Γ=1.8–2.7 y una densidad de la columna de hidrógeno de $N_{\rm H}$=(4.6–7.9)$\times 10^{22}$cm^{-2}. La luminosidad, en el intervalo $0.5 - 10$ keV, fluctuó irregularmente, con picos de $L_{\rm X} \approx 10^{35} - 10^{36}\,{\rm erg\,s^{-1}}$ para una distancia de $4 - 12\,{\rm kpc}$. Basándonos en la evolución del índice fotónico con la luminosidad, proponemos que la fuente es probablemente una binaria de rayos-X poco masiva con una estrella de neutrones situada a varios kpc. De ser cierto, esta fuente sería una buena candidata para buscar pulsaciones coherentes de milisegundos cuando entre de nuevo en erupción.

Key Words: binaries: general — ISM: abundances — stars: individual: XMMSL1 J171900.4–353217 — stars: neutron — X-rays: binaries

1. INTRODUCTION

X-ray binaries are binary systems in which a compact object, either a black hole (BH) or a neutron star (NS), accretes matter from a companion star. When the companion is a low-mass star ($M \lesssim 1{\rm M}_\odot$), the system is known as a low-mass X-ray binary (LMXB). Many LMXBs are transient: they become bright only during outbursts of active accretion, but are more often found in a dim quiescent state.

In quiescence, LMXBs have a low X-ray luminosity of $L_{\rm X} \lesssim^{33}$ erg s^{-1} (e.g., Wijnands et al. 2017). The maximum luminosity that is reached in outburst can vary a lot from source to source, and even from outburst to outburst for a single object. While many LMXBs are bright, with 2–10 keV peak luminosities of $L_{\rm X} \simeq 10^{37} - 10^{39}$ erg s^{-1}, some also exhibit 'mini outbursts' that reach much lower peak luminosities of $L_{\rm X} \simeq 10^{34} - 10^{36}$ erg s^{-1} (e.g., Degenaar

[1]Astronomy and Space Science Department, Faculty of Science, King Abdulaziz University, Kingdom of Saudi Arabia.
[2]Department of Physics, Faculty of Natural and computational Sciences, Debre Tabor University, Ethiopia.
[3]Anton Pannekoek Institute for Astronomy, University of Amsterdam, The Netherlands.
[4]Instituto de Astrofísica de Canarias, Spain.
[5]Departamento de Astrofísica, Universidad de La Laguna, Tenerife, Spain.

& Wijnands 2009; Wijnands & Degenaar 2013; Coti Zelati et al. 2014; Zhang et al. 2019). These are often shorter than regular bright outbursts, although there are also LMXBs that accrete at such a low-luminosity level for extended periods of time (Šimon 2004; Degenaar et al. 2014; Allen et al. 2015; Parikh et al. 2018).

Interestingly, a growing number of systems has been discovered that exhibit maximum outburst luminosities of $L_{\rm X} \simeq 10^{34} - 10^{36}$ erg s^{-1} and seemingly never exhibit brighter outbursts (Sakano et al. 2005; Muno et al. 2005b; Degenaar & Wijnands 2009; Bozzo et al. 2015; Bahramian et al. 2021). These LMXBs belong to the class of very faint X-ray transients (VFXTs; Wijnands et al. 2006). Many of these VFXTs are found near the Galactic center, but this is very likely a selection bias since this region has been regularly surveyed by many X-ray missions. Hence, the brief and dim outbursts of VFXTs are more easily discovered than in other regions of our Galaxy (e.g., Muno et al. 2005b; Sakano et al. 2005; Wijnands et al. 2006; Degenaar et al. 2015).

VFXTs could be intrinsically brighter sources located at large distances (tens of kpc) within the Milky Way, but estimates from thermonuclear bursts could place them nearer[6]. In addition, while inclination effects could possibly make these systems appear fainter than they intrinsically are (e.g., Muno et al. 2005a), this can likely only account for a small fraction of the VFXTs (see King & Wijnands 2006). Many VFXTs are thus expected to be intrinsically faint, i.e. they accrete at low rates. This makes them interesting for a number of scientific reasons. For instance, they probe a little explored mass-accretion regime, hence are valuable for studying accretion physics (e.g., Armas Padilla et al. 2013a; Weng & Zhang 2015; Degenaar et al. 2017). In addition, VFXTs are interesting for testing and improving binary evolution models (e.g. King & Wijnands 2006; Degenaar & Wijnands 2010; Maccarone et al. 2015), and for increasing our understanding of nuclear burning on the surface of accreting NS (e.g., Peng et al. 2007; Degenaar et al. 2010a).

Despite the fact that the number of VFXTs has now grown to a few tens of systems (e.g., Bahramian & Degenaar 2023) and detailed studies of several systems have been performed over the past decade, still much remains to be learned about this source class. For instance, there is no clear picture yet about the distribution of system properties such as the nature of the compact accretor, the type of companion star, and the size of the orbit. Determining whether an LMXB harbors a NS or a BH requires direct measurements of the physical properties of the compact object, such as its mass, or to detect the presence of a solid surface (e.g., through X-ray pulsations or thermonuclear bursts). However, such measurements are often challenging for VFXTs due to their faintness (e.g., making pulsation searches challenging; van den Eijnden et al. 2018) and low accretion rates (e.g., rendering thermonuclear bursts rare; Degenaar et al. 2011).

For some VFXTs, indirect approaches using the ratio between the X-ray and radio or optical/infrared luminosity have been employed to assess the nature of the compact accretor (e.g., Armas Padilla et al. 2011a; Paizis et al. 2011). However, their short outbursts often make it difficult to identify a counterpart for VFXTs at other wavelengths (e.g., Shaw et al. 2020). Furthermore, due to their low accretion rates, not many VXFTs have been detected in the radio band (van den Eijnden et al. 2021) and for finding optical/infrared counterparts additional complications arise from their biased locations in the direction of the Galactic center (i.e., high extinction and crowding; e.g., Bandyopadhyay et al. 2005). Fortunately, an indication of the nature of the accretor can also be obtained by studying the X-ray spectral evolution of VFXTs (Armas Padilla et al. 2011a; Beri et al. 2019; Stoop et al. 2021).

The X-ray properties of LMXBs harboring a NS can be very similar to those containing a BH. However, when comparing their X-ray spectra at low luminosities of $L_{\rm X} \simeq 10^{34} - 10^{36}$ erg s^{-1}, it turns out that confirmed or candidate BH systems have significantly harder spectra than confirmed NSs. In addition, the BH spectra show a strong softening when the X-ray lumninosity evolves below $\simeq 10^{34}$ erg s^{-1}, while NSs start to show clear softening already at higher X-ray luminosities of $L_{\rm X} \simeq 10^{36}$ erg s^{-1} (e.g., Wijnands et al. 2015; Parikh et al. 2017).

Over the last few years, detailed studies have been performed for a growing number of VFXTs and the general conclusion is that due to low statistics on their X-ray spectra, such systems can be satisfactorily described with a simple power-law model, with a soft (black body) component only being distinguishable when high quality (i.e. many counts) data are

[6]Thermonuclear burst, or type-I bursts, are brief (seconds to hours) flashes of X-ray emission caused by unstable nuclear burning of gas accreted onto a neutron star. These explosions are thought to reach the Eddington limit and can therefore be employed to derive a distance to the bursting LMXB (e.g., Kuulkers et al. 2003). They are exhibited by many VFXTs, which place them at distances of only several kpc and they must thus have low intrinsic luminosities (e.g., Cornelisse et al. 2002; Lutovinov et al. 2005; Degenaar et al. 2010a; Bozzo et al. 2015; Keek et al. 2017)

TABLE 1

LOG OF *SWIFT*/XRT OBSERVATIONS

Obs	Observation ID	Date and start time (UT)	Exposure time (ks)	Net count rate (ct s^{-1})
1	00031719001	2010 May 11 16:56	2.0	0.4
2	00031719002	2010 May 31 12:23	1.0	0.1
3	00031719003	2010 June 14 11:44	1.2	0.2
4	00031719004	2010 June 29 06:42	1.7	0.7
5	00031719005	2010 July 13 09:29	1.0	<0.008
6	00031719006	2010 August 20 13:00	2.5	0.3
7	00031719007	2010 October 15 02:10	1.3	<0.002

available (e.g., Armas Padilla et al. 2011a). However, irrespective of what model is fitted to the spectra, VFXTs also become softer with decreasing X-ray luminosity. Their X-ray spectral evolution during an outburst can thus be used as a diagnostic for the nature of the compact accretor.

1.1. *Discovery of XMMSL1 J171900.4–353217*

XMMSL1 J171900.4–353217 was discovered as an X-ray transient in *XMM-Newton* slew data obtained on 2010 March 10 (Read et al. 2010a). The source location was in FOV of *INTEGRAL* observations performed around the same time, but it was not detected (20–40 keV; Bozzo et al. 2010). Markwardt et al. (2010) pointed out that XMMSL1 J171900.4–353217 was likely associated to a faint transient source, XTE J1719–356, detected in *RXTE*/PCA scans of the Galactic bulge since 2010 March.

Observations performed with the X-Ray Telescope (XRT; Burrows et al. 2005) onboard the *Neil Gehrels Swift Observatory* (*Swift*; Gehrels et al. 2004) in 2010 May, showed that the source was still active, i.e. two months after the initial discovery (Read et al. 2010b). Armas Padilla et al. (2010b,a) reported on further *Swift*/XRT observations, performed in 2010 May and June, which showed that the source remained active in soft X-rays, albeit with varying flux. While *Swift*/XRT did no longer detect the source in 2010 July, suggesting it had returned to quiescence (Armas Padilla et al. 2010c), *INTEGRAL* serendipitously detected the source in hard X-rays in August 2010 (20–40 keV; Ishibashi et al. 2010). It was also detected again in soft X-rays with *Swift*/XRT around that time (Pavan et al. 2010). Nothing more was reported on the source after this.

In this work we investigate the nature of the compact accretor in the VFXT XMMSL1 J171900.4–353217 by studying its X-ray spectral evolution as seen with *Swift*/XRT.

2. OBSERVATIONS AND DATA ANALYSIS

XMMSL1 J171900.4–353217 was observed over a 157 days time-span with *Swift*, between 2010 May 11 and October 15 (see Table 1). Seven pointed observations were carried out during this time and we investigate the data collected using the XRT.

2.1. *Description of the Data Reduction*

All XRT data were collected in photon counting (PC) mode. We reduced the data and obtained science products using the HEASOFT software package (v. 6.26). We cleaned the data by running the XRTPIPELINE task in which standard event grades of 0–12 were selected. For every observation, images, count rates and spectra were obtained with the XSELECT (v.2.4) package. We extracted the source events using a circular region with a radius of 52 arcseconds. The background emission was averaged over three circular regions of similar size that were placed on nearby, source-free parts of the image.

The source was detected in 5 of the 7 observations (see Table 1) and for these we extracted spectra. Using GRPPHA, three spectra were grouped to have 10 counts per energy bin, one was grouped to 20 counts per bin (observation ID 00031719004, when the source was brightest), and one to 5 counts per bin (observation ID 00031719002 when the source was faintest).

The spectra were corrected for the fractional exposure loss due to bad columns on the CCD. For this, we created exposure maps with the XRTEXPOMAP task, which were then used as an input to generate the ancillary response files (arf) with the XRTMKARF task. We acquired the response matrix file (rmf) from the HEASARC calibration database (v.12).

2.2. *Pile-Up*

Observation 00031719004 has the highest count rate (0.7 ct s^{-1}) and is affected by pile-up. We tested

this following the steps outlined in the dedicated XRT analysis thread[7]. Following these guidelines, we found that five pixels had to be excluded in the bright core to mitigate the effect of pile-up. The remaining six observations have < 0.5 ct s^{-1} and are not affected by pile-up (see Table 1).

3. RESULTS

3.1. *X-ray Spectral Fitting*

To fit the X-ray spectra, we used XSPEC[8] (v.12.10.1; Arnaud 1996). Given the low count rates (Table 1), we used simple power law (PEGPWRLW) and black body (BBODYRAD) models to describe the data. For both models, we took into account interstellar extinction by including the TBABS model, and used C-statistics due to low data counts. For this absorption model we used abundances set to those of Wilms et al. (2000) and the cross-sections from Verner et al. (1996). Both models yielded the same quality of fit, so that we cannot statistically prefer one model over the other. However, in order to use the Wijnands et al. (2015) method to probe the nature of the compact accretor, we need to use the power-law model. Therefore, we here report on the results from fitting the absorbed power-law model, but we include the results for the absorbed blackbody fits in the Appendix, for completeness.

We also briefly explored whether the spectrum could be composed of two emission components, such as has been seen for VFXTs that have high-quality data available (e.g., Armas Padilla et al. 2011a, 2013a; Degenaar et al. 2017). For this we used the observation with the highest flux (observation ID 00031719004). We first fitted this to an absorbed power law, then added a black body component and re-fitted. This resulted in similar fit parameters as for the single absorbed power-law model. The two-component model adequately fits the spectra by eye, but the extra thermal component is not statistically required (F-test probability > 0.99). It is likely that the low number of counts in the spectrum does not allow us to detect a second component, even if it is present. We therefore did not test this for the other observations, since these have even lower count rates. We conclude that a single-component model can adequately fit the *Swift* spectra.

Using the convolution model CFLUX within XSPEC, and setting the energy range to 0.5 to 10 keV, we determined both the absorbed ($F_{\rm X,abs}$) and unabsorbed fluxes ($F_{\rm X,unabs}$). The results are listed in Table 2. In Figure 1 we show the light curve

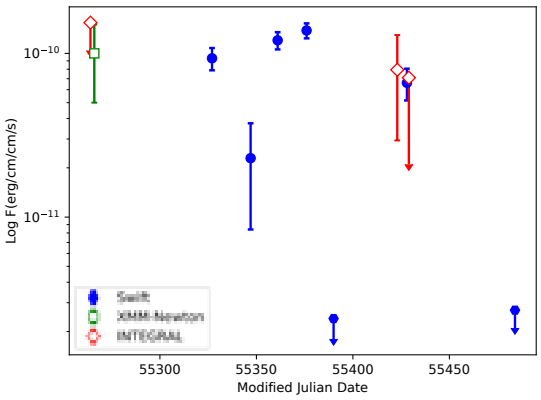

Fig. 1. Evolution of 0.5 – 10 keV unabsorbed flux of XMMSL1 J171900.4–353217, inferred from our spectral analysis of the *Swift*/XRT data (blue filled circles). To show the full outburst, we include points reported in the literature from *INTEGRAL* (red open diamonds) and *XMM-Newton* (green open square), which were converted to 0.5–10 keV for this purpose (see § 3.3 and Table 3). The color figure can be viewed online.

constructed from the unabsorbed fluxes. From the seven XRT observations, the highest unabsorbed flux we measure is $F_{\rm X,unabs} = 13.8 \times 10^{-11}$ erg cm^{-2} s^{-1} in observation 00031719004 (see Figure 1 and Table 2). In Figure 2 we show the *Swift*/XRT spectrum of this observation.

3.2. *Flux Upper Limits for XRT Non-Detections*

In observations 00031719005 and 00031719007 the source was not detected with the XRT. For these observations, we determined the net counts detected at the source position with XSELECT (using similar source and background extraction regions as for the other observations; see § 2.1). For observation 00031719005 (1 ks) we detect 4 counts at the source position and 1 count averaged over the background regions. For observation 00031719007 (1.3 ks), we measure 6 counts for the source and none for the background. Accounting for small number statistics using the tables of Gehrels (1986), we determine a 95% upper limit on the detected net source counts of 7.75 and 11.84 for observations 00031719005 and 00031719007, respectively. Dividing by the exposure times then gives 95% confidence count rate upper limits of $< 7.9 \times 10^{-3}$ ct s^{-1} (00031719005) and $< 9.1 \times 10^{-3}$ ct s^{-1} (00031719007).

To estimate flux upper limits for the non-detections, we used WEBPIMMS[9] to convert the count

[7] https://www.swift.ac.uk/analysis/xrt/pileup.php.
[8] https://heasarc.gsfc.nasa.gov/xanadu/xspec/.
[9] https://heasarc.gsfc.nasa.gov/cgi-bin/Tools/w3pimms/w3pimms.pl.

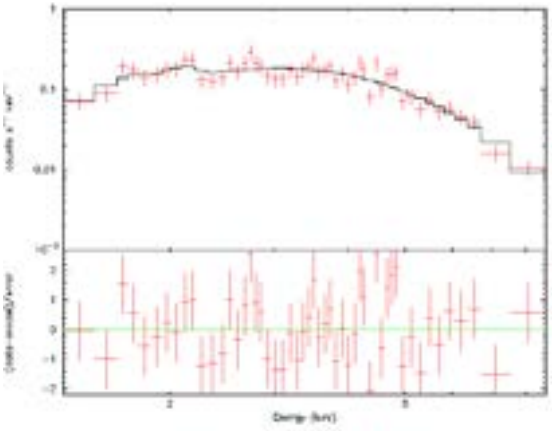

Fig. 2. An X-ray spectrum of XMMSL1 J171900.4–353217 detected with *Swift*/XRT. Upper panel: shows the brightest observation, 00031719004, fitted with an absorbed power law model. Bottom panel: shows the corresponding fit residuals in units of σ. The color figure can be viewed online.

rate upper limits, assuming an absorbed power-law model with a photon index of $\Gamma = 2.49$ and a hydrogen column density of $N_{\rm H} = 5.81 \times 10^{22}$ cm^{-2}. We choose those values because these are the ones we obtained for the observation with the lowest flux (observation 00031719002).

3.3. *X-ray Spectral Evolution*

The distance to XMMSL1 J171900.4–353217 is unknown. We therefore took three different values of 4, 8 and 12 kpc, to calculate the 0.5–10 keV luminosity from the unabsorbed flux. These results are included in Table 2. In Figure 3 we plot the evolution of the power-law index versus luminosity of XMMSL1 J171900.4–353217 along with the sample of NS (red filled circles) and BH (black crosses) LMXBs of Wijnands et al. (2015). We then overplot XMMSL1 J171900.4–353217 as blue open diamonds for different distances of 4, 8, and 12 kpc in subpanels a, b, and c, respectively.

We find that for all distances, our data points fall among the NS sample, but above the BH track. This would suggest that the source is either a proximate ($\lesssim$ 4 kpc) BH, or a NS located around or beyond 4 kpc. Considering the high $N_{\rm H}$ towards the source, both as inferred from our X-ray spectral fitting ($N_{\rm H} \simeq 5 \times 10^{22}$ cm^{-2}) and from Galactic extinction maps ($N_{\rm H} \simeq 1 \times 10^{22}$ cm^{-2}; Bekhti et al. (2016)), we consider a larger distance more likely, and hence tentatively favor a NS nature. However,

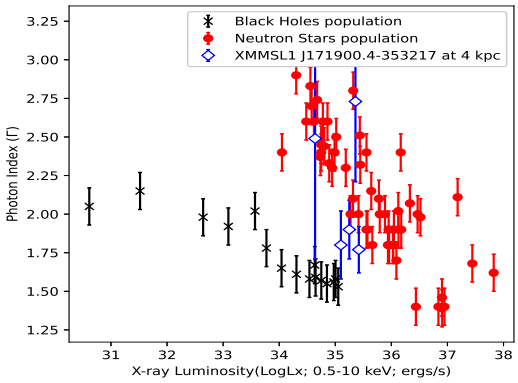

(a)

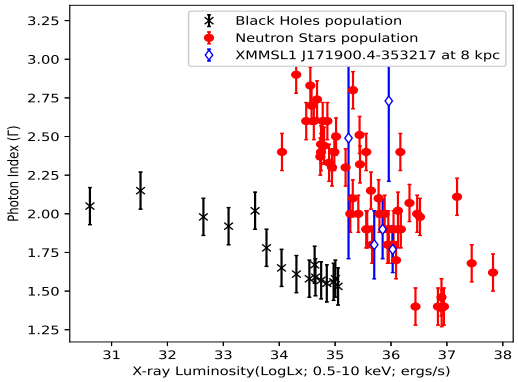

(b)

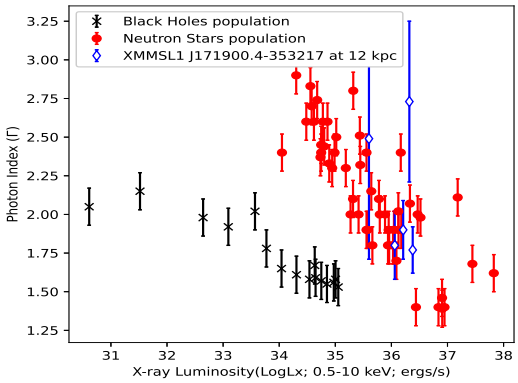

(c)

Fig. 3. Power law index versus X-ray luminosity in the 0.5–10 keV range for XMMSL1 J171900.4–353217 as well as a sample of NS (red circles) and BH (grey crosses) LMXBs (from Wijnands et al. 2015). For XMMSL1 J171900.4–353217 we used three different distances of 4 kpc (panel a), 8 kpc (panel b) and 12 kpc (panel c). The color figure can be viewed online.

TABLE 2

RESULTS FROM ANALYSING THE *SWIFT*/XRT SPECTRA

Obs	$N_{\rm H}$ (10^{22}cm^{-2})	Γ	$F_{\rm X,abs}$ (10^{-11} erg cm^{-2}s^{-1})	$F_{\rm X,unabs}$	$L_{\rm X}$ 4 kpc	$L_{\rm X}$ 8 kpc (10^{35} erg s^{-1})	$L_{\rm X}$ 12 kpc
1	$5.45^{+0.64}_{-0.61}$	1.90 ± 0.19	4.17 ± 0.19	$9.33^{+1.63}_{-1.20}$	$1.78^{+0.32}_{-0.23}$	$7.14^{+1.25}_{-0.92}$	$16.07^{+2.81}_{-5.07}$
2	$5.81^{+2.35}_{-1.98}$	$2.49^{+0.78}_{-0.70}$	$0.57^{+0.12}_{-0.09}$	$2.29^{+4.02}_{-1.03}$	$0.44^{+0.76}_{-0.20}$	$1.73^{+3.08}_{-0.79}$	$3.94^{+6.93}_{-1.77}$
3	$7.85^{+1.87}_{-1.77}$	2.73 ± 0.52	$2.04^{+0.25}_{-0.22}$	$12.02^{+13.09}_{-5.26}$	$2.30^{+2.50}_{-1.01}$	$9.20^{+10.02}_{-4.02}$	$20.7^{+22.55}_{-9.06}$
4	$4.60^{+0.47}_{-0.45}$	1.77 ± 0.15	$7.01^{+0.40}_{-0.25}$	$13.80^{+1.69}_{-1.21}$	$2.64^{+0.32}_{-0.23}$	$10.75^{+1.29}_{-0.93}$	$23.77^{+2.91}_{-2.09}$
5	5.81 fix	2.49 fix	< 0.06	< 0.24	< 0.05	< 0.19	< 0.42
6	$6.67^{+0.89}_{-0.86}$	1.80 ± 0.22	2.95 ± 0.20	$6.61^{+1.33}_{-0.86}$	$1.26^{+0.26}_{-0.16}$	$5.06^{+1.02}_{-0.66}$	$11.38^{+2.29}_{-1.48}$
7	5.81 fix	2.49 fix	< 0.07	< 0.27	< 0.06	< 0.21	< 0.47

TABLE 3

OTHER REPORTED X-RAY FLUX MEASUREMENTS

Observatory (detector)	Date	Reported Brightness (various formats)	$F_{\rm X,abs}$[a]	$F_{\rm X,unabs}$[a]	Reference[b]
			(10^{-11} erg cm^{-2}s^{-1})		
XMM-Newton (PN)	2010 March 10	4.5 c s^{-1} (0.2–10 keV)	4.5	10.2	1
INTEGRAL (IBIS)	2010 March 09	<6 mCrab (20–40 keV)	< 6.82	< 15.40	2
INTEGRAL (IBIS)	2010 August 14	3.0×10^{-11} erg cm^{-2} s^{-1} (20–40 keV)	3.55	7.94	3
INTEGRAL (IBIS)	2010 August 20	$<2.7\times10^{-11}$ erg cm^{-2} s^{-1}(20−40 keV)	<3.2	<7.1	4

[a]The quoted count rates were converted to 0.5–10 keV fluxes using WEBPIMMS and assuming a power-law spectral model. For the first two table entries we used $N_{\rm H} = 5.45 \times 10^{22}$ cm^{-2} and $\Gamma = 1.90$, for the last two $N_{\rm H} = 6.67 \times 10^{22}$ cm^{-2} and $\Gamma = 1.80$. These parameter values match those found from our spectral fitting of *Swift*/XRT data obtained around that time (see Table 2).

[b]References: 1=Read et al. (2010a), 2=Bozzo et al. (2010), 3=Ishibashi et al. (2010), 4=Pavan et al. (2010).

the reader should bear in mind that a BH nature cannot be excluded.

3.4. *Time-Averaged Accretion Rate*

We continue to calculate the time-averaged accretion rate for XMMSL1 J171900.4–353217, since this is an interesting parameter to understand the possible evolution paths of VFXTs (King & Wijnands 2006). We initially assume that the source contains a NS primary and then calculate the mean outburst accretion rate, $\langle \dot{M}_{\rm ob} \rangle$, from the mean unabsorbed flux measured during the outburst. For this purpose, we add the *INTEGRAL* and *XMM-Newton* fluxes reported in the literature to our results obtained with *Swift*.

We used WEBPIMMS to convert reported instrument count rates or 20–40 keV fluxes to unabsorbed 0.5–10 keV fluxes. All information used for these conversions is listed in Table 3. We assumed an absorbed power-law spectral shape. For the *XMM-Newton* and first *INTEGRAL* observations, both performed in March 2010, we used $N_{\rm H} = 5.45 \times 10^{22}$ cm^{-2} and $\Gamma = 1.90$, which are the values we obtained from spectral fitting for the *Swift*/XRT observations performed closest in time (observation 00000031719001; see Tables 1–3). For the other two *INTEGRAL* observations, both performed in 2010 August, we assumed $N_{\rm H} = 6.67 \times 10^{22}$ cm^{-2} and $\Gamma = 1.80$ as found from fitting the *Swift*/XRT spectrum obtained closest in time (observation 00000031719006).

The resulting 0.5–10 keV flux light curve is shown in Figure 1. From all these data points we determine a mean 0.5–10 keV outburst flux of 8.9×10^{-11} erg cm^{-2} s^{-1}. Based on this, we estimate the 0.1–100 keV accretion luminosity by assuming a bolometric correction factor of 3 (following in't Zand et al. 2007). The mass transfer rate of the outburst was then computed using the equation $\langle \dot{M}_{\rm ob} \rangle = R_{\rm Ns} L_{\rm acc} / {\rm G} M_{\rm Ns}$, where ${\rm G} = 6.67 \times 10^{-8}$ cm^{3}g^{-1}s^{-2} is the gravitational constant. Assuming $R_{\rm Ns} = 1.1 \times 10^6$ cm = 11 km and $M_{\rm Ns} = 1.5$ M$_\odot$, the outburst mass accretion rate we obtain is $\langle \dot{M}_{\rm ob} \rangle \simeq 1.7 \times 10^{-10}$ M$_\odot$ yr^{-1}.

We can next estimate the mean long-term averaged accretion rate using $\langle \dot{M}_{\rm long} \rangle = \langle \dot{M}_{\rm ob} \rangle \times t_{\rm ob}/t_{\rm rec}$, where $t_{\rm ob}$ is the outburst duration, $t_{\rm rec}$ is the system's recurrence time, and the ratio of the two represents its duty cycle. Neither the onset nor the fad-

ing of the outburst into quiescence have been observed for XMMSL1 J171900.4–353217, so the total outburst duration is unconstrained.[10] If we assume that the source was continuously active (i.e., only occasionally dropping to non-detectable flux levels) between its first and last detection on 2010 March 9 and 2010 August 20, the minimum outburst duration is 164 days. Since this was the first and only outburst ever observed for the source, its recurrence time is also unconstrained. For the present purpose we assume a duty cycle of 1–10% based on long-term X-ray monitoring of VFXTs in the Galactic center (Degenaar & Wijnands 2009, 2010). This would imply an outburst recurrence time of 4.5–45 yr for XMMSL1 J171900.4–353217, and yields a mean long-term accretion rate of $\langle \dot{M}_{\rm long} \rangle \simeq 0.17 - 1.7 \times 10^{-11}$ M$_\odot$ yr^{-1}.

We note that if the source harbors a black hole accretor, the above estimates for the (long-term) mass accretion rate would be a factor $\simeq 10$ lower due to the mass difference between neutron stars and black holes.

4. DISCUSSION

We report on the properties of the discovery outburst of the X-ray transient XMMSL1 J171900.4–353217, which lasted more than 164 days in 2010. We studied the X-ray spectral evolution of the source using the Swift/XRT data and used the method of Wijnands et al. (2015) to investigate the nature of the accreting object. Based on the evolution of its power-law index with 0.5–10 keV luminosity, we conclude that XMMSL1 J171900.4–353217 is most likely a NS LMXB located at several kpc.

Adding to our *Swift*/XRT results flux measurements reported in the literature (from *XMM-Newton* and *INTEGRAL* observations), we constructed the light curve of the 2010 outburst (see Figure 1). Over the 5.5 months that the source was observed to be active, the maximum 0.5–10 keV unabsorbed flux detected with *Swift*/XRT was $F_{\rm X,unabs}^{\rm peak} = 13.8 \times 10^{-11}$ erg cm^{-2} s^{-1}. For a distance of 8 kpc, this peak flux translates into a luminosity of $L_{\rm X}^{\rm peak} \simeq 1.1 \times 10^{36}$ erg s^{-1}. This classifies XMMSL1 J171900.4–353217 as a VFXT.[11]

We furthermore estimated a mean unabsorbed flux along the observations of $F_{\rm X}^{\rm avg} \simeq 8.9 \times 10^{-11}$ erg cm^{-2} s^{-1}. For a distance of 8 kpc, this translates into a luminosity of $L_{\rm X}^{\rm avg} \simeq 6.8 \times 10^{35}$ erg s^{-1}. We used this information to estimate the average accretion rate along the outburst as $< \dot{M}_{\rm ob} > \simeq 1.7 \times 10^{-10}$ M$_\odot$ yr^{-1}. If the source has a duty cycle of 1–10%, which is not uncommon for LMXBs and VFXTs (Degenaar & Wijnands 2010), we can then estimate a long-term average accretion rate of $< \dot{M}_{\rm long} > \simeq 0.17 - 1.7 \times 10^{-11}$ M$_\odot$ yr^{-1}. This is in the same range as inferred for the VFXTs in the Galactic Center (Degenaar & Wijnands 2009, 2010). Very low long-term average accretion rates can only be explained if these systems have hydrogen poor companions or are born with low companion masses (King & Wijnands 2006). However, the current (faint) accretion activity may not necessarily be representative for the long-term behavior of these systems (Wijnands et al. 2013).

In the past years, several NS LMXBs with similarly low outburst luminosities (hence accretion rates) as XMMSL1 J171900.4–353217 were uncovered to harbor accreting millisecond X-ray pulsars (AMXPs). Examples are IGR J17062–6143 (Strohmayer & Keek 2017), IGR J17591–2342 (Sanna et al. 2018b), IGR J17379–3747 (Sanna et al. 2018a) and IGR J17494–3030 (Ng et al. 2020). All were previously known VXFTs that were observed during (new) outbursts with *NICER*, which detected the X-ray pulsations. Given the similar X-ray spectral properties of XMMSL1 J171900.4–353217 with those sources, we hypothesize that it may also harbor a millisecond X-ray pulsar. Indeed, one of the sources mentioned above was proposed to be a NS based on the same method as we employ here (Armas Padilla et al. 2013b) and later found to be an AMXP (Ng et al. 2020). Therefore, should XMMSL1 J171900.4–353217 enter a new accretion outburst in the future, we encourage X-ray observations (in particular with *NICER*) to search for pulsations that would confirm the NS nature of this source, and allow for a measurement of its orbital period. In case a new outburst occurs, we also encourage dense monitoring of the outburst decay (in particular with *Swift*), since this can also provide an indication of the orbital period and nature of the compact accretor (e.g., Armas Padilla et al. 2011a; Heinke et al. 2015; Stoop et al. 2021).

[10] We note that in the *RXTE*/PCA bulge scans the possibly associated transient XTE J1719–356 seems to be detected on and off between 2010 March and September, but not thereafter. The *RXTE* data therefore does not provide additional constraints on the outburst duration. See `https://asd.gsfc.nasa.gov/Craig.Markwardt/galscan/html/XTE_J1719-356.html`.

[11] We note that Wijnands et al. (2006) uses the 2–10 keV band to define luminosity classes whereas we here use 0.5–10 keV. However, since the 0.5–10 keV luminosity is higher than the 2–10 keV luminosity, our conclusion that XMMSL1 J171900.4–353217 falls in the regime of VFXTs still holds.

TABLE 4

RESULTS FROM XRT SPECTRAL ANALYSIS USING A BLACK-BODY MODEL. X-RAY FLUXES AND LUMINOSITIES ARE GIVEN IN THE 0.5–10 KEV ENERGY BAND

Obs	$N_{\rm H}$ (10^{22} cm^{-2})	kT (keV)	$F_{\rm X_{abs}}$ (10^{-11} erg cm^{-2}s^{-1})	$F_{\rm X_{unabs}}$	$L_{\rm X}$ 4 kpc	$L_{\rm X}$ 8 kpc (10^{35} erg s^{-1})	$L_{\rm X}$ 12 kpc
1	2.23 ± 0.40	$1.32^{+0.08}_{-0.07}$	$3.71^{+0.18}_{-0.16}$	4.47 ± 0.20	$0.85^{+0.04}_{-0.03}$	$3.42^{+0.16}_{-0.18}$	$7.70^{+0.36}_{-0.35}$
2	$2.29^{+1.56}_{-1.29}$	$1.06^{+0.24}_{-0.19}$	$0.50^{+0.10}_{-0.08}$	$0.65^{+0.12}_{-0.11}$	$0.12^{+0.03}_{-0.02}$	0.51 ± 0.09	$1.12^{+0.21}_{-0.19}$
3	$3.38^{+1.26}_{-1.19}$	$1.01^{+0.13}_{-0.11}$	$1.74^{+0.21}_{-0.16}$	$2.51^{+6.61}_{-1.72}$	$0.48^{+1.26}_{-0.33}$	$1.92^{+5.06}_{-1.32}$	$4.32^{+11.39}_{-2.96}$
4	$1.69^{+0.31}_{-0.30}$	$1.34^{+0.07}_{-0.06}$	$6.17^{+0.29}_{-0.28}$	$7.24^{+0.35}_{-0.32}$	$1.38^{+0.07}_{-0.06}$	$5.54^{+0.27}_{-0.24}$	$12.47^{+0.6}_{-0.55}$
5	2.29 fix	1.06 fix	< 0.05	< 0.07	< 0.02	< 0.06	< 0.13
6	$2.96^{+0.60}_{-0.57}$	$1.41^{+0.10}_{-0.09}$	2.63 ± 0.18	3.24 ± 0.15	0.62 ± 0.03	$2.48^{+0.12}_{-0.11}$	5.58 ± 0.26
7	2.29 fix	1.06 fix	< 0.06	< 0.08	< 0.02	< 0.07	< 0.15

Quoted errors reflect 1-σ confidence intervals.

OA is grateful to Sera Markoff and the Anton Pannekoek Institute for organizing and hosting the Advanced Theoretical Astrophysics summer school in 2019, which fostered the collaboration that led to this work. ND was partly supported by a Vidi grant awarded by the Netherlands organization for scientific research (NWO). This work made use of data supplied by the UK *Swift* Science Data Centre at the University of Leicester. M. A. P. acknowledges support from the Spanish ministry of science under Grant PID2020–120323GB-I00. M. A. P. acknowledges support from the Consejeria de Economia, Conocimiento y Empleo del Gobierno de Canarias and the European Regional Development Fund under grant ProID2021010132.

APPENDIX

A1. BLACK-BODY SPECTRAL FITTING RESULTS

For completeness we here report on the results of fitting the *Swift*/XRT spectra of XMMSL1 J171900.4–353217 with an absorbed black body model. For the upper limit calculation of the two XRT non-detections, we now used kT = 1.06 keV and $N_H = 2.29 \times 10^{22}$ cm^{-2}. These are the values we obtained for the observation with the lowest flux (observation ID 00031719002). All results are listed in Table 4.

REFERENCES

Allen, J. L., Linares, M., Homan, J., & Chakrabarty, D. 2015, ApJ, 801, 10, https://doi.org/10.1088/0004-637X/801/1/10

Armas Padilla, M., Degenaar, N., Kaur, R., Wijnands, R., & Yang, Y. 2010a, Atel, 2738, 1

Armas Padilla, M., Degenaar, N., Patruno, A., et al. 2011a, MNRAS, 417, 659, https://doi.org/10.1111/j.1365-2966.2011.19308.x

Armas Padilla, M., Degenaar, N., & Wijnands, R. 2013a, MNRAS, 434, 1586, https://doi.org/10.1093/mnras/stt1114

Armas Padilla, M., Degenaar, N., Yang, Y., Patruno, A., & Wijnands, R. 2010b, Atel, 2656, 1

Armas Padilla, M., Kaur, R., Degenaar, N., et al. 2010c, Atel, 2722, 1

Armas Padilla, M., Wijnands, R., & Degenaar, N. 2013b, MNRAS, 436, 89, https://doi.org/10.1093/mnrasl/slt119

Arnaud, K. A. 1996, ASPC 101, XSPEC: The First Ten Years, Astronomical Data Analysis Software and Systems, 17, 1

Bahramian, A. & Degenaar, N. 2023, in Handbook of X-ray and Gamma-ray Astrophysics, ed. C. Bambi and A. Santangelo, (Singapore:Springer), 120, https://doi.org/10.1007/978-981-19-6960-7

Bahramian, A., Heinke, C. O., Kennea, J. A., et al. 2021, MNRAS, 501, 2790, https://doi.org/10.1093/mnras/staa3868

Bandyopadhyay, R. M., Miller-Jones, J. C. A., Blundell, K. M., et al. 2005, MNRAS, 364, 1195, https://doi.org/10.1111/j.1365-2966.2005.09607.x

Bekhti, N. B., Flöer, L., Keller, R., et al. 2016, A&A, 594, 116, https://doi.org/10.1052/0004-6361/201629178

Beri, A., Altamirano, D., Wijnands, R., Degenaar, N., Parikh, A. S., & Yamaoka, K. 2019, MNRAS, 486, 1620, https://doi.org/10.1093,mnras/stz938

Bozzo, E., Romano, P., Falanga, M., Ferrigno, C., Papitto, A., & Krimm, H. A. 2015, A&A, 579, 56, https://doi.org/10.1051/0004-6361/201526150

Bozzo, E., Weidenspointner, G., Kuulkers, E., Terrier, R., & Carmona, P. K. A. 2010, Atel, 2616, 1

Burrows, D. N., Hill, J. E., Nousek, J. A., et al. 2005, SSRv, 120, 165, https://doi.org/10.1007/s11214-005-5097-2

Cornelisse, R., Verbunt, F., in 't Zand, J., et al. 2002, A&A, 392, 885, https://doi.org/10.1051/0004-6361:20020707
Coti Zelati, F., Campana, S., D'Avanzo, P., & Melandri, A. 2014, MNRAS, 438, 2634, https://doi.org/10.1093/mnras/stt2384
Degenaar, N., Jonker, P., Torres, M., et al. 2010a, MNRAS, 404, 1591, https://doi.org/10.1111/j.1365-2966.2010.16388.x
Degenaar, N., Pinto, C., Miller, J. M., et al. 2017, MNRAS, 464, 398, https://doi.org/10.1093/mnras/stw2355
Degenaar, N. & Wijnands, R. 2009, A&A, 495, 547, https://doi.org/10.1051/0004-6361:200810654
_____. 2010, A&A, 524, 69, https://doi.org/10.1051/0004-6361/201015322
Degenaar, N., Wijnands, R., & Kaur, R. 2011, MNRAS, 414, 104, https://doi.org/10.1111/j.1745-3933.2011.01066.x
Degenaar, N., Wijnands, R., Miller, J. M., et al. 2015, JHEAp, 7, 137, https://doi.org/10.1016/j.jheap.2015.03.005
Degenaar, N., Wijnands, R., Reynolds, M. T., et al. 2014, ApJ, 792, 109, https://doi.org/10.1088/0004-637X/792/2/109
Gehrels, N. 1986, ApJ, 303, 336, https://doi.org/10.1086/164079
Gehrels, N., Chincarini, G., Giommi, P., et al. 2004, ApJ, 611, 1005, https://doi.org/10.1086/422091
Heinke, C. O., Bahramian, A., Degenaar, N., & Wijnands, R. 2015, MNRAS, 447, 3034, https://doi.org/10.1093/mnras/stu2652
in't Zand, J. J. M., Jonker, P. G., & Markwardt, C. B. 2007, A&A, 465, 953, https://doi.org/10.1051/0004-6361:20066678
Ishibashi, W., Bozzo, E., Terrier, R., et al. 2010, Atel, 2803, 1
Keek, L., Iwakiri, W., Serino, M., et al. 2017, ApJ, 836, 111, https://doi.org/10.3847/1538-4357/836/1/111
King, A. R. & Wijnands, R. 2006, MNRAS, 366, 31, https://doi.org/10.1111/j.1745-3933.2005.00126.x
Kuulkers, E., den Hartog, P. R., in't Zand, J. J. M., et al. 2003, A&A, 399, 663, https://doi.org/10.1051/0004-6361:20021781
Lutovinov, A., Revnivtsev, M., Molkov, S., & Sunyaev, R. 2005, A&A, 430, 997, https://doi.org/10.1051/0004-6361:20041677
Maccarone, T. J., Wijnands, R. A. M., Degenaar, N., et al. 2015, arXiv:1501.02769, https://doi.org/10.48550/arXiv.1501.02769
Markwardt, C. B., Strohmayer, T. E., & Swank, J. H. 2010, Atel, 2615, 1
Muno, M. P., Lu, J. R., Baganoff, F. K., et al. 2005a, ApJ, 633, 228, https://doi.org/10.1086/444586
Muno, M. P., Pfahl, E., Baganoff, F. K., et al. 2005b, ApJ, 622, 113, https://doi.org/10.1086/429721
Ng, M., Ray, P. S., Strohmayer, T. E., et al. 2020, Atel, 14124, 1
Paizis, A., Nowak, M. A., Wilms, J., et al. 2011, ApJ, 738, 183, https://doi.org/10.1088/0004-637X/738/2/183
Parikh, A. S., Wijnands, R., Degenaar, N., & Altamirano, D. 2018, Atel, 11869, 1
Parikh, A. S., Wijnands, R., Degenaar, N., et al. 2017, MNRAS, 468, 3979, https://doi.org/10.1093/mnras/stx747
Pavan, L., Terrier, R., Bozzo, E., et al. 2010, Atel, 2807, 1
Peng, F., Brown, E. F., & Truran, J. W. 2007, ApJ, 654, 1022, https://doi.org/10.1086/509628
Read, A. M., Saxton, R. D., & Esquej, P. 2010a, Atel, 2607, 1
Read, A. M., Saxton, R. D., Esquej, P., & Evans, P. A. 2010b, Atel, 2627, 1
Sakano, M., Warwick, R. S., Decourchelle, A., & Wang, Q. D. 2005, MNRAS, 357, 1211, https://doi.org/10.1111/j.1365-2966.2005.08717.x
Sanna, A., Bozzo, E., Papitto, A., et al. 2018a, A&A, 616, 17, https://doi.org/10.1051/0004-6361/201833205
Sanna, A., Ferrigno, C., Ray, P. S., et al. 2018b, A&A, 617, 8, https://doi.org/10.1051/0004-6361/201834160
Shaw, A. W., Heinke, C. O., Maccarone, T. J., et al. 2020, MNRAS, 492, 4344, https://doi.org/10.1093/mnras/staa105
Šimon, V. 2004, A&A, 418, 617, https://doi.org/10.1051&0004-6361:20040037
Stoop, M., van den Eijnden, J., Degenaar, N., et al. 2021, MNRAS, 507, 330, https://doi.org/10.1093/mnras/stab2127
Strohmayer, T. & Keek, L. 2017, ApJ, 836, 23 , https://doi.org/10.3847/2041-8213/aa5e51
van den Eijnden, J., Degenaar, N., Pinto, C., et al. 2018, MNRAS, 475, 2027, https://doi.org/10.1093/mnras/stx3224
van den Eijnden, J., Degenaar, N., Russell, T. D., et al. 2021, MNRAS, 507, 3899, https://doi.org/10.1093/mnras/stab1995
Verner, D. A., Ferland, G. J., Korista, K. T., & Yakovlev, D. G. 1996, ApJ, 465, 487, https://doi.org/10.1086/177435
Weng, S.-S. & Zhang, S.-N. 2015, MNRAS, 447, 486, https://doi.org/10.1093/mnras/stu2610
Wijnands, R. & Degenaar, N. 2013, MNRAS, 434, 1599, https://doi.org/10.1093/mnras/stt1119
Wijnands, R., Degenaar, N., Padilla, M. A., et al. 2015, MNRAS, 454, 1371, https://doi.org/10.1093/mnras/stv1974
Wijnands, R., Degenaar, N., & Page, D. 2013, MNRAS, 432, 2366, https://doi.org/10.1093/mnras/stt599
_____. 2017, JApA, 38, 49, https://doi.org/10.1007/s12036-017-0466-5

Wijnands, R., in't Zand, J. J. M., Rupen, M., et al. 2006, A&A, 449, 1117, https://doi.org/10.1051/0004-6361:20054129
Wilms, J., Allen, A., & McCray, R. 2000, ApJ, 542, 914, https://doi.org/10.1086/317016
Zhang, G. B., Bernardini, F., Russell, D. M., et al. 2019, ApJ, 876, 5, https://doi.org/10.3847/1538-4357/ab12dd

Osman Ahmed: Astronomy and Space Science Department, Faculty of Science, King Abdulaziz University, P.O. Box 80203, Jeddah 21589, Kingdom of Saudi Arabia.
Osman Ahmed: Department of Physics, Faculty of Natural and computational Sciences, Debre Tabor University, P.O. Box 272, South Gondar, Ethiopia.
Nathalie Degenaar and Rudy Wijnands: Anton Pannekoek Institute for Astronomy, University of Amsterdam, Science Park 904, 1098 XH, Amsterdam, The Netherlands.
Montserrat Armas Padilla: Instituto de Astrofísica de Canarias, 38205, San Cristobal de La Laguna, Spain.
Montserrat Armas Padilla: Departamento de Astrofísica, Universidad de La Laguna, E-38206 La Laguna, Tenerife, Spain.

Revista Mexicana de Astronomía y Astrofísica, **60**, 413–413 (2024)

https://doi.org/10.22201/ia.01851101p.2024.60.02.19

ERRATUM: A PECULIAR GALAXY NEAR M104 (RMxAA, 2023, 59, 323)

E. Quiroga

Universidad del Atlantico Medio, Facultad de Comunicacion, Canary Islands, Spain.

Received May 24 2024; accepted May 24 2024

The author, in a previous article, provided details characterizing an object situated at 12:40:07.829 -11:36:47.38 (in J2000) in the halo of M104 as an SBc-type galaxy with a possible active nucleus (Quiroga, 2023). This object was merely listed as IrS in available catalogs, suggesting the designation 'Iris Galaxy'. However, the author mistakenly associated the X-ray emission with this object. The linked emission originates from 12:40:06.24 -11:36:47.7, which is less than 1 arcsecond in Right Ascension and 0.4 arcseconds in Declination from the so-called Galaxia Iris, which, incidentally, was correctly characterized in the coordinates determined by the author (12:40:07.829 -11:36:47.38 in J2000) in catalogs of the Virtual Observatory, such as NED. They are separated in RA by 7.829 - 6.24 = 1.59 seconds or 1.59 x 14.7 = 23.4 arcsec. The position of M104 GCC RZ2551 is 12 40 06.237 -11 36 47.96, coinciding with the X-ray source position within 0.3 arc seconds. Therefore, any assumptions regarding the Lx made in the paper should be disregarded.

Revista Mexicana de Astronomía y Astrofísica, **60**, 415–415 (2024)

https://doi.org/10.22201/ia.01851101p.2024.60.02.20

ERRATUM: COMPUTING POLYTROPIC AND ISOTHERMAL MODELS USING MONTE CARLO METHOD (RMxAA, 2024, 60, 3)

Mohamed I. Nouh[1], Essam A. Elkholy[2,1], and Samah. H. El-Essawy[1]

Received May 28 2024; accepted May 28 2024

The authors extend their appreciation to the Deanship of Scientific Research at Northern Border University, Arar, KSA for funding this research work through the project number (NBU-FFR-2023-0089).

[1]Astronomy Department, National Research Institute of Astronomy and Geophysics(NRIAG), Cairo, Egypt.
[2]Physics Department, College of Science, Northern Border University, Arar, Saudi Arabia.

Revista Mexicana de Astronomía y Astrofísica, **60**, 417–418 (2024)

https://doi.org/10.22201/ia.01851101p.2024.60.02.21

ERRATUM: PHOTOMETRIC ANALYSIS OF TWO K SPECTRAL TYPE CONTACT BINARY SYSTEMS (RMxAA, 2022, 58, 237)

C. Barani[1], M. Martignoni[1], F. Acerbi[1], R. Michel[2], H. Aceves[2], and V. Popov[3]

Received May 29 2024; accepted May 29 2024

We report here some errors in Tables 2 and 3 of our paper "PHOTOMETRIC ANALYSIS OF TWO K SPECTRAL TYPE CONTACT BINARY SYSTEMS", published in RMxAA, Vol. 58, p. 237 (2022). Table 2 refers to the system J135349.

These unfortunate errors have been corrected and the new Table 2 is shown below:

TABLE 2

LIGHT CURVES SOLUTION

	J135349	Error	J150957	Error
i (°)	79.403	0.380	65.226	0.062
T_1 (K)	4760	fixed	4220	fixed
T_2 (K)	4724	15	4032	9
$\Omega_1 = \Omega_2$	2.4320	0.0095	3.5144	0.0023
q	0.3023	0.0047	0.9048	0.0011
f	0.209	0.006	0.158	0.008
L_{1B}	0.7008	0.0045	0.5478	0.0039
L_{2B}	0.2284	0.0021	0.3254	0.0036
L_{1V}	0.7180	0.0041	0.5306	0.0033
L_{2V}	0.2354	0.0019	0.3478	0.0031
L_{1R}	0.7095	0.0038	0.5388	0.0027
L_{2R}	0.2349	0.0012	0.3660	0.0026
L_{1I}	0.7218	0.0036	-	-
L_{2I}	0.2404	0.0012	-	-
Primary				
r (pole)	0.4641	0.0022	0.3748	0.0003
r (side)	0.5012	0.0031	0.3961	0.0004
r (back)	0.5291	0.0042	0.4320	0.0006
Secondary				
r (pole)	0.2699	0.0041	0.3582	0.0003
r (side)	0.2823	0.0050	0.3777	0.0004
r (back)	0.3223	0.0099	0.4147	0.0006
$\Sigma(Res)^2$	0.0024233		0.0014944	

Another error was found in Table 3 for system J150957, for which $R_2(\mathrm{R}_\odot)$ and $L_2(\mathrm{L}_\odot)$ had to be corrected. The new Table 3 is shown below.

We apologise to the readers and are grateful to Dr. D. H. Bradstreet for pointing out the inconsistencies.

[1]Stazione Astronomica Betelguese, Magnago, Italy.
[2]Instituto de Astronomía, UNAM, Ensenada, Baja California, México.
[3]Department of Physics and Astronomy, Shumen University, Bulgaria.

TABLE 3

ESTIMATED ABSOLUTE ELEMENTS

Target	$L_1(\mathrm{L}_\odot)$	$L_2(\mathrm{L}_\odot)$	$R_1(\mathrm{R}_\odot)$	$R_2(\mathrm{R}_\odot)$
J150957	0.170 ± 0.003	0.129 ± 0.007	0.771 ± 0.007	0.737 ± 0.025
J135349	0.275 ± 0.005	0.090 ± 0.008	0.770 ± 0.007	0.448 ± 0.023
	$a(\mathrm{R}_\odot)$	$M_1(\mathrm{M}_\odot)$	$M_2(\mathrm{M}_\odot)$	ρ_1 (g cm^{-3})
J150957	1.922 ± 0.020	0.953 ± 0.030	0.862 ± 0.028	1.27
J135349	1.546 ± 0.020	0.624 ± 0.027	0.189 ± 0.011	1.92
	ρ_2 (g cm^{-3})	Mag Max V	M_V	M_{bol}
J150957	3.03	14.52	7.04	6.13
J130349	2.90	14.77	6.32	5.85
	J	$\log J$	$\log J_{lim}$	J_{lim}
J150957	5.11^{51}	51.71	51.78	6.06^{51}
J130349	9.71^{50}	50.99	51.17	1.48^{51}

AUTHOR INDEX

La *Revista Mexicana de Astronomía y Astrofísica*, fundada en 1974, publica trabajos originales de investigación en todas las ramas de la astronomía, astrofisica y temas vinculados a éstas. Se editan dos números por año y su distribución es gratuita a todas las instituciones relacionadas con los campos cubiertos por esta revista.

La política editorial de la *RMxAA* consiste en enviar a arbitrar los artículos recibidos a especialistas en el campo. Los interesados en publicar en nuestra revista deberán enviar por correo electrónico, a la dirección rmaa@astro.unam.mx, la versión completa de su artículo en formato PostScript o PDF y el archivo LaTeX. Estos archivos deberán ir acompañados de una carta de presentación. Todos los trabajos deben ser preparados en inglés usando la versión más reciente del macro en LaTeX de la *RMxAA* "rmaa.cls" (disponible en https://www.irya.unam.mx/rmaa/). Se requiere un "Abstract" no mayor que 12 líneas, y un "Resumen" en español (este último podrá ser provisto por los editores de ser necesario); también se incluirán de 1 a 6 palabras clave ("Keywords") de la lista de las revistas astronómicas internacionales. Se requiere que cada tabla incluida en el texto esté numerada y con título; las figuras deberán estar en formato PostScript (.ps) o PostScript encapsulado (.eps), estar numeradas y con leyenda explicativa. Se requiere que cada tabla y figura estén mencionadas en el texto. El estilo de las referencias sigue las normas astronómicas internacionales recientes. Para mayor información sobre el estilo de la *RMxAA* se puede consultar el archivo de ejemplo que viene incluido en los macros. La publicación es gratuita para los autores.

En 1995 se inició la Serie de Conferencias de la *Revista Mexicana de Astronomía y Astrofísica*, dedicada a la publicación de las memorias de reuniones astrónomicas efectuadas en México y en otros países del continente. Hasta 1994 las memorias de reuniones astronómicas de la región se publicaron como volúmenes especiales de la *RMxAA*.

Las condiciones de publicación de cada volumen de las memorias de conferencias serán el resultado de un convenio establecido entre la *RMxAC* y los organizadores de cada evento. Los detalles de la publicación, que incluyen fechas y extensión de los textos, serán anunciados por los editores de cada conferencia. Las contribuciones extensas estarán en inglés con un resumen en español (o portugués en caso de las Reuniones regionales). Los resúmenes de las reuniones que no son temáticas tendrán una extensión máxima de 300 palabras incluyendo título, autores y afiliación; serán exclusivamente en inglés. Los macros LaTeX para las memorias se encuentran en http://www.astroscu.unam.mx/~rmaa. Todas las contribuciones y resúmenes deberán estar en estos formatos.

Se concede permiso a los autores de artículos y libros científi-cos para citar trabajos publicados en la *RMxAA* y en la *RMxAC* siempre y cuando se dé la referencia completa. También se permite la reproducción de figuras y tablas bajo las mismas condiciones.

La *RMxAA* aparece indexada en Current Contents, Science Citation Index, Astronomy and Astrophysics Abstracts, Physics Briefs, Publicaciones Científicas en América Latina, Astronomy and Astrophysics Monthly Index, PERIODICA, RedALyC, Latindex y SciELO.

The *Revista Mexicana de Astronomía y Astrofísica*, founded in 1974, publishes original research papers in all branches of astronomy, astrophysics and closely related fields. Two numbers per year are issued and are distributed free of charge to all institutions engaged in the fields covered by the *RMxAA*.

All papers received by the *RMxAA* are sent to a specialist in the field for refereeing. Authors interested in publishing in the *RMxAA* should send their papers to the e-mail address rmaa@astro.unam.mx, in PostScript or PDF format, along with the LaTeX file. A submission letter should also be sent. Papers should be prepared in English, using the most recent version of the *RMxAA* LaTeX document class "rmaa.cls" (available from https://www.irya.unam.mx/rmaa/). An "Abstract" of at most 12 lines is required, as well as a "Resumen" in Spanish. The latter can be provided by the Editors, if necessary. A total of six or fewer "Keywords", taken from the lists of international astronomical journals should be included. Tables should be numbered and include a title. Figures should be submitted in PostScript (.ps) or Encapsulated PostScript (.eps) format, should be numbered, and should include a caption. Both tables and figures should be mentioned in the text. The style of the references follows recent international astronomical usage. For more information about the style norms of *RMxAA* please consult the example included in the LaTeX package. Publication in *RMxAA* is free of charge to authors.

The Conference Series of *Revista Mexicana de Astronomía y Astrofísica* was founded in 1995 to publish the proceedings of astronomical meetings held in Mexico and other countries throughout the continent. Until 1994 such proceedings had been published as special issues of *Revista Mexicana de Astronomía y Astrofísica*.

Conditions of publication of proceedings of each conference will be the result of a mutual agreement between the *RMxAC* and the organizing committee. Details of publication, including length of papers, will be announced by the editors of each event. The extensive contributions should be in English, and should include an abstract in Spanish (or Portuguese for regional meetings). The abstracts of non-thematic meetings should not exceed 300 words including title, authors, and affiliation; they should be exclusively in English. The LaTeX templates specially prepared for proceedings can be obtained at http://www.astroscu.unam.mx/~rmaa; all papers should be submitted in this format.

Authors of scientific papers and books may quote articles published both in *RMxAA* and *RMxAC* provided that a complete reference to the source is given. Reproduction of figures and tables is also permitted on the same basis.

The *RMxAA* is indexed in Current Contents, Science Citation Index, Astronomy and Astrophysics Abstracts, Physics Briefs, Publicaciones Científicas en América Latina, Astronomy and Astrophysics Monthly Index, PERIODICA, RedALyC, Latindex, and SciELO.